SF2A 2015
F. Martins, S. Boissier, V. Buat, L. Cambrésy and P. Petit (eds)

Proceedings of the annual meeting of the French Society of Astronomy & Astrophysics

Toulouse, June 2-5, 2015

Credits: Sébastien Chastanet UPS/OMP. Benh Lieu Song CC BY-SA 3.0 (http://creativecommons.org/licences/by-sa/3.0/)

© Société Francaise d'Astronomie et d'Astrophysique (SF2A) 2015

Contents

© Société Francaise d'Astronomie et d'Astrophysique (SF2A) 2015

Foreword

The annual meeting of the French Society of Astronomy and Astrophysics (*Société Française d'Astronomie et d'Astrophysique* - SF2A), nicknamed *Journées* or *Semaine de l'Astrophysique*, has become a major event in the landscape of French Astronomy. The XXXV$^{\text{th}}$ session, hosted by the *Institut de Recherche en Astrophysique et Planétologie* from June 2 to 5, in Toulouse, did not depart from the tradition.

These *Journées* were very well attended with about 275 professional astronomers and astrophysicists, who participated to plenary sessions organized by the SF2A and to 13 workshops organized by the scientific committees of the *Programmes Nationaux* (PN) and *Actions Spécifiques* (AS) of INSU-CNRS. A 14$^{\text{th}}$ workshop, organized by the SF2A, was dedicated to the integration of young researchers into the economic world.

The talks were exciting and well received. The discussions were very lively and often continued well into the coffee breaks. During the plenary sessions, scientific reviews focused on outstanding scientific results obtained recently by our community. Our special guest, the *Société Canadienne d'Astronomie* (CASCA) represented by Stéphane Courteau, reminded us amusedly the tumultuous birth of the long-standing French-Canadian collaboration. Other general talks led to topical discussions on the organization and the future of French astronomical research in the fast moving national and international environment. In particular, Denis Mourard (INSU) provided the community with a thorough overview of the objectives and available ground-based facilities, just a few months after the workshop on the INSU Mid-term Plan in Giens. Christian Sirmain presented a review of the current and future activities of the Centre National d'Etudes Spatiales (CNES). Michel Marcelin, Benoit Mosser and Christophe Sauty gave an account of the CoNRS section 17, CNAP and CNU section 34 activities.

A large number of SF2A members attended the General Assembly where the annual activity and financial reports of our Society were presented by the new president and treasurer of the SF2A Council, H. Wozniak and A. Palacios. Most important, Françoise Combes was nominated *Membre d'Honneur* of our Society.

Several new features were introduced in 2015. The use of social networks, especially Twitter (#sf2a2015) and Facebook, has been overwhelmingly increased during the meeting, thanks to our community manager (or activist ?) and SF2A board member, P. Petit. Two workshops were organized by the community in reply to a call of opportunity (S09 and S11 workshops). The success of this open call encourages us to continue this action next year. Lunch–meetings were officially scheduled. One was dedicated to the preparation of the next IAU General Assembly in Hawaii and the second focused on the competitions for permanent positions in France.

A key moment of these *Journées* is the awards ceremony (and buffet in the splendid *Salle des Colonnes* of the *Hôtel Dieu*). The SF2A Young Researcher prize was given to Johan Richard by Roland Bacon (both from CRAL). Jérôme Pety (IRAM) and Javier R. Goicoechea (ICMM-CSIC) were awarded the 3$^{\text{rd}}$ SEA-SF2A prize, given by the SF2A president, H. Wozniak. Quentin Kral (LESIA, Observatoire de Paris) was presented with the Thesis prize by M. Deleuil (SF2A board). We warmly thank the sponsors of these prizes, EdP Sciences and the Exelis company for their continuing interest in our science and support to our Society. One traditional sponsor of the Young Researcher prize was sadly missing this year. We hope this situation is only temporary.

Along the *Journées* a number of social, outreach, and cultural events were organized. The SF2A Prize *Découvrir l'Univers* sponsored by EdP Sciences aimed at promoting astronomy among children and young students. Three classrooms were awarded the prize during a special ceremony held in the Cité de l'Espace which offered a party and a planetarium session to the winners. On thursday, Thierry Contini (IRAP) gave a public conference in a packed auditorium of 200 people, on the last results obtained by MUSE on the VLT.

The venue of this conference was made possible through a number of sponsoring organizations and companies: the INSU-CNRS, the CNES, the Service d'Astrophysique du CEA/DSM/IRFU. PN and AS of INSU-CNRS have supported the organization of the workshops. We are extremely grateful to the Observatoire Midi-Pyrénées and the University of Toulouse Paul Sabatier for assisting and hosting the Journées.

The success of the meeting hinged on the efforts of many people. The Local Organizing Committee was

© Société Francaise d'Astronomie et d'Astrophysique (SF2A) 2015

led by Natalie Webb and Pascal Petit and consisted of the further members : Marie-Ange Albouy, Jérôme Ballot, Clément Baruteau, Olivier Berné, Jean-François Botte, Sylvie Etcheverry, Karine Gadré, Dolorès Granat, Laurène Jouve, Rachel Lacôme, Brahim Lamine. Their infallible enthusiasm for preparing this event was undoubtedly a great part of the success. Thanks also to the SF2A board, acting as Scientific Organizing Committee, for its active contribution, and to the editors of these proceedings.

In conclusion the success of these XXXV$^{\rm th}$ *Journées*, which brought together colleagues from all branches of astrophysics, was overwhelming, so that we feel encouraged to think of the organization of the next conference, in Lyons, in June 2016.

Hervé Wozniak, President of the SF2A

List of participants

ABERGEL Alain
AKRAMOV Tohir
ALEXANDROVA Olga
ALVES Marta
AMARD Louis
ATEK Hakim
ATTEIA Jean-luc
AUCLAIR-DESROTOUR Pierre
AUSSEL Hervé
BABUSIAUX Carine
BAILLIE Kévin
BAJAT Armelle
BALLET Jean
BALLOT Jérôme
BARUTEAU Clément
BATZILIS Nikolaos
BAZIN Cyril
BELMONT Renaud
BERNE Olivier
BETH Arnaud
BETRANHANDY Aurore
BIVER Nicolas
BLONDIN Stéphane
BOËR Michel
BöHM Torsten
BOISSIER Samuel
BONNEAU Daniel
BOONE Frédéric
BORGET Fabien
BOSNJAK Zeljka
BOUCHÉ Nicolas
BOUCHET Patrice
BOUCHET Laurent
BOUQUET Alexis
BOURGOIN Adrien
BOURKE Tyler
BOVALO Christophe
BRAINE Jonathan
BREGEON Johan
BRUGGER Bastien
BUAT Véronique
CABANAC Rémi
CAMBRÉSY Laurent
CAVALIÉ Thibault
CELESTIN Sébastien

© Société Francaise d'Astronomie et d'Astrophysique (SF2A) 2015

CERNICHARO Jose
CHADID Merieme
CHAMPION Jason
CHAPILLON Edwige
CHARPINET Stéphane
CHAZALNOËL Pascale
CHEVALLARD Jacopo
CHIAVASSA Thierry
CHOPLIN Arthur
CLAVEL Maïca
COHEN-TANUGI Johann
COMBES Francoise
CONDON Benjamin
CONTINI Thierry
CORBEL Stéphane
CORIAT Mickael
COURCOL Bastien
COURTEAU Stéphane
COUTENS Audrey
COX Nick
CRIDA Aurélien
CRIFO Françoise
CUILLANDRE Jean-charles
DAIGNE Frédéric
DANDOURAS Iannis
DANGER Grégoire
DE BARROS Stéphane
DEAL Morgan
DEFER Eric
DEHEUVELS Sébastien
DELAHAYE Franck
DELEUIL Magali
DELFOSSE Xavier
DEMYK Karine
DENNEFELD Michel
DEPARIS Nicolas
DESPOIS Didier
DETOEUF Adrien
DEVOST Daniel
DI FOLCO Emmanuel
DIBI Salome
DINTRANS Boris
DOLE Hervé
DORVAL Julien
DOUSPIS Marian
DUBERNET Marie Lise
DUBUS Guillaume
DURRET Florence
EGRET Daniel
EL MELLAH Ileyk
ELBAZ David
ELLINGER Yves
ENGRAND Cécile
ERARD Stéphane
ERIC Quirico

FARAH Wael
FARGES Thomas
FECHTENBAUM Sarah
FERNANDEZ Jose
FITOUSSI Thomas
FOENARD Gabriel
FOGLIZZO Thierry
FOUCHET Thierry
FOURNIER Sabrina
FREUNDLICH Jonathan
GALLANT Yves
GALLET Florian
GARGAUD Muriel
GATTANO César
GAURAT Mathieu
GIARD Martin
GIEBELS Berrie
GILLET Nicolas
GIRARD Julien
GODEFROY Michel
GODET Olivier
GOLDWURM Andrea
GONZALEZ Matthias
GRATIER Pierre
GRONDIN Marie-hélène
GROSSO Nicolas
GROULD Marion
GROUSSIN Olivier
GUAITELLA Olivier
GUENEL Mathieu
GUETH Frédéric
GUILET Jérôme
GUILLARD Pierre
GUSDORF Antoine
GUTERMAN Pascal
HABART Emilie
HALBWACHS Jean-louis
HAYWOOD Misha
HÉBRARD Elodie
HEBRARD Guillaume
HEES Aurélien
HERIQUE Alain
HERPIN Fabrice
HERVÉ Anthony
HESS Sébastien
HEUSSAFF Vincent
HILL Vanessa
HOANG Margaux
HUI-BON-HOA Alain
HYPOLITE Delphine
IFFRIG Olivier
IHADDADENE Kevin
ITAM-PASQUET Johanna
JASNIEWICZ Gérard
JAUZAC Mathilde

JIANG Ming
JOBLIN Christine
JOLLY Antoine
JOSSELIN Eric
JOUVE Laurène
KERVELLA Pierre
KILICOGLU Tolgahan
KNöDLSEDER Jürgen
KOECHLIN Laurent
LAFFON Hélène
LAGAGE Pierre-olivier
LAIBE Guillaume
LALANDE Philippe
LAMBERTS Astrid
LAMINE Brahim
LAPORTE Nicolas
LAYCHAK Mary Beth
LE FÈVRE Olivier
LE PONCIN-LAFITTE Christophe
LE TIEC Alexandre
LE TIRAN Loic
LEBRE Agnès
LEBRETON Yveline
LEBRETON Jérémy
LEBRETON Jean-pierre
LEFRANC Valentin
LEININGER Thierry
LEMOINE-GOUMARD Marianne
LIGNIERES François
LOH Alan
LOISON Jean-christophe
LOKHANDWALA Saumya
LOUARN Philippe
LOUVET Fabien
MAKSIMOVIC Milan
MALZAC Julien
MARCELIN Michel
MARET Sébastien
MARIN Frédéric
MARTIN Pierrick
MARTINS Fabrice
MASSERON Thomas
MATHIS Stéphane
MAURY Anaëlle
MEHEUT Héloïse
MEIERHENRICH Uwe
METRIS Gilles
MIGNARD Francois
MIGNON-RISSE Raphaël
MIROUH Giovanni
MONCEAU-BAROUX Rémi
MONTILLAUD Julien
MONTMERLE Thierry
MOREAU Nicolas
MORIN Julien

MOSSER Benoît
MOSSOUX Enmanuelle
MOTTEZ Fabrice
MOUSIS Olivier
MOUTOU Claire
NEINER Coralie
NENON Quentin
NESME Nicolas
OLAGNIER Fleur
ORTHOUS-DAUNAY François-régis
PALACIOS Ana
PALETOU Frédéric
PARADIS Deborah
PAUZAT Françoise
PEILLE Philippe
PELLO Roser
PERICAUD Jessica
PETIT Pascal
PETY Jérôme
PILLERI Paolo
PINÇON Jean-louis
PINTY Jean-pierre
PLOTNIKOV Illya
POMMIER Mamta
PORQUET Delphine
PRAT Vincent
REBOUSSIN Laura
REME Henri
REPOSEUR Thierry
REYLÉ Céline
RICHARD Johan
RICHARD Monier
RIGUCCINI Laurie
RISTORCELLI Isabelle
RODRIGUES Myriam
RODRIGUEZ Jérome
RODRIGUEZ CASTILLO Sarah
ROLAND Bacon
ROLF Walder
RONNET Thomas
ROUDIER Thierry
ROUX Wilhem
ROYER Frédéric
SAKR Ziad
SALMON Sébastien
SALOME Quentin
SARKIS Paula
SARRIA David
SCHIMD Carlo
SERAN Elena
SIELLEZ Karelle
SIMONS Doug
SOUBIRAN Caroline
SOUCAIL Geneviève
STEHLE Chantal

SZOPA Cyril
TAGGER Michel
TASSE Cyril
TAX Tomas
TESSORE Benjamin
TESTON Anthony
THOMAS Guillaume
THOMAS Ivan
TISSERAND Patrick
TOM Piguet
TORCHINSKY Stephen
TREBITSCH Maxime
TROMPIER Francois
TROVA Audrey
TUCKEY Philip
TURON Catherine
VARNIERE Peggy
VASTEL Charlotte
VASYLIEVA Iaroslavna
VAUGLIN Isabelle
VAUPRÉ Solenn
VERGANI Susanna
VINATIER Sandrine
VINCENT Frederic
VIOU Cédric
VUILLAUME Thomas
WEBB Natalie
WOZNIAK Hervé
YASSINE Manal
ZONG Weikai

Session SF2A

Session Plénière

SF2A 2015
F. Martins, S. Boissier, V. Buat, L. Cambrésy and P. Petit (eds)

ESTIMATING STELLAR FUNDAMENTAL PARAMETERS USING PCA: APPLICATION TO EARLY TYPE STARS OF GES DATA

Farah W.[1], Gebran M.[1,], Paletou F.[2] and Blomme R.[3]

Abstract. This work addresses a procedure to estimate fundamental stellar parameters such as $T_{\rm eff}$, log$g$, [Fe/H], and $v \sin i$ using a dimensionality reduction technique called principal component analysis (PCA), applied to a large database of synthetic spectra. This technique shows promising results for inverting stellar parameters of observed targets from Gaia Eso Survey.

Keywords: stars: fundamental parameters, techniques: spectroscopic

1 Introduction

With the introduction of new telescopes and instruments to the scientific astronomical community, and the rapid increase of sky surveys such as SDSS and RAVE, tremendous amount of spectral data is being acquired on a daily basis and with an increasing rate. Therefore, these challenges urged the need of efficient and automated techniques to handle and analyze this huge amount of information. Such automated procedures for classification of stars have been discussed recently using different codes and mathematical approaches. As an example, one can mention the methods used to analyze a spectral library described in Jofré et al. (2014).
In this work, we present a dimensionality reduction technique called PCA, applied to a huge database of synthetic spectra. PCA searches in a high dimensional space for possible correlations, and finds an optimal basis for representing the data in a compact way. Due to the high number of spectra in each synthetic database ($\sim$200 000), and the high number of data points in each spectral domain ($\sim$2 500. Same as observation, see section 2), such technique is crucial for inverting stellar parameters of observed targets from Gaia ESO survey. Using PCA, data can be represented in a fewer number of data points, allowing a fast "nearest neighbor(s)" search between the observed data set and the synthetic spectra. This study is an extension of Paletou et al. (2015) where the H-R domain of application has been extrapolated to stars of types earlier than F, and the training database used in this work is a set of synthetic spectra.

2 Observation

The procedure is applied to more than 800 stars, members of the open clusters NGC3293, NGC6705, and Trumpler14. The observations are part of the GAIA ESO public survey and consist of 2 spectral ranges, one samples the H_δ line region [4030-4200]Å and the second samples the [4400-4550]Å (HR5) region. These spectra were taken using GIRAFFE/FLAMES spectrograph at a resolution R $\approx$ 25 000, and reduced by the GES.

3 Spectral range selection

Balmer lines, due to the broadening caused by the Stark's effect, are excellent indicators of effective temperature and surface gravity (Gray 2005). The reason behind studying H_δ in particular is because this line is formed in deep enough atmospheric layers where LTE can still be considered as a reasonable assumption. Moreover, the HR5 region was chosen since metallic lines (namely Fe II, Mg II, Ti II, ...) are potentially good indicators of rotational velocity and metallicity.

[1] Department of Physics & Astronomy, Notre Dame University - Louaize, Lebanon
[2] Université Paul Sabatier, OMP & IRAP, CNRS, F–31400 Toulouse
[3] Royal Observatory of Belgium, Ringlaan 3, B-1180 Brussels, Belgium

© Société Francaise d'Astronomie et d'Astrophysique (SF2A) 2015

4 Synthetic Spetra

LTE model atmospheres were calculated using ATLAS9 code (Kurucz 1992) and were used as input to the spectrum synthesis code SYNSPEC48 (Hubeny & Lanz 1992) in order to compute a large grid of synthetic line profiles, over the same spectral regions as the observations. Spectra were calculated for T_{eff} between 5 000 and 15 000 K, gravities between 2.0 and 5.0 cgs, rotational velocities between 0 and 200 km s^{-1}, and metalicities between -0.6 and 0.4 dex (only for the HR5 region, whereas a solar [Fe/H] was assumed for the H_δ region), all at a microturbulence of 2 km s^{-1} and at a resolution of 25 000.

5 Procedure

The central idea of principal component analysis is to reduce the dimensionality of a data set in which there are a large number of interrelated variables, while retaining as much as possible of the variation present in the data set (Jolliffe 1986). PCA searches for basis vectors that represent most of the variance in a given database. These vectors ($\vec{e}_k$) are in fact the eigenvectors of the variance-covariance matrix (5.1) of the synthetic data set **S**.

$$C = (\mathbf{S} - \bar{\mathbf{S}})^T.(\mathbf{S} - \bar{\mathbf{S}}) \tag{5.1}$$

Where $\bar{\mathbf{S}}$ being the mean spectrum over all the database.
Once the basis is obtained (adopted a set of 12 vectors, i.e $k = 1, .., 12$), the synthetic spectra and each observation (O) are projected unto this basis to obtain the projected coefficients (5.2 & 5.3)

$$p_{j,k} = (\mathbf{S}_j - \bar{\mathbf{S}}).\vec{e}_k \; {}^* \tag{5.2}$$

$$\rho_k = (\mathbf{O} - \bar{\mathbf{S}}).\vec{e}_k \tag{5.3}$$

Then, a standard chi-squared (5.4) is performed in this low dimensional space in order to achieve a fast inversion of stellar parameters of the observed targets. The parameters of the synthetic spectrum having the minimum d will be considered as the observation fundamental parameters.

$$d_j^{(O)} = \Sigma_{k=1}^{12}(\rho_k - p_{j,k})^2 \tag{5.4}$$

The observation spectra were radial velocity corrected, and those with low signal-to-noise ratio were filtered out. Upon starting the inversion process, the technique showed to be very sensitive to normalization of spectra, thus an iterative "re-"normalization procedure was performed according to Gazzano et al. (2010).

6 Results

In general, inversion based on this technique was performed over the selected stars, and the fundamental parameters of the targets were estimated. An example of the nearest neighbor search is given in figures 1 and 2. The parameters derived by PCA, along with the non-official parameters obtained by WG13 of GES are detailed in table 1.

Table 1. Results derived using PCA along with parameters given by WG13 of GES

	Derived				Given			
Star	$T_{\rm eff}$ (K)	$\log g$ (dex)	$v \sin i$ (km s^{-1})	[Fe/H] (dex)	$T_{\rm eff}$ (K)	$\log g$ (dex)	$v \sin i$ (km s^{-1})	[Fe/H] (dex)
10361733-5809031	14 400	3.6	45	-	14 775	3.84	44	-
10430337-5941536	9 200	4.6	70	0.4	8 633	3.5	75	-

With PCA, we will be contributing by determining stellar parameters to the next GES data release.

* $\mathbf{S}_j$ is the j^{th} spectrum (a row vector) in the database (matrix) **S**.

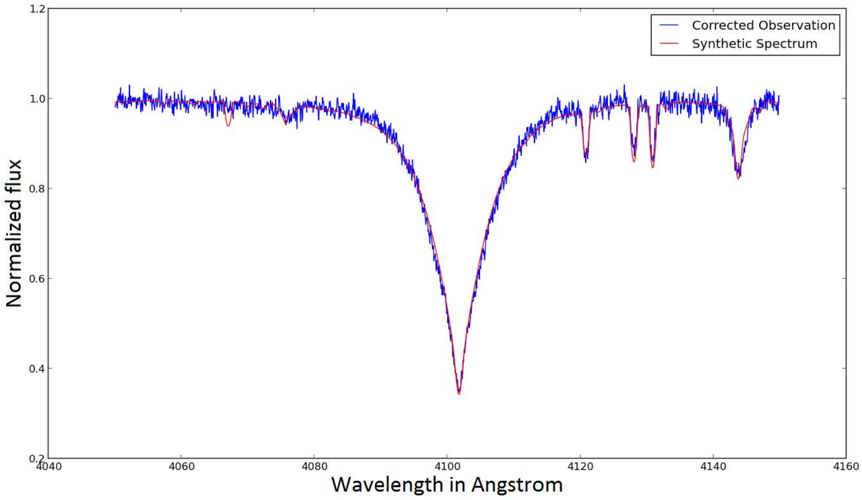

Fig. 1. Example of the fitting of the H_δ line of the star 10361733-5809031 member of NGC3293 cluster, with a synthetic spectrum. Blue being the observed spectrum, while red the fitted synthetic.

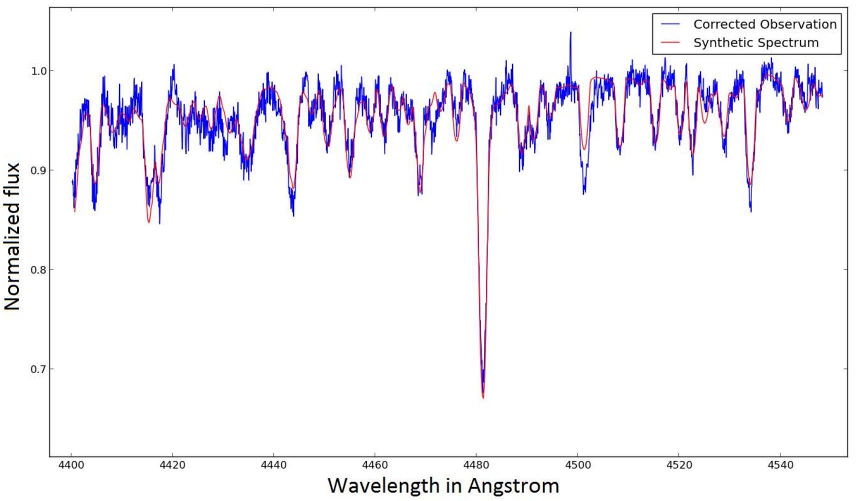

Fig. 2. Example of the fitting of the region containing Fe II, Mg II and Ti II lines of the star 10430337-5941536 member of Trumpler14 cluster, with a synthetic spectrum. Blue being the observed spectrum, while red the fitted synthetic.

7 Conclusions and future work

PCA proved to be a fast and reliable inversion technique, with an ease to implement. An attempt to increase the size of the synthetic database is being performed in order to improve the accuracy in the parameters obtained. Moreover, the merging of two spectral ranges in a one data set is also considered as a future work.

This work is based on observations collected with the FLAMES spectrograph at the VLT/UT2 telescope (Paranal Observatory, ESO, Chile), for the Gaia-ESO Large Public Survey, programme 188.B-3002.

References

Gazzano, J.-C., de Laverny, P., Deleuil, M., et al. 2010, A&A, 523, A91

Gray, D. F. 2005, "The Observation and Analysis of Stellar Photospheres", 3rd Edition, UK: Cambridge University Press, 2005

Hubeny, I., Lanz, T. 1992, A&A, 262, 501

Jofré, P., Heiter, U., Soubiran, C., et al. 2014, A&A, 564, A133

Jolliffe, I. T. 1986, Springer Series in Statistics, Berlin: Springer, 1986,

Kurucz, R.L. 1992, Rev. Mexicana. Astron. Astrofis., 23, 45

Paletou, F., Böhm, T., Watson, V., & Trouilhet, J.-F. 2015, A&A, 573, A67

SF2A 2015
F. Martins, S. Boissier, V. Buat, L. Cambrésy and P. Petit (eds)

MAPPING OPTICALLY VARIABLE QUASARS TOWARDS THE GALACTIC PLANE

J. G. Fernandez-Trincado[1], T. Verdugo[2], C. Reylé[1], A. C Robin[1], J. A. de Diego[3], V. Motta[4], L. Vega[5], J. J. Downes[2, 6], C. Mateu[2,6], A. K. Vivas[7], C. Briceño[7], C. Abad[2], K. Vieira[2], J. Hernández[2], A. Nuñez[8] and E. Gatuzz [9, 10]

Abstract. We present preliminary results of the CIDA Equatorial Variability Survey (CEVS), looking for quasar (hereafter QSO) candidates near the Galactic plane. The CEVS contains photometric data from extended and adjacent regions of the Milky Way disk ($\sim$ 500 sq. deg.). In this work 2.5 square degrees with moderately high temporal sampling in the CEVS were analyzed. The selection of QSO candidates was based on the study of intrinsic optical photometric variability of 14,719 light curves. We studied samples defined by cuts in the variability index ($V_{index} > 66.5$), periodicity index ($Q > 2$), and the distribution of these sources in the plane (A_T, γ), using a slight modification of the first-order of the structure function for the temporal sampling of the survey. Finally, 288 sources were selected as QSO candidates. The results shown in this work are a first attempt to develop a robust method to detect QSO towards the Galactic plane in the era of massive surveys such as VISTA and Gaia.

Keywords: quasar: general - surveys

1 Introduction

In the past few years the intrinsic variability of the QSO (Rengstorf et al. 2004b,a, 2006; Schmidt et al. 2010; Ross et al. 2013; Graham et al. 2014) has been used as an alternative and efficient selection method to distinguish QSO exhibiting variability from the non-variable stellar locus. Additionally, it provides unique information about the physics of the unresolved central source. This technique is free of bias in comparison with the inherent biases present in the traditional methods based in specific cuts in the color-color diagram (Hall et al. 1996; Croom et al. 2001; Richards et al. 2002; Graham et al. 2014).

The intrinsic variability of QSO has been observed in different photometric bands from UV, optical to X-ray. This intrinsic property has been proposed as an efficient method of selection (Rengstorf et al. 2006; MacLeod et al. 2012; Graham et al. 2014), and is commonly quantified using the structure fuction such that the amplitude of variability changes with time (Hughes et al. 1992; Collier & Peterson 2001; Bauer et al. 2009; Welsh et al. 2011). The properties of the variability in QSO have been studied in the literature and they depend on the physical properties of the source, as the presence of radio emission, timescale and others (MacLeod et al. 2012) and the large luminosity of these sources is provided by mass accretion onto super massive black holes in its

[1] Institut Utinam, CNRS UMR 6213, Université de Franche-Comté, OSU THETA Franche-Comté-Bourgogne, Observatoire de Besançon, BP 1615, 25010 Besançon Cedex, France.
[2] Centro de Investigaciones de Astronomía, AP 264, Mérida 5101-A, Venezuela.
[3] Instituto de Astronomía, Universidad Nacional Autónoma de México, Apdo. Postal 70264, México D.F., 04510, Mexico.
[4] Instituto de Física y Astronomía, Universidad de Valparaíso, Avda. Gran Bretaña 1111, Playa Ancha, Valparaíso 2360102, Chile.
[5] Instituto de Astronomía Teórica y Experimental (IATE) - Córdoba, Argentina.
[6] Instituto de Astronomía, UNAM, Ensenada, C.P. 22860, Baja California México.
[7] Cerro Tololo Interamerican Observatory Casilla 603, La Serena, Chile.
[8] Centro de Modelado Científico, Universidad del Zulia, Maracaibo 4001, Venezuela.
[9] Centro de Física, Instituto Venezolano de Investigaciones Científicas (IVIC), Caracas 1040, Venezuela.
[10] Escuela de Física, Facultad de Ciencias, Universidad Central de Venezuela, PO Box 20632, Caracas 1020A, Venezuela.

© Société Francaise d'Astronomie et d'Astrophysique (SF2A) 2015

center (Salpeter 1964; Lynden-Bell 1969; Rees 1984).

Both methods are now used to select QSO candidates, especially in surveys with extended time coverage like the SDSS Strip 82 (MacLeod et al. 2012), MACHO (Pichara et al. 2012), Catalina Real-Time Transient Survey (Drake et al. 2009; Graham et al. 2014) and in the future with Gaia (Mignard 2012). The variability selection is a technique with a high degree of confidence (Graham et al. 2014), and recent studies have shown that variability as method for QSO selection is more accurate and has a higher degree of purity in comparison with the use of color-only cuts (Morganson et al. 2014).

Precise identification of QSOs along the Galactic plane is very valuable for astronomical reference frame purposes. The large extinction present in the area has meant that all QSO-oriented surveys have systematically avoided this region, and the scarcity of confirmed QSO there is evident. Kinematical studies of the Galactic Disk and Bulge, especially when working in small fields of view, would benefit enormously by having a dense and deep "network" on confirmed QSO, to which tie in their observations. For large-scale surveys like Gaia, it is also important to have a large enough number of QSOs identified everywhere on the sky, to improve the overall quality and spatial uniformity of the QSO reference system. Finally, the ICRF always will benefit from adding more new QSO, as the densification of their sources obviously improves the final accuracy of such fundamental reference frame.

The extensive variability survey compiled in the CIDA Equatorial Variability Survey (CEVS) since 2001 has been used so far to study a variety of topics, including RR Lyrae stars, T Tauri stars and young Brown Dwarfs, etc. (e.g. Vivas et al. 2004; Briceño et al. 2005; Downes et al. 2008; Mateu et al. 2012). At high galactic latitudes Rengstorf et al. (2004a,b, 2009) used the QUEST Variability Survey data, predecessor to the CEVS, to conduct a variability survey of QSOs over $\sim$ 190 sq. deg. However, the CEVS has not been applied to extragalactic studies so far, particularly in the search for QSOs.

This paper is organized as follow. In §2 we briefly present the data. The methods are described in §3. The expected contamination is discussed in §4. In §5 we present a preliminar conclusion of this research.

2 Data

The CEVS provides optical multi-epoch information in the V, R and I_c photometric bands. For our work we have combined data from the QUEST* high-galactic latitude survey data, obtained during 1998 to 2001, with the CEVS data collected from 2001 to 2008. The full catalog contains more than 6.5×10^6 sources, observed multiple times from 1998 to 2008. All observations were obtained with the QUEST mosaic camera (16 CCDs) installed at the 1.0/1.5m Jürgen Stock Schmidt telescope located at the National Astronomical Observatory of Venezuela. The survey has been scanned 476 deg^2 of the sky during ten years in a region defined between $60^o \leq \alpha \leq 140^o$ and $-6^o \leq \delta \leq 6^o$ around the Galactic plane. A detailed description of the survey is given in Mateu et al. (2012).

We selected one specific section of the catalog (with a large number of observations in each band, $N > 10$), restricted to the range $85^o \leq \alpha \leq 87.5^o$ and $-1.5^o \leq \delta \leq -0.5^o$, with 14,719 sources covering an area of 2.5 deg^2 near the Galactic plane that also has with observations over 1.96 deg^2 from the SDSS DR9 (Ahn et al. 2012). This region in the CEVS has typically about 30 observations per source.

3 Selection criteria

In subsections 3.1, 3.2 and 3.3 below, we describe three methods (modified in this work), proposed in the literature to explore the intrinsic optical variability, periodicity, and the first-order of the structure function, with the main goal to separate variable QSO and point sources of non-variability sources (more likely associated with the stellar locus).

*Quasar Equatorial Survey Team

3.1 Variability

We adopted a formulation to that of eq. 1 in Rengstorf et al. (2006), in order to characterize the variability over three optical photometric bands, V, R and I_c of the CEVS. For this purpose, we defined the index of variability V_{index} according to the following criteria: (i) A minimum of 10 observations was imposed in each photometric band; (ii) The index $P(\chi^2)$ given by the CEVS, represents the probability of variability for each photometric band, and its value is related to the χ^2 (e.g., Vivas et al. 2004). The V_{index} of a star is redefined in this work as:

$$V_{index} \equiv \sum_{j=1}^{3} \frac{\left(N^j/N_T^j\right) \times \left(1 - P(\chi_j^2)\right) \times 100}{\sum_{j=1}^{3} \left(N^j/N_T^j\right)} = V^{j=1} + V^{j=2} + V^{j=3}, \tag{3.1}$$

where j indexes over filters ($j = 1$ for V, $j = 2$ for R, $j = 3$ for I_c); N^j is the number of observations for the i-th source and N_T^j is the maximum number of observations inside a cone search of 30 arcsec radius centered on the i-th source of the catalog. We have computed V_{index}, for 14,719 sources, and we have found for each photometric band the following percentages of sources for which $V^j \neq 0$: $V^{j=1} = 30.90\%$, $V^{j=2} = 54.77\%$ and $V^{j=3} = 65.35\%$. Figure 1 shows the cumulative probability distribution ($F > V_{index}$) for these 14,719 sources (black line) and 39 spectrally confirmed QSO (red line) from the SDSS DR9. The black vertical dashed line, correspond to the limit $V_{index} = 66.5$ imposed in this work to separate non-variable sources of variable sources, which is the same value proposed by Rengstorf et al. (2006). Finally, we selected 1,931 variable sources with $V_{index} \geq 66.5$, for which the cumulative probability distribution of $F(> 66.5)$ is about 13% and $F(> 66.5) = 5\%$ for the QSO reported in this region of the sky.

3.2 Periodicity

For our pre-selection of 1,931 variable sources in §3.1, we redefined the parameter Q, in order to separate periodic from aperiodic variable sources. We analyzed each light-curve independently, considering a minimum of ten available epochs taken from 1998 to June 2008, for the temporal sampling in the light-curves. The parameter Q, was redefined in a very similar way as eq. 7 in (Rengstorf et al. 2006):

$$Q \equiv \frac{\sum_j \left(N^j/N_T^j\right) \times \left(\frac{\sum_k \left(N^j/N_k^j\right) \times \left(\sigma_T^j/\sigma_k^j\right)^2}{\sum_k \left(N^j/N_k^j\right)}\right) \times \Delta\langle m^j\rangle_{\max}}{\sum_j \left(N^j/N_T^j\right) \times \sigma_T^j}, \tag{3.2}$$

where the index j, N^j and N_T^j are defined as in the previous subsection; the index k correspond to the number of 15-days intervals within the time series of observations of the star; N_k and σ_k correspond to the number of observations in each bin and the standard deviation of the magnitudes by bin in the light curve, respectively; σ_T correspond to the total standard deviation of the magnitudes. Figure 1 shows the Q distribution for our pre-selected 1,931 variable sources. We found 1,481 sources, and 2 spectrally confirmed QSO from SDSS DR9, satisfying the condition of aperiodicity, that is $Q > 2$, based in previous studies (Rengstorf et al. 2006), set to minimize contamination by likely periodic variables.

3.3 First-order of the structure function

So far, we have done a pre-selection of 1,481 sources identified as potential variable and aperiodic QSO in the CEVS. Our final step, consist in identifying the location of QSO candidates in the plane (A_T, γ_T). The first-order of the structure function, which quantify the variability amplitude as a function of time, has been used used for this purpose. We computed an equivalent formulation, rewriting Eq. 3 in Schmidt et al. (2010):

$$M_{i,l}(\Delta t_{i,l}) \equiv \left\langle \sqrt{\frac{\pi}{2}} |\Delta m_{i,l}| - \sqrt{\sigma_i^2 + \sigma_l^2} \right\rangle_{\Delta t}, \tag{3.3}$$

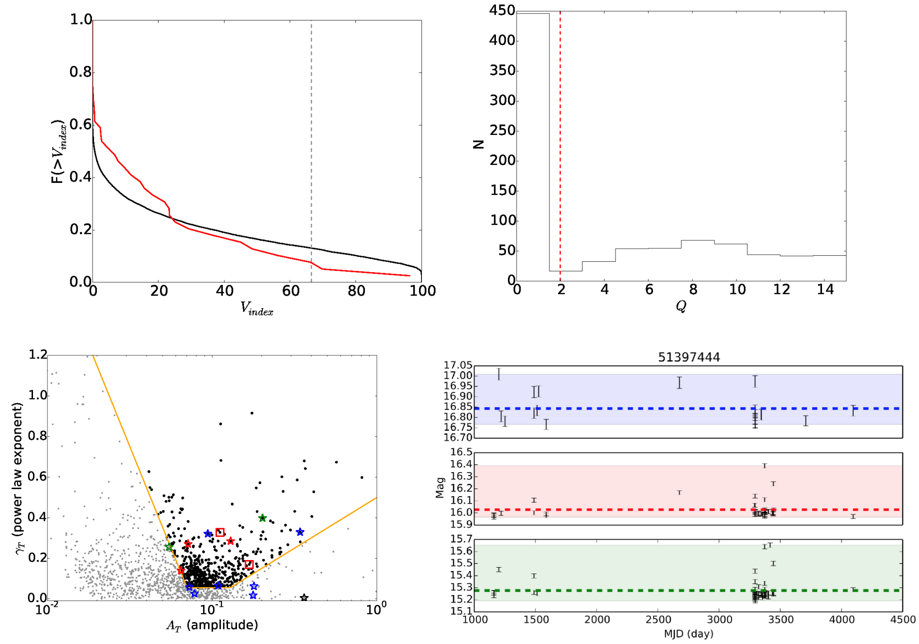

Fig. 1. Top left panel: Cumulative probability distribution ($F > V_{index}$) for 14,719 sources from the CEVS (black line), and QSO spectrally confirmed in the SDSS DR9 (red line) and observed by CEVS. The vertical dashed line corresponds to the limit used in this work ($V_{index} = 66.5$), to rejected non-variable sources ($V_{index} < 66.5$). **Top right panel:** Q_i distributions for 1,931 variable sources. QSOs candidates have $Q > 2$, meaning that they are both variable and aperiodic sources. **Bottom left panel:** QSO candidates parametrized by the structure function in the plane (A_T, γ_T) are shown with black dots and QSO spectrally confirmed are shown in red open squares. All dots correspond to the sample of 1,481 sources analyzed in the third step (see § 3.3). Contaminants in our sample reported in the literature are: binary stars (blue open stars), RR Lyrae (black open star), brown dwarfs (green open stars), variable stars in the CATALINA survey (open red stars). **Bottom left panel:** Example of a QSO candidate light-curve. From top to bottom observations in the photometric bands V, R and I_c respectively, are shown.

where $\Delta m_{i,l}$ is the measured magnitude difference between observation i and l, and σ_i and σ_l are the photometric errors, being $\Delta t_{i,l}$ the time difference between two observations. Thus, the average is taken over all epoch pairs i, l that falls in the bin Δt. In the same way as Schmidt et al. (2010), we parametrized the structure function as:

$$M_{i,l}^{mod}(\Delta t_{i,l} \mid A^j, \gamma^j) \equiv A^j \left(\frac{\Delta t_{i,l}}{1\text{yr}}\right)^{\gamma^j}, \tag{3.4}$$

where the subindex j stands for filter, and can take the values, V, R, I, and:

$$A_T = \frac{\sum_j \left(N^j/N_T^j\right) \times A_j}{\sum_j \left(N^j/N_T^j\right)}, \tag{3.5}$$

and

$$\gamma_T = \frac{\sum_j \left(N^j/N_T^j\right) \times \gamma_j}{\sum_j \left(N^j/N_T^j\right)^j}, \tag{3.6}$$

Figure 1 show the distribution A_T and γ_T for the pre-selected 1,481 sources, and the best fitting values of Eq. (3.4) to Eq. (3.6) to the data. We defined a QSO selection box as Eq. 7 to Eq. 9 in Schmidt et al. (2010), which led us to select a sample of 288 QSO candidates.

The final sample of candidates is shown in the Table 1, containing all the relevant information for each star in it: column 1-10 list ID (CEVS-QSO-XXX; notation adopted in this work), mean V, R and I_c magnitudes, number of times each star was observed in each photometric band and amplitude. The index of variability and aperiodicity are presented in columns 11 and 12 respectively, and column 13 and 14, correspond to the parameters of the structure function (A_T and γ, respectively). Table 1 is published in its entirety in a public repository[†‡]. A sample of the table is shown here for guidance regarding its content.

Table 1. Photometric parameters of QSO candidates from the CIDA Equatorial Variability Survey (CEVS).

ID	$\langle V \rangle$ [mag]	$\langle R \rangle$ [mag]	$\langle I \rangle$ [mag]	Nv	Nr	Ni	AmpV [mag]	AmpR [mag]	AmpI [mag]	Vindex	Q	A_T	γ_T
CEVS-QSO-001	19.323	18.045	17.855	11	41	79	1.009	1.019	0.951	100.00	58.671	0.109	0.285
CEVS-QSO-002	19.449	19.010	18.299	18	43	70	0.566	0.412	0.696	99.99	59.737	0.068	0.253
CEVS-QSO-003	19.371	18.791	18.037	16	47	91	0.875	0.670	0.897	100.00	115.831	0.088	0.232
CEVS-QSO-004	19.438	18.699	17.644	9	45	87	1.072	0.584	0.591	100.00	124.065	0.066	0.126
CEVS-QSO-005	18.747	18.450	17.170	17	49	99	0.947	0.493	0.319	73.36	1243.269	0.049	0.425
CEVS-QSO-006	19.182	17.886	16.372	26	52	90	0.455	0.454	0.357	100.00	986.204	0.341	0.329
CEVS-QSO-007	19.505	18.916	18.172	3	32	36	0.431	0.508	0.517	99.72	28.757	0.115	0.071
CEVS-QSO-008	18.999	18.545	17.540	30	50	78	0.703	1.012	0.607	91.33	54.579	0.062	0.346
CEVS-QSO-009	19.632	18.743	17.851	14	43	69	0.563	0.569	0.561	99.99	6.741	0.132	0.467

4 Expected Milky Way contamination

We have compared the synthetic colour-magnitude diagram computed with the Besançon galaxy model (hereafter BGM) (Robin et al. 2003, 2014), for the same line-of-sight and solid angle studied in this paper. The simulation was generated taking the selection function of the data into account. Since we are near the Galactic plane, we expect a high degree of contamination (foreground stars), not present in previous surveys of QSO using variability. The absence of a complete catalog of confirmed QSOs in this part of the Galaxy makes it difficult to estimate such contamination, a key point to validate our methodology and its application in future surveys like Gaia or VISTA. At this moment we are in the process of determining this contamination, since the CEVS is a not homogeneous survey. However we can do a simple and rough estimate of the more likely contaminants in our sample, namely K and M-type stars, using the BGM and comparing the synthetic colors with those observed in our sample candidates (see Figure 2).

5 Conclusion

In this work, we have used the multi-epoch data in the large scale CEVS to search for low-galactic latitude QSOs by their intrinsic optical variability, using an alternative formulation similar to the proposed in the literature, in order to detect QSO candidates from inhomogeneous temporal sampling.

We have selected 288 QSO candidates according to their variability, aperiodicity and parameters of the structure function, over an area of 2.5 deg^2. Extrapolating these results to the full CEVS with an total area of $\sim$ 500 deg^2, we estimate that is possible to detect 52,000 new QSO candidates in this survey. However, we have shown that the methods presented in this work are sensitive to variations in the temporal sampling of the light curves. This explains the fact our method rejects 95% of the QSO spectroscopically confirmed in the region in common with the SDSS DR9 survey. Follow-up spectroscopic observations for our QSO candidates are currently conducted at the REOSC Spectrograph installed on the 2.15-m telescope at CASLEO, Argentina.

[†] `http://fernandez-trincado.github.io/Fernandez-Trincado/simulations.html`

[‡] jfernandez@obs-besancon.fr

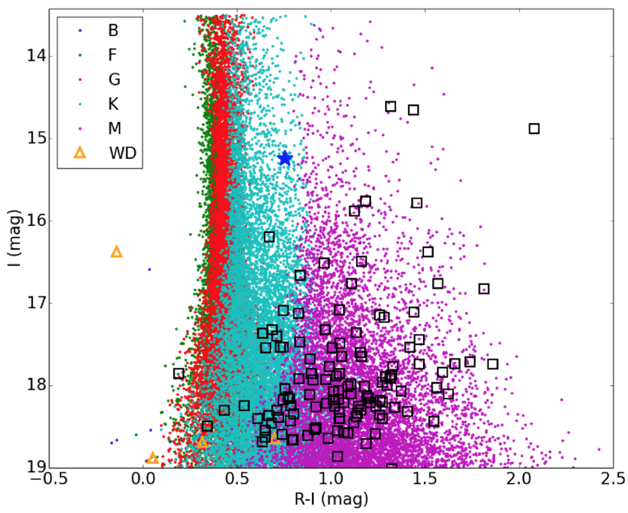

Fig. 2. Color magnitude diagram for QSO candidates (black symbols) with I and R information. The blue star refers to object ID 51397444 showed in Figure 1. The simulation of the Besançon galaxy model is presented with dots of different colors for each stellar population, which are labelled by spectral type (B, F, G, K, M and white dwarfs WD).

In the near future, large spectroscopic surveys as Gaia may help to confirm QSO sources, selected from variability surveys towards the Galactic plane, allowing us to quantify the selection efficiency.

J.G. F.-T. is currently supported by Centre National d'Etudes Spatiales (CNES) through Ph.D grant 0101973 and the Région de Franche-Comté, and by the French Programme National de Cosmologie et Galaxies (PNCG). This research was supported by the Munich Institute for Astro- and Particle Physics (MIAPP) of the DFG cluster of excellence "Origin and Structure of the Universe". V.M. acknowledges the support from FONDECYT 1120741, and Centro de Astrofisica de Valparaiso.

References

Ahn, C. P., Alexandroff, R., Allende Prieto, C., et al. 2012, ApJS, 203, 21
Bauer, A., Baltay, C., Coppi, P., et al. 2009, ApJ, 696, 1241
Briceño, C., Calvet, N., Hernández, J., et al. 2005, AJ, 129, 907
Collier, S. & Peterson, B. M. 2001, ApJ, 555, 775
Croom, S. M., Smith, R. J., Boyle, B. J., et al. 2001, MNRAS, 322, L29
Downes, J. J., Briceño, C., Hernández, J., et al. 2008, AJ, 136, 51
Drake, A. J., Djorgovski, S. G., Mahabal, A., et al. 2009, ApJ, 696, 870
Graham, M. J., Djorgovski, S. G., Drake, A. J., et al. 2014, MNRAS, 439, 703
Hall, P. B., Osmer, P. S., Green, R. F., Porter, A. C., & Warren, S. J. 1996, ApJ, 462, 614
Hughes, P. A., Aller, H. D., & Aller, M. F. 1992, ApJ, 396, 469
Lynden-Bell, D. 1969, Nature, 223, 690
MacLeod, C. L., Ivezić, Ž., Sesar, B., et al. 2012, ApJ, 753, 106
Mateu, C., Vivas, A. K., Downes, J. J., et al. 2012, MNRAS, 427, 3374
Mignard, F. 2012, Mem. Soc. Astron. Italiana, 83, 918
Morganson, E., Burgett, W. S., Chambers, K. C., et al. 2014, ApJ, 784, 92
Pichara, K., Protopapas, P., Kim, D.-W., Marquette, J.-B., & Tisserand, P. 2012, MNRAS, 427, 1284
Rees, M. J. 1984, ARA&A, 22, 471
Rengstorf, A. W., Brunner, R. J., & Wilhite, B. C. 2006, AJ, 131, 1923
Rengstorf, A. W., Mufson, S. L., Abad, C., et al. 2004a, ApJ, 606, 741
Rengstorf, A. W., Mufson, S. L., Andrews, P., et al. 2004b, ApJ, 617, 184
Rengstorf, A. W., Thompson, D. L., Mufson, S. L., et al. 2009, ApJS, 181, 129
Richards, G. T., Fan, X., Newberg, H. J., et al. 2002, AJ, 123, 2945
Robin, A. C., Reylé, C., Derrière, S., & Picaud, S. 2003, A&A, 409, 523
Robin, A. C., Reylé, C., Fliri, J., et al. 2014, A&A, 569, A13
Ross, N. P., McGreer, I. D., White, M., et al. 2013, ApJ, 773, 14
Salpeter, E. E. 1964, ApJ, 140, 796
Schmidt, K. B., Marshall, P. J., Rix, H.-W., et al. 2010, ApJ, 714, 1194
Vivas, A. K., Zinn, R., Abad, C., et al. 2004, AJ, 127, 1158
Welsh, B. Y., Wheatley, J. M., & Neil, J. D. 2011, A&A, 527, A15

SF2A 2015
F. Martins, S. Boissier, V. Buat, L. Cambrésy and P. Petit (eds)

MAPPING THE INNER STELLAR HALO OF THE MILKY WAY FROM 2MASS AND SDSS-III/APOGEE SURVEY

J. G. Fernández-Trincado[1], A. C Robin[1] and C. Reylé[1]

Abstract. The Besançon Galaxy model was used to compare the infrared colour distribution of synthetic stars with those from 2MASS observations taking the selection function of the data into account, in order to study the shape of the stellar halo of the Milky Way, with complemetary spectroscopic data from SDSS-III/APOGEE survey. Furthermore, we compared the generated mock metallicity distribution of the Besançon Galaxy model, to the intrinsic metallicity distribution with reliable stellar parameters from the APOGEE Stellar Parameters and Chemical Abundances Pipeline (ASPCAP). The comparison was carried accross a large volume of the inner part of the Galaxy, revealing that a metal-poor population, [M/H]< -1.2 dex, could fill an extended component of the inner galactic halo. With this data set, we are able to model a more realistic mass density distribution of the stellar halo component of the Milky Way, assuming a six-parameters double power-law model, and reconstruct the behaviour of the rotation curve in the inner part of the Galaxy.

Keywords: Galaxy:structure,Galaxy:disk, Galaxy:halo, Galaxy:formation, Galaxy:stellarcontent

1 Introduction

To perform detailed studies on the kinematics of stars in the Milky Way and its components, as well as to interprete the upcoming six-dimensional phase-space data set produced by the Gaia space mission, a more elaborated description of the Galactic potential of the Milky Way is required. With this purpose, and taking advantage of the well described density profiles for each component of the Besançon Galaxy model (Robin et al. 2003, 2012, 2014), an axisymmetric three-dimensional model for the gravitational field for the inner part of the Galaxy (triaxial bar, stellar halo, central mass), is currently modeled (e.g., Fernández-Trincado et al. 2014, 2015 in prep.), and will be tested using the available spectroscopic surveys as SDSS-III/APOGEE (Alam et al. 2015). The aim of our study is constraint the formation scenarios of the Milky Way central regions, and determine whether the Galactic bulge was predominantely formed by mergers according to Cold Dark Matter (CDM) theory (e.g., Abadi et al. 2003), or from disk instabilities (e.g., Athanassoula 2005), as suggested by its boxy/peanut shape, or if both processes could have affected the inner regions of the Galaxy.

In this paper, we compare the metallicity distribution function of halo (metal-poor) stars predicted by the Besançon Galaxy model with SDSS-III/APOGEE spectroscopic data to infer a constraint on the inner halo density laws.

2 The Milky Way stellar halo

In this section, a brief description of the stellar halo model is outlined.

Robin et al. (2014) has recently suggested that a transition between the Galactic disk and halo of the Milky Way could be smooth enough in the colour-magnitude diagrams, with a halo component dominant at fainter magnitudes, which contribution depends its geometrical shape. In this sense, we attempt to model the

[1] Institut Utinam, CNRS UMR 6213, Université de Franche-Comté, OSU THETA Franche-Comté-Bourgogne, Observatoire de Besançon, BP 1615, 25010 Besançon Cedex, France.

© Société Francaise d'Astronomie et d'Astrophysique (SF2A) 2015

contribution of the stellar halo of the Milky Way using a non-spherical (flattened) density double power-law model (Zhao 1997) with six free parameters (α, β, γ, r_{core}, $\rho_{\odot}$, q),

$$\rho(r) = A^{*}\,(r/r_{core})^{-\gamma}\,[1 + (r/r_{core})^{\alpha}]^{(\gamma-\beta)/\alpha} \tag{2.1}$$

$$A^{*} = \rho_{\odot}\,(r_{\odot}/r_{core})^{\gamma}\,[1 + (r_{\odot}/r_{core})^{\alpha}]^{(\beta-\gamma)/\alpha} \tag{2.2}$$

where $r^2 = X^2 + (Y/p)^2 + (Z/q)^2$ is an axisymmetric radius, and (X, Y, Z) are Galactocentric cartesian coordinates; r_{core} is a scaling radius; $A(\rho_{\odot}, r_{\odot})$ is the normalization, such that, $\rho_{\odot}$ is the local density of the stellar halo in the solar neighborhood ($r_{\odot}$ = 8 kpc); p and q are the axis ratios. Axial symmetry (p = 1) is assumed in this work. The parameters in eq. 2.1 are fitted from 2MASS data (Skrutskie et al. 2006). In Robin et al. (2014), the halo parameters were fitted in the external Galaxy and no constraints on the inner part ($r < 4$ kpc) were used. Here we investigate the extrapolation of the density law in the inner Galaxy with different shapes:

- Shape 1 (double power-law): (α, β, γ, r_{core}, $\rho_{\odot}$, q) = (1, 3.76, 1, 2180 pc, 0.414×10^{-4} M$_{\odot}/pc^3$, 0.77)
- Shape 2 (simple power-law): (α, β, γ, r_{core}, $\rho_{\odot}$, q) = (1, 2.76, 0, 2180 pc, 0.414×10^{-4} M$_{\odot}/pc^3$, 0.77)

3 Results

3.1 SDSS-III/APOGEE bulge fields: An empirical testbed for the inner Galactic regions

We have selected 40 fields from the SDSS-III/APOGEE database, in order to covers the region defined by -5 deg$< l <$ 20 deg and $|b| <$ 20 deg (see Figure 1). We select a sample of $\sim$ 4000 stars with high-quality stellar parameters, and control cuts laid out by García Pérez A. E. et al. (2015, submitted). The Besançon Galaxy model is used with the assumed mass density distribution given in eq. 2.1, and the parametrized form as in Robin et al. (2014) to produce the expected metallicity distribution function of stellar populations, as shown in Figure 2. At low metallicity ([M/H]< -1.2 dex) the model expects little contribution from the triaxial bar, thin-disk and more of the Young/Old thick-disk, and our stellar halo. However, the set of parameters with (α, β, γ, r_{core}, $\rho_{\odot}$, q) = (1, 3.76, 1, 2180 pc, 0.414×10^{-4} M$_{\odot}/pc^3$, 0.77), does not reproduce the number of stars observed beyond [M/H]<-1.2 dex. In the SDSS-III/APOGEE sample it seems that the number of low metallicity stars is much larger than expected from this halo model. To investigate further we show in Figure 1 the distribution in Galactic latitude and longitude of the low metallicity stars. It appears to be not smoothly distributed, but due to variation of extinction in different fields and to the selection function of the APOGEE survey, it is not straightforward to deduce the shape of the stellar halo that could reproduce well the observed distribution. Currently we are fine tuning the parameters of the mass density distribution given in eq. 2.1, taking into account SDSS-III/APOGEE data of the central region of the Galaxy (Fernandez-Trincado et al. 2015 in prep.).

We also expect that a double power-law mass density distribution could be able to explains the observed metallicity distribution function beyond [M/H]< -1.2 dex (Figure 2). However, the parametrized form of eq. 2.1 from 2MASS data, does not reproduce the number of stars observed in the tail of the metallicity distribution function.

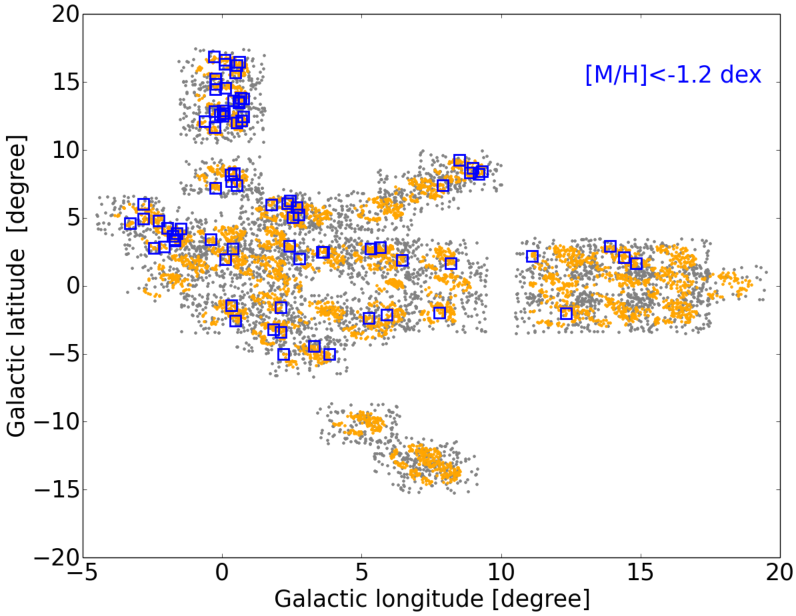

Fig. 1. Spatial distribution of 40 SDSS-III/APOGEE fields (orange dots) included in this study, and the Besançon Galaxy model simulated APOGEE data (grey dots). The low metallicity stars from SDSS-III/APOGEE are shown as blue squares

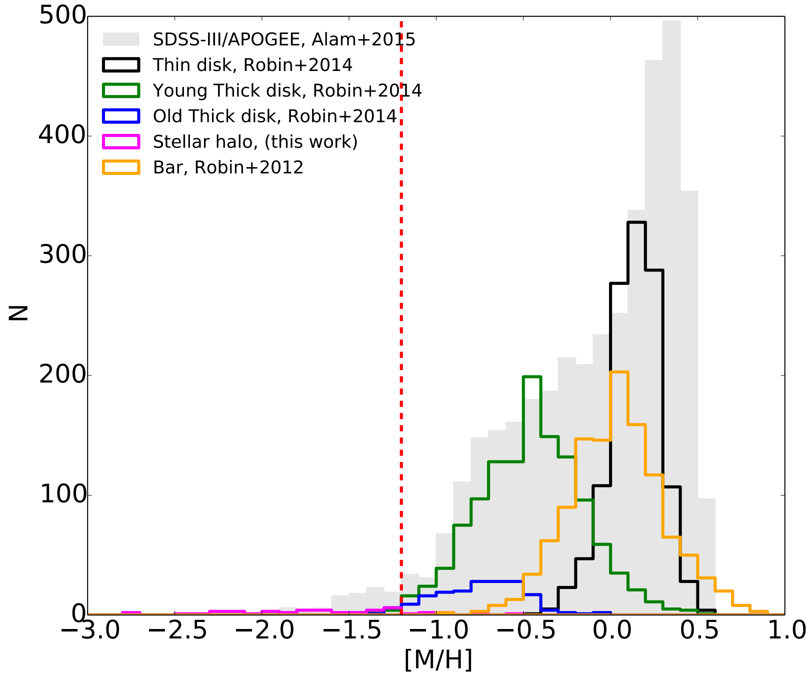

Fig. 2. Metallicity distribution functions in 0.1 dex bins for 40 bulge fields.

3.2 Building the rotation curve for the inner stellar halo shape: Preliminary results

In order to reconstruct the potential for the stellar halo, we approximate the triaxial density by a sum of homogeneous spheroidal surfaces, whose densities approximate the mass density distribution in eq. 2.1, with a step-stair function, according to the adopted stratification method such as that of Schmidt (1956); Pichardo et al. (2004). The circular velocity V_{circ}, for radius $\mathbf{r_{gal}} = \mathbf{r}(\mathbf{X}, \mathbf{Y}, \mathbf{Z} = \mathbf{0})$, is computed as follows:

$$V_{circ}^2 = \mathbf{r_{gal}} \cdot (-\nabla\Phi(r)_{Z=0}) \tag{3.1}$$

Finally, the resulting contributions to the rotation curve of the different stellar halo shapes in §2 are given in Figure 3.

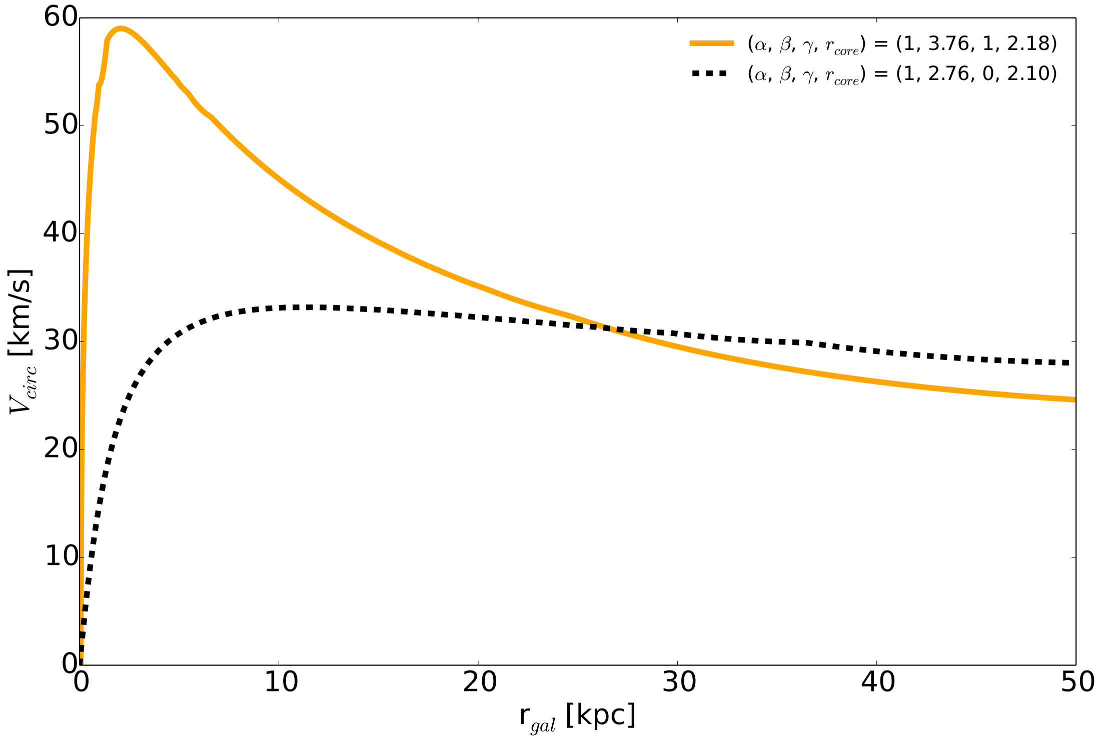

Fig. 3. The contribution to the rotation curve derived from the functional form presented in eq. 2.1. A double power-law density profile describe the orange curve, while that a simple power-law density profile reproduces the black dashed line.

The Besançon Galaxy model contains axisymmetric components (including a three-dimensional model for the stellar halo), and a non-axisymmetric structure associated with the triaxial bar. The new dynamical framework of the Galactic model will be presented in forthcoming paper (Fernández-Trincado et al., in preparation).

J.G.F-T is currently supported by Centre National d'Etudes Spatiales (CNES) through Ph.D grant 0101973 and the Région de Franche-Comté, and by the French Programme National de Cosmologie et Galaxies (PNCG). Besançon Galaxy Model simulations were executed on computers from the UTINAM Institute of the Université de Franche-Comte, supported by the Région de Franche-Comté and Institut des Sciences de l'Univers (INSU). Funding for SDSS-III has been provided by the Alfred P. Sloan Foundation, the Participating Institutions, the National Science Foundation, and the U.S. Department of Energy Office of Science. The SDSS-III web site is http://www.sdss3.org/. SDSS-III is managed by the Astrophysical Research Consortium for the Participating Institutions of the SDSS-III Collaboration including the University of Arizona, the Brazilian Participation Group, Brookhaven National Laboratory, Carnegie Mellon University, University of Florida, the French Participation Group, the German Participation Group, Harvard

University, the Instituto de Astrofisica de Canarias, the Michigan State/Notre Dame/JINA Participation Group, Johns Hopkins University, Lawrence Berkeley National Laboratory, Max Planck Institute for Astrophysics, Max Planck Institute for Extraterrestrial Physics, New Mexico State University, New York University, Ohio State University, Pennsylvania State University, University of Portsmouth, Princeton University, the Spanish Participation Group, University of Tokyo, University of Utah, Vanderbilt University, University of Virginia, University of Washington, and Yale University.

References

Abadi, M. G., Navarro, J. F., Steinmetz, M., & Eke, V. R. 2003, ApJ, 597, 21

Alam, S., Albareti, F. D., Allende Prieto, C., et al. 2015, ApJS, 219, 12

Athanassoula, E. 2005, MNRAS, 358, 1477

Fernández-Trincado, J. G., Robin, A. C., Bienaymé, O., et al. 2014, in EAS Publications Series, Vol. 67, EAS Publications Series, 369–369

Pichardo, B., Martos, M., & Moreno, E. 2004, ApJ, 609, 144

Robin, A. C., Marshall, D. J., Schultheis, M., & Reylé, C. 2012, A&A, 538, A106

Robin, A. C., Reylé, C., Derrière, S., & Picaud, S. 2003, A&A, 409, 523

Robin, A. C., Reylé, C., Fliri, J., et al. 2014, A&A, 569, A13

Schmidt, M. 1956, Bull. Astron. Inst. Netherlands, 13, 15

Skrutskie, M. F., Cutri, R. M., Stiening, R., et al. 2006, AJ, 131, 1163

Zhao, H. 1997, MNRAS, 287, 525

SF2A 2015
F. Martins, S. Boissier, V. Buat, L. Cambrésy and P. Petit (eds)

THE PIC DU MIDI SOLAR SURVEY

L.Koechlin[1] and Observateurs associés[2]

Abstract.
We carry a long term survey of the solar activity with our coronagraphic system at Pic du Midi de Bigorre in the French Pyrenees (CLIMSO). It is a set of two solar telescopes and two coronagraphs, taking one frame per minute for each of the four channels : Solar disk in H-α (656.28 nm), prominences in H-α, disk in Ca II (393.3 nm), prominences in He I (1083 nm), all year long, weather permitting. Since 2015 we also take images of the FeXIII corona (1074.7 nm) at the rate of one every 10 minutes. These images cover a large field: 1.25 solar diameter, 2k*2K pixels, and are freely downloadable form a database.

The improvements made since 2015 concern an autoguiding system for better centering of the solar disk behind the coronagraphic masks, and a new Fe XIII channel at λ =1074.7 nm. In the near future we plan to provide radial velocity maps of the disc and polarimetry maps of the disk and corona. This survey took its present form in 2007 and we plan to maintain image acquisition in the same or better experimental conditions for a long period: one or several solar cycles if possible.

During the partial solar eclipse of March 20, 2015, the CLIMSO instruments and the staff at Pic du Midi operating it have provided several millions internet users with real time images of the Sun and Moon during all the phenomenon.

Keywords: Sun, corona, survey

1 Introduction

Solar astrophysics have a long story at Pic du Midi: coronagraphy was invented there in the 1930's by Bernard Lyot: Lyot (1939, 1945, 1950) Since then, solar observations have been relayed by space probes, but ground-based work keeps its interest for long term surveys. The images from ground based observatories such as Pic du Midi are complimentary to those from space, and may have an advantage in the long run, for example it may turn out easier to finance a long term survey from ground than with space probes.

The survey that we are carrying is in the frame of the "services d'observation" by the Institut National des Sciences de l'Univers (INSU). This survey could not exist without the important contribution of Observateurs Associés (OA) on many aspects : financial support, human resources for data acquisition and software development, and expertise. This association regroups 90 volunteer astronomers, who take turns (one week durations) at Pic du Midi observatory by teams of two: almost every week of the year is covered. There is a detailed story and description of this association on their web site : `http://www.climso.fr` .

The deal offered to the volunteer astronomers is free accommodation for one week at Pic du Midi in exchange of their work during that week. The lodging fees are paid by funding from Université de Toulouse. Observatoire Midi Pyrenees (OMP) and its staff take in charge all the mechanical and heavy logistic aspects.

2 the present instrument

The four telescopes are grouped on an equatorial mount. Two coronagraphs with 20 cm apertures cover the whole sun with a field from 1.002 to 1.25 solar radius: one dedicated to the H-α prominences and the other to the He-I prominences at λ= 1083.0 nm. In addition there are two solar telescopes: one 15 cm aperture centered

[1] Institut de recherche en astrophysique et planétologie (IRAP) Université de Toulouse, CNRS, 14 avenue Edouard Belin, 31400 Toulouse, France
[2] C/O R.Jimenez, 4 rue de la Caoue, 65200 Gerde, France

© Société Francaise d'Astronomie et d'Astrophysique (SF2A) 2015

on the H-α line, and one 9 cm aperture on the Ca-II line at λ= 393.3 nm. These four instruments and the associated data base are operational since march 2007. Details on the instrument and its history can be found on `http://www.climso.fr` , and on `http://bass2000.obspm.fr/solar-spect.php` as well as in Dettwiller & Noens (2008). A quick view of the most recent images is also available there, although a more complete set of images can be downloaded from the databases (see examples in Fig. 1 and Fig. 2). The data base contains images (nominally one per minute per instrument, weather permitting) and films made from these images. An example of image exploitation can be found in Romeuf et al. (2007). Also available are combined images of prominences and solar disk.

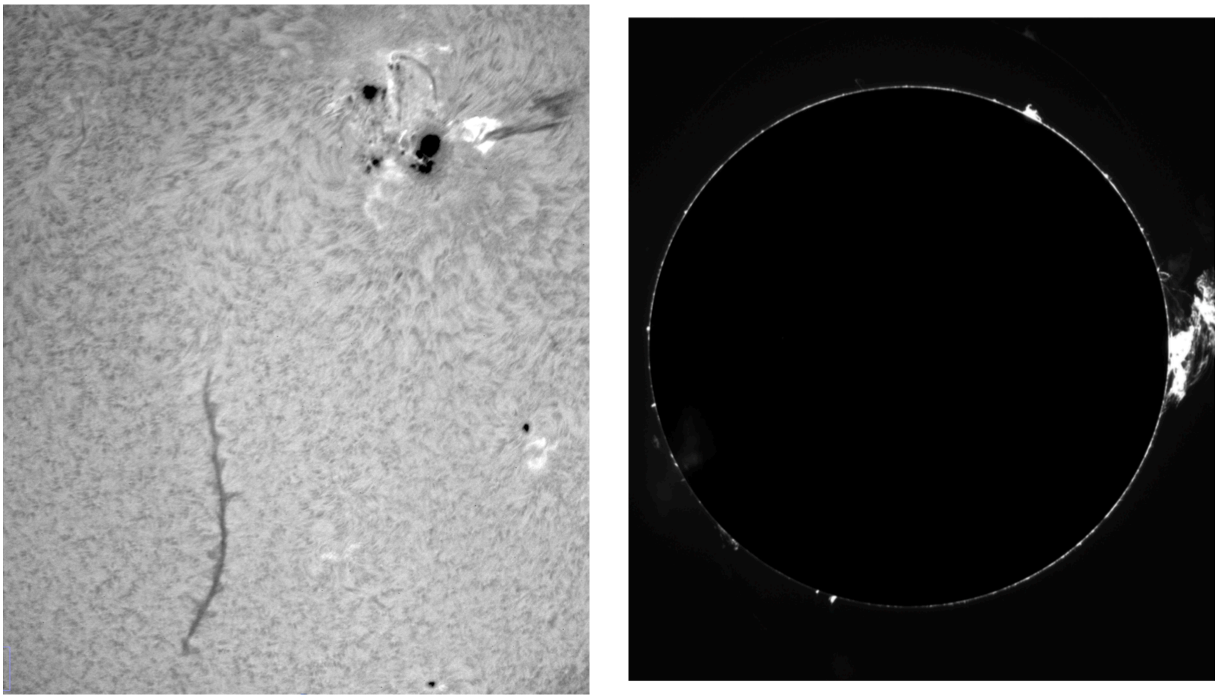

Fig. 1. Left: Detail of the solar chromosphere in Hα (λ=6162.8 nm) taken with the CLIMSO-L1 solar telescope at Pic du Midi. The actual image covers the whole solar disc with the same resolution. **Right:** Ssolar prominence in Hα (λ=6162.8 nm, taken 2015-09-30 at 07:41:37 U.T. with the CLIMSO-C1 coronagraph at Pic du Midi. Images are taken every minute (weather permitting) and sent to a public database. The occulting disc is adjusted to the solar apparent diameter so that the observable field starts at 1.001 solar radius.

3 the autoguiding system

In summer 2014 we added an autoguiding, to achieve a precise superposition (nominally 1 arc second) of the solar disk image onto the coronagraphic mask, in both coronagraphs. A dedicated telescope is placed along one of the coronagraphs, and uses a Fresnel array as objective, Koechlin et al. (2012) : a 50 μm thick copper foil punched with several thousand miniature holes of special shapes and positions (adding up to almost half of the total surface) and focussing the solar light by diffraction. The angular resolution (diffraction limited for monochromatic light) is the same as that of a classical lens of same diameter, here 62 mm. The chromatism induced by the diffractive focusing is strongly reduced by a filter in front of the camera. A 1 nm bandpass filter is good enough here, but diffraction limited imaging requires a slightly narrower bandpass. The frames (one par second) are processed on line: the position of the solar disk is computed by correlation with a circle and

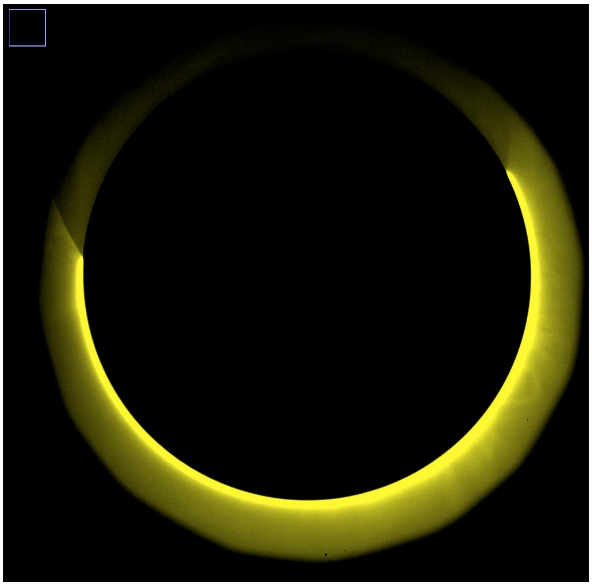
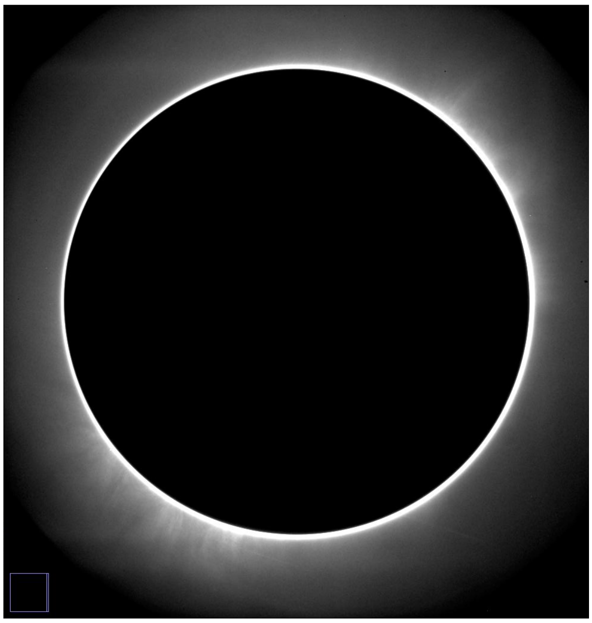

Fig. 2. Left: Solar corona seen with the CLIMSO C2 coronagraph during the partial solar eclipse at pic du midi, 2015-04-20. **Right:** solar corona in Fe XIII seen by coronagraph C2 during a "normal" day and clear sky at pic du midi. The nominal frame rate for the coronal images sent to the data base is one every 10 minutes.

this information is used by the autoguiding system, which sends commands to the equatorial mount to correct the mechanical drifts and low frequencies of atmospheric seeing.

4 The data bases

The Images and films from this survey can be downloaded from: `http://bass2000.bagn.obs-mip.fr/base/sun/index.php` and from: `http://bass2000.obspm.fr/home.php?lang=fr`. We plan to improve the compatibility of the CLIMSO images data base with the Virtual Observatory standards, as well as the interoperability with other databases.

5 Future plans

Our future plans for the instruments are the following:
1. improve the image quality by lucky imaging techniques in real time;
2. improve the image contrast by wavelength modulation and subtraction of references in the continuum;
3. photometric calibration of the images (the solar disc images are already available in W m^{-2} sr^{-1});
4. add several channels showing polarimetry data and velocimetry data.

We do not intend to interrupt the survey in its present form, but add new data types : the longer the time base, the better. The evolutions we are implementing intend to meet better the needs of the scientific community: comments are welcome. Also, if you use these images, which are public and freely available, please source them.

6 Conclusion

The scientific goals and long term plans for this survey are decided in coordination with the "programmes nationaux" of the Institut National des Sciences de l'Univers (INSU). This survey provides a wealth of solar images and films, which are easily downloadable and can be used freely for research or education purposes. We intend to maintain data acquisition on the same spectral channels and in the same or better instrumental setups for as long as possible: we improve the image quality (angular resolution, contrast) but we keep a backwards compatibility with the previous data sets. We also implement new spectral channel and soon new data types such as velocimetry and polarimetry. You are welcome to give us a feedback on how the data is used and how it could be improved.

Special thanks to the OMP staff at Pic du Midi for their dedication and competence in rough conditions. This work has benefited from funding by Université Paul Sabatier, by CNRS and by Fiducial.

References

Lyot, B., 1939, MNRAS 99, 580

Lyot, B., 1945, Ap.J. 101, 255-59

Lyot B., 1950, Comptes rendus des séances de l'Académie des Sciences 231, 461

Dettwiller L, Noens J.-C., 2008, Bull. Un. Prof. Phys. Chim. 102, 1227, (n 908(1))

D. Romeuf, N. Meunier, J.-C. Nons, S. Koutchmy, R. Jimenez, O. Wurmser, S. Rochain, and "Observateurs Associés", 2007, A & A **462**, 731-741, DOI 10.1051/0004-6361:20054159

Koechlin L., Rivet J.-P., Deba P., Serre D., Raksasataya T., Gili R., David J., 2012, Exp Astron 33, 129 DOI 10.1007/s10686-011-9277-7.

SF2A 2015
F. Martins, S. Boissier, V. Buat, L. Cambrésy and P. Petit (eds)

PRIZE OF THE BEST THESIS 2015: STUDY OF DEBRIS DISCS THROUGH STATE-OF-THE-ART NUMERICAL MODELLING

Q. Kral[1] and P. Thébault[2]

Abstract. This proceeding summarises the thesis entitled "Study of debris discs with a new generation numerical model" by Quentin Kral, for which he obtained the prize of the best thesis in 2015.

The thesis brought major contributions to the field of debris disc modelling. The main achievement is to have created, almost ex-nihilo, the first truly self-consistent numerical model able to simultaneously follow the coupled collisional and dynamical evolutions of debris discs. Such a code has been thought as being the "Holy Grail" of disc modellers for the past decade, and while several codes with partial dynamics/collisions coupling have been presented, the code developed in this thesis, called "LIDT-DD" is the first to achieve a full coupling. The LIDT-DD model, which is the first of a new-generation of fully self-consistent debris disc models is able to handle both planetesimals and dust and create new fragments after each collision. The main idea of LIDT-DD development was to merge into one code two approaches that were so far used separately in disc modelling, that is, an N-body algorithm to investigate the dynamics, and a statistical scheme to explore the collisional evolution. This complex scheme is not straightforward to develop as there are major difficulties to overcome: 1) collisions in debris discs are highly destructive and produce clouds of small fragments after each single impact, 2) the smallest (and most numerous) of these fragments have a strongly size-dependent dynamics because of the radiation pressure, and 3) the dust usually observed in discs is precisely these smallest grains. These extreme constraints had so far prevented all previous attempts at developing self-consistent disc models to succeed.

The thesis contains many examples of the use of LIDT-DD that are not yet published but the case of the collision between two asteroid-like bodies is studied in detail. In particular, LIDT-DD is able to predict the different stages that should be observed after such massive collisions that happen mainly in the latest stages of planetary formation. Some giant impact signatures and observability predictions for VLT/SPHERE and JWST/MIRI are given. JWST should be able to detect many of such impacts and would enable to see on-going planetary formation in dozens of planetary systems.

Keywords: planetary system - debris discs - massive collisions - circumstellar matter

1 Introduction

Exoplanet science and more generally the study of extrasolar systems is the fast-growing part of astronomy today. Thanks to the recent spacecrafts Kepler and Corot, as well as ground-based observations from very large telescopes, our knowledge of exoplanets has grown enormously. Exoplanet masses, radii, orbits, atmosphere compositions can be probed using different techniques. Thus, each planetary system observed has its special characteristics that can be compared to our own: the Solar System. Understanding these planetary systems, their formation, their evolution, and searching for hidden components (e.g. planets) that are not bright enough to be observed directly was the main motivations of this thesis.

In extrasolar systems, not only are exoplanets found, but also rocky belts (such as the Kuiper belt in our own Solar System), comets, dust clumps, and gas. All of these with exoplanets, represent what we call a debris disc. Debris discs are found around about one fourth of stars and provide a way to explore the evolution of planetary systems. They also give clues about hidden components in the systems, as will be seen later. As part of the PhD work presented here, a new original approach has been developed to model dust in debris discs, which

[1] Institute of Astronomy, University of Cambridge, Madingley Road, Cambridge CB3 0HA, UK
[2] LESIA-Observatoire de Paris, UPMC Univ. Paris 06, Univ. Paris-Diderot, 92195 Meudon, France

© Société Francaise d'Astronomie et d'Astrophysique (SF2A) 2015

promises to revolutionise our understanding of these objects and extend our knowledge of planetary systems in general.

The study of debris discs is developing rapidly with the increasing quality of spatial and ground-based instruments and the possibility to observe detailed images of such discs. In the recent years, many observations with the space telescopes Hubble and Herschel, as well as the ground-based interferometer ALMA, or new instruments such as SPHERE or GPI, le(a)d to the discovery of structures within discs such as warps, brightness asymmetries, dust clumps, gaps, spiral features, spatial offsets that clearly show that complex physical interactions have to be accounted for when dealing with debris discs. One of the main explanations for the existence of these features is the presence of an exoplanet in the observed extrasolar system. This is how the famous β Pic b planet was first hypothesised indirectly a long time before its actual direct imaging in 2009 (Lagrange et al. 2009). This inclined planet forces the dust in the disc to gain some inclination and creates an observable warp from which we can indirectly infer the presence of a planet.

As well as being an indirect tracer for exoplanets, debris discs can be considered as potential leftovers from the planetary system formation, which tells us about formation of extrasolar systems. Moreover, debris discs are often the most easy component to detect in a planetary system due to their large cumulated dust cross section. Young stars with debris discs can be considered as ideal experimental labs to test planetary formation theories and discover hidden components, but one needs very complex models to handle all the different processes at play. Another area of research that has opened recently deals with "hot" debris discs also called exozodiacal dust (Lebreton et al. 2013). This hot dust close to their host stars should be short-lived, which is not compatible with its high observation rate (about 30% of stars contains hot dust, Absil et al. 2013). Complex interactions need to be modelled to find an explanation to this supposedly common process.

The main research interest of this thesis consists in modelling such discs and their interactions, mainly by developing complex numerical models that aim to make global simulations of such systems. In particular, the thesis was dedicated to develop the first self-consistent model able to couple both dynamical and collisional evolution of grains and planetesimals in such discs.

2 PhD thesis work

The work developed in this thesis mainly consisted in developing new numerical tools to understand debris discs and using them on the data that are already collected. The work can be divided into three parts that are all complimentary to one another. The first part was dedicated to help developing a partial coupling model of debris discs in order to understand the different mechanisms at play, and the limitations that should be overcome to create a full coupling. The heart of the thesis was to develop a powerful code that realises this full coupling and model debris discs in a self-consistent manner by including their interactions with their environments. Then, we started to use this model to learn more about planetary systems and in particular the late stages of planetary formation, which happen to be very chaotic and collisional.

A handful of numerical codes have been developed over the past few years to model debris discs physics, but no one fully succeeded to realise the ambitious goal described above. Motivated by this goal, we investigated the different ways to develop a new generation model able to self-consistently model debris discs, including the two crucial aspects of dynamics and collisions.

As a first test, our team developed a new model called DyCoSS (Thebault et al. 2012). This new algorithm was one of the most sophisticated at time of publication and implements a partial coupling to collisions. It is specifically designed to estimate how collisional lifetimes of grains are affected by dynamical perturbations, and how this variety of collisional lifetimes in turn affects the development of dynamical structures (resonances, PR-drag migrations, etc.). The code allows studying very fine spatial structures and has been used to study debris discs in binaries (Thebault 2012) or discs with an embedded or exterior planet (Thebault et al. 2012, 2014; Lagrange et al. 2012). Fig. 1 shows the structures created by a planet located in a broad disc at steady state. Resonant structures can be observed as well as a density gap at the planet position. This density gap should be empty as this is an unstable zone for the grains, but the constant production of small grains in the inner disc that are pushed on eccentric orbits by radiation pressure fills up the gap and populate it. Very fine structures can be modelled, however, DyCoSS is restricted to very specific setups where the system is at steady state under the influence of only one perturber, and as such shares some similarities with the CGA code (Stark & Kuchner 2009). On top of this, the coupling between dynamics and collisions is only partial as collisions are fully destructive and the fate of collisional fragments is not followed over time. That is why our team decided to develop a totally new approach in parallel that overcomes all of these limitations.

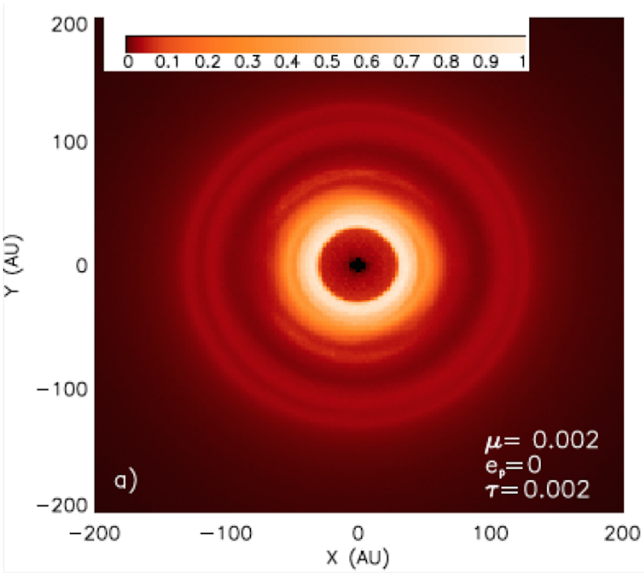

Fig. 1. The effects of a planet at 75 AU embedded within a broad disc (30-130 AU) modelled with a partial coupling code called DyCoSS (Thebault et al. 2012).

The most ambitious part of the PhD was to develop a new state-of-the-art code code, called LIDT-DD, which was the first to merge an N-body code to treat the dynamics of grains and a statistical model to handle dust collisions (Kral et al. 2013). This is a complex process as each collision can create millions of fragments that will themselves collide at the next time step and so on (Charnoz & Taillifet 2012). To make it work over long timescales, some new tools have been developed such as using super-particles (SPs) and many new ideas to be able to regulate smartly the number of SPs within the system, which would otherwise be unmanageable. A SP represents of cloud of particles having the same size and the same orbital parameters. Fig. 2 explains with a diagram how LIDT-DD works over one time step. This can be described in six distinct steps as we follow the evolution of each SP: 1) The orbit of the SP is evolved dynamically (accounting for radiation pressure forces and the gravity of star and surrounding planets), 2) A collisional grid is superimposed on the N-body simulation, 3) Within each cell of the grid, the relative velocities between each grain is worked out, 4) All the fragments resulting from the collisions are created, 5) A sorting algorithm distinguishes the fragments that are really distinct from each other and 6) merges them otherwise.

This new generation model is able, for the first time, to treat accurately and self-consistently dust in complex systems. It is coupled to a radiative transfer code for optically thin discs, which is called GRaTeR (Augereau et al. 1999), and synthetic observations can be produced to compare to actual observed images or spectra. This code opens numerous new possibilities, as it is now possible to follow the dust evolution accurately, in a wide range of systems, where both collisions and dynamics are important.

The first real astrophysical application of the code is the case of violent collisions between sub-planetary mass bodies (Kral et al. 2015). This type of collision is expected during the latest stages of planetary formation. An increasing number of observations show that some discs are too bright to be at collisional steady state given their age, and that some violent transient collisional events could have taken place (Johnson et al. 2012). Our new generation model is able to tackle such an arduous problem for the first time, and leads to some interesting results such as the brightness of such violent phenomena, their timescale, their detectability, as well as being able to predict infallible signature of such events. We perform the first fully self-consistent modelling of the aftermath of massive breakups in debris discs. The initial conditions used to realise this study are shown on Fig. 3. The central star is an A7V and we follow the collisional and dynamical evolution of dust released after the breakup of a Ceres-sized body at 6 AU from the star. This breakup creates rapidly an asymmetric dust disc that is homogenised, by the coupled action of collisions and dynamics, on a timescale of a few 10^5 years. It creates an excess of luminosity that should be detectable in mid-IR photometry, from a 30 pc distance, over a period of $\sim 10^6$ years that exceeds the duration of the asymmetric phase of the disc (of a few 10^5 years). We tried to quantify whether the long-lived asymmetric structures created after such an impact would be observable in a distant planetary system. We created synthetic images with the SPHERE/VLT and MIRI/JWST instruments,

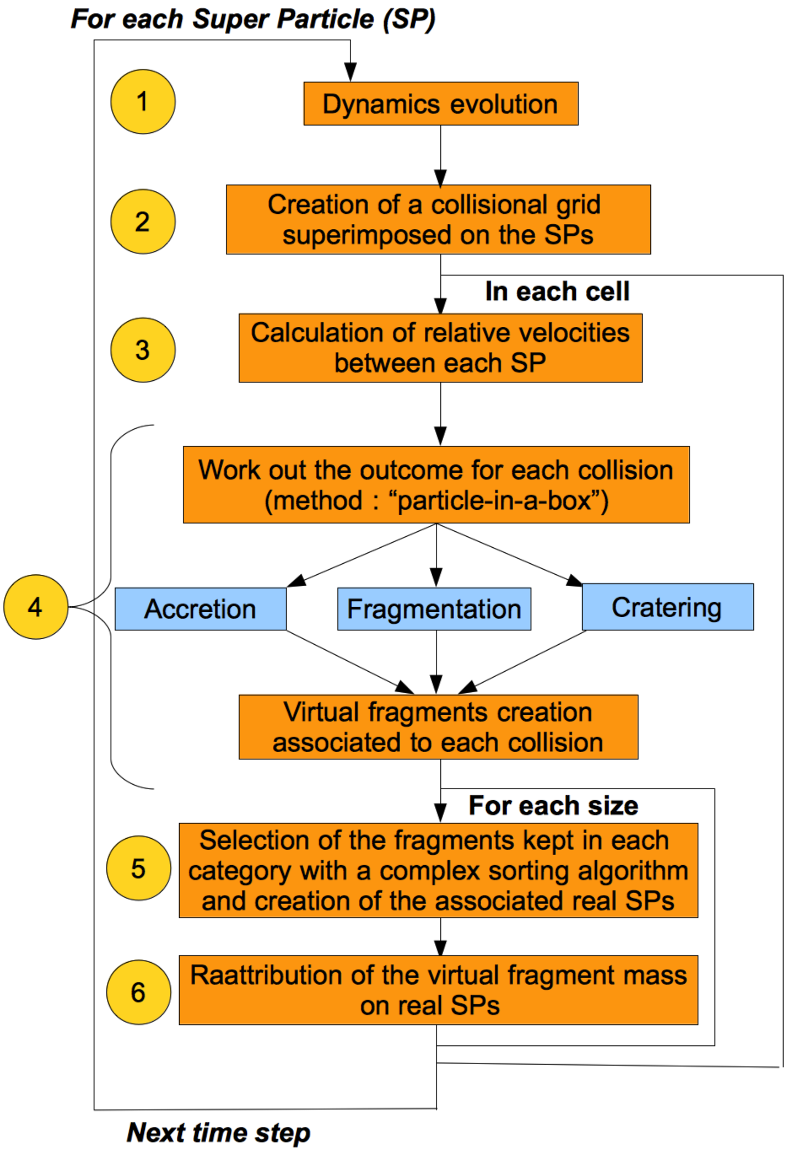

Fig. 2. Simplified diagram showing the time evolution of one time step in LIDT-DD (Kral et al. 2013).

showing that the asymmetries should be clearly visible and resolved from a 10 pc distance for SPHERE and at larger distances for JWST. Images at 1.6μm (marginally), 11.4 and 15.5μm would show the inner disc asymmetry at the collision point, while 23μm images would display the outer disc asymmetry in the dust halo, on the opposite side of the collision point (see Fig. 4). This double asymmetry is a well-defined signature that could be searched for. Confirmed detections of this signature would lead to actual observations of on-going planetary formation, which would be a major advance in our understanding of planetary formation.

3 Perspectives

The global idea of the future research that will be led with the results of this thesis, would be to extend our knowledge of observed planetary systems. This can be done on several fronts, such as having a better understanding of the mechanisms that form planetary systems, or such as trying to extract as much information

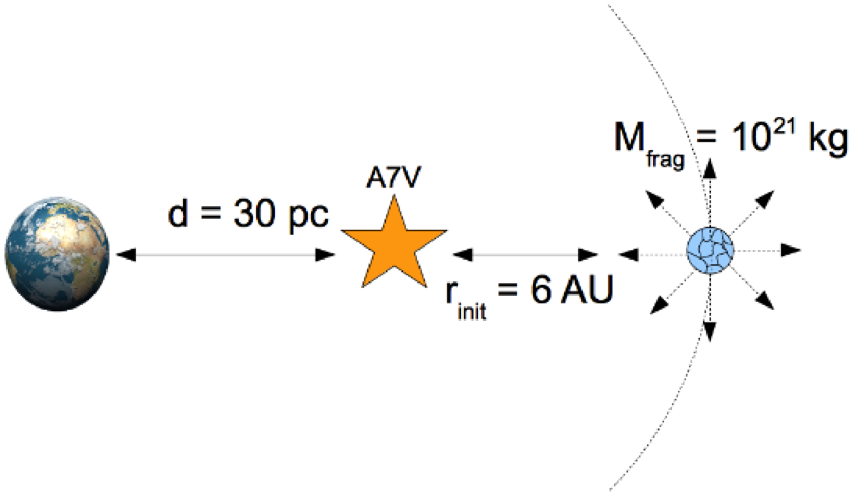

Fig. 3. Initial conditions of the LIDT-DD simulation used to model the aftermath of a massive collision between two asteroid-like objects (Kral et al. 2015).

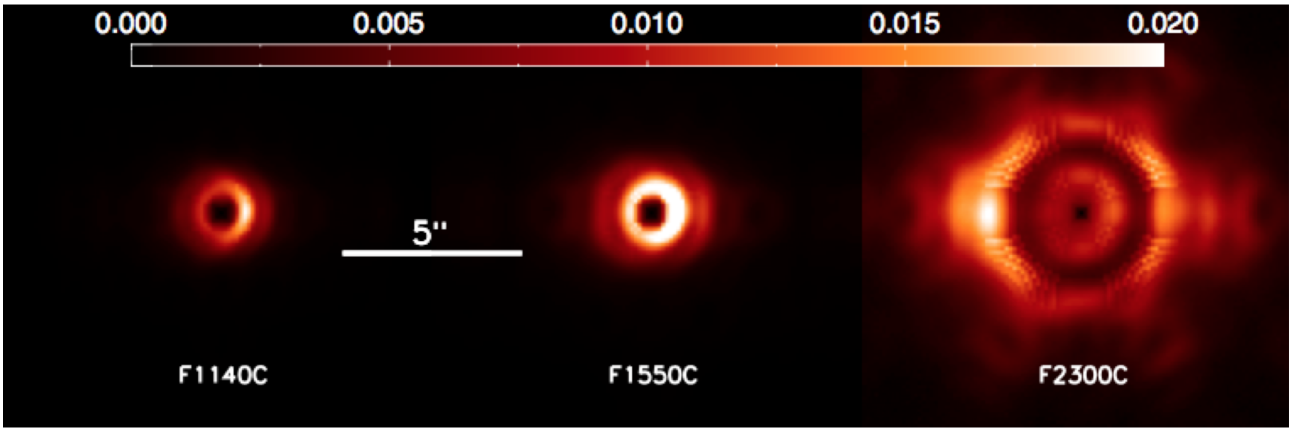

Fig. 4. JWST/MIRI synthetic observation of the aftermath of a massive collision between two asteroid-like objects. Simulation with LIDT-DD (Kral et al. 2015).

as possible from an ensemble of observations that are already collected. The model developed in the thesis, LIDT-DD, can tackle both fronts, and a few interesting problems that could be covered in the near future are presented briefly here below.

An obvious first endeavour would be to explore the full potential of the LIDT-DD code, by investigating very important issues regarding debris discs evolution, and planet formation scenarios that could not be quantitatively investigated with previous non self-consistent codes. A non-exhaustive list of such applications would be planet-disc interactions, the effect of a companion passage on the disc structure, the effect of a violent break-up in such a disc, etc. Another interesting phenomenon called collisional avalanches could also be investigated. It consists in studying the effect of unbound grains created far inside the inner edge of a debris disc (due to a violent break-up or evaporation) ejected quickly by radiation pressure forces and encountering particles from the disc at steady state. A bolting phenomenon or avalanche can be observed and could even possibly explain the recent mysterious observation (Melis et al. 2012), where a circumstellar disc totally disappeared on a very small timescale of about two years.

One of the most urgent problem to solve is the mystery of exozodiacal dust that should not exist so ubiquitously around so many old stars, as this hot dust lifetime is very short. It is a major issue as this hot dust can be within the habitable zone and prevent from observing the “holy grail” of planetary science: *habitable Earth-like planets*. Different scenarios that can create this hot dust have been proposed but could not be modelled numerically with previous codes. LIDT-DD could explore the different paths and bring some new clues concerning the survival of this dust, and in the end, help to observe beyond the dust shield that it forms to see the habitable Earth-like planets.

On a longer timescale, one could also imagine to extend this work to transitional discs (that are not well-understood) or even to a very different case, such as planetary rings. Future applications are numerous and very broad.

QK acknowledge support from the European Union through ERC grant number 279973.

References

Absil, O., Defrère, D., Coudé du Foresto, V., et al. 2013, A&A, 555, A104

Augereau, J. C., Lagrange, A. M., Mouillet, D., Papaloizou, J. C. B., & Grorod, P. A. 1999, A&A, 348, 557

Charnoz, S., & Taillifet, E. 2012, ApJ, 753, 119

Johnson, B. C., Lisse, C. M., Chen, C. H., et al. 2012, ApJ, 761, 45

Kral, Q., Thébault, P., Augereau, J.-C., Boccaletti, A., & Charnoz, S. 2015, A&A, 573, A39

Kral, Q., Thébault, P., & Charnoz, S. 2013, A&A, 558, A121

Lagrange, A.-M., Milli, J., Boccaletti, A., et al. 2012, A&A, 546, A38

Lagrange, A.-M., Gratadour, D., Chauvin, G., et al. 2009, A&A, 493, L21

Lebreton, J., van Lieshout, R., Augereau, J.-C., et al. 2013, A&A, 555, A146

Melis, C., Zuckerman, B., Rhee, J. H., et al. 2012, Nature, 487, 74

Stark, C. C., & Kuchner, M. J. 2009, ApJ, 707, 543

Thebault, P., Kral, Q., & Augereau, J.-C. 2014, A&A, 561, A16

Thebault, P., Kral, Q., & Ertel, S. 2012, A&A, 547, A92

Thébault, P. 2012, A&A, 537, A65

SF2A 2015
F. Martins, S. Boissier, V. Buat, L. Cambrésy and P. Petit (eds)

LA SECTION 17 DU COMITÉ NATIONAL DE LA RECHERCHE SCIENTIFIQUE

M. Marcelin[1]

Abstract. This contribution presents the section 17 of the "Comité National de la Recherche Scientifique" and its activity. Since it concerns mostly French researchers and researchers from French institutes, the rest of the contribution is provided in French language.

Keywords: organization

1 Composition de la Section

La Section 17 du comité national de la recherche scientifique, "Système solaire et Univers lointain", est composée de 18 chercheurs (11 élus et 7 nommés) et 3 ingénieurs (tous élus). Les chercheurs ne sont pas seulement issus du CNRS, mais il y a aussi des astronomes du CNAP, des enseignants-chercheurs ou encore des astrophysiciens du CEA. De ce fait, il s'agit bien d'une représentation de l'ensemble de la recherche scientifique en astrophysique, de même que les autres sections du comité national de la recherche scientifique (41 au total) ne sont pas une simple émanation du CNRS (comme la similarité des sigles CoNRS et CNRS le laisse malheureusement sous-entendre). On retrouve d'ailleurs un peu la même chose au CNAP et au CNU. La durée du mandat des sections était jusque là de 4 ans mais elle passera à 5 ans à partir de 2016, date de fin de la mandature actuelle. La liste détaillée des membres actuellement en exercice est donnée sur le site web de la Section17 : `https://section17.ias.u-psud.fr/foswiki`

2 Rôle de la Section

Parmi les principales prérogatives de la Section 17 on trouve le recrutement et l'évaluation des chercheurs CNRS tout au long de leur carrière, ainsi que les promotions. De plus, la Section participe à l'évaluation des unités de recherche dans lesquelles travaillent des chercheurs dont la thématique relève de ses compétences. La mise en place de l'AERES avait considérablement diminué la participation du comité national à l'évaluation des unités de recherche. Le HCERES (Haut Conseil pour l'Evaluation de la Recherche et l'Enseignement Supérieur) qui remplace l'AERES ne semble pas amener de grand bouleversement au mode de fonctionnement de l'évaluation. On peut toutefois espérer que les élus C des sections (ingénieurs) seront mieux traités et plus systématiquement associés aux comités de visite. La Section 17 s'occupe également de beaucoup de choses moins connues, comme l'attribution des médailles du CNRS (qui, rappelons le, ne sont pas attribuées uniquement à des chercheurs CNRS), l'attribution de la PEDR (Prime d'Encadrement Doctoral et de Recherche) qui succède à la PES, l'accueil en délégation d'enseignants-chercheurs (qui peuvent ainsi bénéficier d'une décharge partielle ou totale de leur enseignement, leur permettant de consacrer plus de temps à leurs activités de recherche), l'évaluation (en vue de financement éventuel par le CNRS) de colloques et écoles thématiques. Chaque section contribue, à mi-mandat, à l'élaboration du rapport de conjoncture du CNRS. En effet, le comité national de la recherche scientifique a pour mission statutaire de procéder à l'analyse de la conjoncture scientifique et de ses perspectives. Ce rapport de conjoncture, résultat d'une consultation très large des communautés scientifiques, se positionne comme un outil de référence dans le paysage de la recherche nationale. Citons enfin la prospective en astronomie et astrophysique de l'INSU, exercice qui a lieu tous les 4 ou 5 ans et auquel la Section 17 participe activement. Le dernier exercice de prospective s'est tenu à la Presqu'île de Giens du 13 au 16 octobre 2014: `http://www.insu.cnrs.fr/prospective-AA-2015`

[1] Aix Marseille Université, CNRS, LAM (Laboratoire d'Astrophysique de Marseille) UMR 7326, 13388, Marseille, France

© Société Francaise d'Astronomie et d'Astrophysique (SF2A) 2015

3 Concours

3.1 *Pré-sélection des candidats sur dossier pour l'audition*

La pré-sélection des dossiers en vue de l'audition, rendue nécessaire par le nombre élevé de candidatures (voisin de 200 en Section 17) a été mise en place en 2012. Elle a permis de réduire à une centaine le nombre de candidats auditionnés en 2013, puis à environ 70 en 2014 et 2015, ce qui a permis de réduire le nombre de sous-jurys de 3 à 2, d'où un meilleur fonctionnement (les candidats étant vus par des sous-jurys plus consistants, le jugement s'en trouve amélioré).

3.2 *Evolution du nombre des admis aux concours CR en Section 17 depuis 2000*

La Figure 1 montre que le nombre d'admis aux concours de chargé de recherche en Section 17 est resté relativement stable au cours des 15 dernières années, compris entre 4 et 6 pour les CR2 et voisin de 2 pour les CR1.

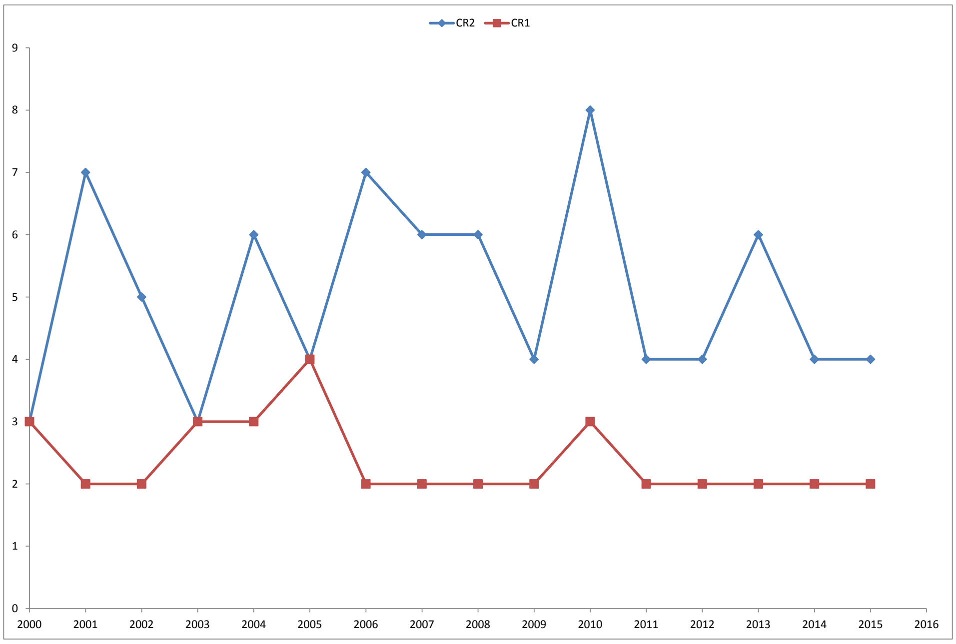

Fig. 1. Nombre d'admis aux concours CR de la Section 17 de 2000 à 2015

3.3 *Age des candidats CR recrutés en Section 17*

L'âge moyen (en terme d'années après la thèse) constaté pour les admis au concours CR1 sur les trois dernières années est de 5,9 ans (avec un minimum de 4,4 ans et un maximum de 7,3 ans). A titre indicatif, l'âge réel moyen de ces admis au concours CR1 est quant à lui de 32,4 ans. Pour le concours CR2, l'âge moyen des admis sur les trois dernières années est de 3,9 ans après la thèse (avec un minimum de 2,4 ans et un maximum de 5,4 ans). L'âge réel moyen de ces admis au concours CR2 est de 31,0 ans.

3.4 *Proportion de femmes candidates et admises aux concours CR en Section 17*

La Figure 2 illustre le problème de l'évaporation des candidates féminines au concours. On y voit le nombre cumulé de candidats en fonction du nombre d'années après la thèse.

Si le nombre d'hommes candidats continue de croitre régulièrement en fonction de l'âge, celui des femmes candidates montre en revanche un plateau très net à partir de 3 à 4 ans après la thèse et qui se poursuit bien

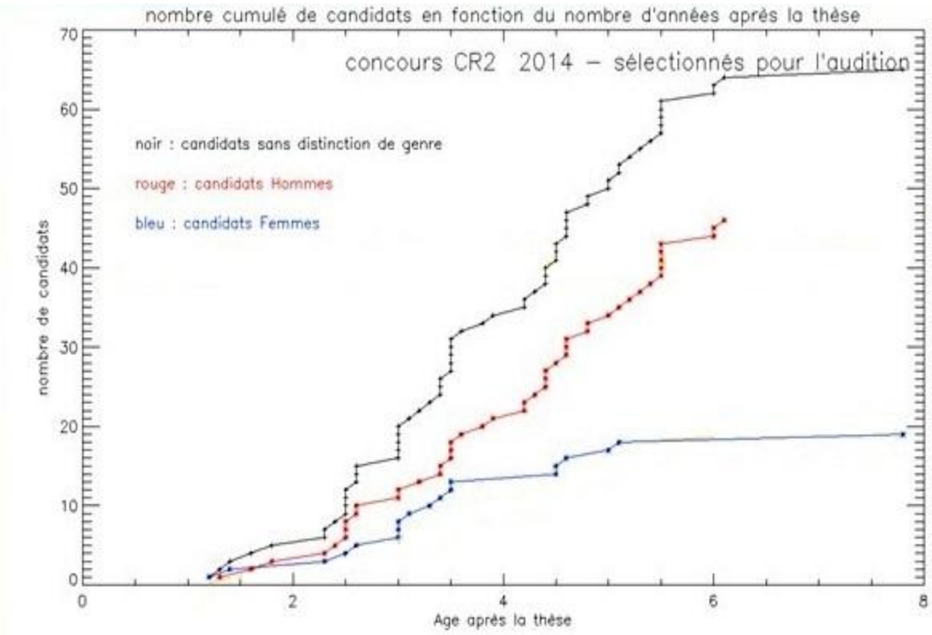

Fig. 2. Nombre cumulé de candidats femmes et hommes aux concours CR de la Section 17 en fonction du nombre d'années après la thèse (courbe en bleu: F, courbe en rouge: H, courbe en noir: F + H).

au-delà. Les conséquences sont donc particulièrement dommageables pour le concours CR1 (qui demande un minimum de 4 ans après la thèse) où l'on trouve de fait une proportion de plus en plus faible de femmes, comme le montre la Figure 3.

Bien qu'il s'agisse de statistiques sur des petits nombres, il est intéressant de voir quelle est la proportion de femmes à différents stades du processus de concours. La Figure 3 donne, pour les trois dernières années, la proportion de femmes admises à concourir, admises à poursuivre (i.e. auditionnées), admissibles et enfin admises aux concours CR2 et CR1 de la Section 17. On y voit de manière évidente la conséquence de l'évaporation des femmes évoquée ci-dessus. Sur les trois dernières années, et malgré une année 2013 sans aucun recrutement de femme ainsi qu'une perte sensible du pourcentage dès le début du processus de concours (lors de la sélection en vue des auditions), on constate que la proportion de femmes recrutées au concours CR2 par la Section 17 reste satisfaisante. De ce fait, malgré l'absence de recrutement de femmes au niveau CR1, la proportion de femmes recrutées au niveau CR (CR2+CR1) par la Section 17 sur les trois dernières années est de 20% et reflète bien la proportion de femmes au sein de la discipline (voir la Figure 4 qui donne la proportion H/F par grade en Section 17, au 31/12/2013).

Bien que le mandat actuel de la Section 17 ne soit couvert qu'aux trois quarts, il est intéressant de regarder l'évolution de la proportion de femmes candidates et lauréates aux concours chercheurs, sur les trois derniers mandats (2004-2008, 2008-2012 et 2012-2016). La Figure 5 montre que les choses restent relativement stables, sauf pour le concours CR1 où aucune femme n'a été recrutée au cours des deux derniers mandats, ce qui résulte vraisemblablement d'une accentuation du phénomène d'évaporation des candidates évoquée ci-dessus.

3.5 Concours CR1 et règle des 3 présentations

A ce sujet, il est bon de rappeler ce qui figure sur le site web du CNRS: "Les candidats ne peuvent se présenter à plus de 3 sessions pour les concours de CR1 ; s'ils ont été deux fois admissibles, ils peuvent se présenter à une 4e session." Attention ! être admissible ne veut pas dire être admis à l'audition (comme le croient malheureusement beaucoup de candidats) mais figurer sur la liste d'admissibilité que la Section publie à l'issue des concours. Il y a ensuite le jury d'admission qui donne la liste définitive des candidats reçus au concours (il s'agit là d'une différence notable avec le CNAP qui est jury d'admission). Il est donc recommandé aux candidats de ne pas gaspiller inutilement leurs cartouches en se présentant trop tôt au concours CR1.

Concours CR2	**2013**	**2014**	**2015**
Admises à concourir	32,7%	35,7%	37,0%
Admises à poursuivre	26,3%	30,3%	35,2%
Admissibles	0%	40%	40%
Admises	0%	50%	50%
Concours CR1	**2013**	**2014**	**2015**
Admises à concourir	26,1%	24,4%	18,1%
Admises à poursuivre	20,9%	12,5%	24,0%
Admissibles	0%	0%	0%
Admises	0%	0%	0%
% d'admises au total (CR2 + CR1)	**0%**	**33,3%**	**33,3%**

Fig. 3. Tableau donnant la proportion de femmes aux concours CR de la Section 17 aux différentes phases du processus de concours pour les trois dernières années.

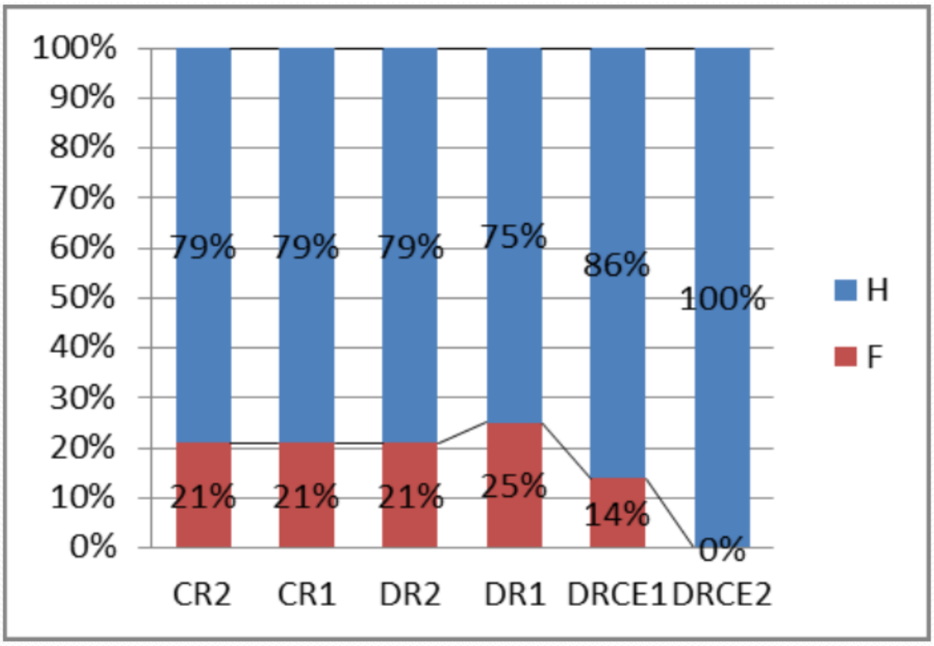

Fig. 4. Proportion H/F par grade en Section 17 (au 31/12/2013).

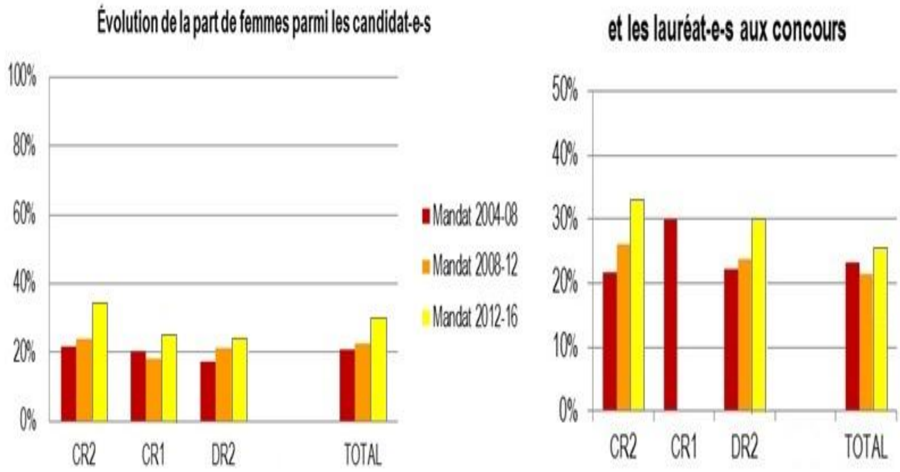

Fig. 5. Proportion de femmes candidates et lauréates aux concours chercheurs (CR et DR) au cours des trois derniers mandats de la Section 17 (2004-2008, 2008-2012 et 2012-2016). N.B. Il manque l'année 2016 pour le dernier.

3.6 Concours DR2

On note une nette baisse du facteur de pression à ce concours. Cela résulte, entre autres, du fait que le nombre de postes ouvert à ce concours a été significativement augmenté au cours des dix dernières années, permettant ainsi de résorber le bouchon qui s'était créé au fil du temps. On notera par ailleurs que la fraction de DR en Section 17 est proche de 50% alors qu'elle est entre 35 et 45% pour la grande majorité des sections du comité national. De ce fait, le nombre de postes DR2 mis au concours en Section 17 a sensiblement diminué au cours des dernières années. Cela n'a pas permis pour autant d'augmenter le nombre de postes CR mis au concours car les candidats reçus au concours DR2 sont généralement des chercheurs issus du CNRS et déjà rémunérés comme CR1 par le CNRS. D'un point de vue budgétaire, il s'agit donc d'une simple promotion et pas d'une création de poste à part entière (ainsi, sur un plan purement comptable, il faudrait supprimer environ 5 postes DR2 pour pouvoir ouvrir 1 poste CR). Note importante: Rappelons que, lors du concours de recrutement DR2 de 2013, le jury d'admission a déclassé 3 candidats qui n'étaient pas titulaires de l'HDR (Habilitation à Diriger des Recherches) et que la Section 17 avait classés en bonne place dans sa liste d'admissibilité. Il est donc fortement recommandé aux candidats de soutenir leur HDR avant de postuler à ce concours (bien que les textes officiels ne l'exigent pas).

3.7 Concours handicap

Chaque année, le CNRS met des postes au concours pour les personnes handicapées. C'est un concours spécifique qui se déroule juste après la session de concours habituelle. Il y a généralement une dizaine de postes ouverts à ce titre, sur l'ensemble des 41 sections et, sur la mandature actuelle, la Section 17 a pu bénéficier d'un tel poste en 2013. Les directeurs d'unité ayant des doctorants ou post-docs au handicap reconnu peuvent contacter le CNRS afin de faire mettre des postes au concours sur leurs thématiques. Ce dispositif permet à des chercheurs handicapés d'être recrutés sur la base d'un contrat d'une période d'un an renouvelable une fois donnant lieu à titularisation. Des détails de la procédure sont donnés sur le site web du CNRS : `http://www.dgdr.cnrs.fr/drhchercheurs/concoursch/handicap/default-fr.htm`

4 Les médailles du CNRS

La répartition des médailles est généralement la suivante:
Médaille de bronze : Une par Section du comité national.
Médaille d'argent : Une par Institut (pour l'INSU : S17, S18, S19 et S30).
Médaille d'or : Une pour tout le CNRS.
L'examen des dossiers se fait chaque année en session d'automne. Les dossiers sont généralement transmis par les directeurs d'unités et par les programmes nationaux, sollicités à cet effet. Rappelons que tout chercheur ou enseignant-chercheur peut recevoir une médaille du CNRS et que celles-ci ne sont pas attribuées uniquement à des chercheurs CNRS. Un biais énorme a été constaté en 2014, pour l'attribution de la médaille de bronze, puisque seules des candidatures masculines avaient été transmises à la Section dans un premier temps...

5 La Prime d'Encadrement Doctoral et de Recherche

La PEDR, tout comme la PES qu'elle a remplacée, est un sujet de discorde parmi les chercheurs, au point que certaines sections du comité national refusent d'examiner les dossiers de demande de PEDR. La Section 17 a néanmoins discuté de l'attribution de cette prime au cours de ces dernières années, même si plusieurs de ses membres n'ont pas souhaité participer à la discussion. Les membres qui y ont participé ont privilégié l'attribution de la prime aux jeunes et évité de reconduire la prime à ceux qui en avaient déjà bénéficié. Une nouveauté cette année, à l'initiative d'Alain Fuchs, président du CNRS, a été l'attribution systématique de cette prime aux nouveaux entrants. De fait cela a réduit environ de moitié le nombre de primes à discuter en Section 17 pour proposition à l'INSU.

SF2A 2015
F. Martins, S. Boissier, V. Buat, L. Cambrésy and P. Petit (eds)

THE GSO DATA CENTRE

F. Paletou[1], J.-M. Glorian[1], V. Génot[1], A. Rouillard[1], P. Petit[1], A. Palacios[2], E. Caux[1] and V. Wakelam[3]

Abstract. Hereafter we describe the activities of the *Grand Sud-Ouest* Data Centre operated for INSU (CNRS) by the OMP–IRAP and the *Université Paul Sabatier* in Toulouse, in a collaboration with the OASU–LAB in Bordeaux and OREME–LUPM in Montpellier.

Keywords: Astronomical databases, Virtual Observatory, Data centers.

1 Introduction

The GSO Data Centre (hereafter OV–GSO) was officially set-up in 2013, after approval by INSU of CNRS. Its role is to support more specific and so-called "reference services" which provide dedicated and communautary services, in relation with relevant astrophysical data. OV–GSO also promotes and encourages the deployment of virtual observatory (VO) techniques, at the regional level.

The actual distribution of regional data centres at the national level can be seen in Fig. (1). OV–GSO covers all the *open and "science ready" data*, and VO-oriented activities of Bordeaux (LAB), Montpellier (LUPM) and Toulouse (IRAP) laboratories for astrophysics.

2 Reference services

2.1 Bass 2000

Bass 2000 was originally set-up in 1996 for the archival and diffusion of all the solar data collected from ground-based observatories having a national participation. At this time, it was essentially giving direct support to the Thémis solar telescope located at the *Observatorio del Teide*, Tenerife (Spain).

The progressive decline of the Thémis community, and the evolution of data management at the era of virtual observatories makes that this service will now focus on the only support to the ground-based instrument under responsability of the *Observatoire Midi–Pyrénées*, that is the CLIMSO set of coronagraphs and narrow-band solar (disk) imagers located at the summit of *Pic du Midi de Bigorre*.

2.2 CDPP

The CDPP is the national centre of expertise concerning terrestrial and planetary plasma data. It was created in 1998 by CNRS/INSU and the French space agency CNES. It assures the long term preservation of data obtained primarily from instruments built using French resources, and renders them readily accessible and exploitable by the international community. The CDPP also provides services to enable on-line data analysis (AMDA, see `amda.cdpp.eu`), and 3D data visualization in context (3DView, see `3dview.cdpp.eu`).

The CDPP also plays an important role in the development of interoperability standards (see e.g., Génot et al. 2014).

[1] Université Paul Sabatier, OMP-IRAP, CNRS, 14 ave. E. Belin, F–31400 Toulouse, France
[2] Université de Montpellier 2, LUPM, CNRS, Place E. Bataillon, F–34095 Montpellier, France
[3] Université de Bordeaux, LAB, CNRS, F–33270 Floirac, France

© Société Francaise d'Astronomie et d'Astrophysique (SF2A) 2015

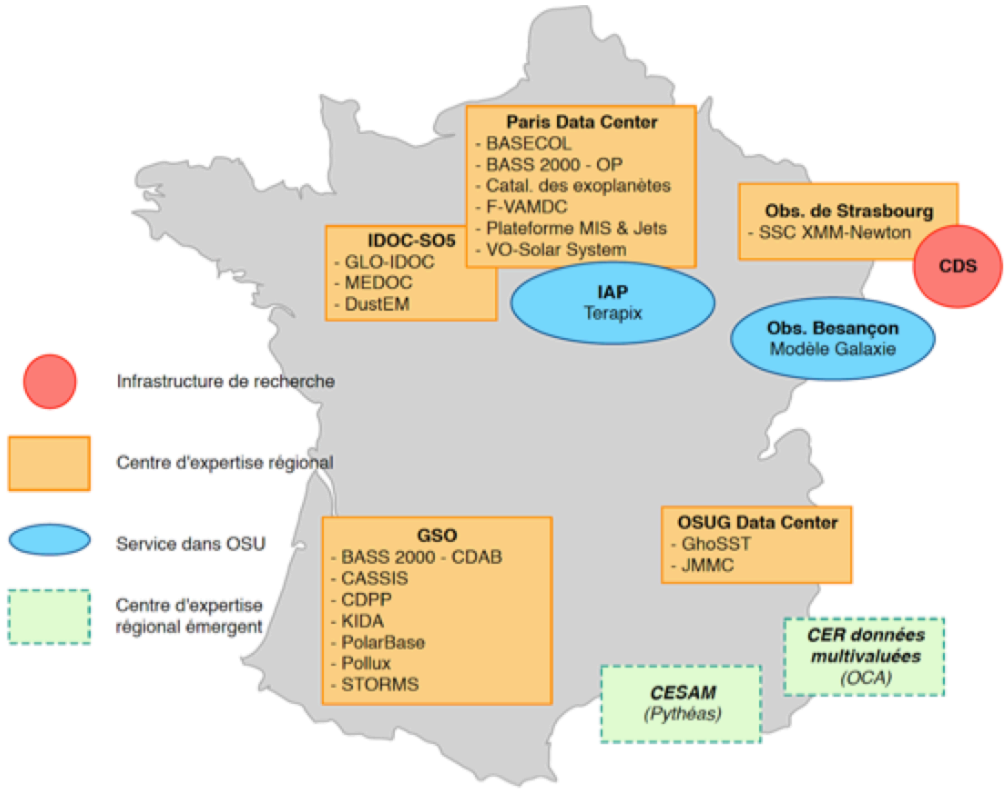

Fig. 1. Actual map of astronomical data services in France. OV–GSO covers the whole south-west area i.e., the (open) data-oriented activities of Bordeaux (LAB), Toulouse (IRAP) and Montpellier (LUPM) astrophysics laboratories.

2.3 STORMS

STORMS, which stands for *Solar Terrestrial ObseRvations and Modeling Service*, is a new public service providing tools and data to perform studies in heliophysics and space weather, and to study and model the influence of solar activity on the geospace environment, as well as on planets or any other solar system bodies (comets, asteroids or spacecrafts).

The main tool it provides so far, `propagationtool.cdpp.eu`, was jointly developed with CDPP. It is meant for the tracking of solar storms, streams and energetic particles in the heliosphere.

2.4 PolarBase

PolarBase was officially opened to the public in 2013. This service distributes high resolution optical stellar spectra from the Espadons@CFHT and Narval@TBL spectropolarimeters.

Reduced spectra, in various Stokes parameters, are delivered to the community, as well as standardizely extracted polarized signatures. A complete description of the database can be found in Petit et al. (2014).

2.5 POLLUX

Pollux is a stellar spectra database proposing access to *theoretical* data. For that purpose, high resolution synthetic spectra and spectral energy distributions have been computed using the best available models of atmosphere (CMFGEN, ATLAS and MARCS), performant spectral synthesis codes (CMF_FLUX, SYNSPEC and TURBOSPECTRUM) and atomic linelists from VALD database and specific molecular linelists for cool stars. Spectral types from O to M are represented for a large set of fundamental parameters: $T_{\rm eff}$, $\log g$, [Fe/H], and specific abundances (Palacios et al. 2010).

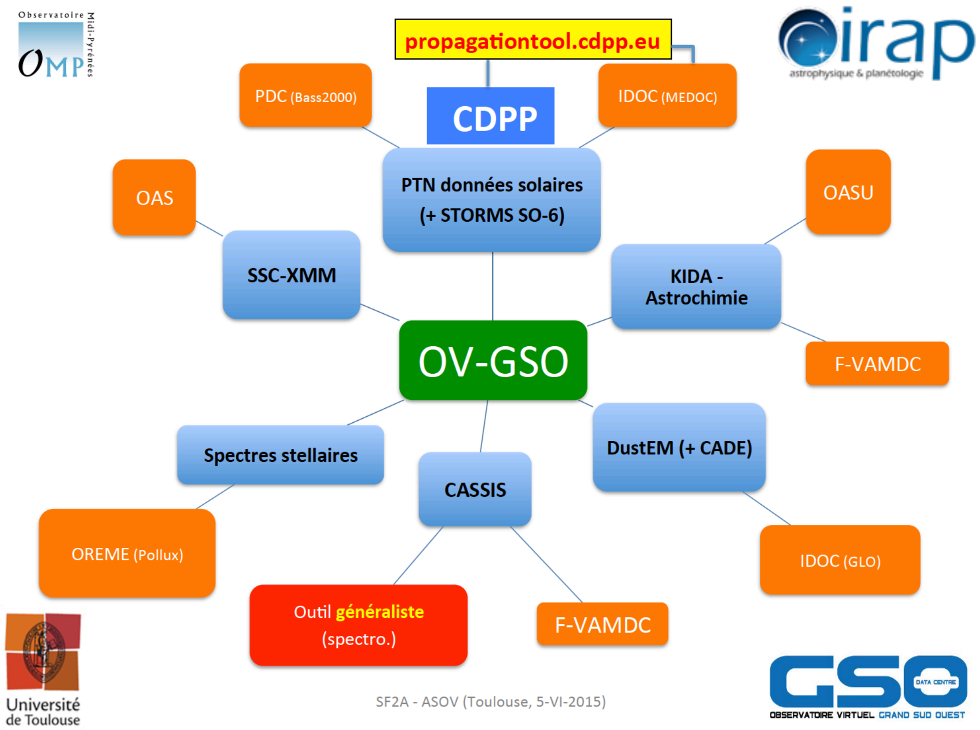

Fig. 2. Connections between OV–GSO and other services and institutes at the national level.

2.6 *CASSIS*

CASSIS started in 2005. It provides an interactive spectrum analyser that was originally proposed for the scientific exploitation of (far-infrared and submillimetric) data from the Herschel Space Observatory. CASSIS allows to visualize observed or synthetic spectra, together with a line identification tool. It can also predict spectra which may be observed by any (single-dish, so far) telescope. Comparison between observations and synthetic spectra (e.g., from Radex) is also possible with the same tool.

CASSIS is now evolving towards a multi-purpose spectral analysis tool, operating beyond its initial range of application.

2.7 *KIDA*

KIDA is a database of kinetic data of interest for astrochemical (interstellar medium and planetary atmospheres) studies. In addition to the available referenced data, KIDA provides recommendations over a number of important reactions. Chemists and physicists can also add their own data to the database.

KIDA also distributes a code, named Nahoon, to study the time-dependent gas-phase chemistry of 0D and 1D interstellar sources. Details about the KIDA database can be found in Wakelam et al. (2012).

3 Management and operations

As of 2015, operations of OV–GSO involve about 10 technical (IT) personnel, and about 25 scientists in the Bordeaux-Toulouse-Montpellier area. The typical annual budget of the data centre is about 50 kEur. Obviously one of the major task of OV–GSO is to guarantee the continuity of all services, and therefore regular upgrades of all hardware devices are made. Another fundamental task of the data centre is to plan and to increment regularly our data storage capability, in an homogeneous way.

We also regularly contribute to the various virtual observatories communities, both at the national and international levels (e.g., IVOA). This concerns our reccurent participation to the bi-yearly so-called Interop meetings of the IVOA, as well as propositions of tutorials (e.g., SpecFlow at `euro-vo.org` scientific tutorials page, or Paletou & Zolotukhin 2014).

Locally, we set-up a monthly dedicated seminar, oriented towards the use and implementation of Virtual Observatory standards and protocols. We are also involved in discussions about more general data issues, at the level of the *Université de Toulouse*. Our various activities can be followed at `ov-gso.irap.omp.eu`

4 Perspectives

Figure (2) finally summarizes the various interactions between OV–GSO and other services and institutes, at the national level (and as of 2015).

We are however already supporting several ongoing projects which should transform into new reference services in a near future. It consists in providing data and tools for the study of emissions of the extended sky (`cade.irap.omp.eu`), and a so-called Multi Frequency Follow-up Inventory Service (`muffins.irap.omp.eu`). Projects are also associated with the data management of the Muse integral-field spectrograph at VLT, as well as high-energy astrophysical data, from spaceborne missions such as XMM (see e.g., `xmmssc.irap.omp.eu`) or Fermi, to the ground-based CTA facility (see e.g., `cta.irap.omp.eu`). An involvement in the data and VO-oriented activities of the space mission Euclid is also planned.

OV–GSO is supported by Cnrs/Insu, the *Université Paul Sabatier, Observatoire Midi–Pyrénées, Toulouse*, and the *Action Spécifique "Observatoire Virtuel"* of Cnrs.

References

Bass 2000: `bass2000.bagn.obs-mip.fr`
CASSIS: `cassis.irap.omp.eu`
CDPP: `cdpp.eu`
KIDA: `kida.obs.u-bordeaux1.fr`
PolarBase: `polarbase.irap.omp.eu`
POLLUX: `npollux.lupm.univ-montp2.fr`
STORMS: `stormsweb.irap.omp.eu`
The GSO Data Centre: `ov-gso.irap.omp.eu`

Génot, V., André, N., Cecconi, B., et al. 2014, Astronomy and Computing, 7, 62
Palacios, A., Gebran, M., Josselin, E., et al. 2010, A&A, 516, A13
Paletou, F., Zolotukhin, I. 2014 [`arXiv:1408.7026`]
Petit, P., Louge, T., Théado, S., et al. 2014, PASP, 126, 469
Wakelam, V., Herbst, E., Loison, J.-C., et al. 2012, ApJS, 199, 21

SF2A 2015
F. Martins, S. Boissier, V. Buat, L. Cambrésy and P. Petit (eds)

INNOVATIVE TECHNOLOGIES FOR AN OFF-AXIS TELESCOPE OPTIMIZED FOR ANTARCTICA

I. Vauglin[1], G. Moretto[1,2], M. Langlois[1] and N. Epchtein[3]

Abstract. It has long been demonstrated that the properties of the atmosphere above the Antarctic Plateau are unique on Earth, especially at Dome C. Already by the end of 2010, the European ARENA network roadmap summarized the exceptional atmospheric conditions that make the site uniquely favorable for infrared astronomy. To capitalize the remarquable Antarctica sites properties, we propose to develop an off-axis telescope, the only concept able to offer the highest possible dynamic range for photometry, the most reduced self thermal emissivity, a high angular resolution and a wide-field. An innovative technology has been proposed to produce the off-axis parabolic mirror and a proposal was submitted to the Horizon-2020 program on this subject (FET).

Keywords: infrared astronomy, instrumentation, Antarctica, optics

1 Introduction

As demonstrated by numerous campaigns since ten years (Aristidi et al. 2009 and references therein, Gredel 2010, and Aristidi et al. 2012), the Concordia scientific station on the Antarctic Plateau gather all the required advantages to become a major site for astronomical observations in the coming years, at all wavelengths but particularly in the infrared. The French-Italian station Concordia, at Dôme C, is successfully operating all year round since 2005. To benefit from the Antarctic performances, several countries have scientific stations, with astronomical observatories, currently operating or under development on other sites of the Antarctic Plateau.
At Concordia, an extremely cold and dry place, the sky transparency, particularly in the infrared, is considerably increased and the thermal infrared sky background radiation is lower by a factor of 10 to 20 in the 2-3 m window, compared to other sites like Mauna Kea or Paranal.
In the medium terms, the future large ground-based and space projects such as E-ELT, ALMA, JWST, EUCLID, GAIA will require new large scale surveys (such as LSST in the Northern hemisphere) to accompany their missions and key-programs to single out and follow-up new sources. We proposed to the ANR a New Generation Infrared Sky Survey (NGISS) from Antarctica, based on an off-axis telescope that could derive the greatest benefit from the polar atmospheric conditions (Vauglin et al. 2013). The only place on Earth where large and deep infrared surveys beyond 2.3μm can be carried out is the Antarctic Plateau. ANGISS is positioned to be able to perform unique and high impact science. It would supersede 2MASS survey by a factor ~ 1000 in sensitivity and ~ 3 in angular resolution and extend the spectral coverage beyond 2.3μm.
Not selected by the ANR, we keep going on with a R&D project of creating an aspheric mirror, based on a novel technology, submitted to FET-H2020.

2 Sciences drivers

The science cases have been extensively debated among the ARENA european network members to identify the highest priorities (see Epchtein et al. 2010 and references therein). The sciences programs proposed for ANGISS

[1] Centre de Recherche Astrophysique de Lyon, UMR 5574, F-69230, Saint-Genis Laval, France, Université Lyon1, Université de Lyon, F-69622, Lyon, France
[2] Institute of Nuclear Physics of Lyon, IN2P3-CNRS, Université de Lyon, F-69622, Lyon, France
[3] retired from Laboratory J-L. Lagrange, UNS, OCA, F-06108, Nice, France

© Société Francaise d'Astronomie et d'Astrophysique (SF2A) 2015

are uniquely possible with the exceptional polar atmospheric conditions of Dôme C using an off-axis telescope. This optical concept allows to minimize light scattering, to reduce self thermal emissivity, to have far superior contrast and to have a filled aperture - that means no azimuthal PSF structure and non missing wavefront errors. Coupled to a specific ground-layer adaptive optics (GLAO) technique matching the very thin turbulent layer of Dôme C (Carbillet et al. 2010), it will lead to a very performant high dynamic range telescope.
Thus, the combination of wavelength range, sensitivity, angular resolution, stability of the sky makes ANGISS unrivaled for studying:
(i) extra-solar planets and low mass K and M–type stars (detection and characterization of exoplanets with the transit and micro-lensing techniques)
(ii) the stellar populations in the Magellanic Clouds and other nearby galaxies to understand star forming processes
(iii) the distant universe: with the H_2 line, which is a tracer of star formation and peaks in the K band for galaxies at $z = 2$ to 3; the Type Ia supernovae light curves in the near infrared, much less affected by dust extinction and reddening in dusty galaxies, to improve constraints on the cosmological parameters.

The expected characteristics of the global system telescope, specific GLAO and infrared camera are given in table 1.

Primary mirror sizes	$\sim 2.5m$ (4m possible)
Configuration	Off-axis 3-mirror combination
Field of View	≥ 1 degree
Sky coverage (mini)	5000 $\deg^2$
Focal plane configuration	16 buttable HgCdTe Hawaii RG4
Spectral range	2-5 μm
Pixel scale	≤ 0.15 arcsec
Final PSF FWHM	0.3 arcsec
Field of view of the camera	40 arcmin $\times$ 40 arcmin
Filter set (3 minimal)	K_d, L_s, L' (+ possibly K_s, M', Grism, narrow bands)
Read out time	5 sec
Integration time per frame (typical)	100 s
Diameter of 80% encircled energy spot	≤ 0.2 arcsec
expected sensitivities (point source)	$K_d \sim 25.3$ / $L_s \sim 20.8$

Table 1. Main characteristics and performances of ANGISS camera on an off-axis telescope equipped with GLAO system

3 Technological developments

A better telescope concept, based on an off-axis optical design that allows excellent dynamic range for photometry, high angular resolution together with a wide field imaging is proposed. Thus, it capitalizes the exceptional atmospheric and environmental Antarctic conditions for astronomical observations over the optical and thermal infrared wavelengths.
One of the main goals of ANGISS project was to to design and build a ~ 50 cm prototype off-axis telescope to validate the concept and to design a GLAO device compliant with the specific atmospheric turbulence properties of the site, concentrated in a very thin layer (≤ 30 m).
To be upmost efficient from this unique environment, the instrument and focal instrumentation must be fully optimized. The three-mirror decentered, not tilted (Moretto et al. 2012 and Moretto et al. 2012b) provides an inherently low scattered light design, minimizing the emissivity of the telescope and is optimized for a wide 1x1 deg field of view. The optical performance across the field is shown in Figure 1. Note that the blur in this system is only weakly dependent on the off-axis angle and the telescope will be entirely seeing limited.

ANGISS has not been funded by ANR. We persevere because the observing conditions are really unique on Earth and also because France and Europe are at the forefront of polar research, having a vast experience in overwintering and operations in polar environnement.

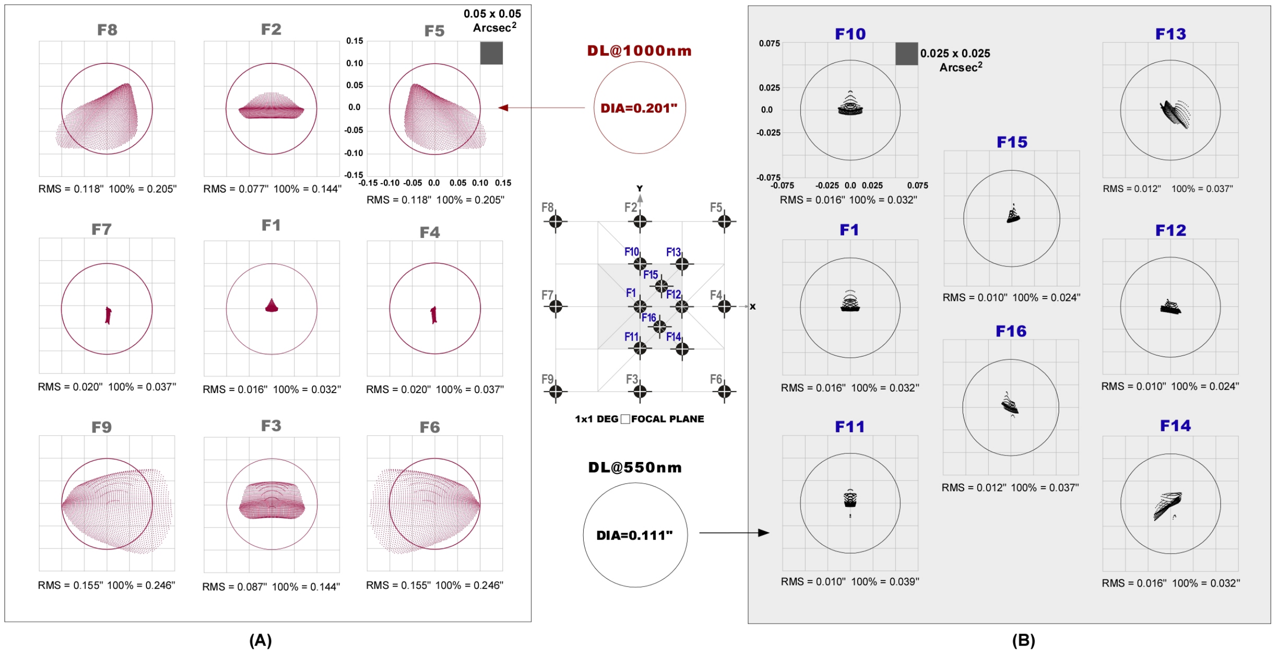

Fig. 1. Geometric optical performance over a flat Field Of View. Left: (A) The PSF computed on the edge and center of a 1×1 deg^2 FOV. Right: (B) The PSF computed across a 0.5 × 0.5 deg^2 FOV. The diffraction limit diameter is 0.111 arcsec at λ = 550 nm and 0.201 arcsec at λ = 1000 nm. Note in (A) : comparing spots F8&F5, F7&F4 and F9&F6 confirm the optical bi-lateral symmetry of the **decentered** system.

We proposed a project to the european Horizon 2020 Work Programme *Future and Emerging Technologies (FET)* called **Live-Mirror** (PI: G. Moretto). Innovative Optics Ltd. has developed a breakthrough *Live Mirror* technology yielding high quality smooth parabolic mirrors with less than 1/10th the scattered light of ordinary polished mirrors. The purpose of the Live-mirror project is to develop a cutting-edge technology aiming at creating large, extremely light-weight, diffraction-limited "live" mirror and optical system. The main goals of our project are to model, optimize and create large light-weight and accurate aspheric optical surfaces generated by a "deterministic non-contact slumping" technique, with extremely smooth optical surface which is never abrasively polished. The large-scale mirror shape is obtained with a controlled active 3D-printed force actuators and sensors.
The purpose of the project is to build and test a 1m diffraction-limited prototype to demonstrate these technologies after which it will be possible to build large precise off-axis parabolic mirrors at much lower cost.

4 Conclusions

Even if the current period is not favorable to future prospects of new telescopes and instruments in Antarctica, we are convinced that a performing camera mounted, with specific GLAO, on a the best possible telescope placed there will lead to major advances in the identified science cases. A medium aperture telescope on the Antarctic Plateau have the potential to undertake tasks previously thought to be possible only in space, for example the imaging and spectroscopy of Earth-like extra-solar planets.
The international efforts to develop astronomy from Antarctica became a Scientific Research Program of Scientific Committee on Antarctic Research (SCAR) in 2010, named Astronomy & Astrophysics from Antarctica (AAA). Broadly stated, its objectives are to coordinate astronomical activities in Antarctica in a way that ensures the best possible outcomes from international investment in Antarctic astronomy, and to maximize the opportunities for productive interaction with other disciplines.
The SCAR AAA third workshop was held on August 2015 in Hawaii during IAU General Assembly bringing together the key players in Antarctic astronomy to further develop SCAR AAA Plan and Tasks for Today (http://subarutelescope.org/Projects/scar_aaa/talks/session8/tasksfortoday.pdf). The efforts made by the French astronomers at Dome C were presented at this meeting.

References

Aristidi E., Fossat E., Agabi K. et al., 2009, A&A, 499, 955

Aristidi E., Agabi K., Fossat E., et al., 2012, Proc. IAU Symposium 288, 300

Carbillet M., Maire A.-L., Le Roux L., et al., 2010 Proc. third ARENA Conference on "An Astronomical Observatory at Concordia(Dome C, Antarctica)", Spinoglio L., Epchtein N., (eds.), EDP EAS Pub. Ser. **Vol. 40**, 157

Epchtein N. and Zinnecker H., 2009, The ARENA roadmap. Proc. of the International Astronomical Union, 5, pp 622-624. doi:10.1017/S1743921310010793.

Epchtein N. (coordinator) and the ARENA consortium, 2010, *A Vision for European Astronomy and Astrophysics at the Antarctic station Concordia, DomeC*, the ARENA roadmap, Novaterra (https://arena.oca.eu)

Gredel, R., 2010, Proc. 3rd ARENA Conf., eds. L. Spinoglio & N. Epchtein, EDP EAS Ser. Vol. 40, 11

Moretto G., Epchtein N., Langlois M., Vauglin I., 2012, Proc. of SPIE Vol. 8444, 84445E, 8

Moretto G.,Vauglin I.,Langlois M., Epchtein N., 2012, Proc. SF2A 2012, Eds S. Boissier, P. de Laverny, N. Nardetto, R. Samadi, D. Valls-Gabaud, H. Wozniak, 707

Vauglin I., Langlois M., Moretto G., 2013, Proc. SF2A 2013, Eds Cambresy L., Martins F., Nuss E., Palacios A., 37

SF2A 2015
F. Martins, S. Boissier, V. Buat, L. Cambrésy and P. Petit (eds)

ULTRA LUMINOUS X-RAY SOURCES

N. A. Webb[2,1] and O. Godet[1,2]

Abstract. Ultra Luminous X-ray sources (ULXs) are X-ray bright objects that are not coincident with the central nucleus of the host galaxy and which have luminosities that exceed the Eddington limit for a stellar mass black hole, typically L > 3 × 10^{39} erg s^{-1} for a black hole of 20 $M_\odot$. The nature of these objects is still unclear. However, it is possible that these sources do not form a single class of objects. Many ULXs may house stellar mass black holes accreting at super-Eddington rates, even if the physical mechanism for such high accretion rates is still not understood. Some ULXs may contain intermediate mass black holes (∼1 × 10^2 − ∼1 × 10^5 $M_\odot$). These elusive black holes are thought to be the building blocks of the more massive supermassive black holes, observed at the centre of many galaxies. Other ULXs may not be accreting black holes at all. Recent evidence for the different types of ULXs is presented in this paper.

Keywords: Stars: black holes, X-rays: binaries, Galaxies: evolution, Accretion, accretion disks

1 Introduction

During the late seventies the X-ray observatory *Einstein* detected non nuclear X-ray sources that have luminosities exceeding the Eddington luminosity ($L_{\rm Edd}$) of a stellar mass black hole (BH, Fabbiano 1989), where $L_{\rm Edd} = 1.3 \times 10^{38} (M/M_\odot)$ erg s^{-1}. These sources are now referred to as ultra-luminous X-ray sources (ULXs). Their nature as a population is still strongly debated, but given the fact that ULXs showed different spectral states, and some ULXs appeared to show spectral state transitions (Kubota et al. 2001), lent weight to the idea that most ULXs are stellar mass black holes accreting super-critically.

The physics describing super-critical accretion is still not clear (e.g. Walton et al. 2013b). Currently, different models are being proposed, e.g. Dotan & Shaviv (2011); Begelman (2002). It has been proposed that ULXs may only seem to exceed the Eddington limit. There are a variety of ways that an accreting source can appear to exceed the Eddington limit, e.g. via relativistic beaming (e.g. Freeland et al. 2006) or via geometric beaming (Paczyńsky & Wiita 1980), and thus appear to exhibit such high luminosities. However, it is generally accepted that many of the lower luminosity ULXs (L < 1 × 10^{41} erg s^{-1}) house stellar mass black holes (3-20 $M_\odot$, e.g. Walton et al. 2011), which are assumed to be accreting above the Eddington limit, as there is little evidence that the high luminosities are due to beaming, as most ULXs are seen to change state. In addition, two X-ray binaries in M 31 have been seen to transit into the ultra-luminous state and then return to their regular state, demonstrating that ULXs can be simply an ultra-luminous state of accreting compact objects (e.g. Middleton et al. 2012, 2013). None the less, there remains the possibility that these ULXs are simply higher mass stellar mass black holes ($20 < M_{BH} \lesssim 100\ M_\odot$) accreting below the Eddington limit e.g. Mapelli & Zampieri (2014); Zampieri & Roberts (2009). Determining the mass of the black hole in these objects is definitive in discerning between these two hypotheses. Also, studying the X-ray spectra (e.g. Gladstone et al. 2009) and X-ray timing properties (e.g. Middleton et al. 2015a), will reveal the physics behind the strong emission observed.

However, ULXs with L > 1 × 10^{41} erg s^{-1}, generally known as hyper luminous X-ray sources (HLXs, Gao et al. 2003) are difficult to explain without evoking more massive black holes, such as Intermediate Mass Black Holes (IMBHs) which have masses ∼1 × 10^2 − ∼1 × 10^5 $M_\odot$ (Gao et al. 2003; Farrell et al. 2009). This is because there is a limit to how much relativistic and geometric beaming is possible if the central object is a stellar mass black hole e.g. Freeland et al. (2006); King (2008). Whilst IMBH are evoked to explain the formation of

[1] Université de Toulouse; UPS-OMP, IRAP, Toulouse, France
[2] CNRS, IRAP, 9 av. Colonel Roche, BP 44346, F-31028 Toulouse cedex 4, France

© Société Francaise d'Astronomie et d'Astrophysique (SF2A) 2015

supermassive black holes ($1 \times 10^6 - 1 \times 10^{10}$ M$_\odot$), either through mergers and/or through (super-) Eddington accretion, (see Greene 2012; Volonteri 2012, for reviews), they remain elusive observationally. If HLXs do contain IMBH, they then become interesting for constraining the formation mechanisms of supermassive black holes.

All the same, a number of proposed ULXs have been shown to be supernova remnants e.g. Mezcua & Lobanov (2011), accreting white dwarfs e.g. Li et al. (2012), background AGN e.g. Dadina et al. (2013), amongst other things. It is clear that ULXs are therefore not a homogeneous sample of sources. Thanks to recent observations of ULXs with (hard) X-ray observatories, such as *XMM-Newton*, *Chandra* and more recently *NuSTAR* (Harrison et al. 2013), coupled with complimentary multi-wavelength observations, the nature of ULXs has been shown to be highly diverse. In this review article we discuss some of the more recent observational results concerning the nature of ULXs and discuss their implications.

2 Stellar mass black holes accreting above the Eddington limit

One of the best ways to unequivocally determine the mass of the accreting object is to determine it using a dynamical mass estimate, i.e. through the radial velocity motion of one or both the stars in the binary system and using Kepler's laws. This is actually difficult to do, as no object is observed to be a ULX in our own galaxy, and such observations are difficult to achieve for ULXs in other galaxies due to the large distances and hence relatively faint sources. Additionally, previous attempts to detect a spectral lines from the companion have revealed blue, almost featureless spectra (e.g. Zampieri et al. 2004; Kaaret & Corbel 2009; Grisé et al. 2012) which are probably dominated by the accretion disc and in some cases show evidence of the surrounding nebula. The companion star is therefore not detected.

Recently, however, Motch et al. (2014) observed a ~64 day period from the ULX P13 in the galaxy NGC 7793 using optical photometry. They confirmed the period using optical spectroscopy of the companion star which they revealed to be a B9Ia star. The mass of the companion star was estimated to be 18-23 M$_\odot$. Using radial velocity measurements and thanks to Kepler's laws, the mass of the black hole was shown to be $\lesssim$ 15 M$_\odot$. The binary has an eccentricity of 0.27-0.41. Given that the X-ray luminosity of the P13 is $\sim 4 \times 10^{39}$ erg s^{-1}, the black hole is accreting at at least twice Eddington, even if it is as massive as 15 M$_\odot$, confirming the stellar mass nature of the black hole, but also demonstrating that the black hole accretes super-critically. Further, this study shows that given the evolved nature of the donor star, the mass transfer must occur on a thermal timescale ($\sim 10^5$ yr) as the supergiant rapidly expands. This is more than an order of magnitude shorter than its main sequence life time. This then implies that supergiant ULXs are much more rare than systems with unevolved mass-donors.

The other major result from Motch et al. (2014) is that they show for the first time that the X-ray spectrum that they observe from P13 and which is typical of many ULXs, with both a medium energy break and a soft X-ray excess, is indeed the signature of an Eddington or super-Eddington regime. This supports the *NuSTAR* results (e.g. Bachetti et al. 2013; Walton et al. 2013a) that many of the lower luminosity ULXs (L $< 1 \times 10^{41}$ erg s^{-1}) are indeed stellar mass black holes accreting super-critically. Understanding the physical mechanism for this extreme accretion is not only useful for understanding the population of ULXs, but also the earliest and most massive super-massive black holes that may require super-critical accretion to achieve such masses at early times e.g. Willott et al. (2010).

3 Intermediate mass black hole candidates

Dozens of HLX sources proposed to house an intermediate mass black hole have been proposed in recent years. However, either these objects are observed only once e.g. Gao et al. (2003) and references therein or they are more often than not, shown to be either foreground or background objects e.g. Sutton et al. (2015). The serendipitous discovery of 2XMM J011028.1–460421 (hereafter Hyper Luminous X-ray source - HLX-1) with XMM-Newton on 23 November 2004 in the outskirts of the edge-on spiral galaxy ESO 243–49 at a distance of 95 Mpc marked a milestone with the most secure identification of a HLX (Farrell et al. 2009; Wiersema et al. 2010). With a 0.2-10 keV unabsorbed luminosity reaching 1.3×10^{42} erg s^{-1} at peak, HLX-1 is the brightest HLX detected so far. Spectral modelling of X-ray data with sophisticated accretion disk models (Davis et al. 2011; Godet et al. 2012b; Straub et al. 2014) and Eddington scaling of X-ray/radio data (Servillat et al. 2011; Webb et al. 2012) gave us a range of mass estimates from 9,000 to 90,000 M$_\odot$, placing it in the IMBH mass range. Multi-wavelength observations of HLX-1 over the past six years showed that HLX-1 displays several properties similar to those observed in stellar mass BH X-ray binaries (Remillard & McClintock 2006), contrary to other lower luminosity ULXs: i) regular outbursts with state transitions, but with X-ray luminosities orders of magnitude larger (Godet et al. 2009; Servillat et al. 2011; Godet et al. 2012b) ; ii) the detection of radio transient emission with ATCA interpreted as discrete jet ejection events following the hard-to-soft transitions (Webb et al. 2012; Cseh et al. 2015); iii) the possible detection of a radio compact jet when the source is in the hard state (Cseh et al. 2015). By modelling HST and *Swift*-XRT data, Farrell et al. (2012) showed that the HLX-1 host could be a globular cluster-like cluster or the stripped nucleus remnant of a dwarf galaxy formed following an interaction with ESO 243-49.

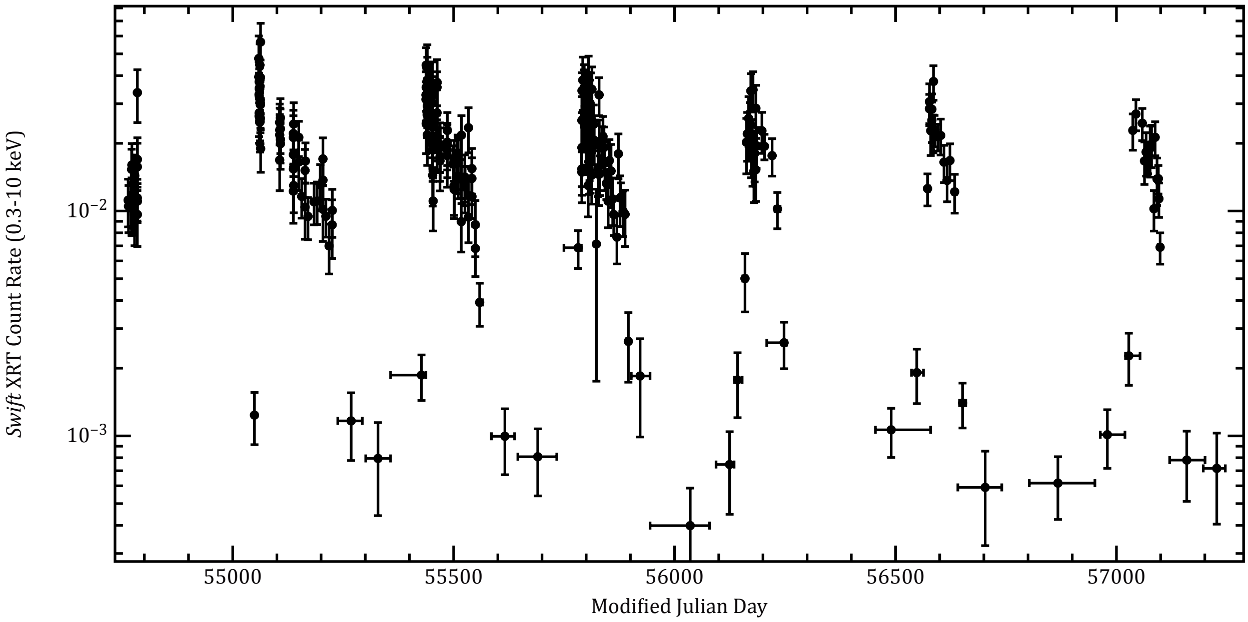

Fig. 1. The Swift X-ray lightcurve of ESO 243-49 HLX-1 from 2008-2015.

The *Swift*-XRT light-curve from 2009 to 2012 shows FRED-like outbursts separated by an apparent recurrence time of nearly a year, see Fig. 1. Since 2013, the time interval between the outbursts has increased by more than a month for the outburst starting in October 2013 (56570 MJD) and around three months for the one starting in January 2015 (57030 MJD). The spectral properties of these two last outbursts are consistent with those seen in previous outbursts, but with a possible moderate spectral softening for the 2015 outburst. Lasota et al. (2011) proposed that the X-ray light-curve is the result of enhanced mass transfer from an Asymptotic Giant Branch star in an eccentric orbit occurring when the star passing at periapsis is tidally stripped. Using contemporary optical (VLT) and X-ray (*Swift*-XRT) observations over the rise of the outburst, Webb et al. (2014) showed that a fraction of the optical emission comes from the accretion disk and that the optical might start just before the X-rays indicating an outside-in outburst and a distance from the delivery-mass radius to the inner edges of the disk to be less than $\sim 10^{11}$ cm. This implies a highly eccentric orbit ($e \rightarrow 1$) and therefore a possibly unstable and potentially short-lived system. From Fig 1, it is also clear that the duration of the outbursts decreases over time until the 2015 outburst. Indeed, the duration of the outbursts decreased from ~ 170 days in 2009 to $\sim 65 - 72$ days in 2013. The duration of the 2015 outburst was slightly longer than that measured in 2013. This might indicate a change in the supply of matter to the IMBH or in the accretion flow.

Godet et al. (2014) investigated through a series of smoothed particle hydrodynamical simulations the origin of the delay in the framework of the mass transfer model and the consequences for the IMBH-star system (e.g. the evolution of the orbital period over time, the system lifetime, the constraints on the donor type). Godet et al. (2014) followed a large number of dynamical timescales (from 6000 to 70000) in order to study the evolution of such a system. Once the system is formed with an eccentricity always close to 1, the orbital period (P) decreases until reaching a minimum. Then, the period tends to increase over several periapsis passages due to tidal effects and increasing mass transfer, leading ultimately to the star ejection. The development of stochastic fluctuations inside the donor could lead to sudden changes in P from orbit to orbit with the appropriate order of magnitude of what has been observed for HLX-1 so far. They also showed that if the HLX-1 orbital period is currently near a minimum ($P \sim 1$ yr) and provided that $M_{BH} > 10^4$ $M_\odot$, the donor has to be a white dwarf (WD) or a stripped giant core. If $P_{\rm min} \sim 1$ yr and $M_{BH} < 10^4$ $M_\odot$, then there is no viable solution for the donor star. Recently, MacLeod et al. (2015) used N-body simulations to investigate the close stellar companions of IMBHs located in globular clusters. They found that most bound companion stars (including white dwarfs) could suffer grazing tidal interactions with the hole.

HLX-1 is clearly very different from regular ULXs and all the observations support the IMBH hypothesis for accreting compact object. Recently, a similar object has been proposed (Heida et al. 2015; Jonker et al. 2010). CXO J122518.6+144545 has shown a maximum luminosity of 2.2×10^{41} erg s^{-1}, with X-ray variability with a factor >60 and repeated outbursts. This will be an interesting object to follow up to confirm its nature. Using radio and X-ray observations and the black hole fundamental (e.g. Falcke et al. 2004), Mezcua et al. (2015) have identified another IMBH candidate of $\sim 5 \times 10^4$ $M_\odot$, so it appears that at least some types of ULXs may host the much sought after IMBH. It would then be instructive to determine their number and distribution, so as to assess their role in the formation of supermassive black holes (e.g. Volonteri 2012; Greene 2012). Other searches for similar sources are therefore underway e.g. Zolotukhin et al. (accepted).

4 Other types of ULXs

As outlined in Sec. 1, ULXs have been shown to be a heterogeneous set of objects. The most extreme and surprising result in recent years is the identification of a neutron star in the ULX M 82 X-2 (Bachetti et al. 2014). M 82 X-2 reaches maximum X-ray luminosities of 1.8×10^{40} erg s^{-1}, is highly variable, and has an X-ray spectrum similar to other ULXs of a similar luminosity. These characteristics would therefore lead us to expect a stellar mass black hole accreting super-critically or a more massive stellar mass black hole accreting at or close to the Eddington limit (see Sec. 2). M 82 was pointed by the hard X-ray observatory *NuSTAR* at the beginning of 2014, for almost 2 Ms to observe the type 1a supernova, SN 2014J. M 82 X-2 was also in the field of view and the long exposure revealed a highly periodic signal (pulse period 1.37 s, 30 σ significance) from this ULX. Not only was a pulse detected, a strong spin up of the period of 2.2×10^{-10} s s^{-1} was discovered and a longer period of 2.53 d was also identified. Only a very compact object (neutron star or black hole) can have such a short period, but to have such a rapid spin up, the object requires a surface, demonstrating that the accreting object is a neutron star and thus emits at 100 times the Eddington limit.

This result implies that ULXs may not only host black holes as their compact object, but also host neutron stars. It also shows that an object can (appear to) emit at highly super-Eddington luminosities for extended periods. This surprising result has triggered a lot of work in understanding how this could occur. Bachetti et al. (2014) suggest that the neutron star may have a fan beam geometry and if viewed at a favourable angle, the observed pulse profile could be produced and the accretion stream could become sufficiently collimated to generate the observed luminosities. Shao & Li (2015) show that just after the onset of Roche lobe overflow in a system like M 82 X-1 with a companion star of mass > 5.2 M$_\odot$, the mass ratio of the stars is such that the mass transfer rate can not be stable and increases rapidly to become super-Eddington, allowing the binary to transition to a ULX for $\sim 10^5$ years. Thus it would be possible to have a population of neutron star X-ray binaries contributing significantly to the ULX population. Shao & Li (2015) show that high-mass and intermediate-mass X-ray binaries dominate the neutron star ULX population in M 82- and Milky Way-like Galaxies, respectively. Wiktorowicz et al. (2015) support this by showing that several binary evolutionary channels lead to phases of very high mass transfer rate in close Roche lobe overflow binaries, so that any ULX, including the most luminous ones, may potentially be a short-lived phase in the life of a binary star.

5 Discussion

As discussed above, the term ULX denotes a highly inhomogeneous group of objects, some which appear to be accreting super-critically, whilst others below the Eddington limit. Not only that, the accreting compact object ranges from neutron stars and stellar mass black holes and quite probably all the way to intermediate mass black holes. As the number of ULXs grows, it is quite likely that sub-groups of these objects will be formed, above and beyond the standard ULX and HLX division. Indeed, some authors have already attempted to make this sub-division. Gladstone (2013) propose a third class, the 'Extreme Ultra Luminous X-ray Sources' composed of objects with X-ray luminosity of 2×10^{40} erg s^{-1} - 1×10^{41} erg s^{-1}. This luminosity range includes the break in the X-ray luminosity function in our local Universe and the luminosity due to accretion onto extreme massive stellar remnant black hole accretors. Sutton et al. (2013) defined an empirical classification scheme based on spectral morphology and timing properties. Below $\sim 3 \times 10^{39}$ erg s^{-1} the disc X-ray spectra are broad, consistent with a population of stellar mass black holes (M $\lesssim 20$ M$_\odot$), accreting at, or just above, the Eddington limit. ULXs with luminosities above this value and up to $\sim 2 \times 10^{40}$ erg s^{-1} with broad X-ray spectra may be powered by accretion onto larger black hole primaries, although higher beaming factors remain a possibility. Brighter sources show either hard ultraluminous spectra with fractional variability much less than 10% or soft ultraluminous spectra with 10-30% fractional variability. This is thought to be due to the large winds created at these high luminosities and the spectral and timing differences are due to viewing angle, where looking down the opening angle of the wind, the geometrically-beamed hard emission from the central source dominates, and at higher inclinations to our line-of-sight a wind-dominated soft ultraluminous spectrum is seen. This creates a unified model for the majority of ULXs, but does not allow us to distinguish between neutron star or intermediate mass black hole accretors, for example, see e.g. Middleton et al. (2015a).

Obviously more work remains to be done to validate this model and understand where the outliers to this generalisation fit in. Continued observations to monitor the variability of all types of ULXs with *Swift* and in the future with *SVOM* (e.g. Godet et al. 2012a), will allow us to understand the transitions between ULX spectral states, that are for the most part, quite different to those observed for sub-Eddington X-ray binaries. Using the high resolution gratings on *XMM-Newton* and *Chandra* should also give us some insight into the nature and importance of the wind in ULXs (e.g. Middleton et al. 2015b). These winds may also be investigated by studying the optical emission-line nebulae that are sometimes seen around ULXs, and are thought to be due to shock-ionised driven jets, outflows or disc winds and/or because of photo-ionisation from the X-ray and UV emission around the black hole. In the future, sensitive radio observatories such as the *SKA* will be able to look for emission emanating from (possible) jets and nebulae in ULXs, extending recent work carried out with the VLBI (Mezcua et al. 2013). This will enable us to constrain whether the source is in a low hard state, as oppose to the hard ultra-luminous state, for example, giving us the nature of the compact accretor. The nebulae can also serve as a calorimeter, implying the total intrinsic power of the ULX, (e.g. Pakull & Mirioni 2002, 2003). They can be used to understand how outflows and photo-ionisation can play a role in the behaviour of the ULX and on its surrounding environment (e.g. Pakull & Mirioni 2002, 2003). In the optical, future surveys such as the *Large Synoptic Survey Telescope* (*LSST*)* from 2022, will observe the sky using an 8.4 m telescope. This will allow us to identify new and monitor known transient ULXs in order to identify ULXs under-going state transition. Observations with the proposed *Extremely Large Telescopes* which should be able to achieve excellent signal to noise for good resolution spectra of ULX companion stars, will allow us to make dynamical mass measurements of many of the known (and still to be found) ULXs in a similar way to Motch et al. (2014), thus allowing us to unequivocally determine the nature and mass of the compact accretor. Future X-ray observations with the X-ray observatory *Athena* (Nandra et al. 2013) will be able to probe the accretion regime, allowing us to finally understand these diverse and extreme objects.

References

Bachetti, M., Harrison, F. A., Walton, D. J., et al. 2014, Nature, 514, 202

Bachetti, M., Rana, V., Walton, D. J., et al. 2013, ApJ, 778, 163

Begelman, M. C. 2002, ApJ, 568, L97

Cseh, D., Webb, N. A., Godet, O., et al. 2015, MNRAS, 446, 3268

Dadina, M., Masetti, N., Cappi, M., et al. 2013, A&A, 559, A86

Davis, S. W., Narayan, R., Zhu, Y., et al. 2011, Astrophys. J., 734, 111

Dotan, C. & Shaviv, N. J. 2011, MNRAS, 413, 1623

Fabbiano, G. 1989, in European Southern Observatory Conference and Workshop Proceedings, Vol. 32, European Southern Observatory Conference and Workshop Proceedings, ed. E. J. A. Meurs & R. A. E. Fosbury, 325

Falcke, H., Körding, E., & Markoff, S. 2004, A&A, 414, 895

Farrell, S. A., Servillat, M., Pforr, J., et al. 2012, ApJ, 747, L13

Farrell, S. A., Webb, N. A., Barret, D., Godet, O., & Rodrigues, J. M. 2009, Nature, 460, 73

Freeland, M., Kuncic, Z., Soria, R., & Bicknell, G. V. 2006, MNRAS, 372, 630

Gao, Y., Wang, Q. D., Appleton, P. N., & Lucas, R. A. 2003, ApJ, 596, L171

Gladstone, J. C. 2013, Mem. Soc. Astron. Italiana, 84, 629

* `http://www.lsst.org/lsst/`

Gladstone, J. C., Roberts, T. P., & Done, C. 2009, MNRAS, 397, 1836

Godet, O., Barret, D., Webb, N. A., Farrell, S. A., & Gehrels, N. 2009, Astrophys. J., 705, L109

Godet, O., Lombardi, J. C., Antonini, F., et al. 2014, ApJ, 793, 105

Godet, O., Paul, J., Wei, J. Y., et al. 2012a, in Society of Photo-Optical Instrumentation Engineers (SPIE) Conference Series, Vol. 8443, Society of Photo-Optical Instrumentation Engineers (SPIE) Conference Series, 1

Godet, O., Plazolles, B., Kawaguchi, T., et al. 2012b, ApJ, 752, 34

Greene, J. E. 2012, Nature Communications, 3, 1304

Grisé, F., Kaaret, P., Corbel, S., et al. 2012, ApJ, 745, 123

Harrison, F. A., Craig, W. W., Christensen, F. E., et al. 2013, ApJ, 770, 103

Heida, M., Jonker, P. G., & Torres, M. A. P. 2015, MNRAS, 454, L26

Jonker, P. G., Torres, M. A. P., Fabian, A. C., et al. 2010, MNRAS, 407, 645

Kaaret, P. & Corbel, S. 2009, ApJ, 697, 950

King, A. R. 2008, MNRAS, 385, L113

Kubota, A., Mizuno, T., Makishima, K., et al. 2001, ApJ, 547, L119

Lasota, J.-P., Alexander, T., Dubus, G., et al. 2011, ApJ, 735, 89

Li, K. L., Kong, A. K. H., Charles, P. A., et al. 2012, ApJ, 761, 99

MacLeod, M., Trenti, M., & Ramirez-Ruiz, E. 2015, ArXiv e-prints [arXiv] 1508.07000

Mapelli, M. & Zampieri, L. 2014, ApJ, 794, 7

Mezcua, M., Farrell, S. A., Gladstone, J. C., & Lobanov, A. P. 2013, MNRAS, 436, 1546

Mezcua, M. & Lobanov, A. P. 2011, Astronomische Nachrichten, 332, 379

Mezcua, M., Roberts, T. P., Lobanov, A. P., & Sutton, A. D. 2015, MNRAS, 448, 1893

Middleton, M. J., Heil, L., Pintore, F., Walton, D. J., & Roberts, T. P. 2015a, MNRAS, 447, 3243

Middleton, M. J., Miller-Jones, J. C. A., Markoff, S., et al. 2013, Nature, 493, 187

Middleton, M. J., Sutton, A. D., Roberts, T. P., Jackson, F. E., & Done, C. 2012, MNRAS, 420, 2969

Middleton, M. J., Walton, D. J., Fabian, A., et al. 2015b, ArXiv e-prints [arXiv] 1509.06760

Motch, C., Pakull, M. W., Soria, R., Grisé, F., & Pietrzyński, G. 2014, Nature, 514, 198

Nandra, K., Barret, D., Barcons, X., et al. 2013, ArXiv e-prints [arXiv] 1306.2307

Paczyńsky, B. & Wiita, P. J. 1980, A&A, 88, 23

Pakull, M. W. & Mirioni, L. 2002, ArXiv Astrophysics e-prints astro-ph/0202488

Pakull, M. W. & Mirioni, L. 2003, in Revista Mexicana de Astronomia y Astrofisica Conference Series, Vol. 15, Revista Mexicana de Astronomia y Astrofisica Conference Series, ed. J. Arthur & W. J. Henney, 197–199

Remillard, R. A. & McClintock, J. E. 2006, ARA&A, 44, 49

Servillat, M., Farrell, S. A., Lin, D., et al. 2011, Astrophys. J., 743, 6

Shao, Y. & Li, X.-D. 2015, ApJ, 802, 131

Straub, O., Godet, O., Webb, N., Servillat, M., & Barret, D. 2014, A&A, 569, A116

Sutton, A. D., Roberts, T. P., Gladstone, J. C., & Walton, D. J. 2015, MNRAS, 450, 787

Sutton, A. D., Roberts, T. P., & Middleton, M. J. 2013, MNRAS, 435, 1758

Volonteri, M. 2012, Science, 337, 544

Walton, D. J., Fuerst, F., Harrison, F., et al. 2013a, ApJ, 779, 148

Walton, D. J., Miller, J. M., Harrison, F. A., et al. 2013b, ApJ, 773, L9

Walton, D. J., Roberts, T. P., Mateos, S., & Heard, V. 2011, MNRAS, 416, 1844

Webb, N., Cseh, D., Lenc, E., et al. 2012, Science, 337, 554

Webb, N. A., Godet, O., Wiersema, K., et al. 2014, ApJ, 780, L9

Wiersema, K., Farrell, S. A., Webb, N. A., et al. 2010, Astrophys. J., 721, L102

Wiktorowicz, G., Sobolewska, M., Sagondowski, A., & Belczynski, K. 2015, ApJ, 810, 20

Willott, C. J., Albert, L., Arzoumanian, D., et al. 2010, AJ, 140, 546

Zampieri, L., Mucciarelli, P., Falomo, R., et al. 2004, ApJ, 603, 523

Zampieri, L. & Roberts, T. P. 2009, MNRAS, 400, 677

Session 01

Rosetta

SF2A 2015
F. Martins, S. Boissier, V. Buat, L. Cambrésy and P. Petit (eds)

SUBSURFACE CHARACTERIZATION OF 67P/CHURYUMOV-GERASIMENKO'S ABYDOS SITE

B. Brugger[1], O. Mousis[1], A. Morse[2], U. Marboeuf[3], L. Jorda[1], A. Guilbert-Lepoutre[4], D. Andrews[2], S. Barber[2], P. Lamy[1], A. Luspay-Kuti[5], K. Mandt[5], G. Morgan[2], S. Sheridan[2], P. Vernazza[1] and I.P. Wright[2]

Abstract. We investigate the subsurface structure of comet 67P/Churyumov-Gerasimenko at the landing site of Rosetta's descent module Philae. We use a cometary nucleus model with an optimized parametrization and assume an initial composition derived from Rosetta/ROSINA measurements. We compare the CO and CO_2 outgassing rates derived from our model with those measured *in situ* by the Ptolemy experiment aboard the Philae module on November 12, 2014. We find results that allow us to place two main constraints on the subsurface structure of this region: a low CO/CO_2 molar ratio is needed in the nucleus, and the dust/ice mass ratio is higher at Abydos than in the rest of the nucleus. These specific constraints on Abydos support the statement of an important heterogeneity in 67P/Churyumov-Gerasimenko's nucleus.

Keywords: comets: individual (67P/Churyumov-Gerasimenko), solid state: volatile, methods: numerical

1 Introduction

On November 12, 2014, Rosetta's descent module Philae landed on the Abydos site of comet 67P/Churyumov-Gerasimenko (67P). Among the instruments onboard Philae, the Ptolemy mass spectrometer performed the analysis of several samples collected from the surface and atmosphere of the comet (Morse et al. 2015), with the detection of H_2O, CO and CO_2 giving a value of 0.07 ± 0.04 for the CO/CO_2 molar ratio. This value is substantially different from the production rates measured in 67P's coma by the ROSINA double mass spectrometer aboard the Rosetta spacecraft. Thus we investigate the structure of the subsurface of the Abydos site. To do so, we employ a cometary nucleus model with an updated set of thermodynamic parameters relevant for 67P, assuming that the composition of the solid phase located beneath the landing site initially corresponds to the value in the coma. Thus, we selected the measurements performed by ROSINA on August 7, 2014 (the spacecraft's closest flyby date of the Abydos region), giving a CO/CO_2 molar ratio of 1.62 ± 1.34 (Hässig et al. 2015). The comparison of the production rates derived from our model with those measured by Ptolemy allows us to place important constraints on the structure (layering and composition) of the subsurface of Philae's landing site.

2 The cometary nucleus model

The one-dimensional cometary nucleus model used in this work is the one depicted in Marboeuf et al. (2012). This model considers an initially homogeneous sphere composed of a predefined porous mixture of ices and dust in specified proportions. It describes heat transmission, gas diffusion, sublimation/recondensation of volatiles within the nucleus, water ice phase transition, dust release, and dust mantle formation. Using a 3D geometric

[1] Aix Marseille Université, CNRS, LAM (Laboratoire d'Astrophysique de Marseille) UMR 7326, 13388, Marseille, France (bastien.brugger@lam.fr)
[2] Planetary and Space Sciences, Department of Physics, The Open University, Walton Hall, Milton Keynes MK7 6AA, UK
[3] Space Science & Planetology, Physics Institute, University of Bern, Sidlerstrasse 5, 3012 Bern, Switzerland
[4] Institut UTINAM, UMR 6213 CNRS-Université de Franche-Comté, Besançon, France
[5] Department of Space Science, Southwest Research Institute, 6220 Culebra Rd., San Antonio, TX 78228, USA

© Société Francaise d'Astronomie et d'Astrophysique (SF2A) 2015

model developed by Jorda et al. (2014), we determine orbital parameters of comet 67P as well as we correctly reproduce the illumination conditions at Abydos (see Table 1). Porosity and dust/ice mass ratio in the cometary material have been chosen to match the value of the nucleus' density determined by Jorda et al. (2014) (510 $\pm$ 20 kg/m^3).

In addition to water ice and dust, the solid phase of our model includes CO and CO_2 whose abundances, inferred from the ROSINA observations of August 7, 2014, are $CO/H_2O = 0.13 \pm 0.07$ and $CO_2/H_2O = 0.08 \pm 0.05$ (Hässig et al. 2015). In this model, water ice is fully crystalline, making it impossible to trap volatile molecules. Thus, CO and CO_2 are crystallized in the pores of the matrix beside water ice.

Table 1. Modeling parameters for the nucleus

Parameter	Value	Reference
Rotation period (hr)	12.4	Mottola et al. (2014)
Obliquity (degree)	52.25	
Argument of subsolar meridian at perihelion (degree)	-111	
Co-latitude (degree)	-21	
Initial radius (km)	2.43	
Bolometric albedo (%)	1.5	Fornasier et al. (2015)
Dust/ice ratio	4 $\pm$ 2	Rotundi et al. (2014)
Porosity (%)	65 $\pm$ 15	Iida et al. (2010)
Density (kg/m^3)	510 $\pm$ 20	Jorda et al. (2014)
Thermal inertia (W K^{-1} m^{-2} s$^{1/2}$)	50	Leyrat et al. (2015)
CO/CO_2 initial ratio	1.62 $\pm$ 1.34	Hässig et al. (2015)

3 Thermal evolution of the subsurface at Abydos

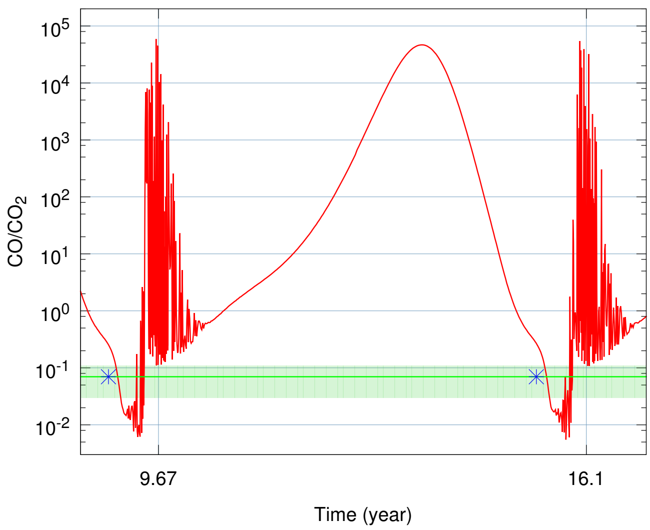

Fig. 1. Evolution of the CO/CO_2 outgassing ratio at Abydos during one orbit. The green line and area represent the Ptolemy central value and its range of uncertainty, respectively. The blue dots correspond to the measurement epoch (November 12, 2014). Vertical lines show the passages at perihelion.

Figure 1 represents the evolution of the CO/CO_2 ratio outgassing throughout the surface of the Abydos site as a function of the orbital evolution of 67P. This process is entirely following the sublimation of CO and CO_2 in the pores of nucleus material, leading to interfaces of sublimation of both species that reach deeper layers in the nucleus, until perihelion is reached and the ablation of the surface erases the progression of these interfaces. Thus, the outgassing rates of both molecules follow the same trend at Abydos during each orbit, irrespective of the considered period. Because the sublimation interface of CO_2 is closer to the surface, its production rate is more sensitive to illumination conditions than CO. The CO/CO_2 ratio thus varies over several orders of magnitude, depending on the comet's position on its orbit. Close to perihelion, this ratio crosses the range of values measured by Ptolemy (0.07 ± 0.04) and reaches a minimum.

A quantitative characterization of our simulation is made possible by measuring the delay taken by the CO/CO_2 ratio to match the value measured by Ptolemy on November 12, 2014 - using the actual measurement epoch as a reference. To improve the results of a simulation, we minimize this time difference by exploring the parameters' ranges of values. This study shows that two quantities have a strong influence on the time difference: the initial CO/CO_2 ratio in the nucleus, and the dust/ice mass ratio. With $CO/CO_2 = 0.46$ and a dust/ice ratio of 6 or higher (because of the suspected heterogeneity of 67P's nucleus), we are able to match Ptolemy's measurement epoch with about 50 days difference, corresponding to less than 2% of error on 67P's cometary year (6.44 terrestrial years).

4 Conclusion

Our model allows us to place constraints on the structure and composition of the comet's subsurface at Abydos: a low initial CO/CO_2 ratio is needed in the composition of the subsurface of Abydos to better match the measure performed by Ptolemy. The minimal value of the range measured by ROSINA in 67P's coma for this quantity is at least needed at Abydos to obtain results under 2% of error. Beside, the dust/ice mass ratio has to be taken in the upper values of the range determined by Rotundi et al. (2014) for 67P. Values even higher for the dust/ice ratio are desirable if we want to improve the time difference to match Ptolemy's data, supporting the hypothesis of a heterogeneous nucleus for 67P.

O.M. acknowledges support from CNES. This work has been partly carried out thanks to the support of the A*MIDEX project (n° ANR-11-IDEX-0001-02) funded by the "Investissements d'Avenir" French Government program, managed by the French National Research Agency (ANR).

References

Fornasier, S., Hasselmann, P. H., & Barucci, M. A., et al. 2015, A&A, in press (eprint arXiv:1505.06888)

Hässig, M., Altwegg, K., Balsiger, H., et al. 2015, Science, 347, 276

Iida, Y., Tsuchiyama, A., Kadono, T., et al. 2010, Meteoritics and Planetary Science, 45, 1302

Jorda, L., Gaskell, R. W., Hviid, S. F., et al. 2014, AGU Fall Meeting Abstracts, 3943

Leyrat, C., Erard, S., Capaccioni, F., et al. 2015, EGU General Assembly Conference Abstracts, 17, 9767

Marboeuf, U., Schmitt, B., Petit, J.-M., Mousis, O., & Fray, N. 2012, A&A, 542, A82

Morse, A., Mousis, O., Sheridan, S., et al., A&A, in press

Mottola, S., Lowry, S., Snodgrass, C., et al. 2014, A&A, 569, L2

Rotundi, A., Rietmeijer, F. J. M., Ferrari, M., et al. 2014, Meteoritics and Planetary Science, 49, 550

Rubin, M., Altwegg, K., Balsiger, H., et al. 2015, Science, 348, 232

SF2A 2015
F. Martins, S. Boissier, V. Buat, L. Cambrésy and P. Petit (eds)

SIMULATION OF THE ELECTROSTATIC CHARGING OF PHILAE ON 67P/CHURYUMOV-GERASIMENKO AND OF ITS INTERACTION WITH THE DUSTS.

S. L. G. Hess[1], P. Sarrailh[1], J.-C. Matéo-Vélez[1], J. Forest[2], B. Jeanty-Ruard[2] and F. Cipriani[3]

Abstract. ROSETTA's probe Philae landed on a dust covered soil. This dust may be ejected from the ground through many mechanisms (other than spacecraft landing) : micro-meteorite impacts, electrostatic charging and soil outgassing. In any cases, the dust grains charge electrostatically in the ambient plasma and this charge impacts the dust interaction with the spacecraft, which is itself differentially charged due to its partial exposure to the solar UV light. Using the DUST addition to the Spacecraft-Plasma Interaction Software (SPIS) routinely used to compute the charge state of the spacecraft surfaces, we simulate the electrostatic charging of Philae as well as its dust environment. SPIS-DUST allows one to compute the electrostatic charging of the dust grains on the ground and in the plasma, and to model their ejection and their recollection by the probe. We simulated one cometary day of the Philae environment at different distances from the sun to observe the variation of the dust collection with Philae's local time.

Keywords: Comet, Rosetta, Philae, Dust

1 Introduction

The Rosetta spacecraft reached comet 67P/Churyumov-Gerasimenko on August 2014 and was inserted into orbit, on November Philae separated from Rosetta and landed on the comet. After a first touchdown close to the expected landing site, Philae bounced and finally stopped in a more chaotic region after several touchdowns (Biele et al. 2015). In particular, the lander attitude and its position close to a cliff jeopardized its chances to survive. Eventually, the probe received enough power from the sun later in Rosetta's mission and brought new information on the comet surface. Among Philae missions, the Dust Impact Monitor collects dusts. Although it is expected that most of the dusts will be ejected from the ground because of the sublimation of volatile materials in the soil, these neutral dust grains will interact with the plasma and acquire an electric charge that can modify their interaction with Philae and its instruments. The present study concentrates on the determination of the importance of dust charging on the dust collection by Philae.

2 Numerical Model

2.1 SPIS

The Spacecraft-Plasma Interaction Software (SPIS) is an open source tool (available along with a more detailed description at `http://dev.spis.org`) for the simulation of the charging of materials in a plasma environment (Roussel et al. 2008, 2012). First developed to simulate the charge of artificial satellites in space (Roussel et al. 2008), it was later developed to simulate plasma experiments on the ground (Matéo-Vélez et al. 2008), scientific probes aboard interplanetary probes (Guillemant et al. 2012, 2013), and is currently being extended to allow for the simulation of the dust charging and transport (Hess et al. 2015). This simulation scheme is essentially electrostatic, even though a background magnetic field can be set that acts on the particle motions. The electric

[1] ONERA - The French Aerospace Lab, 31055 Toulouse, France
[2] Artenum, 75010 Paris, France
[3] ESA/ESTEC, 2201 AZ Noordwijk, The Netherlands

© Société Francaise d'Astronomie et d'Astrophysique (SF2A) 2015

potential is computed by solving the Poisson equation across the simulation domain.
SPIS allows for the use of multiple schemes for the description of the particle populations such as Particle-In-Cell (PIC) and Poisson-Boltzman, multiple spatial scales (unstructured tetrahedral meshes), and multiple times scales for the simulation of the plasma and the interactions with materials (Roussel et al. 2012).
In the present simulation, we model the bulk solar wind species (electrons and protons) as PIC populations. A minor (100 m^{-3}) hot (1 keV) component of each solar wind species is added to model the plasma environment in the comet wake. This hot component is not drifting and is modeled by a Poisson-Boltzmann approximation. Neutrals and dust grains are modeled as PIC populations. All populations have the same time step than the Poisson equation solver, except the dust grains that have a time step 10^5 times larger. This permits us to numerically speed-up the dust motion and to allow for their simulation in realistic times, but it has no impact on the physical model since the dust characteristic time scales remain larger than that of the other species.

Fig. 1. Geometry of the simulation domain. The domain cross-section is 50x50 meter. Philae is close to the center. The comet rotation axis is approximately directed toward the top of the page on this picture.

In a similar way, the spacecraft and comet surface potentials are computed over a larger time step than the plasma potential. This permits us to compute these potentials in realistic times without modifying the results of the simulation since we are only interested by long scale variations and not by transient phenomena that could occur at the plasma time scales.
The simulation domain is based on the digital terrain model published by the CNES, but was reproduced by hand to simply the topology. The domain cross-section is 50x50 meters and the box height is 130 m. This height is needed to correctly reproduce the potential barrier above the sunlit surfaces. Philae is at its real size, but its geometry was simplified, as its legs and instruments are not reproduced. The mesh size is fixed but adapted to the expected Debye length across the simulation domain. The typical cell size is 8 m on the open boundary and 1 m on the surface.

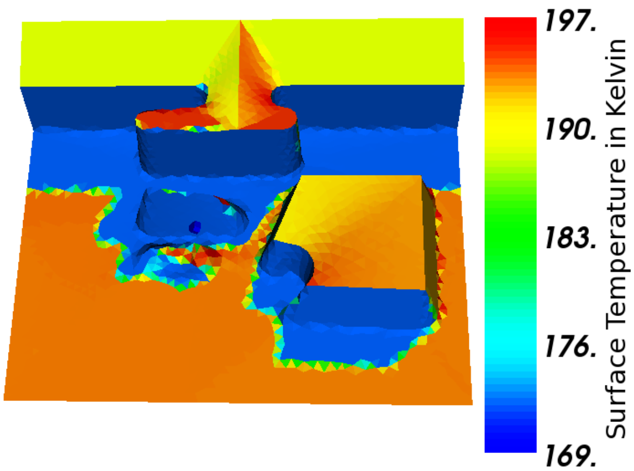

Fig. 2. Temperature of the comet surface computed using the simple model implemented in SPIS. The local time is noon. Philae surface temperatures are not computed.

Parameter	Value
cold e^-, H^+ densities	2E6 m^{-3}
hot e^-,H^+ densities	100 m^{-3}
cold e^-, H^+ bulk velocities	400 $km.s^{-1}$
cold e^-,H^+ temperature	10 eV
hot e^-,H^+ temperature	1 keV
albedo A	0.04
solar flux $\Phi_\odot$	340 $W.m^{-2}$
emissivity ϵ	1
soil thermal inertia† $\mathcal{I}$	450 $W.m^{-2}.K^{-1}.s^{1/2}$
ice fraction f_{H_2O}	0.3
ice specific heat $\mathcal{L}$	1100 J/K/kg
isotherm temperature† T_0	184 K

Table 1. Parameters used in the plasma and thermal models. †Parameters that are computed from material characteristics and from the model.

2.2 Dust physics

The dust particles and their physics have been introduced in a new version of SPIS that will be publicly released in 2015, as the SPIS 5.2 version. The dust population differs from the plasma or neutral population in that all

particles do not share the same characteristics (different radii,...) that may evolve with time (charge). SPIS allows the user to define distributions for the characteristics of the dust on the ground, in particular for their radii. SPIS computes the dust interaction with the plasma (plasma collection and secondary emission) and with the solar photons (photo-emission) to determine the charge state of the dust grains in the plasma.
The charge evolution both influences and depends on the dust motion in the plasma. It also participate to the dust ejection from the ground. The computation of the dust charging on the ground is more complex than that in the plasma, as a dusty surface is a complex composite material for which no physical models exist that describe its electrostatic behavior. SPIS computes the dust grain charging on the ground by assimilating the irregular surface to a "bed of nails" of different sizes on which the charge and the electric field are computed using a tip effect model. The size distribution of the tips and the charge and electric field enhancements are related through the model, which is described in details in Hess et al. (2015). If the electrostatic forces are strong enough and cannot be balanced by gravitational and cohesive forces, the dust is ejected.
In the present simulation we use the material characteristics of the lunar regolith to model the comet soil (see description in Hess et al. 2015). It is now set that 67P soil is composed of carbon-rich regolith (Capaccioni et al. 2015) which strongly differs from lunar silicates, but in absence of a complete characterization of this material, we use a better know material instead.

2.3 *Thermal model and sublimation*

The dust ejection from the ground due to electrostatic charging may not be the dominant process on a comet, where the sublimation of the volatile material (water and carbon oxides ices) in the ground may carry small dusts. In the present study, we developed a model of dust ejection caused by volatile material sublimation. In this case, the dust grain ejection occurs because of the neutral pressure rather than because of the electrostatic force. Thus, dust ejection strongly depends on the neutral outgassing flux, which itself depends on the soil composition and on its thermal behavior. Several studies have been - and are still- performed to give accurate models of the comet thermal behavior, taking into account many physical processes. Such a model is however out of the scope of the present study. We rather introduced a very simple toy-model of the surface temperature of the comet, T, which only depends on the instantaneous lighting of the surface:

$$\epsilon\sigma T^4 - (1-A)\mathcal{T}\Phi_\odot + \mathcal{I}(T-T_0)\sqrt{4/P} + f_{H_2O}\rho_{sat}v_T\mathcal{L} = 0 \tag{2.1}$$

First term stands for the power radiated by the ground, depending on the emissivity, ϵ. Second term stands for the incoming power from the sun, which depends on the albedo, A and on a transfer function $\mathcal{T}$. Third term stands for the power diffused in depth, depending of the thermal inertia, $\mathcal{I}$, on the comet period, P, and on an isotherm temperature, T_0 taken as the average temperature of the comet. Last term stand for the power lost by sublimation, depending on the water ice fraction, f_{H_2O}, the saturation density, ρ_{sat}, the vapor atoms thermal velocity across the surface, v_T, and the specific heat, $\mathcal{L}$. Parameters that have been used are shown in Table 1. Because we assumed lunar regolith in an ice matrice, neglecting porosity, our estimate of the thermal inertia is several times larger that that deduced from observations (Gulkis et al. 2015; Spohn et al. 2015), but is in the range of older models Davidsson & Gutiérrez (2005). At 2 AU, the surface temperature varies between 169 K and 198 K, whereas more complex simulation, like that of Tenishev et al. (2011), give value between 165 K and 197 K. We consider than this small discrepancy is not of primary importance given the actual knowledge of the comet surface and the accuracy needed for the present study.

3 Simulations

We perform simulations of Philae and comet soil charging in a solar wind condition at 2 AU from the sun: the UV flux is 0.25 times that at Earth, the solar wind density is 2.10^6 m^{-3}, and all the other parameters are the same than for the lunar case. The simulations are first run in a 12:00LT configuration for the equivalent of 1.13 hours in order to initialize it and then for 12.5 hours with the direction of the solar wind species bulk velocities and of the photon changing in accordance with the local time.
In order to investigate the role of dust charging in the interaction between Philae and its environment, we perform three simulations: first one only takes into account the dust ejection due to its charging on the ground, the outgassing and the neutral dust ejection by outgassing are turned off. In a second simulation, we take into account the dust ejection due to outgassing along with the electrostatic charging. In a last simulation, we turn off the electrostatic charging of the dusts, both on the ground and in the plasma, i.e. all dust grains are neutral.

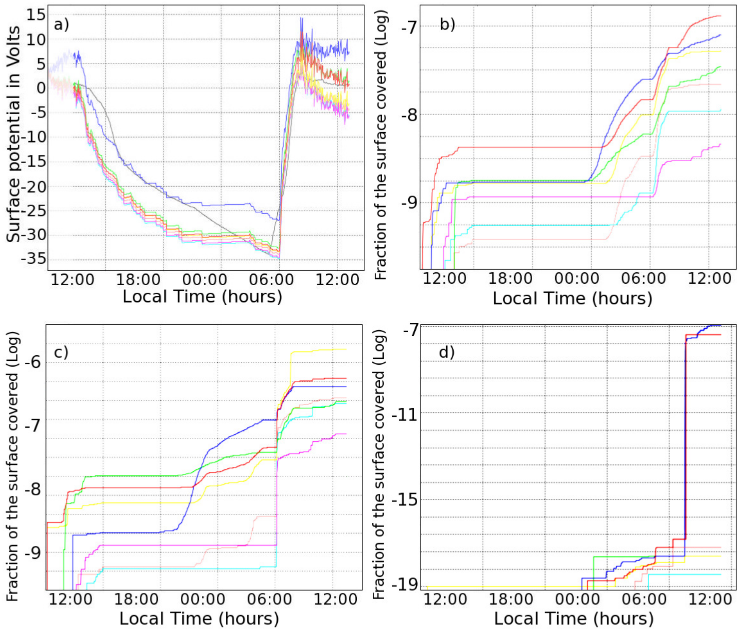

Fig. 3. Evolution of the surface potentials on the different electrical nodes (a). Fraction of the surface covered for runs with electrostatic charging and no outgassing (b), outgassing and charging (c) outgassing and no charging (d). Color code: black= comet surface, dark blue= Philae top, light blue= Philae bottom and instrument side. Red, yellow, green, pink, purple= Philae solar panel sides, counted in the clockwise direction (when seen from above) starting after the instrument side (In this configuration, red is directed upward and purple downward).

Panel a of Fig. 3 shows the evolution of the averaged surface potential over different elements: the comet surface (black), Philaes top solar panel (dark blue) and the other surface elements of Philae (see Figure caption for details). At noon, all of the surfaces are a few Volts positive, because of the photo-electron emission. Shortly after 13:00LT the surface potentials drop abruptly as Philae gets into the shade. The surface potential only decrease noticeably after 15:00LT. The surface potentials of Philae decrease until 00:00LT when they stabilize thanks to the secondary emission caused by the hot plasma populations. The ground secondary emission yield is much lower than that of Philae surfaces, so its potential continues to decrease. Then, all potentials increase abruptly around 06:00LT when the surfaces are sunlit again.

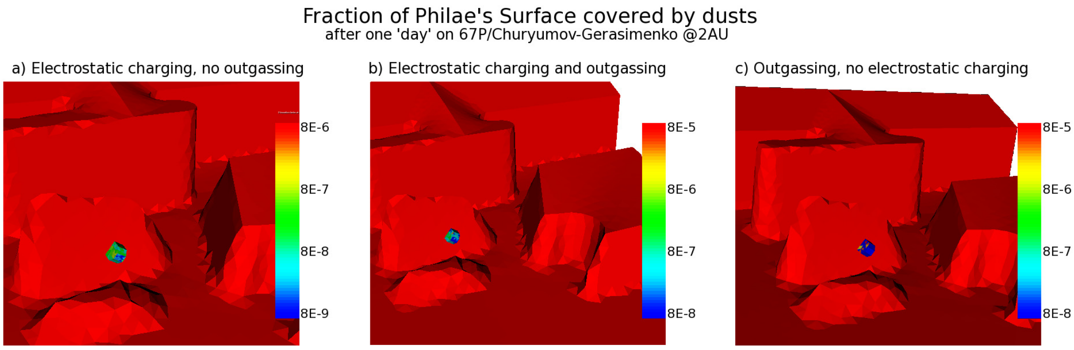

Fig. 4. Fraction of the Philae's surface covered by dust, in log scale, after a simulation lasting for one cometary day ($\simeq$ 12h30). **Left:** In the case for which the dusts are allowed to charge electrostatically in the plasma and on the surface, leading to their ejection. The dust ejection due to outgassing is not included in this simulation. **Middle:** In the case for which the dust ejection due to outgassing is simulated and the dusts are allowed to charge electrostatically in the plasma and on the surface, leading to their ejection. **Right:** In the case for which the dust ejection due to outgassing is simulated but the dusts are not allowed to charge electrostatically neither the plasma nor on the surface.

The other panels of 3 show the evolution of the fraction of the surface cover by dusts (same color code, but the ground is not plotted), for the three cases we simulated. In the case without electrostatic charging, the dust deposit is very low and only concerns the panel facing the +z direction. The two other cases are very similar, except for a dust deposit about one order of magnitude larger in the case with outgassing. The differences in the amount of dust deposited can be clearly seen on Fig. 4 which shows maps on the fraction of the surface covered by dust in the three cases we simulated.
For simulations with electrostatic charging, the dust collection by the surfaces is directly related to the exposure to the sunlight: the top solar panel (dark blue) of Philae is amongst the most covered, whereas the solar panel of Philae which is directed toward the ground (purple) is the less covered. It is also highly correlated with the potential difference between the surfaces and the ground. The time evolution clearly shows that dust grains are collected once a surface is more positive than the ground. This is due to the fact that the ground potential is negative, so that the emitted dusts are negatively charged and attracted by positive potentials. Most of the dust is collected around 06:00LT, when the sunrise.

4 Conclusions

We performed simple simulation of Philae on 67P/Churyumov Gerasimenko using generic parameters for the comet composition that would have to be refined using the results of the ongoing experiments to accurately model the environment of Philae. Nonetheless, our purpose was to investigate the effect of the electrostatic charging of the dust grains on their interaction with Philae. We showed that even if the dominant dust production mechanism is the ejection of neutral dust caused by the sublimation of volatile material in the soil, the subsequent charging of the dust increased the dust collection by about an order of magnitude. This is an important effect that should be taken into account to interpret Philae's dust measurements.

The SPIS-DUST development has been funded under ESA Contract No. 4000107327/12/NL/AK

References

Biele, J., Ulamec, S., Maibaum, M., et al. 2015, Science, 349, 019816
Capaccioni, F., Coradini, A., Filacchione, G., et al. 2015, Science, 347
Davidsson, B. J. R. & Gutiérrez, P. J. 2005, Icarus, 176, 453
Guillemant, S., Génot, V., Matéo-Vélez, J.-C., Ergun, R., & Louarn, P. 2012, Ann. Geophys., 30, 1075
Guillemant, S., Génot, V., Vélez, J.-C., et al. 2013, IEEE Transactions on Plasma Science, 41, 3338
Gulkis, S., Allen, M., von Allmen, P., et al. 2015, Science, 347
Hess, S., Sarrailh, P., Matéo-Vélez, J.-C., et al. 2015, IEEE Transactions on Plasma Science, 43, 2799
Matéo-Vélez, J.-C., Roussel, J., Sarrail, D., et al. 2008, IEEE Transactions on Plasma Science, 36, 2369
Roussel, J., Dufour, G., Matéo-Vélez, J.-C., et al. 2012, IEEE Transactions on Plasma Science, 40, 183
Roussel, J., Rogier, F., Dufour, G., et al. 2008, IEEE Transactions on Plasma Science, 36, 2360
Spohn, T., Knollenberg, J., Ball, A. J., et al. 2015, Science, 349, 020464
Tenishev, V., Combi, M. R., & Rubin, M. 2011, The Astrophysical Journal, 732, 104

Session 02

Prparation scientifique JWST

SF2A 2015
F. Martins, S. Boissier, V. Buat, L. Cambrésy and P. Petit (eds)

30 YEARS OF COSMIC FULLERENES

O. Berné[1], J. Montillaud[2], G. Mulas[3] and C. Joblin[1]

Abstract. In 1985, "During experiments aimed at understanding the mechanisms by which long-chain carbon molecules are formed in interstellar space and circumstellar shells", Harry Kroto and his collaborators serendipitously discovered a new form of carbon: fullerenes. The most emblematic fullerene (i.e. C_{60} "buckminsterfullerene"), contains exactly 60 carbon atoms organized in a cage-like structure similar to a soccer ball. Since their discovery impacted the field of nanotechnologies, Kroto and colleagues received the Nobel prize in 1996. The cage-like structure, common to all fullerene molecules, gives them unique properties, in particular an extraordinary stability. For this reason and since they were discovered in experiments aimed to reproduce conditions in space, fullerenes were sought after by astronomers for over two decades, and it is only recently that they have been firmly identified by spectroscopy, in evolved stars and in the interstellar medium. This identification offered the opportunity to study the molecular physics of fullerenes in the unique physical conditions provided by space, and to make the link with other large carbonaceous molecules thought to be present in space : polycyclic aromatic hydrocarbons.

Keywords: subject, verb, noun, apostrophe

1 The presence of large carbonaceous molecules in space : the PAH hypothesis

About 30 years ago, the presence of bands in emission (the strongest of which are found at 3.3, 6.2, 7.7, 8.6, 11.2 and 12.7 μm) in the mid-infrared spectrum of our Galaxy was observed. Soon after that, it was proposed by Léger & Puget (1984) and then Allamandola et al. (1985) that these bands result from the emission of large carbonaceous molecules from the family of Polycyclic Aromatic Hydrocarbons (PAHs), present in the gas phase and heated by the absorption of single UV photons. Since then, PAHs have been invoked to be part of numerous key processes in interstellar and circumstellar environments (e.g. the formation of H_2, heating of the neutral gas, UV extinction etc.) and are widely used as tracers of physical conditions and star-formation in galaxies. Yet, even though it is widely accepted, the gas phase PAH model remains an hypothesis because no specific PAH molecule could be identified up to date. This is mainly because there exists a large number of PAH molecules (it is a "family" of molecules) and the mid-infrared emission bands are broad are not specific enough to identify individual species from the PAH family.

2 The serendipitous discovery of the C_{60} molecule

About at the same time the PAH model was proposed, H. Kroto and his collaborators serendipitously formed, in the laboratory, a new molecule made of 60 carbon atoms arranged as the vertices of a soccer ball (C_{60} , Fig. 2). It is worth noting that, in the original Nature paper (Kroto et al. 1985), the authors of the discovery present a photograph of a soccer ball as their Fig. 1. Because of the resemblance of the geometry of this molecule with the buildings of architect Buckminster Fuller, they coined the name "Buckminsterfullerene" for this new molecule. In fact, there exists a whole class of pure carbon molecules with icosahedral geometries of different

[1] IRAP Université de Toulouse; UPS-OMP; IRAP; Toulouse, France CNRS; 9 Av. colonel Roche, BP 44346, F-31028 Toulouse cedex 4, France
[2] Institut Utinam, CNRS UMR 6213, OSU THETA, Université de Franche-Comté, 41bis avenue de l'Observatoire, 25000 Besançon, France
[3] Istituto Nazionale di Astrofisica – Osservatorio Astronomico di Cagliari – strada 54, localit Poggio dei Pini, 09012– Capoterra (CA), Italy

© Société Francaise d'Astronomie et d'Astrophysique (SF2A) 2015

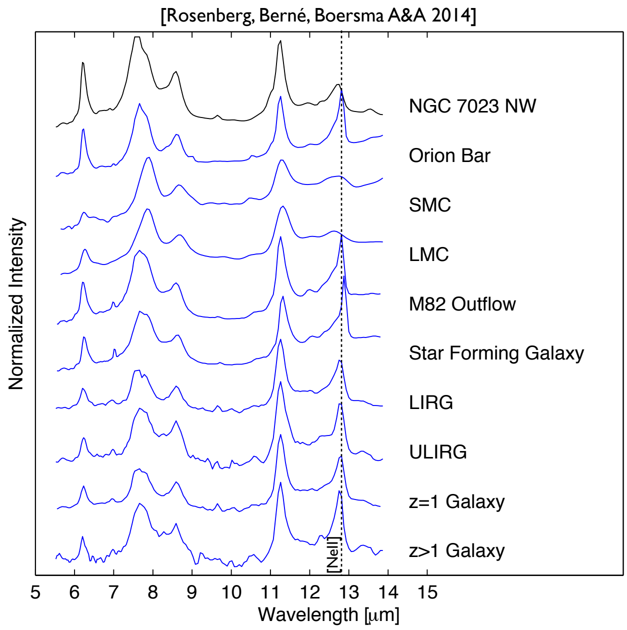

Fig. 1. Mid-infrared spectra of UV-irradiated regions in the Milky Way and other galaxies obtained with the IRS instrument on- board the Spitzer Space Telescope and showing the main PAH bands. (see Rosenberg et al. 2014 for details).

sizes and shapes, which belong to the family of fullerenes. The discovery of C_{60} and fullerenes had a strong impact on the development of nanotechnologies, and H. Kroto and his colleagues received the Nobel prize in 1996 for this discovery. Yet, it should not be forgotten that, in their 1985 paper, the future Nobel laureates start their article by "During experiments aimed at understanding the mechanisms by which long-chain carbon molecules are formed in interstellar space and circumstellar shells", i.e. that their main goal was to understand interstellar and circumstellar chemistry.

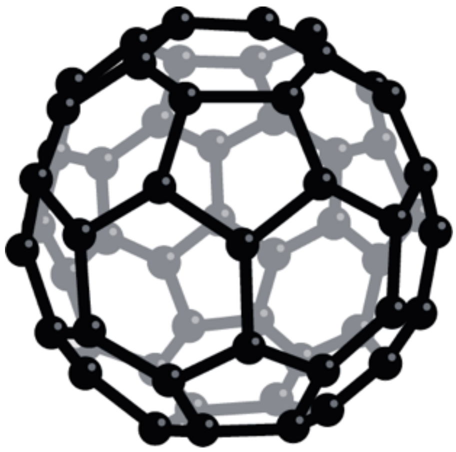

Fig. 2. Structure of the C_{60} molecule, "Buckminsterfullerene". Figure credit L. Cadars.

3 The search and discovery of C_{60} in space

C_{60} has been sought for by astronomers since its discovery in 1985. The first serious evidence of the presence of C_{60}, in reality its cation i.e. C_{60}^{+}, was given by Foing & Ehrenfreund (1994) who detected two weak absorption bands in the diffuse interstellar medium with wavelengths close to those measured in the laboratory for the electronic transitions of C_{60}^{+}. Unfortunately, the laboratory data were obtained using matrix isolation techniques, which do not allow a precise enough measurement of the band positions for a definitive identification. Therefore, this detection remained debated for nearly two decades. It was only in 2010 that clear evidence for the presence of C_{60} was provided. This time, it was with the detection in emission of the main vibrational bands (Fig. 3) of the neutral C_{60} molecule, in two reflection nebulae by Sellgren et al. (2010) and in an evolved star by Cami et al. (2010). While this discovery was an important step, it raised a number of question for astrochemistry :

- How is C_{60} formed in space ?
- C_{60} was detected in its neutral form, while given the harsh conditions of the ISM one could expect to detect the cationic form of the molecule, i.e. C_{60}^{+}
- It was proposed by Sellgren et al. (2010) that C_{60} is in the gas phase and heated by single UV photons, as in the PAH model, but Cami et al. (2010) suggest that C_{60} is stuck on the surface of grains at thermal equilibrium with the radiation field.

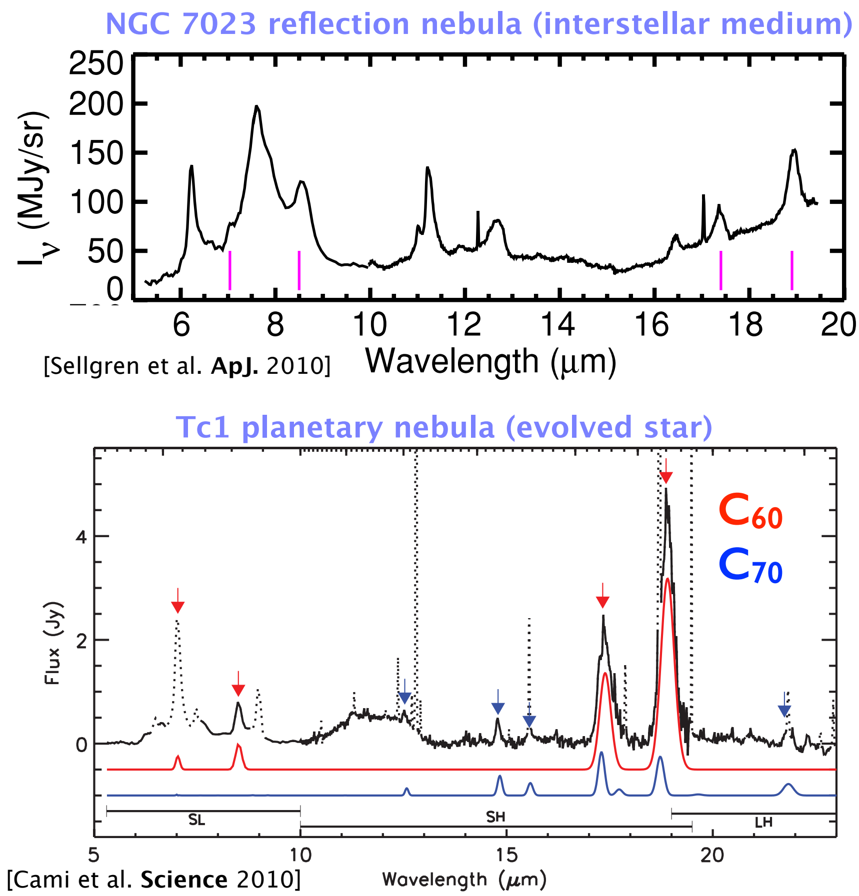

Fig. 3. Spitzer spectra of the NGC 7023 reflection nebula and TC 1 planetary nebula in which the main signatures of the C_{60} molecule are observed. In the case of NGC 7023, the PAH bands are also present. Figures from Sellgren et al. (2010) and Cami et al. (2010).

4 The formation of C_{60}

One question related to fullerenes, and in particular C_{60}, concerns their formation pathway. Recently, "top-down" schemes where larger carbon clusters shrink to reach C_{60} have been proposed (Chuvilin et al. 2010; Zhang et al. 2013; Pietrucci & Andreoni 2014), and can be opposed to the traditional "bottom-up" approach where C_{60} is built up from small gas-phase species (Kroto & McKay 1988; Heath 1992; Hunter et al. 1994; Dunk et al. 2013). Using infrared observations of the NGC 7023 nebula, Berné & Tielens (2012) found evidence of an increase of the abundance of C_{60} with increasing UV field, while the abundance of PAHs decreases. This was interpreted by these authors as evidence for the formation of C_{60} from large PAHs ($N_C > 60$) under UV irradiation, a top-down mechanism similar to the one observed by Chuvilin et al. (2010). García-Hernández et al. (2010, 2011) and Micelotta et al. (2012) proposed a similar mechanism where the starting materials are more complex, such as hydrogenated amorphous carbon instead of PAHs. Top-down scenarios are particularly appealing, given that the densities prevailing in the ISM are many orders of magnitude too low to allow for a bottom-up formation (i.e. starting from small gas-phase species) over reasonable timescales. Berné et al. (2015) proposed the first detailed model of the top-down photochemistry of interstellar fullerenes (Fig. 4). PAHs are assumed to be formed in the envelopes of evolved stars (Frenklach & Feigelson 1989; Cherchneff et al. 1992; Merino et al. 2014) and then to be injected in the ISM. According to Berné et al. (2015), under UV irradiation, large PAHs, ($60 < N_C \lesssim 1000$) are first fully dehydrogenated into small graphene flakes, dehydrogenation being by far the dominant dissociation channel (see Montillaud et al. 2013, and references therein). Additional UV irradiation enables these flakes to fold into closed cages. Once the cages are closed, they can lose C_2 units if they continue to absorb energy (Irle et al. 2006). Because of the low densities prevailing in the ISM, the reverse reaction, that is, addition of C_2, is too slow to balance photodissociation and therefore the molecule will shrink. Once a system has reached C_{60}, it will remain in this form for a very long time because it is remarkably stable. Berné et al. (2015) find that, with this route, it is possible to convert about 1% of the interstellar PAHs into C_{60}. This efficiency results in predicted abundances that are comparable to the observed ones. It should be noted that C_{60} was recently formed in the laboratory (Zhen et al. 2014) in a top down manner similar to the one described in this theoretical model, i.e. from the irradiation of PAH molecules in the gas phase. However, the detailed steps taken to convert PAHs to C_{60} in this top down scheme are still a subject of debate within specialists (see discussion in Berné et al. 2015).

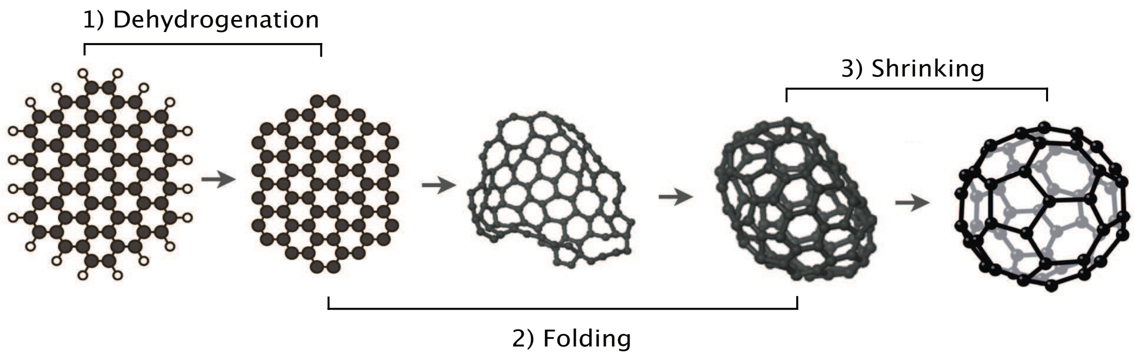

Fig. 4. Schematic representation of the evolutionary scenario for the "top-down" formation of fullerenes from PAHs under UV irradiation. From Berné et al. (2015).

5 The detection of C_{60}^{+}

Recently, Berné et al. (2013) examined in detail the *Spitzer* IRS spectra of the NGC 7023 reflection nebula, at a position close (7.5") to its illuminating B star HD 200775, and found four previously unreported bands at 6.4, 7.1, 8.2, and 10.5 μm (Fig. 5), in addition to the classical bands attributed to PAHs and neutral C_{60}. These 4 bands are observed only in this region of the nebula (Fig. 5), while C_{60} emission is still present slightly farther away from the star, and PAH emission even farther away. Based on this observation Berné et al. (2013) suggested that these bands could be due to C_{60}^{+}. In addition, they conducted quantum chemistry calculations to determine the theoretical positions of the C_{60}^{+} bands. These theoretical band positions were found to match very well with the observed ones (Fig. 5). On this basis, Berné et al. (2013) concluded that the cationic form of C_{60} , i.e. C_{60}^{+} is also present in the ISM. In 2015, further evidence for the presence of C_{60}^{+} in the ISM was provided by Campbell et al. (2015) who measured in the laboratory a gas phase electronic spectrum of C_{60}^{+}. The measured positions of the electronic bands were found to be in very good agreement with the bands observed by Foing & Ehrenfreund (1994) (See sect. 3). The detection of an ion, C_{60}^{+} , in emission, confirms the idea that large carbon molecules exist in the gas phase in the ISM and that their emission is caused by the absorption of individual UV photons as initially suggested by Sellgren et al. (2010). This brings strong evidence that the PAH model (Sect. 1) is correct.

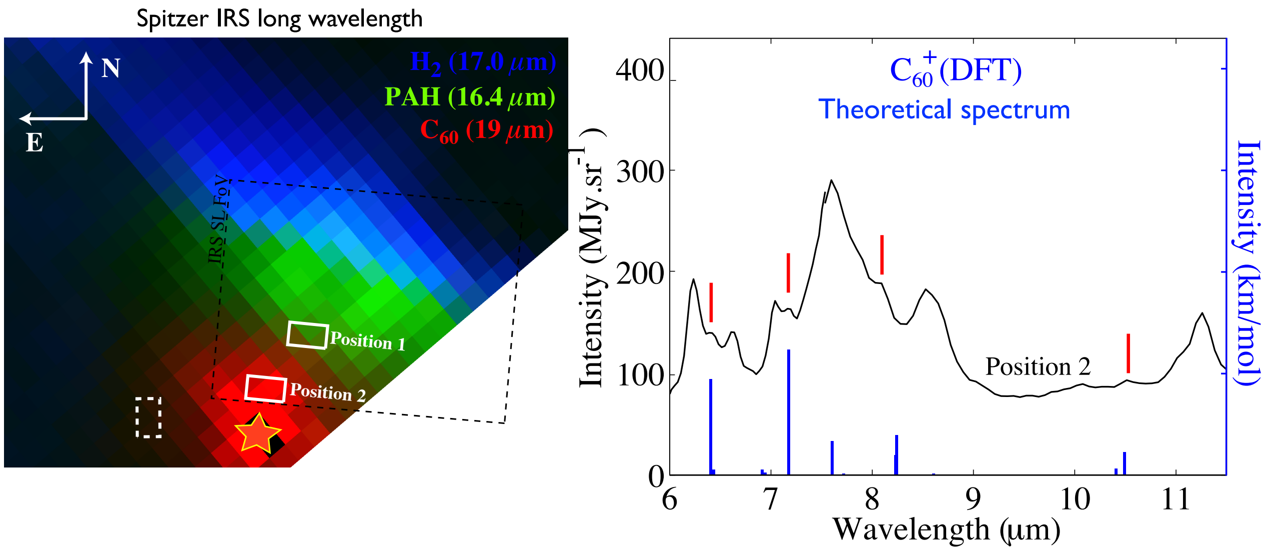

Fig. 5. *Left:* False-color image of the NGC 7023 nebula such as the one presented in Sellgren et al. (2010), obtained from integrating different components in the *Spitzer*-IRS LL spectral cube. Red is the emission integrated in the C_{60} 19μm band. Green is the emission of the PAH 16.4 μm band. Blue is the emission integrated in the H_2 (0-0) S(0) 17.0 μm band. *Right:* Spectrum at positions 1 (see Berné et al. 2013 for spectrum at position 2) in the image. Error bars are not shown here but are comparable to the width of the line. The red lines indicate the four newly detected bands attributed to C_{60}^{+}. The DFT calculated spectrum is shown as a bar graph in blue. See Berné et al. (2013) for details.

6 Conclusions

30 years after it was discovered in the laboratory, there is now convincing evidence that C_{60} and likely other fullerenes are present in space (indeed there is evidence for C_{70} in TC1, see Fig. 3). In the ISM, C_{60} is probably formed by a top down mechanism from PAHs, but it is possible that other mechanisms are at play in the dense envelopes of evolved stars. It was shown that C_{60} exists in the gas phase in the ISM and is heated by single UV photons emitted by massive stars. This confirms the emission mechanism put forward by the PAH model 30 years ago. The presence of neutral and cationic fullerenes indicates that the molecule is stable in both states and that the ionization fraction of C_{60} will depend on the local physical conditions. This opens the possibility to use C_{60} and C_{60}^{+} emission bands as a proxy of the physical conditions, mainly radiation field which controls the ionization and gas density which controls the electron recombination rate.

This work was supported by the CNRS program "Physique et Chimie du Milieu Interstellaire" (PCMI).

References

Allamandola, L. J., Tielens, A. G. G. M., & Barker, J. R. 1985, ApJ, 290, L25
Berné, O., Montillaud, J., & Joblin, C. 2015, A&A, 577, A133
Berné, O., Mulas, G., & Joblin, C. 2013, A&A, 550, L4
Berné, O. & Tielens, A. G. G. M. 2012, Proceedings of the National Academy of Science, 109, 401
Cami, J., Bernard-Salas, J., Peeters, E., & Malek, S. E. 2010, Science, 329, 1180
Campbell, E. K., Holz, M., Gerlich, D., & Maier, J. P. 2015, Nature, 523, 322
Cherchneff, I., Barker, J. R., & Tielens, A. G. G. M. 1992, ApJ, 401, 269
Chuvilin, A., Kaiser, U., Bichoutskaia, E., Besley, N. A., & Khlobystov, A. N. 2010, Nature Chemistry, 2, 450
Dunk, P. W., Adjizian, J.-J., Kaiser, N. K., et al. 2013, Proceedings of the National Academy of Sciences, 110, 18081
Foing, B. H. & Ehrenfreund, P. 1994, Nature, 369, 296
Frenklach, M. & Feigelson, E. D. 1989, ApJ, 341, 372
García-Hernández, D. A., Kameswara Rao, N., & Lambert, D. L. 2011, ApJ, 729, 126
García-Hernández, D. A., Manchado, A., García-Lario, P., et al. 2010, ApJ, 724, L39
Heath, J. R. 1992, in Fullerenes, ed. G. Hammond & V. Kuck, 1–23
Hunter, J. M., Fye, J. L., Roskamp, E. J., & Jarrold, M. F. 1994, The Journal of Physical Chemistry, 98, 1810
Irle, S., Zheng, G., Wang, Z., & Morokuma, K. 2006, The Journal of Physical Chemistry B, 110, 14531, pMID: 16869552
Kroto, H. W., Heath, J. R., Obrien, S. C., Curl, R. F., & Smalley, R. E. 1985, Nature, 318, 162
Kroto, H. W. & McKay, K. 1988, Nature, 331, 328
Léger, A. & Puget, J. L. 1984, A&A, 137, L5
Merino, P., Švec, M., Martinez, J. I., et al. 2014, Nature Communications, 5
Micelotta, E. R., Jones, A. P., Cami, J., et al. 2012, ApJ, 761, 35
Montillaud, J., Joblin, C., & Toublanc, D. 2013, A&A, 552, A15
Pietrucci, F. & Andreoni, W. 2014, Journal of Chemical Theory and Computation, 10, 913
Rosenberg, M. J. F., Berné, O., & Boersma, C. 2014, A&A, 566, L4
Sellgren, K., Werner, M. W., Ingalls, J. G., et al. 2010, Astrophys. J., 722, L54
Zhang, J., Bowles, F. L., Bearden, D. W., et al. 2013, Nature Chemistry, 5, 880
Zhen, J., Castellanos, P., Paardekooper, D. M., Linnartz, H., & Tielens, A. G. G. M. 2014, ApJ, 797, L30

SF2A 2015
F. Martins, S. Boissier, V. Buat, L. Cambrésy and P. Petit (eds)

SHEDDING LIGHT ON COSMIC REIONIZATION WITH THE JAMES WEBB SPACE TELESCOPE

J. Chevallard[1]

Abstract. Current observational constraints on cosmic reionization mainly rely on CMB-based measures of the electron Thomson scattering optical depth τ_e, and on the absorption signatures of neutral hydrogen on the spectra of distant QSOs and GRBs afterglow. These, however, only probe the last phase of reionization (QSOs and GRBs), or its duration (τ_e), therefore leaving most of the reionization history unconstrained. The origin of H-ionizing photons is also largely uncertain. While several observations suggest that star forming galaxies may be the primary sources of these photons, many uncertain quantities prevent a rigorous quantification of their role in ionizing the IGM. With the launch of JWST, scheduled in 2018, a new window will open to study cosmic reionization. The large wavelength coverage, unique sensitivity and different spectroscopic and imaging capabilities of JWST will provide new constraints on both the reionization history and contribution of different sources to the Universe ionizing budget. In this contribution, I will review current observational constraints on cosmic reionization, and discuss the role of JWST to improve our understanding of this phase.

Keywords: cosmic reionization, JWST

1 Introduction

Cosmic reionization is the last ‘phase transition’ experienced by the Universe. It starts with the appearance of the first sources of ionizing radiation, namely Population III stars and quasars. These, along with further generations of metal-enriched stars, create bubbles of ionized gas which grow, eventually percolating. By redshift $z \sim 6$ hydrogen in the intergalactic medium (IGM) has been fully ionized. Understanding the details of cosmic reionization requires measuring the properties of H-ionized bubbles and their evolution with time, and identifying the sources responsible for the production of H-ionizing photons. Our current knowledge of this phase is limited by the difficulty of measuring the rest-frame UV emission of distant, faint sources. The James Webb Space Telescope (JWST), and in the future Extremely Large Telescopes (ELTs) and the Square Kilometre Array (SKA), will open new windows to study in detail this phase. In the next sections, I will briefly recall the basic (analytic) formalism adopted to describe cosmic reionization, and briefly summarise the main characteristics of the different instruments onboard JWST. I will then discuss different observational constraints on the reionization history and sources of ionizing radiation, focusing on the role of JWST to improve these constraints. I will conclude with a summary.

2 Basic formalism

Cosmic reionization can be described with a differential equation expressing the competing processes of hydrogen ionization by Lyman-continuum photons (with $E > 13.6$ eV) and hydrogen recombination (e.g. Madau et al. 1999):

$$\frac{dQ_{\mathrm{HII}}}{dt} = \frac{f_{\mathrm{esc}}\,\dot{n}_{\mathrm{ion}}}{\langle n_{\mathrm{H}} \rangle} - \frac{Q_{\mathrm{HII}}}{t_{\mathrm{rec}}}\,, \tag{2.1}$$

where Q_{HII} indicates the volume filling fraction of ionized hydrogen, $\dot{n}_{\mathrm{ion}}$ the comoving production rate of hydrogen ionizing photons within galaxies, f_{esc} the escape fraction of these photons into the IGM, $\langle n_{\mathrm{H}} \rangle$ the

[1] Scientific Support Office, Directorate of Science and Robotic Exploration, ESA/ESTEC, Keplerlaan 1, 2201 AZ Noordwijk, The Netherlands

© Société Francaise d’Astronomie et d’Astrophysique (SF2A) 2015

comoving average number density of hydrogen atoms, and $t_{\rm rec}$ the average recombination time of hydrogen.* The variation of the volume fraction of ionized hydrogen with time (the term on the left side of Equation 2.1) therefore depends on the availability of H-ionizing photons, produced by stars and AGN within galaxies and escaping into the IGM (first term on the right side of equation 2.1), and on the physical conditions of the IGM (density, temperature and ionisation fields), which determine the recombination rate of ionized H (second term on the right side of equation 2.1). We note that while equation 2.1 is an approximation, it provides an intuitive understanding of the different ingredients affecting cosmic reionization. Moreover, it has been shown that equation 2.1 provides an excellent approximation to more complex models (Finlator et al. 2012). Understanding the details of cosmic reionization therefore means constraining all physical quantities, and their time dependence, entering equation 2.1.

3 James Webb Space Telescope

JWST is a joint effort of three major space agencies, NASA, ESA and CSA, and is expected to be launched in October 2018. Equipped with a ~ 6.5 m primary mirror (7× HST collecting area) and observing in a wide wavelength range, from the near- to mid-infrared, it will represent a real 'game changer' for the characterisation of the most distant galaxies in the Universe and of cosmic reionization. JWST is equipped with four main instruments, a Near-InfraRed Camera (NIRCam), Near-InfraRed Spectrograph (NIRSpec), Mid-InfraRed Instrument (MIRI), and Near-InfraRed Imager and Slitless Spectrograph (NIRISS). Below, we briefly summarise the main characteristics of these instruments. All quoted sensitivities refer to a point source, an integration time of 10^4 s, and S/N=10.

NIRCam covers the wavelength range 0.6 to 5.0 μm, with a field-of-view (FoV) of ~ 10 arcmin^2. Its unique sensitivity will allow high S/N observations of 10 nano Jy sources, extending, and improving, HST sensitivity up to 5 μm.

NIRSpec provides a complete set of spectroscopic capabilities in the range 0.6 to 5 μm, with resolution ranging from R ~ 100 (prism) to R ~ 1000 and 2700 (gratings). Three different slits will allow one to perform slit spectroscopy at R ~ 100, 1000 and 2700, while the 'multi-object spectrograph' (MOS) mode will allow one to observe multiple sources on a ~ 11.5 arcmin^2 FoV. Finally, the 'integral filed unit' (IFU) mode will allow one to take 3D data cubes on a 3×3 arcsec FoV. NIRSpec sensitivity will allow the detection at low-resolution (R $= 100$) of the continuum of ~ 100 nano Jy sources, and emission lines in the medium resolution mode down to a luminosity of $\sim 10^{-18}\,\rm erg\,s^{-1}\,cm^{-2}$.

NIRISS will be able to take broad-band images in the range 1 to 5 μm in a ~ 5 arcmin^2 FoV. Although about 10 times less sensitive than NIRSpec in the same wavelength range, it will also perform R ~ 150 grism spectroscopy in the range 1 to 2.5 μm.

MIRI covers the range 5 to 28 μm, providing broad-band imaging on a ~ 2.3 arcmin^2 FoV, with a sensitivity decreasing from 0.1 micro Jy at $\lambda \sim 5$ μm (~ 2 dex better than *Spitzer*), to 30 micro Jy at $\lambda \sim 28$ μm (~ 1 dex better than *Spitzer*). MIRI also provides slit low-resolution spectroscopy R ~ 100 in the range 5 to 10 μm, with a sensitivity varying (from the blue to the red side) from 1 to 10 micro Jy (~ 1.5 dex better than *Spitzer*). IFU spectroscopy provides a resolution R $= 3000$ at $\lambda = 5$ μm, decreasing to R $= 1000$ at $\lambda = 28$ μm, allowing one to measure line luminosities down to $\sim 10^{-17}\,\rm erg\,s^{-1}\,cm^{-2}$ at $\lambda = 5$ μm (~ 2 dex better than *Spitzer*), and $\sim 10^{-16}\,\rm erg\,s^{-1}\,cm^{-2}$ at $\lambda = 28$ μm (> 1 dex better than *Spitzer*).

4 Observational constraints on cosmic reionization and the role of JWST

Current observations, such as the Cosmic Microwave Background (CMB) radiation, spectra from high-redshift quasars (QSOs) and Gamma Ray Bursts (GRBs) afterglow, mainly constrain the end and duration of the reionization process. The main reason for this is the difficulty of obtaining high-quality rest-frame UV spectra of $z \geq 6$ sources from the ground. JWST will revolutionise this situation, (potentially) contributing to the improvement of several current, and proposed, observational constraints, except for those based on CMB observations.

*Equation 2.1 does not account for collisional ionization and implicitly assumes that the ionization sources are widely separated, as it mixes mass-averaged (ionization fraction) and volume-averaged (recombination time) quantities (see the discussion in section 5 of Finlator et al. 2012).

4.1 Cosmic Microwave Background

The most accurate estimate of the electron Thomson scattering optical depth τ_e obtained by the *Planck* team corresponds to a redshift of *instantaneous* reionization $z_{\rm re} \sim 8.8$ ($\tau_e \sim 0.066$). This was obtained by combining the CMB temperature, polarisation and lensing maps obtained by *Planck* with measurements of Baryon Acoustic Oscillation from different galaxy/QSOs redshift surveys (Planck Collaboration et al. 2015). The major limitation of using τ_e to constrain the cosmic reionization history is its dependence on the time *integral* of $Q_{\rm HII}(t)$, which means that an infinite number of potential reionization histories (with equal integral) are consistent with the same value of τ_e. Independent observations are therefore required to constrain the evolution of the H-ionized fraction with time, and of the sources responsible for the production of H-ionizing photons.

4.2 Constraints from background sources

Another family of observational constraints relies on measurements of the light emitted by luminous, distant sources, such as QSOs and GRBs afterglow. The signatures of neutral hydrogen in the spectra of these sources allow one to probe the intervening IGM between source and observer. Different signatures have been used in the past to constrain the fraction and distribution of neutral H along the line-of-sight. These include the 'Gunn-Peterson' (GP, Gunn & Peterson 1965) trough and distribution of 'dark gaps' in the spectra of distant QSOs, and the Lyα damping wing in the spectra of QSOs and GRBs.

The GP trough is the complete absorption of photons with $\lambda_{\rm em} \leq \lambda_{{\rm Ly}\alpha}$ (i.e., $\lambda_{\rm em} < 1216$ Å), caused by the presence of clouds of neutral hydrogen along the QSO line-of-sight, and the resonant scatter of photons with frequency coinciding with the rest frequency of Lyα at the cloud frame. Measurements of the GP trough in $z \sim 6$ QSOs indicate a rapid increase of the hydrogen neutral fraction in the IGM (e.g. Fan et al. 2006). However, these measurements are insensitive to neutral fractions $f_{\rm HI} \geq 10^{-4}$, due to the Lyα line saturation, and they probe single line-of-sights of a highly inhomogeneous IGM.

In some cases, the flux blueward Lyα is not completely absorbed, but shows regions of complete absorption spaced out by regions with non-null flux. The distribution of these 'dark gaps' can be used to infer the properties of a partly ionized IGM. In particular, the number of these regions, their redshift and extension (in redshift space) are related to the time and size evolution of H-ionized bubbles, and their clustering properties (e.g. Fan et al. 2006).

The spectra of background QSOs and GRBs afterglows contains other signatures of the state of IGM. The effect of intervening clouds of neutral hydrogen is expected to create a characteristic 'damping wing' redward $\lambda_{{\rm Ly}\alpha}$ (Miralda-Escudé 1998). The advantage of such a measurement is that it allows one to probe much larger $f_{\rm HI}$ than the GP trough. Tentative detections of the Lyα damping wing have appeared in the literature in last few years, both adopting a QSO at $z = 7.08$ (Mortlock et al. 2011; Bolton et al. 2011) and a GRB afterglow at $z = 5.91$ (Totani et al. 2014) as background sources, with claims of a substantial H neutral fraction ($f_{\rm HI} \geq 0.1$) at these redshifts.

The major challenge in improving the above constraints stands in the difficulty of obtaining high-quality, rest-frame far-UV spectra of sources at $z \geq 7$ with ground-based telescopes. This will change with NIRSpec, which will be able to take high S/N ratio, medium resolution (R=1000 and 2700) spectra of bright QSOs and GRBs afterglows at $z > 7$, probing the rest-frame UV spectrum (around Lyα) of these objects. Moreover, NIRCam may alleviate the problem of the rarity of high-z bright QSOs, by providing new, and more numerous, lower luminosity QSOs candidates for the spectroscopic follow-up with NIRSpec.

4.3 Lyα emitters

A different class of observables is related to the measurements of Lyα photons emitted by galaxies. Both the occurrence of these galaxies, called 'Lyman-alpha emitters' (LAE), over the global Lyman-break population, and the redshift evolution of their luminosity function, provide useful constraints on cosmic reionization. Resonant scattering of Lyα photons make them very sensitive to the presence of neutral hydrogen along the line-of-sight, hence LAE can in principle be used to trace the last phase of cosmic reionization (e.g. Stark et al. 2010; Tilvi et al. 2014; Konno et al. 2014; Matthee et al. 2015; Bacon et al. 2015). However, the interpretation of observed trends in the LAE population is hampered by other effects, acting within or nearby the emitters, which can also affect the observability of Lyα emission. These include the effect of dust attenuation, gas kinematics and gas geometry (i.e. 'covering fraction'), which all influence the Lyα photons escape fraction. Other difficulties in using LEA to study cosmic reionization are the need to observe large areas of sky, to obtain statistical significant samples, and the difficulty of correcting for incompleteness, i.e. unobserved emitters. This problem appears even more serious after recent observations with the *MUSE* integral-field unit spectrograph, which have revealed the ubiquitous presence of an 'extended' Lyα emission around galaxies at $3 \leq z \leq 6$. This can have important consequences on the calculation of LEA luminosity function evolution, given the effect of surface brightness limits and aperture sizes (Wisotzki et al. 2015).

Besides the LAE luminosity function, the clustering properties of LAE can be used to constraint different reionization scenarios. Simulations have suggested that such a measurement is less sensitive to the intrinsic evolution of the sources than them LAE luminosity function. In particular, the redshift evolution of HII bubbles (size, clustering) is predicted to leave unique imprints on the clustering properties of LAE at scales ≥ 1 Mpc (e.g. McQuinn et al. 2007; Zheng et al. 2011; Jensen et al. 2014; Sobacchi & Mesinger 2015).

JWST will likely give a substantial contribution for the interpretation of the LAE luminosity function evolution, by allowing one to characterise the physical properties of LAE. The unique spectroscopic capabilities of NIRSpec will allow the measurement of several nebular emission lines in the spectra of distant ($z \geq 6$) LAE, allowing one to constrain the dust and gas (ionization state, metallicity) properties of these galaxies. This will be a promising way to separate the effect of the intrinsic evolution of the sources and of the H neutral fraction on their luminosity function evolution. JWST will also allow the identification of LAE at redshifts not covered by the *MUSE* instrument at the VLT. The LAE identification can be performed by appealing to the 'prism' mode of NIRSpec, and to the slitless spectrograph on NIRISS. This will allow the detection of faint LAE, hence pushing the LEA luminosity function to low fluxes, and allowing a measurements of the LAE clustering signal at small scales. The major challenge for this type of study is the relatively small FoV of NIRSpec (compared to ground-based telescopes), which would require ~ 100 pointings to scan a large enough area of ~ 1000 arcmin^2.

4.4 Nebular emission lines

A fundamental, and largely unknown, quantity entering equation 2.1 is the escape fraction of H-ionizing photons from galaxies. This depends on the gas and dust properties in star forming regions. Recently, Verhamme et al. (2015) proposed the use of the Lyα line profile to measure the properties of distant star forming regions. The shape of the line, and in particular its peak and width, are in fact sensitive to the geometry of gas, i.e. its 'covering factor', and density distribution (optically thin vs thick). The medium resolution mode ($R \sim 2700$) of NIRSpec will be sufficient to provide high-quality measurements of Lyα profiles of very distant galaxies.

Another way to constrain the gas properties of high-z star forming regions is to combine information from Balmer emission lines and UV continuum. As shown by Zackrisson et al. (2013), the 'leak' of UV photons produced within star forming regions is predicted to leave an impact on the equivalent width of hydrogen Balmer lines, at fixed UV slope. This picture is however complicated by the effect of dust, metallicity and variation in the galaxy star formation history, which also affect nebular emission and UV continuum slope. For this, a complete characterisation of the physical properties of such galaxies is required. This can be accomplished by combining the different instrument onboard JWST: NIRSpec will provide ratios of different emission lines, that can be sued to constrain the gas metallicity and dust content; NIRCam will allow one to measure the shape of the rest-frame far-UV; MIRI will allow one to access the rest-frame optical/NIR, which is sensitive to the past history of star formation.

4.5 UV luminosity function

In the last years, theoretical and observational evidence has accumulated pointing towards a dominant role of low-mass star forming galaxies in providing the bulk of H-ionizing photons necessary for cosmic reionization. Many works have suggested that the contribution of other sources, such as mini-QSOs (e.g. Willott et al. 2010; McQuinn 2012; Grissom et al. 2014), high-mass X-ray binaries (e.g. Mirabel et al. 2011; McQuinn 2012) and Pop. III stars (e.g. Paardekooper et al. 2013; Wise et al. 2014; Kulkarni et al. 2014) is secondary. Observationally, the detected steepening of the galaxy UV luminosity function with increasing redshift (e.g. Atek et al. 2014; Bouwens et al. 2015b; Oesch et al. 2014) suggests that these low-mass galaxies were more abundant in the early Universe ($z \geq 6$) than at more recent times, hence potentially providing enough H-ionizing photons to reionize the IGM (e.g. Robertson et al. 2015; Bouwens et al. 2015a). Major uncertainties, however, affect such an interpretation: the quality of current data do not allow to break the degeneracies between the different parameters describing the galaxy UV luminosity function, such as faint-end slope, normalization, and magnitude of the exponential cutoff (e.g. Finkelstein et al. 2015). Also, current, deep surveys cannot resolve magnitudes fainter than $M_{\mathrm{UV}} \sim -17$, except in a few lensed fields (e.g. Atek et al. 2015b,a), hence any interpretation relies on an extrapolation of the observed luminosity function by several magnitudes. Finally, the luminosity function itself must be converted to the production rate of H-ionizing photons within galaxies, and to the number of these photons escaping the galaxies. This 'escape fraction' is observationally unconstrained at $z \geq 2$

JWST will likely play a pivotal role also in the determination of the far-UV luminosity function at high-z. Deep observations with NIRCam will allow the measurement of the galaxy UV luminosity function at $z \geq 6$ down to $M_{\rm UV} \sim -15$. Even deeper observations would however be required to detect the predicted turn-over of the luminosity function at $M_{\rm UV} \leq -13$, due to the effect of stellar and supernova feedback on low mass ($\log(\mathrm{M_{vir}/M_\odot}) \leq 8.5$) haloes (e.g. Gnedin & Kaurov 2014; Wise et al. 2014).

5 Conclusions

Despite great observational efforts, our current knowledge of cosmic reionization is limited by the difficulty of measuring the rest-frame UV emission of galaxies at $z \geq 6$. This situation will be revolutionised with the launch of JWST. The complementarity of the different instruments onboard JWST will allow to trace the state of the IGM at $z \geq 7$ by using background sources (NIRSpec and NIRCam), to study the evolution of LAE down to faint magnitudes (NIRSpec and NIRISS), to precisely characterise the properties of gas in high-redshift star forming regions (NIRSpec), and of stellar population in primeval galaxies (NIRCam, NIRSpec and MIRI), besides providing the most accurate measurements of the galaxy UV luminosity function and its redshift evolution (NIRCam).

Thanks to Pierre Ferruit, Chris Willott, Marcia Rieke and Massimo Stiavelli for providing me with precious material for this review.

References

Atek, H., Richard, J., Jauzac, M., et al. 2015a, ArXiv e-prints [arXiv] 1509.06764
Atek, H., Richard, J., Kneib, J.-P., et al. 2014, ApJ, 786, 60
Atek, H., Richard, J., Kneib, J.-P., et al. 2015b, ApJ, 800, 18
Bacon, R., Brinchmann, J., Richard, J., et al. 2015, A&A, 575, A75
Bolton, J. S., Haehnelt, M. G., Warren, S. J., et al. 2011, MNRAS, 416, L70
Bouwens, R. J., Illingworth, G. D., Oesch, P. A., et al. 2015a, ApJ, 811, 140
Bouwens, R. J., Illingworth, G. D., Oesch, P. A., et al. 2015b, ApJ, 803, 34
Fan, X., Strauss, M. A., Becker, R. H., et al. 2006, AJ, 132, 117
Finkelstein, S. L., Ryan, Jr., R. E., Papovich, C., et al. 2015, ApJ, 810, 71
Finlator, K., Oh, S. P., Özel, F., & Davé, R. 2012, MNRAS, 427, 2464
Gnedin, N. Y. & Kaurov, A. A. 2014, ApJ, 793, 30
Grissom, R. L., Ballantyne, D. R., & Wise, J. H. 2014, A&A, 561, A90
Gunn, J. E. & Peterson, B. A. 1965, ApJ, 142, 1633
Jensen, H., Hayes, M., Iliev, I. T., et al. 2014, MNRAS, 444, 2114
Konno, A., Ouchi, M., Ono, Y., et al. 2014, ApJ, 797, 16
Kulkarni, G., Hennawi, J. F., Rollinde, E., & Vangioni, E. 2014, ApJ, 787, 64
Madau, P., Haardt, F., & Rees, M. J. 1999, ApJ, 514, 648
Matthee, J., Sobral, D., Santos, S., et al. 2015, MNRAS, 451, 400
McQuinn, M. 2012, MNRAS, 426, 1349
McQuinn, M., Hernquist, L., Zaldarriaga, M., & Dutta, S. 2007, MNRAS, 381, 75
Mirabel, I. F., Dijkstra, M., Laurent, P., Loeb, A., & Pritchard, J. R. 2011, A&A, 528, A149
Miralda-Escudé, J. 1998, ApJ, 501, 15
Mortlock, D. J., Warren, S. J., Venemans, B. P., et al. 2011, Nature, 474, 616
Oesch, P. A., Bouwens, R. J., Illingworth, G. D., et al. 2014, ApJ, 786, 108
Paardekooper, J.-P., Khochfar, S., & Dalla Vecchia, C. 2013, MNRAS, 429, L94
Planck Collaboration, Ade, P. A. R., Aghanim, N., et al. 2015, ArXiv e-prints [arXiv] 1502.01589
Robertson, B. E., Ellis, R. S., Furlanetto, S. R., & Dunlop, J. S. 2015, ApJ, 802, L19
Sobacchi, E. & Mesinger, A. 2015, MNRAS, 453, 1843
Stark, D. P., Ellis, R. S., Chiu, K., Ouchi, M., & Bunker, A. 2010, MNRAS, 408, 1628

Tilvi, V., Papovich, C., Finkelstein, S. L., et al. 2014, ApJ, 794, 5
Totani, T., Aoki, K., Hattori, T., et al. 2014, PASJ, 66, 63
Verhamme, A., Orlitová, I., Schaerer, D., & Hayes, M. 2015, A&A, 578, A7
Willott, C. J., Delorme, P., Reylé, C., et al. 2010, AJ, 139, 906
Wise, J. H., Demchenko, V. G., Halicek, M. T., et al. 2014, MNRAS, 442, 2560
Wisotzki, L., Bacon, R., Blaizot, J., et al. 2015, ArXiv e-prints [arXiv] 1509.05143
Zackrisson, E., Inoue, A. K., & Jensen, H. 2013, ApJ, 777, 39
Zheng, Z., Cen, R., Trac, H., & Miralda-Escudé, J. 2011, ApJ, 726, 38

SF2A 2015
F. Martins, S. Boissier, V. Buat, L. Cambrésy and P. Petit (eds)

AN EXTREME [O iii] EMITTER AT $z = 3.2$: A LOW METALLICITY LYMAN CONTINUUM SOURCE

S. de Barros[1] and E. Vanzella[1]

Abstract. We investigate the physical properties of a Lyman continuum emitter candidate at $z = 3.212$ with photometric coverage from U to MIPS 24μm band and VIMOS/VLT and MOSFIRE/Keck spectroscopy. Investigation of the UV spectrum confirms a direct spectroscopic detection of the Lyman continuum emission with $S/N > 5$. Non-zero Lyα flux at the systemic redshift and high Lyman-α escape fraction suggest a low H I column density. The weak C and Si low-ionization absorption lines are also consistent with a low covering fraction along the line of sight. The [O III]$\lambda\lambda4959, 5007$+Hβ equivalent width is one of the largest reported for a galaxy at $z > 3$ (EW([O III]$\lambda\lambda4959, 5007 +$ Hβ) $\simeq 1600Å$, rest-frame; 6700Å observed-frame) and the NIR spectrum shows that this is mainly due to an extremely strong [OIII] emission. The large observed [O III]/[O II] ratio (> 10) and high ionization parameter are consistent with prediction from photoionization models in case of a density-bounded nebula scenario. This source is currently the first high-z example of a Lyman continuum emitter exhibiting indirect and direct evidences of a Lyman continuum leakage and having physical properties consistent with theoretical expectation from Lyman continuum emission from a density-bounded nebula.

Keywords: Galaxies: high-redshift; Galaxies: evolution; Galaxies: ISM; Galaxies: starburst

1 Introduction

A number of surveys at $1 < z < 3.5$ both from the ground and with the Hubble Space Telescope (*HST*), have looked for ionizing photons by means of imaging or spectroscopy and there have been some claims of detections (Steidel et al. 2001; Shapley et al. 2006; Nestor et al. 2013; Mostardi et al. 2013, 2015). However several other surveys reported only upper limits (Siana et al. 2010; Bridge et al. 2010; Malkan et al. 2003; Vanzella et al. 2010, 2012; Boutsia et al. 2011; Grazian et al. 2015). Attempts at identifying individual galaxies at $z > 1$ with Lyman continuum (LyC, < 912Å) emission have so far been unsuccessful and have provided upper limits on the f_{esc}(LyC) of the order of few percent ($< 5\%$; Vanzella et al. 2012; Siana et al. 2015). This could be due to the rarity of relatively bright ionizing sources, as a consequence of the combination of view-angle effects (Cen & Kimm 2015), stochastic intergalactic opacity (Inoue & Iwata 2008; Inoue et al. 2014) and possibly intrinsically low escaping ionizing radiation on average, in the luminosity regime explored so far ($L > 0.1L^*$, e.g., Vanzella et al. 2010).

We have identified two Lyman continuum leakers in Vanzella et al. (2015), hereafter V15: *Ion1* and *Ion2*. These galaxies have been selected as Lyman continuum emitters through a photometric selection which is based on the comparison between the observed photometric fluxes and colors probing the Lyman continuum emission and predictions from the combination of spectral synthesis models (e.g., Bruzual & Charlot 2003) and intergalactic medium (IGM) transmissions (Inoue et al. 2014).

In this work we present the source with one of the largest [O III]$\lambda\lambda4959, 5007$ line equivalent width currently known (EW $\sim 1500Å$, rest-frame) at $z > 3$ and with a plausible leakage of ionizing radiation. Ultraviolet (VLT/VIMOS), optical and NIR (Keck/MOSFIRE) rest-frame spectroscopy are presented, as well as a detailed multi-frequency analysis with the aim to test possible signatures of linking Lyman continuum.

[1] INAF–Osservatorio Astronomico di Bologna, via Ranzani 1, I-40127 Bologna, Italy, email: stephane.debarros@oabo.inaf.it

© Société Francaise d'Astronomie et d'Astrophysique (SF2A) 2015

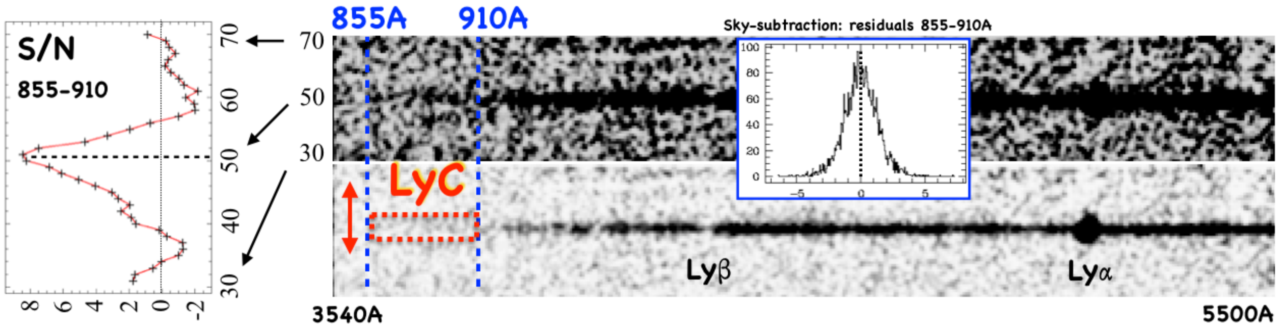

Fig. 1. Two-dimensional LR VIMOS UV spectrum of *Ion2*. We show the moving average calculated within a rectangular aperture (855-910Å × 1.25", red-dotted rectangle) in the spatial direction divided by its r.m.s. on the left side. A signal is detected at $\lambda < 912\AA$ with $S/N > 5$. The inset shows the pixel distribution of the background after sky-subtraction in the region 855-910Å (derived from the S/N spectrum). No significant systematic effects are present.

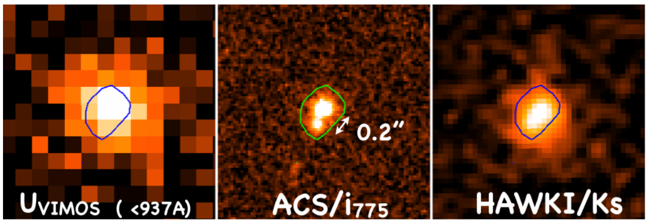

Fig. 2. Ground based VLT/VIMOS U-band observation of *Ion2* at a resolution of 0.2"/pixel (left panel). The contour of the system (derived from the ACS/i_{775} band, center panel) is indicated and superimposed in blue to the VIMOS U-image and to the HAWK-I K_s image (right panel). The cutouts are 2.6" vs. 2.6".

2 Spectroscopic detection and spatial distribution of the Lyman continuum emission

The VIMOS LR spectrum of *Ion2* shows a clear signal detected blueward the Lyman limit. We performed a careful reanalysis of the *Ion2* low-resolution UV spectrum by computing the moving average of the flux at $\lambda < 910\AA$ and we find a signal with $S/N > 5$ (Figure 1). While several systematics can affect the derivation of the LyC signal (e.g., background substraction, Shapley et al. 2006), we use different methods of sky subtraction (ABBA method and polynomial fitting with different orders) and they all provide consistent results. In particular the same moving average in the LyC region calculated over the S/N two-dimensional spectrum we derived with ABBA method (see Vanzella et al. 2014) produces stable results with no significant systematics and a signal ($> 5\sigma$) at the same spatial position of the target. This signal can be interpreted as a direct detection of the Lyman continuum emission, but the presence of the two components in the *HST* images can cast some doubts about the origin of this detection. However, assuming that the faintest component keeps the same magnitude as the derived B_{435} magnitude (27.25±0.24; V15) at shorter wavelengths, the average S/N in the range 3600-3840Å is ~ 0.5 per pixel (from ETC). Averaging over 20 pixels, as we did in Figure 1, we would expect $S/N \sim 2.2$. In addition, the B-band dropout signature of such a component ($B - V = 0.62$, V15) between the B_{435} and V_{606} prevents a possible increased emission approaching the U-band, unless an emission feature is boosting the U-band magnitude. In such a case the only possible line would be [O II]λ3727 which would also imply a certain amount of star-formation activity, that in turns would be detectable through Balmer and/or Oxygen lines in the wide spectral range probed here. The most likely explanation is that the spectroscopic detection is due to a Lyman continuum emission emerging from the brightest *Ion2* component. Furthermore, the ground-based VLT/VIMOS U-band spatial distribution shows that most of the U-band flux is emitted from the brightest component (Figure 2).

However, the U-band probes both ionizing *and* non-ionizing photons ($\lambda < 937\AA$), so a fraction of the signal is not due only to Lyman continuum photons, and the ground-based observations are clearly limited in terms of resolution, as seen in Figure 2.

The only way to clarify the exact position and the detailed spatial distribution of the Lyman continuum emission is to perform dedicated *HST* observations. A proposal to observed *Ion2* with *HST*/F336W (17 orbits) has been recently approved (PI: Vanzella, cycle 23). Hopefully, emission line diagnostics can be used to characterize the gaseous and stellar content of *Ion2* and provide some hints about a Lyman continuum leakage, as discussed in the next Section.

3 Lyman continuum leakage signatures

We use VLT/VIMOS and Keck/MOSFIRE spectroscopy to obtain a wide *Ion2* spectral coverage with $850\mathring{A} < \lambda < 5700\mathring{A}$ (rest-frame).

The first property derived from emission lines is the spectroscopic redshift. As already reported in V15, the C III]$\lambda1906.68-1908.68$ transition is clearly detected in the VIMOS MR spectrum (with $S/N = 8$). This feature shows a symmetric shape with a relatively large FWHM ($= 400\mathrm{km\,s^{-1}}$) with respect to other lines like Lyα and [O III], suggesting the two components have similar intensities, even if they are blended and non resolved. The redshift we derive from C III] is fully consistent with the redshift of Oxygen lines 4959–5007Å identified in the MOSFIRE spectrum. This provides a robust estimate of the systemic redshift, $z = 3.2127 \pm 0.0008$.

We derive ionization parameter, Oxygen and Carbon abundances using a modified version of the HII-CHI-mistry code (Pérez-Montero 2014), adapted to provide metallicity, C/O and ionization parameter in a Te-consistent framework, based on the comparison of the observed UV and optical nebular lines with a grid of CLOUDY photoionization models (Ferland et al. 2013). The derived abundances and ionization parameter are $12 + \log(\mathrm{O/H}) = 8.07 \pm 0.44$, $\log(\mathrm{C/O}) = -0.80 \pm 0.13$, and $\log U = -2.25 \pm 0.81$. Both set of lines lead to low metallicity and high ionization parameter (in the following, we consider the results obtain with all the line measurements and upper limits). *Ion2* metallicity is similar to the typical green pea metallicity ($12 + \log(\mathrm{O/H}) = 8.05 \pm 0.14$, Amorín et al. 2010). The metallicity and ionization parameter are also consistent with extreme emission-line galaxies up to $z \sim 3.5$ (Amorín et al. 2014b,a, 2015). The metallicity of *Ion2* is also consistent with the mean metallicity of star-forming galaxies selected through their extreme EW([O III]) (Maseda et al. 2014; Amorín et al. 2015; Ly et al. 2014).

We compare the metallicity and the ionization parameter with the results presented in Nakajima & Ouchi (2014). Overall, *Ion2* has a lower metallicity than all other galaxy populations presented in their work and one of the highest ionization parameter. The higher ionization parameter is in line with a possible Lyman continuum leaking that could be explained with a low neutral hydrogen column density. Also, the *Ion2* extreme [O III]$\lambda5007$/[O II] ratio, the metallicity, and the ionization parameter are consistent with CLOUDY models with a non zero Lyman continuum escape fraction (Nakajima & Ouchi 2014, , Figure 11).

The identification of Lyman continuum leakage from Green pea galaxies is a current line of research (e.g., Jaskot & Oey 2014; Nakajima & Ouchi 2014; Borthakur et al. 2014; Yang et al. 2015) and the Green pea nature of *Ion2* and its LyC leakage represent the first concrete attempt to link these two properties. *Ion2* represents an extreme case of Green pea galaxy, being the highest redshift ($z > 3$) ultra-strong Oxygen emitter (with EW([O III]$\lambda\lambda4959, 5007$) ~ 1100Å) currently known. The Lyman continuum leakage observed in *Ion2* allow us to investigate the relationship between the LyC leakage and physical and morphological properties. However, as shown in Stasińska et al. (2015), the [O III]/[O II] ratio is also related to the specific star formation rate and the metallicity: the [O III]/[O II] ratio increases with increasing sSFR and decreasing metallicity. For *Ion2* the observed ratio is ≥ 15 making *Ion2* as an outlier in the Oxygen abundance vs. [O III]/[O II] ratio relation and the EW(Hβ) (i.e., sSFR) vs. [O III]/[O II] ratio (Figure 2, Stasińska et al. 2015): *Ion2* ratio is higher by ~ 0.6 dex for the observed EW(Hβ) and the ratio is higher by ~ 1 dex compared to galaxies in the SDSS sample with similar metallicities. The *Ion2* [O III]/[O II] ratio is also higher than what is expected for the derived stellar mass, SFR, and sSFR (Nakajima & Ouchi 2014). Therefore, we conclude that the extreme [O III]/[O II] ratio is due to unusual physical conditions (density-bounded nebula), which imply a low column density of neutral gas, and so favor leakage of ionizing photons (Nakajima & Ouchi 2014).

4 Conclusions

We present new observations with the Keck/MOSFIRE NIR spectrograph and a new analysis of the UV spectrum of a Lyman continuum emitter candidate. Our main results can be summarized as follows:

- a new analysis of the UV spectrum shows a signal consistent with a direct detection of ionizing photons with $S/N > 5$;

- the Lyα emission at the systemic redshift, the high Lyα escape fraction, the non detection of low-ionization absorption lines are consistent with a low neutral hydrogen column density, while velocity separation of the two Lyα peaks is in tension with expectation (e.g., Verhamme et al. 2015);
- we find low metallicity ($\sim 1/6 Z_{\odot}$), strongly subsolar C/O ratio and high ionization parameter ($\log U = -2.25$) using a T_e-consistent method, in good agreement with previous results at $z \sim 2-3$;
- *Ion2* exhibit one of the largest [O III]/[O II] ratio observed at $z > 3$ and similar large ratios are predicted for galaxies with low metallicities and Lyman continuum leakage (Nakajima & Ouchi 2014);

A complete analysis of *Ion2* can be found in de Barros et al. (2015). In the near future, our approved proposal to observe *Ion2* with *HST*/F336W will hopefully shed new light on the nature of this source (PI: Vanzella).

We thank M. Tosi, F. Annibali, M. Brusa and H. Atek for useful discussions. We acknowledge the financial contribution from PRIN-INAF 2012.

References

Amorín, R., Grazian, A., Castellano, M., et al. 2014a, ApJ, 788, L4
Amorín, R., Pérez-Montero, E., Contini, T., et al. 2015, A&A, 578, A105
Amorín, R., Sommariva, V., Castellano, M., et al. 2014b, A&A, 568, L8
Amorín, R. O., Pérez-Montero, E., & Vílchez, J. M. 2010, ApJ, 715, L128
Borthakur, S., Heckman, T. M., Leitherer, C., & Overzier, R. A. 2014, Science, 346, 216
Boutsia, K., Grazian, A., Giallongo, E., et al. 2011, ApJ, 736, 41
Bridge, C. R., Teplitz, H. I., Siana, B., et al. 2010, ApJ, 720, 465
Bruzual, G. & Charlot, S. 2003, MNRAS, 344, 1000
Cen, R. & Kimm, T. 2015, ApJ, 801, L25
de Barros, S., Vanzella, E., Amorín, R., et al. 2015, ArXiv e-prints [arXiv] 1507.06648
Ferland, G. J., Porter, R. L., van Hoof, P. A. M., et al. 2013, å, 49, 137
Grazian, A., Fontana, A., Santini, P., et al. 2015, A&A, 575, A96
Inoue, A. K. & Iwata, I. 2008, MNRAS, 387, 1681
Inoue, A. K., Shimizu, I., Iwata, I., & Tanaka, M. 2014, MNRAS, 442, 1805
Jaskot, A. E. & Oey, M. S. 2014, ApJ, 791, L19
Ly, C., Malkan, M. A., Nagao, T., et al. 2014, ApJ, 780, 122
Malkan, M., Webb, W., & Konopacky, Q. 2003, ApJ, 598, 878
Maseda, M. V., van der Wel, A., Rix, H.-W., et al. 2014, ApJ, 791, 17
Mostardi, R. E., Shapley, A. E., Nestor, D. B., et al. 2013, ApJ, 779, 65
Mostardi, R. E., Shapley, A. E., Steidel, C. C., et al. 2015, ApJ, 810, 107
Nakajima, K. & Ouchi, M. 2014, MNRAS, 442, 900
Nestor, D. B., Shapley, A. E., Kornei, K. A., Steidel, C. C., & Siana, B. 2013, ApJ, 765, 47
Pérez-Montero, E. 2014, MNRAS, 441, 2663
Shapley, A. E., Steidel, C. C., Pettini, M., Adelberger, K. L., & Erb, D. K. 2006, ApJ, 651, 688
Siana, B., Shapley, A. E., Kulas, K. R., et al. 2015, ApJ, 804, 17
Siana, B., Teplitz, H. I., Ferguson, H. C., et al. 2010, ApJ, 723, 241
Stasińska, G., Izotov, Y., Morisset, C., & Guseva, N. 2015, A&A, 576, A83
Steidel, C. C., Pettini, M., & Adelberger, K. L. 2001, ApJ, 546, 665
Vanzella, E., de Barros, S., Castellano, M., et al. 2015, A&A, 576, A116
Vanzella, E., Fontana, A., Pentericci, L., et al. 2014, A&A, 569, A78
Vanzella, E., Guo, Y., Giavalisco, M., et al. 2012, ApJ, 751, 70
Vanzella, E., Siana, B., Cristiani, S., & Nonino, M. 2010, MNRAS, 404, 1672
Verhamme, A., Orlitová, I., Schaerer, D., & Hayes, M. 2015, A&A, 578, A7
Yang, H., Malhotra, S., Gronke, M., et al. 2015, ArXiv e-prints [arXiv] 1506.02885

SF2A 2015
F. Martins, S. Boissier, V. Buat, L. Cambrésy and P. Petit (eds)

WARM MOLECULAR HYDROGEN AT HIGH REDSHIFT WITH THE JAMES WEBB SPACE TELESCOPE

P. Guillard[1], F. Boulanger[2], M. D. Lehnert[1], P. N. Appleton[3] and G. Pineau des Forêts[2, 4]

Abstract. The build-up of galaxies is regulated by a complex interplay between gravitational collapse, galaxy merging and feedback related to AGN and star formation. The energy released by these processes has to dissipate for gas to cool, condense, and form stars. How gas cools is thus a key to understand galaxy formation. *Spitzer Space Telescope* infrared spectroscopy revealed a population of galaxies with weak star formation and unusually powerful H_2 line emission. This is a signature of turbulent dissipation, sustained by large-scale mechanical energy injection. The cooling of the multiphase interstellar medium is associated with emission in the H_2 lines. These results have profound consequences on our understanding of regulation of star formation, feedback and energetics of galaxy formation in general. The fact that H_2 lines can be strongly enhanced in high-redshift turbulent galaxies will be of great importance for the *James Webb Space Telescope* observations which will unveil the role that H_2 plays as a cooling agent in the era of galaxy assembly.

Keywords: Galaxies: evolution, interstellar medium, molecular gas, turbulence, accretion, feedback – stars: formation – ISM: turbulence, kinematics, dynamics – Infrared: ISM

1 Introduction: gas heating and cooling in galaxy assembly

In the ΛCDM framework, galaxies are assembled from the collapse of gas in virialized dark matter haloes (e.g White & Rees 1978; Fall & Efstathiou 1980). The most outstanding question in all contemporary theoretical studies of galaxies evolution is what processes regulate the gas content of galaxies, that is, the balance between accretion and mass loss. This balance, and thus the build-up of baryonic mass in galaxies, is regulated by a complex interplay between gravitational collapse, gas accretion, galaxy merging and feedback related to active galactic nuclei (AGN) activity and star formation (e.g. Dekel & Birnboim 2006). It is this competition between the rates of inflow, outflow, and star formation that gives the properties and physical characteristics of the galaxies we observe today. What currently limits our understanding of galaxy formation is how does the gas respond to those feedback mechanisms, which may inject sufficient mechanical energy into the interstellar medium (ISM) to have a major impact on star formation and galaxy assembly, thus potentially regulating the growth of galaxies (Lehnert et al. 2015; Guillard et al. 2015). Those feedback processes will be particularly important during the early phases of galaxy evolution at high redshift, when galaxies were gas-rich and most of the stars in the universe were formed.

The energy injected by feedback processes has to be dissipated for gas to cool and form stars. Observations of galaxies experiencing strong feedback and turbulence (e.g. galaxy interactions, AGN, cluster cooling flows) show that a significant fraction of this energy cascades down to small scales and is dissipated through line emission. This turbulent cascade is associated with the formation of multiphase ISM and one of the dominant cooling channel is through H_2 line emission (Guillard et al. 2009, 2012b). H_2 is a natural outcome of gas cooling, and the material from which stars are formed. Being affected by star formation, massive central black holes, and inflows and outflows of gas, H_2 plays an important role in all stages of galaxy formation and evolution

[1] Sorbonne Universités, UPMC Université Paris 6 et CNRS, UMR 7095, Institut d'Astrophysique de Paris, 98 bis bd Arago, 75014 Paris, France.
[2] Institut d'Astrophysique Spatiale, UMR 8617, CNRS, Université Paris-Sud, Bat. 121, 91405 Orsay, France
[3] NASA Herschel Science Center, Infrared Processing & Analysis Center, California Institute of Technology, Pasadena, CA 91125, USA
[4] Observatoire de Paris, LERMA, UMR 8112, CNRS, 61 Avenue de l'Observatoire, 75014 Paris, France

© Société Francaise d'Astronomie et d'Astrophysique (SF2A) 2015

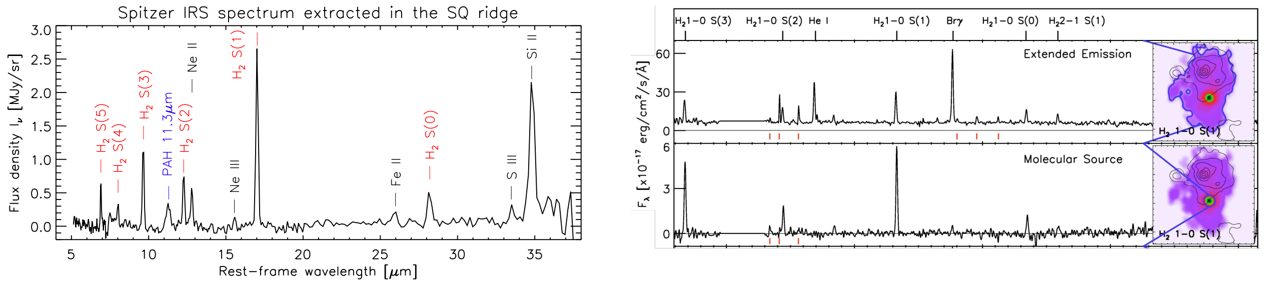

Figure 1. *Left:* Spitzer IRS mid-infrared spectrum of the Stephan's Quintet intra-group medium (Appleton et al. 2006; Cluver et al. 2010). *Right:* Integrated VLT/SINFONI near-infrared spectra of two regions (a compact and extended one) in the overlap area of the Antennae galaxies (Herrera et al. 2011). In the right panel, blue contours mark the aperture from which each spectrum was extracted. In both sources, the spectra show prominent H_2 rotational and ro-vibrational lines, respectively. The H_2 emission is originating from the dissipation of turbulent energy driven by large-scale gas dynamics, a galaxy hitting a tidal filament for Stephan's Quintet and the formation of bound clouds through accretion for the Antennae overlap region.

(Boulanger et al. 2009). In this paper, we stress the unique capability of the James Webb Space Telescope to detect and characterize H_2 line emission at the peak of the star-forming activity of the Universe. Those observations will be key to study the structure and phase distribution of the gas, because they will allow us to estimate the cooling, turbulent dissipation, and dynamical times.

2 H_2 line emission as a probe of the energetics of molecular gas

Excitation of rotation-vibration levels of H_2 can occur through different mechanisms. Collisional excitation with atoms and molecules (e.g. Flower 1998; Le Bourlot et al. 2002), absorption of UV photons followed by fluorescence (e.g. Gautier et al. 1976; Black & van Dishoeck 1987), heating by hard X-rays penetrating into the molecular clouds (Maloney et al. 1996; Tine et al. 1997), and cosmic ray heating (Dalgarno et al. 1999), which has mainly been discussed for the strong H_2 emission in cooling-flow filaments (Ferland et al. 2008).

Rotational and ro-vibrational lines of molecular hydrogen (H_2) have become an important diagnostic tool for shocks in the galactic (e.g. Allen & Burton 1993; Falgarone et al. 2005; Hewitt et al. 2009; Ingalls et al. 2011) and extra-galactic interstellar medium (e.g. Wright et al. 1993; Appleton et al. 2006; Veilleux et al. 2009; Ogle et al. 2010; Beirão et al. 2015). Two examples are given in Figure 1. Pure rotational lines of H_2 (0-0 S(0), 0-0 S(1), etc.) are found in the mid-infrared between $3 - 30\,\mu$m and trace warm gas with typical temperatures of a few 100 K to 1000 K. Ro-vibrational lines of H_2 (e.g., 1-0 S(1) at $2.12\,\mu$m) are observed in the near-infrared and trace hotter gas with temperatures of a few 1000 K. According to shock models, H_2 line ratios can be used to infer the pre-shock gas characteristics (density, magnetic field) and shock properties (velocity, non-dissociative – C-type – or dissociative – J-type –) (Flower & Pineau des Forêts 2010; Guillard et al. 2009, 2012b).

3 Tracing the kinetic energy dissipation associated with feedback processes at $z \sim 1.5 - 3.5$ with JWST

The *James Webb Space Telescope* will be, 15 years after the *Spitzer Space Telescope*, the next mission to have access to rotation-vibration H_2 transitions. As such, it will play a critical role in the context of galaxy evolution since H_2 represents an important, if not dominant, cooling agent in the energetics of galaxy formation. Observations by the InfraRed Spectrograph (IRS) onboard the *Spitzer Space Telescope* unveiled a significant and diverse population of low-z objects where the mid-infrared rotational line emission of H_2 is strongly enhanced ($L_{\rm H_2} \sim 10^{40} - 10^{44}$ erg s^{-1}), while star formation is suppressed (see Figure 2). This suggest that shocks are the primary cause of the H_2 emission (Guillard et al. 2009). This sample of *H_2-luminous sources* includes galaxies in several key phases of their evolution, dominated by, for instance, gas accretion onto bright central galaxies in clusters (Egami et al. 2006), galaxy interactions (Appleton et al. 2006), or galactic winds driven by star formation (e.g. M82 Beirão et al. 2015), and radio-loud AGN (Ogle et al. 2010; Guillard et al. 2012b). In those sources, the turbulent dissipation time is longer than the dynamical time, the mechanical energy contained in the molecular phase being dominant over the thermal energy of the gas (e.g. Guillard et al. 2012a).

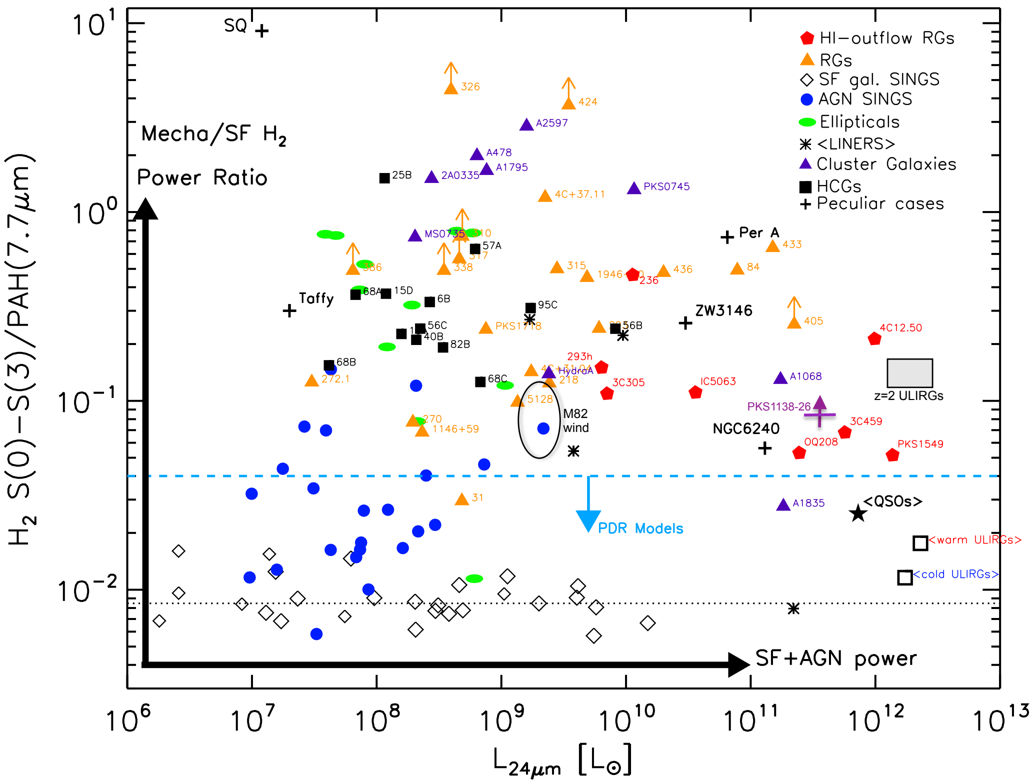

Figure 2. Ratio of the mid-IR H_2 line luminosities (summed over S(0) to S(3)) to the PAH 7.7μm emission vs. 24μm continuum luminosity (updated from Guillard et al. 2012b). This ratio indicates the relative contribution of mechanical heating (shocks) and star-formation (SF) power (UV excitation). The red pentagons are nearby radio galaxies with fast (>1000 km/s) HI outflows observed with *Spitzer IRS* (Guillard et al. 2012b). The orange triangles and green ellipses are samples of radio galaxies (respectively Ogle et al. 2010; Kaneda et al. 2008). These H_2-luminous galaxies stand out above SF and AGN galaxies from the SINGS survey (Roussel et al. 2007). The H_2 emission in these sources cannot be accounted by UV or X-ray photon heating. The blue dashed line shows the upper limit given by the Kaufman et al. (2006) PDR models ($n_H = 10^4\,\mathrm{cm}^{-3}$, $G_{UV} = 10$). For comparison, a few other types of H_2-luminous galaxies are shown: the Stephan's Quintet (SQ) and Taffy galaxy collisions (Cluver et al. 2010; Peterson et al. 2012), other Hickson Compact Groups (black squares, Cluver et al. 2013), the ZW 3146 (Egami et al. 2006) and Perseus A (Johnstone et al. 2007) clusters, and the NGC 6240 merger (Armus et al. 2006). The black ellipse shows the *Spitzer IRS* observations of the M82 wind (Beirão et al. 2015), the black rectangle shows the detection of H_2 in stacked *Spitzer* spectra of $z = 2$ ULIRGs (Fiolet et al. 2010), and the purple cross the detection of H_2 in the Spider Web (PKS1138-26) radio galaxy protocluster (Ogle et al. 2012).

Constraining the impact of merging and AGN feedback on the formation and evolution of massive galaxies can only be addressed through direct H_2 line observations at $z \sim 2$, near the cosmologically most active period of star formation, galaxy interactions and AGN activity. By analogy to what is observed on local H_2-luminous objects, we expect the mid-IR lines to be the dominant cooling lines for warm, 10^{2-3} K, gas in the strongly shocked, highly turbulent, colliding flows in galaxy interactions (e.g. the galaxy-wide shock in Stephan's Quintet, Guillard et al. 2009), but also, e.g., in AGN-driven outflows. High gas velocity dispersions measured in $z \sim 2$ actively star-forming galaxies show that the gas kinematics in these systems was strongly disturbed compared to galaxies today (e.g. Lehnert et al. 2009). The molecular gas is observed to be highly turbulent and therefore the warm H_2 emission is expected to be more frequent and more powerful than at low-z, as suggested by H_2 detections in $z \approx 2$ infrared-luminous galaxies (Fiolet et al. 2010; Ogle et al. 2012). In those sources, H_2 line emission is likely powered by the dissipation of turbulence, which could originate from star formation (supernovae), radiation pressure, or gas accretion.

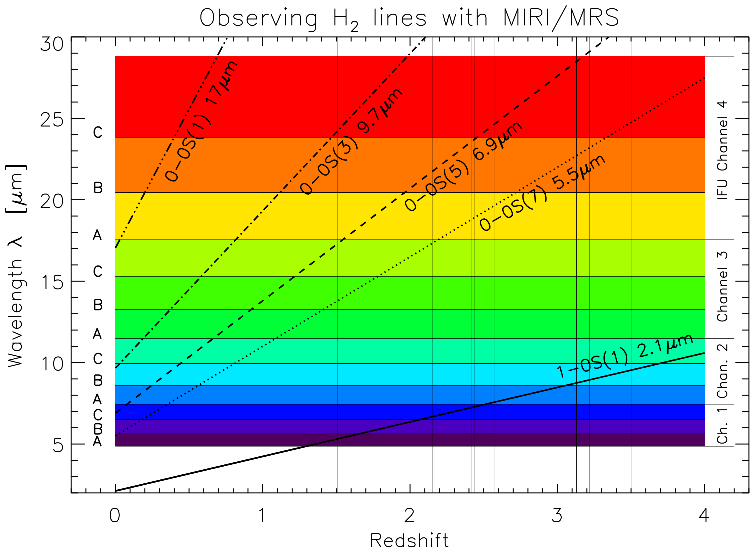

Figure 3. Observing H_2 lines at high-redshift with JWST/MIRI. The observed wavelengths of some H_2 lines are shown as a function of the redshift. The colored bars indicate the channels and bands of the Medium Resolution Spectrometer (MRS) of the MIRI instrument. One observation corresponds to four sub-bands, like 1A, 2A, 3A, 4A for instance (see Guillard, P. 2010, for technical details about the MRS operations). The vertical lines indicate the redshifts of some high-z radio-galaxies that might be interesting to look at with MIRI.

Covering a wavelength range of $4.9 - 28.6\,\mu$m, the MIRI Medium Resolution Spectrometer (MRS, Wells et al. 2015) will be the first Integral Field Unit (IFU) instrument to provide the sensitivity and resolving power to spatially and spectrally resolve H_2 and forbidden ionized gas lines at rest-frame near-IR and mid-IR wavelengths, out to $z = 1.5 - 3.5$ (Figure 3). Covering $0.6 - 5\,\mu$m in the near-infrared, NIRSPEC (Posselt et al. 2004) will allow the detection of ro-vibrational lines at very high sensitivity (0.6×10^{-21} W m^{-2} for 1h) and spectral resolution ($R \approx 3000$ for the IFU mode). Both the MRS and NIRSPEC IFUs will have comparable spectral resolutions to the SINFONI near-infrared IFU on the VLT (see Figure 1, right panel). The JWST instruments will allow us to directly investigate the physical state and the kinematics of the ionized gas and the warm (> 150 K) molecular gas that is dynamically heated by the dissipation of mechanical energy associated with galaxy merging and AGN feedback. To establish the energy budget of the warm molecular gas and shock diagnostics, we shall use the near-IR ro-vibrational lines, e.g. the H_2 1-0 S(1) $2.12\,\mu$m line, and the mid-IR pure rotational H_2 0-0 S(3) $9.7\,\mu$m and S(5) $6.9\,\mu$m lines. The forbidden ionized gas lines (e.g. [Ne II], [Ne III]) will be used to compare the kinematics of the molecular gas with that of the ionized gas and complement the shock diagnostics (Gusdorf 2015). The synergy with NIRSPEC will be helpful to observe the CO bandheads and Ca II triplet to estimate the stellar kinematics. This will allow to estimate the ratio between the bulk galaxy rotation and the gas velocity dispersion in these high-z objects, and provide an absolute rest-frame in which to interpret the gas motions as blueshift or redshift.

4 Conclusions and perspectives

Rotation-vibration H_2 transitions observed in the mid- and near-infrared appear as key tracers of the energetics of galaxy formation and evolution. They complement the CO transitions which usually trace the bulk of the molecular gas that is too cold to emit in H_2. The powerful infrared H_2 line emission observed in a large sample of extragalactic sources is believed to be powered by the dissipation of turbulent energy, provided by large-scale shocks from galaxy collisions, radio jet feedback, star formation and gas accretion. In some cases, the line emission represents a significant fraction of the total molecular gas mass and bolometric luminosity of the galaxies. By observing routinely those lines, the JWST should allow us to relate the star formation activity and the gas accretion rates to the turbulence of the gas. This has potentially far-reaching implications, from the physics of the multiphase ISM, regulation of star formation in the most massive galaxies, and the formation of the first galaxies.

References

Allen, D. A. & Burton, M. G. 1993, Nature, 363, 54

Appleton, P. N., Xu, K. C., Reach, W., et al. 2006, ApJ, 639, L51

Armus, L., Bernard-Salas, J., Spoon, H. W. W., et al. 2006, ApJ, 640, 204

Beirão, P., Armus, L., Lehnert, M. D., et al. 2015, MNRAS, 451, 2640

Black, J. H. & van Dishoeck, E. F. 1987, ApJ, 322, 412

Boulanger, F., Maillard, J. P., Appleton, P., et al. 2009, Experimental Astronomy, 23, 277

Cluver, M. E., Appleton, P. N., Boulanger, F., et al. 2010, ApJ, 710, 248

Cluver, M. E., Appleton, P. N., Ogle, P., et al. 2013, ApJ, 765, 93

Dalgarno, A., Yan, M., & Liu, W. 1999, ApJS, 125, 237

Dekel, A. & Birnboim, Y. 2006, MNRAS, 368, 2

Egami, E., Rieke, G. H., Fadda, D., & Hines, D. C. 2006, ApJ, 652, L21

Falgarone, E., Verstraete, L., Pineau Des Forêts, G., & Hily-Blant, P. 2005, A&A, 433, 997

Fall, S. M. & Efstathiou, G. 1980, MNRAS, 193, 189

Ferland, G. J., Fabian, A. C., Hatch, N. A., et al. 2008, MNRAS, 386, L72

Fiolet, N., Omont, A., Lagache, G., et al. 2010, A&A, 524, A33+

Flower, D. R. 1998, MNRAS, 297, 334

Flower, D. R. & Pineau des Forêts, G. 2010, MNRAS, 406, 1745

Gautier, III, T. N., Fink, U., Larson, H. P., & Treffers, R. R. 1976, ApJ, 207, L129

Guillard, P., Boulanger, F., Lehnert, M. D., et al. 2015, A&A, 574, A32

Guillard, P., Boulanger, F., Pineau Des Forêts, G., & Appleton, P. N. 2009, A&A, 502, 515

Guillard, P., Boulanger, F., Pineau des Forêts, G., et al. 2012a, ApJ, 749, 158

Guillard, P., Ogle, P. M., Emonts, B. H. C., et al. 2012b, ApJ, 747, 95

Guillard, P. 2010, PhD thesis, IAS, Université Paris Sud 11

Gusdorf, A. 2015, ArXiv e-prints

Herrera, C. N., Boulanger, F., & Nesvadba, N. P. H. 2011, A&A, 534, A138

Hewitt, J. W., Rho, J., Andersen, M., & Reach, W. T. 2009, ApJ, 694, 1266

Ingalls, J. G., Bania, T. M., Boulanger, F., et al. 2011, ApJ, 743, 174

Johnstone, R. M., Hatch, N. A., Ferland, G. J., et al. 2007, MNRAS, 382, 1246

Kaneda, H., Onaka, T., Sakon, I., et al. 2008, ApJ, 684, 270

Kaufman, M. J., Wolfire, M. G., & Hollenbach, D. J. 2006, ApJ, 644, 283

Le Bourlot, J., Pineau des Forêts, G., Flower, D. R., & Cabrit, S. 2002, MNRAS, 332, 985

Lehnert, M. D., Nesvadba, N. P. H., Tiran, L. L., et al. 2009, ApJ, 699, 1660

Lehnert, M. D., van Driel, W., Le Tiran, L., Di Matteo, P., & Haywood, M. 2015, A&A, 577, A112

Maloney, P. R., Hollenbach, D. J., & Tielens, A. G. G. M. 1996, ApJ, 466, 561

Ogle, P., Boulanger, F., Guillard, P., et al. 2010, ApJ, 724, 1193

Ogle, P., Davies, J. E., Appleton, P. N., et al. 2012, ApJ, 751, 13

Peterson, B. W., Appleton, P. N., Helou, G., et al. 2012, ApJ, 751, 11

Posselt, W., Holota, W., Kulinyak, E., et al. 2004, in Society of Photo-Optical Instrumentation Engineers (SPIE) Conference Series, Vol. 5487, Optical, Infrared, and Millimeter Space Telescopes, ed. J. C. Mather, 688–697

Roussel, H., Helou, G., Hollenbach, D. J., et al. 2007, ApJ, 669, 959

Tine, S., Lepp, S., Gredel, R., & Dalgarno, A. 1997, ApJ, 481, 282

Veilleux, S., Rupke, D. S. N., & Swaters, R. 2009, ApJ, 700, L149

Wells, M., Pel, J.-W., Glasse, A., et al. 2015, PASP, 127, 646

White, S. D. M. & Rees, M. J. 1978, MNRAS, 183, 341

Wright, G. S., Geballe, T. R., & Graham, J. R. 1993, in Evolution of Galaxies and their Environment, ed. J. M. Shull & H. A. Thronson, 195–196

SF2A 2015
F. Martins, S. Boissier, V. Buat, L. Cambrésy and P. Petit (eds)

SHOCKS, STAR FORMATION AND THE JWST

A. Gusdorf[1]

Abstract. The interstellar medium (ISM) is constantly evolving due to unremitting injection of energy in various forms. Energetic radiation transfers energy to the ISM: from the UV photons, emitted by the massive stars, to X- and γ-ray ones. Cosmic rays are another source of energy. Finally, mechanical energy is injected through shocks or turbulence. Shocks are ubiquitous in the interstellar medium of galaxies. They are associated to star formation (through jets and bipolar outflows), life (via stellar winds), and death (in AGB stellar winds or supernovae explosion). The dynamical processes leading to the formation of molecular clouds also generate shocks where flows of interstellar matter collide. Because of their ubiquity, the study of interstellar shocks is also a useful probe to the other mechanisms of energy injection in the ISM. This study must be conducted in order to understand the evolution of the interstellar medium as a whole, and to address various questions: what is the peculiar chemistry associated to shocks, and what is their contribution to the cycle of matter in galaxies ? What is the energetic impact of shocks on their surroundings on various scales, and hence what is the feedback of stars on the galaxies ? What are the scenarios of star formation, whether this star formation leads to the propagation of shocks, or whether it is triggered by shock propagation ? What is the role of shocks in the acceleration of cosmic rays ? Can they shed light on their composition and diffusion processes ? In order to progress on these questions, it is paramount to interpret the most precise observations with the most precise models of shocks. From the observational point of view, the James Webb Space Telescope represents a powerful tool to better address the above questions, as it will allow to observe numerous shock tracers in the infrared range at an unprecedented spatial and spectral resolution.

Keywords: shock waves – astrochemistry – stars: formation – ISM: jets and outflows – ISM: kinematics and dynamics – Infrared: ISM

1 Different shock environments

Observations over the past few decades have shown that, in the early stages of low-mass star formation, the process of mass accretion is almost always associated with mass ejection in the form of collimated jets. The jets impact on the parent cloud, driving a shock front through the collapsing interstellar gas. Large cavities, called bipolar outflows, are carved in the ambient medium, which is accelerated, compressed and heated by the shock wave. This paradigm was proposed by Snell et al. (1980) and has been regularly verified in such environments (see, for example, figure 1, and Arce et al. 2007; Frank et al. 2014 for reviews), including recent high-angular-resolution observations by ALMA (e.g. Codella et al. 2014). Comparisons of observations in these jet/outflow regions with 1D shock models such as the Paris-Durham model (Flower & Pineau des Forêts 2015) have been extensively performed in the last decade. The aim is often to constrain the physical conditions (e.g. Giannini et al. 2004, 2006; Dionatos et al. 2010). It can additionnally be to understand the chemistry of a given species, such as SiO (e.g. Gusdorf et al. 2008a,b, 2015b) or/and CH_3OH and NH_3 (e.g. Flower et al. 2010; Flower & Pineau des Forêts 2012). Of course, when properly understood, the chemistry of this species can in turn allow to better characterize the physical conditions prevailing in the shocked gas. Recently, the column densities of H_2O inferred from observations in various low-mass star forming regions have raised some concern that models (e.g. Kaufman & Neufeld 1996; Flower & Pineau Des Forêts 2010; Gusdorf et al. 2011) might have overestimated its abundance. This discrepancy could be due to the underestimate of the effects of the protostellar radiation field in models, but this assumption has not been tested yet. In any case, directly

[1] LERMA, Observatoire de Paris, PSL Research University, CNRS, UMR 8112, F-75014, Paris, France; Sorbonne Universités, UPMC Univ. Paris 6, UMR 8112, LERMA, F-75005, Paris, France

© Société Francaise d'Astronomie et d'Astrophysique (SF2A) 2015

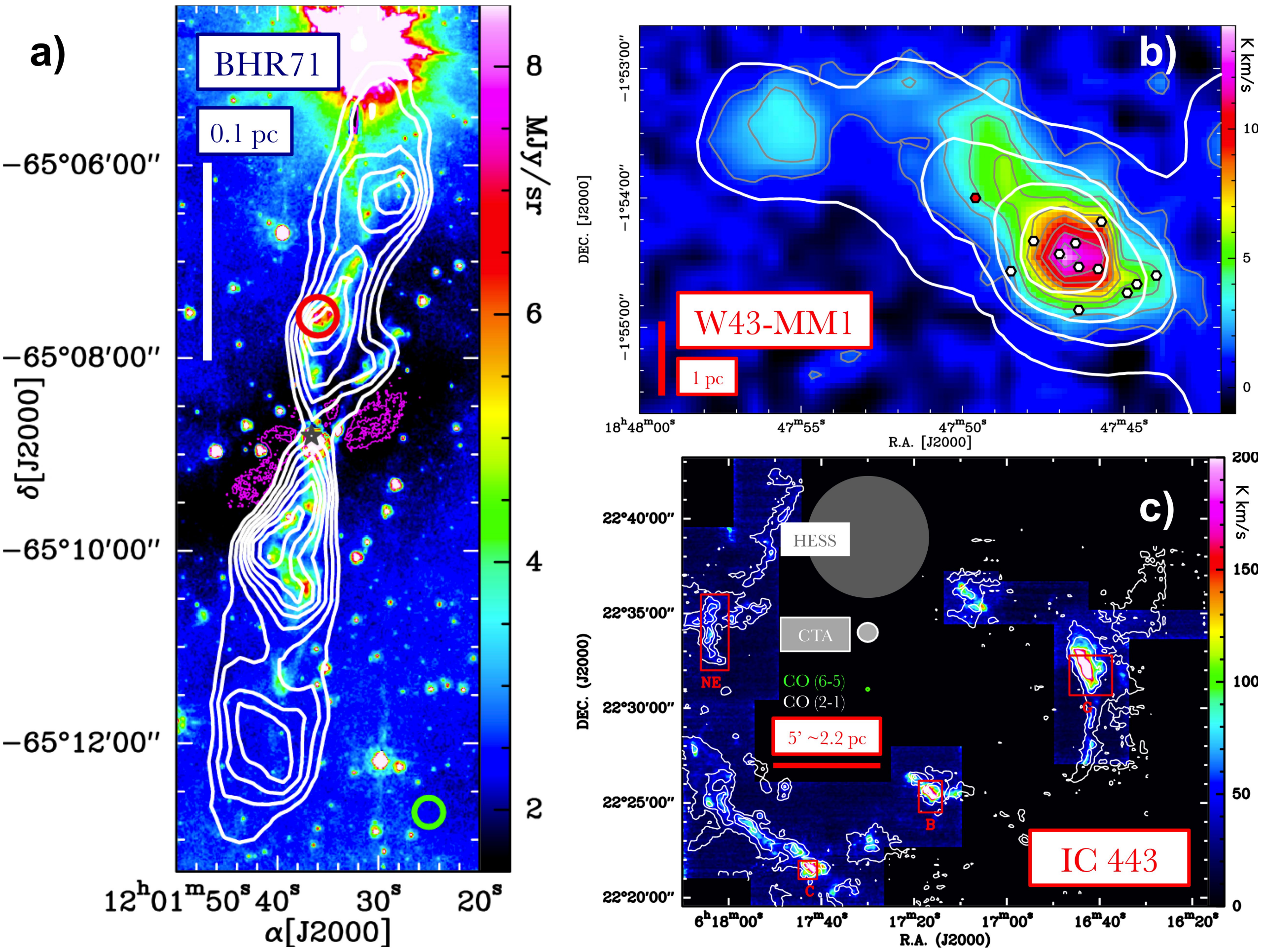

Fig. 1. The ubiquity of shocks in the interstellar medium. Note the sizes indicated in the various panels. **a):** The BHR71 bipolar outflow system driven by two young proto-stars, seen in colours and red contours at 8 μm by *Spitzer*/IRAC, and in white contours in the CO (3–2) emission line by the APEX telescope; adapted from Gusdorf et al. (2015b). **b):** The W43-MM1 ridge, seen in colours and grey contours in the SiO (2–1) transition (adapted from Nguyen-Lu'o'ng et al. 2013). The white contours are column density contours. The white hexagons mark the position of massive dense cores identified by Louvet et al. (2014). The red hexagon is a dense core. **c):** The IC 443 supernova remnant, seen in the CO (6–5) (colours) and (2–1) (white contours) transitions. The typical beam size of the CO observations is also shown, as well as those of current (HESS) and future (CTA) γ-ray observatories (Gusdorf et al., prep., I).

comparing observed line integrated intensities to modelled ones does not seem to yield such a discrepancy (e.g. Flower & Pineau des Forêts 2013; Neufeld et al. 2014) in low-mass star forming environments.

One of the major shortcomings of such models is their simple geometry. In the case of the Paris-Durham model, the choice was made to keep a 1D geometry in order to optimize the numerical treatment of microscopic physical and chemical processes, as a 3D shock model including 1000 chemical reactions would still take too much time to run. Recently, attempts have been made to overcome this difficulty. In Kristensen et al. (2008) and Gustafsson et al. (2010), the 1D shock models have been stitched on 2D or 3D structures, ultimately and successfully allowing to compare modelled maps of integrated intensity with observations. The Paris-Durham model has also been combined with dynamical MHD disk wind models in order to account for the observations of molecular counterparts to atomic jets, very close to the protostars and at very early evolutionary stages (Panoglou et al. 2012 and Yvart et al., in prep.). Probability density functions of 1D shock layers have also been generated in order to statistically account for a more complex shock structure (Lesaffre et al. 2013).

Interestingly, these latest shock models somehow included the effects of the protostellar radiation field. Such an inclusion is paramount when studying shocks in regions of more massive star formation, as massive protostars radiate significant amounts of energy in the UV range (see Tan et al. 2014 for a review). Mostly because of this extra ingredient, the paradigm for the formation of massive stars is less established than for their low-mass counterpart. The key question is to determine whether massive stars form from a dense core in a scaled-up version of the low-mass scenario, or if alternative processes should be invoked, such as competitive accretion or coalescence of low-mass protostars. A way to build a consistent view on star formation is to compare observations with models in regions of shocks associated to the formation of protostars of various masses. This implies a development of a new class of shock models, called 'irradiated' because they must include the influence of the protostellar radiation field. Indeed, Lefloch et al. (2015) have been able to successfully reproduce CO observations of a shock in an intermediate-mass protostellar outflow, but e.g. Leurini et al. (2014), Gusdorf et al. (2015a), and Gusdorf et al., submitted to A&A, have quantified the shortcomings of non-irradiated shock models to fit H_2O, OH, or C^+ observations in regions of massive star formation. The implementation of irradiated shock models is ongoing (e.g. Lesaffre et al. 2013, Melnick & Kaufman 2015) and is key to constrain the scenarios of massive star formation, but also its chemical and energetic impact. It is also important to be able to distinguish regions where shocks are irradiated by an external radiation source from regions where the shocks itself is a source of UV radiation, a situation that occurs in fast shocks (e.g. Hollenbach & McKee 1989).

The implementation of the effects of a mild irradiation is also necessary to better understand the peculiar physics and chemistry at work in the dense filaments whose formation is the result of dynamical accretion processes themselves at the origin of the formation of molecular clouds. In these converging flows, dense and low-velocity shocks are observed (see figure 1 and e.g. Nguyen-Lu'o'ng et al. 2013, Duarte-Cabral et al. 2014). Studying these regions where streams of matter collide or converge is a way to understand the ongoing massive star formation, often clustered in some regions of the ridge (Louvet et al. 2014). It is also a way to confront our models with a new chemistry where thermal effects can dominate the sputtering of grains, resulting e.g. in the detection of extended, and narrow emission of SiO transitions for instance (Louvet et al., in prep.). It is finally a way to quantify whether these extended and very common regions contribute to the energetic balance of galaxies, through measurements of the flux from their high-lying CO transitions (Gusdorf et al., in prep., II).

The objective of quantifying the high-J CO emission from shock regions, or more generally the energetic impact they could have on large scales, is also significant when studying supernova remnants (SNRs; see figure 1), given their size. In such regions, various studies have shown that non irradiated models of shocks, stationary (Gusdorf et al. 2012, Neufeld et al. 2014) or not (Cesarsky et al. 1999, Anderl et al. 2014), can reproduce the observations of CO, H_2 and/or H_2O. In old SNRs, the detailed characterisation of the interstellar content can also serve to support the study of cosmic-ray (CR) related questions. Indeed, these objects are usually detected at very high energy by γ-ray telescopes such as HESS, *Fermi*, VERITAS or MAGIC (e.g. Aharonian et al. 2008, Abdo et al. 2010). CRs have been accelerated to high energies in the past, then trapped in the shocked/dense region. The γ-ray emission is the signature of interactions involving the hadronic (π^0 decay) or leptonic (Inverse Compton, Bremstrahlung, synchrotron emission) part of CRs on the one hand, and the dense and often shocked medium in the other hand. Characterizing shocks is hence essential to understand the contribution of these processes to the high energy spectra, and to support the study of CRs acceleration, composition and diffusion.

2 The JWST contribution

With an expected launch in 2018, the JWST will be a powerful tool to support the study of shocks. First, it will allow to observe pure rotational line emission from H_2. H_2 is an important molecule in the ISM and particularly in shocked regions. Indeed, it is an abundant molecule, a key partner in chemical and collisional processes leading to the formation and excitation of other species. Since its rotational levels lie at a few hundreds to a few thousands of K, its excitation traces the dense, warm medium, and H_2 hence constitutes an important cooling agent of shocked regions. Constraining the physical conditions prevailing in the H_2 emitting gas is an unavoidable step when performing detailed chemical studies, and represent a potential benefit to every study already mentioned. This is all the more true in regions that were not observed by the ISO or *Spitzer* telescopes. This is the case of the filaments and ridges that constitutes one of the important legacies of the *Herschel* telescope and whose studies started when no further observation of rotational line emission from H_2 was possible with *Spitzer*. Observing the H_2 emission in various environments with MIRI will also allow to better understand the processes of its formation at the surface of grains, and to place tighter constraints on its excitation processes. From the point of view of H_2 and more generally, the gain in angular resolution of the JWST with respect to those afforded by ISO, or the *Spitzer* telescopes should allow to resolve the shock structures. Simultaneously the gain in sensitivity will allow to map larger regions on bipolar outflows our supernova remnants, an essential step when assessing the energetic impact of an entire object on its surroundings. Such detailed observations will also provide strong constraints for multi-dimensional shock modelling. This gain in sensitivity should also allow to study the propagation of shocks in the more diffuse medium, where H_2 emission is expected to be fainter.

Insight will also be gained from the JWST in terms of chemistry, as a lot of filters have been designed to target specific lines or features (H_2, CO, H_2O ice, CH_4, CO, CO_2,...). When it comes to shocks, the detailed characterization of the ionization state of the gas is key to investigate the nature of shocks. In particular, the observation of atomic and ionized species, such as [Ar II], [Ne II], [Ne III], [S III], [S I], [Fe II], [Fe III], [O I] should allow to quantify the dissociative nature of shocks, and the degree or origin of their irradiation. The observations of H_2O and the product of its dissociation such as OH and [OI] should also contribute to understand their potential to dissociate the ISM (see, e.g. Tappe et al. 2008, 2012 on the use of *Spitzer* observations of OH to probe the potential of 40 km s^{-1} shocks to generate self-irradiation). Incidently, the ionization fraction reached in a shock is also a key parameter when it comes to assessing its potential to accelerate cosmic rays (Padovani et al., subm. to A&A). Moreover, the observation of numerous molecules (HD, H_3O^+, CH_4, HCN,...) by the JWST will allow to address more specific chemical questions. Finally, the JWST will allow to probe the composition of ice mantles, yielding new constraints on the formation paths of complex molecules.

3 Perspectives

Beyond its unquestionable intrinsic value, the JWST will arrive at a unique time in astronomy, where windows of unprecedented quality are open at all the wavelength of the electromagnetic spectrum. Its strength will not only reside in its added value, but also in its complementarity with other observatories. Used with the VLT (and high resolution receivers such as CRIRES or VISIR), the JWST will provide the most comprehensive view on H_2 emission in terms of spectral and spatial resolutions and mapping capacities. Beyond infrared diagnoses, there will be a natural complementarity of the JWST with sub-mm to far infrared telescopes such as the IRAM-30m, APEX, *Herschel* or SOFIA, to investigate the chemistry of the ISM in greater details than ever. This complementarity extends towards the high energies, as the combination of the JWST with X- (ATHENA) and γ-ray (HESS, *Fermi*, MAGIC, VERITAS, and more importantly CTA) telescopes will allow to better describe fast shocks and to improve our understanding of CRs related questions. Finally, shock astrophysics will benefit from the combined use of the JWST with ALMA, that will allow to probe the effect of shocks not only in our own Galaxy, but in all galaxies, thus tracing the shocks effects in the history of the Universe (see P. Guillard's contribution).

References

Abdo, A. A., Ackermann, M., Ajello, M., et al. 2010, ApJ, 718, 348
Aharonian, F., Akhperjanian, A. G., Bazer-Bachi, A. R., et al. 2008, A&A, 481, 401
Anderl, S., Gusdorf, A., & Güsten, R. 2014, A&A, 569, A81
Arce, H. G., Shepherd, D., Gueth, F., et al. 2007, Protostars and Planets V, 245
Cesarsky, D., Cox, P., Pineau des Forêts, G., et al. 1999, A&A, 348, 945
Codella, C., Cabrit, S., Gueth, F., et al. 2014, A&A, 568, L5
Dionatos, O., Nisini, B., Cabrit, S., Kristensen, L., & Pineau Des Forêts, G. 2010, A&A, 521, A7
Duarte-Cabral, A., Bontemps, S., Motte, F., et al. 2014, A&A, 570, A1
Flower, D. R. & Pineau Des Forêts, G. 2010, MNRAS, 406, 1745
Flower, D. R. & Pineau des Forêts, G. 2012, MNRAS, 421, 2786
Flower, D. R. & Pineau des Forêts, G. 2013, MNRAS, 436, 2143
Flower, D. R. & Pineau des Forêts, G. 2015, A&A, 578, A63
Flower, D. R., Pineau Des Forêts, G., & Rabli, D. 2010, MNRAS, 409, 29
Frank, A., Ray, T. P., Cabrit, S., et al. 2014, Protostars and Planets VI, 451
Giannini, T., McCoey, C., Caratti o Garatti, A., et al. 2004, A&A, 419, 999
Giannini, T., McCoey, C., Nisini, B., et al. 2006, A&A, 459, 821
Gusdorf, A., Anderl, S., Güsten, R., et al. 2012, A&A, 542, L19
Gusdorf, A., Cabrit, S., Flower, D. R., & Pineau Des Forêts, G. 2008a, A&A, 482, 809
Gusdorf, A., Giannini, T., Flower, D. R., et al. 2011, A&A, 532, A53
Gusdorf, A., Guesten, R., Menten, K. M., et al. 2015a, ArXiv e-prints [arXiv] 1509.08367
Gusdorf, A., Pineau Des Forêts, G., Cabrit, S., & Flower, D. R. 2008b, A&A, 490, 695

Gusdorf, A., Riquelme, D., Anderl, S., et al. 2015b, A&A, 575, A98
Gustafsson, M., Ravkilde, T., Kristensen, L. E., et al. 2010, A&A, 513, A5
Hollenbach, D. & McKee, C. F. 1989, ApJ, 342, 306
Kaufman, M. J. & Neufeld, D. A. 1996, ApJ, 456, 611
Kristensen, L. E., Ravkilde, T. L., Pineau Des Forêts, G., et al. 2008, A&A, 477, 203
Lefloch, B., Gusdorf, A., Codella, C., et al. 2015, A&A, 581, A4
Lesaffre, P., Pineau des Forêts, G., Godard, B., et al. 2013, A&A, 550, A106
Leurini, S., Gusdorf, A., Wyrowski, F., et al. 2014, A&A, 564, L11
Louvet, F., Motte, F., Hennebelle, P., et al. 2014, A&A, 570, A15
Melnick, G. J. & Kaufman, M. J. 2015, ApJ, 806, 227
Neufeld, D. A., Gusdorf, A., Güsten, R., et al. 2014, ApJ, 781, 102
Nguyen-Lu'o'ng, Q., Motte, F., Carlhoff, P., et al. 2013, ApJ, 775, 88
Panoglou, D., Cabrit, S., Pineau Des Forêts, G., et al. 2012, A&A, 538, A2
Snell, R. L., Loren, R. B., & Plambeck, R. L. 1980, ApJ, 239, L17
Tan, J. C., Beltrán, M. T., Caselli, P., et al. 2014, Protostars and Planets VI, 149
Tappe, A., Forbrich, J., Martín, S., Yuan, Y., & Lada, C. J. 2012, ApJ, 751, 9
Tappe, A., Lada, C. J., Black, J. H., & Muench, A. A. 2008, ApJ, 680, L117

SF2A 2015
F. Martins, S. Boissier, V. Buat, L. Cambrésy and P. Petit (eds)

PREPARING JWST OBSERVATIONS AT THE FRONTIERS OF THE UNIVERSE

N. Laporte[1], F. E. Bauer[1], D. Bina[2], F. Boone[2], I. Chillingarian[3], L. Infante[1], S. Kim[1], R. Pelló[2], I. Pérez-Fournon[4], A. Streblyanska[4] and P. Troncoso[1]

Abstract. Pushing even further the limits of the observable Universe is one of the most exciting challenge of modern astronomy. During the last decade, several space and ground-based telescopes have been involved in this quest leading to the discovery of hundred of objects at z>6. Therefore, the physical properties of the galaxies emitting light during the first billion years of the Universe are better constrained and we are just starting to understand their role during the reionization process. In the following, we discuss how the last flagship program of the *Hubble* Space Telescope, namely the *Frontier Fields*, is preparing the first JWST observations at the frontiers of the Universe and how the exceptional capabilities of this future space telescope will benefit to the study of the early Universe.

Keywords: Galaxies: distances and redshifts, Galaxies: evolution, Galaxies: formation, Galaxies: high-redshift, Galaxies: photometry, Galaxies: star formation

1 Introduction

One of the main questions of modern astronomy is undoubtedly the study of the earliest stages of the Universe, and more particularly the study of the first luminous objects. Within the last ten years, considerable advances have been made to push ever further the limits of the observable Universe. To date the most distant object confirmed by spectroscopic observations has emitted light around 600 million years after the Big-Bang (Zitrin et al. 2015), and it is $\sim$ 60 times less massive than the Milky Way. However, only a dozen secured objects are currently known at such early epoch, making the conclusions on their properties, environment or evolution during cosmic times difficult. The arrival of large surveys aiming to study the most distant objects, such as the *Hubble Ultra Deep Field* or the on-going *Frontier Fields*, has strongly increased the number of very high-redshift candidates (e.g. Ellis et al. 2013, Bouwens et al. 2015). Moreover, the arrival of the future *James Webb Space Telescope* (JWST - Gardner et al. 2009) by the end of 2018, will open a new cosmic time window allowing to study in details the properties of the primeval galaxies.

2 The HST Frontier Fields

In October 2013, the *Hubble* Space Telescope started observations of six massive galaxies clusters as part of its new flagship program, "The Frontier Fields", aiming to obtain the deepest data using strong gravitational lensing. The data are reduced by the *Space Telescope Science Institute* and released few days after observations. The *Spitzer* Space Telescope is also involved in this project allowing to increase the wavelength coverage with extremely deep data up to $\sim$5μm. Several teams have also provided lens models and amplification maps for all clusters (Bradač et al. 2009, Richard et al. 2014, Merten et al. 2011, Zitrin et al. 2013, Johnson et al. 2014 and Mohammed et al. 2014). To date, four clusters have been already observed by *Hubble* : Abell 2744, MACSJ0416.1-2403, MACSJ0717.5+3745 and MACS1149.5+2223 reaching a depth of 29.0 AB at 5σ.

[1] Instituto de Astrofísica, Pontificia Universidad Católica, Santiago (CHILE)
[2] Institut de Recherche en Astrophysique et Planètologie, Toulouse (FRANCE)
[3] Harvard-Smithsonian Center for Astrophysics, Boston (US)
[4] Instituto de Astrofísica de Canarias, La Laguna (SPAIN)

© Société Francaise d'Astronomie et d'Astrophysique (SF2A) 2015

2.1 Search for z>6.5 objects

The most popular method used to identify very high-z sources on a photometric dataset is the Lyman Break technique (Steidel et al. 1996) combining color selection with strong non-detection criteria in bands bluewards of the break. Our team applied this method for the three first Frontier Fields clusters, namely Abell 2744 (Laporte et al. 2014), MACSJ0416.1-2403 (Laporte et al. 2015b, Infante et al. 2015) and MACSJ0717+3745 (Laporte et al. in prep) and selected ∼100 objects at z>6.5. Recently, several studies (e.g. Smit et al. 2014) have shown that z∼8 objects display two breaks in magnitude in their Spectral Energy Distribution (SED) : one around the Lyman-α emission, called Lyman break, and another one around 4μm, the 4000Å break. Among all the z∼8 objects selected on FF images, 3 display such a break between HST and *Spitzer* data (Figure 1) confirming the high-z hypothesis for these sources. All the z>8 galaxies spectroscopically confirmed so far display these two breaks (Finkelstein et al. 2013, Oesch et al. 2015, Zitrin et al. 2015). Therefore, the detection of both the Lyman-α and 4000AA breaks strongly reduce the probability for these objects to be low-z interlopers.

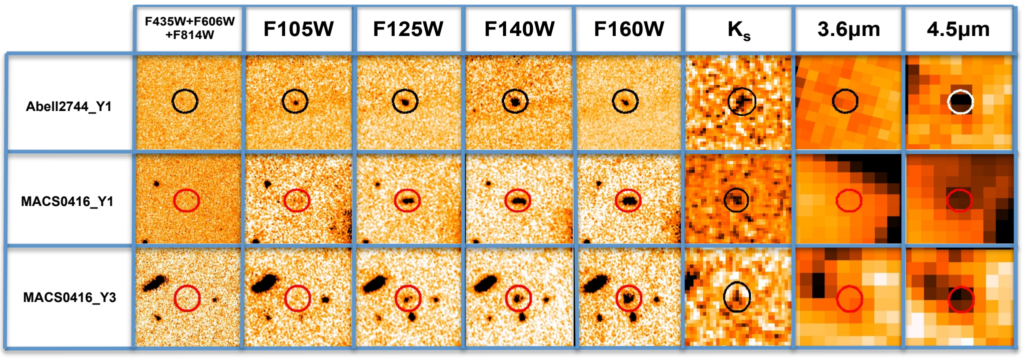

Fig. 1. z∼8 candidates displaying a break around 4μm that could be associated to the 4000Å break at high-redshift (from Laporte et al. 2014, Laporte et al. 2015b).

2.2 Properties of the z>6.5 candidates

We adopted a SED-fitting approach to estimate the photometric properties of sources in our sample, such as the redshift, Star Formation Rate (SFR), dust content or stellar mass, using "new Hyperz"* (Bolzonella et al. 2000). We also took benefit from the high quality of HST data to measure their size following the method described in Oesch et al. (2010), and then to study the evolution of their size as a function of the UV luminosity (Figure 2.a). The huge number of z>6.5 candidates selected in the 3 first *Frontier Fields* allows to give robust constraints on the evolution of their physical parameters, and on the evolution of the luminosity distribution of objects as well. We computed the UV Luminosity Function in the redshift range covered by the FF survey using a method taking into account the uncertainties on photometric redshift (see details in Laporte et al. 2015a). Thanks to the depth of this new survey, we are able to probe the faint end of this function up to very high redshift (z∼10 - Figure 2.b - Infante et al. 2015).

3 The need for a JWST Frontier Fields

The HST *Frontier Fields* will strongly increase the number of objects with redshift ranging from 7 to 9, and thus will provide robust constraints on the properties and evolution of objects up to ≈ 0.5 billion years after the Big-Bang. However according to the current paradigm, the first galaxies were formed at higher redshift and are expected to be extremely faint, i.e. well below the limit of current telescopes (Lacey et al. 2011). Therefore the future *James Webb Space Telescope*, thanks to its 6.5m diameter mirror, will play a crucial role in the study of the early Universe by opening a new cosmic time window. Moreover, the NIRCam instrument (Rieke et al. 2003) will provide high data quality over a continuous wavelength range from 0.6 to 5μm enabling to detect Lyman-α and 4000Å breaks, as described in the previous section, up to z ∼12 (Figure 3), and therefore to identify robust primeval galaxies.

*latest version available at : www.ast.obs-mip.fr/users/roser/newhyperz/

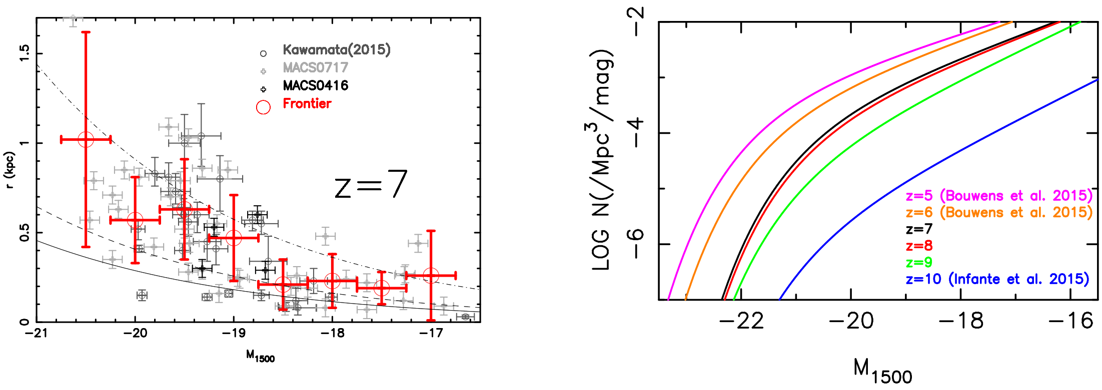

Fig. 2. Left : (a) Evolution of the half-light radius as a function of the UV luminosity for all z ~7 objects selected on the 3 first *Frontier Fields* dataset (see Laporte et al. in prep for more details). **Right** : (b) Evolution of the UV Luminosity Function estimated from *Frontier Fields* samples.

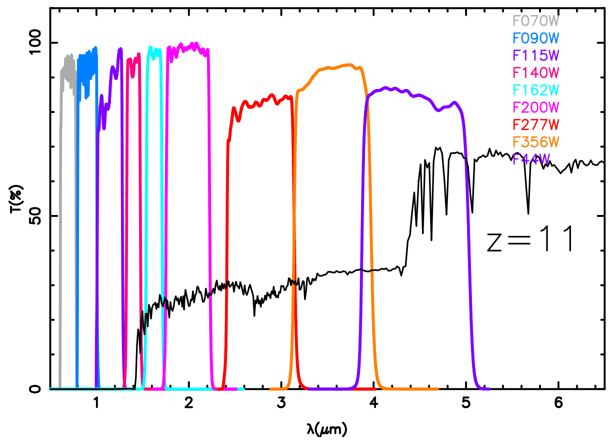

Fig. 3. Filters transmissions of the future JWST NIRCam instrument covering a continuous wavelength range from 0.6 to 5μm. SED of a starburst at z ~11 is overplotted showing the capabilities of the JWST to detect Lyman-α and 4000Å breaks at such high redshift.

We estimated the number of Lyman Break Galaxies expected in the full *Frontier Fields* survey by integrating the UV Luminosity Function evolution equations published in Bouwens et al. (2015) over the comoving volume explored assuming the mass models provided by the CATS team (Richard et al. 2014). About 200 objects at z >7.5 are expected in the ~35 arcmin^2 covered by these 1000h *Hubble* survey. Assuming the same amount of observing time, the depth that will be reached by NIRCam images will be 30.5 AB at 5σ, and the expected number of z>7.5 objects expected in a FF like survey will be about 5 times more than what is expected in the HST FF (Table 3). More particularly, at the highest redshift, only ~10 galaxies at z>10.5 are expected in the HST survey, whereas >100 would be detected in a JWST *Frontier Fields* survey, allowing to study properties of objects emitting light ≈350 million years after the Big-Bang.

4 Conclusions

The HST *Frontier Fields* survey has already demonstrated its huge capabilities by identifying >100 objects at z>6.5, with several at z ~10 (Zitrin et al. 2014, Infante et al. 2015). The use of gravitational lensing, that

Redshift range	N_{obj} *HST FF*	N_{obj} *JWST FF*
$7.5 < z < 8.5$	98^{+150}_{-36}	505^{+929}_{-216}
$8.5 < z < 9.5$	46^{+105}_{-20}	273^{+772}_{-139}
$9.5 < z < 10.5$	21^{+72}_{-11}	148^{+623}_{-86}
$10.5 < z < 11.5$	10^{+47}_{-6}	81^{+495}_{-53}
$11.5 < z < 12.5$	1 ± 1	44^{+392}_{-30}

Table 1. Comparison between the expected number of LBGs in the HST *Frontier Fields* survey (left) and in a similar observing time survey using JWST (right) assuming the UV Luminosity Function evolution published in Bouwens et al. (2015).

amplified light coming from background sources, allows to put the first constraints on the faint-end of the UV Luminosity Function at very high-redshift, and thus to better constrain the role played by the first galaxies during the Epoch of Reionization. However, the number of >10 sources highlighted is not sufficient to study in details properties of primeval galaxies that are expected to be extremely faint, i.e. well below the limit of current telescopes. The arrival of the *James Webb Space Telescope* by the end of 2018 will open a new luminosity window and thus will be able to detect >100 galaxies at z>10.5 in a *Frontier Fields* like survey.

We acknowledge support from CONICYT-Chile grants Basal-CATA PFB-06/2007 (NL, LI, FEB, SK), Gemini-CONICYT #32120003 (NL), "EMBIGGEN" Anillo ACT1101 (FEB), FONDECYT 1141218 (FEB), and Project IC120009 "Millennium Institute of Astrophysics (MAS)" of the Iniciativa Científica Milenio del Ministerio de Economía, Fomento y Turismo (FEB) and the French Agence Nationale de la Recherche bearing the reference ANR-09-BLAN-0234 (RP, DB) This work is based on observations made with the NASA/ESA Hubble Space Telescope, obtained at the Space Telescope Science Institute (STScI), which is operated by the Association of Universities for Research in Astronomy, Inc., under NASA contract NAS 5-26555. The HST image mosaics were produced by the Frontier Fields Science Data Products Team at STScI. This work is based in part on observations made with the Spitzer Space Telescope, which is operated by the Jet Propulsion Laboratory, California Institute of Technology under a contract with NASA.

References

Bolzonella, M., Miralles, J.-M., & Pelló, R. 2000, A&A, 363, 476

Bouwens, R. J., Illingworth, G. D., Oesch, P. A., et al. 2015, ApJ, 803, 34

Bradač, M., Treu, T., Applegate, D., et al. 2009, ApJ, 706, 1201

Ellis, R. S., McLure, R. J., Dunlop, J. S., et al. 2013, ApJ, 763, L7

Finkelstein, S. L., Papovich, C., Dickinson, M., et al. 2013, Nature, 502, 524

Gardner, J. P., Mather, J. C., Clampin, M., et al. 2009, in Astrophysics in the Next Decade, ed. H. A. Thronson, M. Stiavelli, & A. Tielens, 1–4020

Infante, L., Zheng, W., Laporte, N., et al. 2015, ApJ[arXiv] nan

Johnson, T. L., Sharon, K., Bayliss, M. B., et al. 2014, ApJ, 797, 48

Lacey, C. G., Baugh, C. M., Frenk, C. S., & Benson, A. J. 2011, MNRAS, 412, 1828

Laporte, N., Pérez-Fournon, I., Calanog, J. A., et al. 2015a, ApJ, 810, 130

Laporte, N., Streblyanska, A., Clement, B., et al. 2014, A&A, 562, L8

Laporte, N., Streblyanska, A., Kim, S., et al. 2015b, A&A, 575, A92

Merten, J., Coe, D., Dupke, R., et al. 2011, MNRAS, 417, 333

Mohammed, I., Liesenborgs, J., Saha, P., & Williams, L. L. R. 2014, MNRAS, 439, 2651

Oesch, P. A., Bouwens, R. J., Carollo, C. M., et al. 2010, ApJ, 709, L21

Oesch, P. A., van Dokkum, P. G., Illingworth, G. D., et al. 2015, ApJ, 804, L30

Richard, J., Jauzac, M., Limousin, M., et al. 2014, MNRAS, 444, 268

Rieke, M. J., Baum, S. A., Beichman, C. A., et al. 2003, in Society of Photo-Optical Instrumentation Engineers (SPIE) Conference Series, Vol. 4850, IR Space Telescopes and Instruments, ed. J. C. Mather, 478–485

Smit, R., Bouwens, R. J., Labbé, I., et al. 2014, ApJ, 784, 58

Steidel, C. C., Giavalisco, M., Pettini, M., Dickinson, M., & Adelberger, K. L. 1996, ApJ, 462, L17

Zitrin, A., Labbe, I., Belli, S., et al. 2015, ArXiv e-prints [arXiv] 1507.02679

Zitrin, A., Meneghetti, M., Umetsu, K., et al. 2013, ApJ, 762, L30

Zitrin, A., Zheng, W., Broadhurst, T., et al. 2014, ApJ, 793, L12

SF2A 2015
F. Martins, S. Boissier, V. Buat, L. Cambrésy and P. Petit (eds)

THE INFRARED SIGNATURES OF VERY SMALL GRAINS IN THE UNIVERSE SEEN BY JWST

P. Pilleri[1, 2], O. Berné[1,2] and C. Joblin[1,2]

Abstract. The near- and mid-IR spectrum of many astronomical objects is dominated by emission bands due to UV-excited polycyclic aromatic hydrocarbons (PAH) and evaporating very small grains (eVSG). Previous studies with the ISO, *Spitzer* and AKARI space telescopes have shown that the spectral variations of these features are directly related to the local physical conditions that induce a photo-chemical evolution of the band carriers. Because of the limited sensitivity and spatial resolution, these studies have focused mainly on galactic star-forming regions. We discuss how the advent of JWST will allow to extend these studies to previously unresolved sources such as near-by galaxies, and how the analysis of the infrared signatures of PAHs and eVSGs can be used to determine their physical conditions and chemical composition.

Keywords: Photon-dominated regions, Polycyclic Aromatic Hydrocarbons, James Webb Space Telescope.

1 Introduction

The infrared (IR) and (sub-)millimetre emission of star-forming galaxies is due to gas and dust in photon-dominated regions (PDR, for a review, see Hollenbach & Tielens 1997). In these regions, ultraviolet (UV) photons from nearby massive stars illuminate the interstellar matter, creating a transition between the HII region and the neutral molecular gas. PDRs are seen in our Galaxy at the border of molecular clouds, in reflection nebulae, proto-planetary disks and the envelopes of evolved stars. To understand the shaping and evolution of these objects and, at larger scales, of starburst galaxies, it is key to understand the micro-physics that regulate the thermal and chemical balance of PDRs. Indeed, the physics and chemistry of these sources are strongly influenced by the interaction of UV photons with very small (nanometer-size) dust particles. These particles absorb most of the UV photons, re-emitting the majority of the energy in the IR domain and using a small fraction of it to heat the gas. Using the IR features to trace the evolution of the dust populations, one can therefore hope to evaluate their impact on the thermal balance and the chemistry.

In the mid-IR domain (3-20 μm), the spectrum of PDRs presents a series of emission bands that are usually attributed to polycyclic aromatic hydrocarbons (PAH; Leger & Puget 1984; Allamandola et al. 1985), evaporating very small grains (eVSG; Pilleri et al. 2012) and to buckminsterfullerne (C_{60}; Sellgren et al. 2010), superimposed to a (generally weak) continuum. It also shows rotational lines of molecular hydrogen (H_2; e.g. Habart et al. 2011), and can also display fine structure lines of atoms with ionisation potential lower than 13.6 eV (such as Silicon and Sulfur), as well as absorption bands of ices at the surface of micrometer-size grains (Boogert et al. 2015). The ro-vibrational lines of simple molecules such as acetylene (C_2H_2) have also been detected in the dense PDRs associated with the inner envelopes of evolved stars (Cernicharo et al. 2001) or with proto-planetary disks (Carr & Najita 2008). The sub-mm and mm domains also contain a wealth of information on the morphology, dynamics and chemical richness of PDRs. In this domain, we observe the emission of rotational lines of molecules with a permanent dipole moment, recombination lines of atomic carbon and hydrogen, and the continuum due to micrometer-size grains at thermal equilibrium. In the following, we show that the observations of both the IR and (sub-)mm domains with sufficient sensitivity and spatial resolution is an important tool in the study of galactic and extragalactic PDRs.

[1] Université de Toulouse; UPS-OMP; IRAP; Toulouse, France
[2] CNRS; IRAP; 9 Av. colonel Roche, BP 44346, F-31028 Toulouse cedex 4, France

© Société Francaise d'Astronomie et d'Astrophysique (SF2A) 2015

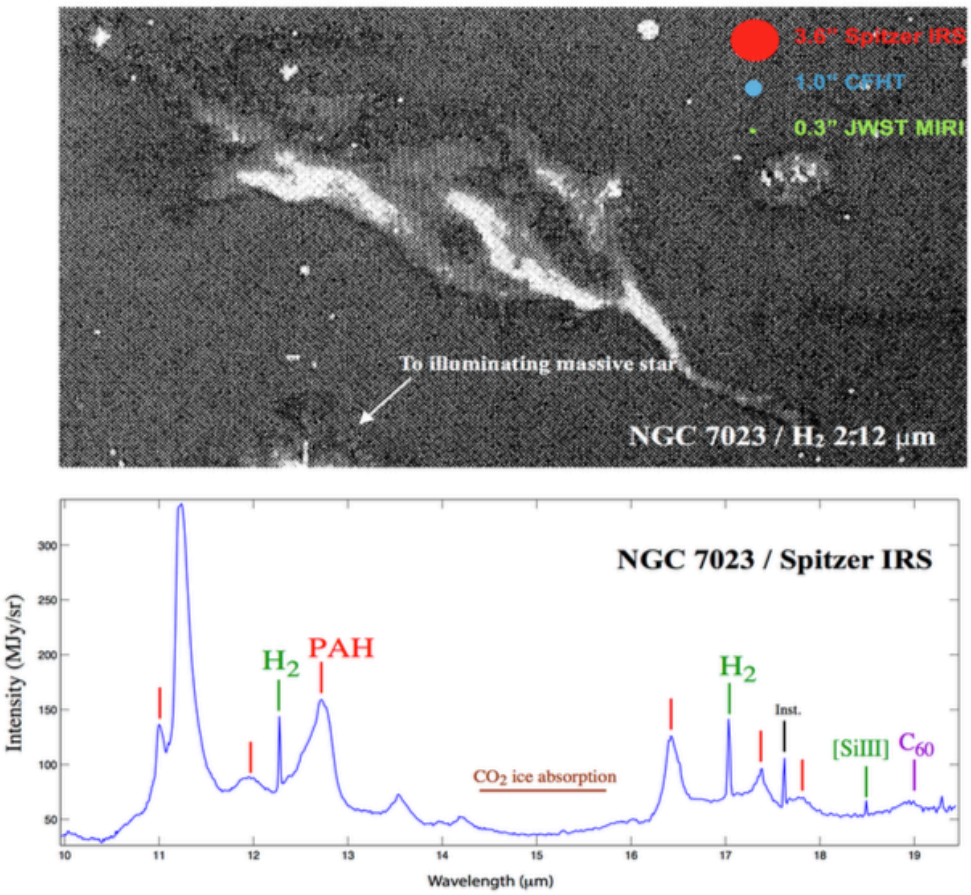

Fig. 1. *Top:* Image of the vibrationally-excited H_2 line at 2.12 μm in the north-west PDR of NGC 7023 (Lemaire et al. 1996). The bright filamentary structures correspond to the border of the molecular cloud, illuminated by the UV photons from the massive star HD 200775. The PDR corresponds to the transition region from atomic to molecular gas, and to the zone in which very small grains are evaporated into PAHs (Berné et al. 2007; Pilleri et al. 2012). The coloured circles represent the spatial resolution of the *Spitzer*-IRS and JWST-MIRI spectrometers, and that of the H_2 image at 2.12 μm. *Bottom:* mid-IR spectrum toward the H_2 filaments obtained with the *Spitzer*-IRS spectrometer with average spectral resolution (R∼600). The signatures of the different dust and gas populations are shown. These same signatures are often seen in different astronomical objects such as proto-planetary disks, planetary neabulae and starburst galaxies.

2 Resolving steep chemical variations: JWST and the evaporation of very small grains

Spectral mapping observations with the *Spitzer* Space Telescope and with the IRAM telescopes of several PDRs have shown that the transition region between the atomic and molecular gas hosts a number of processes that determine the chemical evolution of hydrocarbon material: for instance, IR observations have shown that eVSGs of aliphatic / aromatic composition are evaporated into free-flying PAHs (Berné et al. 2007; Pilleri et al. 2012, 2015). The comparison with mm observations suggests that the photo-destruction of PAHs and eVSGs also releases small hydrocarbons in the gas phase (Pety et al. 2005; Pilleri et al. 2013; Guzmán et al. 2015; Cuadrado et al. 2015).

With the advent of ALMA, we are now peering into the details of the molecular gas in PDRs with an unprecedented angular resolution, similar to that achieved by the *Hubble* Space Telescope in the visible. Figure 1 shows the intensity map of the vibrationally excited H_2 line at 2.12 μm of the reflection nebula NGC 7023 ($d = 430$ pc) and its mid-IR spectrum obtained with the *Spitzer*-IRS spectrograph. This region hosts structures at different gas densities from a very diluted atomic gas at $n_H \sim 10^3\,\mathrm{cm}^{-3}$ in the cavity (Berné & Tielens 2012) to dense filaments with $n_H \sim 10^5 - 10^6\,\mathrm{cm}^{-3}$ that are located $\sim 50''$ north-west of the star. The filaments have angular scales of the order of 1-2$''$ (e.g., Fuente et al. 1996; Lemaire et al. 1996, Fig. 1). Only space-based observatories can provide enough sensitivity and spectral coverage to fully study these filaments, but until now they have been limited to an angular resolution of few arcsec. Thus, it is not yet possible to resolve the gradients in temperature, density and chemical abundances that are associated with these structures. Only JWST will be able to obtain spectral cubes of sufficiejnt sensibility, frequency coverage and spatial resolution to obtain a complete view of the chemical evolution of PAHs and eVSGs at these spatial scales and understand the processes that drive the physical and chemical evolution of these objects.

3 The mid-IR spectrum of PDRs as tracers of the physical conditions

The spectral properties (position, absolute and relative intensity, shape) of the infrared bands are linked to the nature of their carriers, to the physical conditions in the emitting regions (that determine the excitation conditions of the band carriers), and to the morphology of the source (that influences the radiative transfer). Thus, the analysis of the IR spectrum can be used to obtain insights on these properties.

The PAHTAT toolbox (Pilleri et al. 2014) allows to fit an observed mid-IR spectrum using a set of template spectra for ionised and neutral PAHs and eVSGs. In Pilleri et al. (2012), we have shown that the fraction of carbon atoms contained in eVSGs (f_C) decreases significantly with increasing intensity of the UV radiation field, G_0. Thus, given a mid-IR spectrum presenting emission of PAHs and eVSGs, PAHTAT allows to estimate the intensity of the local UV field. We applied PAHTAT to all the spectra contained in the *Spitzer*-IRS 3D cube of NGC 7023 NW. Figure 2 shows a map of G_0 obtained with this method (for details, see Pilleri et al. 2015). The UV field intensity decreases by over 2 order of magnitude in only few arcsec due to the absorption by very small dust particles in the thin filaments shown in Fig. 1.

PAHTAT also allows to derive the selective extinction (A_V) by taking into account the absorption of micron-sized grains (silicates) along the line of sight. Figure 2 compares the map of A_V with the intensity of the CS $J = 2-1$ emission observed at the Plateau de Bure Interferometer (PdBI, A. Fuente, priv. comm.). The CS intensity presents a peak that corresponds spatially to the peak in the A_V derived by PAHTAT, indicating that its emission arises from a clump of high (column) density.

We applied the same method to the *Spitzer*-IRS spectral cube of the starburst galaxy M 82 and obtained maps of both G_0 and A_V (Fig. 2, right panel). The results show a very high extinction ($A_V > 30$) in the lines of sight close to the plane of the galaxy, with individual peaks in the NE, SW and in the center. These values are consistent with previous analysis of mid-IR spectra obtained by Beirão et al. (2008). As in the case of NGC 7023, the extinction peak correlates very well with high-density tracers such as CS $J = 3-2$ (Ginard et al. 2015). Because the extinction in the galactic plane is so extreme, it is difficult to probe precisely the intensity of the UV field in the disk. However, the map of G_0 obtained with PAHTAT shows a clear asymmetry between the northern and southern halos, the latter presenting a higher G_0 compared to the former. This is consistent

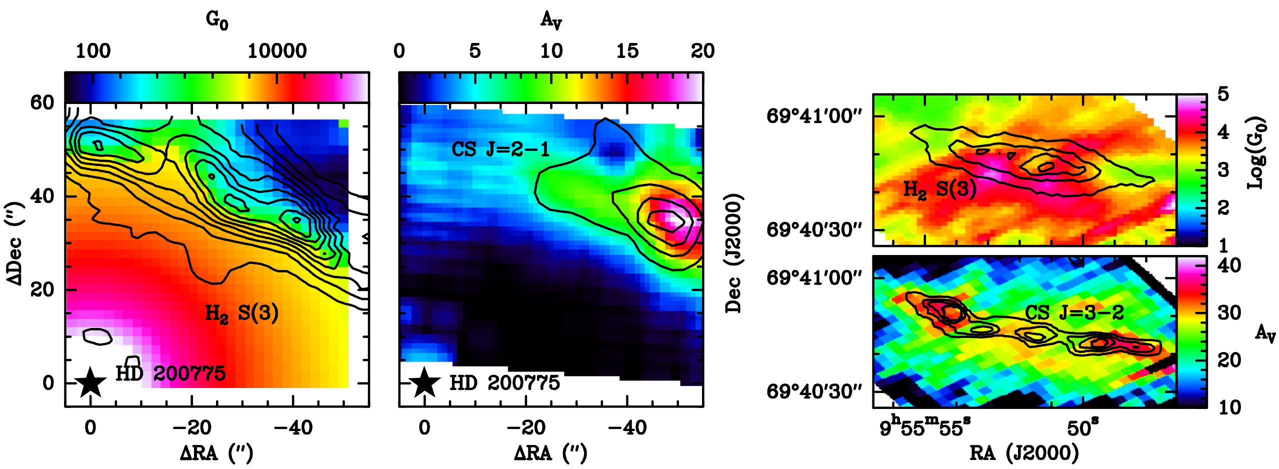

Fig. 2. *Left:* maps of the UV radiation field intensity (G_0; first panel, for details, see Pilleri et al. 2015) and of the line-of-sight extinction (A_V, second panel) for NGC 7023 as derived from the PAHTAT tool (Pilleri et al. 2012) applied to the *Spitzer*-IRS data cube. The contours represent the H_2 S(3) emission and CS $J = 2-1$ emission (Plateau de Bure Interferometer; Fuente et al., priv. comm.) *Right:* Same as the left panel, for the starburst galaxy M82. Overlaid are the H_2 S(3) and CS $J = 3-2$ (Ginard et al. 2015).

with direct observations of the far-UV luminosity of this source (Hoopes et al. 2005) and is likely explained by a higher star formation rate in the south.

4 Conclusions

The analysis of the mid-IR emission of very small dust particles provides complementary information to characterise the properties of PDRs compared to molecular data in the mm for instance. We have shown that mid-IR observations can be used as a probe of physical conditions such as the UV radiation field intensity and the extinction along the observed line of sight.

The emission of PAHs is also found to correlate with that of the fine structure line of ionised carbon (C^+) at 158 μm (Joblin et al. 2010). This line is often used as a tracer of star formation but its observation at high spatial resolution is challenging. If the PAH bands can be used as a complementary proxy to measure the star formation rate, JWST will be able to do so at an unprecedented physical scale for near-by and more distant galaxies.

We thank A. Fuente for providing the CS $J = 2 - 1$ map of NGC 7023.
P. Pilleri gratefully acknowledges financial support from the Centre National d'Etude Spatiales (CNES).
The research leading to these results has also received funding from the European Research Council under the European Union's Seventh Framework Programme (FP/2007-2013) ERC-2013-SyG, Grant Agreement n. 610256 NANOCOSMOS.
This work was supported by the CNRS program Physique et Chimie du Milieu Interstellaire (PCMI)
The IRS was a collaborative venture between Cornell University and Ball Aerospace Corporation funded by NASA through the Jet Propulsion Laboratory and Ames Research Centre.

References

Allamandola, L. J., Tielens, A. G. G. M., & Barker, J. R. 1985, ApJ, 290, L25
Beirão, P., Brandl, B. R., Appleton, P. N., et al. 2008, ApJ, 676, 304
Berné, O., Joblin, C., Deville, Y., et al. 2007, A&A, 469, 575
Berné, O. & Tielens, A. G. G. M. 2012, Proceedings of the National Academy of Science, 109, 401
Boogert, A. C. A., Gerakines, P. A., & Whittet, D. C. B. 2015, ARA&A, 53, 541
Carr, J. S. & Najita, J. R. 2008, Science, 319, 1504
Cernicharo, J., Heras, A. M., Tielens, A. G. G. M., et al. 2001, ApJ, 546, L123
Cuadrado, S., Goicoechea, J. R., Pilleri, P., et al. 2015, A&A, 575, A82
Fuente, A., Martin-Pintado, J., Neri, R., Rogers, C., & Moriarty-Schieven, G. 1996, A&A, 310, 286
Ginard, D., Fuente, A., García-Burillo, S., et al. 2015, A&A, 578, A49
Guzmán, V. V., Pety, J., Goicoechea, J. R., et al. 2015, ApJ, 800, L33
Habart, E., Abergel, A., Boulanger, F., et al. 2011, A&A, 527, A122
Hollenbach, D. J. & Tielens, A. G. G. M. 1997, ARA&A, 35, 179
Hoopes, C. G., Heckman, T. M., Strickland, D. K., et al. 2005, ApJ, 619, L99
Joblin, C., Pilleri, P., Montillaud, J., et al. 2010, A&A, 521, L25
Leger, A. & Puget, J. L. 1984, A&A, 137, L5
Lemaire, J. L., Field, D., Gerin, M., et al. 1996, A&A, 308, 895
Pety, J., Teyssier, D., Fossé, D., et al. 2005, A&A, 435, 885
Pilleri, P., Joblin, C., Berné, O., Montillaud, J., & Okada, Y. 2014, in IAU Symposium, Vol. 303, IAU Symposium, ed. L. O. Sjouwerman, C. C. Lang, & J. Ott, 208–210
Pilleri, P., Joblin, C., Boulanger, F., & Onaka, T. 2015, A&A, 577, A16
Pilleri, P., Montillaud, J., Berné, O., & Joblin, C. 2012, A&A, 542, A69
Pilleri, P., Treviño-Morales, S., Fuente, A., et al. 2013, A&A, 554, A87
Sellgren, K., Werner, M. W., Ingalls, J. G., et al. 2010, ApJ, 722, L54

SF2A 2015
F. Martins, S. Boissier, V. Buat, L. Cambrésy and P. Petit (eds)

MORPHO-KINEMATIC OF DISTANT GALAXIES WITH JWST AND MOSAIC

M. Rodrigues[1], F. Hammer[1], M. Puech[1] and H. Flores[1]

Abstract. The combination of high spatial resolution from space imagery and 3D spectroscopy from ground is a remarkable tool to dissect distant galaxies and their internal motions. Using HST and VLT observations, we have captured the strong evolution of disk galaxies over the past 8 billion years ($z \sim 1$), which suggests disk (re)formation after gas rich mergers. At higher lookback time, the morpho-kinmatics of galaxies is strongly limited by the lower signal-to-noise and coarse spatial resolution of the observations. In the next decade, the synergy between JWST/NIRCAM and MOSAIC the futur MOS at the E-ELT will allow us to capture the morpho-kinematics up to the first galaxies and unveil the physical processes dominating their formation. The lesson learned at intermediate redshift will allow us to optimize the specification for MOSAIC to achieve the morpho-kinematics follow-up of galaxies from z∼4 to z=0.

Keywords: Extragalatic, Kinematics, Instrumentation

1 Introduction

Stamping the epoch of emergence of the disc galaxy population is a critical observational constraint for galaxy formation models. In the nearby Universe, the disk/merger ratio can be estimated using morphological studies, because mergers are easily recognizable by their characteristic morphological features (bridges, tidal tails, etc...). With increasing redshift, the classification of galaxies using imagery alone is jeopardized by observational limitations - cosmological dimming, coarser spatial resolution of the observations - and by possible changes in the properties of certain galaxy types. Kinematic studies from integrated field spectroscopy (IFS) observations are seen as a crucial tool to overcome the limitation of morphological classification. Accessing the internal kinematics of galaxies allow us to probe directly their dynamical and evolutionary state, and prevent us to be biases by star-forming regions or dust. In the past 10 years, many kinematic surveys have been carried on (see for a complete review Glazebrook 2013), e.g.: CALIFA at $z \sim 0$ (Husemann et al. 2013), IMAGES at $z \sim 0.6$ (Flores et al. 2006; Yang et al. 2008), MASSIV at $z \sim 1$ (Epinat et al. 2010, 2012), KMOS^{3D} at $z \sim 1-2$ (Wisnioski et al. 2015)and AMAZE/LSD at z∼ 3 (Gnerucci et al. 2011). These studies have led to discrepant results on the evolution of the disk/merger ratio. While several authors argue that the fraction of discs remains constant from z=0 to z∼2 (Förster Schreiber et al. 2006; Shapiro et al. 2008; Sobral et al. 2013; Wisnioski et al. 2015), other studies found a strong evolution of the fraction of rotating disks over the past 8 Gyrs (Yang et al. 2008; Epinat et al. 2010). These contradictory results are due to the heterogenous methodologies used to classify rotating disks. In section 2, we show that the limitations of kinematic classifications can be overcome with the addition of deep imagery. This has led us to propose a new classification based on the morpho-kinematic properties of galaxies. In section 3, we will discuss the synergie between JWST/NIRCAM and E-ELT/MOSAIC to unveil the nature of distant galaxies up to $z \sim 4$.

2 Morpho-kinematic classification of $z \sim 1$ galaxies

Hung et al. (2015) have shown that kinematic classifications tend to give an upper limit of the fraction of rotating disks. These systematics are due to two reasons. The first one is that integral-field observations of distant galaxies can only probe the ionized gas. However, the distribution of gas does not always follow the distribution of mass, in particular during merger events. Secondly, observations are restricted to a few spatial

[1] GEPI, Observatoire de Paris, CNRS, Univ. Paris Diderot

© Société Francaise d'Astronomie et d'Astrophysique (SF2A) 2015

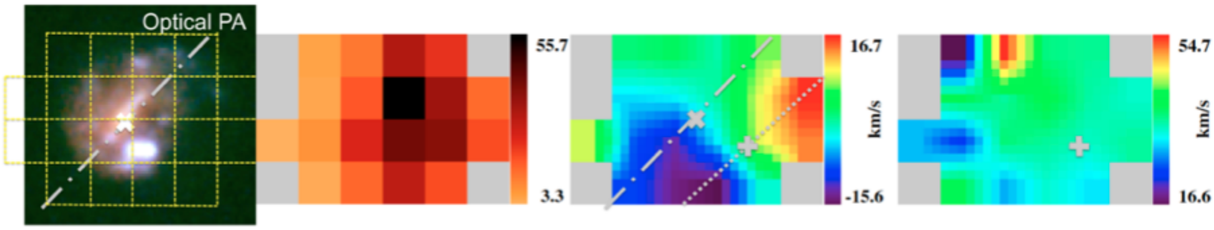

Fig. 1. Exemple of a galaxy with a velocity field consistant with a rotation (third panel). Deep imagery from the HST (left panel) shows that the major axis of the stellar component is misaligned respect to the gas kinematics. Unrelaxed systems can be easily distinguish by strong misalignment between the gas (IFU) and stars (imagery)

resolution elements and the outer isophotes are dramatically affected by low S/N. To overcome this, deep space imagery is needed to add constraints on the distribution of stars. Figure 1 illustrates how unrelaxed systems can be easily distinguished when combining kinematics and deep imagery observations, evidencing a strong misalignement between the gas (IFU) and stars (imagery). In Hammer et al. (2009), we presented a *morpho-kinematic* classification of distant galaxies which includes the morphological information provided by deep HST imagery into the kinematics classification. The classification follows a decision tree (Hammer et al. 2016) based on several morphological and kinematics parameters.

The morpho-kinematic classification requires 3D spectroscopy observations and deep HST imagery observations in several bands to construct surface brightness profiles and color maps. Deep imagery in at least one rest-frame band over 4000Å is mandatory to recover the stellar mass distribution. The decision tree allows us to classify galaxies into 3 morpho-kinematic categories :

- Rotating spiral disks: these targets present both spiral morphologies (exponential disk profile, spirals arms and/or bars) and kinematics consistant with a rotating disk (spider diagram, peak of dispersion coincides with the center of rotation and optical center).
- Semi-relaxed systems: this category includes objects that possess either a rotational velocity field and a peculiar morphology or a velocity field discrepant from rotation and a spiral morphology.
- Non-relaxed systems: these galaxies have complex kinematics (without velocity gradient) and peculiar morphologies.

In Hammer et al. (2009), we have applied this methodology to a representative sample of $z \sim 0.6$ galaxies observed with the HST ACS camera and the multi-IFUs spectrographe FLAMES/GIRAFFE at the VLT. We found that half of the present-day spirals had peculiar morphologies and anomalous kinematics at $z \sim 0.6$ (Neichel et al. 2008; Yang et al. 2008; Puech et al. 2008a), and conclude for a strong evolution of the number of disk galaxies over the past 8 billion years. This result favorises a scenario of disk formation through a mechanism of disk (re)formation after gas rich mergers (Hammer et al. 2005, 2009). Using archive data from the $KMOS^{3D}$ survey (Wisnioski et al. 2015), we are now extending our study at $z \sim 1$. The preliminary results indicate that the number of disk galaxies continue to decrease with increasing redshift, with only 25% of galaxies being rotating disk at $z \sim 1$.

3 The nature of distant galaxies with JWST and MOSAIC/E-ELT

At present time, morpho-kinematic studies of distant galaxies can be conducted in representative samples up to $z \sim 1$. At higher redshift, only the most massive and luminous galaxies are reachable with the actual instrumentation. In the next decade, the synergy provided by HST and VLT to morpho-kinematic studies will be renew with JWST and the E-ELT. These two telescopes will allow us to unveil the nature of galaxies in mass selected sample up to $z \sim 4$. The near-infrared imager embarked on JWST, NIRCAM, will give us deep and high resolution images of distant galaxies at wavelength above 4000Å (rest-frame). The set of simulations conducted in the framework of the E-ELT design reference mission* have shown that NIRCAM/JWST will be

*`http://www.eso.org/sci/facilities/eelt/science/drm/`

able to observed $0.5M^*$ galaxies up to $z \sim 4$. On the other hand, the futur multi-IFU spectrograph for the E-ELT, MOSAIC (Hammer et al. 2014), will provide us with spatially-resolved kinematics of distant galaxies. The multi-IFU mode of MOSAIC will have the following specifications:

- FOV IFU $\sim$2.0×2.0 arcsec;
- Multiplex$\sim$ 10 IFUs;
- Spatial pixel scale$\sim$ 80 mas in H-band using the multi-object adaptive optic systems (MOAO) ;
- Encircle Energy$\sim$ 30% EE in 2 spatial spatial pixels;
- R>4000-5000;
- λ-coverage: 0.8 - 1.8 μm.

The IFU observation allow us to retrieve spatial resolved map for $0.5M^*$ galaxies at $z \sim 4$, see simulation in Figure 2 (Puech et al. 2008b). In the framework of a futur legacy survey with MOSAIC, it would be possible to carry on a large kinematic survey of a mass-selected sample, previously defined from deep JWST observations at $1 < z < 4$. Assuming a multiplex of ten, 240 galaxies would require $\sim$12.5 nights of MOSAIC observations, against $\sim$250 nights in a single IFU instrument.

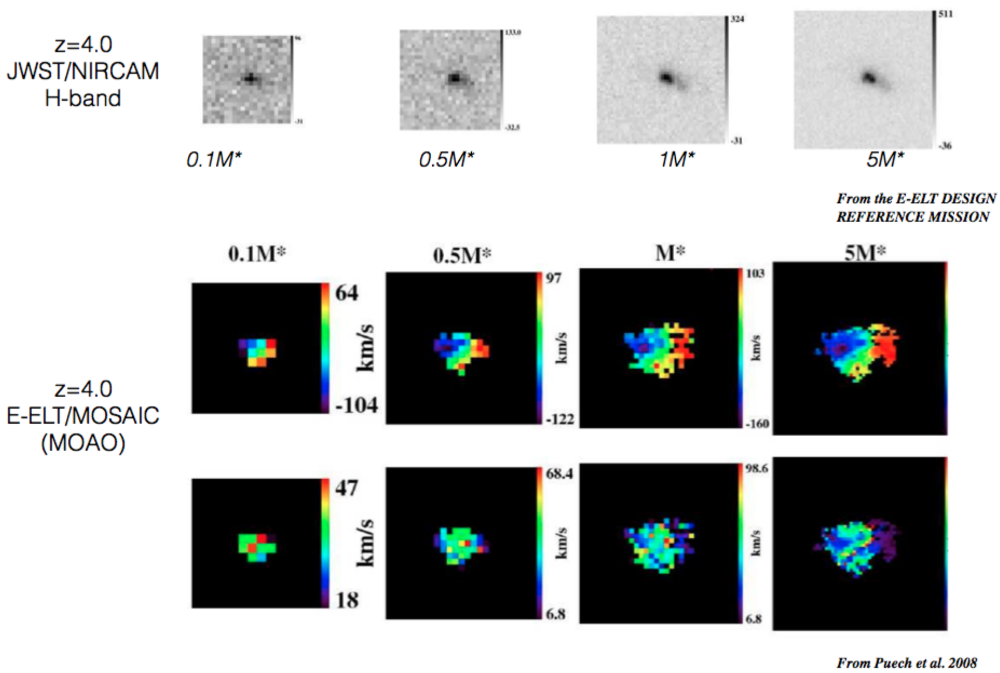

Fig. 2. NIRCAM/JWST simulation of $z \sim 4$ galaxies spanning stellar masses between $0.1M^*$ and $5M^*$ in H-band (upper-panel) and velocity and dispersion maps from MOSAIC/E-ELT with multi-object adaptive optic (MOAO).

References

Epinat, B., Amram, P., Balkowski, C., & Marcelin, M. 2010, MNRAS, 401, 2113

Epinat, B., Tasca, L., Amram, P., et al. 2012, A&A, 539, A92

Flores, H., Hammer, F., Puech, M., Amram, P., & Balkowski, C. 2006, A&A, 455, 107

Förster Schreiber, N. M., Genzel, R., Lehnert, M. D., et al. 2006, ApJ, 645, 1062

Glazebrook, K. 2013, PASA, 30, 56

Gnerucci, A., Marconi, A., Cresci, G., et al. 2011, A&A, 528, A88

Hammer, F., Barbuy, B., Cuby, J. G., et al. 2014, in Society of Photo-Optical Instrumentation Engineers (SPIE) Conference Series, Vol. 9147, Society of Photo-Optical Instrumentation Engineers (SPIE) Conference Series, 27

Hammer, F., Flores, H., Elbaz, D., et al. 2005, aap, 430, 115

Hammer, F., Flores, H., Puech, M., & Rodrigues, M. 2016, "Studying Distant Galaxies: a Handbook of Methods and Analysis", one edn. (World Scientific), iSBN 978-1-84816-944-9

Hammer, F., Flores, H., Puech, M., et al. 2009, A&A, 507, 1313

Hung, C.-L., Rich, J. A., Yuan, T., et al. 2015, ApJ, 803, 62

Husemann, B., Jahnke, K., Sánchez, S. F., et al. 2013, A&A, 549, A87

Neichel, B., Hammer, F., Puech, M., et al. 2008, A&A, 484, 159

Puech, M., Flores, H., Hammer, F., et al. 2008a, A&A, 484, 173

Puech, M., Flores, H., Lehnert, M., et al. 2008b, MNRAS, 390, 1089

Shapiro, K. L., Genzel, R., Förster Schreiber, N. M., et al. 2008, ApJ, 682, 231

Sobral, D., Swinbank, A. M., Stott, J. P., et al. 2013, ApJ, 779, 139

Wisnioski, E., Förster Schreiber, N. M., Wuyts, S., et al. 2015, ApJ, 799, 209

Yang, Y., Flores, H., Hammer, F., et al. 2008, A&A, 477, 789

SF2A 2015
F. Martins, S. Boissier, V. Buat, L. Cambrésy and P. Petit (eds)

MODELING SMALL GALAXIES DURING THE EPOCH OF REIONISATION

M. Trebitsch[1], J. Blaizot[1] and J. Rosdahl[2]

Abstract. Small galaxies are thought to be the main contributors to the ionising budget of the Universe before reionisation was complete. There have been a number of numerical studies trying to quantify their ionising efficiency through the *escape fraction* $f_{\rm esc}$. While there is a clear trend that $f_{\rm esc}$ is higher for smaller haloes, there is a large scatter in the distribution of $f_{\rm esc}$ for a single halo mass. We propose that this is due to the intrinsic burstiness of star formation in low mass galaxies. We performed high resolution radiative hydrodynamics simulations with Ramses-RT to model the evolution of three galaxies and their ionising efficiency. We found that the variability of $f_{\rm esc}$ follows that of the star formation rate. We then discuss the consequences of this variability on the observability of such galaxies by JWST.

Keywords: radiative transfer, methods: numerical, galaxies: dwarfs, galaxies: formation, galaxies: high redshift, reionization.

1 Introduction

One of the key science projects of the upcoming *James Webb Space Telescope* (JWST) is to probe the end of the Dark Ages, around $z \sim 15$, when the first stars and galaxies formed. The apparition of these first sources of light marked the beginning of the Epoch of Reionisation (EoR), during which the matter in the Universe experienced a transition, from fully neutral to fully ionised. It is very appealing to link this phase transition to the formation of the first galaxies. Indeed, even if quasars produce much more ionising photons, the evolution of the quasar space density at high redshift seems to indicate that there are not enough of them to dominate the ionising background during the EoR (Haardt & Salvaterra 2015).

This favours a reionisation model in which galaxies are the main sources of ionising radiation. However, observational constraints from deep surveys such as the UDF12 campaign indicates that the galaxies detected by those surveys do not produce enough ionising radiation to reionise the Universe by $z \sim 6$ (Robertson et al. 2013). This tension disappears if the luminosity function is extended to fainter galaxies, down to $M_{\rm UV} \lesssim -13$. While these faint, low mass galaxies are thought to dominate the ionising budget of the Universe at high z, they have never been observed yet. Understanding their physical properties, formation histories and how ionising radiation can escape from them is therefore crucial to be able to prepare the next generation of deep surveys with the JWST.

In the past few years, there have been a number of numerical studies (see e.g. Kimm & Cen 2014; Wise et al. 2014; Paardekooper et al. 2015; Ma et al. 2015, for recent results) trying to address the formation of those small galaxies, and to quantify the *escape fraction* of ionising photons, which is the amount of radiation escaping from them. This typically requires very high resolution simulations, capable of resolving details in the insterstellar medium (ISM). Despite the variety of methods used for the modelling of star formation, supernova feedback, or radiative transfer, most of the recent simulations agree on the fact that the escape fraction $f_{\rm esc}$ decreases mass of the host dark matter halo $M_{\rm vir}$. However, there is a large scatter in the $f_{\rm esc}$ vs. $M_{\rm vir}$ relation, that needs to be understood. We present here our contribution to the community effort to model those galaxies with cosmological simulations.

[1] Université de Lyon, Lyon, F-69003, France;
Université Lyon 1, Observatoire de Lyon, 9 avenue Charles André, Saint-Genis Laval, F-69230, France;
CNRS, UMR 5574, Centre de Recherche Astrophysique de Lyon;
École Normale Supérieure de Lyon, Lyon, F-69007, France
[2] Leiden Observatory, Leiden University, P.O. Box 9513, 2300 RA Leiden, the Netherlands

© Société Francaise d'Astronomie et d'Astrophysique (SF2A) 2015

2 Simulation methodology

We performed cosmological simulations with the code Ramses-RT (Rosdahl et al. 2013), an extension of the cosmological code Ramses (Teyssier 2002) that solves the equations of radiative hydrodynamics (RHD) for astrophysical flows on an adaptive grid. Ramses-RT follows the coupled evolution of gas and radiation, allowing us to track the ionisation state of the gas in the simulation. We use the zoom technique to achieve the very high resolution needed to resolve the structure of the ISM. We focus on three haloes of masses $M_{\rm vir} \sim 8 \times 10^7 M_\odot$ for the smallest onne, $6 \times 10^8 M_\odot$ for the intermediate one, and $2 \times 10^9 M_\odot$ for the largest one.

The haloes were selected in a dark-matter (DM) only simulation using 512^3 particles in a $10h^{-1}$ Mpc box. We then generated multigrid initial conditions using the Music code (Hahn & Abel 2011), using 3 additional levels of refinement, giving a DM particle mass of $\sim 2000 M_\odot$. We ran the simulation for one billion year, down to $z \sim 5.6$, with a maximum of 21 levels of refinment, allowing for a cell size of $\Delta x \sim 7$ pc. Radiation is modeled using three photon groups (ionising HI, He I, He II). We use the same supernova (SN) feedback recipe as in Kimm & Cen (2014), where after 10 Myr, each star particle deposits in the ISM the amount momentum and metals corresponding to the phase of the SN explosion that can be resolved. We use a new recipe for star formation (Devriendt et al. in prep.), where we account for the turbulence in the star-forming cloud.

3 Bursty assembly of small galaxies

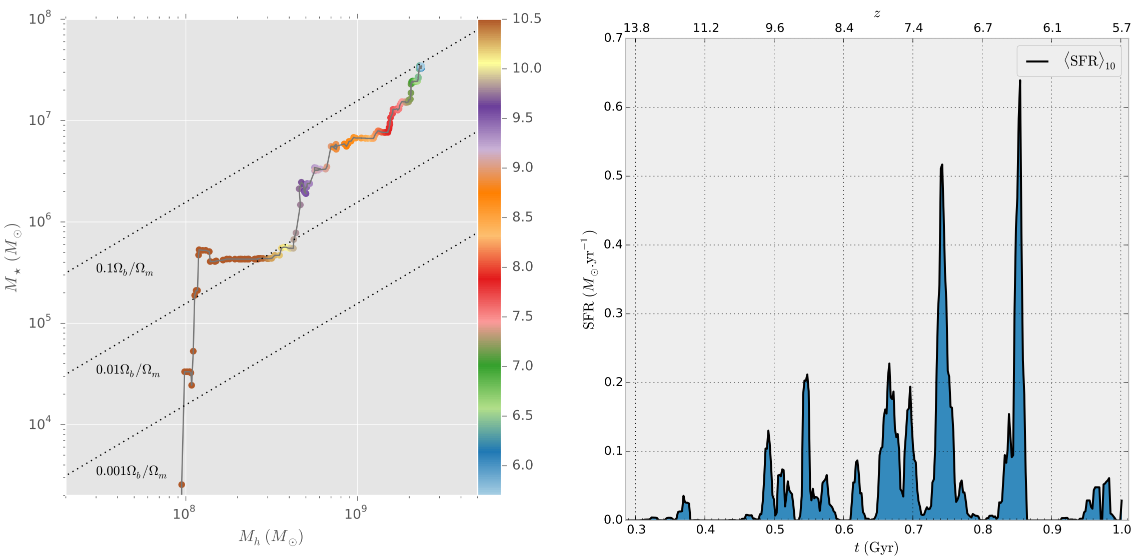

Fig. 1. Left: Stellar mass to halo mass relationship for the most massive halo studied. The the dotted lines corresponds to a stellar fraction of 10%, 1% and 0.1% of the baryons in the halo, and the colours note the redshift. **Right:** Star formation history of the galaxy.

We present on Fig. 1 the assembly history of the most massive halo we targeted on our study. On the left panel, we show the evolution of the stellar mass to halo mass relationship with redshift, and on the right panel, we display the time evolution of the star formation rate (SFR) of the galaxy. In all the haloes, roughly between 1% and 10% of the baryons are converted into stars at all times, and a striking feature of the left panel is the presence of several plateaus indicating a growth of the galaxy with no associated star formation. The right panel provides a natural explanation for this: in this low mass regime, star formation happens by bursts. A few Myr after the beginning of a star formation episode, the most massive stars will end their life, and the resulting supernovae will heat and remove large amounts of gas from the ISM, quenching the star formation for a while. After some time, the gas will cool down in the halo, and return to the galaxy, fueling a new episode of star formation.

This cycle of star formation episodes followed by outflow has very strong consequences for the escape of ionising radiation. Indeed, the supernovae will completely disrupt the star forming clouds in which most of the young stars live. This will vastly increase the ionising efficiency of the neighbouring young stars. We

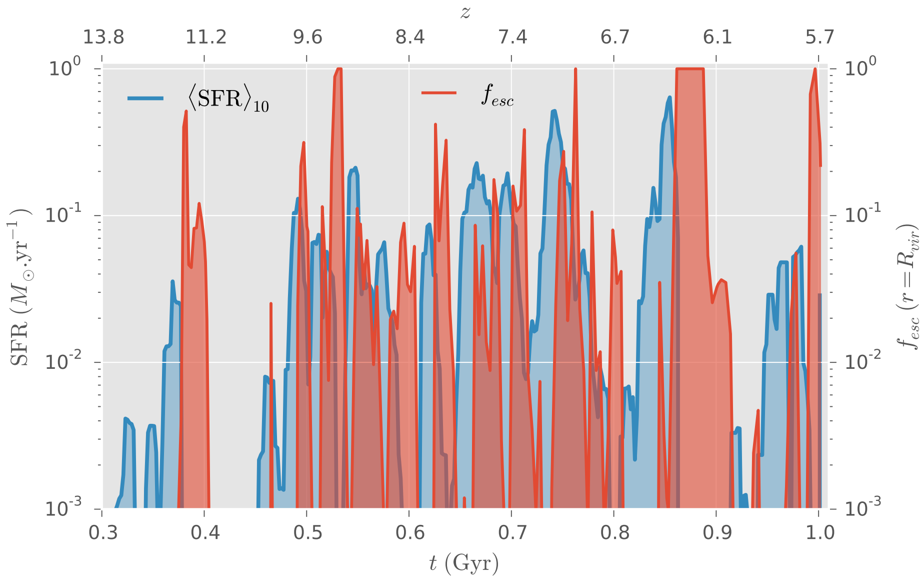

Fig. 2. In blue, evolution of the SFR with time. The evolution of the escape fraction f_{esc} at the halo virial radius is show in red.

show on Fig. 2 the time evolution of both the SFR (in blue) and the escape fraction f_{esc} (in red). There is a clear correlation between the two curves, and f_{esc} starts to rise typically 10 Myr after the beginning of a star formation episode, which is the age at wich the star particles explode in supernovae in our simulations.

4 Observational implications

Using the models of Bruzual & Charlot (2003), we computed the UV magnitude of the three galaxies we modelled to assess their observability with JWST. So far, our computations include neither dust nor IGM attenuation. We find that the most massive galaxy can reach absolute UV magnitudes as high as $M_{\mathrm{UV}} \lesssim -18$, but spend most of its time at $M_{\mathrm{UV}} \gtrsim -15$. We can expect that this kind of small, high-z galaxy will be seen in deep JWST surveys, especially if they are in a starburst episode.

We show on Fig. 3 the correlation between the UV magnitude and the ionising flux escaping the halo. While there is a clear trend that brighter galaxies are in general leaking more ionising photons, there is a large scatter. This means that selection only galaxies brighter than $M_{\mathrm{UV}} = -16$ will miss a large portion of galaxies that are actively contributing to the ionisation budget of the Universe. Conversely, a survey targeting the galaxies emitting more than 10^{50} photons per second would need to go deeper than $M_{\mathrm{UV}} = -14$ to be complete.

5 Conclusions

We have performed high resolution RHD simulations of three dwarf galaxies at $z \sim 6$ to investigate their ionising properties. We found that the cycle of star formation episodes followed by SN explosions will result in a highly varying escape of ionising radiation that can explain the scatter found in other studies. This highlights that it is critical to model star formation and feedback properly at small scale to accurately study the escape of ionising photons in high z galaxies.

We then used simple SED modelling to assess the visibility of such galaxies. We found that the UV magnitude of these galaxies varies a lot with time (following the evolution of the SFR), between $M_{\mathrm{UV}} \sim -12$ and $M_{\mathrm{UV}} \sim -18$. Deep surveys with JWST will probably detect galaxies like these ones, but only when they are in a "bright" phase. We also found that there is only a loose correlation between UV magnitude and ionising emissivity.

MT and JB aknowledge support from the Lyon Institute of Origins under grant ANR-10-LABX-66, and from the ORAGE project from the Agence Nationale de la Recherche under grand ANR-14-CE33-0016-03.

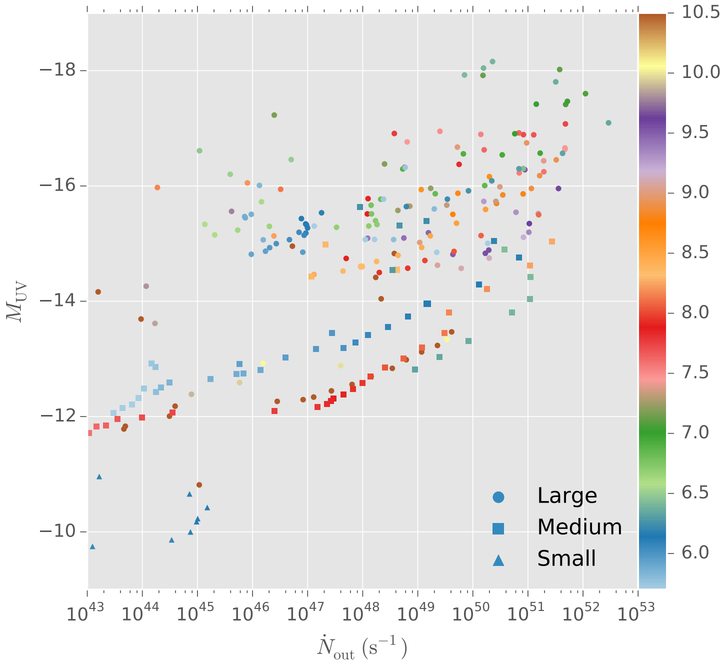

Fig. 3. Ionising flux escaping the halo vs. UV magnitude. The different symbols represents the three different haloes, and the colours represent the redshift.

References

Bruzual, G. & Charlot, S. 2003, MNRAS, 344, 1000

Devriendt, J., Slyz, A., & Kimm, T. in prep.

Haardt, F. & Salvaterra, R. 2015, A&A, 575, L16

Hahn, O. & Abel, T. 2011, MNRAS, 415, 2101

Kimm, T. & Cen, R. 2014, ApJ, 788, 121

Ma, X., Kasen, D., Hopkins, P. F., et al. 2015, MNRAS, 453, 960

Paardekooper, J.-P., Khochfar, S., & Dalla Vecchia, C. 2015, MNRAS, 451, 2544

Robertson, B. E., Furlanetto, S. R., Schneider, E., et al. 2013, ApJ, 768, 71

Rosdahl, J., Blaizot, J., Aubert, D., Stranex, T., & Teyssier, R. 2013, MNRAS[arXiv] 1304.7126

Teyssier, R. 2002, A&A, 385, 337

Wise, J. H., Demchenko, V. G., Halicek, M. T., et al. 2014, MNRAS, 442, 2560

Session 03

Atelier de l'AS GRAM : 100 ans après la relativité générale, point actuel sur Gravitation, Références, Astronomie, Métrologie

SF2A 2015
F. Martins, S. Boissier, V. Buat, L. Cambrésy and P. Petit (eds)

A NEW 4-D DYNAMICAL MODELLING OF THE MOON ORBITAL AND ROTATIONAL MOTION DEVELOPED AT POLAC

A. Bourgoin[1], C. Le Poncin-Lafitte[1], S. Bouquillon[1], G. Francou[1] and M.-C. Angonin[1,]

Abstract. Nowadays, General Relativity (GR) is very well tested within the Solar System using observables given by the tracking of spacecraft (Bertotti et al. 2003), Very Long Baseline Interferometry (Lambert & Le Poncin-Lafitte 2009, 2011) and Lunar Laser Ranging -LLR- (Merkowitz 2010). These tests are mainly based on two frameworks: the Parametrized Post Newtonian (PPN) and the search for a fifth force. However other frameworks are available and can be used to look for deviations from GR. In this context, we present the ongoing work concerning LLR performed at POLAC (Paris Observatory Lunar Analysis Center) in SYRTE, Paris Observatory. We focus on a new generation of software that simulates the observable (the round trip time of photons) from a given space-time metric (Hees et al. 2012). This flexible approach allows to perform simulations in any alternative metric theories of gravity. The output of these software provides templates of anomalous residuals that should show up in real data if the underlying theory of gravity is not GR. Those templates can be used to give a rough estimation of the constraints on the additional parameters involved in the alternative theory. To succeed, we are building a numerical lunar ephemeris which integrates the differential equations governing the orbital and rotational motion of bodies in the Solar System. In addition, we integrate the difference between the Terrestrial Time (TT) and the Barycentric Dynamical Time (TDB) to make the ephemeris self-consistent. Special attention is paid to the computation of partial derivatives since they are integrated numerically from the variational equations.

Keywords: general relativity, fundamental physics

1 Context

Since 1969 LLR is one of the best tool to constrain GR. However these constraints are generally computed within two frameworks : PPN formalism (Will 1993) and the fifth force framework (Fischbach & Talmadge 1999). Therefore, parameters involved in these two formalism, are very well estimated and point towards GR. For instance, the solution of Williams et al. (2004) yields a numerical test of the equivalence principle with LLR comparable with the present laboratory limit at one part over 10^{13}. It also improved constraints on the strong equivalence principle parameter η (=0 in GR), PPN parameter of non linearity β (=1 in GR), geodetic precession effect and $\dot{G}/G$. Soffel et al. (2008) consider a potential test of the gravitomagnetism effect and the link with the preferred frame parameter α_1 (=0 in GR) appearing in the usual PPN framework. Finally, for the search of a fifth force Müller et al. (2005) performed LLR analysis of the inverse square law by fitting Yukawa perturbation terms.

Most of the time, tests realised in the PPN formalism, are performed in fully-conservative metric theories. However looking for deviations from GR in semi-conservatives, non-conservatives metric theories or even in other phenomenological frameworks like SME (Colladay & Kostelecký 1997, 1998) could be very interesting. Indeed many alternative theories to GR predict for instance a violation of the Lorentz symmetry at different levels. In this attempt, we are building a new numerical lunar ephemeris computed in alternative frameworks to GR and which will be fit on LLR data.

---

[1] SYRTE, Observatoire de Paris, PSL Research University, CNRS, Sorbonne Universités, UPMC Univ. Paris 06, LNE, 61 avenue de l'observatoire, 75014 Paris, France

© Société Francaise d'Astronomie et d'Astrophysique (SF2A) 2015

2 Main effects

Considering the high accuracy of the LLR data, we have to model all the dynamical effects with theoretical signal larger than 1 cm over the Earth-Moon distance. The most important are (i) the point-mass interactions, (ii) figure potential, (iii) tides and spin deformations of (iv) anelastic bodies and (v) lunar librations.

(i) The numerical integration of the positions of point-mass bodies is done in the International Celestial Reference System (ICRS). We use the post-Newtonian Eistein-Infeld-Hoffmann (EIH) equations of motion in PPN framework, see e.g. Klioner & Soffel (2000). The difference between TT and TDB is also integrated.

(ii) The Moon, the Sun and the Earth are not considered as point-mass bodies. We use spherical harmonics to describe their figure potential. We expand the Earth potential up to degree 4 in zonal harmonic, up to degree 4 in zonal, sectoral and tesseral harmonic for the Moon and only the 2^{nd} degree in zonal harmonic is considered for the Sun.

(iii) We take into account distortions (due to tides and spin variation) raised upon the Earth and the Moon since they are closed to each other. These distortions induce variations in 2^{nd} degree harmonic of the two extended bodies. Subsequently, the impact on the orbital motion of point-mass body is computed with the figure potential formalism described in (ii).

(iv) Distortions are evaluated considering anelastic bodies. Since anelastic bodies don't react immediately to a perturbation, there is a time delay in their reaction because of the dissipation inside them. To consider this dissipation for tides, we introduce a phase lag between the position of a tide raising body and the direction of the tidal bulge. For the spin velocity vector, we consider dissipation by computing the angular velocity vector at time t minus time delay.

(v) We orientate the Moon in ICRS thanks to the three Euler's angles (ϕ, θ, ψ). Their evolution in time is given by Euler's equation of motion which relates the change in Moon angular velocity vector with the Moon total moment inertia tensor and its time derivative. Torques acting on the Moon come from different contributions: (a) interactions of point-mass bodies with the non-spheric potential of the Moon; (b) interaction between the figure of the Earth and the one of the Moon. (c) geodetic precession effect.

3 Partials derivatives

One of the most important specificity of our approach compared to others numerical ephemeris, is the computation of partials from variational equations. In the least squares procedure partials represent the link between the computed and the observed values. We choose to integrate them at the same time than the equations of motion with the ODEX integrator (Hairer et al. 1993). In the standard least squares fit applied to LLR, the new parameters vector $\boldsymbol{x}$ is determined from the initial parameters vector $\boldsymbol{x_0}$ as well as the range measured and the range numerically integrated $f(\boldsymbol{x_0})$. We also need $f'(\boldsymbol{x_0})$ the partial derivative matrix, computed from the variational equations. It depends on initial values of the solution vector : $\boldsymbol{x_0} = {}^{\mathrm{T}}(\rho_1^i, \cdots, \rho_n^i, \zeta^i;\ \dot{\rho}_1^i, \cdots, \dot{\rho}_n^i, \dot{\zeta}^i;\ p^l)$, where $i = 1, \cdots, 3$; $l = 1, \cdots, m$; $\boldsymbol{p}$ being the physical parameters vector, $\boldsymbol{\rho}_{\mathrm{A}}$ the position vector of body A, $\dot{\boldsymbol{\rho}}_{\mathrm{A}}$ the velocity vector of body A, $\boldsymbol{\zeta}$ the three Euler's angles and $\dot{\boldsymbol{\zeta}}$ their time derivatives. Then, for $i = 1, \cdots, 3$, $A = 1, \cdots, n$ and $j = 1, \cdots, 6(n+1)+m$, we integrate the $3n[6(n+1)+m]$ following equations :

$$\left\{ \begin{aligned} \frac{\mathrm{d}}{\mathrm{d}t}\left(\frac{\mathrm{d}\rho_{\mathrm{A}}^i}{\mathrm{d}x_0^j}\right) &= \frac{\mathrm{d}\dot{\rho}_{\mathrm{A}}^i}{\mathrm{d}x_0^j} \\ \frac{\mathrm{d}}{\mathrm{d}t}\left(\frac{\mathrm{d}\dot{\rho}_{\mathrm{A}}^i}{\mathrm{d}x_0^j}\right) &= \sum_{\mathrm{B},k} \frac{\partial \alpha_{\mathrm{A}}^i}{\partial \rho_{\mathrm{B}}^k}\frac{\mathrm{d}\rho_{\mathrm{B}}^k}{\mathrm{d}x_0^j} + \sum_{\mathrm{B},k} \frac{\partial \alpha_{\mathrm{A}}^i}{\partial \dot{\rho}_{\mathrm{B}}^k}\frac{\mathrm{d}\dot{\rho}_{\mathrm{B}}^k}{\mathrm{d}x_0^j} + \sum_{k} \frac{\partial \alpha_{\mathrm{A}}^i}{\partial \zeta^k}\frac{\mathrm{d}\zeta^k}{\mathrm{d}x_0^j} + \sum_{k} \frac{\partial \alpha_{\mathrm{A}}^i}{\partial \dot{\zeta}^k}\frac{\mathrm{d}\dot{\zeta}^k}{\mathrm{d}x_0^j} + \frac{\partial \alpha_{\mathrm{A}}^i}{\partial x_0^j} \end{aligned} \right. ,$$

where $\boldsymbol{\alpha}_{\mathrm{A}} = \ddot{\boldsymbol{\rho}}_{\mathrm{A}}(\boldsymbol{x_0})$ is the absolute acceleration vector of body A. We obtain a similar expression for $\mathrm{d}\zeta^i/\mathrm{d}x_0^j$ where $\boldsymbol{\alpha}_{\mathrm{A}}$ is replaced by $\ddot{\boldsymbol{\zeta}}$ the acceleration over the three Euler angles. Partial derivatives in the second member are computed analytically and directly implemented into the software. The numerical integration of the $\mathrm{d}\rho_{\mathrm{A}}^i/\mathrm{d}x_0^j$ quantities let to compute the partial derivatives matrix $f'(\boldsymbol{x_0})$. Using this semi-numerical method, we integrate partials at the same time than the equations of motion unlike a purely numerical method.

4 Comparison with INPOP13c

We present a comparison between our numerical solution and INPOP13c (Fienga et al. 2014). Currently, the two dynamical modelling are closed to each other except three main differences: (a) into our numerical solution, the Earth orientation is forced with the IAU-routines of SOFA (Wallace 1998), whereas it is integrated into INPOP13c; (b) we consider the perturbation upon the Earth-Moon vector of the 70 biggest asteroids, while the effect of 300 is computed into INPOP13c; (c) INPOP13c takes into account a flat ring in order to model the remaining asteroids of the main belt, which is not present in our software.

In Fig. 1, 2 and 3 we compare the two dynamical modelling by taking initial conditions (positions and velocities) of bodies as well as values of physical parameters provided by INPOP13c at J2000. We have integrated the differential equations with our software and plotted the differences between our solution and INPOP13c. In Fig. 1 is shown the difference over the Earth-Moon distance on the left panel and the distribution around the mean value on the right panel. In Fig. 2 is plotted the differences over the 6 Keplerian elements of the Moon, and the three Euler's angles and their time derivatives in Fig. 3.

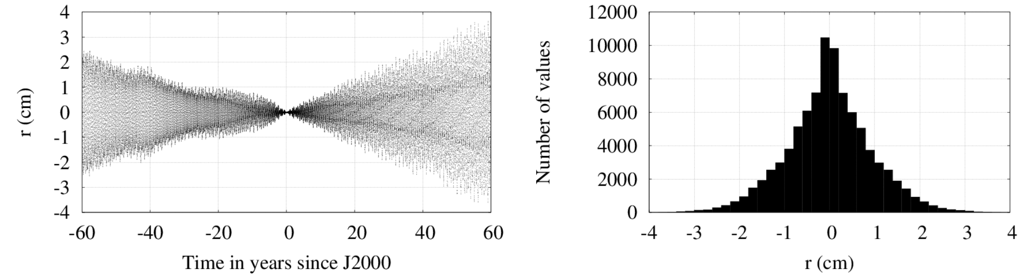

Fig. 1. Left: Difference over the Earth Moon distance after an integration with initial conditions provided by INPOP13c. The x axis is TDB time expressed in years since J2000. **Right:** Distribution of this difference around the mean value.

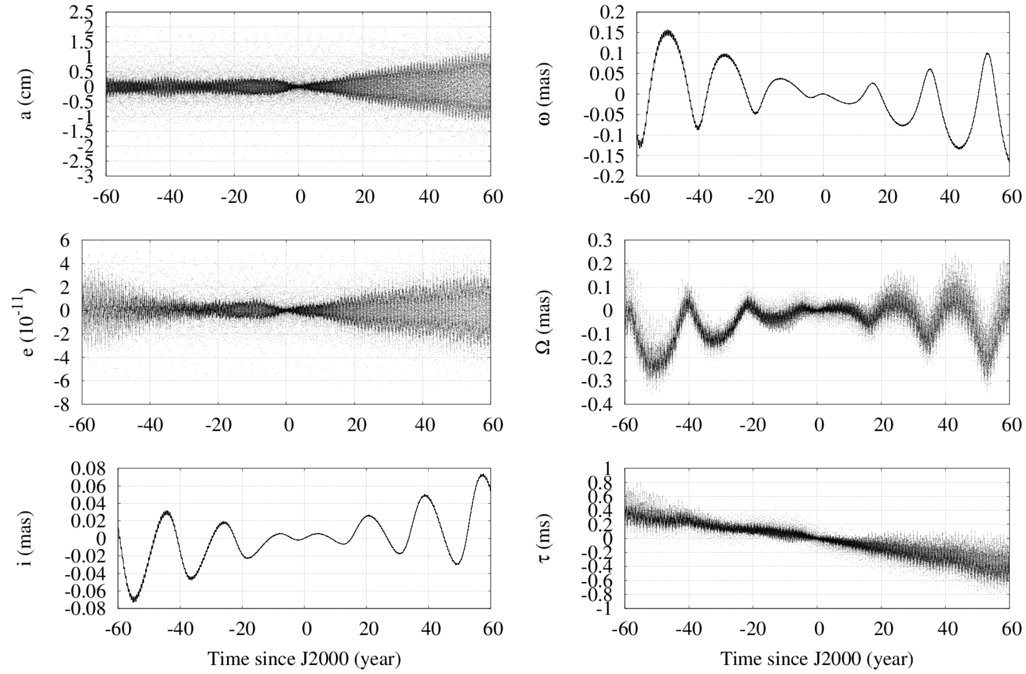

Fig. 2. Differences over the 6 keplerian elements of the Moon after an integration with initial conditions provided by INPOP13c. The x axis is TDB time expressed in years since J2000.

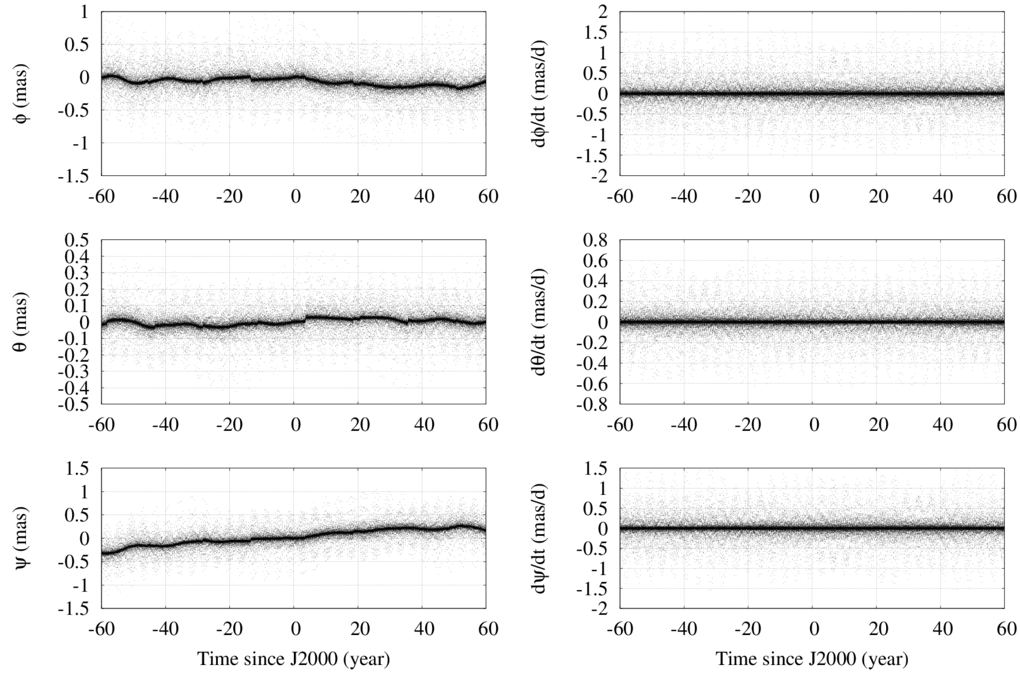

Fig. 3. Differences over the 3 Euler's angles and their time derivatives after an integration with initial conditions provided by INPOP13c. The x axis is TDB time expressed in years since J2000.

5 Conclusion

Our numerical solution of the orbital and rotational motion of the Moon, is very closed to the one of INPOP13c over a time span of 120 years old centred at J2000, as shown with Fig. 1, 2 and 3. The remaining signal on Fig. 1 and 2 is totally explained by the differences of the two modelling (see Sec. 4) while no significant remaining signal is found on Fig. 3. Currently we are fitting our numerical solution to LLR data with the CAROLL reduction software available in POLAC using partial derivatives computed from variational equations.

References

Bertotti, B., Iess, L., & Tortora, P. 2003, Nature, 425, 374

Colladay, D. & Kostelecký, V. A. 1997, Phys. Rev. D, 55, 6760

Colladay, D. & Kostelecký, V. A. 1998, Phys. Rev. D, 58, 116002

Fienga, A., Manche, H., Laskar, J., Gastineau, M., & Verma, A. 2014, ArXiv e-prints

Fischbach, E. & Talmadge, C. L. 1999, The Search for Non-Newtonian Gravity

Hairer, E., Norsett, S. P., & Wanner, G. 1993, Solving Ordinary Differential Equation I. Nonstiff Problems, ed. Springer-Verlag (Springer Series in Computational Mathematics)

Hees, A., Lamine, B., Reynaud, S., et al. 2012, Classical and Quantum Gravity, 29, 235027

Klioner, S. A. & Soffel, M. H. 2000, Physical Review D, 62, 024019

Lambert, S. B. & Le Poncin-Lafitte, C. 2009, A&A, 499, 331

Lambert, S. B. & Le Poncin-Lafitte, C. 2011, Astronomy and Astrophysics, 529, A70+

Merkowitz, S. M. 2010, Living Reviews in Relativity, 13, 7

Müller, J., Williams, J. G., & Turyshev, S. G. 2005, ArXiv General Relativity and Quantum Cosmology e-prints

Soffel, M., Klioner, S., Müller, J., & Biskupek, L. 2008, Physical Review, 78, 024033

Wallace, P. T. 1998, Highlights of Astronomy, 11, 191

Will, C. M. 1993, Theory and Experiment in Gravitational Physics

Williams, J. G., Turyshev, S. G., & Boggs, D. H. 2004, Physical Review Letters, 93, 261101

SF2A 2015
F. Martins, S. Boissier, V. Buat, L. Cambrésy and P. Petit (eds)

COMPARISON OF OFFICIAL IVS NUTATION TIME SERIES FROM VLBI ANALYSIS

C. Gattano[1], S. Lambert[1] and C. Bizouard[1]

Abstract. We carried out comparisons between the official IVS nutation time series using VLBI data. We studied differences between those time series and differences between derived products such as amplitude and phase of nutation components, including free core nutation, and noise color.

Keywords: VLBI, Analysis Strategy, Celestial Reference Frame, Precession-nutation

1 Introduction

Very Long Baseline Interferometry (VLBI) is the only technique that determines the Earth's nutation at submilliarcsecond (mas) accuracy. With its 35 years of observations and at the rate of about two sessions per week during the last decade, it allows to estimate nutation over periods from 14 days and up to almost 20 years. The quality of nutation estimates is fundamental for further use in geophysics for, e.g., inferring Earth's interior parameters relevant to the mantle, the core, and the inner core (e.g., Mathews et al. 1991, 1995, 2002). But VLBI data analysis is complex. Even if the observational data set is the same for everyone, there are as much different nutation time series that there are analysists, and therefore analysis strategies, in the International VLBI Service for Geodesy and Astrometry (IVS; Schuh & Behrend 2012). We propose here to quantify the differences.

2 Data Set

We carried out a comparison of several nutation time series provided by different analysis centers of the IVS: Geoscience Australia (AUS00007, Australia), Bundesamt für Kartographie und Geodäsie (BKG00014, Germany), Centro di Geodesia Spaziale (CGS2014A, Italy), Goddard Space Flight Center (GSF2014A, USA), Institute of Applied Astronomy (IAA2007A, Russia), Observatoire de Paris (OPA2015A, France), Astronomical Institute of St.-Petersbufg University (SPU00004, Russia), U. S. Naval Observatory (USN2015A, USA), Vienna University of Technologie (VIEEOP13, Austria) and the IVS combined time series (IVS14Q2X) which is computed with the transformed and weighted normal equations of several operational analysis center solutions (Böckmann et al. 2010). The nutation time series used in this study are offsets according to an IAU precession-nutation model in dX, dY parametrization (Capitaine et al. 1986). You can use the tool following this link to get all the previous nutation time series in the parametrization you want.

Solution technical descriptions are summarized in Table 1 where we display the analysis options that are connected to nutations. VIEEOP13 is added because it uses VieVs software but we do not know its technical details. Globally, all solutions are obtained by similar analysis strategies except for some steps concerning: **(1)** the status of radio sources (are their positions locally or globally estimated, fixed, constrained?); **(2)** the wet zenith troposphere delay a priori at the observing elevation (mapping function); **(3)** the wet zenith troposphere delay and gradient estimation strategy and interval; **(4)** the clock offset estimation strategy and interval.

Concerning the first item, several works reported a non negligible influence of the instability of the targeted radio sources in Earth orientation parameter estimates (Dehant et al. 2003; Feissel-Vernier 2003; Feissel-Vernier et al. 2005, 2006; Lambert et al. 2008). The use of the ICRF1 (Ma et al. 1998) or its extension (Fey et al. 2004), which axes stability was estimated around 0.25 mas in place of the current ICRF2 (Fey et al. 2015) which is more stable by a factor of 5 could lead to detectable perturbations in the nutation time series. Concerning the VLBI analysis software package, five analysis centers use CALC/SOLVE, three use OCCAM and one uses VieVs.

[1] SYRTE, Observatoire de Paris, PSL Research University, CNRS, Sorbonne Universites, UPMC Univ. Paris 06, LNE, 61 avenue de lObservatoire, 75014 Paris, France

© Société Francaise d'Astronomie et d'Astrophysique (SF2A) 2015

		AUS	BKG	CGS	GSF	IAA	OPA	SPU	USN
CRF	a priori	ICRF1 Ext.2	ICRF2	ICRF2	ICRF2	ICRF1 Ext.2	ICRF2	ICRF1 Ext.2	ICRF2
	NNR	ICRF1	ICRF2	ICRF2	ICRF2	ICRF1	ICRF2	ICRF1	ICRF2
	global/local	0/0	all/0	969/1720	1670/NL	0/0	all-NL/NL	0/0	846/852
Precession a priori		IAU1976	IAU2006	IAU2006	IAU2006	IAU2000A	IAU2006	IAU1976	IAU2006
Nutation a priori		IAU1980	IAU2000A	IAU2000A	IAU2000A	IAU2000A	IAU2000A	IAU1980	IAU2000A
IERS Conventions		2000	2010	2003	2010	2003	2010	2003	2010
Tropo.	mapping	VMF	VMF	VMF	VMF	VMF	VMF	VMF	NMF
	ZTD	RW	1h LS	60mn LS	20mn LS	RW	20m LS	RW	20m LS
	gradients	constant	24h offset	6h LS	6h LS	-	6h offset	constant	6h LS
Clock interval		RW	1h LS	1h Q	1h Q	RW	1h Q	RW	1h Q
Elevation cutoff		quality flag	5°	5°	5°	quality flag	5°	quality flag	5°
Software package		OCCAM	CALC/ SOLVE	CALC/ SOLVE	CALC/ SOLVE	OCCAM	CALC/ SOLVE	OCCAM	CALC/ SOLVE

Table 1. Analysis strategies of different analysis centers. NNR: no-net rotation applied to the defining sources; NL: 39 sources called "non linear" in Fey et al. (2015); LS: linear spline; Q: quadratic polynomial; RW: Random Walk process; VMF/NMF: Vienna (Boehm et al. 2006)/Niell (1996) mapping function.

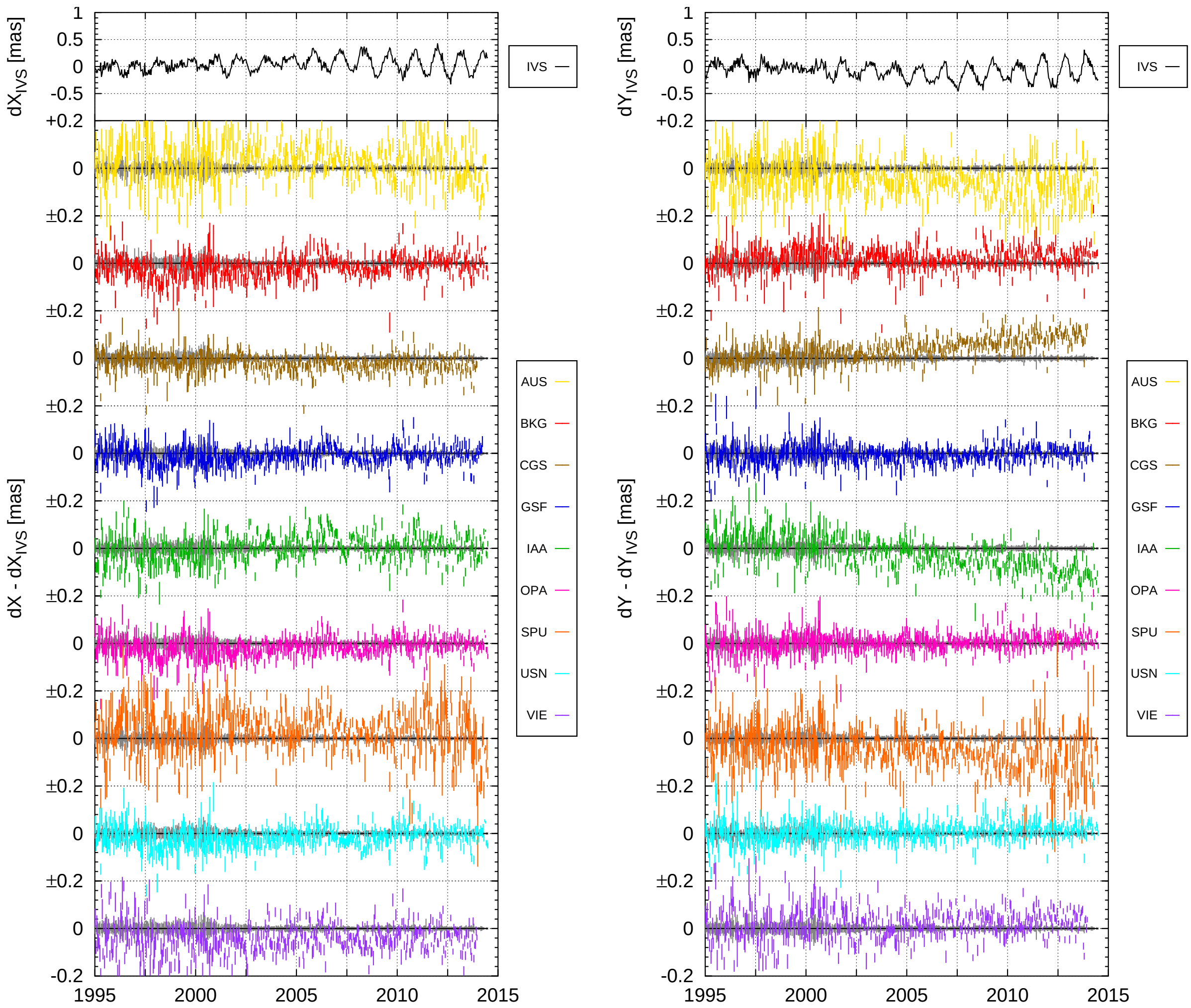

Fig. 1. Differences of nutation time series with respect to the IVS combination. The reference IVS time series is shown on the top.

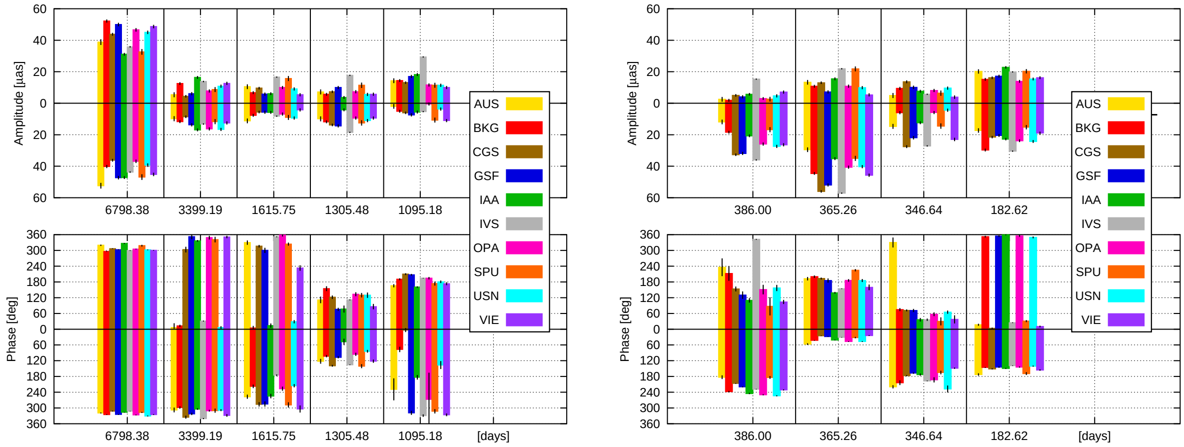

Fig. 2. Least Square adjustment of amplitude and phase of principal nutations.

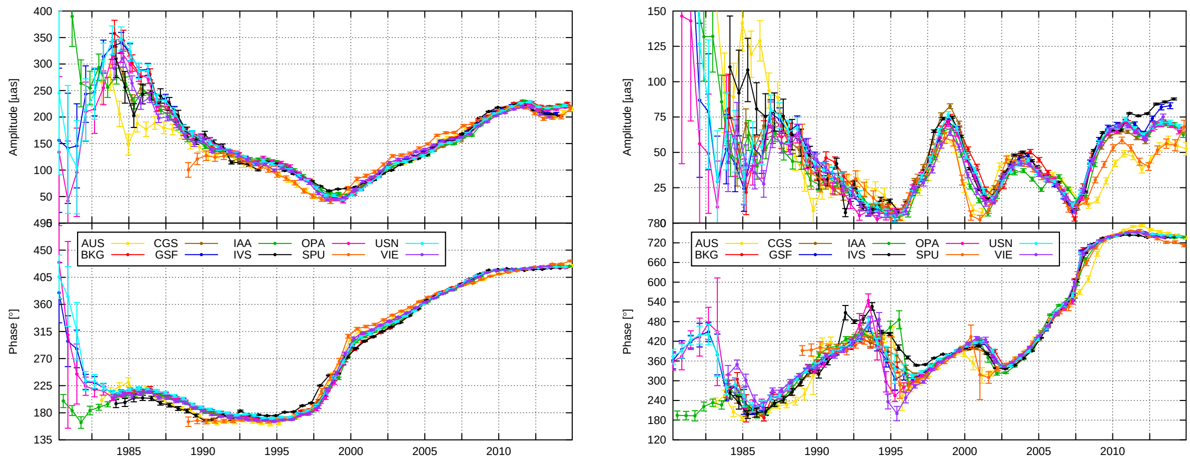

Fig. 3. Least square adjustment over a 7-yr sliding window every 0.6 years of amplitude and phase of the free core nutation (FCN) and retrograde annual nutation.

3 Analysis and results

Figure 1 displays differences of each center's time series with respect to the IVS combined series. For each graph, we plot error bars of center's solution in color and error bars of IVS-combined's solution (top plot) in grey. We use the IVS combined time series as references purely for sake of clarity. At no time, we consider the IVS combined time series better than the others. Drifts that appear on AUS, IAA and SPU graphes are likely due to the use of a different precession model as a priori precession : IAU1976 (Lieske et al. 1977), IAU2000 (Mathews et al. 2002) or IAU2006 (Capitaine et al. 2005). Drift on CGS graph comes from another unknown origin.

Even if, globally, time series are similar at the level of tenths of a mas, we can see that they significantly diverge at some dates in the sense that error bars do not account for the differences. Figures 2 show adjustments of principal lunisolar nutations and figures 3 show more detailed on the time-variable amplitudes and phases of the free core nutation (FCN), known at period of 430.21 days in retrograde motion, and the annual retrograde nutation. The complete adjustment is composed of 21 prograde and retrograde waves of prominent amplitudes used in the latest Earth nutation theory of Mathews et al. (2002). They were adjusted by least square method over all the available data between 01.01.1979 and 01.01.2015. For the FCN and annual nutation, the least square adjustment was done over a 7-yr sliding window every 0.6 years between those dates.

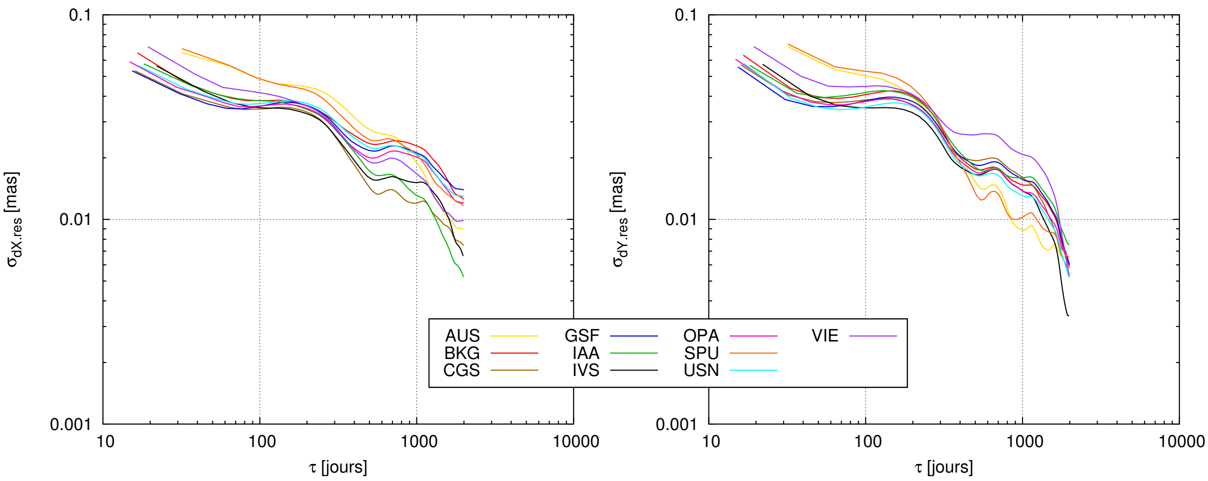

Fig. 4. Allan standard deviation of residual nutation time series.

From one solution to another, figures reveals that the difference in amplitude for a given nutation do not exceed 30 μas. Surprisingly, IVS often present the furthest value with respect to the others. It seems that the combination process creates artifacts that affect the nutation components. SPU, AUS and IAA show also some divergences at some dates. Those three are using the OCCAM software (see table 1). Software may also affect results of nutation adjustment. Notice that the annual nutation shows a period of phase instability between 1992 and 1997. The excitation mechanism of both the FCN and the annual retrograde nutation should be investigated in the future, especially to understand their amplitude variability and the cancellation of the annual retrograde nutation amplitude in 1995, 2002(?) and 2007.5. This mechanism likely originates in external fluid layer mass exchanges but the difficulty in modeling high frequency behavior of the atmosphere prevents one from any verification (de Viron et al. 2005; Lambert 2006).

4 Noise characterization

In the previous section, we adjusted a number of prominent nutation components and removed them from the time series, such that residuals can be considered as close to a noise. We computed Allan standard deviation samples σ_{A} defined for a time sampling interval τ as (Allan 1966; Rutman 1978)

$$\sigma^2_{\mathrm{A}}(t,\tau) = \frac{1}{2}\left(\bar{y}_t + \bar{y}_{t+\tau}\right)^2, \tag{4.1}$$

where y is a data set and $\bar{y}_t$ is the mean of data along the τ-duration interval which begins at t. Then we computed the Allan standard deviation by averaging over time using overlapped samples. This algorithm is called AVAR in the litterature. It provides an unbiased estimator for the true variance in the case of white frequency noise modulation. The Allan standard deviation of the residual series are displayed in Fig. 4. We investigate noise on time scales from 15 days and up to about 5 years. In the graphes, a slope of -0.5 indicates the presence of a white frequency noise, while a constant reveals a flicker noise and a slope of 0.5, a random walk noise.

At low time scales, residual nutation time series can be considered as a white noise. After a 500 days time scale, it is difficult to distinguish between white noise and colored noise because of the bumps. Those successive bumps indicate the presence of a residual periodic signal. The time scale for the top of the first bump gives us the half-period of this signal, the time scale of the second bump gives three halves times the period, etc... In our case the period is approximately 450 days. Solutions are also gathered between software users (see table 1), that means BKG, CGS, GSF, OPA, USN (CALC SOLVE users), AUS, IAA, SPU (OCCAM users) and VIE (VieVs user). This fact is remarkable on the dY graph at 1000 days. Only IAA do not follow its group and CGS do not follow CALC/SOLVE group for the dX component. It means that the noise amplitude certainly be software dependent.

5 Conclusion

We compared the nutation time series made available by different analysis centers using their own VLBI analysis configurations. These differences affect the nutation at the level of 30 μas. No analysis configuration shows up in this study. But a dependance on software used appears, especially on the noise characterization. More thorough analyses are needed to separate the effects due to delay modeling, constraints, and parameterization.

Although small compared to, e.g., the stability of the current celestial reference frame (Fey et al. 2015), differences between nutation series raise some questions about the observability of tiny phenomenon that are currently under investigation by the geophysical community. In particular, we can cite **(1)** the determination of the quality factor (damping factor) of the FCN which is linked to deformability of the core-mantle interface as well as possible topographic and electromagnetic couplings (Mathews et al. 2002; Koot et al. 2008, 2010), and **(2)** the determination of the period of the free inner core nutation (FICN) which is currently very uncertain (Rogister & Valette 2009). In a work in preparation, we also include multi-techniques combination EOP in our comparison and we consider a more thorough spectral analysis to extract periodic components, so that the characterization of the internal noise of each series is more relevant.

References

Allan, D. W. 1966, IEEE Proceedings, 54, 221

Böckmann, S., Artz, T., Nothnagel, A., & Tesmer, V. 2010, Journal of Geophysical Research (Solid Earth), 115, 4404

Boehm, J., Werl, B., & Schuh, H. 2006, Journal of Geophysical Research (Solid Earth), 111, 2406

Capitaine, N., Souchay, J., & Guinot, B. 1986, Celestial Mechanics, 39, 283

Capitaine, N., Wallace, P. T., & Chapront, J. 2005, A&A, 432, 355

de Viron, O., Schwarzbaum, G., Lott, F., & Dehant, V. 2005, Journal of Geophysical Research (Solid Earth), 110, 11404

Dehant, V., Feissel-Vernier, M., de Viron, O., et al. 2003, Journal of Geophysical Research (Solid Earth), 108, 2275

Feissel-Vernier, M. 2003, A&A, 403, 105

Feissel-Vernier, M., Ma, C., Gontier, A.-M., & Barache, C. 2005, A&A, 438, 1141

Feissel-Vernier, M., Ma, C., Gontier, A.-M., & Barache, C. 2006, A&A, 452, 1107

Fey, A. L., Gordon, D., Jacobs, C. S., et al. 2015, AJ, 150, 58

Fey, A. L., Ma, C., Arias, E. F., et al. 2004, AJ, 127, 3587

Koot, L., Dumberry, M., Rivoldini, A., de Viron, O., & Dehant, V. 2010, Geophysical Journal International, 182, 1279

Koot, L., Rivoldini, A., de Viron, O., & Dehant, V. 2008, Journal of Geophysical Research (Solid Earth), 113, 8414

Lambert, S. B. 2006, A&A, 457, 717

Lambert, S. B., Dehant, V., & Gontier, A.-M. 2008, A&A, 481, 535

Lieske, J. H., Lederle, T., Fricke, W., & Morando, B. 1977, A&A, 58, 1

Ma, C., Arias, E. F., Eubanks, T. M., et al. 1998, AJ, 116, 516

Mathews, P. M., Buffett, B. A., Herring, T. A., & Shapiro, I. I. 1991, J. Geophys. Res., 96, 8243

Mathews, P. M., Buffett, B. A., & Shapiro, I. I. 1995, J. Geophys. Res., 100, 9935

Mathews, P. M., Herring, T. A., & Buffett, B. A. 2002, Journal of Geophysical Research (Solid Earth), 107, 2068

Niell, A. E. 1996, J. Geophys. Res., 101, 3227

Rogister, Y. & Valette, B. 2009, Geophysical Journal International, 176, 368

Rutman, J. 1978, IEEE Proceedings, 66, 1048

Schuh, H. & Behrend, D. 2012, Journal of Geodynamics, 61, 68

SF2A 2015
F. Martins, S. Boissier, V. Buat, L. Cambrésy and P. Petit (eds)

TESTING THE RAY-TRACING CODE GYOTO

M. Grould[1], T. Paumard[1] and G. Perrin[1]

Abstract. In the next few years, the near-infrared interferometer GRAVITY will observe the Galactic Center. Astrometric data will be obtained with an expected accuracy of 10 μas. In order to analyze those future data, we have developed a code named GYOTO to compute orbits and ray-trace images. We want to assess the validity and accuracy of GYOTO in a variety of contexts, in particular for stellar astrometry in the Galactic Center.

Keywords: Galactic Center, Black hole physics, Gravitational lensing

1 Introduction

GYOTO* (General relativitY OrbiT of Observatoire de Paris) is a ray-tracing code developed by Vincent et al. (2011). It integrates null and time-like geodesics in any analytical metrics and numerical metrics. This last property makes GYOTO a unique ray-tracing code. GYOTO can compute images and spectra for a variety of astrophysical objects, such as moving stars or accretion disks, around a Kerr black hole. Thanks to its particularity, it can also compute images or trajectories of stars orbiting exotic objects such as a boson star (Grandclément et al. 2014).

The main motivation for the development of GYOTO was to interpret the data to be obtained with the second generation VLTI instrument GRAVITY (Eisenhauer et al. 2011). This instrument will observe stars and flares orbiting Sgr A*. It will probe space-time near the central object with an expected astrometric accuracy of 10 μas. The stellar orbits measured by GRAVITY will be affected by several effects such as periastron shift and Lense-Thirring effects (Will 2008, Merritt et al. 2010). In additions, the individual astrometric measurements will be affected by relativistic effects: time delay and lensing (Bozza & Mancini 2012). All these effects need to be considered in apparent orbit model that will be fitted to the GRAVITY data, allowing to constrain the nature of Sgr A* using the GRAVITY data. Since the goal of GRAVITY is to deliver astrometry at an accuracy of 10 μas, models need to be more accurate than this value, in order to not limit the accuracy of final results. We therefore aim for a model with an astrometric accuracy of 1 μas. In this paper, we study the accuracy of GYOTO in order to determine whether this tool can be used as a foundation for a future apparent orbit model to fit the GRAVITY data. Using the star images computed by GYOTO it will be possible to get the apparent position of the star. However, the accuracy of this position will depend on the precision of the photon trajectories. Null geodesics need to be properly computed by the integrator implemented in GYOTO in order to take into account the correct bending effect. Beside, because of the 2" of field-of-view of GRAVITY, a wide range of distances between stars and Sgr A* will be possible. GYOTO has never been used in such a configuration, we need to ensure that geodesics are well computed.

We first focus on the Einstein ring radius. The aims are both to compare our numerical results with analytical study on the Einstein ring radius performed by Sereno and De Luca in 2008 (Sereno & de Luca 2008), and to check if the numerical error is sufficiently low, which means inferior or equal to 1 μas. The comparison between GYOTO and the approximation is a validation of GYOTO in the weak deflection limit (WDL), however we also have to check if this ray-tracing code is valid in the strong deflection limit (SDL). To do so, we choose to compare null geodesics computed in GYOTO and with another code named Geokerr† (Dexter & Agol 2009).

[1] LESIA, Observatoire de Paris, CNRS, Universit Pierre Marie Curie, Universit Paris Diderot, 5 place Jules Janssen, 92190 Meudon, France
*freely available at the URL `http://GYOTO.obspm.fr`
†freely available at the URL `http://www.astro.washington.edu/users/agol/geokerr/`

© Société Francaise d'Astronomie et d'Astrophysique (SF2A) 2015

2 The Einstein ring

To understand how the Einstein ring is formed, we remind basics of gravitational lensing using a Schwarzschild lens. Then, we focus on Einstein ring obtained with a Kerr black hole. In both cases we consider a static observer. The spin axis coincides with the z-axis. Spherical coordinates of the observer and the source, relative to the lens L, are noted $(r_0, \vartheta_0, \phi_0)$ and $(r_s, \vartheta_s, \phi_s)$, respectively. Without loss of generality we choose to work in the equatorial plane: $\vartheta_0 = \frac{\pi}{2}$, $\phi_0 = 0$ and $\vartheta_s = \frac{\pi}{2}$. This yields $(x_0, 0, 0)$ for the observer and $(x_s, y_s, 0)$ for the source. We note M the lens mass and a the spin of the black hole ranging from 0 (Schwarzschild black hole) to 1 (extremal Kerr black hole). In this paper, we use two different units for the distance: parsecs and geometrical units. This last unit is equal to $\frac{GM}{c^2}$, with G the Newton's constant and c the speed of light, but we will consider $G = c = 1$ and note it M.

2.1 Schwarzschild lens

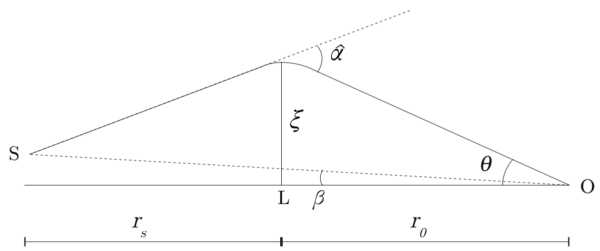

Fig. 1. Spatial projection of a Schwarzschild lensing situation: S corresponds to the source, L to the lens and O to the observer.

Using the notation of Fig.1, we can write the useful lens equation (Schneider et al. 1992):

$$\boldsymbol{\beta} = \boldsymbol{\theta} - \frac{r_s}{(r_s + r_0)} \hat{\boldsymbol{\alpha}}(\boldsymbol{\xi}), \tag{2.1}$$

with $\boldsymbol{\beta}$ the unlensed angular position of the source, $\boldsymbol{\theta}$ the lensed angular position of the source equal to $\boldsymbol{\xi}/r_0$ and $\hat{\boldsymbol{\alpha}}$ the deflection angle depending on the impact parameter $\boldsymbol{\xi}$. The latter angle is also called the Einstein angle whose expression is equal to $\hat{\boldsymbol{\alpha}}(\boldsymbol{\xi}) = \frac{2R_S}{\boldsymbol{\xi}}$ with $R_S = \frac{2GM}{c^2}$ the Schwarzschild radius. We can rewrite the lens equation as:

$$\boldsymbol{\theta}^2 - \boldsymbol{\beta}\boldsymbol{\theta} - \alpha_0^2 = 0, \tag{2.2}$$

with $\alpha_0 = \sqrt{2R_S \frac{r_s}{r_0(r_s+r_0)}}$. The magnification of the source in the lens plane is function of the lensed and unlensed angles as:

$$A = J^{-1} = \left| det \frac{\partial \boldsymbol{\beta}}{\partial \boldsymbol{\theta}} \right|^{-1}. \tag{2.3}$$

A is infinite when $J = 0$. In the source plane, these positions are called caustics points (or primary caustic). For a Schwarzschild lens, the caustic is a line behind the lens starting from it and extending toward infinity (Rauch & Blandford 1994). If the source lies on the caustic line then $\beta = 0$. Thus, the solution of the lens equation is $\theta = \alpha_0$. A circle called critical curve is formed in the lens plane with a radius of α_0. Considering the source as a star the observer sees the well-known Einstein ring. The radius of the ring corresponds to the critical curve radius so we get $\alpha_0 = \theta_E$ with θ_E the Einstein ring radius. If the star does not lie on the caustic, the observer will see two images named primary and secondary images. These images are formed by lensing effects. Light rays are deviated because of the curvature of space-time by the black hole. At the caustic points, the lensed images merge into the Einstein ring.

2.2 Kerr black hole lens

In the Kerr black hole case, there is also a primary caustic but it is not a line anymore (Rauch & Blandford 1994, Bozza 2008). Rauch & Blandford (1994) were the first to discover that the primary caustic is a tube with an astroid (four-cusped) cross-section. At large distances the cross-section is symmetric but becomes distorted near the horizon. Besides, the closer the source to the black hole the larger the tube shifts with respect to the Schwarzschild's case. Very far from the black hole the shift is still significant but the size of the caustic (distance between the right and the left cusp of the astroid cross-section) decreases and tends to zero. To form the critical curve with this caustic, the source must cover all of the astroid cross-section.

An analytical study of the Einstein ring radius was made by Sereno and De Luca in 2006 and 2008 (Sereno & de Luca 2006, Sereno & de Luca 2008). Their analytical approximation is obtained in the WDL. In this regime, photons do not wind around the black hole which means $r_s >> R_S$ and the minimum distance between the photon and the lens r_{min_γ} must satisfy: $R_S << r_{min_\gamma}$. In this regime, the primary caustic is only shifted and keeps a symmetric shape. Because of the shift of the caustic, the critical curve is not centered on the black hole. In Sereno & de Luca 2008, the Einstein ring radius (or critical curve radius) equation is developed through a Taylor expansion of the light-like geodesics in $\varepsilon = \frac{\theta_E}{4D}$ where $D = \frac{r_s}{r_s + r_0}$ and θ_E is the Einstein ring radius. The equation presents in this paper is expressed in the equatorial plane. The radius of the Einstein ring is given by:

$$\Theta_E \simeq \theta_E \left\{ 1 + \frac{15\pi}{32}\varepsilon + \left[4\left(1 + D^2\right) - \frac{675\pi^2}{2048} \right] \varepsilon^2 + \frac{15\pi}{8}\varepsilon^3 \left[D + 4D^2 - \frac{9(272 - 25\pi^2)}{1024} - \frac{a^2}{8} \right] \right\}. \tag{2.4}$$

The left and the right radius of the critical curve are equal and depend on the spin in the third-order term in ε.

To validate GYOTO in the WDL, we estimate the Einstein ring radius with GYOTO and make a comparison with the formula (2.4). To reproduce the observational conditions of GRAVITY, we consider an observer at $r_0 = 8$ kpc from a black hole of mass M equal to $4.31 \times 10^6 M_\odot$. We also consider a source far enough from the black hole to be compliant with the domain of validity of this approximation. For each distance of the source, we estimate the error made on the Einstein ring radius. Since the goal of this paper is to determine if the accuracy of GYOTO is better than 1 μas, we only consider the maximum error of this parameter.

3 Results

3.1 Weak deflexion limit

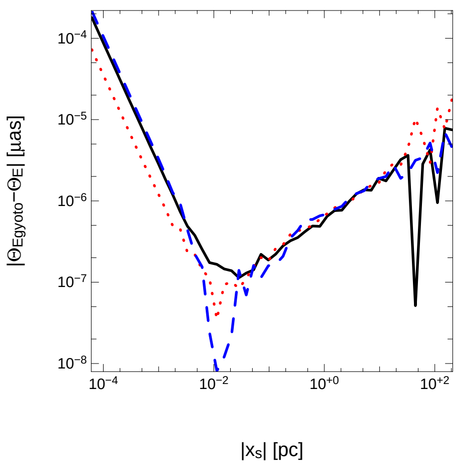

Fig. 2. Absolute difference between the analytical approximation Θ_E and Einstein ring radius measured with GYOTO. The types of line denote different values of the spin: 0.2 in solid, 0.5 in dotted and 0.9 in dashed.

On Fig.2 we present the absolute difference between the analytical approximation (2.4) and Einstein ring radius measured with GYOTO, obtained for three different spins. For all the range of the parameter, the differences are always extremely small ($\sim 10^{-2}\mu$m). On the plot two different regimes can be observed. For small x_s, the curve is marked by a smooth, power-law decrease: GYOTO and the numerical approximation agree better and better for larger and larger values of x_s. After reaching a minimum, the curve raises again, which a much more noisy appearance. This is due to the fact that, for small x_s, GYOTO is better than the analytical approximation. The difference between the two traces the order of the approximation. On the other hand, for large values of x_s, the approximation wins over GYOTO and the difference is dominated by the numerical error of GYOTO. The maximal errors of the parameter evaluated with GYOTO, and for each spin, are all smaller than $10^{-3}\mu$as. The ray-tracing code is very accurate, even for sources far behind the black hole (e.g. $\delta_{\Theta_{Egyoto}} = 1.6^{-4}\mu$as at 200 parsecs).

The requirement on accuracy ($\leq 1\mu$as) is largely met in the weak field regime. However, an equivalent test is necessary in the SDL regime.

3.2 Strong deflexion limit

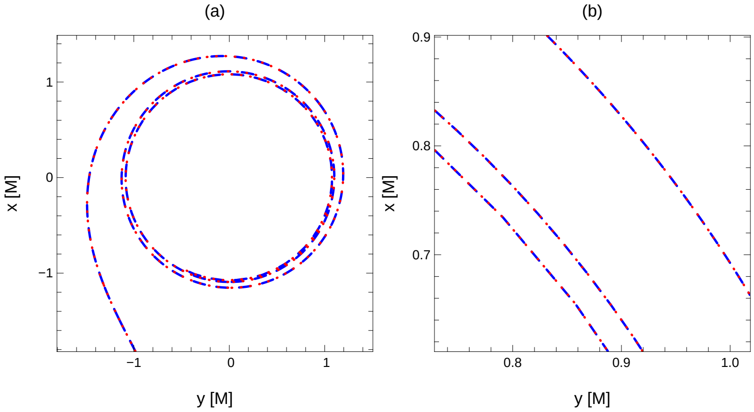

Fig. 3. Null geodesics computed with GYOTO (dotted) and Geokerr (dashed). We consider a spin of 0.998 and a photon launched from the center of the screen. (b) is a zoom of geodesics plotted on (a): δ_x and δ_y on (b) is about $4 \times 10^{-4}M$.

The aim of this subsection is to check if null geodesics computed with GYOTO in the SDL are accurate enough. To do so, we decided to compare photon trajectories computed with GYOTO with those computed with the ray-tracing code Geokerr. Contrary to GYOTO, Geokerr computes photon coordinates semi-analytically reducing the equations of motion expressed in the Hamiltonian formulation to Carlson elliptic integrals.

The comparison is made using the same observer coordinates and black hole parameters as before. We evaluate null geodesics for three different values of the spin (0, 0.5 and 0.998) and we consider photons launched from the center of the observer screen ($\alpha = \delta = 0$). We first compute the geodesics with Geokerr and get the dates of each point of the photon trajectory. Then, to get the null geodesics with GYOTO, we interpolate the positions of photons with our ray-tracing code considering these dates.

The difference between positions evaluated with GYOTO and those evaluated with Geokerr are smaller than $10^{-3}\mu$as for a spin equal to 0.2, 0.5 or 0.998. This shows a very good consistency between the two ray-tracing codes. Even for a photon which is not launched from the center of the screen (α =1.2 μpc), with $a = 0.998$, we find a very small error ($\sim 6 \times 10^{-4}M$). An example of computed null geodesics with both codes are shown on Fig.3.

4 Conclusions

The Galactic Center is a unique laboratory to observe stars close enough to a compact object to test General Relativity. Thanks to GRAVITY it will be possible to measure astrometric positions of stars orbiting Sgr A* with an expected astrometric precision of 10 μas. We have shown that GYOTO is extremely accurate even in complex configurations. For the purpose of the interpretation of the future astrometric positions observed by GRAVITY, GYOTO is accurate enough to model star trajectories and fit the GRAVITY data.

We want to thank Eric Gourgoulhon, Claire Somé, Jason Dexter and Stefan Gillessen for helpful discussions.

References

Bozza, V. 2008, Phys. Rev. D, 78, 063014
Bozza, V. & Mancini, L. 2012, ApJ, 753, 56
Dexter, J. & Agol, E. 2009, ApJ, 696, 1616
Eisenhauer, F., Perrin, G., Brandner, W., et al. 2011, The Messenger, 143, 16
Grandclément, P., Somé, C., & Gourgoulhon, E. 2014, Phys. Rev. D, 90, 024068
Merritt, D., Alexander, T., Mikkola, S., & Will, C. M. 2010, Phys. Rev. D, 81, 062002
Rauch, K. P. & Blandford, R. D. 1994, ApJ, 421, 46
Schneider, P., Ehlers, J., & Falco, E. E. 1992, Gravitational Lenses
Sereno, M. & de Luca, F. 2006, Phys. Rev. D, 74, 123009
Sereno, M. & de Luca, F. 2008, Phys. Rev. D, 78, 023008
Vincent, F. H., Paumard, T., Gourgoulhon, E., & Perrin, G. 2011, Classical and Quantum Gravity, 28, 225011
Will, C. M. 2008, ApJ, 674, L25

SF2A 2015
F. Martins, S. Boissier, V. Buat, L. Cambrésy and P. Petit (eds)

TESTS OF GRAVITATION WITH GAIA OBSERVATIONS OF SOLAR SYSTEM OBJECTS

A. Hees[1], D. Hestroffer[2], C. Le Poncin-Lafitte[3] and P. David[2]

Abstract. In this communication, we show how asteroids observations from the Gaia mission can be used to perform local tests of General Relativity (GR). This ESA mission, launched in December 2013, will observe –in addition to the stars– a large number of small Solar System Objects (SSOs) with unprecedented astrometric precision. Indeed, it is expected that about 360,000 asteroids will be observed with a nominal sub-mas precision.

Here, we show how these observations can be used to constrain some extensions to General Relativity. We present results of SSOs simulations that take into account the time sequences over 5 years and geometry of the observations that are particular to Gaia. We present a sensitivity study on various GR extensions and dynamical parameters including: the Sun quadrupolar moment J_2, the parametrized post-Newtonian parameter β, the Nordtvedt parameter η, the fifth force formalism, the Lense-Thirring effect, a temporal variation of the gravitational parameter $GM_\odot$ (a linear variation as well as a periodic variation), the Standard Model Extension formalism, ... Some implications for planetary ephemerides analysis are also briefly discussed.

Keywords: Gaia, asteroids, tests of gravitation, General Relativity

1 Introduction

This year marks the centenary of the publication of the classical theory of General Relativity (GR), the current paradigm to describe the gravitational interaction. Since its publication in 1915, GR has been confirmed by experimental observations. Although very successful so far, it is nowadays commonly admitted that GR is not the ultimate theory of gravitation. Attempts to develop a quantum theory of gravitation or to unify gravitation with the others fundamental interactions lead to deviation from GR. Moreover, observations requiring the introduction of Dark Matter and Dark Energy are sometimes interpreted as a hint that gravitation presents some deviations from GR at large scales.

GR is built upon two fundamental principles. The first principle is the Einstein Equivalence Principle (EEP) which gives to gravitation a geometric nature. More precisely, EEP implies that gravitation can be identified to space-time curvature which is mathematically described by a space-time metric $g_{\mu\nu}$. If the EEP postulates the existence of a metric, the second building of GR specifies the form of this metric. The metric tensor is determined by solving the Einstein field equations which can be derived from the Einstein-Hilbert action.

The EEP has been thoroughly tested (Will 2014, and references therein) by considering Universality of Free Fall experiments (Schlamminger et al. 2008; Adelberger et al. 2009; Williams et al. 2009; Müller et al. 2012), constancy of the constants of Nature (Uzan 2011; Rosenband et al. 2008; Guéna et al. 2012; Minazzoli & Hees 2014; Hees et al. 2014e), redshift experiments (Vessot et al. 1980; Delva et al. 2015), anisotropy in the velocity of light (Will 2014), ...

On the other hand, in the last 50 years, mainly two formalisms have been used to test the form of the metric: the parametrized post-Newtonian (PPN) formalism fully described in Will (1993) and the fifth force formalism described in Talmadge et al. (1988); Adelberger et al. (2009). The PPN formalism is making a nice interface

[1] Department of Mathematics, Rhodes University, Grahamstown 6140, South Africa. a.hees@ru.ac.za
[2] IMCCE, Observatoire de Paris - PSL Research University, UPMC Universités P06, Université Lille 1, CNRS, France
[3] SYRTE, Observatoire de Paris, PSL Research University, CNRS, Sorbonne Universités, UPMC Univ. Paris 06, LNE, 61 avenue de l'Observatoire, 75014 Paris, France

© Société Francaise d'Astronomie et d'Astrophysique (SF2A) 2015

between theoretical developments and observations by parametrizing deviations from GR at the level of the space-time metric by means of 10 dimensionless coefficients. The fifth force formalism considers a modification of the Newtonian potential of the form of a Yukawa potential. The parameters entering these formalisms have been severely constrained by diverse measurements (for a review, see Will 2014): spacecraft tracking (Bertotti et al. 2003; Konopliv et al. 2011), Lunar Laser Ranging (Williams et al. 2009; Müller et al. 2012), planetary ephemerides (Fienga et al. 2011; Pitjeva & Pitjev 2013; Verma et al. 2014; Fienga et al. 2015), Very Long Baseline Interferometry (Lambert & Le Poncin-Lafitte 2009), etc... Despite very stringent constraints, we have strong theoretical motivations to pursue these tests and to consider formalisms beyond the standard PPN and fifth force formalism (for some motivations, see for example Hees et al. 2012, 2014c,d).

Launched in December 2013, the ESA Gaia mission is scanning regularly the whole celestial sphere once every 6 months providing high precision astrometric data for a huge number ($\approx$ 1 billion) of celestial bodies. In addition to stars, it is also observing SSOs, in particular asteroids. One can estimate that about 360 000 asteroids will be regularly observed. The high precision astrometry (at sub-mas level) will allow us to perform competitive tests of gravitation and to provide new constraints on alternative theories of gravitation. These constraints will be complementary to the ones existing currently since relying on different bodies, on different type of observations and therefore sensitive to other systematics.

In this communication, we report the first results of a sensitivity study of Gaia SSOs observations to several modifications of the gravitation theory. Correlations between the different dynamical parameters (in particular with the Sun quadrupolar moment) are also assessed.

2 Simulations and parameters estimation

We have simulated the trajectories of asteroids using the standard post-Newtonian equations of motion in a heliocentric frame. The mutual interactions between the asteroids are neglected, the Sun oblateness parameter J_2 is considered and the perturbations from the different planets and the Moon are modelled by using INPOP10e ephemerides (Fienga et al. 2013). The initial conditions used for the simulations are provided by the ASTORB database* and a match between the asteroids trajectories with the Gaia scanning law is performed to find the observation times for each asteroid. Simultaneously with the equations of motion, we integrate the variational equations (for a detailed presentation of the method, see Hestroffer et al. (2010); Mouret & Mignard (2011); Mouret (2011)). The simulated asteroid trajectories are transformed into astrometric observables as well as their partial derivatives with respect to the parameters considered in the covariance analysis. The parameters considered here are twofolds: (i) local parameters specific to each asteroid (e.g. their 6 initial conditions) and (ii) global parameters that are common for all asteroids (the Sun J_2 and the parameters that characterize the gravitation theory). Our sensitivity study is performed by computing the covariance matrix to assess the correlations between the estimated parameters and the formal uncertainties reachable using Gaia observations. In this proceedings, the simulations performed include only 10,000 asteroids and the astrometric accuracy used is 0.2 mas. Full simulations of 360,000 asteroids with updated and better precision are ongoing and will be published in the future.

3 Sensitivity study to various global parameters

In all the following, we consider modifications of the gravitation theory that do not produce any important effects on the light propagation. Therefore, we concentrate on the orbital dynamics only and neglect any modification in the propagation of the light. Simulations using the Time Transfer Formalism (Teyssandier & Le Poncin-Lafitte 2008; Hees et al. 2012, 2014b,a) have been performed to ensure that the effects of the considered gravitation modifications on the light propagation can safely be neglected.

In the following subsections, we report a sensitivity study performed by a global inversion that includes the 6 initial conditions for each of the 10,000 asteroids, the Sun J_2 and the parameters characterizing the gravitation theory.

*see http://www.naic.edu/~nolan/astorb.html

3.1 Sun quadrupolar moment, PPN parameter and Nordtvedt effect

First of all, we consider the standard PPN parameter β (Will 1993, 2014). It is well known that this parameter is highly correlated with the Sun quadrupole moment J_2. Indeed, the secular advances of the perihelia produced by these two parameters are given by

$$\left\langle \frac{d\omega}{dt} \right\rangle = (2 + 2\gamma - \beta) n \frac{GM}{c^2 a(1-e^2)} + \frac{3}{2} n \frac{J_2 R_e^2}{a^2(1-e^2)^2}\,, \tag{3.1}$$

where ω is the argument of the perihelia, GM is the Sun gravitational parameter, c the speed of light, γ and β are the PPN parameters, J_2 the Sun quadrupole moment, R_e the Sun equatorial radius, a the semimajor axis of the orbit considered, e its eccentricity and $n = (GM/a^3)^{1/2}$ the mean motion. In this analysis, we use $\gamma = 1$ since this parameter is better determined by other types of observations like the Shapiro time delay (Bertotti et al. 2003) and by Gaia itself that will be able to constrain it at the level of 10^{-6} by observing light deflection (Mignard & Klioner 2010).

The fact that a large number of asteroids are considered with various different orbital parameters helps to decorrelate the two parameters. In this simulation, we obtain a sensitivity around $\sigma_{J_2} \sim 10^{-7}$ and $\sigma_\beta \sim 7\times10^{-4}$ with a correlation coefficient of 0.56 between the two parameters. These sensitivities are 1 order of magnitude lower than the ones obtained with planetary ephemerides (Pitjeva & Pitjev 2014; Verma et al. 2014; Fienga et al. 2015). The consideration of the complete set of asteroids (360,000 instead of 10,000) will improve slightly our current estimation. Planetary ephemerides will likely remain more powerful but Gaia will provide an independent and complementary estimation.

In addition to these two parameters, we also consider a violation of the Strong Equivalence Principle (SEP). Such a violation appears in all alternative theories of gravitation. One effect produced by a violation of the SEP is that the trajectories of self-gravitating bodies depend on their gravitational self energy Ω (violation of the universality of free fall). It is characterized by a difference between the gravitational and the inertial mass usually parametrized by the Nordtvedt parameter η

$$m_g = m_i + \eta \frac{\Omega}{c^2}\,, \tag{3.2}$$

where m_g is the gravitational mass and m_i is the inertial mass. Using the same modelling as in (Mouret 2011), the estimated uncertainty on η using simulations of 10,000 asteroids is 9×10^{-4}. This parameter does not change the estimations on the β and J_2 parameters and is not correlated to them. The only constraint available currently on η is provided by Lunar Laser Ranging measurements and is at the level of 4.5×10^{-4} (Williams et al. 2009).

Moreover, in the PPN framework, the η parameter is unambiguously related to the PPN parameters (Will 1993) by the relation

$$\eta = 4\beta - \gamma - 3\,. \tag{3.3}$$

Instead of estimating 3 independent parameters (J_2, β and η), one can introduce the last relation and estimate only two of them (J_2 and β). By doing so, the estimated uncertainty on J_2 and β becomes $\sigma_{J_2} \sim 9 \times 10^{-8}$ and $\sigma_\beta \sim 2\times10^{-4}$. Considering a violation of the SEP predicted by the PPN framework leads to an improvement in the estimation of the β PPN parameter. Moreover the correlation coefficient between β and J_2 drops from 0.56 to 0.18, which can be a considerable improvement. Similar conclusion holds for planetary ephemerides analysis and this gives a strong motivation to consider violation of the SEP with planetary ephemerides gravitation tests.

3.2 Lense-Thirring effect

The Lense-Thirring effect is a purely relativistic frame-dragging effect produced by the angular momentum of bodies. While the Lense-Thirring effect from the Earth has been detected with the LAGEOS satellite (Ciufolini & Pavlis 2004) (see nevertheless the controversy raised in Iorio et al. (2011)) and with the Gravity Probe B mission (Everitt et al. 2011). The Sun Lense-Thirring has never been directly detected so far. Such a direct measurement would provide a new way to estimate the Sun angular momentum, an important quantity to assess interior models of the Sun (Pijpers 2006). Possibilities to measure the Sun Lense-Thirring effect has been mentioned in (Iorio et al. 2011; Iorio 2011, 2012b,a). Nevertheless, as mentioned in (Folkner et al. 2014), planetary ephemerides analysis does not allow to disentangle the Sun Lense-Thirring from the Sun J_2 (even with the latest Messenger data). The two effects are completely correlated. This is partially due to the fact that all planets are orbiting in a very similar plane with a nearly circular orbit. Considering the asteroids can help since they provide a wide range of different orbital parameters especially including larger inclinations that may reduce this correlation. With the 10,000 asteroids considered in this study, the uncertainty on the Sun Lense-Thirring is a factor 5 larger than its actual value. This means that a direct detection of this effect with Gaia observations seems difficult. This conclusion should be reassessed by the consideration of the full set of asteroids. Moreover, the combination of the Gaia dataset with radar observations performed at UCLA (Margot & Giorgini 2010) may also improve this conclusion. Finally, it would be interesting to assess the gain that an analysis combining planetary ephemerides with Gaia observations would bring.

Nevertheless, even if a detection of the Sun Lense-Thirring seems to be unreachable, the fact to not include this effect in the modelling of the orbital dynamics produce biases in the estimation of the other parameters. Our simulations indicate that not including the Lense-Thirring in the equations of motion leads to a bias at the level of 10^{-8} on J_2 and at the level of 5×10^{-5} on the β PPN parameter. Similar conclusions seem to hold for planetary ephemerides, which is also mentioned by Iorio et al. (2011) and Folkner et al. (2014) for the J_2.

3.3 Fifth force formalism

The fifth force formalism consists in a Yukawa modification of the Newtonian potential (Talmadge et al. 1988; Adelberger et al. 2009). This Yukawa modification is parametrized by a range of interaction λ and by an intensity α. Constraints on these two parameters can be found for example in Fig. 31 of (Konopliv et al. 2011). At astronomical scales, the constraints are provided mainly by Lunar Laser Ranging and by ranging to Mars spacecraft. With simulation of 10,000 asteroids, we estimate the uncertainty on α for different fixed values of λ. At the level of $\lambda = 10^{10}$ m, the uncertainty on α is slightly larger than the one from ranging to Mars spacecraft while for $\lambda = 10^{11}$ m, our estimated uncertainty improves the current constraint by a factor 5. Therefore, this seems to be a very promising test. The correlation with the Sun mass needs nevertheless to be assessed (see the related discussion by Konopliv et al. (2011)).

3.4 Temporal variation of the gravitational constant

A lot of alternative theories of gravitation promotes the gravitation constant G to a dynamical field (typically to a scalar field). In this case, G becomes space-time dependant and can evolve for example with the cosmological evolution. Therefore, this class of models predicts a non-vanishing value of $\dot{G}$ in the Solar System. Our covariance study of the observations of 10,000 asteroids over 5 years indicates that Gaia will be able to constrain a linear evolution of the gravitational constant $\dot{G}/G$ at the level of 10^{-12} yr^{-1} (or more precisely $d \ln GM_\odot/dt$). The correlation with the Sun J_2 is very weak (see also (Mouret 2011)). The best current estimations on $\dot{G}/G$ are at the level of 10^{-13} yr^{-1} and are provided by planetary ephemerides (Konopliv et al. 2011; Fienga et al. 2015).

Moreover, very recently, it has been reported that the measurements of the gravitational constant G seem to undergo some periodic variations (Anderson et al. 2015) with a 5.9 years period. This analysis has been confirmed by Schlamminger et al. (2015) even if the conclusion has been weakened. We have performed a simulation including a periodic variation of G. This shows that asteroid observations from Gaia will be able to constrain the relative amplitude of the oscillations at the level of 10^{-10}. This accuracy is 5 orders of magnitude smaller than the amplitude predicted by Anderson et al. (2015); Schlamminger et al. (2015). No correlation is expected with the Sun J_2. This means that Gaia will be able to rule out such a temporal variation of G. Note that, as mentioned by Iorio (2015), the current planetary ephemerides analysis is also able to rule out this time variation with a similar accuracy.

3.5 Standard Model Extension formalism

The Standard Model Extension (SME) formalism has been developed to systematically describe violations of the Lorentz symmetry in all sectors of physics, including the gravitational sector. Consequences of SME on gravitational observations are developed into details in (Bailey & Kostelecký 2006; Kostelecký & Tasson 2011). In the linearized gravity approximation, the gravitational sector of the minimal SME is described by a space-time metric that depends on a symmetry trace-free tensor $\bar{s}^{\mu\nu}$. It can be shown that the orbital dynamics is insensitive to $\bar{s}^{TT}$ (Bailey & Kostelecký 2006) and therefore depends on 8 independent parameters: $\bar{s}^{XX} - \bar{s}^{YY}$, $\bar{s}^{XX} + \bar{s}^{YY} - 2\bar{s}^{ZZ}$, $\bar{s}^{XY}$, $\bar{s}^{XZ}$, $\bar{s}^{YZ}$, $\bar{s}^{TX}$, $\bar{s}^{TY}$ and $\bar{s}^{TZ}$. The heliocentric equations of motion can be found in (Bailey & Kostelecký 2006).

The covariance analysis performed by considering 10,000 asteroids leads to the estimated uncertainties presented in Table 1. These uncertainties are better than the current best estimations of the SME parameters available in the literature (Kostelecký & Russell 2011). In particular, they are better than the ones obtained with planetary ephemerides (Iorio 2012c; Hees et al. 2015). This is due to the variety of the asteroids orbital parameters while planetary ephemerides use only 8 planets with similar orbital parameters (same orbital planes and nearly circular orbits). Therefore, the estimation of the SME parameters with planetary ephemerides are degraded by these correlations (see the discussion in Hees et al. (2015)). Using our set of asteroids, the correlation matrix for the SME parameters is very reasonable: the three most important correlation coefficients are 0.71, -0.68 and 0.46. All the other correlations are below 0.3. Moreover, the Sun J_2 is not correlated to these parameters. Therefore, Gaia offers a unique opportunity to constrain Lorentz violation through the SME formalism. A combined analysis with planetary ephemerides analysis (Hees et al. 2015), Lunar Laser Ranging (Battat et al. 2007) and atom interferometry (Müller et al. 2008) would also be very interesting. Our analysis needs to be extended to include gravity-matter Lorentz violation parametrized by $(\bar{a})^\mu$ coefficients in the SME framework.

Table 1. Sensitivity on the SME gravity parameters.

SME parameters	Sensitivity (σ)
$\bar{s}^{XX} - \bar{s}^{YY}$	9×10^{-12}
$\bar{s}^{XX} + \bar{s}^{YY} - 2\bar{s}^{ZZ}$	2×10^{-11}
$\bar{s}^{XY}$	4×10^{-12}
$\bar{s}^{XZ}$	2×10^{-12}
$\bar{s}^{YZ}$	4×10^{-12}
$\bar{s}^{TX}$	1×10^{-8}
$\bar{s}^{TY}$	2×10^{-8}
$\bar{s}^{TZ}$	4×10^{-8}

4 Conclusion

In this communication, we have presented different possibilities to use asteroid observations from Gaia to perform different test of the gravitation theory. The estimation of the β PPN parameter and of a linear time dependance of the gravitational constant ($d \ln GM_\odot/dt$) would not be as good as the current estimations from planetary ephemerides. Nevertheless, the expected constraints are very complementary since they do not suffer from the same systematics errors.

Moreover, we have shown that the asteroid orbits are sensitive to a violation of the Strong Equivalence Principle through the η parameter. In the framework of the PPN formalism, this η parameter is related to the standard PPN parameters and this relation can help to reduce the correlation between the Sun J_2 and the PPN parameter β. Similar conclusion holds for planetary ephemerides analysis.

We have shown that the Sun Lense-Thirring effect is too weak to be detected with such dataset. Nevertheless, it would be interesting to see if a combination of the Gaia dataset with radar observations of ateroids (Margot & Giorgini 2010) or with planetary ephemerides can lead to a first dynamical detection of the Sun angular momentum through the Lense-Thirring. Nevertheless, we have shown that not including the Sun Lense-Thirring in the equations of motion leads to a bias in the estimation of the Sun J_2 and of the β PPN parameter. Similar conclusions hold for planetary ephemerides analysis.

The asteroid trajectories are also sensitive to a fifth force and can be used to improve constraints in this formalism.

Finally, the number of asteroids and the variety of their orbital parameters provide a unique opportunity to constrain Lorentz violation through the Standard Model Extension formalism. The wide orbital parameters allows to decorrelate the SME parameters and will allow us to produce the best estimations on the SME parameters.

Extended simulations considering the full set of asteroids (360,000 asteroids instead of 10,000 considered in this analysis) with refined astrometric precision (instead of 0.2 mas) and possible mission extension (6 years) are currently on-going. We are also currently assessing the improvement provided by combining the Gaia dataset with radar observations (Margot & Giorgini 2010) that are complementary in the time frame and orthogonal to astrometric telescopic observations.

A.H. thanks the GRAM for financial support to attend this meeting and acknowledges support from “Fonds Spécial de Recherche” through a FSR-UCL grant and from a GREAT-ESF exchange grant. A.H. thanks Q. G. Bailey for interesting discussions about SME and L. Iorio for his interesting comments. C.L.P.L. thanks GRAM and GPHYS from Paris Observatory for financial support.

References

Adelberger, E. G., Gundlach, J. H., Heckel, B. R., Hoedl, S., & Schlamminger, S. 2009, Progress in Particle and Nuclear Physics, 62, 102

Anderson, J. D., Schubert, G., Trimble, V., & Feldman, M. R. 2015, EPL (Europhysics Letters), 110, 10002

Bailey, Q. G. & Kostelecký, V. A. 2006, Phys. Rev. D, 74, 045001

Battat, J. B. R., Chandler, J. F., & Stubbs, C. W. 2007, Physical Review Letters, 99, 241103

Bertotti, B., Iess, L., & Tortora, P. 2003, Nature, 425, 374

Ciufolini, I. & Pavlis, E. C. 2004, Nature, 431, 958

Delva, P., Hees, A., Bertone, S., Richard, E., & Wolf, P. 2015, ArXiv e-prints [arXiv] 1508.06159

Everitt, C. W. F., Debra, D. B., Parkinson, B. W., et al. 2011, Physical Review Letters, 106, 221101

Fienga, A., Laskar, J., Exertier, P., Manche, H., & Gastineau, M. 2015, Celestial Mechanics and Dynamical Astronomy, 123, 325

Fienga, A., Laskar, J., Kuchynka, P., et al. 2011, Celestial Mechanics and Dynamical Astronomy, 111, 363

Fienga, A., Manche, H., Laskar, J., Gastineau, M., & Verma, A. 2013, ArXiv e-prints [arXiv] 1301.1510

Folkner, W. M., Williams, J. G., Boggs, D. H., Park, R., & Kuchynka, P. 2014, IPN Progress Report, 42

Guéna, J., Abgrall, M., Rovera, D., et al. 2012, Physical Review Letters, 109, 080801

Hees, A., Bailey, Q. G., Le Poncin-Lafitte, C., et al. 2015, Phys. Rev. D, 92, 064049

Hees, A., Bertone, S., & Le Poncin-Lafitte, C. 2014a, Phys. Rev. D, 90, 084020

Hees, A., Bertone, S., & Le Poncin-Lafitte, C. 2014b, Phys. Rev. D, 89, 064045

Hees, A., Folkner, W. M., Jacobson, R. A., et al. 2014c, in Proceedings of the Journées 2013 ”Systèmes de Référence Spatio-Temporels”, ed. N. Capitaine, Observatoire de Paris (Observatoire de Paris), 241

Hees, A., Folkner, W. M., Jacobson, R. A., & Park, R. S. 2014d, Phys. Rev. D, 89, 102002

Hees, A., Lamine, B., Reynaud, S., et al. 2012, Classical and Quantum Gravity, 29, 235027

Hees, A., Minazzoli, O., & Larena, J. 2014e, Phys. Rev. D, 90, 124064

Hestroffer, D., Mouret, S., Mignard, F., Tanga, P., & Berthier, J. 2010, in IAU Symposium, Vol. 261, IAU Symposium, ed. S. A. Klioner, P. K. Seidelmann, & M. H. Soffel, 325–330

Iorio, L. 2011, Advances in Space Research, 48, 1403

Iorio, L. 2012a, Sol. Phys., 281, 815

Iorio, L. 2012b, General Relativity and Gravitation, 44, 719

Iorio, L. 2012c, Classical and Quantum Gravity, 29, 175007

Iorio, L. 2015, ArXiv e-prints [arXiv] 1504.07233

Iorio, L., Lichtenegger, H. I. M., Ruggiero, M. L., & Corda, C. 2011, Ap&SS, 331, 351

Konopliv, A. S., Asmar, S. W., Folkner, W. M., et al. 2011, Icarus, 211, 401

Kostelecký, V. A. & Russell, N. 2011, Reviews of Modern Physics, 83, 11

Kostelecký, V. A. & Tasson, J. D. 2011, Phys. Rev. D, 83, 016013

Lambert, S. B. & Le Poncin-Lafitte, C. 2009, A&A, 499, 331

Margot, J.-L. & Giorgini, J. D. 2010, in IAU Symposium, Vol. 261, IAU Symposium, ed. S. A. Klioner, P. K. Seidelmann, & M. H. Soffel, 183–188

Mignard, F. & Klioner, S. A. 2010, in IAU Symposium, Vol. 261, IAU Symposium, ed. S. A. Klioner, P. K. Seidelmann, & M. H. Soffel, 306–314

Minazzoli, O. & Hees, A. 2014, Phys. Rev. D, 90, 023017

Mouret, S. 2011, Phys. Rev. D, 84, 122001

Mouret, S. & Mignard, F. 2011, MNRAS, 413, 741

Müller, H., Chiow, S.-W., Herrmann, S., Chu, S., & Chung, K.-Y. 2008, Physical Review Letters, 100, 031101

Müller, J., Hofmann, F., & Biskupek, L. 2012, Classical and Quantum Gravity, 29, 184006

Pijpers, F. P. 2006, Methods in helio- and asteroseismology (Imperial College Press)

Pitjeva, E. V. & Pitjev, N. P. 2013, MNRAS, 432, 3431

Pitjeva, E. V. & Pitjev, N. P. 2014, Celestial Mechanics and Dynamical Astronomy, 119, 237

Rosenband, T., Hume, D. B., Schmidt, P. O., et al. 2008, Science, 319, 1808

Schlamminger, S., Choi, K.-Y., Wagner, T. A., Gundlach, J. H., & Adelberger, E. G. 2008, Physical Review Letters, 100, 041101

Schlamminger, S., Gundlach, J. H., & Newman, R. D. 2015, Phys. Rev. D, 91, 121101

Talmadge, C., Berthias, J.-P., Hellings, R. W., & Standish, E. M. 1988, Physical Review Letters, 61, 1159

Teyssandier, P. & Le Poncin-Lafitte, C. 2008, CQG, 25, 145020

Uzan, J.-P. 2011, Living Reviews in Relativity, 14, 2

Verma, A. K., Fienga, A., Laskar, J., Manche, H., & Gastineau, M. 2014, A&A, 561, A115

Vessot, R. F. C., Levine, M. W., Mattison, E. M., et al. 1980, Physical Review Letters, 45, 2081

Will, C. M. 1993, Theory and Experiment in Gravitational Physics, ed. Will, C. M.

Will, C. M. 2014, Living Reviews in Relativity, 17, 4

Williams, J. G., Turyshev, S. G., & Boggs, D. H. 2009, International Journal of Modern Physics D, 18, 1129

SF2A 2015
F. Martins, S. Boissier, V. Buat, L. Cambrésy and P. Petit (eds)

THE TIME TRANSFER FUNCTIONS: AN EFFICIENT TOOL TO COMPUTE RANGE, DOPPLER AND ASTROMETRIC OBSERVABLES

A. Hees[1], S. Bertone[2,3], C. Le Poncin-Lafitte[2] and P. Teyssandier[2]

Abstract. Determining range, Doppler and astrometric observables is of crucial interest for modelling and analyzing space observations. We recall how these observables can be computed when the travel time of a light ray is known as a function of the positions of the emitter and the receiver for a given instant of reception (or emission). For a long time, such a function–called a reception (or emission) time transfer function–has been almost exclusively calculated by integrating the null geodesic equations describing the light rays. However, other methods avoiding such an integration have been considerably developped in the last twelve years. We give a survey of the analytical results obtained with these new methods up to the third order in the gravitational constant G for a mass monopole. We briefly discuss the case of quasi-conjunctions, where higher-order enhanced terms must be taken into account for correctly calculating the effects. We summarize the results obtained at the first order in G when the multipole structure and the motion of an axisymmetric body is taken into account. We present some applications to on-going or future missions like Gaia and Juno. We give a short review of the recent works devoted to the numerical estimates of the time transfer functions and their derivatives.

Keywords: subject, verb, noun, apostrophe

1 Observables computed from the Time Transfer Functions

Many observations in the Solar System rest on the measurement of the travel time of light rays. Modelling the light propagation requires a mathematical tool defined as follows. Assume that space-time is covered by a single system of coordinates $x^0 = ct, \boldsymbol{x} = (x^i)$, where $i = 1, 2, 3$. Consider a light ray emitted at time t_A at a point of spatial coordinates $\boldsymbol{x}_A$ and received at time t_B at a point of spatial coordinates $\boldsymbol{x}_B$. Here, light rays are null geodesic paths (light propagating in a vacuum). The light travel time $t_B - t_A$ may be regarded as a function of the variables $\boldsymbol{x}_A, t_B, \boldsymbol{x}_B$, so that one can write

$$t_B - t_A = \mathcal{T}_r(\boldsymbol{x}_A, t_B, \boldsymbol{x}_B). \tag{1.1}$$

$\mathcal{T}_r$ may be called the "(reception) time transfer function" (TTF)*. As we shall see below, the interest of this function is not confined to the range experiments: knowing $\mathcal{T}_r$ is sufficient for modelling observations based on the Doppler-tracking or the gravitational bending of light (astrometry).

1.1 Radioscience observables

Suppose that the above-mentioned signal is exchanged between two observers $\mathcal{O}_A$ and $\mathcal{O}_B$. The range observable can directly be computed from the TTF as it is defined as the difference of proper time between the reception and emission of the signal

$$R(\tau_B) = c(\tau_B - \tau_A) = c(\tau_B - \tau_A(t_A = t_B - \mathcal{T})). \tag{1.2}$$

[1] Department of Mathematics, Rhodes University, Grahamstown 6140, South Africa
[2] Observatoire de Paris, SYRTE, CNRS/UMR 8630, LNE, UPMC, 61 avenue de l'Observatoire, F-75014 Paris, France
[3] currently at Astronomical Institute, University of Bern

*In this communication, we generally omit the term "reception" for the sake of brevity. Note that similar results can be derived from the "(emission) time transfer function" $\mathcal{T}_e$ defined by $t_B - t_A = \mathcal{T}_e(t_A, \boldsymbol{x}_A, \boldsymbol{x}_B)$.

© Société Francaise d'Astronomie et d'Astrophysique (SF2A) 2015

Let ν_A and ν_B be the frequencies of the signal as measured at $(ct_A, \boldsymbol{x}_A)$ by $\mathcal{O}_A$ and at $(ct_B, \boldsymbol{x}_B)$ by $\mathcal{O}_B$, respectively. The ratio ν_B/ν_A is given by (see, e.g., (see, e.g., Teyssandier et al. 2008, and Refs. therein)

$$\frac{\nu_B}{\nu_A} = \frac{[(g_{00} + 2g_{0i}\beta^i + g_{ij}\beta^i\beta^j)^{1/2}]_{x_A}}{[(g_{00} + 2g_{0i}\beta^i + g_{ij}\beta^i\beta^j)^{1/2}]_{x_B}} \frac{(k_0)_{x_B}}{(k_0)_{x_A}} \frac{1 + (\beta^i \widehat{k}_i)_{x_B}}{1 + (\beta^i \widehat{k}_i)_{x_A}}, \tag{1.3}$$

where the quantities $g_{\alpha\beta}$ are the components of the metric, $\beta^i_{x_A} = [dx^i_A/cdt]_{t_A}$ and $\beta^i_{x_B} = [dx^i_B/cdt]_{t_B}$ are the coordinate velocities divided by c of $\mathcal{O}_A$ at time t_A and $\mathcal{O}_B$ at time t_B, respectively. The quantities $\widehat{k}_i$ are defined by $\widehat{k}_i = k_i/k_0$, where the k_α are the covariant components of the vector k^μ tangent to the light ray described by affine parametric equations. One has (Le Poncin-Lafitte et al. 2004)

$$\left(\widehat{k}_i\right)_A = c\frac{\partial \mathcal{T}_r}{\partial x^i_A}, \qquad \left(\widehat{k}_i\right)_B = -c\frac{\partial \mathcal{T}_r}{\partial x^i_B}\left[1 - \frac{\partial \mathcal{T}_r}{\partial t_B}\right]^{-1}, \qquad \frac{(k_0)_B}{(k_0)_A} = 1 - \frac{\partial \mathcal{T}_r}{\partial t_B}. \tag{1.4}$$

Substituting these relations in (1.3) yields ν_B/ν_A in terms of the derivatives of the TTF as follows

$$\frac{\nu_B}{\nu_A} = \frac{[(g_{00} + 2g_{0i}\beta^i + g_{ij}\beta^i\beta^j)^{1/2}]_{x_A}}{[(g_{00} + 2g_{0i}\beta^i + g_{ij}\beta^i\beta^j)^{1/2}]_{x_B}} \frac{1 - \frac{\partial \mathcal{T}_r}{\partial t_B} - c\beta^i_{x_B}\frac{\partial \mathcal{T}_r}{\partial x^i_B}}{1 + c\beta^i_{x_A}\frac{\partial \mathcal{T}_r}{\partial x^i_A}}, \tag{1.5}$$

a formula which can also be inferred without using (1.3), as it is shown in Hees et al. (2012).

1.2 Astrometric observables

Let $\{\lambda_{\underline{\alpha}}, \underline{\alpha} = 0, 1, 2, 3\}$ be an orthonormal comoving tetrad attached to $\mathcal{O}_B$ ($\lambda_{\underline{0}}$ coincides with the unit 4-velocity vector of $\mathcal{O}_B$). The direction of the light ray as measured by $\mathcal{O}_B$ is defined by a unit vector proportional to the orthogonal projection of k^μ on the rest frame of $\mathcal{O}_B$ at x_B. The spatial components $n^{\underline{i}}$ of this vector in the basis $\{\lambda_{\underline{i}}\}$ is given by (see, e.g. Brumberg 1991)

$$n^{\underline{i}} = -\left(\frac{\lambda^0_{\underline{i}} + \lambda^j_{\underline{i}}\widehat{k}_j}{\lambda^0_{\underline{0}} + \lambda^j_{\underline{0}}\widehat{k}_j}\right)_{x_B}, \tag{1.6}$$

where $\lambda^\mu_{\underline{\alpha}}$ denote the components of the 4-vector $\lambda_{\underline{\alpha}}$ in the natural basis associated to the coordinates (x^μ). It follows from (1.4) that each $n^{\underline{i}}$ can be expressed in terms of the derivatives of the TTF.

An analogous conclusion can be drawn for the angular separation ϕ between two point-like sources S and S' as measured by $\mathcal{O}_B$ at x_B. Indeed, one has (Teyssandier & Le Poncin-Lafitte 2006)

$$\sin^2\frac{\phi}{2} = -\frac{1}{4}\left[\frac{\left(g_{00} + 2g_{0k}\beta^k + g_{kl}\beta^k\beta^l\right) g^{ij}(\widehat{k}_i - \widehat{k}'_i)(\widehat{k}_j - \widehat{k}'_j)}{(1 + \beta^m\widehat{k}_m)(1 + \beta^l\widehat{k}'_l)}\right]_B, \tag{1.7}$$

where the quantities $\widehat{k}_i$ and $\widehat{k}'_i$ are related to the light rays arriving from S and S', respectively.

2 A survey of the method proposed to compute the TTFs

Two approaches exist to determine the light propagation in metric theories of gravity. The most widespread method consists in solving the null geodesic equations. Analytical solutions have been developed within the first post-Newtonian (1pN) or first post-Minkowksian (1pM) approximation dealing with static monopoles (Shapiro 1964), static mass multipole moments (Kopeikin 1997), moving monopoles (Kopeikin & Schäfer 1999; Klioner 2003b), moving multipole moments (Kopeikin & Makarov 2007),... After the pioneering papers by Richter & Matzner (1983) and Brumberg (1987), an analytical solution has been derived within the 2pM approximation for a static monopole, with a metric containing three arbitrary post-Newtonian parameters (Klioner & Zschocke 2010). Finally, the gravitational deflection of the image of a star when observed at a finite distance from a static monopole has been obtained up to the 2pM order in Ashby & Bertotti (2010). On the other hand, a numerical treatment based on a shooting method has been proposed in San Miguel (2007).

The other approach enables to determine the TTFs without integrating the null geodesic equations. Initially grounded on Synge's world function (see John (1975) for the Schwarzschild space-time, and then Linet & Teyssandier (2002), Le Poncin-Lafitte et al. (2004) for much more general cases), this approach is now based on the direct determination of the TTFs (Teyssandier & Le Poncin-Lafitte 2008).

3 Post-Minkowskian expansion of the TTF

We assume that the metric may be expanded in a series in powers of the gravitational constant G:

$$g_{\mu\nu}(x,G) = \eta_{\mu\nu} + \sum_{n=1}^{\infty} g_{\mu\nu}^{(n)}(x,G), \tag{3.1}$$

where $\eta_{\mu\nu} = \mathrm{diag}\,\{1,-1,-1,-1\}$ is the Minkowski metric and $g_{\mu\nu}^{(n)}(x,G)$ stands for the term of order G^n. Then, it may be supposed that $\mathcal{T}_r$ is represented by an asymptotic expansion in a series in powers of G:

$$\mathcal{T}_r(\boldsymbol{x}_A, t_B, \boldsymbol{x}_B) = \frac{R_{AB}}{c} + \sum_{n=1}^{\infty} \mathcal{T}_r^{(n)}(\boldsymbol{x}_A, t_B, \boldsymbol{x}_B), \tag{3.2}$$

where $R_{AB} = |\boldsymbol{x}_B - \boldsymbol{x}_A|$ and $\mathcal{T}_r^{(n)}$ stands for the perturbation term of order G^n. It is shown in Teyssandier & Le Poncin-Lafitte (2008) that each $\mathcal{T}_r^{(n)}$ can be expressed by an iterative procedure as a line integral whose the integrand involves only the terms $g_{\mu\nu}^{(k)}$ and $\mathcal{T}_r^{(l)}$ such that $k \leq n-1$, $l \leq n-1$, with an integration taken along the straight line passing through x_B defined by

$$x^\alpha = z^\alpha(\lambda), \quad z^0(\lambda) = x_B^0 - \lambda R_{AB}, \quad z^i(\lambda) = x_B^i - \lambda(x_B^i - x_A^i), \quad 0 \leq \lambda \leq 1. \tag{3.3}$$

So, computing the TTFs never requires the knowledge of the real null geodesics followed by the photons.

4 Application to static, spherically symmetric space-times

The procedure outlined in section 3 allows the determination of the TTF and the direction of light propagation in a static spherically symmetric space-time at any order in G (Teyssandier 2014). This determination can also be obtained by an iterative solution of an integro-differential equation derived from the null geodesic equations (Linet & Teyssandier 2013). Denoting by M the mass of the central body and assuming the metric to be a generalization of the Schwarzschild ds^2 written in the form

$$ds^2 = \left(1 - \frac{2m}{r} + 2\beta\frac{m^2}{r^2} - \frac{3}{2}\beta_3\frac{m^3}{r^3} + \cdots\right)(dx^0)^2 - \left(1 + 2\gamma\frac{m}{r} + \frac{3}{2}\epsilon\frac{m^2}{r^2} + \frac{1}{2}\gamma_3\frac{m^3}{r^3} + \cdots\right)d\boldsymbol{x}^2, \tag{4.1}$$

where $r = |\boldsymbol{x}|$, $m = GM/c^2$ and the coefficients $\beta, \beta_3, \gamma, \epsilon, \gamma_3$, are post-Newtonian parameters equal to 1 in general relativity, the two methods lead to expressions† as follow for the first three terms in Eq. (3.2):

$$\mathcal{T}^{(1)}(\boldsymbol{x}_A, \boldsymbol{x}_B) = \frac{(1+\gamma)m}{c}\ln\left(\frac{r_A + r_B + R_{AB}}{r_A + r_B - R_{AB}}\right), \tag{4.2}$$

$$\mathcal{T}^{(2)}(\boldsymbol{x}_A, \boldsymbol{x}_B) = \frac{m^2}{r_A r_B}\frac{R_{AB}}{c}\left[\kappa\frac{\arccos \boldsymbol{n}_A.\boldsymbol{n}_B}{|\boldsymbol{n}_A \times \boldsymbol{n}_B|} - \frac{(1+\gamma)^2}{1 + \boldsymbol{n}_A.\boldsymbol{n}_B}\right], \tag{4.3}$$

$$\mathcal{T}^{(3)}(\boldsymbol{x}_A, \boldsymbol{x}_B) = \frac{m^3}{r_A r_B}\left(\frac{1}{r_A} + \frac{1}{r_B}\right)\frac{R_{AB}}{c(1 + \boldsymbol{n}_A.\boldsymbol{n}_B)}\left[\kappa_3 - (1+\gamma)\kappa\frac{\arccos \boldsymbol{n}_A.\boldsymbol{n}_B}{|\boldsymbol{n}_A \times \boldsymbol{n}_B|} + \frac{(1+\gamma)^3}{1 + \boldsymbol{n}_A.\boldsymbol{n}_B}\right], \tag{4.4}$$

where $\boldsymbol{n}_A = \boldsymbol{x}_A/r_A$, $\boldsymbol{n}_B = \boldsymbol{x}_B/r_B$ and $\kappa = 2(1+\gamma) - \beta + 3/4\varepsilon$, $\kappa_3 = 2\kappa - 2\beta(1+\gamma) + (3\beta_3 + \gamma_3)/4$.

Equation (4.2) is equivalent to the well-kown formula due to Shapiro and (4.3) recovers the expression already obtained in Teyssandier & Le Poncin-Lafitte (2008), and then in Klioner & Zschocke (2010). On the other hand, (4.4) is a recent result and shows the fecondity of the new procedures.

It follows from Eqs. (4.2)-(4.4) that at least for $n \leq 3$, an enhancement of the contribution proportional to $(1+\gamma)^n$ appears in configurations of quasi-conjunction, i.e. when the unit 3-vectors $\boldsymbol{n}_A$ and $\boldsymbol{n}_B$ are almost opposite $(1 + \boldsymbol{n}_A.\boldsymbol{n}_B \sim 0)$. A result inferred in Ashby & Bertotti (2010) by an 'asymptotic reasoning' is thus rigorously confirmed. The 2pM enhanced term in (4.3) will be required for analyzing data in future missions like for example BepiColombo (Iess et al. 2009), as it may be seen on Figs. 2 and 3 in Hees et al. (2014b). The

†Note that owing to the static character of the metric, $\mathcal{T}_r$ does not depend on t_B. So we may remove the index r.

3pM enhanced contribution from the Sun may reach 30 ps for a light ray grazing the Sun (see Table 1 in Linet & Teyssandier 2013). Taking this contribution into account will therefore be necessary for modelling space mission proposals like ODYSSEY (Christophe et al. 2009), LATOR (Turyshev 2009) or ASTROD (Braxmaier et al. 2012), designed to measure the 1pN parameter γ at the level of 10^{-7}-10^{-8}.

The light deflection has been calculated and discussed within the 2pM approximation in Klioner & Zschocke (2010), Ashby & Bertotti (2010) and Teyssandier (2012). The enhanced 2pM term, proportional to $(1+\gamma)^2$, can reach 16 microarcsecond (μas) for a ray grazing Jupiter (see right of Fig. 2) and is therefore required in the analysis of Gaia data (see, e.g., de Bruijne 2012). In Linet & Teyssandier (2013) and Hees et al. (2014b), it is noted that for a ray grazing the Sun, the 2pM and 3pM enhanced contributions amount to 3 milliarcsecond (mas) and 12 μas, respectively. The last value is to be compared with the 2pM contribution due to the 2pN parameter κ, as illustrated on the left of Fig. 2.

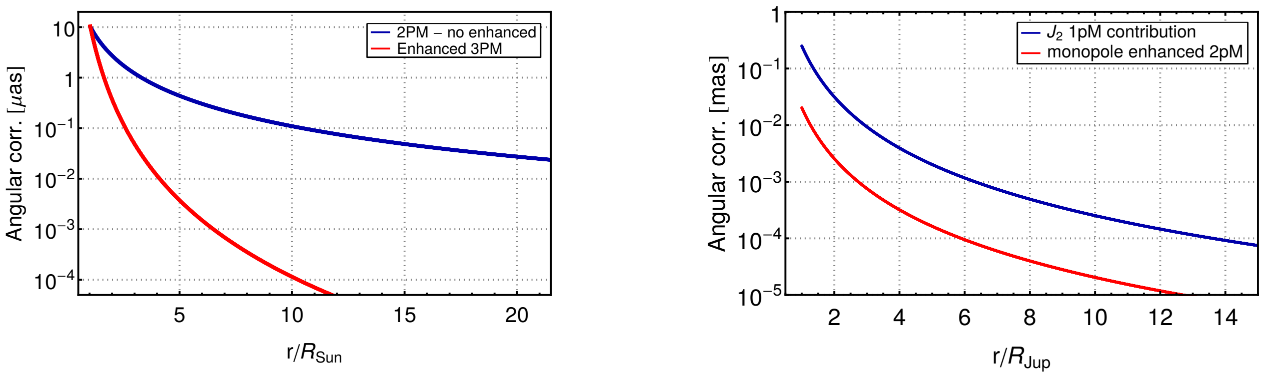

Fig. 1. Left: Contribution of the 2pM term proportional to κ and the 3pM enhanced term on the light deflection for a Sun grazing ray. – Right: Contribution of Jupiter J_2 at 1pM order and contribution of the enhanced 2pM Jupiter monopole term on the deflection of a Jupiter grazing light ray.

5 Effects due to the asphericity and/or the motion of bodies

The gravitational potential of an axisymmetric body is parametrized amongst others by its mass multipole moments J_n. Using a property previously established in Kopeikin (1997) and recovered later (see Teyssandier et al. 2008, and Refs. therein), explicit formulas for the contributions of each J_n to the TTF and its first derivatives have been given in Le Poncin-Lafitte & Teyssandier (2008). Thus, it becomes possible to calculate the influence of any J_n on the gravitational light deflection. These results generalize the expressions previously obtained in various papers for $n = 1$ and $n = 2$ (see, e.g, Klioner 2003a; Kopeikin & Makarov 2007, and Refs. therein). Recall that the Jupiter J_2 must be taken into account in the analysis of Gaia (see Crosta & Mignard 2006, and references therein) or VLBI observations (see the right of Fig. 1) since it produces a deflection amounting to 240 μas for a grazing light ray. A similar conclusion holds for the Juno mission (see Anderson et al. (2004)) since it is shown in Hees et al. (2014a) that the influence of the quadrupole moment of Jupiter reaches the level of the cm for the range and the level of 10 μm/s for the Doppler (see left of Fig. 2). Some of these effects will be relevant in the data reduction since the expected accuracies for Juno are of 10 cm on the range and 1 μm/s on the Doppler.

The procedure outlined in section 3 noticeably facilitates the determination of the TTF of a uniformly moving axisymmetric body within the 1pM approximation. Denote by $\tilde{\mathcal{T}}_r^{(1)}$ the 1pM TTF corresponding to the body at rest. When this body is uniformly moving with a coordinate velocity $\boldsymbol{v} = c\boldsymbol{\beta}$, it is shown in Hees et al. (2014a) that the 1pM TTF can be written as

$$\mathcal{T}_r^{(1)}(\boldsymbol{x}_A, t_B, \boldsymbol{x}_B) = \Gamma(1 - \boldsymbol{N}_{AB}.\boldsymbol{\beta})\tilde{\mathcal{T}}_r^{(1)}(\boldsymbol{R}_A + \Gamma R_{AB}\boldsymbol{\beta}, \boldsymbol{R}_B) \, , \tag{5.1}$$

where $\Gamma = (1-\beta^2)^{-1/2}$ is the Lorentz factor and

$$\boldsymbol{R}_X = \boldsymbol{x}_X - \boldsymbol{x}_p(t_0) + \frac{\Gamma^2}{1+\Gamma}\boldsymbol{\beta}\left[\boldsymbol{\beta}.(\boldsymbol{x}_X - \boldsymbol{x}_p(t_0))\right] - \Gamma\boldsymbol{v}(t_B - t_0) \, , \tag{5.2}$$

with $\boldsymbol{x}_p(t_0)$ being the position of the deflecting body at an arbitrary time t_0 usually chosen between $t_B - R_{AB}/c$ and t_B. This recent and general result is particularly simple. The first derivatives of the right-hand side of (5.1) are easily calculated. For a moving monopole, using Eq. (4.2) for $\tilde{\mathcal{T}}_r^{(1)}$ and Eq. (5.1) gives

$$\mathcal{T}_r^{(1)}(\boldsymbol{x}_A, t_B, \boldsymbol{x}_B) = (1+\gamma)m\Gamma(1-\boldsymbol{\beta}.\boldsymbol{N}_{AB}) \ln \frac{|\boldsymbol{R}_A + \Gamma R_{AB}\boldsymbol{\beta}| + R_B + \Gamma R_{AB}(1-\boldsymbol{\beta}.\boldsymbol{N}_{AB})}{|\boldsymbol{R}_A + \Gamma R_{AB}\boldsymbol{\beta}| + R_B - \Gamma R_{AB}(1-\boldsymbol{\beta}.\boldsymbol{N}_{AB})}. \tag{5.3}$$

This formula recovers the expression obtained in Kopeikin & Schäfer (1999) and Klioner (2003a) using longer calculations. A low velocity expansion of this result is obtained in Bertone et al. (2014). To finish, let us mention that using a similar method but a symmetric trace free (STF) decomposition of the gravitational potential, Soffel & Han (2014) have also determined the expression of the TTF produced by a moving body with arbitrary static multipoles, but their result is only valid in the slow velocity approximation.

In Hees et al. (2014a), these results are applied in the context of the Juno mission to discuss the effects of the mass and the quadrupole moment of Jupiter when the motion of this planet is taken into account. The effect of the motion of Jupiter's monopole is represented on the right of Fig. 2. This contribution is smaller than the expected Juno Doppler accuracy and can safely be ignored in the reduction of the observations. Nevertheless, it is important to point out that this numerical estimate depends highly on the geometry of the probe orbit and should be reassessed in the context of other space missions. In particular, this contribution depends on the quantity $\boldsymbol{\beta}.\boldsymbol{N}_{AB}$ and on the presence of conjunctions (which is not the case for Juno owing its polar orbit, but will be the case in other missions). The deflection of light produced by the motion of Jupiter monopole is of the order of 0.04 μas for a grazing light ray and can safely be ignored for current observations.

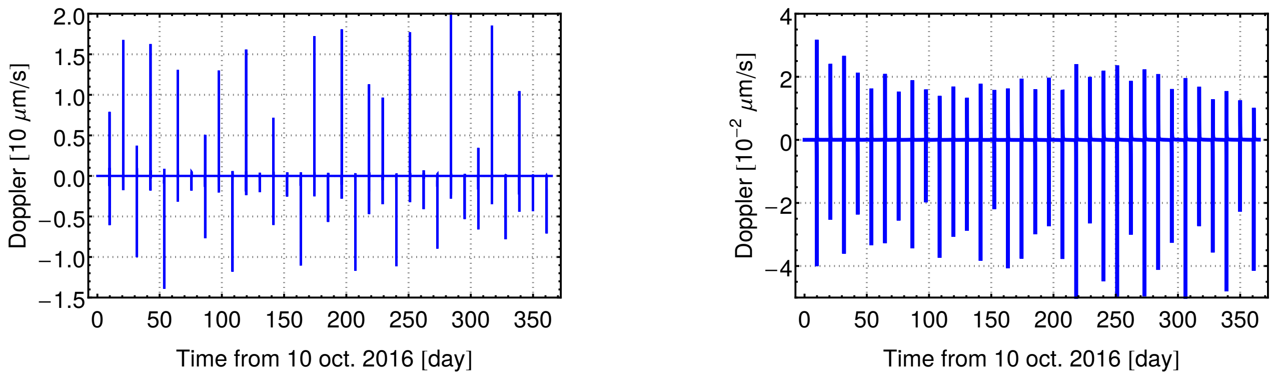

Fig. 2. Left: Effect of Jupiter J_2 on a Doppler link between Juno and Earth. Right: Effect of Jupiter's velocity on a Doppler link between Juno and Earth.

6 Numerical determination of the TTFs and their derivatives

The TTF formalism lends itself well to the numerical simulations of the light propagation in curved space-time. This is useful when no analytical expressions can be found or when systematic comparisons of the propagation of light in different space-times are discussed. This approach is fully developed within the 2pM approximation in Hees et al. (2014b). The iterative procedure mentioned in Sect. 3 gives

$$\mathcal{T}_r^{(1)} = \int_0^1 n\left[z^\alpha(\lambda); g_{\alpha\beta}^{(1)}, R_{AB}\right] d\lambda, \tag{6.1}$$

$$\frac{\partial \mathcal{T}_r^{(1)}}{\partial x^i_{A/B}} = \int_0^1 n_{A/B}\left[z^\alpha(\lambda); g_{\alpha\beta}^{(1)}, g_{\alpha\beta,\sigma}^{(1)}, \boldsymbol{x}_A, \boldsymbol{x}_B\right] d\lambda, \tag{6.2}$$

for $\mathcal{T}_r^{(1)}$ and its first derivatives, and then

$$\mathcal{T}_r^{(2)} = \int_0^1 \int_0^1 l\left[z^\alpha(\mu\lambda); g_{\alpha\beta}^{(2)}, g_{\alpha\beta}^{(1)}, g_{\alpha\beta,\sigma}^{(1)}, \boldsymbol{x}_A, \boldsymbol{x}_B\right] d\mu\, d\lambda\,, \tag{6.3}$$

$$\frac{\partial \mathcal{T}_r^{(2)}}{\partial x^i_{A/B}} = \int_0^1 \int_0^1 l_{A/B} \left[z^\alpha(\mu\lambda); g^{(2)}_{\alpha\beta}, g^{(2)}_{\alpha\beta,\sigma}, g^{(1)}_{\alpha\beta}, g^{(1)}_{\alpha\beta,\sigma}, g^{(1)}_{\alpha\beta,\sigma\delta}, \boldsymbol{x}_A, \boldsymbol{x}_B \right] d\mu\, d\lambda \,, \tag{6.4}$$

for $\mathcal{T}_r^{(2)}$ and its first derivatives, where the functions n, n_A, n_B, l, l_A and l_B can be explicitly written (see Hees et al. 2014b). All the integrations are taken over the straight line defined by Eqs. (3.3).

This kind of procedure avoids the numerical integration of the full set of geodesic equations, which is unnecessarily time consuming since we are only concerned by a single 'time function'. It has been successfully applied to simulate range, Doppler and astrometric observations within some alternative theories of gravity in order to find signatures differing from the predictions of general relativity (see Hees et al. 2012, 2014c, 2015), and more recently to compute the propagation of light in the field of arbitrarily moving monopoles, when no analytical solution is available (Hees et al. 2014a).

7 Conclusion

This survey shows that the TTF formalism is a powerful tool for computing the range, Doppler and astrometric (VLBI) observables involved in Solar System experiments. The iterative method summarized in section 3 is very effective in deriving analytical and numerical solutions. The simplicity of this method relies mainly on the fact that one never has to determine the real trajectory of the photon in order to perform an explicit calculation of the TTF. We have reviewed some of the analytical expressions derived using this formalism. This method has been successfully applied to determine the light propagation in a static spherically symmetric space-time up to the 3pM order and a generic procedure enabling to compute higher order terms has been developed. It has also been applied to determine the influence of the motion and asphericity of bodies on the light propagation. The result is obtained by simple calculations. We have assessed the influence of different terms in the observation of space missions like Gaia or Juno. Finally, the TTF formalism turns out to be very well adapted to the numerical simulations of the effects observable in the Solar System.

A.H. thanks the GRAM for financial support to attend this meeting and acknowledges support from “Fonds Spécial de Recherche” through a FSR-UCL grant.

References

Anderson, J. D., Lau, E. L., Schubert, G., & Palguta, J. L. 2004, in Bulletin of the American Astronomical Society, Vol. 36, AAS/Division for Planetary Sciences Meeting Abstracts #36, 1094

Ashby, N. & Bertotti, B. 2010, Classical and Quantum Gravity, 27, 145013

Bertone, S., Minazzoli, O., Crosta, M., et al. 2014, Classical and Quantum Gravity, 31, 015021

Braxmaier, C., Dittus, H., Foulon, B., et al. 2012, Experimental Astronomy, 34, 181

Brumberg, V. A. 1987, Kinematika i Fizika Nebesnykh Tel, 3, 8

Brumberg, V. A. 1991, Essential relativistic celestial mechanics, ed. Brumberg, V. A. (Adam Hilger)

Christophe, B., Andersen, P. H., Anderson, J. D., et al. 2009, Experimental Astronomy, 23, 529

Crosta, M. T. & Mignard, F. 2006, Classical and Quantum Gravity, 23, 4853

de Bruijne, J. H. J. 2012, Ap&SS, 341, 31

Hees, A., Bailey, Q. G., Le Poncin-Lafitte, C., et al. 2015, Phys. Rev. D, 92, 064049

Hees, A., Bertone, S., & Le Poncin-Lafitte, C. 2014a, Phys. Rev. D, 90, 084020

Hees, A., Bertone, S., & Le Poncin-Lafitte, C. 2014b, Phys. Rev. D, 89, 064045

Hees, A., Folkner, W. M., Jacobson, R. A., & Park, R. S. 2014c, Phys. Rev. D, 89, 102002

Hees, A., Lamine, B., Reynaud, S., et al. 2012, Classical and Quantum Gravity, 29, 235027

Iess, L., Asmar, S., & Tortora, P. 2009, Acta Astronautica, 65, 666

John, R. W. 1975, Exp. Tech. Phys., 23, 127

Klioner, S. A. 2003a, AJ, 125, 1580

Klioner, S. A. 2003b, Astron. Astrophys., 404, 783

Klioner, S. A. & Zschocke, S. 2010, Classical and Quantum Gravity, 27, 075015

Kopeikin, S. M. 1997, Journal of Mathematical Physics, 38, 2587

Kopeikin, S. M. & Makarov, V. V. 2007, Phys. Rev. D, 75, 062002

Kopeikin, S. M. & Schäfer, G. 1999, Phys. Rev. D, 60, 124002

Le Poncin-Lafitte, C., Linet, B., & Teyssandier, P. 2004, CQG, 21, 4463

Le Poncin-Lafitte, C. & Teyssandier, P. 2008, Phys. Rev. D, 77, 044029

Linet, B. & Teyssandier, P. 2002, Phys. Rev. D, 66, 024045

Linet, B. & Teyssandier, P. 2013, Classical and Quantum Gravity, 30, 175008

Richter, G. W. & Matzner, R. A. 1983, Phys. Rev. D, 28, 3007

San Miguel, A. 2007, General Relativity and Gravitation, 39, 2025

Shapiro, I. I. 1964, Physical Review Letters, 13, 789

Soffel, M. H. & Han, W.-B. 2014, ArXiv e-prints [arXiv] 1409.3743

Teyssandier, P. 2012, Classical and Quantum Gravity, 29, 245010

Teyssandier, P. 2014, in De Gruyter Studies in Mathematical Physics 22, Vol. 2, Frontiers in Relativistic Celestial Mechanics, ed. S. M. Kopeikin (De Gruyter)

Teyssandier, P. & Le Poncin-Lafitte, C. 2006, ArXiv General Relativity and Quantum Cosmology e-prints arXiv:gr-qc/0611078

Teyssandier, P. & Le Poncin-Lafitte, C. 2008, CQG, 25, 145020

Teyssandier, P., Le Poncin-Lafitte, C., & Linet, B. 2008, in Astrophysics and Space Science Library, Vol. 349, Lasers, Clocks and Drag-Free Control: Exploration of Relativistic Gravity in Space, ed. H. Dittus, C. Lammerzahl, & S. G. Turyshev, 153

Turyshev, S. G. 2009, Astronomy Letters, 35, 215

SF2A 2015
F. Martins, S. Boissier, V. Buat, L. Cambrésy and P. Petit (eds)

THE SAGITTARIUS TIDAL STREAM AS A GRAVITATIONNAL EXPERIMENT IN THE MILKY WAY

G. F. Thomas[1], B. Famaey[1], R. Ibata[1], F. Lüghausen[2] and P. Kroupa[2]

Abstract. Modified Newtonian Dynamics (MOND or Milgromian dynamics) gives a successful description of many galaxy properties that are hard to understand in the classical framework. The rotation curves of spiral galaxies are, for instance, perfectly reproduced and understood within this framework. Nevertheless, rotation curves only trace the potential in the galactic plane, and it is thus useful to test the shape of the potential outside the plane. Here we use the Sagittarius tidal stream as a gravitational experiment in the Milky Way, in order to check whether MOND can explain both its characteristics and those of the remnant dwarf spheroidal galaxy progenitor. We show that a MOND model of the Sagittarius stream can both perfectly reproduce the observed positions of stars in the stream, and even more strikingly, perfectly reproduce the observed properties of the remnant. Nevertheless, this first model does not reproduce well the observed radial velocities, which could be a signature of a rotating component in the progenitor or of the presence of a massive hot gaseous halo around the Milky Way.

Keywords: Modified gravity, Sagittarius, galaxy, stream

1 Introduction

Some discrepancies appear at galactic scales between the observations and the predictions from ΛCDM simulations. Indeed, in rotationally supported galaxies the asymptotic velocity is related to the baryonic mass via the baryonic Tully-Fisher, which has intrinsically negligible scatter (McGaugh 2012), the shape of rotation curves in dark matter dominated galaxies is not correlated with V_{max} but rather with the baryonic surface density (Famaey & McGaugh 2012; Oman et al. 2015), and many observations indicate that dynamical friction is not as efficient as expected in ΛCDM (Kroupa 2015). Galaxy merger simulations such as those of the Antenna galaxies can produce long tidal tails as observed only if DM halos are truncated to almost one-tenth of the actual virial radius.

These problems disappear if we consider that gravity is effectively modified on galaxy scales as proposed by Milgrom (1983), a paradigm known as Modified Newtonian Dynamics (MOND) where the gravitational law is effectively modified in the weak acceleration regime, typically when the acceleration falls under a_0, a new constant with the dimension of acceleration (of order 10^{-10} m.s^{-2}). However it is currently impossible to explain the observations at the cosmological scales without adding some sort of DM, or at least a new degree of freedom behaving as a collisionless dust fluid on these scales.

In galaxies, the shape of the rotation curve gives us information about the potential only in the galactic plane, and the best tracers of the potential outside this plane are the tidal streams. They are the consequences of the stripping of satellites galaxies while they orbit the host galaxy. The most studied of them is the Sagittarius Stream in our own Milky Way galaxy (Ibata et al. 1994). The presence of a remnant progenitor dwarf spheroidal galaxy (Sgr dSph) for this stream is the source of a lot of information about the initial conditions of this satellite and on the potential. This stream has been heavily studied through N-body simulations (Law et al. 2005; Law & Majewski 2010) or by various analytical models, mostly ignoring dynamical friction, by, e.g., spraying particles at Lagrange points at different time steps (Varghese et al. 2011; Küpper et al. 2012). However, a full study of

[1] Observatoire astronomique de Strasbourg, Université de Strasbourg, CNRS, UMR 7550, 11 rue de l'Université, F-67000 Strasbourg, France
[2] Helmholtz-Institut für Strahlen-und Kernphysik, Universität Bonn, Nussallee 14-16, D-53115 Bonn, Germany

© Société Francaise d'Astronomie et d'Astrophysique (SF2A) 2015

streams in a modified gravity framework is still lacking. The only study dates back to Read & Moore (2005) who concluded that the orbit of a single point mass was very similar to that of a point mass in a spherical DM halo.

In Sec.2 we present a brief overview of how we modelled the initial satellite galaxy and the MW in MOND. The results of our simulations are developed in Sec.3 and our conclusions and perspectives are treated in Sec.4.

2 Constructing the model

2.1 The QuMOND formulation

The classical Newtonian action for a set of particles generated by the matter density distribution ρ generating the Newtonian potential Φ_N is given by :

$$S_N = S_{kin} + S_{in} + S_{grav} = \int \frac{\rho \mathbf{v}^2}{2} d^3x\, dt - \int \rho \Phi_N d^3x\, dt - \int \frac{|\nabla \Phi_N|^2}{8\pi G} d^3x\, dt \tag{2.1}$$

The equations of motion and the Poisson equation result through the variation of this action w.r.t. the coordinates or to the potential itself.

Proposed by Milgrom (2010), QuMOND is a non-relativistic formulation of the MONDian paradigm where the matter action is unmodified but where the gravitational action (the third term of equation 2.1) is generalized by introducing an auxiliary acceleration field (Milgrom 2010; Famaey & McGaugh 2012). Finally the MONDian potential Φ can be computed by the MONDian Poisson equation :

$$\nabla^2 \Phi = 4\pi G(\rho_b + \rho_{ph}) \tag{2.2}$$

where ρ_b is the baryonic matter density that generates the Newtonian potential Φ_N with the classical Newtonian Poisson equation $\rho_b = (\nabla^2 \Phi_N)/(4\pi G)$ and ρ_{ph} is the phantom dark matter (PDM) density. The PDM is an effective matter density and can be seen as a mathematical ansatz that is useful for interpreting MOND in the dark matter language. This density results directly from the baryonic density :

$$\rho_{ph} = \nabla \left[\tilde{\nu} \left(\frac{|\nabla \Phi_N|}{a_0} \right) \nabla \Phi_N \right] \tag{2.3}$$

$\tilde{\nu}(y)$ is the interpolation ν-function and $\tilde{\nu}(y) \to 0$ when $y \gg 1$ (Newtonian regime) and $\tilde{\nu}(y) \to y^{-1/2} - 1$ when $y \ll 1$ (Deep MOND regime) that gives the variation of the potential beside the Newtonian potential over the acceleration. In our work we use 3 different ν-functions :

- the simple ν-function defined by Famaey & Binney (2005) : $\tilde{\nu}(y) = \frac{1+(1+4y^{-1})^{1/2}}{2} - 1$
- the standard ν-function : $\tilde{\nu}(y) = \left[\frac{1+(1+4y^{-2})^{1/2}}{2}\right]^{1/2} - 1$
- the exponential ν-function : $\tilde{\nu}(y) = (1 - e^{-y^2})^{-1/4} + (1 - \frac{1}{4})e^{-y^2} - 1$

With this formulation it is very easy to determine the potential by solving twice the Poisson equation and once the equation 2.3. In this way, all grid-based N-body methods can be adapted to do MONDian simulations. We use hereafter the AMR code Phantom-Of-Ramses (POR) developed by Lüghausen et al. (2014) based on the code Ramses (Guillet & Teyssier 2011).

2.2 Modelling the Milky Way

We assume that the purely baryonic Milky Way is well modelled by the first model of Dehnen & Binney (1998) without the dark halo component. This model features a double exponential stellar disk of $3.52 \times 10^{10} M\odot$ to fit the thin and the thick component with a scale length of 2 kpc and the two scales heights of 0.3 and 1 kpc, respectively. The bulge and the interstellar medium components have respectively a mass of $0.518 \times 10^{10} M\odot$ and $1.69 \times 10^{10} M\odot$.

The host galaxy has a direct importance on the internal dynamic of the dwarf accreted galaxy. Indeed, MOND is a non-linear theory which breaks the strong equivalence principle (SEP), this means that the external field effect (EFE), produced by the host galaxy, affects the internal dynamics of the dwarf. The EFE effectively truncates the satellite's PDM halo therewith making it more susceptible to disruption.

2.3 Modelling the Sagittarius galaxy

The Sagittarius galaxy is a dSph whose observed density is well modelled by a King profile (see Binney & Tremaine 2008). To be self-consistent in MONDian dynamics, we used a MONDified King model where the density $\rho_{b,\,King}$ can be calculated by the Eq.2.4 with ψ being the MONDian binding potential.

$$\rho_{b,\,King} \propto e^{\psi/\sigma} erf\left(\frac{\sqrt{\psi}}{\sigma}\right) - \sqrt{\frac{4\psi}{\pi\sigma^2}}\left(1 + \frac{2\psi}{3\sigma^2}\right) \tag{2.4}$$

The MONDian binding potential ψ is determined by the Newtonian binding potential ψ_N and the density by Eq.2.5, since a King profile has spherical symmetry.

$$\begin{aligned} \nabla^2\psi_N &= -4\,\pi\,G\,\rho_{b,\,King} \\ \nabla\psi &= \nu\left(\tfrac{\nabla\psi_N}{a_0}\right)\nabla\psi_N \end{aligned} \tag{2.5}$$

We then integrate Eq.2.4 inside-out to get a stable King profile in MOND. The velocities are drawn from the corresponding phase-space distribution function, using the MOND potential to determine the energy.

We assume that the current position and velocity of the remnant of the Sgr dSph is the same as in Law & Majewski (2010) : $(l,\,b) = (5.6, -14.2)$ (Majewski et al. 2003), at a distance of 28 kpc (McConnachie 2012), a radial velocity of $v_{rad} = 171$ km.s^{-1} and an apparent proper motion of $(\mu_l\ \cos b,\, \mu_b) = (-2.16,\, 1.73)$ mas. yr^{-1}. The initial position is determined by launching the galaxy backward for about 4 Gyr.

3 Results

We want the features of the remnant at the end of the simulations to be similar to those observed. Our best initial model which can match the current observation is a King sphere with a mass $M_{b,\,0Gyr} = 5.8.10^7$ M$_\odot$ and a half-light radius $r_h = 0.41$kpc which gives after 4 Gyr a baryonic mass of $M_{b,\,4Gyr} \sim 2.5.10^7$ M$_\odot$, a half light radius $r_{h,\,4Gyr} = 0.6$ kpc and a velocity dispersion $\sigma_{rad,\,4Gyr} = 11$ km/s in agreement with the observation of Majewski et al. (2003) (here after called M03).

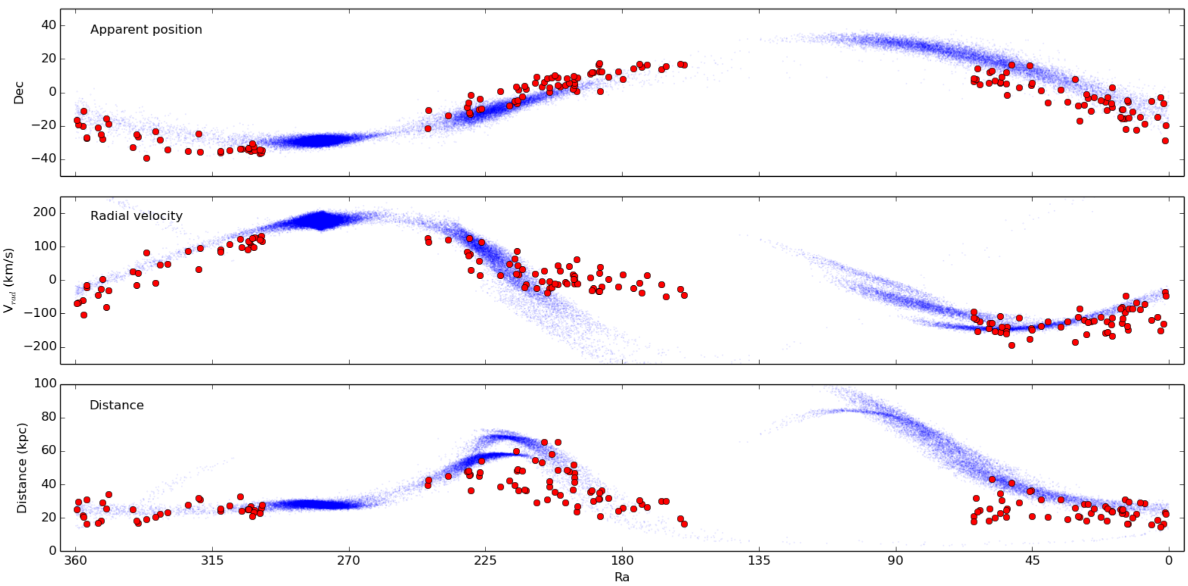

Fig. 1. Apparent position, radial velocity and distances of the stellar particles of our simulation in blue and stars from M03 in red.

On Figure 1, the apparent position of the particles of our simulation fits well the observed positions of the stars from the Sagittarius stream selected by M03. However, the amplitude of the radial velocity between RA=160-240 is more pronounced in the simulations than in the observations.

4 Conclusions and perspectives

We showed that a MOND model of the Sagittarius stream can both perfectly reproduce the observed positions of stars in the stream, and even more strikingly, perfectly reproduce the observed properties of the remnant. Nevertheless, this first model shows interesting deviations from the observed radial velocities between RA=160-240.

This behaviour of the radial velocities could actually be the signature of a rotating progenitor with $V_{flat} \simeq 33$ km.s^{-1}. Indeed, the angular momentum of a rotating dwarf spiral galaxy decreases during the accretion by the loss of stars, thus can produce a dSph remnant after 4 Gyr. Since the remnant is not rotating, the rotating material must either be in a disk, or MOND gravity must have a slow-down effect on the rotation.

A lack of baryonic matter can also explain the radial velocity in our simulation. Indeed, assuming a universal baryon fraction of 0.165 (Komatsu et al. 2011), the predicted baryonic mass of the MW is of $1.65 - 3.3 \times 10^{11}$ $M_{\odot}$, well above the observed baryonic mass ($\sim 0.6 \times 10^{10} M_{\odot}$). This lack of matter could be explain by a hot gaseous halo (T$\sim 10^6$ K) with a mass of about 10^{11} $M_{\odot}$, which could be non-spherically symmetric, and needs to be included in our future works.

References

Binney, J. & Tremaine, S. 2008, Galactic Dynamics, 2nd edn. (Princeton University Press), 920
Dehnen, W. & Binney, J. 1998, MNRAS, 294, 429
Famaey, B. & Binney, J. 2005, MNRAS, 363, 603
Famaey, B. & McGaugh, S. S. 2012, Living Reviews in Relativity, 15, 10
Guillet, T. & Teyssier, R. 2011, Journal of Computational Physics, 230, 4756
Ibata, R. A., Gilmore, G., & Irwin, M. J. 1994, Nature, 370, 194
Komatsu, E., Smith, K. M., Dunkley, J., et al. 2011, ApJS, 192, 18
Kroupa, P. 2015, Canadian Journal of Physics, 93, 169
Küpper, A. H. W., Lane, R. R., & Heggie, D. C. 2012, MNRAS, 420, 2700
Law, D. R., Johnston, K. V., & Majewski, S. R. 2005, ApJ, 619, 807
Law, D. R. & Majewski, S. R. 2010, ApJ, 714, 229
Lüghausen, F., Famaey, B., & Kroupa, P. 2014, ArXiv e-prints [arXiv] 1405.5963
Majewski, S. R., Skrutskie, M. F., Weinberg, M. D., & Ostheimer, J. C. 2003, ApJ, 599, 1082
McConnachie, A. W. 2012, AJ, 144, 4
McGaugh, S. S. 2012, AJ, 143, 40
Milgrom, M. 1983, ApJ, 270, 365
Milgrom, M. 2010, MNRAS, 403, 886
Oman, K. A., Navarro, J. F., Fattahi, A., et al. 2015, ArXiv e-prints [arXiv] 1504.01437
Read, J. I. & Moore, B. 2005, MNRAS, 361, 971
Varghese, A., Ibata, R., & Lewis, G. F. 2011, MNRAS, 417, 198

Session 04

Atelier du PNHE

SF2A 2015
F. Martins, S. Boissier, V. Buat, L. Cambrésy and P. Petit (eds)

PROPERTIES OF OPTICALLY THICK CORONAE AROUND ACCRETING BLACK HOLES

R. Belmont[1, 2], A. Różańska[3], J. Malzac[1,2], B. Czerny[4] and P.-O. Petrucci[5, 6]

Abstract. Accreting black holes are complex sources exhibiting several spectral components (disc, jet, hot corona etc). The exact nature and the interplay between these components is still uncertain, and constraining the accretion flow in the vicinity of the compact object has become a key problem to understand the general physics of accretion and ejection.

In the past years, the X-ray spectra of several X-ray binaries and AGN have suggested the existence of a new type of coronae in the inner part of their accretion disk. These coronae are warm (about 1 keV) and have Thomson optical depths of about $\tau \approx 10$, much larger than the standard comptonizing medium inferred in black hole systems. However, simple radiative models based on the diffusion approximation are unable to sustain a large temperature over such high optical depths, therefore questioning existence of these thick coronae.

Here we investigate the radiative and hydrostatic properties of slabs, thick coronae covering a standard accretion disc. A precise modelling of the radiation transfer shows that the observed temperature inversion can be reproduced, provided that most of the accretion power is dissipated in this upper layer and that the medium is strongly magnetised.

Keywords: Radiative transfer, Scattering, Methods: analytical, Accretion, accretion disks

1 Introduction

The X-ray spectrum of accreting black holes is usually modelled with several components. The softer component is a multi-temperature blackbody originating from the accretion disk. The inner disk temperature is about 10 eV in AGN and 1 keV in X-ray binaires. At higher energy, the spectrum is often modelled with a comptonisation component resulting from the up-scattering of cold disc photons in a hot corona located in the innermost parts of the accreting system. The coronal temperature and optical depth are similar in AGN and X-ray binaries in their low-hard state, namely $k_BT \sim 100$ keV and $\tau \sim 1$ respectively.

These two components, with the addition of reflection features, are able to reproduce many observations of accreting black holes. However, many sources have shown an excess in the intermediate band. In X-ray binaires, this excess is seen in the $2 - 10$ keV band when the sources are in the *very high state*. Although this component can also been explained by a complex structure of the accretion disk (i.e. different from a standard disc, Shakura & Sunyaev 1973), or a contribution from the jet, it has been proposed that it results from comptonisation in a warm ($k_BT \sim 1$ keV) and optically thick ($\tau \sim 3 - 10$) corona covering the inner accretion disc (e.g. Zhang et al. 2000). The issue is most common in AGN, where the so-called *soft excess* is observed below 2 keV. Here also, several explanations have been proposed, as blurred, ionised reflection (Fabian et al. 2004; Crummy et al. 2006), smeared absorption by an outflowing medium (Gierliński & Done 2006; Schurch et al. 2009). However comptonisation in a warm and optically thick corona sucessfuly allows to reproduce the broad band spectrum of many sources, such as NGC5548 (Magdziarz et al. 1998), PG1211+143 (Janiuk et al.

[1] Université de Toulouse, UPS-OMP, IRAP, Toulouse, France
[2] CNRS; IRAP; 9 Av. colonel Roche, BP44346, F-31028 Toulouse cedex 4, France
[3] Copernicus Astronomical Center, Bartycka 18, 00-716 Warsaw, Poland
[4] Center for Theoretical Physics, Al. Lotników 32/46, 02-680 Warsaw, Poland
[5] Université de Grenoble Alpes, IPAG, F-38000 Grenoble, France
[6] CNRS, IPAG, F-38000 Grenoble, France

© Société Francaise d'Astronomie et d'Astrophysique (SF2A) 2015

2001), Mrk 359 (Czerny et al. 2003), RE1034+396 (Done et al. 2012), Mrk 509 (Petrucci et al. 2013), and many others (Jin et al. 2012). The temperature is similar to that in X-ray binaires ($k_B T \sim 1$ keV), the optical depth is always much larger than unity ($\tau \sim 10-20$), and the covering factor is large, suggesting a slab, sandwich-like geometry.

Hot atmospheres are common in astrophysical sources (e.g. in the sun) and can be expected from several processes (e.g. enhanced dissipation, external illumination). However such hot upper layers are commonly thought to remain optically thin. This simple result is based on two facts:

- First, in a plane-symmetric, sandwich geometry, radiation can only escape from the upper layers, so that the radiation flux is directed upward, away from the disk-atmosphere boundary.
- Second, when a medium is optically thick ($\tau >> 1$), radiation cannot escape freely. It is trapped and only diffuses slowly out of the medium. Moreover, the local spectrum at some altitude is a blackbody with the local temperature. In this diffusion approximation, the local radiation energy density and the local flux scale as $U_{\mathrm{rad}} \propto T^4$ and $F_{\mathrm{rad}} \propto -T^3 dT/dz$ respectively, where z is the altitude measured from the disc mid plane.

Therefore, the temperature can only decrease with altitude from the disc-atmosphere boundary, in contradiction with observations of a warm and thick upper layers.

Here is a summary of a recent work we have done on this problem (Rozanska et al. 2015). We show that the diffusion is not valid with the inferred properties of warm and thick coronae, and we perform a more precise analysis of radiation transfer in such layers. We fist derive the properties of the radiation field by solving the radiation transfer equation (section 2). Then, we derive the temperature profile by solving the energy equation (section 3). And last, we compute the hydrostatic structure of the corona. Conclusions follow in the last section.

2 Radiation profile

The diffusion approximation is valid for optically thick media. When both scattering and absorption are involved, it means that the *effective* optical depth $\tau_* \approx \sqrt{\tau_a(\tau_a+\tau_s)} >> 1$ is much larger than unity (where τ_a and τ_s are the absorption and scattering optical depth respectively). Here, comptonisation models of the X-ray excess lead to *Thomson* optical depths as large as $\tau_s \approx 10-20$. However, as the inferred temperature is also large, the absorption optical depth (dominated by bremmstrahlung absorption) is small, and the effective optical depth remains moderate. The diffusion approximation therefore does not hold and the radiation transfer equation must be solved.

In the following, we define τ the Thomson optical depth as measured downwards, from the atmosphere surface. We consider an atmosphere of total, Thomson optical depth τ_c. For seek of simplicity, we assume a uniform dissipation per unit optical depth and solid angle: Q. The total power dissipated in the atmosphere is $F_c = 4\pi Q \tau_c$. The atmosphere covers a standard disk with vertically integrated dissipation F_d. The coronal dissipation is parametrised by the ratio

$$\chi = F_c/F_{\mathrm{tot}} \tag{2.1}$$

where $F_{\mathrm{tot}} = F_c + F_d$ is the total dissipation. The slab, grey (frequency integrated) radiation transfer equation for specific intensity I then reads: $-\cos\theta dI/d\tau = J - I + Q$, where J is the angle-averaged intensity and angle θ is measured from the vertical direction. It can be solved by computing its first moments and using a closure relation. The first moment gives an equation on the flux: $-dF/d\tau = 4\pi Q$. With the boundary condition at the base $F(\tau_c) = F_d$, the solution is: $F/F_{\mathrm{tot}} = 1 - \chi\tau/\tau_c$. The flux increases upwards because of local dissipation. The second moment gives an equation on the radiation pressure: $cdP_{\mathrm{rad}}/d\tau = F$, where c is the speed of light. Using the Eddington approximation ($U_{\mathrm{rad}} = 3P_{\mathrm{rad}}$), and assuming no incoming flux at the atmosphere surface leads to the upper boundary condition $P_{\mathrm{rad}}(0) = 2F_{\mathrm{tot}}/(3c)$, which gives the solution:

$$cP_{\mathrm{rad}}/F_{\mathrm{tot}} = 2/3 + \tau - \chi\tau^2/(2\tau_c) \tag{2.2}$$

As expected, the radiation pressure decreases with altitude since radiation can only escape from the top.

3 Temperarure profile

As the effective optical depth is not expected to be larger than unity, the temperature does not scale as $T \propto U_{\mathrm{rad}}^{1/4}$. Rather it is computed by assuming that Compton up-scattering is the dominant cooling mechanism:

Model number	β_m	F_{Edd}/F_{tot}	χ	τ_c	kT_{av} (keV)
1	0	1	0.98	5.21	3.91
2	50	1	0.98	19.9	0.42
3	50	6	0.98	8.76	1.68
4	50	1	0.4	15.9	0.23
5	50	3	0.4	7.08	0.88
6	50	1	0.02	9.28	2.68 $\times 10^{-2}$

Table 1. Properties of models shown in other figures.

$Q = Q_c = 4c(U_{\rm rad}/4\pi)(k_B T/m_e c^2)$, where m_e is the electron mass. This gives:

$$\frac{k_B T}{m_e c^2} = \frac{\chi}{12\tau_c}\left(\frac{2}{3} + \tau - \frac{\chi}{2}\frac{\tau^2}{\tau_c}\right)^{-1} \tag{3.1}$$

Examples of temperatures profiles are shown in Fig. 1 (left) for various values of τ_c and χ. As the radiation

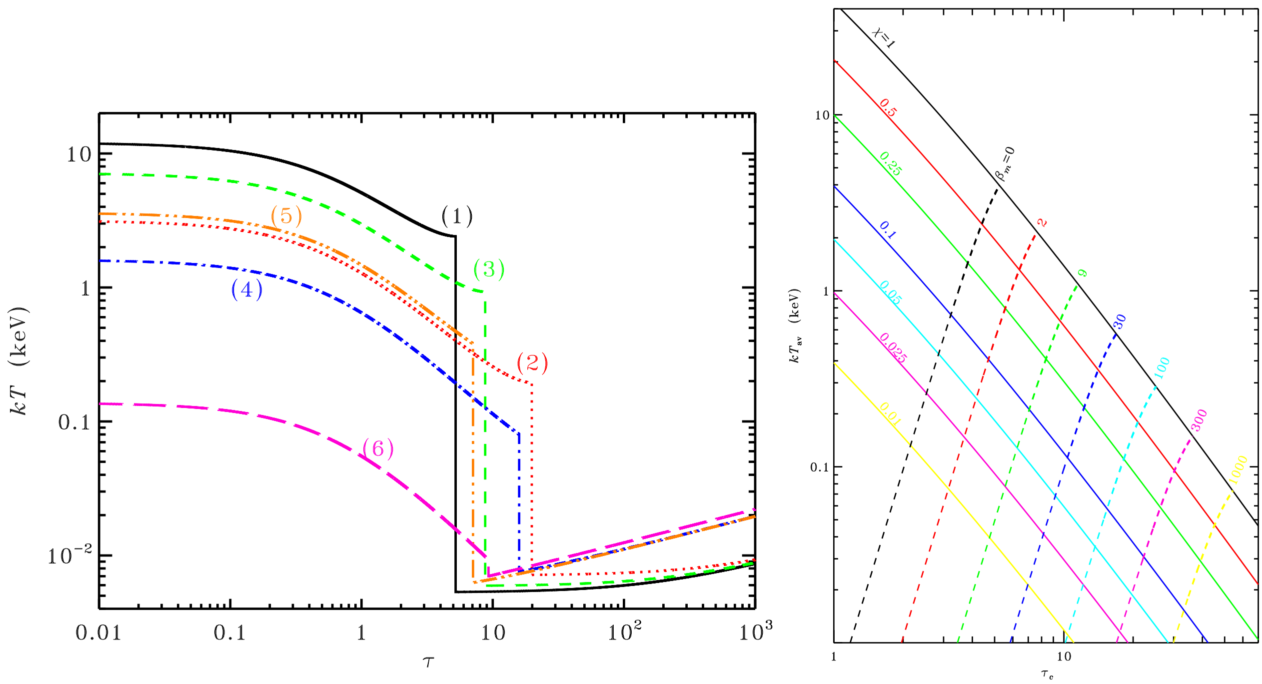

Fig. 1. Left: Local temperature as a function of the Thomson optical depth for models defined in Tab. 1. Temperature in the underlying disk was computed using the diffusion approximation with negligible dissipation. **Right:** Average temperature of the corona, as a function of its optical depth τ_c (solid lines) for different values of the dissipation χ. Dashed lines show the maximal optical depth above which free-free cooling starts dominating over Compton cooling.

field is weaker in the upper layers of the atmosphere, Compton cooling is less efficient, producing a larger temperature. In Compton-dominated atmospheres, a temperature inversion is therefore found, as suggested by observations. Interestingly, the temperature remains bounded, even when most of the accretion power is dissipated in the corona. The surface temperature is: $k_B T_0 = 6\chi(\tau_c/10)^{-1}$ keV. Even with $\chi = 1$, it cannot not exceed a few keV. Moreover, the observed spectrum is likely to be comparable to the comptonisation in a uniform medium with average temperature $T_{\rm av} = \int_0^{\tau_c} T d\tau/\tau_c$, smaller than the surface temperature. This average temperature is shown in Fig. 1 (right). It is found that atmospheres with temperature of $k_B T_{\rm av} \sim 1$ keV and Thomson optical depth $\tau_c \leq 15$ can be reproduced, provided that most of the dissipation occurs in this layer ($\chi \sim 1$).

4 Hydrostatic structure

In static equilibrium, the total pressure must balance gravity: $dP/d\tau = GMz/(\kappa_{es}R^3)$ where G is the gravitational constant, M the black hole mass, R the radial distance to the black hole, and κ_{es} the electron scattering opacity. The total pressure is composed by radiation pressure $P_{\rm rad}$, and gas pressure $P_{\rm gas}$. We also include a possible contribution P_B of the magnetic field, with uniform ratio $\beta_m = P_B/P_{\rm gas}$. For simplicity, we assume that the atmosphere is thin, at some fixed altitude z_c, so that gravity is also uniform within the entire atmosphere. For a given coronal altitude z_c, matter can only be in static equilibrium as long as the total flux $F_{\rm tot}$ remains below a critical flux $F_{\rm Edd}$ (akin a slab version of the Eddington limit) and given by: $\kappa_{es}F_{\rm Edd}/c = GMz_c/R^3$. Solving the hydrostatic equilibrium with a no gas-pressure boundary condition at the atmosphere surface yields the following profiles for the gas pressure and density:

$$\frac{cP_{\rm gas}}{F_{\rm tot}} = \frac{\tau}{1+\beta_m}\left(\frac{F_{\rm Edd}}{F(\tau)} - 1 + \frac{\chi}{2}\frac{\tau}{\tau_c}\right) \tag{4.1}$$

$$\frac{m_e}{\mu m_p}\frac{c^3\rho}{F_{\rm tot}} = \frac{12\tau_c}{\chi}\frac{\tau}{1+\beta_m}\left(\frac{F_{\rm Edd}}{F(\tau)} - 1 + \frac{\chi}{2}\frac{\tau}{\tau_c}\right)\left(\frac{2}{3} + \tau - \frac{\chi}{2}\frac{\tau^2}{\tau_c}\right) \tag{4.2}$$

Examples of density profiles are shown in Fig. 2. Both quantities decrease with altitude. Deep in the atmosphere,

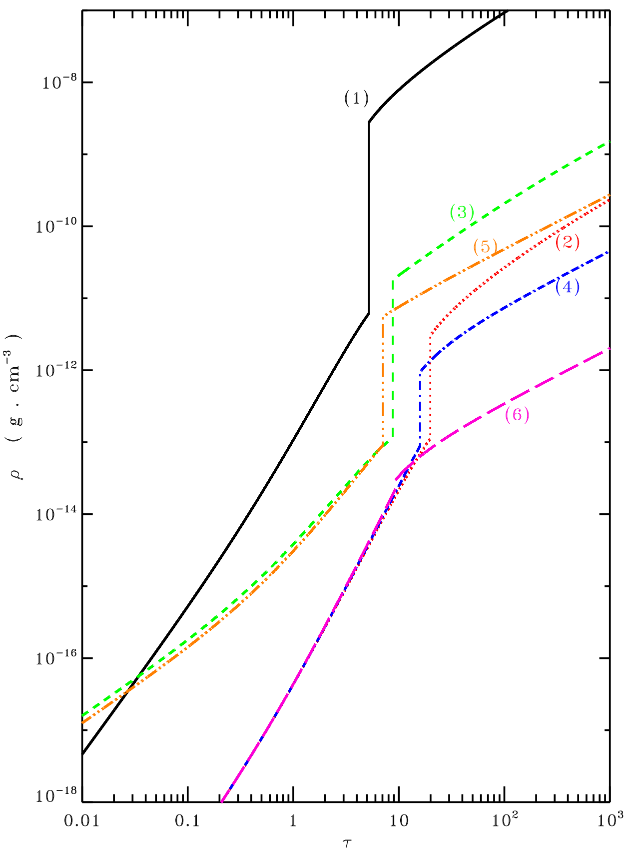

Fig. 2. Local gas density as a function of Thomson optical depth, for the models presented in Tab. 1. Temperature in the underlying disk was computed using the diffusion approximation with negligible dissipation.

the temperature is the lowest and the density the largest, so that free-free cooling is the most efficient mechanism. For a temperature inversion to remain possible, the latter has to remain negligible compared to Compton cooling. For given dissipation rate χ, magnetic ratio β_m, and altitude z_c, comparing the two cooling rates gives a maximal possible optical depth. This is shown in dashed lines in Fig. 1 (right). It is found that in unmagnetised coronae, the maximal optical depth is about $\tau_c = 5 - 6$ in the most favorable situation (i.e. for maximal dissipation $\chi = 1$, and lowest altitude $F_{\rm tot} = F_{\rm Edd}$). This is too thin to account for the observed properties of the observed coronae. However, at a given altitude, any additional magnetic pressure reduces the gas pressure, hence the free-free cooling. Super-equipartition fields with $P_B/P_{\rm gas} = 50 - 100$ allow for warm corona with $k_B T_{\rm av} \approx 1$ keV up to $\tau_c = 10 - 15$.

5 Conclusions

We have investigated the properties of dissipative, warm ($k_B T \sim 1$ keV), optically thick ($\tau_{es} \sim 10-20$) coronae on the top of standard accretion discs. Contrary to what is usually done, the diffusion approximation cannot be used in such hot media and the radiation transfer equation must be solved. This gives the profiles for flux and radiation energy density. In turn, balancing the dissipation with Compton cooling determines the temperature. We find that the dissipation can sustain a hot temperature down to optical depths compatible with observations, provided that most of the accretion power is dissipated in the atmosphere (as oppose as in the disc). Solving the hydrostatic equation determines the gas pressure and density. We find that these quantities remain low enough for the Compton cooling to be the dominant cooling mechanism in the entire atmosphere, only if the medium is strongly magnetized.

This research was conducted within the scope of the HECOLS International Associated Laboratory, supported in part by the Polish NCN grant DEC-2013/08/M/ST9/00664. AR and BC were supported by NCN grants No. 2011/03/B/ST9/03281, 2013/10/M/ST9/00729, and by Ministry of Science and Higher Education grant W30/7.PR/2013. They have received funding from the European Union Seventh Framework Program (FP7/2007-2013) under grant agreement No.312789. This research has also received fundings from PNHE in France, and from the french Research National Agency: CHAOS project ANR-12-BS05- 0009 (http://www.chaos-project.fr). JM and POP also acknowledge fundings from CNRS/PICS.

References

Crummy, J., Fabian, A. C., Gallo, L., & Ross, R. R. 2006, MNRAS, 365, 1067

Czerny, B., Nikołajuk, M., Różańska, A., et al. 2003, A&A, 412, 317

Done, C., Davis, S. W., Jin, C., Blaes, O., & Ward, M. 2012, MNRAS, 420, 1848

Fabian, A. C., Miniutti, G., Gallo, L., et al. 2004, MNRAS, 353, 1071

Gierliński, M., & Done, C. 2006, MNRAS, 371, L16

Janiuk, A., Czerny, B., & Madejski, G. M. 2001, ApJ, 557, 408

Jin, C., Ward, M., Done, C., & Gelbord, J. 2012, MNRAS, 420, 1825

Magdziarz, P., Blaes, O. M., Zdziarski, A. A., Johnson, W. N., & Smith, D. A. 1998, MNRAS, 301, 179

Petrucci, P.-O., Paltani, S., Malzac, J., et al. 2013, A&A, 549, A73

Rozanska, A., Malzac, J., Belmont, R., Czerny, B., & Petrucci, P.-O. 2015, A&A, 580, A77

Schurch, N. J., Done, C., & Proga, D. 2009, ApJ, 694, 1

Shakura, N. I., & Sunyaev, R. A. 1973, A&A, 24, 337

Zhang, S. N., Cui, W., Chen, W., et al. 2000, Science, 287, 1239

SF2A 2015
F. Martins, S. Boissier, V. Buat, L. Cambrésy and P. Petit (eds)

SYSTEMATIC SPECTRAL ANALYSIS OF GX 339–4: EVOLUTION OF THE REFLECTION COMPONENT

M. Clavel[1], J. Rodriguez[1], S. Corbel[1] and M. Coriat[2]

Abstract. Black hole X-ray binaries display large outbursts, during which their properties are strongly variable. We develop a systematic spectral analysis of the 3–40 keV *RXTE*/PCA data in order to study the evolution of these systems and apply it to GX 339–4. Using a phenomenological model to account for the reflection process we provide a first overview of the evolution of the fluorescent iron line at 6.4 keV and of the associated smeared absorption edge at 7.1 keV, for all GX 339–4's outbursts monitored by the *RXTE* mission during its 16-year lifetime.

Keywords: accretion, accretion discs;, black hole physics, X-rays: binaries, Stars: individuals: GX 339–4

1 Introduction

Along the course of their large outbursts, the spectral shape of black hole X-ray binaries (BHXB) varies, tracing the evolution of a jet (or a corona), of an accretion disk and of the associated reflection processes. How these physical structures form and evolve over time is still under investigation (e.g. Remillard & McClintock 2006). To better constrain the theoretical models, one needs to compare the simulation outputs with the real observations, applying the same methods to both data sets. Therefore, we are developing a systematic procedure to reduce the *RXTE*/PCA data (Sec. 2) and to perform the corresponding spectral analysis (Sec. 3). In order to test our method and to obtain an initial set of generic spectral properties for BHXB, we use GX 339–4 which undergoes frequent outbursts, as prime example (e.g. Dunn et al. 2008). For this source, the spectral model chosen to account for the reflection processes is of great importance since an incomplete model can lead to the spurious detection of a high-temperature disk (Clavel et al. 2015). We present here a first overview of the reflection parameters we obtained using a phenomenological model including both a Gaussian iron line at 6.4 keV and the associated smeared absorption edge at 7.1 keV (Sec. 4).

2 RXTE/PCA observations and data reduction

GX 339–4's recurrent outbursts have been monitored with a large number of observatories at all wavelengths. In order to have a uniform spectral coverage over a maximum number of observations, we decided to restrict our systematic spectral analysis of GX 339–4 to the 3–40 keV *RXTE*/PCA data.

The *RXTE* mission operated from December 1995 to January 2012, providing a quasi-systematic follow-up of the X-ray binary outbursts over 16 years. We reduced all the 1389 Proportional Counter Array (PCA) observations available for GX 339–4*. We used the `HEASOFT` software suite v6.16 to reduce the corresponding data in a standard way, restricting it to the top layer of Proportional Counter Unit 2 (PCU2)†. We time-filtered the data, using *maketime* and *xtefilt*, to remove PCU2 breakdowns and to restrict it to the times when the elevation angle above the Earth is greater than 10°, and when the satellite pointing offset is less than 0.02°. The PCA response file was computed using *pcarsp* and the instrumental noise was estimated using *pcabackest*

---

[1] Laboratoire AIM, UMR 7158, CEA/CNRS/Univ. Paris Diderot, CEA DSM/IRFU/SAp, F-91191 Gif-sur-Yvette, France
[2] Université de Toulouse, UPS-OMP, CNRS, IRAP, 9 av. Colonel Roche, BP 44346, F-31028 Toulouse cedex 4, France

*This corresponds to all *RXTE*/PCA observations pointing within one degree from GX 339–4, ignoring slew and raster observations, as well as observations containing data gaps possibly affecting the data (obsIDs ending with G, T or U).

†PCU2 is the only unit which was active during all *RXTE* observations, and, for our study, the spectra are not significantly improved when adding the photon counts from PCU2's second and third layers.

© Société Francaise d'Astronomie et d'Astrophysique (SF2A) 2015

with the background model pca_bkgd_cmbrightvle_eMv20051128.mdl. All observation/background spectra and average count rates were then extracted using *saextrct*. For PCA observations having a net average count rate lower than 40 cts s^{-1} over the full energy range, the instrumental background estimation was replaced by the one calculated from model pca_bkgd_cmfaintl7_eMv20051128.mdl. All spectra were binned in order to have at least 200 counts per resultant channel and a systematic error of 0.6% was added to account for instrumental uncertainties. In this work we present 3–10 keV lightcurves and spectral fits obtained in the 3–40 keV energy range. Following Clavel et al. (2015), we assume that the astrophysical background present in these data is negligible for observations having an average count rate over 0.77 cts s^{-1} in the 3–10 keV range. The observations having average count rates below this threshold are not considered further in this paper.

3 Spectral analysis

Following the method proposed by Dunn et al. (2010), we perform a systematic analysis of the 1260 spectra[‡] obtained for GX 339–4. For each observation, we test the presence of several spectral components using `XSPEC` software v12.8.2 models and chi-squared fitting routines, as well as parameter constraints discussed by Dunn et al. (2008), Plant et al. (2014) and Clavel et al. (2015).

3.1 Phenomenological model set

In addition to the non-thermal component modeled by an absorbed power law, PHABS×POWERLAW[§], we test the presence of a thermal emission coming from the accretion disk modeled by a multi-temperature black-body EZDISKBB, and of a reflection component modeled by both a GAUSSIAN emission line and a smeared edge, SMEDGE. The latter component accounts for both the neutral iron absorption edge at 7.1 keV and the broad reflection hump, also called Compton hump, arising around 20 keV. Along with the Gaussian line, this component provides a sufficient model for the reflection process. Indeed, within the 3–40 keV range and with the *RXTE*/PCA energy resolution, this reflection model allows for good chi-square fits, it also prevents the detection of nonphysical parameters and gives results that are coherent with more-sophisticated self-consistent reflection models, such as XILLVER (Clavel et al. 2015; García et al. 2013). Our phenomenological model set can be summarized as follow,

$$\text{phabs} \times (\text{powerlaw} + \textit{ezdiskbb} + \textbf{gaussian}) \times \textbf{smedge} \tag{3.1}$$

where the disk component (in italic) and of the reflection component (in bold) are included only if they are statistically significant (see Sec. 3.2 for the model selection procedure). The column density corresponding to the photoelectric absorption PHABS is set to $N_H = 0.4 \times 10^{22}\,\mathrm{cm}^{-2}$. The Gaussian line energy is fixed to $E_{\rm line} = 6.4$ keV, the SMEDGE threshold energy to $E_{\rm edge} = 7.1$ keV, its smearing width to $W = 15$ keV and the index for photoelectric cross section to $a = -2.67$. All the other parameters (power law photon index Γ and normalization $I_{\rm pwl}$, disk maximal temperature $T_{\rm max}$ and normalization $I_{\rm disk}$, Gaussian normalization $I_{\rm line}$, edge maximum absorption factor at energy threshold $\tau_{\rm max}$) are left free to vary within physical ranges and are initialized at typical values in order to increase the chance of converging rapidly to a consistent fit.

3.2 Procedure to select the best fit model

Our systematic analysis performs the spectral fit of each observation with four models (POWERLAW, POWERLAW+REFLECTION, POWERLAW+DISK and POWERLAW+DISK+REFLECTION). We then identify the model having the best chi-square and use the `XSPEC` F-statistic test to check the statistical relevance of any optional components (i.e. any disk and/or reflection components), based on a comparison of chi-squares (χ^2) and degrees of freedom.

We are aware that the F-test we use is limited to data sets having a Gaussian statistic (which is the case considering the data large count rates and the consequent binning applied to the spectra, see Sec. 2) and cannot be used to test the presence of a Gaussian line (Protassov et al. 2002) nor of a multiplicative component

[‡]127 observations out of the 1389 we reduced are considered as dominated by the Galactic ridge emission and are therefore excluded from our spectral analysis (see Sec. 2 and Clavel et al. 2015). Two other observations also had to be ignored due to data reduction issues preventing a full spectral analysis.

[§]A model including a broken power law and/or a high energy cut-off, as tested by Dunn et al. (2010), are not statistically needed within the energy range of our analysis (3–40 keV).

(Orlandini et al. 2012). Therefore, similarly to what is done by (Dunn et al. 2010) we added a test on the iron line parameters: it is considered statistically relevant only if its normalization is at least $2\,\sigma$ above zero. When the emission line is detected, the edge should also be present in the spectrum. However, this multiplicative component may not be statistically needed for the fit. This is why we decide to include the SMEDGE in the best fit model only if the following two conditions are fulfilled: (i) the Gaussian line is required, (ii) the edge is significantly improving the overall fit (lowering the reduced χ^2 from more than 2.5 down to about 1).

The phenomenological models we are testing are quite simple. Therefore, for most of the observations, the best fit model selection can easily be done by eye. When this is the case, the automatic procedure gives results that are in good agreement with what one would expect. For this reason, we decide not to investigate for more complex statistical tests. Apart from few isolated observations (less than 1% of our sample), all best fit models have reduced χ^2 around 1 and the uncertainties we provide correspond to the $1\,\sigma$ error bars.

4 Standard spectral evolution of GX 339–4

Our data set is made of 1260 observations spread over the entire life time of the *RXTE* mission, sampling five major outbursts of GX 339–4 (see the source lightcurve and the corresponding hardness ratio in Fig. 1, panels A and B). These events all follow a standard cycle that can be summarized as follow: (i) an intensity rise in the hard state, best modeled by an absorbed power law, (ii) a transition to the soft state, with the detection of an additional disk component, (iii) an intensity decrease in the soft state, where the disk component is dominating the spectra, (iv) a transition back to the hard state, with the disappearance of the disk, and (v) an intensity decrease with a source remaining in the hard state.

Within these cycles, we identified the observations whose best fit models include a reflection component (Fig. 1, panel A). They correspond to the high count rate observations having a sufficient exposure time. This means that a relatively high statistic is needed to significantly detect the reflection component in a given spectrum. When this is the case, the iron line flux seems to follow the evolution of the source average count rate, starting from $I_{\rm line} \sim 10^{-4}\,{\rm ph\,cm^{-2}\,s^{-1}}$ for the lowest count rate observations ($\sim 20\,{\rm cts\,s^{-1}}$) up to few $10^{-2}\,{\rm ph\,cm^{-2}\,s^{-1}}$ for the brightest ones (Fig. 1, panel C). In the hard state the smeared absorption edge is also statistically required and the corresponding maximum absorption factor is relatively stable with a typical value $\tau_{\rm max} \sim 1$. In the soft state this absorption component is not needed, likely because the higher energy part of the spectrum is then often poorly constrained. At the transitions between these two states, the smeared absorption edge is sometimes detected with a maximum absorption factor higher than 1.5 (Fig. 1, panel D). The origin of these extreme values is still under investigation but it could be associated to a disk component which is not detected by our systematic analysis. Indeed, these higher values are coupled with increasing values of the photon index (Clavel et al. 2015). If the later is fitting a soft excess in the spectrum, the absorption edge could then artificially create a break in the model, separating the soft and the hard components. This hypothesis will need to be tested using additional data from a broader energy range, in order to better constrain both the low and high energy parts of the GX 339–4 spectrum in the transition phases.

5 Conclusion

Our systematic analysis of the *RXTE*/PCA data between 3 and 40 keV highlights similar trends for all GX 339–4 outbursts, and it is important to disentangle the variations tracing the true evolution of the source from the one generated by the analysis itself. In this work we present a first overview of the evolution of the parameters related to the reflection model composed of an iron fluorescent line emission at 6.4 keV and of the associated smeared absorption edge at 7.1 keV. The first component is well defined in all observations having a sufficient statistic, while the second is mainly detected in the hard state. The absorption edge is also significantly required in part of the observations covering the transitions between the hard and soft states. However, for the latter observations, the high value of the absorption factor could also be due to the non-detection of a low-temperature disk component. Therefore, physical inputs on the source, as well as multi-wavelength observations, will be crucial to fully test our systematic analysis and to provide the generic properties of GX 339–4. This extensive study is beyond the scope of this paper and will be presented in a future publication (Clavel et al. in prep).

The authors acknowledge funding support from the French Research National Agency: CHAOS project ANR-12-BS05-0009 (http://www.chaos-project.fr).

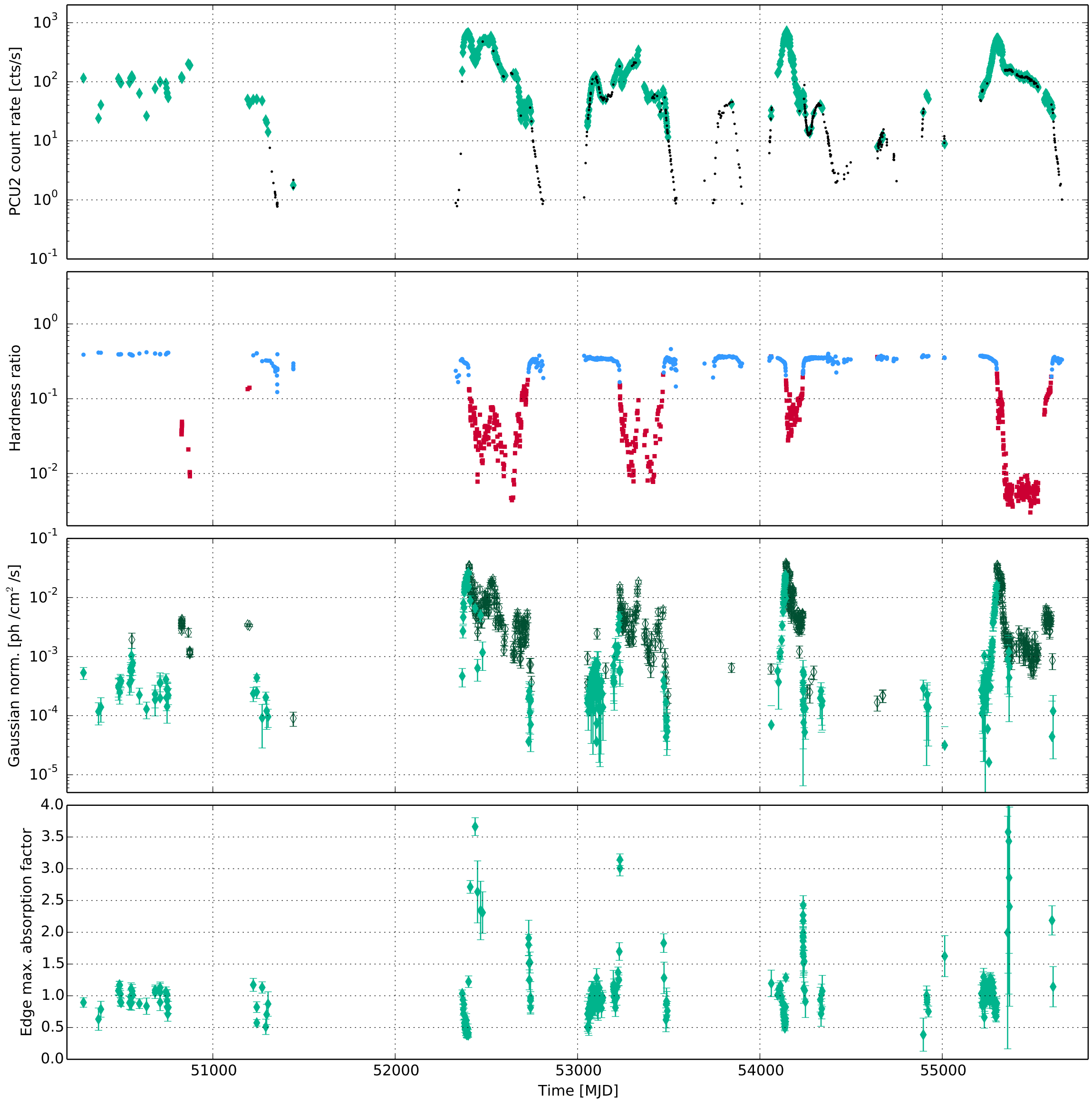

Fig. 1. *RXTE*/PCA lightcurve of all GX 339–4 observations having an average count rate above 0.77 cts s^{-1} and the best fit parameters related to the reflection component. From top to bottom: *(A)* 3–10 keV lightcurve with a color coding highlighting whether the observation best model includes a reflection component (green diamonds) or not (black dots); *(B)* The hardness ratio of each observation defined as the ratio of the 6–10 keV flux over the 3–6 keV one. The color coding highlights whether a disk component is statistically needed (red squares) or not (blue circles) ; *(C)* The intensity of the Gaussian emission line, whether the smeared absorption edge is statistically needed (green diamonds) or not (dark green empty diamonds); *(D)* The 7.1 keV maximum absorption of the SMEDGE component.

References

Clavel, M., Rodriguez, J., Corbel, S., & Coriat, M. 2015, AN, submitted
Dunn, R. J. H., Fender, R. P., Körding, E. G., Belloni, T., & Cabanac, C. 2010, MNRAS, 403, 61
Dunn, R. J. H., Fender, R. P., Körding, E. G., Cabanac, C., & Belloni, T. 2008, MNRAS, 387, 545
García, J., Dauser, T., Reynolds, C. S., et al. 2013, ApJ, 768, 146
Orlandini, M., Frontera, F., Masetti, N., Sguera, V., & Sidoli, L. 2012, ApJ, 748, 86
Plant, D. S., Fender, R. P., Ponti, G., Muñoz-Darias, T., & Coriat, M. 2014, MNRAS, 442, 1767
Protassov, R., van Dyk, D. A., Connors, A., Kashyap, V. L., & Siemiginowska, A. 2002, ApJ, 571, 545
Remillard, R. A. & McClintock, J. E. 2006, ARA&A, 44, 49

SF2A 2015
F. Martins, S. Boissier, V. Buat, L. Cambrésy and P. Petit (eds)

A GAMMA-RAY TRANSIENT AT THE POSITION OF DG CVN

A. Loh[1], S. Corbel[1, 2], G. Dubus[3] and on behalf of the Fermi-LAT Collaboration

Abstract. Solar flares are regularly detected by the Large Area Telescope (LAT) on board the *Fermi* satellite, however no gamma-ray emission from other stellar eruptions has ever been captured. A recent *Swift* detection of a powerful outburst originating from the nearby binary star DG CVn, with optical and radio counterparts, gave us an opportunity to measure the 0.1–100 GeV emission from this kind of objects for the first time. We performed a deep LAT study over the past six years of the *Fermi* mission and we report a significant gamma-ray excess in November 2012, at a position consistent with this binary at a 2σ confidence level. Since no multi-wavelength coverage was available in 2012 and because no high-energy emission was detected during the recent X-ray superflare, we discuss the possible origin of this gamma-ray transient.

Keywords: Acceleration of particles, stars: flare, gamma-rays: stars, stars: individual (DG CVn).

1 Introduction

Wide-field surveys and rapid response capabilities have offered the keys to discover unanticipated classes of transient sources. The high-energy sky above 100 MeV proves to be intensely variable and the *Fermi* satellite is at the forefront of detecting such events. Indeed, its main instrument, the Large Area Telescope (LAT, Atwood et al. 2009), combines a high sensitivity, a wide field of view, a large energy range, and operates in a sky-survey mode most of the time. This nearly complete mapping and continuous monitoring of the sky led to the discovery of new and sometimes unexpected gamma-ray source classes such as microquasars (Fermi LAT Collaboration et al. 2009) or Galactic novae (Ackermann et al. 2014).

The hard X-ray transient monitor Burst Alert Telescope (BAT) on board *Swift* detected on 2014 April 23 a powerful and rare outburst (Drake et al. 2014) from the DG Canum Venaticorum system (hereafter DG CVn, also known as GJ 3789 or G 165−8AB). DG CVn is a M-dwarf binary whose components are separated by $0\farcs2$ (Mason et al. 2001; Beuzit et al. 2004) in rapid rotation ($v \sin i = 55.5\,\mathrm{km\,s^{-1}}$, Delfosse et al. 1998; Mohanty & Basri 2003). Riedel et al. (2014) indicate that the system lies at 18 pc from the Earth and that it is relatively young (~ 30 Myr, confirmed by estimations from Caballero-García et al. 2015), explaining its intense activity.

The brightness of this event was high enough so that *Swift* triggered an automatic follow-up with the Arcminute Microkelvin Imager radio telescope at 15 GHz (Fender et al. 2015). Radio observations started within 6 minutes after the trigger and captured a bright 100 mJy flare. Some additional smaller flares occurred during the next four days before the return at a quiescent radio level (2–3 mJy, as detected by Bower et al. 2009). DG CVn's radio detection suggests production of synchrotron emission from electrons accelerated during the initial phase of the stellar flare. These non-thermal particles are thought to deposit their energy in the lower stellar atmosphere where the density is higher, heating the medium and possibly producing X-ray thermal radiation from the plasma (e.g. Neupert 1968). Caballero-García et al. (2015) measured a delay between hard X-ray and optical emissions, that can be attributed to this Neupert effect. The accelerated particles could also lose their energy via pion decay or Bremsstrahlung processes depending on their leptonic or hadronic nature. This would result in high-energy emission that may be detectable by the LAT.

[1] Laboratoire AIM (CEA/IRFU - CNRS/INSU - Université Paris Diderot), CEA DSM/IRFU/SAp, F-91191 Gif-sur-Yvette, France
[2] Station de Radioastronomie de Nançay, Observatoire de Paris, CNRS/INSU, USR 704 Univ. Orléans, OSUC, F-18330 Nançay, France
[3] UJF-Grenoble 1/CNRS-INSU, Institut de Planétologie et d'Astrophysique de Grenoble (IPAG) UMR 5274, Grenoble F-38041, France

© Société Francaise d'Astronomie et d'Astrophysique (SF2A) 2015

2 Search for high-energy gamma-ray emission with the LAT

We report here the analysis of the P302 LAT data from *Fermi* launch in August 2008 to September 2014, six years later. The reduction and analysis of the LAT products were performed with the *Fermi* Science Tools (version 10-00-02) using the Instrument Response Functions `P8R2_SOURCE_V6` and the corresponding diffuse models for the Galactic and isotropic emissions. The source model file used to constrain the diffuse and nearby point-source emissions is based on the Third *Fermi*-LAT Source Catalog (3FGL, Acero et al. 2015). We added the model of DG CVn at the position (RA = 202.°94, Dec. = 29.°28, J2000) with a power-law spectrum.

As the binary star lies far away from the Galactic plane, the likelihood analysis over the full LAT data set easily converged and we used the Test Statistic (defined as $\mathrm{TS} = 2\Delta \log L$, where the difference compares the likelihood functions L with and without the addition of DG CVn) to quantify the statistical significance of the presence of the point-source with respect to the background. Including the DG CVn source model does not seem essential for the fitting procedure over six years as its derived TS value is about 19.7 (approximatively just over 4σ for 2 degrees of freedom, Mattox et al. 1996) with a mean gamma-ray flux of $(3.9 \pm 1.6) \times 10^{-9}\,\mathrm{ph\,cm^{-2}\,s^{-1}}$. A low TS value over a large time scale could mean that either the steady gamma-ray flux, if present, is lower than the LAT sensitivity or the gamma-ray emission is transient (e.g. during an outburst).

2.1 Long-term variability

The binary star's light-curve was built using 4-day time bins (Fig. 1) over the entire range of *Fermi* observations to identify time periods where a gamma-ray emission is significantly detected at the position of DG CVn. We computed 95 per cent upper-limits on the high-energy flux when the TS value was below 25 ($\sim 5\sigma$) using the (semi-)Bayesian method of Helene (1991) as implemented in the `pyLikelihood` module provided with the Science Tools. Otherwise, we provide integrated gamma-ray fluxes along with 1σ statistical error bars.

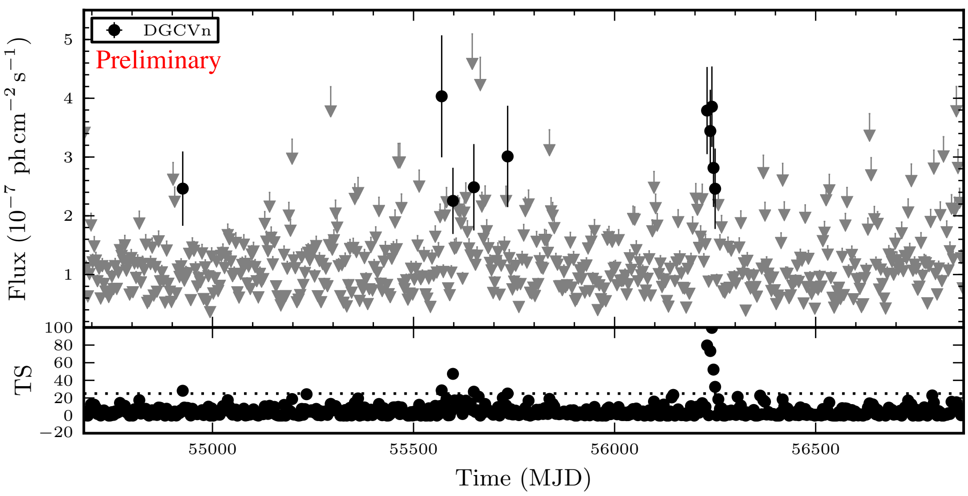

Fig. 1. 4-day exposure LAT light-curve (0.1–100 GeV) obtained by fitting a point-source at DG CVn position. Upper-limits (grey arrows) or gamma-ray fluxes given with 1σ statistical errors (black dots) are derived whether the Test Statistic (bottom panel) falls below or above the defined threshold value of 25 (horizontal dotted line) respectively.

Most of the time, including a point-source at DG CVn's position does not improve the fitting of the region (i.e. TS < 25), thus we are only able to provide upper-limits on the binary star flux for the corresponding periods. However, a few data points exceed the TS threshold. We identified the spurious detections related to local fluctuations or outbursts originating from nearby sources. For instance, the gamma-ray excess around MJD 55600, which reaches a 47 TS value, is time-coincident with a flaring episode of the nearby blazar 3FGL J1332.8+2723 and has been detected by the weekly *Fermi All-Sky Variability Analysis* (FAVA, Ackermann et al. 2013a) between 2011 February 7 and 14. Due to the large PSF of the instrument, some of its softest photons may have been included during the model fitting of DG CVn, resulting in an artificial TS excess for the latter source, although situated 1.°9 away (Ackermann et al. 2013b).

Apart from these spurious detections, one can clearly distinguish a significant excess around MJD 56240 (2012 November 9) where five measurements present a TS value between 32 and 99. Again, this gamma-ray flare has been previously reported by the FAVA. The automatic analysis detected a significant transient event lasting for about three weeks (from 2012 October 29 to November 19) and incorrectly associated it with the blazar 3FGL J1332.8+2723 responsible for the outburst previously mentioned (see Sec. 2.2).

We also note the absence of any gamma-ray counterpart for the X-ray/radio superflare which occurred on 2014 April 23 (MJD 56770.88). 40 days encompassing the outburst were investigated in details but no significant gamma-ray emission can be associated with a point-source at the position of DG CVn. A single 1-day measurement presents a TS value just above 9 with a mean flux of $(2.0 \pm 1.2) \times 10^{-7}\,\mathrm{ph\,cm^{-2}\,s^{-1}}$ eight days before the X-ray flaring episode but this could be due to a statistical fluctuation.

2.2 November 2012 outburst

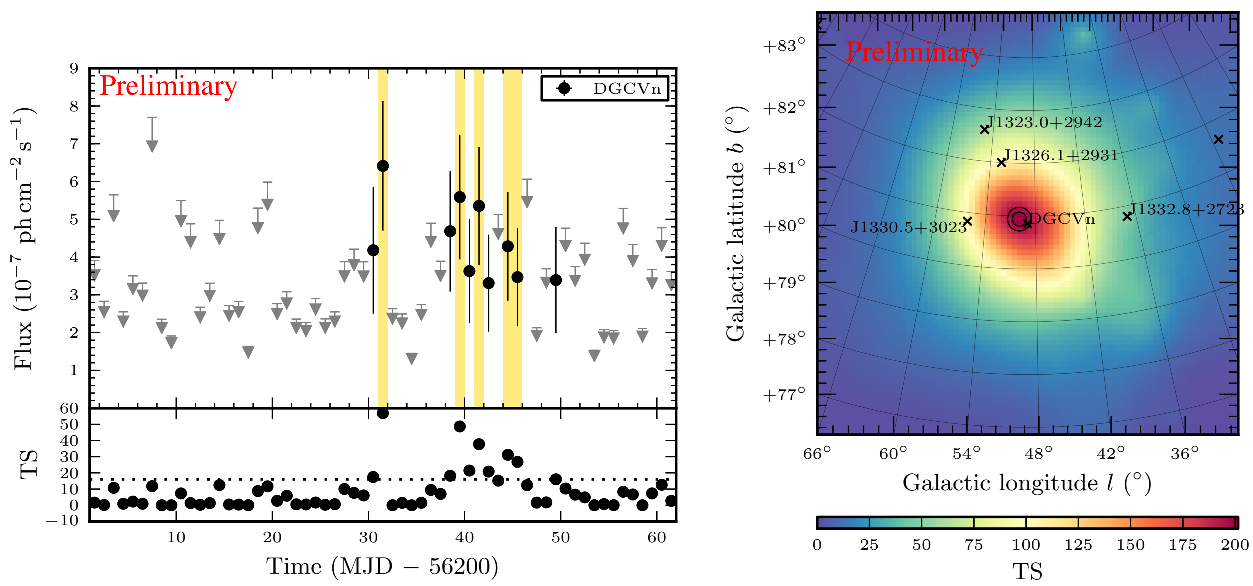

Fig. 2. Left: One-day bin light-curve built over the 61-day interval encompassing the most significant gamma-ray excess in Fig. 1. Black data points correspond to TS > 16 measurements. Yellow shaded periods represent the daily measurements for which the TS value is above 25. **Right:** $8^\circ \times 8^\circ$ residual TS map computed over the stacked TS > 25 period. 68 and 95 per cent containment regions of the *Fermi* source localisation are overplotted.

The 1-day bin light-curve over 61 days encompassing the MJD 56240 flare (Fig. 2, left) unveils a gamma-ray flare evolving over several days. The addition of a point-source at the position of DG CVn seems significant with a TS value up to 57. It starts on MJD 56230 with a peak flux of $(6.4 \pm 1.7) \times 10^{-7}\,\mathrm{ph\,cm^{-2}\,s^{-1}}$ one day later before a six day quenching. We detect a re-ignition around MJD 56238 followed by a slow decrease of the gamma-ray flux over eight days. A hint for another small hump two days after can be distinguished although associated with a lower TS.

We stacked the data corresponding to the days when DG CVn's model addition significantly improve the sensitivity (i.e. 2012 October 31, November 8, 10, 13, 14, all yellow shaded in Fig 2 left). The likelihood analysis yields a TS of about 197 for a mean gamma-ray flux of $(4.9 \pm 0.7) \times 10^{-7}\,\mathrm{ph\,cm^{-2}\,s^{-1}}$ and a power-law index of -2.42 ± 0.14. Fig. 2 (right) displays the residual TS map during the excess. The best-fit is at the position (RA $= 202\overset{\circ}{.}81$, Dec. $= 29\overset{\circ}{.}41$, $0\overset{\circ}{.}18$ from DG CVn) with 68 and 95 per cent containment radii r68 $= 0\overset{\circ}{.}13$ and r95 $= 0\overset{\circ}{.}22$. There is thus a 2σ significance agreement between DG CVn and the gamma-ray peak positions.

3 Discussion and conclusion

Regarding the TS map (Fig. 2, right) and the localisation, we can rule out the FAVA association of the November 2012 flare with the blazar 3FGL J1332.8+2723. Moreover, the TS peak displayed on the bottom panel of the Fig. 1 is clearly above the TS distribution. This feature has not been found in the other analyses that we performed at the position of several active stars. Besides, the flare is spread over several consecutive days, which ensures an unlikely statistical noise origin.

Without any known counterpart and considering the localisation uncertainty, it is not clear whether or not the binary star DG CVn is responsible for the observed transient event. Active stars are indeed not known to produce such high-energy and long-lasting outbursts. On the other hand, the April 2014 superflare (Drake et al. 2014) as well as the radio counterpart (Fender et al. 2015) were totally unexpected, indicating that DG CVn may be an extreme system. It is possible that a major outburst happened and remained unnoticed by a lack of simultaneous monitoring at other wavelength. Such unique and interesting behaviour would require further investigations.

If not originating from DG CVn system, the flare could come from an Active Galactic Nucleus (AGN) since AGNs account for the vast majority of high-latitude ($|b| > 10°$) *Fermi*-LAT sources (more than 71 per cent according to Ackermann et al. 2015, 3LAC catalogue). Among them, 98 per cent are blazars (either Flat Spectrum Radio Quasars FSRQs or BL Lacertae objects). Blazar light-curves are known for their variability on a wide range of time scales and display strong flares due to internal shocks or sporadic increases of the accretion flow feeding the jets. We have listed three association candidates. Two quasars are located within the containment region (namely J133059.8+293005 and J133031.5+292854, Véron-Cetty & Véron 2010, respectively $0\overset{\circ}{.}10$ and $0\overset{\circ}{.}17$ away from the best fit position). The flat-spectrum radio source GB6 J1331+2932 (with a 19.6 ± 0.2 mJy flux density, Muñoz et al. 2003), $0\overset{\circ}{.}13$ away from the *Fermi*-LAT localisation, may also be worth investigating since this high-Galactic latitude source is likely to be an AGN (either a blazar or a compact radio galaxy core).

AL and SC acknowledge the financial support from the UnivEarthS Labex programme of Sorbonne Paris Cité (ANR-10-LABX-0023 and ANR-11-IDEX-0005- 02).
The *Fermi*-LAT Collaboration acknowledges support for LAT development, operation and data analysis from NASA and DOE (United States), CEA/Irfu and IN2P3/CNRS (France), ASI and INFN (Italy), MEXT, KEK, and JAXA (Japan), and the K.A. Wallenberg Foundation, the Swedish Research Council and the National Space Board (Sweden). Science analysis support in the operations phase from INAF (Italy) and CNES (France) is also gratefully acknowledged.

References

Acero, F., Ackermann, M., Ajello, M., et al. 2015, ApJS, 218, 23
Ackermann, M., Ajello, M., Albert, A., et al. 2013a, ApJ, 771, 57
Ackermann, M., Ajello, M., Albert, A., et al. 2014, Science, 345, 554
Ackermann, M., Ajello, M., Allafort, A., et al. 2013b, ApJ, 765, 54
Ackermann, M., Ajello, M., Atwood, W. B., et al. 2015, ApJ, 810, 14
Atwood, W. B., Abdo, A. A., Ackermann, M., et al. 2009, ApJ, 697, 1071
Beuzit, J.-L., Ségransan, D., Forveille, T., et al. 2004, A&A, 425, 997
Bower, G. C., Bolatto, A., Ford, E. B., & Kalas, P. 2009, ApJ, 701, 1922
Caballero-García, M. D., Šimon, V., Jelínek, M., et al. 2015, MNRAS, 452, 4195
Delfosse, X., Forveille, T., Perrier, C., & Mayor, M. 1998, A&A, 331, 581
Drake, S., Osten, R., Page, K. L., et al. 2014, The Astronomer's Telegram, 6121, 1
Fender, R. P., Anderson, G. E., Osten, R., et al. 2015, MNRAS, 446, L66
Fermi LAT Collaboration, Abdo, A. A., Ackermann, M., et al. 2009, Science, 326, 1512
Helene, O. 1991, Nuclear Instruments and Methods in Physics Research A, 300, 132
Mason, B. D., Wycoff, G. L., Hartkopf, W. I., Douglass, G. G., & Worley, C. E. 2001, AJ, 122, 3466
Mattox, J. R., Bertsch, D. L., Chiang, J., et al. 1996, ApJ, 461, 396
Mohanty, S. & Basri, G. 2003, ApJ, 583, 451
Muñoz, J. A., Falco, E. E., Kochanek, C. S., Lehár, J., & Mediavilla, E. 2003, ApJ, 594, 684
Neupert, W. M. 1968, ApJ, 153, L59
Riedel, A. R., Finch, C. T., Henry, T. J., et al. 2014, AJ, 147, 85
Véron-Cetty, M.-P. & Véron, P. 2010, A&A, 518, A10

SF2A 2015
F. Martins, S. Boissier, V. Buat, L. Cambrésy and P. Petit (eds)

THE EMISSION OF COMPACT JETS POWERED BY INTERNAL SHOCKS

Julien Malzac[1,2] and Samia Drappeau[1,2]

Abstract. The emission of steady compact jets observed in the hard spectral state of X-ray binaries is likely to be powered by internal shocks caused by fluctuations of the outflow velocity. The dynamics of the internal shocks and the resulting spectral energy distribution (SED) of the jet is very sensitive to the shape of the Power Spectral Density (PSD) of the fluctuations of the jet Lorentz factor. It turns out that Lorentz factor fluctuations injected at the base of the jet with a flicker noise power spectrum (i.e. $P(f) \propto 1/f$) naturally produce the canonical flat SED observed from radio to IR band in X-ray binary systems in the hard state. This model also predicts a strong, wavelength dependent, variability that resembles the observed one. In particular, strong sub-second variability is predicted in the infrared and optical bands. The assumed fluctuations of the jet Lorentz factor are likely to be triggered by the variability of the accretion flow which is best traced by the X-ray emission. In the case of GX339-4 for which high quality and simultaneous multi-wavelength data are available, we performed simulations assuming that the fluctuation of the jet Lorentz factor have the same PSD as the observed X-ray PSD. The synthetic SED calculated under this assumption provides a remarkable match to the observed radio to IR SED. In this case the model also produces strong mid-infrared spectral variability that is comparable to that reported in this source.

Keywords: accretion, accretion discs – black hole physics – shock waves – relativistic processes –radiation mechanisms: non-thermal – X-rays: binaries

1 Properties of the internal shock model

Steady compact jets are probably the most common form of jets in X-ray binaries. They appear to be present in all black hole and neutron star binaries when in the hard X-ray spectral state. They have an approximatively flat Spectral Energy Distribution (SED) extending from the radio to the mid-IR (e.g. Fender et al. 2000; Corbel & Fender 2002; Chaty et al. 2003; Migliari et al. 2011). These flat spectra are usually ascribed to self-absorbed synchrotron emission from conical compact jets (Blandford & Königl 1979) under the assumption of continuous energy replenishment of the adiabatic losses. The compensation of these energy losses is crucial for maintaining this specific spectral shape (Kaiser 2006).

Internal shocks provide a possible mechanism to compensate the adiabatic losses by dissipating energy and accelerating particles at large distance from the black hole. Internal shocks caused by fluctuations of the outflow velocity are indeed widely believed to power the multi-wavelength emission of jetted sources such as γ-ray bursts (Rees & Meszaros 1994; Daigne & Moscovitch 1998), active galactic nuclei (Rees 1978; Spada et al. 2001), or microquasars (Kaiser, Sunyaev & Spruit 2000; Jamil et al. 2010). Internal shocks models usually assume that the jet can be discretised into homogeneous ejectas. Those ejectas are injected at the base of the jet with variable velocities and then propagate along the jet. At some point, the fastest fluctuations start catching up and merging with slower ones. This leads to shocks in which a fraction of the bulk kinetic velocity of the shells is converted into internal energy. Part of the dissipated energy goes into particles acceleration, leading to synchrotron and also, possibly, inverse Compton emission. Recently, however, Jamil et al. (2010) developed an internal shock model for the emission of jets in X-ray binaries, and concluded that energy dissipation through internal shocks only is not enough to produce a flat SED. Nevertheless, most studies of the internal shock model so far, including that of Jamil et al. (2010), have implicitly assumed that the Fourier Power Spectral Density (PSD) of the velocity fluctuations injected at the base of the jet is flat (i.e. white noise). In fact, the energy

[1] Université de Toulouse; UPS-OMP; IRAP; Toulouse, France
[2] CNRS; IRAP; 9 Av. colonel Roche, BP 44346, F-31028 Toulouse cedex 4, France

© Société Francaise d'Astronomie et d'Astrophysique (SF2A) 2015

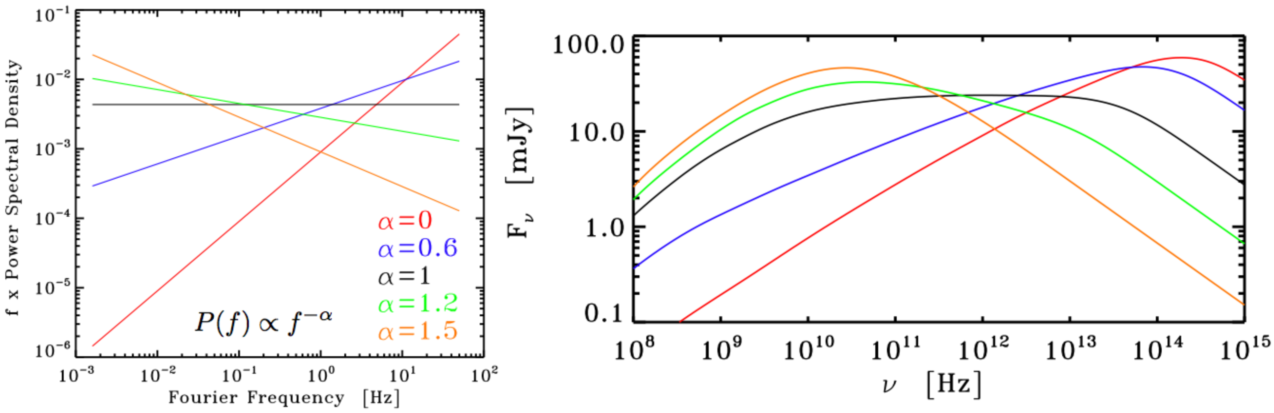

Fig. 1. Simulation of the internal shock model with a power-law PSD of the Lorentz factor fluctuations ($P(f) \propto f^{-\alpha}$). The top left panel shows the shape of the injected PSDs, for the indicated values of the α index. The right panel shows the jet SED calculated for an inclination angle of 40 degrees and a distance to the source of 2 Kpc. See Malzac (2014) for details.

dissipation profile of the internal shocks is very sensitive to the shape of the PSD of the velocity fluctuations. Indeed, let us consider a fluctuation of the jet velocity of amplitude Δv occuring on a time scale Δt. This leads to the formation of a shock at a downstream distance $z_s \propto \Delta t/\Delta v$. In this shock the fraction of the kinetic energy converted into internal energy will be larger for larger Δv. From these simple considerations we see that the distribution of the velocity fluctuation amplitudes over their time scales (i.e. the PSD) is going to determine where and in which amount the energy of the internal shocks is deposited. Malzac (2014) used Monte-Carlo simulations to study this dependance and found that independently of the details of the model flat radio-IR SEDs are obtained for a flicker noise PSD of the fluctuations of the jet Lorentz factor. This result is illustrated by Fig. 1, which compares the SEDs obtained for PSD of the Lorentz factor of the jet with a power-law shape with varying index α: $P(f) \propto f^{-\alpha}$. For larger α the fluctuations of the Lorentz factor have, on average, longer time-scales and therefore more dissipation occurs at larger distances from the black hole. One can see from Fig. 1 that the SED is very sensitive to the value of α, for $\alpha = 1$ (i.e. flicker noise) the dissipation profile scales like z^{-1} and the specific energy profile is flat. In other words, the internal shocks compensate exactly for the adiabatic losses. As result the SED is flat over a wide range of photon frequencies. In fact, this result can also be obtained analytically (Malzac 2013). The case of flicker noise fluctuations of the jet Lorentz factor may therefore be relevant to the observations of compact jets.

An interesting feature of the internal shock model is that it naturally predicts strong variability of the jet emission. Figure 2 shows sample light curves and power spectra obtained from the simulation with $\alpha = 1$. The jet behaves like a low-pass filter. As the shells of plasma travel down the jet, colliding and merging with each other, the highest frequency velocity fluctuations are gradually damped and the size of the emitting region increases. The jet is strongly variable in the optical and IR bands originating primarily from the base of the emitting region and becomes less and less variable at longer frequencies produced at larger distances from the black hole. The observations also show significant flickering in the Infrared and optical band (Kanbach et al. 2001; Casella et al. 2010; Gandhi et al. 2010). At least part of this fast IR/optical variability is likely to arise from the jet, possibly through internal shocks. Another interesting property of the observed variability is the existence of correlations with the fast X-ray variability originating from the accretion flow. In particular, Casella et al. (2010) measured de cross-correlation function of the X-ray and IR light curves and found significant correlation between the two bands with the infrared photons lagging behind the X-rays by about 100 ms. Casella et al. (2010) interpreted this time-lag as the propagation time of the ejected shells from the accretion flow to the infrared emitting region in the jet. In the framework of the internal shock model this observation suggests that the fluctuations of the jet Lorentz factor are related to the X-ray variability of the source.

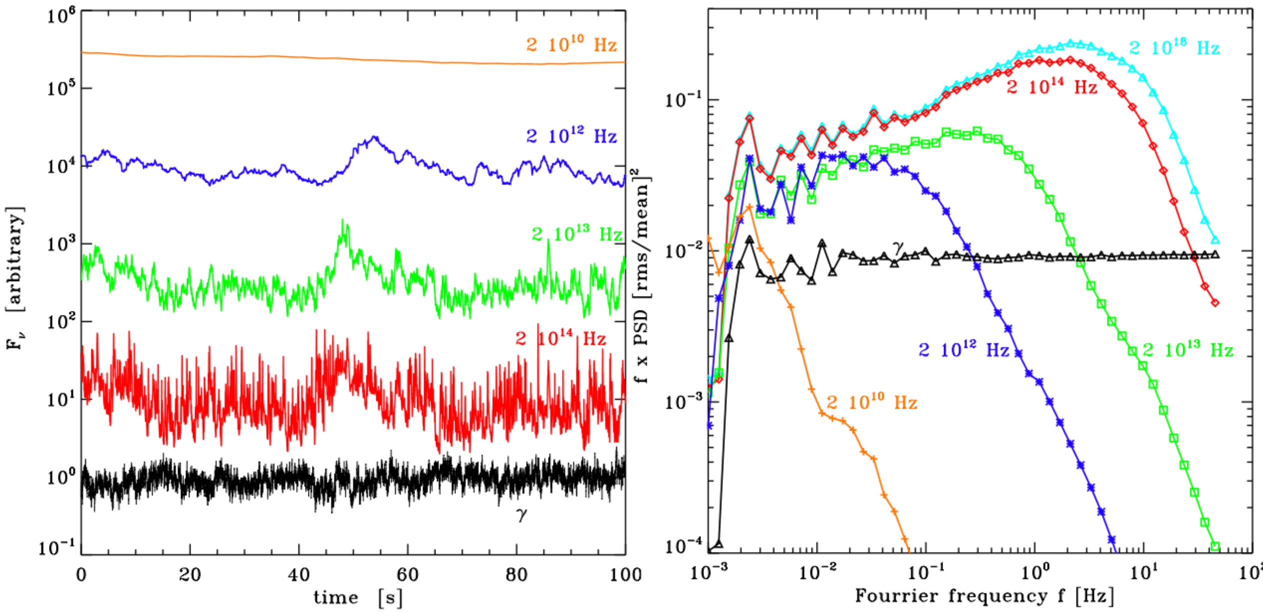

Fig. 2. Synthetic light curves (left, rescaled) and power spectra at various indicated frequencies resulting from the simulation with $\alpha = 0$. The injected fluctuations of the Lorentz factor are also shown.

2 Are the jet Lorentz factor fluctuations related to the X-ray variability ?

In fact, if the jet is launched from the accretion disc, the variability of the jet Lorentz factor must be related to that of the accretion disc. And we know, both from theory (see e.g. Lyubarskii 1997) and from observations (see e.g. Gilfanov & Arefiev 2005) that accretion discs tend to generate flicker noise variability. Therefore flicker noise fluctuations of the jet Lorentz factor are not unexpected. In X-ray binaries the variability of the accretion flow is best traced directly by the X-ray light curves. Those sources indeed exhibit a strong variability over a very broad range of time scales. This is consistent with the idea that the fluctuations of the jet Lorentz factor may be related to the X-ray variability. Although this variability is close to flicker noise, it appears to be more complex. The left panel of Fig. 3) shows an actual X-ray PSD of the black hole binary GX339-4 . As can be seen on this figure, in the hard state, which is the spectral state associated to the presence of compact radio jets, the short time-scale X-ray variability is dominated by a band limited noise that is well described in terms of 4-5 broad Lorentzians (e.g. Nowak 2000; van der Klis 2006).

This variability could be a good proxy for the assumed fluctuations of the jet. The right panel of Fig. 3 shows the resulting time averaged SED obtained if one assume that the Lorentz factor fluctuations have a PSD that is exactly the observed X-rays. This synthetic SED is compared to multi wavelength observation that are nearly simultaneous with the X-ray timing data (see Gandhi et al. 2011 for details). The model appears to reproduce pretty well the radio to infrared data. This agreement is striking because the shape of the SED depends almost uniquely on the assumed shape of the PSD of the fluctuations. Although the model has a number of free parameters (jet power, inclination angle, time-averaged jet Lorentz factor...) that could be tuned to fit the data, those parameters only allow to modify the flux normalisation or shift it in the photon frequency direction (Drappeau et al. submitted), but they have very little effects on the overall shape of the SED.

The four mid-infrared flux measurements at 1.36×10^{13}, 2.50×10^{13}, 6.52×10^{13} and 8.82×10^{13} Hz that are shown on Fig. 3 were obtained with the Wide field Infrared Survey Explorer (WISE; Wright et al. 2010) they represent an average over 13 epochs, sampled at multiples of the satellite orbital period of 95 minutes and with a shortest sampling interval of 11 s, when WISE caught the source on two consecutive scans. These data have revealed a strong variability of the mid-infrared emission (see Gandhi et al. 2011). The light curves of these observations are shown in Fig. 4 (left panel) and compared to light curves obtained from the same simulation that gives a good fit to the observed radio-IR SED (right panel). The model appears to predict a variability of similar amplitude to that observed by WISE.

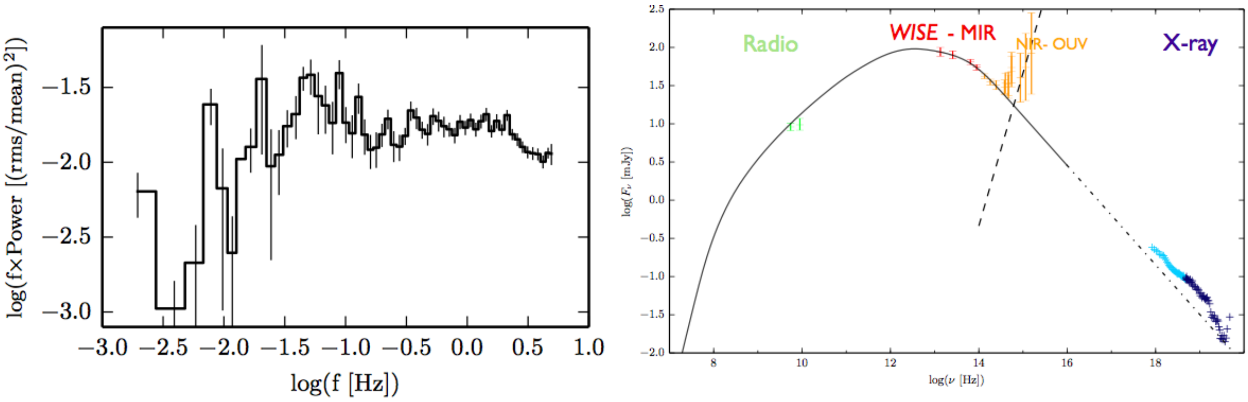

Fig. 3. Left: the observed X-ray PSD of GX 339-4 during the observations presented in Gandhi et al. (2011). Right: the SED measured by Gandhi et al. (2011) compared to a simulated jet SED obtained assuming that the jet Lorentz factor fluctuations have exactly the PSD as the X-ray flux.

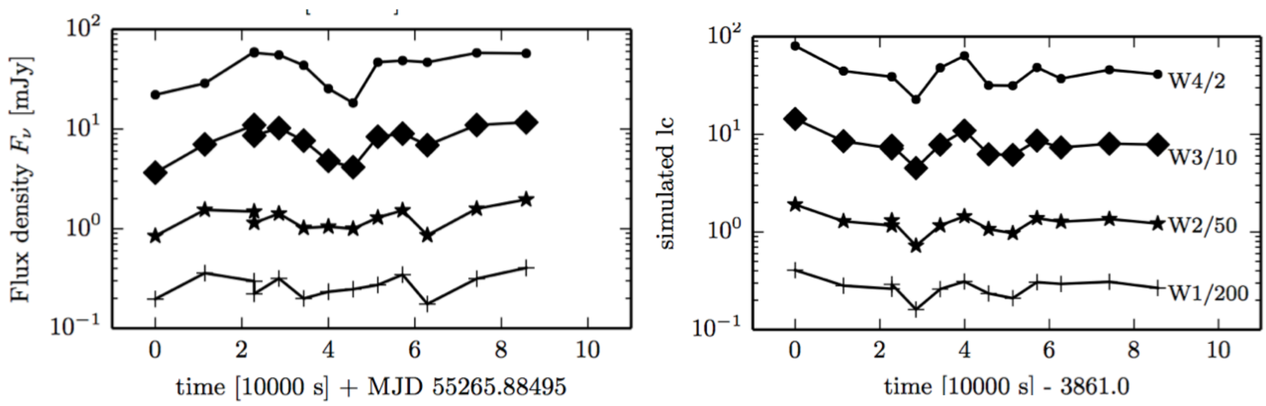

Fig. 4. Left: the observed mid-infrared variability as observed by WISE in 4 bands. Right: sample synthetic light curves obtained from the same simulation shown in Fig. 3.

3 Conclusion

Internal shocks naturally lead to the formation of the observed SEDs of compact jets and also predict a strong, wavelength dependent, variability that resembles the observed one. The assumed velocity fluctuations of the jet must originate in the accretion flow. The model thus predicts a strong connection between the observable properties of the jet in the radio to IR bands, and the variability of the accretion flow as observed in X-rays. If the model is correct, this offers a unique possibility to probe the dynamics of the coupled accretion and ejection processes leading to the formation of compact jets.

References

Blandford R. D., Königl A., 1979, ApJ, 232, 34

Casella P., et al., 2010, MNRAS, 404, L21

Chaty S., et al., 2003, MNRAS, 346, 689

Corbel S., Fender R. P., 2002, ApJ, 573, L35

Daigne F., Mochkovitch R., 1998, MNRAS, 296, 275

Drappeau, S., Malzac, J., Belmont, R., Gandhi, P., & Corbel, S. 2015, MNRAS, 447, 3832

Fender R. P., et al., 2000, MNRAS, 312, 853

Gandhi P., et al., 2010, MNRAS, 407, 2166

Gandhi P., et al., 2011, ApJ, 740, L13

Gilfanov M., Arefiev V., 2005, astro, arXiv:astro-ph/0501215

Jamil O., Fender R. P., Kaiser C. R., 2010, MNRAS, 401, 394

Kaiser C. R., Sunyaev R., Spruit H. C., 2000, A&A, 356, 975

Kaiser C. R., 2006, MNRAS, 367, 1083

Kanbach G., Straubmeier C., Spruit H. C., Belloni T., 2001, Natur, 414, 180

Lyubarskii Y. E., 1997, MNRAS, 292, 679

Malzac J., 2013, MNRAS, 429, L20

Malzac J., 2014, MNRAS, 443, 299

Migliari S., Miller-Jones J. C. A., Russell D. M., 2011, MNRAS, 415, 2407

Nowak M. A., 2000, MNRAS, 318, 361

Rees M. J., 1978, MNRAS, 184, 61P

Rees M. J., Meszaros P., 1994, ApJ, 430, L93

van der Klis M., in Compact stellar X-ray sources, Lewin & van der Klis (eds), Cambridge University Press, 2006, arXiv:astro-ph/0410551

Spada M., Ghisellini G., Lazzati D., Celotti A., 2001, MNRAS, 325, 1559

Wright N. J., Drake J. J., Civano F., 2010, ApJ, 725, 480

SF2A 2015
F. Martins, S. Boissier, V. Buat, L. Cambrésy and P. Petit (eds)

THE OPTICAL POLARIZATION SIGNATURES OF FRAGMENTED EQUATORIAL DUSTY STRUCTURES IN ACTIVE GALACTIC NUCLEI

F. Marin[1] and M. Stalevski[2,3,4]

Abstract. If the existence of an obscuring circumnuclear region around the innermost regions of active galactic nuclei (AGN) has been observationally proven, its geometry remains highly uncertain. The morphology usually adopted for this region is a toroidal structure, but other alternatives, such as flared disks, can be a good representative of equatorial outflows. Those two geometries usually provide very similar spectroscopic signatures, even when they are modeled under the assumption of fragmentation. In this lecture note, we show that the resulting polarization signatures of the two models, either a torus or a flared disk, are quite different from each other. We use a radiative transfer code that computes the 2000 – 8000 Å polarization of the two morphologies in a clumpy environment, and show that varying the sizes of a toroidal region has deep impacts onto the resulting polarization, while the polarization of flared disks is independent of the outer radius. Clumpy flared disks also produce higher polarization degrees ($\sim$ 10 % at best) together with highly variable polarization position angles.

Keywords: radiative transfer, polarization, galaxies: active, galaxies: nuclei, galaxies: Seyfert

1 Introduction

The presence of an optically thick, equatorial, dusty region around the core of active galactic nuclei (AGN) has been predicted by polarimetric observations from the Lick 3m telescope (Antonucci & Miller 1985) and revealed thanks to mid-infrared interferometry (Jaffe et al. 2004; Wittkowski et al. 2004) at the *Very Large Telescope*. This obscuring torus is a fundamental region that explains the polarization dichotomy observed in radio-quiet AGN: along type-1 viewing angles (close to the AGN pole), the observed net polarization position angle is mainly parallel to the symmetry axis of the system, while at type-2 orientations (close to the edge of the system), the polarization angle is perpendicular. Hiding the innermost regions of AGN behind a dust wall is also necessary to explain the absence of broad lines in the optical spectra of type-2 Seyfert galaxies. It has been shown by Antonucci & Miller (1985) and Miller & Goodrich (1990) that polarization can unveil those broad lines in the polarized flux spectra of type-2 AGN, demonstrating the power of polarimetry.

Studying AGN under the scope of polarization can be achieved thanks to numerical modeling (e.g. Kartje 1995; Wolf & Henning 1999; Young 2000), but all those codes are limited to scattering inside uniform-density regions. As a bulky hydrostatic dusty region is inconsistent with self-gravitational stability, it is more likely to consist of individual, optically thick, molecular clumps in collision-free orbits that are sustaining the vertical height of the torus (Krolik & Begelman 1988; Pier & Krolik 1992). Hence, it is necessary to use radiative transfer codes that are able to handle multiple scattering in a clumpy environment, such as SKIRT in the optical and infrared bands (Baes et al. 2011; Stalevski et al. 2012; Camps & Baes 2015), or STOKES in the optical, ultraviolet and X-ray bands (Goosmann & Gaskell 2007; Marin et al. 2012). The later code has been recently upgraded to account for thousands of individual scattering regions (Marin et al. 2015) and will be used here to investigate the impact of fragmentation onto two different geometries of circumnuclear regions.

In this lecture note, the optical polarimetric investigation of dusty clumpy tori and flared disks will be presented in Sect. 2.1 and Sect. 2.2, respectively. We discuss our results and conclude this note in Sect. 3.

[1] Astronomical Institute of the Academy of Sciences, Boční II 1401, CZ-14100 Prague, Czech Republic
[2] Departmento de Astronomia, Universidad de Chile, Camino del Observatorio 1515, Santiago, Chile
[3] Astronomical Observatory, Volgina 7, 11060 Belgrade, Serbia
[4] Sterrenkundig Observatorium, Universiteit Gent, Krijgslaan 281-S9, Gent, 9000, Belgium

© Société Francaise d'Astronomie et d'Astrophysique (SF2A) 2015

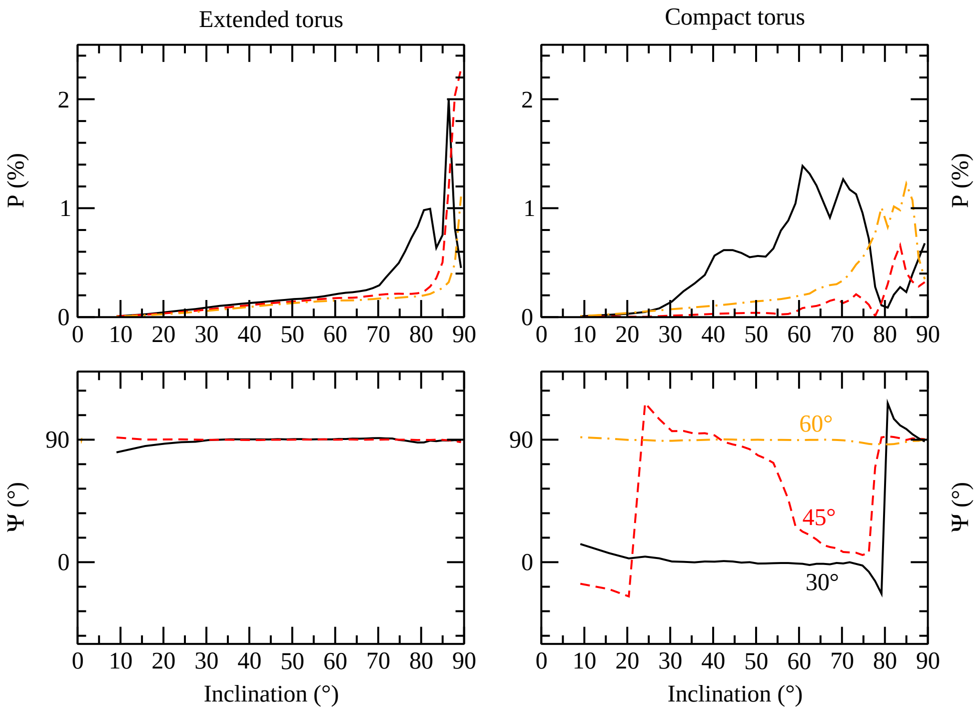

Fig. 1. Polarization degree P (top) and polarization position angle Ψ (bottom) for an extended (left column) and a compact clumpy torus (right column). Polarization is plotted as a function of the observer's viewing angle for three different half-opening angles of the torus (solid black line: 30°, dashed red line: 45°, and dot-dashed orange line: 60°), defined with respect to the symmetry axis of the model.

2 Polarization modeling

We used the Monte Carlo radiative transfer code STOKES (Goosmann & Gaskell 2007; Marin et al. 2012, 2015) to compute the optical polarization of two different equatorial models, using torus and flared disk morphologies. Both geometries are investigated using a clumpy medium composed of hundreds of constant-density spheres filled with a Milky Way dust mixture. Each optically-thick clump has a radius of 0.3 pc and an optical depth in the V-band of 50. We fixed the filling factor of the models to 25 %. Both geometries have an inner radius of 0.25 pc, a distance to the accretion disk corresponding to the dust sublimation radius for $L_{AGN} \approx 4 \times 10^{44}$ erg s^{-1}, assuming T = 1500 K for the dust sublimation temperature (Barvainis 1987). Note that, since here we are interested in polarization only, and not thermal dust re-emission, the actual AGN luminosity used in the models does not matter. The outer radius of the torus is not fixed by the unified model of AGN and is thought to span from a couple of parsecs to about 100 pc. Recent observations (Gandhi et al. 2015) and studies (Marin et al. 2015) tend to rule out extended dusty structures along the equator but this needs to be investigated further. This is particularly true as infrared spectral energy distributions are often not able to provide constraints on the outer dust radius (e.g. Alonso-Herrero et al. 2011). Hence, we adopt two different outer radii for our models; either 100 pc or 6 pc (Heymann & Siebenmorgen 2012). We allow the torus half-opening angle to vary between 30°, 45°, and 60°, with respect to the symmetry axis of the model. Finally, we simulate the irradiating continuum using an isotropic point-like source emitting an unpolarized flux according to power-law intensity spectrum $F_* \propto \nu^{-\alpha}$ with $\alpha = 1$.

2.1 Fragmented tori

The resulting 2000 – 8000 Å polarization degree P and polarization angle Ψ of different fragmented tori are integrated and plotted in Fig. 1 against the inclination of the observer. An inclination of 0° corresponds to a pole-on view and 90° corresponds to an edge-on viewing angle.

In the case of an extended clumpy torus (Fig. 1 left column), the resulting polarization P increases with inclination, up to a maximum value that depends on the half-opening angle of the system. A maximum of

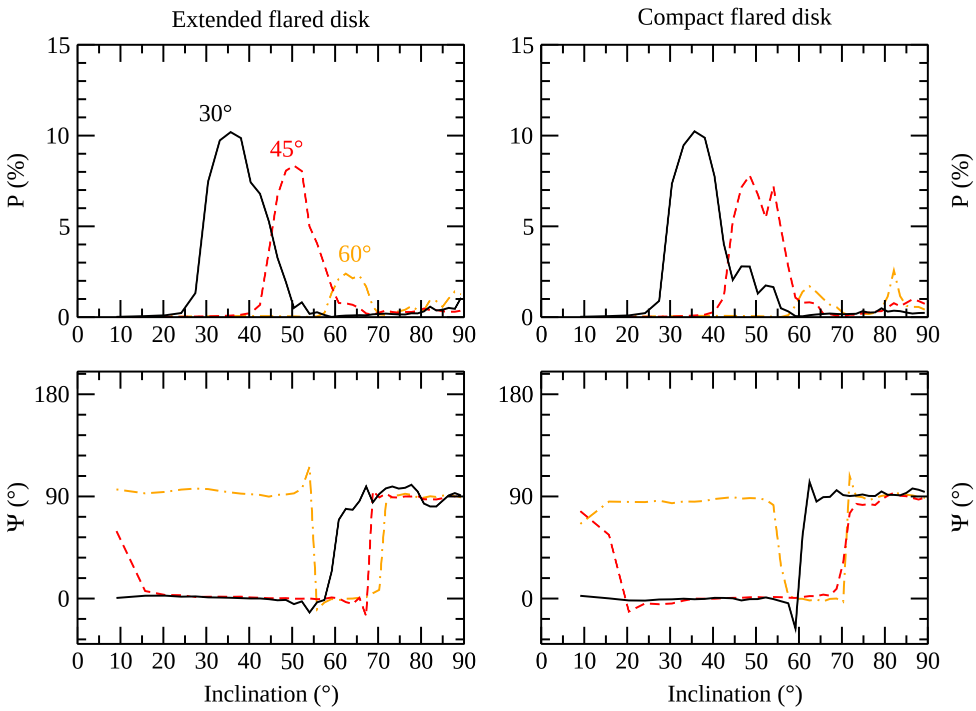

Fig. 2. Same as Fig. 1, but for fragmented flared disks.

2 % is detected at extreme inclinations for tori with large half-opening angles. This is the result of multiple scattering between the dust clouds in an environment that enables radiation to escape even at inclinations where obscuration is maximum. The associated polarization position angle is equal to 90°, i.e. parallel to the projected symmetry axis of the torus. This is a geometrical effect predicted by Kartje (1995) and already reproduced in Marin et al. (2015), where photons scatter off the side walls of the dust structure and naturally yield parallel Ψ values.

Looking at compact dusty tori (Fig. 1 right column), the maximum value of P is lower (~ 1 %) but does not peak as in the case of extended tori. This is due to the compactness of the model: the torus being smaller in diameter while sustaining a similar height (scaled with the half-opening angle), the region has a less oblate morphology. Hence, the angular dependence of opacity provides higher obscuration at intermediate inclinations and radiation escapes with more difficulty from the funnel. This geometrical effect also has an impact on the polarization angle as photons do not longer scatter preferentially along the midplane, resulting in polarization position angles orthogonal to the scattering plane for the cases where the half-opening angle of the model is lower than 60°. At large opening angles, where the resulting structure is geometrical flat, scattering will naturally produce parallel polarization angles.

2.2 Fragmented flared disks

The geometry of a flared disk is completely different from a torus, as the ratio of the disk thickness to the distance from the central black hole increases outward. Hence, we expect different signatures in terms of polarization.

Fig 2 (left column) shows the polarization resulting from an extended flared disk. P drastically increases at viewing angles that matches the half-opening angle of the flared disk, with a maximum polarization degree of ~ 10 % for a geometrically puffed-up region. The low P before this peculiar inclination is due to a direct view of the central engine, that emits unpolarized photons, hence diluting the net polarization percentage. The decrease of P when the observer's line-of-sight exceeds the flared disk horizon is due to canceling contribution of radiation with a perpendicular polarization angle scattered from the inner walls of the disk and photons scattered along the midplane, thus carrying a parallel Ψ. This trend can be observed in the polarization angle plot (Fig 2 bottom left), where the competition between parallel and perpendicular polarization drives the resulting P. At maximum inclinations, $\Psi = 90°$, such as in the torus cases, for the same reasons: the gaps between the clouds allow photons that have scattered close to the equator to escape, carrying a parallel polarization position angle.

Focusing on compact flared disks (Fig 2 right column), we find very similar results. This is due to the fact that reducing the outer radius of the dusty region does not change its global geometry. The amount of P and the inclination-dependent behavior of Ψ are thus the same as in the case of an extended flared disk.

3 Discussion and conclusion

The radiative transfer modeling undertaken in this lecture note confirms that polarization is a unique tool to distinguish between various dusty equatorial morphologies. The polarization signatures of clumpy tori and flared disks qualitatively and quantitatively show contrasts: a torus cannot produce as high degrees of polarization as a flared disk (especially for half-opening angles lower than 60°), and their inclination-dependent Ψ signatures are clearly different. Polarimetry also allows to put constraints on the outer radius of toroidal structures as varying their maximal extension impacts their net polarization. In the case of fragmented flared disks, changing the outer dust radius results in no polarimetric differences due to the geometry of the system: squeezing its width does not alter the maximal height of the disk, in contrast to tori.

The high polarization degrees found for flared disk models (up to 10 %), when the observer's line-of-sight is grazing the edge of the disk, is a feature that might have an impact onto a more complete AGN model. In particular, this could be a hint to explain the high (> 2 %) polarization degrees of some type-1 AGN (e.g. Fairall 51, IC 4329A or Mrk 1239, see Marin 2014). As shown on Fig. 2 (top row), this would be also consistent with the perpendicular polarization position angle found for most (but not all) of those highly polarized Seyfert-1s. It implies that those objects would be seen at a very limited inclination range. However, this hypothesis must be explored in details with more complete AGN modeling, as the polarimetric results might change when equatorial and polar electron scattering regions are added.

This work has been supported by the COST Action MP1104 "Polarization as a tool to study the Solar System and beyond". MS acknowledges support by FONDECYT through grant No. 3140518 and Ministry of Education, Science and Technological Development of the Republic of Serbia through the projects Astrophysical Spectroscopy of Extragalactic Objects (176001) and Gravitation and the Large Scale Structure of the Universe (176003).

References

Alonso-Herrero, A., Ramos Almeida, C., Mason, R., et al. 2011, ApJ, 736, 82
Antonucci, R. R. J. & Miller, J. S. 1985, ApJ, 297, 621
Baes, M., Verstappen, J., De Looze, I., et al. 2011, ApJS, 196, 22
Barvainis, R. 1987, ApJ, 320, 537
Camps, P. & Baes, M. 2015, Astronomy and Computing, 9, 20
Gandhi, P., Hoenig, S. F., & Kishimoto, M. 2015, ArXiv e-prints [arXiv] 1502.02661
Goosmann, R. W. & Gaskell, C. M. 2007, A&A, 465, 129
Heymann, F. & Siebenmorgen, R. 2012, ApJ, 751, 27
Jaffe, W., Meisenheimer, K., Röttgering, H. J. A., et al. 2004, Nature, 429, 47
Kartje, J. F. 1995, ApJ, 452, 565
Krolik, J. H. & Begelman, M. C. 1988, ApJ, 329, 702
Marin, F. 2014, MNRAS, 441, 551
Marin, F., Goosmann, R. W., & Gaskell, C. M. 2015, A&A, 577, A66
Marin, F., Goosmann, R. W., Gaskell, C. M., Porquet, D., & Dovčiak, M. 2012, A&A, 548, A121
Miller, J. S. & Goodrich, R. W. 1990, ApJ, 355, 456
Pier, E. A. & Krolik, J. H. 1992, ApJ, 399, L23
Stalevski, M., Fritz, J., Baes, M., Nakos, T., & Popović, L. C. 2012, MNRAS, 420, 2756
Wittkowski, M., Kervella, P., Arsenault, R., et al. 2004, A&A, 418, L39
Wolf, S. & Henning, T. 1999, A&A, 341, 675
Young, S. 2000, MNRAS, 312, 567

SF2A 2015
F. Martins, S. Boissier, V. Buat, L. Cambrésy and P. Petit (eds)

STUDY OF THE X-RAY ACTIVITY OF SGR A* DURING THE 2011 XMM-NEWTON CAMPAIGN

Enmanuelle Mossoux[1], Nicolas Grosso[1], Frédéric H. Vincent[2] and Delphine Porquet[1]

Abstract. Sgr A* is the closest supermassive black hole ($\sim 4 \times 10^6$ M$_\odot$) located at the dynamical center of our galaxy. It has a very low bolometric luminosity ($\sim 9.4 \times 10^{-9}$ times the Eddington luminosity) and, consequently, a very low mass accretion rate ($\sim 10^{-6}$ M$_\odot$/yr) but flaring activity can be observed in near-infrared, X-ray, sub-millimeter and radio. To constrain the origin of such events, it is important to investigate the timing and spectral properties of these flares, especially in X-rays. During the 2011 XMM-Newton campaign (whose total exposure was ∼226 ks) in coordination with the 1.3 mm Very-Long-Baseline Interferometry array, two X-ray flares have been observed in the $2 - 10$ keV energy band. To perform the timing analysis of the light curves, we apply the Bayesian-blocks method to the XMM-Newton event lists, using a two-step algorithm to correct for any detector flaring background. Furthermore, we compute X-ray smoothed light curves in order to have better accuracy on the substructures and the amplitude of the flares. The first X-ray flare was observed on March 30, 2011 with a peak amplitude of about 3 times the non-flaring level. It is characterized by two sub-flares: the first one is very short (∼458 s) with an unabsorbed peak-luminosity of $\sim 9.4 \times 10^{34}$ erg s^{-1}, whereas the second one is longer (∼1542 s) with a lower unabsorbed peak- luminosity ($\sim 6.8 \times 10^{34}$ erg s^{-1}). The waiting time between the two sub-flares (∼1000 s) is one of the smallest ever observed. If we compare this value with those observed during the 2012 Chandra XVP campaign, we can favor the hypothesis that this event is a single flare rather than two distinct sub-flares. We developed a hotspot model to explain the double-peaks shape of the light curve of this flare with the gravitational lensing and Doppler boosting. However, the decrease of the flux back to the quiescent level between the two substructures cannot be satisfactorily reproduced with this simple model. This observation allows us to reject this flaring model even when it is made slightly more complex than a simple hotspot. The very rapid flux variation during the first sub-flare allow us to constrain the distance and the size of the flaring source. Since the proper time around a supermassive black hole is always longer than the observed duration due to the time dilatation in strong gravity field and assuming that the rise and decay phases are due to magnetic energy heating and synchrotron cooling of infrared photons, respectively, we derive a range to the radial distance of $4 - 100(+19, -29)$ rg with rg=0.04 AU. The corresponding source radii at this distance are $1.8 - 2.87 \pm 0.01$ rg.

Keywords: Galaxy: center, X-rays: Sgr A*, radiation mechanisms: general

1 Introduction

Our Galaxy hosts Sgr A* the closest supermassive black hole at a distance of about 8 kpc (Genzel et al. 2010; Falcke & Markoff 2013). It has a mass $M_{\rm BH} = 4 \times 10^6\ M_\odot$ (Schödel et al. 2002; Ghez et al. 2008; Gillessen et al. 2009) and is usually in a steady state, emitting predominately at radio to submillimeter wavelengths. The detections of flares from Sgr A* have provided a valuable way to scrutinize accreting matter close to the event horizon. The X-ray flare frequency is 1.1 (1.0-1.3) flare per day with $L_{2-8\ \rm keV} \geq 10^{34}$ erg s^{-1} (Neilsen et al. 2013). The bulk of X-ray flares detected so far have faint-to-moderate amplitudes (Baganoff et al. 2003; Neilsen et al. 2013), and three very bright flares have been observed to share very similar spectral properties (Porquet et al. 2003, 2008; Nowak et al. 2012). When near-infrared (NIR) and X-ray flares are detected simultaneously, their light curves have similar shapes, and there is no apparent delay (< 3 min) between the peaks of flare

[1] Observatoire Astronomique de Strasbourg, Université de Strasbourg, CNRS, UMR 7550, 11 rue de l'Université, F-67000 Strasbourg, France.
[2] Nicolaus Copernicus Astronomical Center, ul. Bartycka 18, 00-716 Warszawa, Poland.

© Société Francaise d'Astronomie et d'Astrophysique (SF2A) 2015

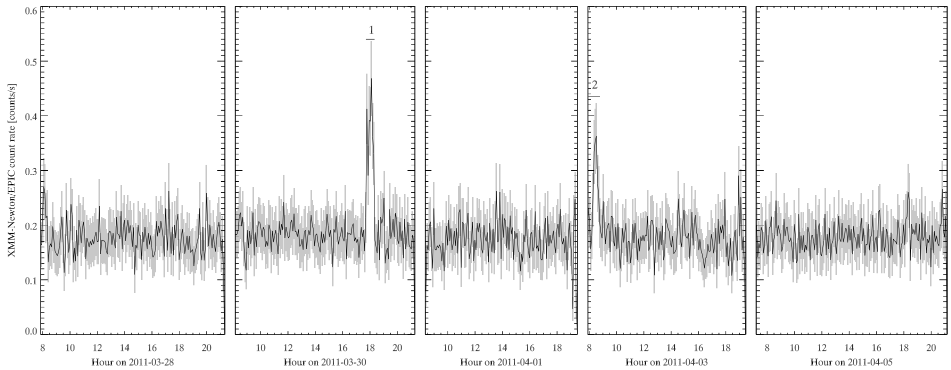

Fig. 1. pn+MOS1+MOS2 light curves of Sgr A* in the 2−10 keV energy range binned on 300 s. The X-ray flares are labeled from 1 to 2. The horizontal lines below these labels are the flare durations.

emission (e.g., Yusef-Zadeh et al. 2006; Dodds-Eden et al. 2009; Eckart et al. 2012). The current interpretation is that both X-ray/NIR flares come from a region close to the event horizon, while delayed sub-mm (e.g., ≈ 100 min; Marrone et al. 2008) and mm peaks (up to 5 hours; Yusef-Zadeh et al. 2009) have been interpreted as the adiabatic cooling of an expanding relativistic plasma blob. While NIR flares are known to be due to synchrotron emission (Eisenhauer et al. 2005; Eckart et al. 2006), the X-ray flare emission mechanism has not been settled yet, with arguments for synchrotron (Dodds-Eden et al. 2009; Barrière et al. 2014), inverse Compton (Yusef-Zadeh et al. 2012), and synchrotron self-Compton (Eckart et al. 2008) models.

We report here the results published in Mossoux et al. (2015a,b) of the 2011 XMM-Newton campaign for Sgr A* observation.

2 XMM-Newton observations: data processing and timing analysis

The 2011 observational campaign of Sgr A* with XMM-Newton (AO-8, 5×33 ks; PI: D. Porquet) was scheduled on 2011 Mar. 28 and 30 and Apr. 1, 3, and 5 for a total effective exposure of ≈ 226 ks. The data were reduced using the Science Analysis Software (SAS) package (v.13.5 and CCF of 04/04/2014) and filtered in the 2−10 keV energy range. The pn on-axis Half Energy Width is $\approx 20''$ at 1.5 keV (Ghizzardi 2002). To extract the events coming from Sgr A*, we thus define the source+background (src+bkg) region as a $10''$-radius disk around the VLBI radio position of Sgr A* (Reid et al. 1999). For each observation and detector, we first built the src+bkg and the bkg (extracted from a $3'\times 3'$ region on the same CCD) light curves. After applying relative corrections, we create the bkg-subtracted light curves. Finally, the light curves of the three detectors were summed to produce the total light curve shown in Fig. 1.

To identify the flaring and non-flaring levels under a certain probability using the *unbinned* event arrival time, we used the Bayesian blocks analysis proposed by Scargle (1998) and improved by Scargle et al. (2013a). This recursive algorithm performs a segmentation of the event list into blocks with statistically different count-rates levels. The time defining two successive blocks is called a change point. To use this algorithm, we have to calibrate the prior estimate of the number of change points to the false detection probability ($p = e^{-3.5}$; Neilsen et al. 2013; Nowak et al. 2012) and the number of points in the observation. We also correct the blocks count rate from the observation time lost during the CCD read out and we reject the time where the camera did not observe. The blocks count rate is also corrected from the background count rate by applying successively the Bayesian blocks algorithm on the bkg and src+bkg region and then applying the algorithm on the src+bkg region with a weight adjusting the Voronoi time-interval in order to subtract the average background (Scargle et al. 2013b). The non-flaring level is defined as the count rate of the longest block and the flaring levels are the highest blocks. This algorithm gives us the duration of the flaring and non-flaring levels with better accuracy than in a binned light curve since it uses the best temporal resolution available. Moreover, it has a better detection efficiency compared to previous methods which only detect a flare if its peak on the binned light curve is higher than 3 times the standard deviation of the non-flaring light curve. The Bayesian blocks analysis is applied independently on each cameras. The non flaring level is about 0.18 count s^{-1} during all observations which is consistent with the one previously observed with XMM-Newton (e.g., in 2007, Porquet et al. 2008). Two X-ray flares are detected on 2011 Mar. 30 and Apr. 3.

To improve the characterization of the amplitude and the time of a local maximum or minimum, we compute a smoothed light curve by applying a density estimator (Silverman 1986; Feigelson & Babu 2012) on the *unbinned* event arrival times. We use the Epanechnikov kernel (inverse parabola shape) with a window width of the kernel

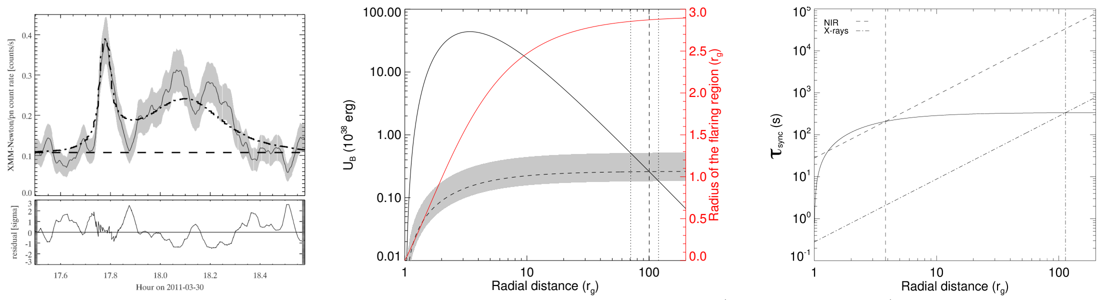

Fig. 2. *Left panel:* Best-fitting theoretical light curve of a rotating hotspot (dot-dashed line) plotted over the pn smoothed light curve (solid line, with 1σ error in gray) of the 2011 Mar. 30 flare. The non-flaring level is the horizontal dashed line. The lower panel gives the residual in units of the standard deviation of the binned light curve. *Middle panel:* Magnetic energy vs. radial distance. The solid line is the distribution of the magnetic energy (left y-axis). The dashed line and gray band are the flare total energy and its errors with 90% confidence level, respectively. The vertical lines are the upper limits to the distance. The red line is the radius of the emitting region (right y-axis). *Right panel:* Synchrotron cooling time vs. radial distance. The solid line is $\Delta\tau_{\rm decay}(r)$. The vertical lines are the lower limits to the radial distance.

of 100 s since it is defined on a finite support which allows us to control any boundary effects. The density estimator is also corrected from the background count rate by applying the same weight than for the Bayesian blocks analysis. The error of the smoothed light curve is assumed to be Poissonnian. The smoothed light curve of the first flare is superimposed to the binned light curve in Fig. 2 (left panel). This flare has 211 ± 25 counts and an amplitude of 0.284 ± 0.013 count s^{-1} (computed using the smoothed light curve). It is characterized by two components: a short (~ 458 s) and symmetrical subflare and a longer (~ 1542 s) and fainter symmetrical subflare separated by only ~ 1000 s. Between these two subflares, the smoothed light curve returns to a level consistent with the non-flaring state during less than 100 s. The second flare has more than 154 ± 24 counts and an amplitude of 0.165 ± 0.012 count s^{-1}.

3 Gravitational lensing of a hotspot-like structure

We modeled the two subflares of the 2011 Mar. 30 flare with a single mechanism since its shape could be the signature of a gravitational lensing of a hotspot-like structure: the primary maximum is the gravitational lensing of the light emitted by the hotspot when it is on the opposite side of the black hole with respect to the observer whereas the secondary maximum is the relativistic beaming of the light emitted when the source is moving toward the observer. The hotspot has a spherical and optically thin structure in solid rotation around the black hole with Keplerian angular velocity and its emitted spectrum is assumed to follow a power law. Maps of the observed spectrum were computed by using the open-source ray-tracing code `GYOTO` (Vincent et al. 2011). The light curve is obtained by summing each of these maps over all pixels and solid angle to compute a flux. Our hotspot model is defined by three physical parameters: the orbital radius r, the hotspot radius R and the black hole inclination i. The spin parameter has a low impact on the light curve, thus it is fixed to $a = 0.99$. The left panel of Fig. 2 shows the best fit that is found for the following values: $r = 12r_{\rm g}, R = 1.4r_{\rm g}, i = 86.5°$ with $r_{\rm g} = 0.04$ au the gravitational radius ($\chi^2_{red} = 0.85$). This figure clearly shows that the local minimum of the light curve, in between the two bumps at around 17.53 h, is not well fit by the hotspot model. This inadequacy is sufficient to reject this simple model without adding some ad hoc new components since a hotspot-like model will always produce a local minimum at a higher level than the non-flaring level.

4 Constraining the radial distance of the first 2011 Mar. 30 subflare

We consider that the short duration of the rise phase of the first subflare ($\Delta t_{\rm rise} = 115$ s) places a limit to the size of the flaring region (e.g., Dodds-Eden et al. 2009). We compute the proper-to-observed time ratio ($\Delta\tau(r) > \Delta t$) due to time dilation in strong gravity field.

We constrain the radius of the spherical flaring region by considering that the Alfven velocity cannot be higher than the speed of light (Dodds-Eden et al. 2009): $R < c\Delta\tau_{rise}$. This leads to an upper limit on the volume V of the flaring region used to compute the magnetic energy: $U_{\rm B} = \frac{B^2 V}{8\pi}$ with $B = B_{1R_{\rm S}} 2r_{\rm g}/r$ the magnetic field vs. the radial distance r (see Barrière et al. 2014, and references therein). The average luminosity of the first subflare is $L^{\rm unabs}_{2-10\ {\rm keV}}({\rm flare}) = 5.8^{+5.7}_{-1.7} \times 10^{34}$ erg s^{-1}. If we assume a maximum efficiency, the upper limit to the radial distance is obtained from the balance between the flare total energy and the magnetic energy. The result is $r < 100^{+19}_{-29}\ r_{\rm g}$ and the corresponding radius of the flaring region at this distance is $R = 2.87 \pm 0.01\ r_{\rm g}$

(see Fig. 2, middle panel).

The electrons that are accelerated by the release of the magnetic energy cool by emitting synchrotron radiation with the following timescale: $\tau_{\rm sync} = 8\ (B/30\ {\rm G})^{-3/2}\ \left(\nu/10^{14}\ {\rm Hz}\right)^{-1/2}$ min (Dodds-Eden et al. 2009). This synchrotron cooling timescale must be equal to the decay time of the first subflare. If the X-ray photons are the primary source of synchrotron cooling, we derive $r > 114\ r_{\rm g}$, which is not consistent with the previously derived upper limit since sustained heating must also be present during the decay phase. Thus, we consider the synchrotron cooling time of NIR photons which leads to $r > 4\ r_{\rm g}$ with the flaring region outside the event horizon.

5 Conclusions

We have reported the data analysis of the XMM-Newton 2011 campaign for the observation of Sgr A*. We used the Bayesian-blocks algorithm and a density estimator applied on the unbinned event arrival time to constrain the duration, the position, and the amplitude of the X-ray flares with better accuracy. We observed two X-ray flares: on 2011 Mar. 30 and Apr. 03. The first flare is composed of two subflares: a very short-duration one and a longer and less luminous one. We modeled its two subflares with a single physical phenomenon using the gravitational lensing of a hotspot-like structure. However, the consistency of the observed flux level between the two subflare peaks with the non-flaring level led us to conclude that the light curve of this X-ray flare cannot satisfactorily be reproduced by a gravitational lensing event. Using the short duration of the first 2011 Mar. 30 subflare, we conclude that $4\ r_{\rm g} < r < 100^{+19}_{-29}\ r_{\rm g}$ in this subflare for $B_{1R_{\rm S}} = 100$ G. The corresponding radii of the flaring region at these distances are $1.8\ r_{\rm g} < R < 2.87 \pm 0.01\ r_{\rm g}$.

References

Baganoff, F. K., Maeda, Y., Morris, M., et al. 2003, ApJ, 591, 891
Barrière, N. M., Tomsick, J. A., Baganoff, F. K., et al. 2014, ApJ, 786, 46
Dodds-Eden, K., Porquet, D., Trap, G., et al. 2009, ApJ, 698, 676
Eckart, A., Baganoff, F. K., Schödel, R., et al. 2006, A&A, 450, 535
Eckart, A., García-Marín, M., Vogel, S. N., et al. 2012, A&A, 537, A52
Eckart, A., Schödel, R., García-Marín, M., et al. 2008, A&A, 492, 337
Eisenhauer, F., Genzel, R., Alexander, T., et al. 2005, ApJ, 628, 246
Falcke, H. & Markoff, S. B. 2013, Classical and Quantum Gravity, 30, 244003
Feigelson, E. D. & Babu, G. J. 2012, Modern statistical method for astronomy with R applications, ed. Cambridge University Press (Cambridge, UK)
Genzel, R., Eisenhauer, F., & Gillessen, S. 2010, Reviews of Modern Physics, 82, 3121
Ghez, A. M., Salim, S., Weinberg, N. N., et al. 2008, ApJ, 689, 1044
Ghizzardi, S. 2002, In flight calibration of the PSF for the pn camera (EPIC-MCT-TN-012), Tech. rep.
Gillessen, S., Eisenhauer, F., Fritz, T. K., et al. 2009, ApJ, 707, L114
Marrone, D. P., Baganoff, F. K., Morris, M. R., et al. 2008, ApJ, 682, 373
Mossoux, E., Grosso, N., Vincent, F. H., & Porquet, D. 2015a, A&A, 573, A46
Mossoux, E., Grosso, N., Vincent, F. H., & Porquet, D. 2015b, A&A, 580, C2
Neilsen, J., Nowak, M. A., Gammie, C., et al. 2013, ApJ, 774, 42
Nowak, M. A., Neilsen, J., Markoff, S. B., et al. 2012, ApJ, 759, 95
Porquet, D., Grosso, N., Predehl, P., et al. 2008, A&A, 488, 549
Porquet, D., Predehl, P., Aschenbach, B., et al. 2003, A&A, 407, L17
Reid, M. J., Readhead, A. C. S., Vermeulen, R. C., & Treuhaft, R. N. 1999, ApJ, 524, 816
Scargle, J. D. 1998, ApJ, 504, 405
Scargle, J. D., Norris, J. P., Jackson, B., & Chiang, J. 2013a, ApJ, 764, 167
Scargle, J. D., Norris, J. P., Jackson, B., & Chiang, J. 2013b, 2012 Fermi Symp. Proc. – eConf C121028 [arXiv:1304.2818v1]
Schödel, R., Ott, T., Genzel, R., et al. 2002, Nature, 419, 694
Silverman, B. W. 1986, Density Estimation for Statistics and Data Analysis, ed. C. . Hall (Chapman & Hall)
Vincent, F. H., Paumard, T., Gourgoulhon, E., & Perrin, G. 2011, Classical and Quantum Gravity, 28, 225011
Yusef-Zadeh, F., Bushouse, H., Wardle, M., et al. 2009, ApJ, 706, 348
Yusef-Zadeh, F., Roberts, D., Wardle, M., Heinke, C. O., & Bower, G. C. 2006, ApJ, 650, 189
Yusef-Zadeh, F., Wardle, M., Dodds-Eden, K., et al. 2012, AJ, 144, 1

SF2A 2015
F. Martins, S. Boissier, V. Buat, L. Cambrésy and P. Petit (eds)

A STUDY OF THE CYG X-1 SPECTRAL COMPONENTS IN RADIO, X, AND γ-RAYS: HIGH ENERGY POLARIMETRY, SPECTROSCOPY, AND THE RELATION WITH THE SPECTRAL STATE

J. Rodriguez[1], V. Grinberg[2], P. Laurent[3], Marion Cadolle Bel[4], Katja Pottschmidt[5], Guy Pooley[6], Arash Bodaghee[7], Jörn Wilms[8] and Christian Gouiffès[1]

Abstract. We present an analysis of AMI-Ryle (15 GHz) and INTEGRAL (0.01–2 MeV) observations of Cygnus X-1 performed between early 2003 and late 2012. The observations are separated into distinct spectral states thanks to a model-independent approach based on data acquired with All Sky Monitors. The multi-wavelength state-dependent properties of the source are then studied: a compact radio jet is detected in the hard and intermediate states and is absent in the soft state. We clearly detect a high energy tail dominating the 0.4–2 MeV emission in the hard state. This component is highly polarized and we suggest it to be the signature of jet emission at high energies.

Keywords: accretion, accretion disks, black hole physics, stars: individual (Cyg X-1), X-ray binaries, radio observations, X-ray observations, polarimetry

1 Introduction

The black hole binary (BHB) Cygnus X-1 (Cyg X-1) was the first Galactic source thought to host a black hole hole (Bolton 1975). Recent estimates led to a black hole mass of $\mathrm{M_{BH}} = 14.8 \pm 1.0\,\mathrm{M_\odot}$ (Orosz et al. 2011). The donor star is HDE 226868 (Bolton 1972; Walborn 1973) an O supergiant star. This system is located at a distance of $d = 1.86 \pm 0.12\,\mathrm{kpc}$ from Earth (Reid et al. 2011; Xiang et al. 2011), making it one of the closest BHBs known so far.

Although Cyg X-1 has a high mass companion, a difference compared to most BHBs, the presence of a variable accretion disc, a corona, and jets make it a prototypical object to study the properties of accretion flows, and their connections with ejections of material. Spectral states were indeed first defined from the spectra observed in this source: Cyg X-1 can be found in both the so-called "low" hard state (LHS) or "high" soft state (HSS); between 2003 and 2010 it was predominantly in the LHS. between 2010 and 2014 (**TBC**) Cyg X-1 spent most of its time in the HSS (e.g. Grinberg et al. 2013). Partial (or "failed") transitions from the LHS to the HSS, during which Cyg X-1 and can be found in a transitional or intermediate state (IS, e.g., Pottschmidt et al. 2003), are sometimes seen. Cyg X-1 belongs to the pair of Galactic microquasars where compact relativistic jets in the LHS have directly been imaged with VLBI technics (Stirling et al. 2001).

In Cyg X-1 the presence of a high energy spectral tail extending up to the MeV domain is known for almost 20 years (e.g. Grove et al. 1998). Its presence has recently been confirmed with the two main instruments onboard the ESA's INTErnational Gamma-Ray Astrophysics Laboratory (*INTEGRAL*) by Cadolle Bel et al. (2006) and Laurent et al. (2011) with IBIS, and Jourdain et al. (2012) with SPI. In Laurent et al. (2011), we have shown that the $\geq 400\,\mathrm{keV}$ emission of Cyg X-1 was polarized at a level of about 70%, a result independently confirmed by Jourdain et al. (2012) using SPI data. Both studies, however, made use of the whole dataset available at the time of their publication regardless of the source spectral state.

[1] Laboratoire AIM, CEA-Saclay, France
[2] MIT, Cambridge, USA
[3] Laboratoire APC & CEA-Saclay, Paris, France
[4] Max Planck Computing and Data Facility, Garching, Germany
[5] CRESST, University of Maryland, Baltimore & NASA GSFC, Greenbelt, USA
[6] Astrophysics, Cavendish Laboratory, Cambridge, UK
[7] Georgia College & State University, Milledgeville, USA
[8] Dr. Karl Remeis-Sternwarte and ECAP, Friedrich Alexander Universität Erlangen-Nürnberg, Bamberg, Germany

© Société Francaise d'Astronomie et d'Astrophysique (SF2A) 2015

2 Separation of the data into spectral states

In order to improve the analysis and the understanding of the origin of hard X-ray tails it is important to separate the observations by spectral states. This way the spectral parameters and, hence, the properties of the emitting media, are not mixed and can be better interpreted. We used model-independent criterion based on all-sky monitors that is fully described and tested in Grinberg et al. (2013) to separate all the *INTEGRAL* (0.02–2 MeV) and AMI-Ryle (15 GHz) observations of Cyg X-1 obtained between 2003 and December 2012. The details of the data reduction are given in Rodriguez et al. (2015). Fig. 1 shows the Ryle-AMI (15 GHz) and *INTEGRAL*/IBIS (20–40 keV) long term light-curves with a color coding indicating the spectral state of the source as deduced with the above criteria (see Grinberg et al. 2013; Rodriguez et al. 2015, for all details of the method and the application to the current dataset).

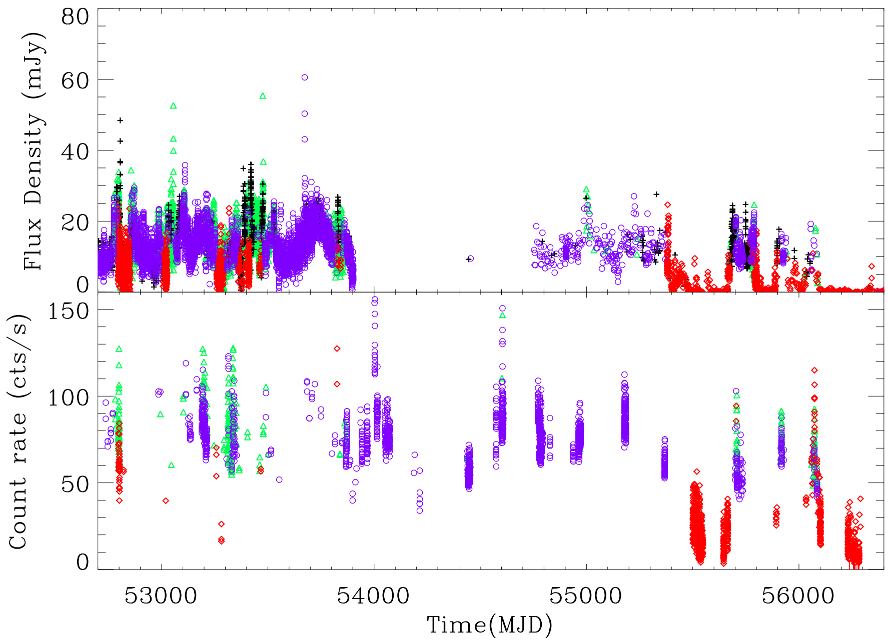

Fig. 1. Long-term 15 GHz Ryle-AMI (upper panel) and 20–40 keV *INTEGRAL*/IBIS (lower panel) light curves of Cyg X-1. The color coding indicates the spectral state of the source: purple is for the LHS, green for the IS, red for the HSS, and black shows observations where a classification was not possible.

3 State dependent analysis

3.1 Radio behavior: a compact jet in the LHS

Cyg X-1 is very variable in radio (Fig. 1). It shows quiescent periods, periods with relatively steady activity and flares. Our spectral classification shows that, as in other sources, the specific radio behavior is related to the spectral state: little or no radio emission is seen in the HSS, while the LHS is associated with a definite radio activity. Flares seem to occur in conjunction with or close to transitions from one state to another. Considering the entire data base we estimate the following mean state resolved radio fluxes: $\langle F_{15\,\mathrm{GHz,LHS}}\rangle = 13.5\,\mathrm{mJy}$, $\langle F_{15\,\mathrm{GHz,IS}}\rangle = 15.4\,\mathrm{mJy}$, and $\langle F_{15\,\mathrm{GHz,HSS}}\rangle \lesssim 9\,\mathrm{mJy}$. The level of radio detection and the relative steadiness of the source is compatible with the presence of a compact jet in the LHS as already seen in this source and others (e.g. Stirling et al. 2001; Corbel et al. 2003; Coriat et al. 2011).

3.2 High energy spectral analysis: a hard tail in the LHS

Fig. 2 shows the state-resolved 0.01–2 MeV *INTEGRAL* spectra. The 0.01–0.4 MeV spectra are all well represented by either a cut-off powerlaw or thermal Comptonization and a reflection component, even though the spectral shapes and fluxes are obviously different (see Rodriguez et al. 2015, for the details of the spectral modeling, and the spectral parameters obtained).

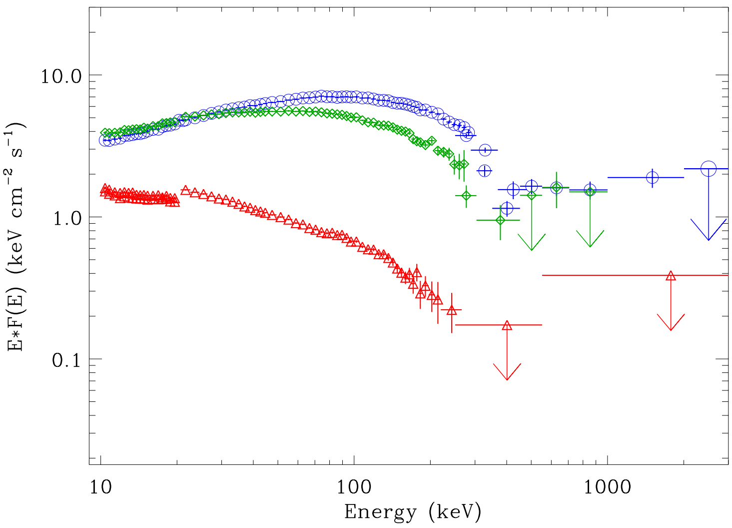

Fig. 2. *INTEGRAL* "ν-Fν" spectra of Cyg X-1 in all three states. Blue is the LHS, green the IS, and red the HSS.

This model, however, fails at reproducing the 0.4–2 MeV LHS spectrum, and the inclusion of an additional $\Gamma = 1.4^{+0.2}_{-0.3}$ power law is needed in this state. The 0.4–1 MeV flux of this component is 1.9×10^{-9} erg cm^{-2} s^{-1}. It is not required in the other states with 3σupper limits of 1.5×10^{-9} erg cm^{-2} s^{-1}and 0.9×10^{-9} erg cm^{-2} s^{-1}in the IS and HSS respectively.

3.3 Polarimetric analysis: a 0.4–1 MeV polarized signal in the LHS

To study the properties of high energy polarization we took advantage of the two-layer nature of the IBIS detectors and consider only the events that interact in both the low and high energy detectors. In case of a polarized signal, Compton diffusion from the upper layer into the lower one preferentially follows a direction perpendicular to the polarization angle (e.g. Forot et al. 2007; Rodriguez et al. 2015, and references therein). By studying the distribution of detected counts with respect to the azimuthal angle (hereafter referred to as polarigrams) one can estimate the level of polarization (if any) and the polarization angle (PA). Fig. 3 shows

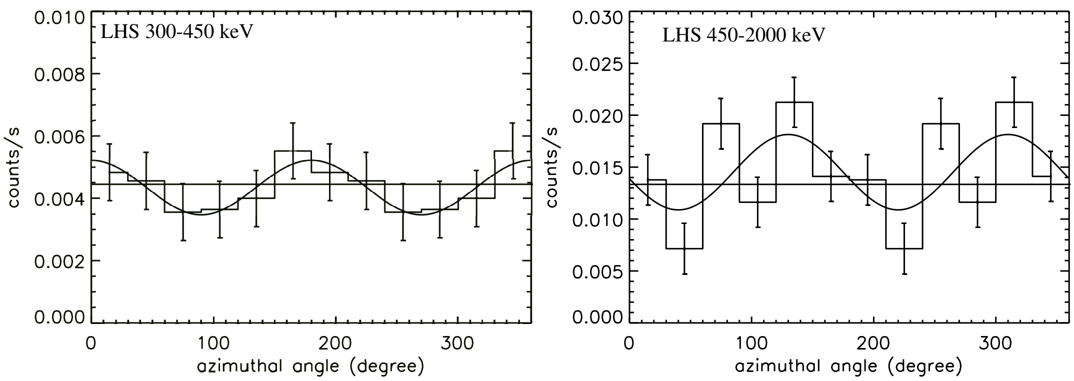

Fig. 3. LHS polarigrams. **Left:** 300–450 keV **Right:** 450–2000 keV.

the polarigrams obtained from the LHS data in two spectral domains, one corresponding to the energies where the source spectrum is dominated by the Comptonized component (below 450 keV) and one where the source spectrum is dominated by the hard tail (above 450 keV). While the lower energy polarigram is compatible with a flat line, the high energy one shows the definite presence of polarized emission. We estimate a polarization fraction of 75±32% with a polarization angle PA=$40° \pm 14°$. We do not detect any polarized signal in the HSS with an upper limit for the polarization fraction of 70% between 0.4–2 MeV. In the IS the short exposure time does not allow us to obtain a meaningful constraint.

4 Conclusions

Our state dependent analysis shows :

- The 0.01–400 keV spectra of Cyg X-1 are well represented by either a cut-off power law or (thermal) Comptonization and a reflection component, with parameters that are clearly distinct from one state to another.
- The presence of a hard tail dominating the 0.4–1 MeV emission in the LHS.
- The hard tail is below the detection sensitivity in the other states and we obtain a 3σ upper limit on the hard tail flux in the HSS that is half the flux emitted in the LHS.
- We detect a clear polarized signal in the 0.4–2 MeV LHS data only. In the other states we estimate an upper limit for the polarized fraction of 70% between 0.4–2 MeV in the HSS, and we do not obtain meaningful constraint in the IS.
- Radio emission is clearly detected in the LHS and in the IS. The level of radio in the HSS is compatible with no or little emission.

The large polarization value implies synchrotron radiation and a very ordered magnetic field. A jet is a natural medium for synchrotron emission, and all models of jets rely on the presence of an ordered magnetic field, and predict synchrotron emission. Our observations do show the presence of a jet in the state where the polarized tail is found. We therefore favor a jet origin for the hard tail polarized component. We note that a coronal origin has recently been suggested as the origin of the polarized signal (Romero et al. 2014). This however relies on an underlying synchrotron emitting medium (taken to be the corona) which undergoes Compton scattering in the corona. While this suggestion opens interesting possibilities, it would need the corona to be highly structured (in its innermost regions) in order to produce the polarized (synchrotron) signal. The coronal optical depth/density also needs to be rather low, to not exceed the low number of Compton scatterings necessary to maintain the high level of polarization. While the cannot completely exclude such a geometry, we think that it needs too much fine tuning, and we clearly favor the interpretation which we think is better supported by observational facts, namely the presence of a jet.

5 Literature citations

References

Bolton, C. T. 1972, Nature, 235, 271
Bolton, C. T. 1975, ApJ, 200, 269
Cadolle Bel, M., Sizun, P., Goldwurm, A., et al. 2006, A&A, 446, 591
Corbel, S., Nowak, M. A., Fender, R. P., Tzioumis, A. K., & Markoff, S. 2003, A&A, 400, 1007
Coriat, M., Corbel, S., Prat, L., et al. 2011, MNRAS, 414, 677
Forot, M., Laurent, P., Lebrun, F., & Limousin, O. 2007, ApJ, 668, 1259
Grinberg, V., Hell, N., Pottschmidt, K., et al. 2013, A&A, 554, A88
Grove, J. E., Johnson, W. N., Kroeger, R. A., et al. 1998, ApJ, 500, 899
Jourdain, E., Roques, J. P., Chauvin, M., & Clark, D. J. 2012, ApJ, 761, 27
Laurent, P., Rodriguez, J., Wilms, J., et al. 2011, Science, 332, 438
Orosz, J. A., McClintock, J. E., Aufdenberg, J. P., et al. 2011, ApJ, 742, 84
Pottschmidt, K., Wilms, J., Nowak, M. A., et al. 2003, A&A, 407, 1039
Reid, M. J., McClintock, J. E., Narayan, R., et al. 2011, ApJ, 742, 83
Rodriguez, J., Grinberg, V., Laurent, P., et al. 2015, ApJ, 807, 17
Romero, G. E., Vieyro, F. L., & Chaty, S. 2014, A&A, 562, L7
Stirling, A. M., Spencer, R. E., de la Force, C. J., et al. 2001, MNRAS, 327, 1273
Walborn, N. R. 1973, ApJ, 179, L123
Xiang, J., Lee, J. C., Nowak, M. A., & Wilms, J. 2011, ApJ, 738, 78

SF2A 2015
F. Martins, S. Boissier, V. Buat, L. Cambrésy and P. Petit (eds)

EQUILIBRIUM OF SELF-GRAVITATING TORI IN SPHERICAL GRAVITATIONAL AND DIPOLAR MAGNETIC FIELDS

A.Trova[1], V. Karas[1], P. Slaný[2] and J. Kovář[2]

Abstract. We investigate a new model for equilibria of self-gravitating fluid tori with electric charge that are embedded in gravitational potential and a dipolar magnetic field produced by the central mass. We find that the shape and the vertical structure of the massive torus are influenced by effects of self-gravity which were neglected in our previous work (Slaný et al. 2013). We show the impact of self-gravity on the morphology of figures of equilibrium, depending on the rotation of the fluid and the strength of the magnetic field.

Keywords: hydrodynamics – tori: rotation – gravitation – methods: numerical – magnetic field.

1 Introduction

In active galactic nuclei (AGN), the study of equilibrium of toroidal figure of perfect fluid are important to understand the physics and structure of accretion discs (Kozlowski et al. 1978; Abramowicz et al. 1978). This subject has been treated in great detail (Stuchlík et al. 2000; Font & Daigne 2002; Kucáková et al. 2011; Slaný et al. 2013; Kovář et al. 2014). AGN are composed of dusty tori and a central compact body that is frequently associated with a supermassive black hole (the mass typically $M \simeq 10^6$–$10^9 M_\odot$ (Krolik 2004; Eckart et al. 2005)). At a distance of 10^4–10^5 gravitational radii ($R_g \equiv GM/c^2 \approx 1.5(M/M_\odot)$ km) these tori become self-gravitating. At the same time this distance is large enough to reduce the effects of General Relativity (essential near the center) to negligible level (Shlosman & Begelman 1987; Huré 1998). Then we can use the Newtonian limit to study the vertical and radial structures of these objects (Frank et al. 1985).

In this paper we describe an approximate model where self-gravity of the torus material, central mass effect and non-vanishing electric charge density interact to define the radial and vertical structure of an equilibrium configuration. The idea is to use the same method as Slaný et al. (2013) and add the term of self-gravity. In section 2, we give the basic equations and assumptions of our work. In section 3, we use these equations to build a toy-model for equilibrium of tori surrounded by a central mass which produce a dipolar magnetic field and a spherical gravitational field. The section 4 is dedicated to the conclusion.

2 Basic equations and hypothesis

2.1 Equilibrium equation

The Bernoulli equation governs the tori equilibrium in the Newtonian limit. It is given by

$$-\frac{1}{\rho_{\rm m}}\vec{\nabla}P - \vec{\nabla}\Psi_{Sg} - \vec{\nabla}\Psi_c - \vec{\nabla}\Phi + \frac{\vec{\mathcal{L}}}{\rho_{\rm m}} = 0, \tag{2.1}$$

where P, Ψ_{Sg}, Ψ_c, Φ, $\mathcal{L} = q\rho_{\rm m} v_\phi \vec{e_\phi}$ and $\rho_{\rm m}$ are the pressure, the self-gravitating potential of the torus, the central mass potential, the rotational potential, the Lorentz force and the mass-density, respectively. The orbital

[1] Astronomical Institute, Academy of Sciences, Boční II, Prague, CZ-141 31, Czech Republic
[2] Institute of Physics, Faculty of Philosophy and Science, Silesian University in Opava Bezručovo nám. 13, CZ-746 01 Opava, Czech Republic

© Société Francaise d'Astronomie et d'Astrophysique (SF2A) 2015

Test 1 $d_{\rm t} = 0$	$b = 1.44$, $c = -0.5$ and $r_c = 25 \to e \sim 0.439$ and $a \sim 7.33 \times 10^{-2}$
Test 2 $d_{\rm t} = 0.1$	$b = 1.44$, $c = -0.5$ and $r_c = 25 \to e \sim 0.409$ and $a \sim 0.147$
Test 3 $d_{\rm t} = 0.5$	$b = 1.44$, $c = -0.5$ and $r_c = 25 \to e \sim 0.285$ and $a \sim 0.443$.

Table 1. Description of the three tests for equatorial tori..

velocity $v_\phi = \frac{K_2}{R}$ for a constant angular velocity ($K_2 = \text{const}$), q is the specific charge. After a first integration, we can write

$$\frac{P}{\rho_{\rm m}} + \Psi_{Sg} + \Psi_c + \Phi + M = \text{Const} \tag{2.2}$$

where M' is the "magnetic potential" given by $\vec{\nabla} M' = -\frac{\vec{\mathcal{L}}}{\rho_{\rm m}}$.

2.2 Hypothesis

We assumed that the fluid is stationary, axially symmetrical and symmetric with respect to the mid-plane. We are working with an orbital velocity profile with constant angular momentum. Then the centrifugal potential is given by $\Phi = \frac{K_2^2}{2R^2}$. The fluid is incompressible, $\rho_{\rm m} = \text{const}$ and is embedded in an external dipolar magnetic field, which is given, in cylindrical coordinates, by

$$B_R = \frac{3\mu Z R}{\sqrt{R^2+Z^2}^5}, \quad B_\phi = 0, \quad B_Z = \frac{\mu(2Z^2 - R^2)}{\sqrt{R^2+Z^2}^5}. \tag{2.3}$$

Lastly we work with a specific charge distribution, $q(R, Z)$, described in Slaný et al. (2013) (named family II). In cylindrical coordinates (R, θ, Z),

$$q(R, Z) = C \left(\frac{R}{\sqrt{R^2+Z^2}}\right)^3 \tag{2.4}$$

with $C = \text{Const}$.

3 Influence of self-gravity

Normalization of equation (2.1) is given by

$$a\tilde{P} = -d_{\rm t}\tilde{\Psi}_{\rm Sg} - \tilde{\Psi}_c - b\tilde{\Phi} - e\tilde{M} + c, \tag{3.1}$$

with a, b, $d_{\rm t}$, e and c constants which depend on various parameters,such as the central mass, the torus mass, the rotation law, the specific charge and the radius of pressure maximum r_c. In particular, the constant $d_{\rm t}$ is the ratio of the torus mass with the central mass. It represents the strength of self-gravity. It is the main parameter of our work. We are going to vary with this parameter to see the influence of the self-gravity on the morphology of the equilibrium solutions. The tori equilibrium exists only if it can exist a maximum of pressure (mathematical conditions on the function $\tilde{P}$ given by equation 3.1). According to this conditions, we have two possibilities. The equilibrium can exist (1) for equatorial tori, and (2) for off-equatorial tori.

3.1 Equatorial tori

The method is to select a value for the maximum of pressure ($R = r_c, Z = 0$) and check if the mathematical conditions are valid. Next, we have to impose a value for the constants b, c and $d_{\rm t}$. The value of e are given by the conditions and a is the maximum of pressure. To see the influence of self-gravity, we vary the parameter $d_{\rm t}$. We decided to choose three values $d_{\rm t} = 0$ (no self-gravity) and $d_{\rm t} = 0.1$ and $d_{\rm t} = 0.5$. The values of other constants are in table 1.

The map, corresponding to the parameters described in table 1, are represented in figure 1. $d_{\rm t} = 0$ is plotted at the left, $d_{\rm t} = 0.1$ in the middle and $d_{\rm t} = 0.5$ at the right. We can see that there is no change in the morphology of the solution. The pressure field has a toroidal shape for each value of $d_{\rm t}$. The shape, the vertical and radial structure change with the strength of the self-gravity. The maximum of pressure raises with the value of $d_{\rm t}$, see value of a in table 2.

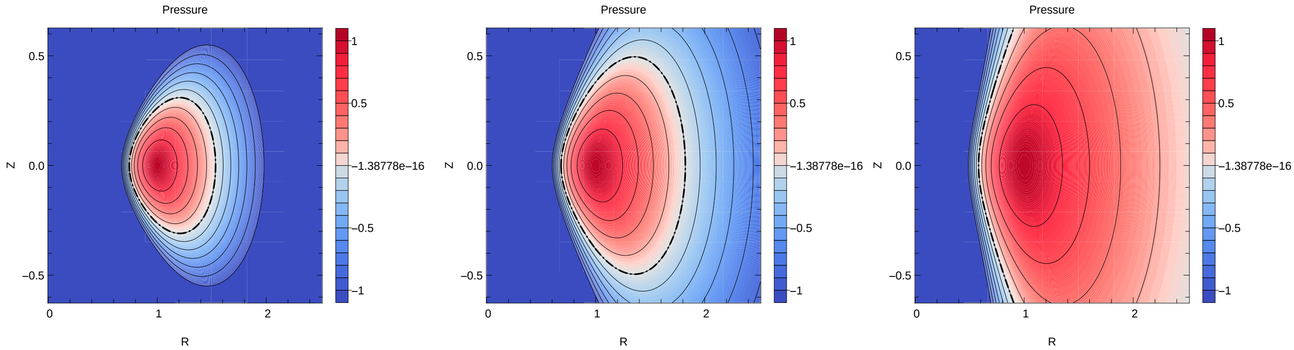

Fig. 1. Map of normalized pressure given by equation (3.1) with the parameters described in table 1. $d_t = 0$ corresponds to the map at the left, $d_t = 0.1$ in the middle, and $d_t = 0.5$ on the right.

Test 1 $d_t = 0$	$c = -0.2$ and $r_c = 20 \rightarrow b = 0.471$, $e \sim -1.12$ and $a \sim 0.114$
Test 2 $d_t = 0.1$	$c = -0.2$ and $r_c = 20 \rightarrow b = 0.495$, $e \sim -1.21$ and $a \sim 0.151$
Test 3 $d_t = 0.5$	$c = -0.2$ and $r_c = 20 \rightarrow b = 0.590$, $e \sim -1.58$ and $a \sim 0.299$.

Table 2. Description of the three tests for off-equatorial tori.

3.2 *Off-equatorial tori*

We set-up the same test and use the same method for off-equatorial tori too. We choose a location for the maximum of pressure ($R = r_c, Z = z_c \neq 0$), and check if the conditions are satisfied. Next we set the constant c. The parameters b and e are given by the conditions of existence of the solutions. As before a is the maximum of pressure and is given by equation (3.1). All these variables are given in table 2.

The map, corresponding to the table 2 and equation (3.1), is plotted in figure 2, $d_t = 0$ at the left, $d_t = 0.1$ in the middle and $d_t = 0.5$ at the right. The same effects, as for equatorial tori, appear in this case. The maximum of pressure raises with the value of d_t (see value of a in table 2), the vertical and radial structure change too. The difference with the previous case is the change in the morphology of the pressure field. We can see that for $d_t = 0$, the field has two lobes above and below the equatorial plane. But for $d_t = 0.1$ and $d_t = 0.5$ the two lobes are linked with each other across the equatorial plane.

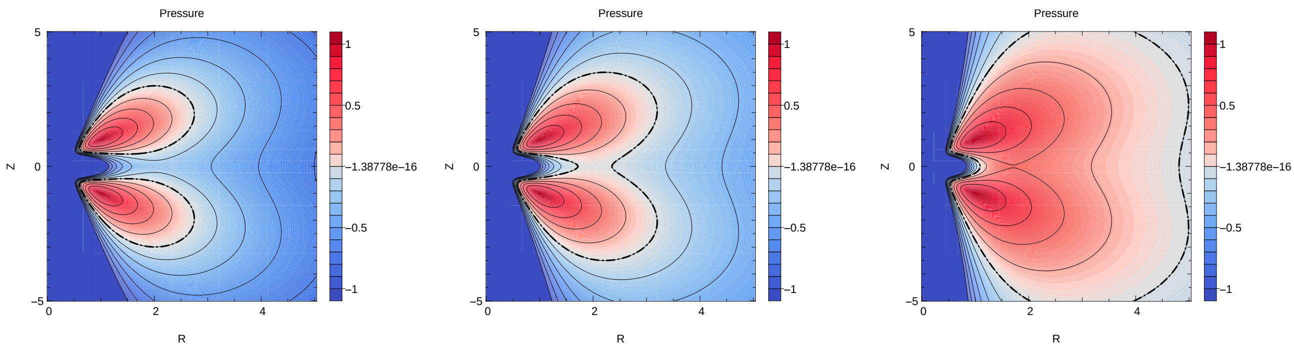

Fig. 2. same as 1 but for off-equatorial tori and for parameters described in 2.

4 Conclusions

In this paper, we analyse the impact of the self-gravity on the conditions of existence of charged fluid tori and their morphology. We consider these tori as a fluid, whose particles carry electrical charges. The fluid is considered as perfect and incompressible. The latter is embedded in the gravitational potential and the dipolar magnetic field due to the central mass and the gravitational force produced by itself (the self-gravity). Our study follow the work done by Slaný et al. (2013) where they neglect the self-gravity. We add the self-gravity term

to the equilibrium equation to find stationary tori configurations and see the impact of this self-gravitational force on the morphology of solutions.
We found different interesting results. We saw that the morphology of tori are similar to the non-selfgravitating case. We found the toroidal configuration and the toroidal off-equatorial configurations (see figure 1 and the graphic at the left of figure 2). A new morphology appears. The two toroidal off-equatorial objects are linked by the mid -plane (see graphics in the middle and at the left of figure 2). An other effect of the self-gravity is that the maximum of pressure seems to raise with the value of $d_{\rm t}$ and the torus becomes thicker, which makes sense because higher gravity implies higher pressure to balance the forces. It will be interesting to test other form for the specific charged (Trova et al. in prep) and to elaborate this model, with a non approximated self-gravity. We can use a SCF (self-consistent field) method (Ostriker & Mark 1968; Blinnikov 1975; Hachisu 1986) which consist to find by an iteration scheme the equilibrium configuration. In this case, the self-gravitational potential is calculated with Poisson's equation. The benefit of this is the possibility to study various equations of state too. Finally it will be interesting to add the magnetic field produced by the torus itself.

References

Abramowicz, M., Jaroszynski, M., & Sikora, M. 1978, A&A, 63, 221

Blinnikov, S. I. 1975, Soviet Ast., 19, 151

Eckart, A., Schödel, R., & Straubmeier, C. 2005, The black hole at the center of the Milky Way

Font, J. A. & Daigne, F. 2002, MNRAS, 334, 383

Frank, J., King, A. R., & Raine, D. J. 1985, Accretion power in astrophysics

Hachisu, I. 1986, ApJS, 61, 479

Huré, J.-M. 1998, A&A, 337, 625

Kovář, J., Slaný, P., Cremaschini, C., et al. 2014, Phys. Rev. D, 90, 044029

Kozlowski, M., Jaroszynski, M., & Abramowicz, M. A. 1978, A&A, 63, 209

Krolik, J. 2004, Nature, 429, 29

Kucáková, H., Slaný, P., & Stuchlík, Z. 2011, J. Cosmology Astropart. Phys., 1, 33

Ostriker, J. P. & Mark, J. W.-K. 1968, ApJ, 151, 1075

Shlosman, I. & Begelman, M. C. 1987, Nature, 329, 810

Slaný, P., Kovář, J., Stuchlík, Z., & Karas, V. 2013, ApJS, 205, 3

Stuchlík, Z., Slaný, P., & Hledík, S. 2000, A&A, 363, 425

SF2A 2015
F. Martins, S. Boissier, V. Buat, L. Cambrésy and P. Petit (eds)

IMPACT OF QPOS ON THE ENERGY SPECTRUM OF MICROQUASARS

P. Varniere[1] and R. Mignon-Risse[1]

Abstract. The presence of QPOs in the Power Density Spectra of x-ray binaries is quite ubiquitous and is often modeled as a hot structure orbiting in the disk. While we have been using timing and PDS to determine the presence and explore the possible origin of QPOs, they are, up to now, absent from the spectral analysis. Here we are using a simple analytical model to mimic the hot structure of several QPO models in order to determine their impact on the energy spectrum.

Keywords: microquasars, QPO, Xray

1 Introduction

When looking at the Power Density Spectrum of microquasars the most striking features are the presence of Quasi-Periodic Oscillations. Those Low-Frequency (< 30Hz) and High-Frequency (> 40Hz) QPOs cannot be neglected in the PDS, indeed, the LFQPO alone can have a rms of up to 30%. There are a lot of distinct models to describes them, but most of them imply a warm/hot structure orbiting the disk causing the X-ray modulation.

Nevertheless, when looking at the same data through the energy spectrum the disk is considered smooth with a monotonic temperature profile. If such a featureless disk can easily model states where there is no QPO or even if the QPO has a low impact (meaning low rms), it is incoherent to use it to describe states with prominent QPOs. Here we are checking if the structure at the origin of QPOs also has a measurable impact on the energy spectrum and its fits.

While it is hard to look at a direct impact on the energy spectrum because of its shape, we can look at a possible impact of the presence of QPOs on different correlations between the fit parameters. Then we will use our simplified model (Varniere & Vincent 2015, 2016) to compute energy emission from a disk having an increasingly strong QPO.

Using our model with the module `fakeit` from XSPEC we will be able create a synthetic spectrum of the system { disk with QPO and corona } which then can be fitted similarly to regular observations. The resulting parameters can then be plotted against the real correlation and see if the behavior found in presence of QPOs can be related to the difference in the temperature profile.

2 Link between the disk parameters and QPOs

It has been asserted early on that the properties of the LFQPOs, in particular their frequency, are related to parameters of the disk (Varniere *et al.* 2002) obtained through spectral fitting. As there is much less data for HFQPOs, no similar study has been led yet but HFQPOs seem to be linked with the presence of LFQPOs of type A or B (Remillard *et al.* 2002). Using data from XTE J1550-564 during the outburst of 98-99 and 2000, both known to harbor HFQPOs, we reduced the data and looked at the behavior of the different spectral parameters depending if there is or not a QPO observed.

Unsurprisingly it is for the disk parameters that we see a clear change in the behavior depending if there is or not a HFQPO detected. Indeed, on Fig. 1. we see that a departure from the correlation between r_{in} and T_{in}

[1] AstroParticule & Cosmologie (APC), UMR 7164, Universit Paris Diderot, 10 rue Alice Domon et Leonie Duquet, 75205 Paris Cedex 13, France.

© Société Francaise d'Astronomie et d'Astrophysique (SF2A) 2015

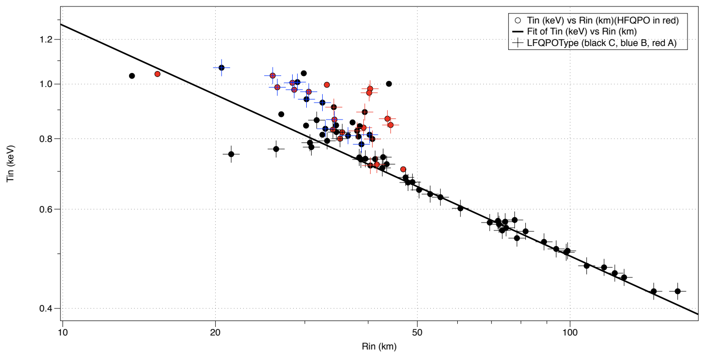

Fig. 1. Correlation between the inner edge position and inner edge temperature as given by the spectral fits for the outburst of 98-99 and 2000 of XTE J1550-564. Red dots represent observations with HFQPOs detected while there is none in the black dots. The crosses represent the type of LFQPO, black for the common type C, blue for type B and red for type A.

when HFQPOs or type A/B LFQPO are observed. As a side note we are looking to see if the few points that depart from the correlation without a published HFQPO frequency have or not some high frequency structure fine enough to be a HFQPO.

As all those data points come from the spectral fitting, it is possible that the departure from the correlation is rooted by the presence of a QPO/warm structure which cause the fit by a smooth disk to fail and gives unrealistic small values for the inner edge of the disk. To test that we need to be able to fit a disk with such structure in a controlled, hence simulated, manner.

3 Simple model for the temperature profile

QPO models often connect the signal modulations to the presence of structures embedded in the disk. Such structures include axisymmetric (see e.g. Bursa *et al.* 2004; Schnittman *et al.* 2006b; Vincent *et al.* 2014), or precessing tori (Schnittman *et al.* 2006c; Ingram *et al.* 2009) or hotspots (Karas *et al.* 1992; Schnittman & Bertschinger 2004; Tagger & Varniere 2006; Pechacek *et al.* 2013).

Our main concern here is not the origin of the structure, but the consequences on the emission. This means that, rather than taking full magnetohydrodynamic (MHD) simulations of the different models proposed to explain QPOs we are interested in, we decided to create a simple, analytical, model for the different structures in order to test more cleanly the different parameters. Indeed, in a full fluid simulation changing one parameter in the initial condition can have repercussions on several observable parameters and therefore it is harder to study the different effects separately.

We take a pertubative a pproach to the disk temperature profile by adding to the disk hydrostatic equilibrium temperature $T_0(r) \propto r^{-1}$ a component that depends on time, radius and azimuthal angle $T_1(t,r,\varphi) = T_0(r)d(r)\, s(r-r_s,\varphi)$. This allows us to minimize the number of parameters to characterize the structures in the disk while keeping a similar framework. $r_s = r_s(t,\varphi)$ represents the structure added to in the equilibrium disk in time-dependent polar coordinates, it can either be a torus or a hotspot. We choose to decompose T_1 as a height function d that depends only on r and a shape function s which is finite only near the disc structure we are studying. This allows us to keep the same structure to take into account a variety of shapes mimicking a variety of models. For simplicity we take the shape function to be gaussian and the height function to be a power-law of r only and related to the equilibrium temperature $T_0(r)$. This provides a simple but useful framework to model a disk with added perturbative structures. Within this framework the perturbed temperature reads

$$T(t,r,\varphi) \quad = \quad T_0(r) \times \left[1 + \gamma\left(\frac{r_c(t)}{r}\right)^{\beta} \exp\left(-\frac{1}{2}\left(\frac{r - r_s(t,\varphi)}{\delta}\right)^2\right)\right] \tag{3.1}$$

where $r_c(t)$ is the position of the temperature maximum in the disk (the center of the torus or hotspot). This quantity is allowed to be a function of time. The quantity β measures how fast the temperature decreases from the maximum at r_c, δ parametrizes the radial extent of the structure while γ is the maximum amplitude of the perturbation.

Using these simple models we are able to reproduce several observables such as, for example, the rms amplitude of QPOs as shown in Varniere & Vincent (2015, 2016), hence validating this simple model as representing a disk with a QPO.

Using those parametrized temperature profiles we have created XSPEC models of disks having such structure (`disktor` and `diskblob`, which will be made available once optimized). This allow two things: first we can fit observations with our non-monotonic disk profile and second, using the procedure `fakeit` in XSPEC we created synthetic spectra of a power-law plus the disk emission taking into account the presence of a warm/hot structure. It is this that we will use here to access if the change in the temperature profile does indeed impact the spectrum and hence the fitted parameters.

4 Impact on the energy spectrum fitting

In order to see if the presence of a HFQPO in the disk can reproduce the departure seen in Fig. 1. we computed severals sets of synthetic spectra with the physical parameters of XTE J1550-564. Each set consists of a regular, diskbb-like, disk with slowly increasing structure parameters aiming to reproduce the time evolution effect of a growing QPO and an 'origin point'(with a QPO amplitude of 0) on the (r_{in}, T_{in}) diagram. We then fitted the sets of synthetic spectra with XSPEC following the standard procedure.

The results of the fit from the synthetic spectra are represented as grey stars on Fig. 2. in the case of an 'origin point', at $(45, 0.7)$. They occupy the same space as the HFQPO/type B LFQPO data points from XTE J1550-564 hence strengthening the link between QPO, hot spot, and fit-difficulties. Other sets of parameters, not shown here, reach the type A LFQPOs.

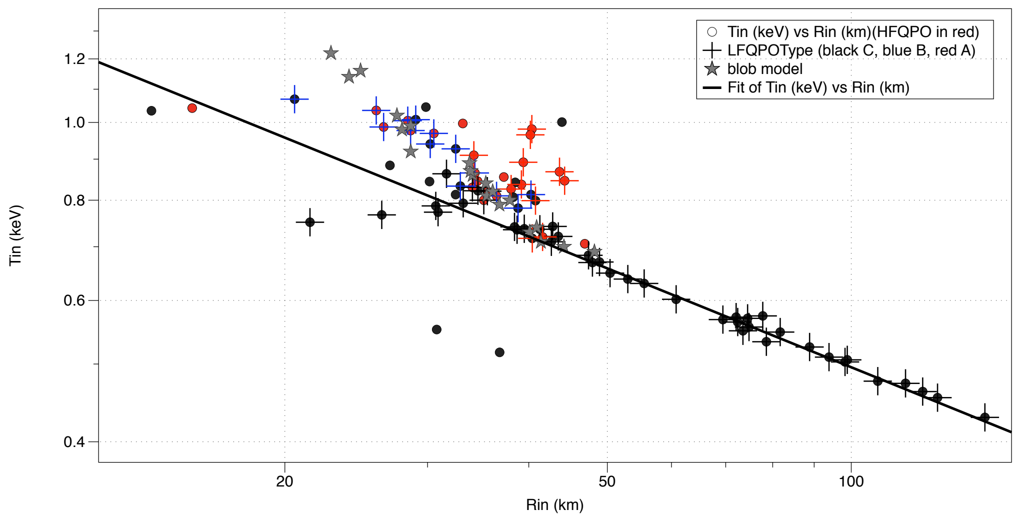

Fig. 2. Correlation between the inner edge position and inner edge temperature as given by the spectral fits for the outburst of 98-99 and 2000 of XTE J1550-564. Red dots represent observations with HFQPOs detected while there is none in the black dots. The crosses represent the type of LFQPO, black for the common type C, blue for type B and red for type A. The grey stars are the result of the synthetic spectra fit.

Following the evolution of the grey stars we see that as soon as the QPO has a non-zero amplitude there is an error on the disk parameters. The error is growing with the QPO amplitude but already with a 5% rms for the QPO we get an error of about 14% on T_{in} and 12% on r_{in}. This error is mostly going toward smaller r_{in} and higher T_{in}, indeed in our case of a 'real' inner edge at 45km we get some fit results up to about 20km for an rms of 20%. We see that, even with RXTE resolution and range, neglecting the QPO in the spectral analysis leads to large errors. As a side note, such departure from correlation could be used to detect, purely from spectral analysis, the possible presence of HFQPOs.

5 Conclusions

Using a simple model to mimic the emission from a disk with a non-monotonic temperature, as has been theorized to be the case in the presence of QPOs, we have created synthetic spectra with increasingly strong QPOs. This allowed us to study in a clean environment the impact of a QPO on the energy spectrum and determine if we can neglect them in the spectral fit.

First, our simulated observations are coherent with the departure from correlation seen in the T_{in}-r_{in} diagram of XTE J1550-564 in presence of HFQPO and LFQPOs B or A. In the case of very small amplitude QPOs there is a negligible impact on the energy spectrum and it can be ignored in the spectral fit. Nevertheless, in the case of an amplitude as small as 5% rms we cannot neglect the presence of the hot structure as it leads to significant errors in the fits. Especially those errors tend to give a smaller inner radius and higher inner temperature. Therefore there is a need to improve the disk fitting by taking into account the structures at the origin of the QPOs if we want to constraint the disk parameters in their presence.

PV acknowledges financial support from the French Programme National des Hautes Energies (PNHE) and the UnivEarthS Labex program at Sorbonne Paris Cite (ANR-10-LABX- 0023 and ANR-11-IDEX-0005-02). Computing was done at the FACe (Francois Arago Centre) in Paris.

References

Bursa M., Abramowicz M. A., Karas V., Kluzniak W., 2004, The Astrophysical Journal Letter, 617, L45

Feroci, M., et al., 2014, Proceedings of the SPIE, 9144, 2

Ingram, A., Done, C., Fragile, P. C., MNRAS, 397, L101

Karas, V., Vokrouhlicky, D., Polnarev, A. G., 1992, MNRAS, 259, 569

Pechacek, T., Goosmann, R. W., Karas, V., Czerny, B., Dovciak, M., 2013, A&A, 556, A77

Schnittman J. D., Bertschinger E., 2004, The Astrophysical Journal, 606, 1098

Schnittman J. D., Rezzolla L., 2006, The Astrophysical Journal Letter, 637, L113.

Schnittman, J. D., Homan, J., Miller, J. M., 2004, ApJ, 642, 420

2002, ApJ, 564, 962.

Tagger, M. & Varniere, P., 2006, ApJ, 652, 1457.

Varniere, P.; Rodriguez, J.; Tagger, M., 2002, A&A, 387, 497.

Varniere, P. & Vincent, F.H., 2016, to be submitted A&A.

Varniere, P. & Vincent, F.H., 2015, proceeding de la SF2A.

Vincent, F. H.; Mazur, G. P.; Straub, O.; Abramowicz, M. A.; Kluzniak, W.; Torok, G.; Bakala, P., 2014, A&A, 563, A109.

SF2A 2015
F. Martins, S. Boissier, V. Buat, L. Cambrésy and P. Petit (eds)

IMPACT OF THE QPO MODELS ON THE PULSE PROFILE

P. Varniere[1] and F. H. Vincent[2]

Abstract. Quasi-periodic oscillations (QPO) are an important probe of the timing properties of black-hole binaries. Many models are proposed in order to account for these features and it is difficult to differentiate them with current data. Here we aim to look at the actual pulse profile from each model in order to see how they could be differentiated and what kind of sources are the best targets for such a test. We consider three classes of simple models: elongated hot spots, tori and spirals. We perturb the equilibrium temperature of a thin disk to create these structures. The perturbed disk is supposed to emit blackbody radiation at the local temperature. Radiation is ray-traced in the Schwarzschild metric to a distant observer. We study the dependency with the source inclination of the pulse profile for different frequencies for these three models. The departure from a pure sinusoid of certain models at high inclination will be visible in the power density spectra by a higher presence of harmonics. In particular, hot spots and spirals lead to a (complete or partial) harmonic series which is lacking for a radially oscillating tori. We conclude that analyzing the first harmonics of the dominant power density spectrum peak for high-inclination sources is an interesting probe and it might make it possible to differentiate between axisymmetric (tori) and non-axisymmetric (hotspots and spirals) models.

Keywords: black hole, QPO, general realtivity

1 Introduction

Up to now QPO models have been focusing mainly on explaining the frequency (or frequencies) observed in the power density spectrum (PDS). While it is essential, it is just the first accessible observable and all of the models fulfilled this requirement as they were created for it. It is therefore interesting to take those same models and look at how they compare for other observables. Some we already have as the root mean square (rms) amplitude, some we do not yet have complete access to such as the pulse profile. This will allow us to see what would be necessary to differentiate between the models, in particular in the context of the next generation of instruments, but also what are the best candidate observables with present data.

2 From the disk emission to the Pulse profile

2.1 Simple model for the temperature profile

QPO models often connect the signal modulations to the presence of structures embedded in the disk. Such structures include axisymmetric (see e.g. Bursa *et al.* 2004; Schnittman *et al.* 2006b; Vincent *et al.* 2014), or precessing (Schnittman *et al.* 2006c; Ingram *et al.* 2009) tori, hotspots (Karas *et al.* 1992; Schnittman & Bertschinger 2004; Tagger & Varniere 2006; Pechacek *et al.* 2013) and spirals (Tagger & Pellat 1999; Varniere *et al.* 2002; Varniere & Blackman 2005; Karas *et al.* 2007).

Our main concern here is not the origin of the structure, but the consequences on the emission. This means that, rather than taking full magnetohydrodynamic (MHD) simulations of the different models proposed to explain QPOs we are interested in, we decided to create a simple, analytical, model for the different structures in order to test more cleanly the different parameters. Indeed, in a full fluid simulation changing one parameter

[1] AstroParticule & Cosmologie (APC), UMR 7164, Universit Paris Diderot, 10 rue Alice Domon et Leonie Duquet, 75205 Paris Cedex 13, France.
[2] LESIA, CNRS UMR 8109, Observatoire de Paris, Universite Pierre et Marie Curie, Universite Paris Diderot, 92190 Meudon, France

© Société Francaise d'Astronomie et d'Astrophysique (SF2A) 2015

in the initial condition can have repercussions on several observable parameters and therefore it is harder to study the different effects separately.

We take a pertubative approach to the disk temperature profile by adding to the disk hydrostatic equilibrium temperature $T_0(r) \propto r^{-1}$ a component that depends on time, radius and azimuthal angle $T_1(t,r,\varphi) = T_0(r)d(r)\,s(r-r_s,\varphi)$. This allows us to minimize the number of parameters to characterize the structures in the disk while keeping a similar framework. The quantity $r_s = r_s(t,\varphi)$ represents the structure added to the equilibrium disk in time-dependent polar coordinates, it can either be a torus, a hotspot or a spiral. We choose to decompose T_1 as a height function d that depends only on r and a shape function s which is finite only near the disc structure we are studying. This allows us to keep the same structure to take into account a variety of shapes mimicking a variety of models. For simplicity we take the shape function to be gaussian and the height function to be a power-law of r only and related to the equilibrium temperature $T_0(r)$. This provides a simple but useful framework to model a disk with added perturbative structures. Within this framework the perturbed temperature reads

$$T(t,r,\varphi) \quad = \quad T_0(r) \times \left[1 + \gamma \left(\frac{r_c(t)}{r}\right)^{\beta} \exp\left(-\frac{1}{2}\left(\frac{r - r_s(t,\varphi)}{\delta}\right)^2\right)\right] \tag{2.1}$$

where $r_c(t)$ is the position of the temperature maximum in the disk (the center of the torus or hotspot). This quantity is allowed to be a function of time. The quantity β measures how fast the temperature decreases from the maximum at r_c, δ parametrizes the radial extent of the structure while γ is the maximum amplitude of the perturbation.

2.2 The general relativistic ray-tracing code GYOTO

In order to simulate the observed light-curve, we use the open-source general relativistic ray-tracing code GYOTO (Vincent *et al.* 2011). We assume the structure to be at rest in a reference frame corotating with the disk at the Keplerian velocity at radius r_c. Null geodesics are integrated backward in time from a distant observer to the disk. When the disk is hit, the outgoing flux is assumed to follow the blackbody law at the local temperature. We are using the (*Schwarzschild* or *full-GR* case in the following) taking into account the Schwarzschild metric, thus all special and general relativistic effects for a non-rotating black hole.

3 Modulation from an axi-symetrical torus

The first model we study is the resulting flux modulation coming from the radial oscillation of a torus. The position of the torus is defined bt $r_c(t) = r_{c,o}(1 + A\sin(\Omega(r_{c,o})\sqrt{1 - r_{LSO}/r_{c,o}}t))$. Here we choose the amplitude of the oscillation $A = 0.1$. This corresponds to adding to a non- oscillating torus a velocity perturbation of the order of a few percent of the local Keplerian velocity, so this is a rather big oscillation, but the dominating motion is of course still azimuthal.

On the right of Fig. 1. we show the lightcurves at inclination 20° in the case of a torus positioned at $r_c \in \{2,3,4,6,8\}r_{LSO}$ while the other parameters are identical. The shape of the lightcurve stays consistent with a higher amplitude sinusoid while keeping the mean value at the same phase location. The increase in the rms amplitude is to be expected, indeed the amplitude of the torus oscillation is about 10% of its average position, therefore when the torus is further away in the disk the variation in position also increases thus causing a stronger modulation.

On the left of Fig. 1. we show the same lightcurves but this time seen at a high inclination of 70°. Similarly to what we saw at low inclination the shape of the lightcurves stay consistent with a sinusoid whose amplitude increased as the structure gets further away in the disk.

Observationally, this would mean that, while the rms amplitude of the QPO increase with inclinations, the pulse shape is unaffected and the PDS would not show variation on the harmonic content between high and low inclination systems.

4 Modulation from non axi-symetrical structure: an elongated blob or spiral

A lot of QPO models imply the presence of a non axi-symetrical structure in the disk. Here we take two of those structures to see how the pulse profile and hence the PDS would behave as a function of distance and

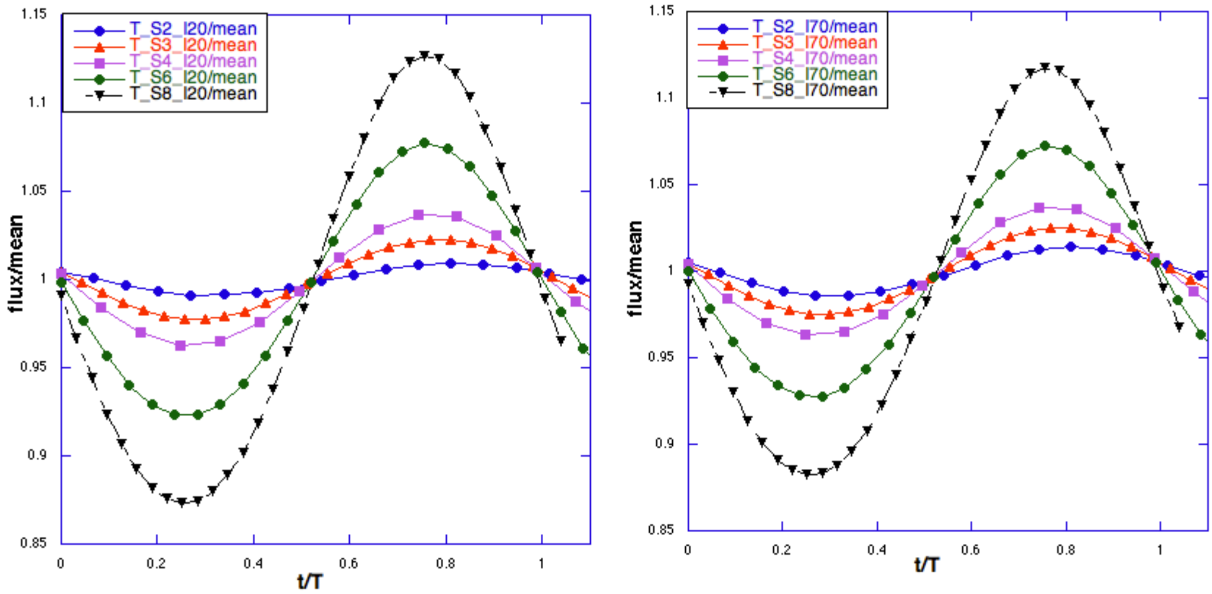

Fig. 1. Comparison of one period of the light curves obtained in the case of a torus at different positions in the disk. The legend of the graph shows T for a torus, S followed by a number represent r_c and I is for the inclination. **Left:** Case of a 20° inclination. **Right:** Case of a 70° inclination. All of them are sinusoidal for both inclination.

inclination.

First, we look at the case of a large, heavily sheared, hotspot of azimuthal extend $\delta\varphi = \pi$, this is a final stage of any blob that is not sustained by any instability, indeed shear will tend to circularize any overdensity. We see on the left if Fig. 2 that having the position of the blob further away in the disk also has no detectable effect of the shape of the light curve. Still, there is a very small departure from a pure sinusoide that gets

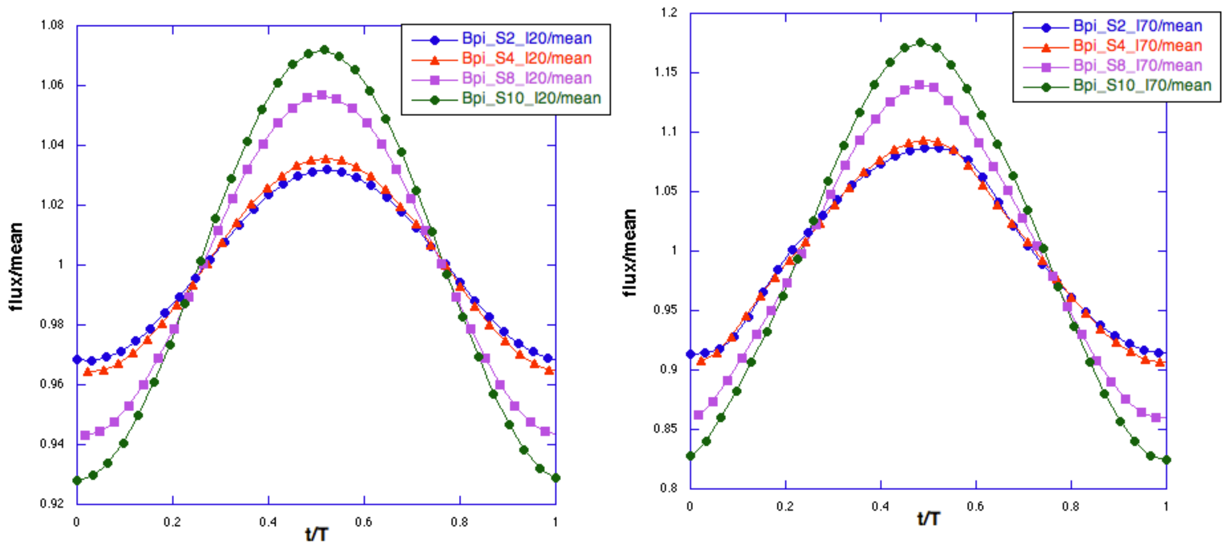

Fig. 2. Comparison of one period of the light curves obtained in the case of an elongated blob at different positions in the disk. **Left:** Case of a 20° inclination. **Right:** Case of a 70° inclination. A slight departure from a pure sinusoide is visible at high inclination, seemingly more visible for structures further away in the disk.

stronger as the structure moves further away in the disk (this is well below 1% of the rms of the main peak even at $r_c = 10$ thus not detectable among the noise). Similarly as in the torus case, the rms amplitude increases with the radius of the structure, though it is not as pronounced in the case of the blob. Indeed, the increase in rms comes from the fact that, while changing r_c, we keep the ratio r_c to the inner edge of the disk constant, hence reducing the average, unmodulated, flux.

When we look at the system from a higher inclination, as we can see on the right of Fig. 2, there is a clear departure from a sinusoide that gets stronger as the blob is further away in the disk. Such a change in the pulse shape will have an strong impact when looking at the PDS. From looking at just the torus and the hotspot cases we see that, while providing the required increase in rms with inclination, the pulse profile from those two models differ widely between low inclination and high inclination systems. This will have detectable consequences on the PDS as one will have a higher harmonic content for a high inclination system than for a low one, while there is no change for the radially oscillating torus.

Just as excepted from the similitude of their modulation mechanism, we see on Fig. 3. a similar trend for the case of a one-arm spiral perturbing the disk. Once again the lightcurve has a slight, barely visible, departure from a sinusoide and when looking at Fourier space a small first harmonic might be detected, especially when the spiral is further out in the disk.

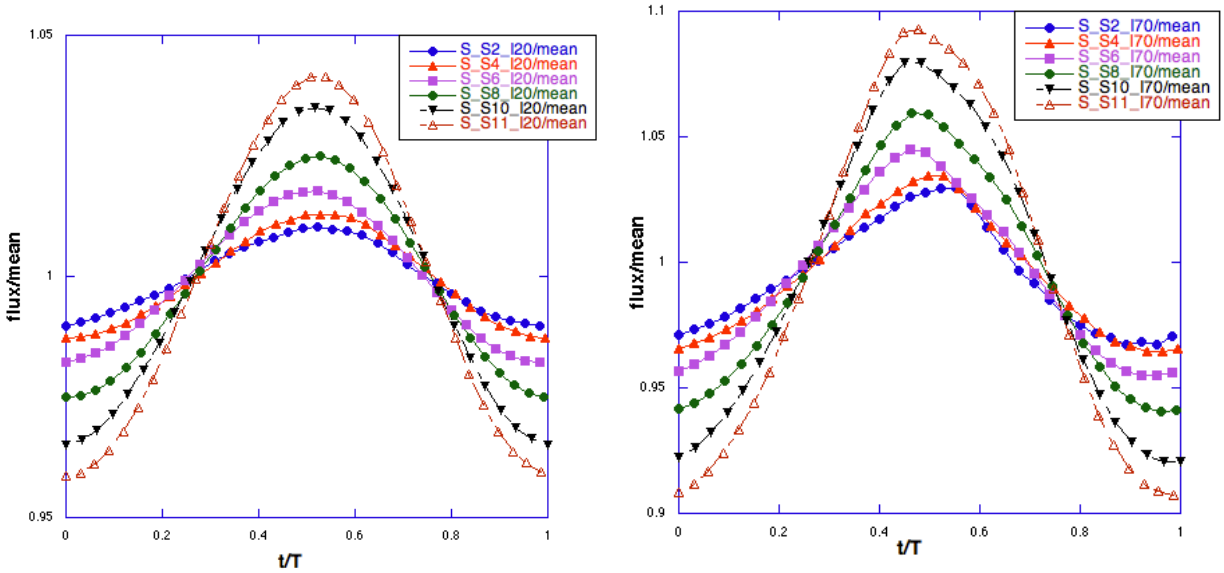

Fig. 3. Comparison of one period of the light curves obtained in the case of a spiral at different positions in the disk. **Left:** Case of a 20° inclination. **Right:** Case of a 70° inclination. There is a definite departure from a sinusoide at high inclination, seemingly increasing for structures further away in the disk.

This is even more visible at higher inclinations as shown on the right of Fig. 3. As in the case of the hotspot the shape of the pulse is strongly affected by the inclination.

The main difference with Fig. 2 is in the detailed shape of the pulse which is clearly not symmetrical with respect to the average value for the spiral, meaning the time spent at higher flux than the mean value will be shorter than the time spent at lower flux. While this is hardly detectable now, we might find some high inclinations system having a strong QPO in which we can try to assess the time spent above and below the mean value.

5 Conclusions

Here we have computed and compared the pulse profile of three QPO models. From this, it seems that the only axi-symmetrical model we studied, a simple radially oscillating torus, would be distinguishable from the other, non-axi-symmetrical, models by the lack of change in its harmonic contents between high and low inclination systems. It is therefore interesting to start looking at the harmonic content of sources at different inclinations to see if a statistically significant change with inclination is detected.

Distinguishing between the different non-axi-symmetrical models would be more difficult and would require finding stable high inclination systems with strong QPOs in which we could compare the difference between the average and the mean of the light curve. This might be feasible with the next generation of X-ray missions.

PV acknowledges financial support from the French Programme National des Hautes Energies (PNHE) and the UnivEarthS Labex program at Sorbonne Paris Cite (ANR-10-LABX- 0023 and ANR-11-IDEX-0005-02). Computing was done at the FACe (Francois Arago Centre) in Paris. FHV acknowledges financial support from the Polish NCN grant 2013/09/B/ST9/00060.

References

Bursa M., Abramowicz M. A., Karas V., Kluzniak W., 2004, The Astrophysical Journal Letter, 617, L45

Feroci, M., et al., 2014, Proceedings of the SPIE, 9144, 2

Ingram, A., Done, C., Fragile, P. C., MNRAS, 397, L101

Karas, V., Vokrouhlicky, D., Polnarev, A. G., 1992, MNRAS, 259, 569

Karas, V., Dovciak, M., Eckart, A., Meyer, L., 2007, Proceedings of RAGtime 8/9

Pechacek, T., Goosmann, R. W., Karas, V., Czerny, B., Dovciak, M., 2013, A&A, 556, A77

Schnittman J. D., Bertschinger E., 2004, The Astrophysical Journal, 606, 1098

Schnittman J. D., Rezzolla L., 2006, The Astrophysical Journal Letter, 637, L113.

Schnittman, J. D., Homan, J., Miller, J. M., 2004, ApJ, 642, 420

2002, ApJ, 564, 962.

Tagger, M. & Pellat, R., 1999, 349, 1003.

Tagger, M. & Varniere, P., 2006, ApJ, 652, 1457.

Varniere, P. & Blackman, E.G., 2005, New Astronomy, Volume 11, Issue 1, p. 43.

Varniere, P.; Rodriguez, J.; Tagger, M., 2002, A&A, 387, 497.

Varniere, P. & Mignon-Risse, R., 2016, to be submitted A&A.

Varniere, P. & Mignon-Risse, R., 2015, proceeding de la SF2A.

Vincent, F. H., Paumard, T., Gourgoulhon, E., & Perrin, G. 2011, Classical and Quantum Gravity, 28, 225011.

Vincent, F. H.; Mazur, G. P.; Straub, O.; Abramowicz, M. A.; Kluzniak, W.; Torok, G.; Bakala, P., 2014, A&A, 563, A109.

Session 05

CFHT : Programmes scientifiques, MSE, SPIRou et CFIS

SF2A 2015
F. Martins, S. Boissier, V. Buat, L. Cambrésy and P. Petit (eds)

SCALING LAWS TO QUANTIFY TIDAL DISSIPATION IN STAR-PLANET SYSTEMS

P. Auclair-Desrotour[1,2], S. Mathis[2,3] and C. Le Poncin-Lafitte[4]

Abstract. Planetary systems evolve over secular time scales. One of the key mechanisms that drive this evolution is tidal dissipation. Submitted to tides, stellar and planetary fluid layers do not behave like rocky ones. Indeed, they are the place of resonant gravito-inertial waves. Therefore, tidal dissipation in fluid bodies strongly depends on the excitation frequency while this dependence is smooth in solid ones. Thus, the impact of the internal structure of celestial bodies must be taken into account when studying tidal dynamics. The purpose of this work is to present a local model of tidal gravito-inertial waves allowing us to quantify analytically the internal dissipation due to viscous friction and thermal diffusion, and to study the properties of the resonant frequency spectrum of the dissipated energy. We derive from this model scaling laws characterizing tidal dissipation as a function of fluid parameters (rotation, stratification, diffusivities) and discuss them in the context of star-planet systems.

Keywords: hydrodynamics, waves, turbulence, planet-star interactions, planets and satellites: dynamical evolution and stability

1 Introduction

Planetary fluid layers and stars are affected by tidal perturbations resulting from mutual gravitational and thermal interactions between bodies. These perturbations generate velocity fields which are at the origin of internal tidal dissipation because of the friction/diffusion applied on them. Over long timescales, the energy dissipated in a planetary system impacts the orbital dynamics of this later (Efroimsky & Lainey 2007; Auclair-Desrotour et al. 2014). The architecture of the system thus evolves. At the same time, the rotation of its components and the orientation of their spin is modified while they are submitted to an internal heating. However, solids and fluids are not affected by tides in the same way. While the solid planetary tidal response takes the form of a delayed visco-elastic elongation, internal and external fluid shells such as liquid cores and atmospheres behave as waveguides having their own resonant frequency ranges (Ogilvie & Lin 2004, 2007; Gerkema & Shrira 2005). Because of its great complexity, tidal dissipation resulting from this behaviour has been studied in numerous theoretical works, especially for stellar interiors and gaseous giant fluid envelopes, over the past decades (see e.g. Zahn 1966a,b,c, 1975, 1977, 1989; Ogilvie & Lin 2004; Wu 2005; Ogilvie & Lin 2007; Remus et al. 2012; Cébron et al. 2012, 2013), which highlighted the crucial role played by the internal structure of bodies and their dynamical properties (rotation, stratification, diffusivities). It is therefore very important to understand the physical mechanisms responsible for tidal dissipation in fluid layers.

Tidal waves that can propagate in these layers belong to well-identified families:

- inertial waves due to the rotation of the body and which have the Coriolis acceleration as restoring force,
- gravity waves due to the stable stratification of the layers and driven by the Archimedean force,
- Alfvén waves due to magnetic field (if the fluid is magnetized) and driven by magnetic forces.

[1] IMCCE, Observatoire de Paris, UMR 8028 du CNRS, UPMC, 77 Av. Denfert-Rochereau, 75014 Paris, France
[2] Laboratoire AIM Paris-Saclay, CEA/DSM - CNRS - Université Paris Diderot, IRFU/SAp Centre de Saclay, F-91191 Gif-sur-Yvette Cedex, France
[3] LESIA, Observatoire de Paris, CNRS UMR 8109, UPMC, Univ. Paris-Diderot, 5 place Jules Janssen, 92195 Meudon, France
[4] SYRTE, Observatoire de Paris, UMR 8630 du CNRS, UPMC, 77 Av. Denfert-Rochereau, 75014 Paris, France

© Société Francaise d'Astronomie et d'Astrophysique (SF2A) 2015

As demonstrated by Ogilvie & Lin (2004) for inertial waves, the amplitude of tidal dissipation strongly depends on the tidal frequency contrary to the case of solids. It is also obviously linked to internal properties of the layer such as its turbulent viscosity, thermal diffusivity, rotation and stratification. Indeed, several dissipative mechanisms are involved. The most important of them are viscous friction in turbulent convective zones, thermal diffusion in radiative zones, and Ohmic diffusion in the case of magnetized fluids. In this work, we ignore magnetic effects and focus on gravito-inertial waves damped through viscosity and thermal diffusion. Hence, we give an overview of the analytical results established in Auclair Desrotour et al. (2015). We refer the reader to this paper for more details. Generalizing the approach described by Ogilvie & Lin (2004), given in Appendix A of their paper, we consider an idealized local section of a fluid layer submitted to an academic tidal forcing with periodic boundary conditions. This model allows us to compute analytic expressions of energies dissipated by viscous friction and thermal diffusion. Then, we use these results to identify the control parameters of the system, to determine the possible asymptotic regimes of the tidal response and to give simple scaling laws characterizing a dissipation spectrum. Hence, in Sect. 2, we present the local model. We summarize the obtained results in Sect. 3 and give our conclusions in Sect. 4.

2 Physical set-up

2.1 Local model

Our local model is a Cartesian fluid box of side length L centered on a point M of a planetary fluid layer, or star (see Fig. 1). Let be $\mathscr{R}_O : \{O, \mathbf{X}_\mathrm{E}, \mathbf{Y}_\mathrm{E}, \mathbf{Z}_\mathrm{E}\}$ the reference frame rotating with the body at the spin frequency Ω with respect to $\mathbf{Z}_\mathrm{E}$.The spin vector $\boldsymbol{\Omega}$ is thus given by $\boldsymbol{\Omega} = \Omega \mathbf{Z}_\mathrm{E}$. The point M is defined by the spherical coordinates (r, θ, φ) and the corresponding spherical basis is denoted $\left(\mathbf{e}_r, \mathbf{e}_\theta, \mathbf{e}_\varphi\right)$. We also define the local Cartesian coordinates $\mathbf{x} = (x, y, z)$ and reference frame $\mathscr{R} : \left\{M, \mathbf{e}_x, \mathbf{e}_y, \mathbf{e}_z\right\}$ associated with the fluid box, which is such that $\mathbf{e}_z = \mathbf{e}_r$, $\mathbf{e}_x = \mathbf{e}_\varphi$ and $\mathbf{e}_y = -\mathbf{e}_\theta$. In this frame, the local gravity acceleration, assumed to be constant, is aligned with the vertical direction, i.e. $\mathbf{g} = -g\mathbf{e}_z$, and the spin vector is decomposed as follows: $\boldsymbol{\Omega} = \Omega\left(\cos\theta \mathbf{e}_z + \sin\theta \mathbf{e}_y\right)$, where θ is the colatitude. The fluid is Newtonian and locally homogeneous, of kinematic viscosity ν and thermal diffusivity κ. To complete the set of parameters, we introduce the Brunt-Väisälä frequency N given by

$$N^2 = -g\left[\frac{d\log\rho}{dz} - \frac{1}{\gamma}\frac{d\log P}{dz}\right], \tag{2.1}$$

where $\gamma = (\partial \ln P/\partial \ln \rho)_S$ is the adiabatic exponent (S being the specific macroscopic entropy), and P and ρ are the radial distributions of pressure and density of the background, respectively. These distributions are assumed to be rather smooth to consider P and ρ constant in the box. The regions studied are stably stratified ($N^2 > 0$) or convective ($N^2 \approx 0$ or $N^2 < 0$). At the end, we suppose that the fluid is in solid rotation with the whole body.

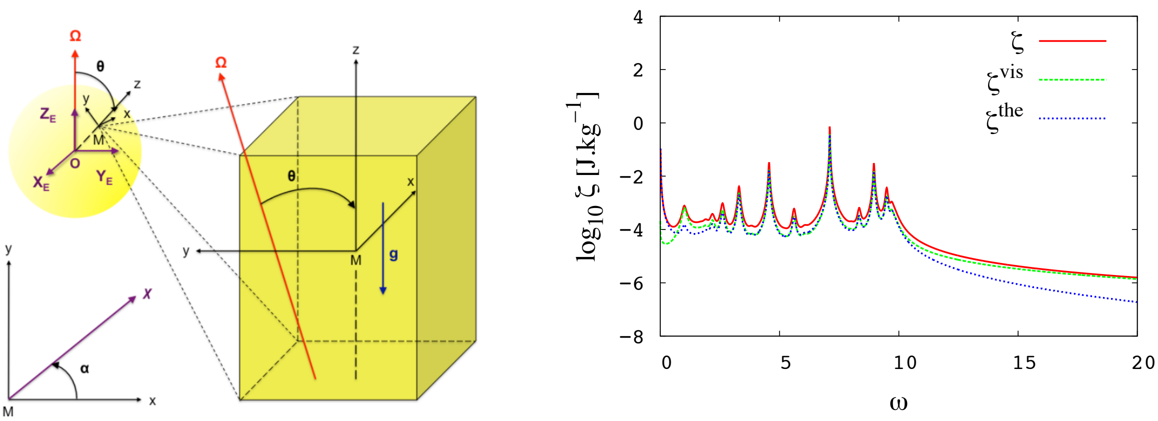

Fig. 1. Left: Local Cartesian model, frame, and coordinates. **Right:** Energy dissipated (ζ) and its viscous and thermal components, ζ^{visc} and ζ^{therm} respectively, as functions of the reduced tidal frequency (ω) for $\theta = 0$, $A = 10^2$, $E = 10^{-4}$ and $K = 10^{-2}$, which gives $P_r = 10^{-2}$ (see Sect. 2 for the definition of these quantities).

2.2 Analytic expressions of dissipated energies

The fluid is perturbed by a tidal force $\mathbf{F} = \left(F_x, F_y, F_z\right)$, periodic in time (denoted t) and space, at the frequency χ. Its tidal response takes the form of local variations of pressure p', density ρ', velocity field $\mathbf{u} = (u, v, w)$ and buoyancy $\mathbf{B}$, which is defined as follows:

$$\mathbf{B} = B\mathbf{e}_z = -g\frac{\rho^{'}(\mathbf{x}, t)}{\rho}\mathbf{e}_z\,. \tag{2.2}$$

Introducing the dimensionless time and space coordinates, tidal frequency, normalized buoyancy, and force per unit mass

$$T = 2\Omega t, \quad X = \frac{x}{L}, \quad Y = \frac{y}{L}, \quad Z = \frac{z}{L}, \quad \omega = \frac{\chi}{2\Omega}, \quad \mathbf{b} = \frac{\mathbf{B}}{2\Omega}, \quad \mathbf{f} = \frac{\mathbf{F}}{2\Omega}, \tag{2.3}$$

and using the Navier-Stokes, continuity and heat transport equations, we compute a solution of the tidally forced waves and perturbation, denoted $s = \{p', \rho', \mathbf{u}, \mathbf{b}, \mathbf{f}\}$, of the form $s = \Re\left[\sum s_{mn} e^{i2\pi(mX+nZ)} e^{-i\omega T}\right]$, where $\Re$ stands for the real part of a complex number. In this expression, m and n are the longitudinal and vertical degrees of Fourier modes and s_{mn} the associated coefficient. At the end, the expressions of the energies dissipated per mass unit over a rotation period by viscous friction and thermal diffusion are obtained:

$$\zeta^{\rm visc} = 2\pi E \sum_{(m,n)\in\mathbb{Z}^{*2}} \left(m^2 + n^2\right)\left(\left|u_{mn}^2\right| + \left|v_{mn}^2\right| + \left|w_{mn}^2\right|\right), \quad \zeta^{\rm therm} = 2\pi K A^{-2} \sum_{(m,n)\in\mathbb{Z}^{*2}} \left(m^2 + n^2\right)\left|b_{mn}\right|^2. \tag{2.4}$$

In these expressions, A, E (the Ekman number) and K are the control parameters of the system, given by

$$A = \left(\frac{N}{2\Omega}\right)^2, \quad E = \frac{2\pi^2\nu}{\Omega L^2}, \quad \text{and} \quad K = \frac{2\pi^2\kappa}{\Omega L^2}. \tag{2.5}$$

3 Asymptotic regimes and scaling laws

Using Eq. (2.4), it is possible to plot $\zeta^{\rm visc}$ and $\zeta^{\rm therm}$ as functions of the tidal frequency (e.g. Fig. 1, right). The dissipation spectrum appears to be highly resonant, and its properties strongly depend on the control parameters identified above. By studying the analytic solution given by the model, we determine the asymptotic regimes of the tidal response (Fig. 2). Let us recall the Prandtl number of the system, $P_{\rm r} = \nu/\kappa$. Four different behaviours are identified. Each of them corresponds to a colored region on the map:

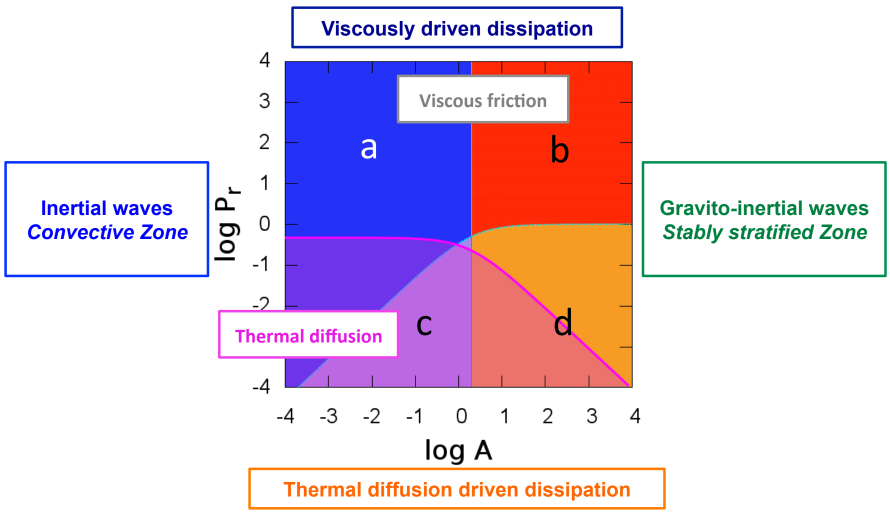

Fig. 2. Map of the asymptotic behaviours of the tidal response. The horizontal (vertical) axis measures the parameter A ($P_r = \nu/\kappa$) in logarithmic scales. Regions on the left correspond to inertial waves (**a** and **c**), and to gravito-inertial waves on the right (**b** and **d**). The fluid viscosity (thermal diffusivity) drives the behaviour of the fluid in regions **a** and **b** (**c** and **d**). The pink (grey) zone corresponds to the regime of parameters where $\zeta^{\rm therm}$ ($\zeta^{\rm visc}$) predominates in tidal dissipation.

1. $A \ll A_{mn}$ and $P_r \gg P_{r;mn}$: inertial waves controlled by viscous diffusion (blue);
2. $A \gg A_{mn}$ and $P_r \gg P_{r;mn}$: gravity waves controlled by viscous diffusion (red);
3. $A \ll A_{mn}$ and $P_r \ll P_{r;mn}$: inertial waves controlled by thermal diffusion (purple); and
4. $A \gg A_{mn}$ and $P_r \ll P_{r;mn}$: gravity waves controlled by thermal diffusion (orange),

where A_{mn} and $P_{r;mn}$ are the vertical and horizontal transition parameters associated with the mode (m, n). Besides, we may identify the regions where the fluid response is mainly damped by thermal diffusion (pink) or by viscous friction (grey). The transition, materialized by the pink line, corresponds to $P_r = P_r^{\rm diss}$. The model allows us to compute, for all regimes, analytical formulae quantifying properties of the dissipation spectrum such as the number $N_{\rm kc}$, positions ω_{mn}, width l_{mn} and height H_{mn} of the resonant peaks, the height of the non-resonant background $H_{\rm bg}$, which corresponds to the equilibrium tide, and the sharpness ratio $\Xi = H_{11}/H_{\rm bg}$. Some of these formulae are given in Fig. 3. We finally deduce from these analytic solutions the scaling laws characterizing the dissipation regimes of Fig. 2, summarized in Table 1.

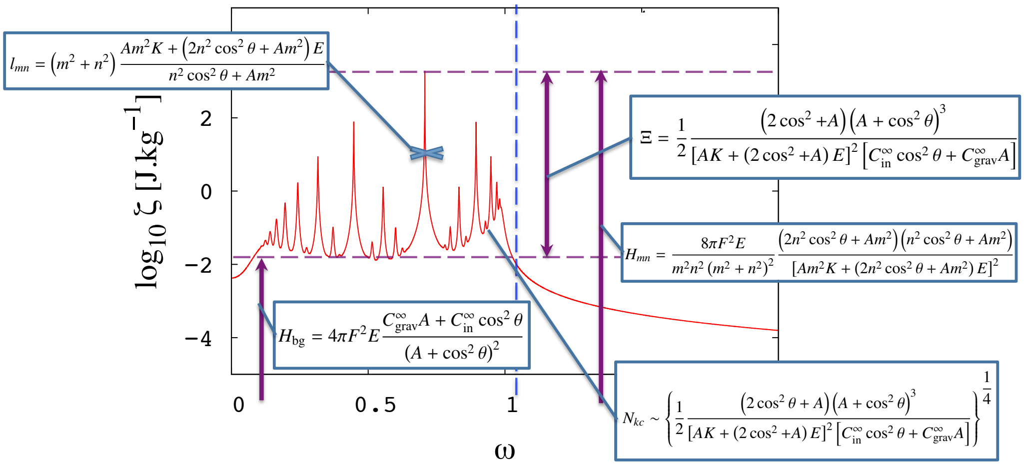

Fig. 3. Energy dissipated by viscous friction as a function of the reduced tidal frequency (ω) and the formulae giving the properties of the spectrum as functions of the colatitude and control parameters of the box (A, E and K).

4 Conclusions

In this work, we have explored the physics of tidal dissipation in fluid layers by using an analytic local model. This approach allowed us to identify the physical parameters that control the tidal response of a non-magnetized fluid. From the analytic expressions obtained for energies, we determined the possible regimes of tidal dissipation, which may be dominated either by inertial or gravity waves, and controlled either by viscous friction or thermal diffusion. Furthermore, we note that below a given critical Prandtl number, the principal damping mechanism is heat diffusion (on the contrary, tidal dissipation above this Prandtl number is due to viscous friction essentially). At the end, we established the scaling laws quantifying the properties of dissipation frequency spectra as functions of the control parameters of the model for each identified behaviour. This study will be completed in forthcoming works with the case of magnetized fluid layers.

This work was supported by the French Programme National de Planétologie (CNRS/INSU), the CNES-CoRoT grant at CEA-Saclay, the ”Axe fédérateur Etoile” of Paris Observatory Scientific Council, and the International Space Institute (ISSI; team ENCELADE 2.0).

<table>
<tr><th>Domain</th><th colspan="2">$A \ll A_{11}$</th><th colspan="2">$A \gg A_{11}$</th></tr>
<tr><td>$P_r \gg P_{r;11}^{\text{reg}}$</td><td colspan="2">$l_{mn} \propto E$
$\omega_{mn} \propto \dfrac{n\cos\theta}{\sqrt{m^2+n^2}}$
$H_{mn} \propto E^{-1}$
$N_{\text{kc}} \propto E^{-\frac{1}{2}}$
$H_{\text{bg}} \propto E$
$\Xi \propto E^{-2}$</td><td colspan="2">$l_{mn} \propto E$
$\omega_{mn} \propto \dfrac{m\sqrt{A}}{\sqrt{m^2+n^2}}$
$H_{mn} \propto E^{-1}$
$N_{\text{kc}} \propto A^{\frac{1}{4}}E^{-\frac{1}{2}}$
$H_{\text{bg}} \propto A^{-1}E$
$\Xi \propto AE^{-2}$</td></tr>
<tr><td rowspan="2">$P_r \ll P_{r;11}^{\text{reg}}$</td><td>$P_r \gg P_{r;11}$</td><td>$l_{mn} \propto E$
$\omega_{mn} \propto \dfrac{n\cos\theta}{\sqrt{m^2+n^2}}$
$H_{mn} \propto E^{-1}P_r^{-1}$
$N_{\text{kc}} \propto E^{-\frac{1}{2}}$
$H_{\text{bg}} \propto EP_r^{-1}$
$\Xi \propto E^{-2}$</td><td>$P_r \gg P_{r;11}^{\text{diss}}$</td><td>$l_{mn} \propto EP_r^{-1}$
$\omega_{mn} \propto \dfrac{m\sqrt{A}}{\sqrt{m^2+n^2}}$
$H_{mn} \propto E^{-1}P_r^{2}$
$N_{\text{kc}} \propto A^{\frac{1}{4}}E^{-\frac{1}{2}}P_r^{\frac{1}{2}}$
$H_{\text{bg}} \propto A^{-1}E$
$\Xi \propto AE^{-2}P_r^{2}$</td></tr>
<tr><td>$P_r \ll P_{r;11}$</td><td>$l_{mn} \propto AEP_r^{-1}$
$\omega_{mn} \propto \dfrac{n\cos\theta}{\sqrt{m^2+n^2}}$
$H_{mn} \propto A^{-2}E^{-1}P_r$
$N_{\text{kc}} \propto A^{-\frac{1}{2}}E^{-\frac{1}{2}}P_r^{\frac{1}{2}}$
$H_{\text{bg}} \propto EP_r^{-1}$
$\Xi \propto A^{-2}E$</td><td>$P_r \ll P_{r;11}^{\text{diss}}$</td><td>$l_{mn} \propto EP_r^{-1}$
$\omega_{mn} \propto \dfrac{m\sqrt{A}}{\sqrt{m^2+n^2}}$
$H_{mn} \propto A^{-1}E^{-1}P_r$
$N_{\text{kc}} \propto A^{\frac{1}{4}}E^{-\frac{1}{2}}P_r^{\frac{1}{2}}$
$H_{\text{bg}} \propto A^{-2}EP_r^{-1}$
$\Xi \propto AE^{-2}P_r^{2}$</td></tr>
</table>

Table 1. Scaling laws for the properties of the energy dissipated in the different asymptotic regimes. The parameter $P_{r;11}^{\text{diss}}$ indicates the transition zone between a dissipation led by viscous friction and a dissipation led by heat diffusion. The parameter A_{11} indicates the transition between tidal inertial and gravity waves. The parameter $P_{r;11}^{\text{reg}}$ is defined as $P_{r;11}^{\text{reg}} = \max\left\{P_{r;11}, P_{r;11}^{\text{diss}}\right\}$.

References

Auclair-Desrotour, P., Le Poncin-Lafitte, C., & Mathis, S. 2014, A&A, 561, L7

Auclair Desrotour, P., Mathis, S., & Le Poncin-Lafitte, C. 2015, A&A, 581, A118

Cébron, D., Bars, M. L., Gal, P. L., et al. 2013, Icarus, 226, 1642

Cébron, D., Le Bars, M., Moutou, C., & Le Gal, P. 2012, A&A, 539, A78

Efroimsky, M. & Lainey, V. 2007, Journal of Geophysical Research (Planets), 112, 12003

Gerkema, T. & Shrira, V. I. 2005, Journal of Fluid Mechanics, 529, 195

Ogilvie, G. I. & Lin, D. N. C. 2004, ApJ, 610, 477

Ogilvie, G. I. & Lin, D. N. C. 2007, ApJ, 661, 1180

Remus, F., Mathis, S., & Zahn, J.-P. 2012, A&A, 544, A132

Wu, Y. 2005, ApJ, 635, 688

Zahn, J. P. 1966a, Annales d'Astrophysique, 29, 313

Zahn, J. P. 1966b, Annales d'Astrophysique, 29, 489

Zahn, J. P. 1966c, Annales d'Astrophysique, 29, 565

Zahn, J.-P. 1975, A&A, 41, 329

Zahn, J.-P. 1977, A&A, 57, 383

Zahn, J.-P. 1989, A&A, 220, 112

SF2A 2015
F. Martins, S. Boissier, V. Buat, L. Cambrésy and P. Petit (eds)

NEWS FROM THE CFHT/ESPADONS SPECTROPOLARIMETER

C. Moutou[1], L. Malo[1], N. Manset[1], L. Selliez-Vandernotte[1] and M.-E. Desrochers[1]

Abstract. The ESPaDOnS spectropolarimeter has been in use on the Canada-France-Hawaii Telescope (CFHT) since 2004, for studying stars, galactic objects and planets. ESPaDOnS is used in queued service observing mode since 2008, which allows an optimization of the science outcome. In this article, we summarize the new functionalities and analyses made on ESPaDOnS operations and data for the present and future users. These modifications include: signal-to-noise ratio based observing, radial velocity nightly drifts, the OPERA pipeline under development, the measurement of H2O content in the Maunakea sky, and the use of ESPaDOnS with the neighbour telescope Gemini.

Keywords: Observatory, spectrograph, stars

1 Introduction

The ESPaDOnS spectropolarimeter is used in three different modes: Star-only (single fiber on the star, highest resolving power, 81000), Star+Sky (68000 resolving power, second fiber observes the sky background), and Polarimetric (68000 resolving power, linear or circular polarisation). With its twin instrument NARVAL at Telescope Bernard Lyot, ESPaDOnS has the unique capability of measuring the magnetic topologies of stars. Recent examples of ESPaDOnS results are given in, e.g., Donati et al. (2015); Shultz et al. (2015); Melendez et al. (2015); Martins et al. (2015); Sabin et al. (2015); Walker et al. (2015). While ESPaDOnS is highly efficient, cover the totality of the visible bandpass (370-1050nm) and benefits from the exquisite conditions at Maunakea 4200m-high Observatory, its performances and global science outcome can still be optimized in a number of ways. In the following, we summarize the directions taken by the observatory staff to improve the consistency, reliability and performance of ESPaDOnS operations. This report is also meant to help present and future users to understand their data better and/or to plan more efficiently their future ESPaDOnS observing campaigns.

2 Signal-to-noise based observations

ESPaDoNS is operated in queued service observing mode since 2008, from Phase 2 information provided by the users: instrumental configuration, exposure time per exposure, sequence strategy, science priorities, finding charts, sky constraints and potentially timing parameters. Then the queue for a given night is built from the entire database of observations, by a queue coordinator who minimizes the telescope motion, the instrumental changes (only two modes out of the three can be used in a given night), and maximizes the science outcome, while trying to accomodate all timing constraints. Backup queues are also prepared with alternate targets. This queue can be executed as such during the night, if the conditions are good and stable; the observer can also pick any observation from the queue, skipping or re-ordering observations as needed . If conditions are bad and/or variable, the remote observer can repeat high priority observations or switch to low priority snapshot programs. However, when conditions are better than median, the stellar signal increases rapidly and it would be possible to fit in more observations and increase the overall quality of the collected data. For this reason, the CFHT observatory aims at offering an operational strategy based on the measured signal-to-noise ratio (SNR) rather than fixed exposure times for ESPaDonS. Note that this mode is already used for some MegaPrime imaging surveys (Cuillandre et al. 2014), allowing an homogeneous depths in a wide field of view. For ESPaDOnS, in addition to adapt exposure times as a function of observing conditions, an SNR-based operation would also

[1] CFHT, Kamuela HI 96743, USA

© Société Francaise d'Astronomie et d'Astrophysique (SF2A) 2015

allow to homogeneize the quality of the numerous polarimetric sequences (10 to 15 identical observations spread over two weeks).

In order to set up the SNR mode, the observatory needs additional information from the users, namely: 1) the magnitude and effective temperature of the target, 2) the goal SNR per pixel and per intensity spectrum. By using this information, when available, we were able to estimate that 25 to 30% of the exposure time would have been saved, by observing at the requested SNR and not beyond. The science validation of this new mode requires that the users provide the observatory staff with relevant and complete information. One way to verify this in a systematic way is to use the instrument model (exposure time calculator*) with adequate ranges of image quality and airmass. The user can now iterate with the different values of exposure time, external constraints and goal SNR, in the Phase 2 web tool, until all information is consistent in the database.

Second, the remote observer needs a realtime estimate of the SNR during the night, or even during the exposure. This is possible with the exposuremeter, a photodiode that collects a small part of the light going through the spectrograph. By comparing exposuremeter counts and final SNR as measured by the pipeline (examples in Figure 1), we were able to calibrate the realtime flux and estimate the realtime behaviour of the SNR. This calibration depends on the instrumental mode and requires adjustements for the spectrograph temperature, which affects the mechanical structure of the optical mounts. The realtime estimate of the SNR is presently (Sept 2015) in testing, for further validation. When deemed a robust estimate, the observer will be able to trigger the anticipated readout of the exposure in the cases where the goal SNR has been reached before the expected end of the exposure. A final complication comes from the fact that the SNR for ESPaDOnS can be defined at several places in the spectrum, which is freely specified by the user, while the calibration of the exposuremeter is done at a specific wavelength (755nm, center of order 30). So it is first necessary to use the exposure time calculator from the database to derive the goal SNR at order 30, from the goal SNR at any wavelength provided by the user. Users are also encouraged to use order 30 as their new reference for goal SNR requests!

With a simultaneous monitoring of the flux count entering the spectrograph, one could also prevent saturated exposures -for program relying on extreme SNR values- but mostly, the gain in exposure time would be beneficial to the whole user community. The SNR operation mode with ESPaDOnS could be made available in 2016A, provided that all tools are validated and robust, and at the discretion of the users. Indeed, some programs may be inadequate for SNR mode observations: time critical sequences, targets of very variable magnitude, moving targets or very faint objects.

3 Radial velocity shifts and precision

ESPaDOnS is not an optimized velocimeter: the spectrograph is not actively controlled in temperature nor pressure, the fiber injection is not scrambled, and there is no possible simultaneous wavelength calibration as in high-precision radial-velocity spectrographs. However, the spectral range and resolution allow to obtain a good precision on the spectrum of Earth atmosphere bands, and to correct at first order for the wide velocity shift that occurs during the night. The wavelength calibration of the spectrograph, done in the afternoon or the morning, results in an error of about 200 m/s. There are ways to reduce this error, by improving the pipeline (see section 5). By observing known exoplanets, previous studies have shown that a residual scatter of $\sim$20 m/s remains on the stellar radial velocity measurement, when the Least Square Deconvolution intensity profile is used (Donati & Brown 1997) and when the measurement is corrected for the spectrograph shift as measured on the telluric spectrum (Moutou et al. 2007). On a very short timescale of 1 hour, the scatter is of the order of 10 m/s.

The typical shift during a night is of the order of 200 to 500 m/s, depending on the temperature and pressure evolution. The behaviour of the drift also depends on the range of these parameters, and can be linear or sinusoid-like, or anything in between! In the coming month, this drift evolution will be continuously monitored on ESPaDOnS data, to spot any change of the behaviour due to the recent installation of a second external, passive, thermal enclosure. Although passive, the new enclosure should limit the temperature changes on a given timescale; also, it immediately resulted in a new temperature range (the spectrograph has become warmer), which may affect the mechanical distortions and the residual spectral shifts.

*http://etc.cfht.hawaii.edu/esp/

4 Water content above Maunakea

With its spectral coverage of 370-1050nm, the ESPaDOnS spectra contain a wealth of information about the Earth atmosphere features. As the mean telluric band is extracted from the spectra by the pipeline, for the correction of the spectral shift, this profile can also be used for calibrating the water content in the sky at the time of the observation. The equivalent width of the telluric profile (EW) has been correlated to the simultaneous measurement of the water absoption by the Caltech Submm Observatory ontop Maunakea[†]. The following equations are used to derive the precipitable water vapor from the ESPaDOnS spectra:

$$PWVesp(zenith) = 2.5335 - 1.608 \times EW + 0.200 \times EW^2 \tag{4.1}$$

$$PWVesp = 1./airmass * (PWVesp(zenith) - 0.296 \times (airmass - 1.)) \tag{4.2}$$

where $PWVesp$ is the value at the observed $airmass$ and $PWVesp(zenith)$ the value at zenith.

Using more than 1 year of data where this measurement is available, we could derive some statistical values, which are useful for specific programs limited by the water content in the spectra and more generally, for the future CFHT/SPIRou programs (where water content will directly affect the radial-velocity precision). During 50% of the time, the PWV in the atmosphere is less than 2.5mm H2O during nights where ESPaDOnS is used, and at the real observed airmasses.

5 OPERA pipeline

The standard pipeline of ESPaDOnS is Libre-Esprit (Donati & Brown 1997). It conducts the pre-processing of the spectra, recognizes the order from flatfield calibration exposures, performs the wavelength calibration, uses optimal extraction to derive the final spectra, calculates polarization from 4 polarimetric sub-exposures, and subtracts the sky spectrum for data taken in the Star+Sky mode. Libre-Esprit, is embedded in the data flow software Upena and used daily to process the ESPaDOnS nights and provide users with final products.

The OPERA pipeline has started development a few years ago to fulfill additional needs from the users: get intermediate products, and use a two-amplifier readout mode of the detector that would reduce the readout overheads by about a factor of two. OPERA is also used for the reduction of GRACES data (see below), for which the processing parameters are different. Fine tuning of OPERA algorithms is still underway but made a lot of progress in the last year (Martioli, Malo et al, in prep.). Both OPERA and Libre-Esprit products will be distributed to users in 2016, in order for the observatory to get feedback before OPERA pipeline eventually becomes the new standard.

Special care has been put into the spectral calibration into OPERA. The selection of Thorium and Neon lines from the atlas and from the observed lamp exposures has been optimized, with the result that the radial-velocity scatter per order is of the order of 50 to 70 m/s. A combination of long and short exposures on the spectral lamp also prevents some of the saturated lines to blur out the neighbour orders. This gain of radial-velocity precision is promising and may open new science capability.

Finally, the 2-amplifier mode is still being tested, but its reduction poses no issue with the OPERA pipeline, although the noise properties are different than in 1-amplifier images and changing along the chip. Science validation is yet needed before this 2-amplifier mode is offered for observations.

6 Meeting the giants: GRACES

GRACES stands for Gemini Remote Access to CFHT ESPaDOnS Spectrograph. It is literally the links between the neighbour 8m telescope located at about 200m from the CFHT dome and the ESPaDOnS spectrograph. A 270m fiber has been deployed that feeds ESPaDOnS when it is not used by CFHT. GRACES has two spectroscopic modes (no polarimetric mode) with resolving powers of 67k and 40k and covers the same spectral range than ESPaDOnS, although the bluest part of the spectrum is less efficient. Lamp calibration and fiber injection are provided by the Gemini North GMOS instrument. First tests and science results obtained with GRACES are described in Chene et al. (2014) and Malo et al (in prep).

As foreseen in the agreement between both observatories, the CFHT community will receive a few nights of observing at Gemini North or South in compensation for the use of ESPaDOnS (with a ratio 3/20). A first call for proposals should appear in 2016B (March 2016).

[†] `http://cso.caltech.edu/tau/`

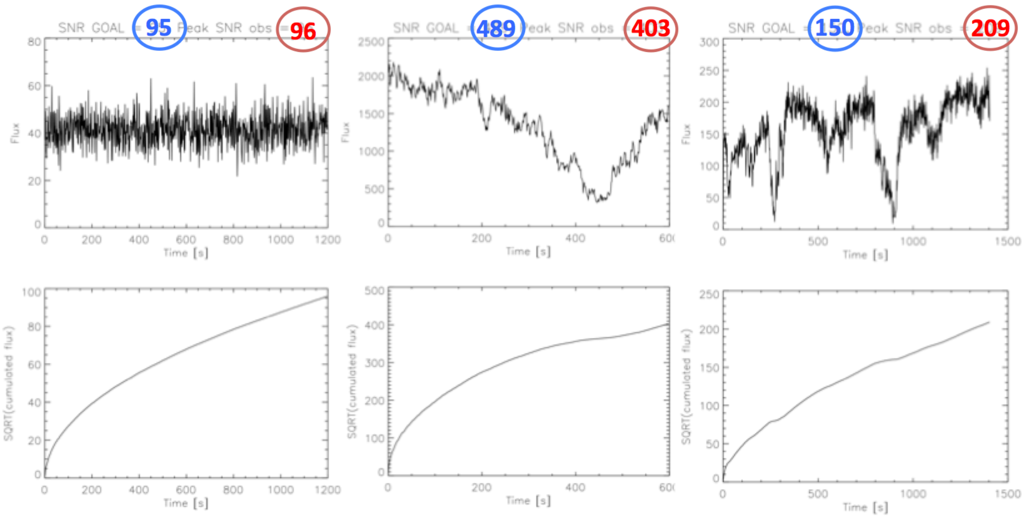

Fig. 1. Three examples of exposuremeter plots are shown: (left), the conditions are stable and the goal SNR (95) is achieved (96); (middle), the flux is altered by a cloud -or degrading image quality- and the goal SNR (489) is not achived (403), meaning we should repeat the exposure; (right) the flux is altered during the exposure, but the goal SNR (150) has nevertheless been exceeded, so that the exposure could have been reduced in realtime. The plots below show the realtime estimate of the SNR based on the exposuremeter counts.

References

Chene, A.-N., Padzer, J., Barrick, G., et al. 2014, in Society of Photo-Optical Instrumentation Engineers (SPIE) Conference Series, Vol. 9151, Society of Photo-Optical Instrumentation Engineers (SPIE) Conference Series, 47

Cuillandre, J., Mahoney, B., & Withington, K. 2014, in Astronomical Society of the Pacific Conference Series, Vol. 485, Astronomical Data Analysis Software and Systems XXIII, ed. N. Manset & P. Forshay, 81

Donati, J.-F. & Brown, S. F. 1997, A&A, 326, 1135

Donati, J.-F., Hébrard, E., Hussain, G. A. J., et al. 2015, MNRAS, 453, 3706

Martins, F., Hervé, A., Bouret, J.-C., et al. 2015, A&A, 575, A34

Melendez, J., Tucci Maia, M., & Ramirez, I. 2015, in Astronomical Society of the Pacific Conference Series, Vol. 496, Astronomical Society of the Pacific Conference Series, ed. S. M. Rucinski, G. Torres, & M. Zejda, 411

Moutou, C., Donati, J.-F., Savalle, R., et al. 2007, A&A, 473, 651

Sabin, L., Wade, G. A., & Lèbre, A. 2015, MNRAS, 446, 1988

Shultz, M., Wade, G. A., Alecian, E., & BinaMIcS Collaboration. 2015, MNRAS, 454, L1

Walker, G., Bohlender, D., Maier, J., & Campbell, E. 2015, ArXiv e-prints [arXiv] 1509.06818

SF2A 2015
F. Martins, S. Boissier, V. Buat, L. Cambrésy and P. Petit (eds)

SPIROU: A SPECTROPOLARIMETER FOR THE CFHT

C. Moutou[1], I. Boisse[2], G. Hébrard[3,4], E. Hébrard[6], J.-F. Donati[8], X. Delfosse[10], D. Kouach[12] and the SPIRou team

Abstract. SPIRou is a near-infrared spectropolarimeter and high-precision radial-velocity instrument, to be mounted on the 3.6m Canada-France-Hawaii telescope ontop Maunakea and to be offered to the CFHT community from 2018. It focuses on two main scientific objectives : (i) the search and study of Earth-like planets around M dwarfs, especially in their habitable zone and (ii) the study of stellar and planetary formation in the presence of stellar magnetic field. The SPIRou characteristics (complete coverage of the near infrared wavelengths, high resolution, high stability and efficiency, polarimetry) also allow many other programs, e.g., magnetic fields and atmospheres of M dwarfs and brown dwarfs, star-planet interactions, formation and characterization of massive stars, dynamics and atmospheric chemistry of planets in the solar system.

Keywords: spectrograph, exoplanets, stellar formation, spectropolarimetry

1 Introduction

SPIRou is a near-infrared spectropolarimeter designed for the detection of exoplanets around low-mass stars and for the detection of magnetic fields of young stellar objects. It is currently under construction with a first light foreseen in fall 2017. SPIRou will then be available to the community in 2018. An overview of the key aspects of SPIRou's design is given in Artigau et al. (2014). Delfosse et al. (2013) and Santerne et al. (2013a) detailed several aspects of the science cases. In this article, we will recall the science goals and challenges (Section 2), present the status of the instrument development (Section 3) and describe the SPIRou Legacy Survey (Section 4) as presently foreseen for the Canada-France-Hawaii Telescope (CFHT).

2 The SPIRou science

2.1 The Quest for Earth-like planets around M dwarfs

One objective of the current exoplanet science is to find and characterise habitable Earths and Super Earths. Among the 1600 planets detected (and many more candidates), very few are in the habitable zone (sphere around a star where liquid water can be stable of the surface) of their host stars, and none is equivalent to Earth. On

[1] Canada-France-Hawaii Telescope Corporation, 65-1238 Mamalahoa Hwy, Kamuela, HI 96743, USA
[2] Université Aix-Marseille / CNRS-INSU, LAM / UMR 7326, 13388 Marseille, FRANCE
[3] IAP / UMR 7095, CNRS / Université Pierre & Marie Curie, 98 bis boulevard Arago, 75014 Paris, France
[4] Observatoire de Haute-Provence, CNRS, Université d'Aix-Marseille, 04870, Saint-Michel-l'Observatoire, France
[5] Université de Toulouse, UPS-OMP, IRAP, 14 avenue E. Belin, Toulouse, F-31400 France
[6] CNRS, IRAP / UMR 5277, Toulouse, 14 avenue E. Belin, F31400 France
[7] Université de Toulouse, UPS-OMP, IRAP, 14 avenue E. Belin, Toulouse, F-31400 France
[8] CNRS, IRAP / UMR 5277, Toulouse, 14 avenue E. Belin, F31400 France
[9] Université Grenoble Alpes, IPAG, BP 53, F38041 Grenoble Cedex 09, France
[10] CNRS, IPAG / UMR 5274, BP 53, F38041 Grenoble Cedex 09, France
[11] Université de Toulouse, UPS-OMP, IRAP, 14 avenue E. Belin, Toulouse, F-31400 France
[12] CNRS, IRAP / UMR 5277, Toulouse, 14 avenue E. Belin, F31400 France

© Société Francaise d'Astronomie et d'Astrophysique (SF2A) 2015

another hand, very few planets are known around M dwarfs. Finally, observing the planetary architecture as a function of the stellar host mass is important to constrain planet formation models.

The long-term goal of exploring the atmospheric composition of the telluric, potentially habitable exoplanets starts with the discovery of such objects in the solar neighbourhood and the statistical description of their properties. Ideally, one would need to complete a catalog of habitable terrestrial planets, allowing future space missions to concentrate on planet characterization without wasting time on their detection. In addition, statistical properties of planets around M dwarfs can provide key information on planetary formation, and in particular on the sensitivity of planet formation to initial conditions in the protoplanetary disc. Recent simulations indeed suggest that planet populations change very significantly for M dwarfs of increasing masses (Alibert et al in preparation). M dwarfs also vastly dominate the stellar population in the Solar neighborhood and are likely hosting most planets in our Galaxy; this makes such studies even more crucial. Finally, pioneering studies with HARPS at the ESO 3.6m telescope demonstrated that super-Earths with orbital periods ¡100 d are more numerous around M dwarfs than around Sun-like stars, with an occurrence frequency close to 90% (Bonfils et al. 2013); moreover, about half of these super-Earths are potentially located in the habitable zones of their host stars.

The exoplanetary scientists have several reasons to focus on low-mass M dwarfs around which small/low-mass planets are easier to detect. Indeed, the radial-velocity signal of a planet is inversely proportional to $M_\star^{2/3}$, so the method is more favorable to the coolest dwarf stars. It is also faster and easier to detect planets in the habitable zone of low-mass stars since it is located at a distance where planets orbital periods are in the range 10 to 50 days, thanks to a lower stellar temperature and to the fact that the radial-velocity semi-amplitude is proportional to $P_{orb}^{-1/3}$.

Since M dwarfs are faint in the visible, we designed the SPIRou spectropolarimeter in the infrared, so that it is optimised for accurate radial-velocity measurements on M dwarfs. Two challenges will have yet to be faced when pursuing the search for telluric planets in the habitable zones of M dwarfs with SPIRou. First, numerous telluric lines are present in the near-infrared part of the spectra. These lines do not have an equal contribution on each observation depending on time and weather conditions. One should carefully mask or remove them, before deriving the radial-velocity of the star. The second limitation is the level of activity of low-mass M dwarfs. We are currently investigating several reseach directions to mitigate this problem (see Sect. 2.3).

The quest for low-mass planets around very low mass stars is a major science goal that requires large amounts of time.

2.2 Characterization of transiting exoplanets

Numerous ground- and space-based photometric surveys have been used to detect new transiting planets and several others are in project. Exoplanets transiting in front of their host stars are particularly interesting objects as they allow numerous key studies to be performed. This includes accurate radius, mass, and density measurements, atmospheric studies in absorption through transits and in emission through occultations, dynamic analyses from possible timing variations or obliquity measurements.

With precise masses of transiting exoplanets, the atmospheric models can be efficiently tested. For instance, the presence of an atmosphere and its composition strongly depend on these fundamental parameters, as shown by the difference between CoRoT-7b and GJ 1214b (larger radius for a similar mass for the latter): the atmosphere can be dominated by water or by hydrogen, leading to different chemistry and various densities. The diversity of mass or density in the regime of Earth-like exoplanets and super-earthes is striking, and requires a greater sample, and accurate mass measurements, to become useful constraints for the theory (Valencia et al. 2010; Lopez & Fortney 2014; Valencia et al. 2013).

M dwarfs are advantageous hosts for transiting planets studies, as for the radial-velocity method. Their small radii make deeper the transits of telluric planets, and the reduced size of their habitable zone makes more frequent and probable the transits of a potentially habitable planet. SPIRou is thus well optimized to perform the radial velocity follow up of photometric surveys observing M dwarfs to detect transiting planets. Since the rate of false positives could be significant, in particular those due to blended or unblended binaries, the first goal of this follow up is to establish the planetary nature of the transiting candidates. For such validated transiting planets, the radial velocities are then used to characterize the systems and in particular to measure the mass, eccentricity, and obliquity of the planets. They are also used to characterize the host stars and to search for possible extra companions. SPIRou is expected to play an important role in the follow up of planetary candidates transiting in front of M dwarfs detected by photometric surveys, including ExTra, NGTS, K2, TESS, or PLATO.

Finally, as the magnetic field of the host stars will also be obtained by SPIRou for each planet detection, it will be possible to investigate the role of the magnetic field to shape the evolution of planets, through evaporation or stellar wind interactions. Such studies in transiting systems, where the relative inclinations are better constrained and the planet masses are well known, are particularly interesting.

2.3 Filtering out the radial-velocity activity jitter using the spectropolarimetry

To diagnose the radial velocity jitter, several complementary approaches are commonly used, mostly making use of chromospheric activity indicators like excess flux in the cores of the Hα and Ca II H&K, or measurements of spectral line asymmetries. For the use of SPIRou, we investigate how we can use spectropolarimetry to better characterize and ultimately model the radial-velocity jitter. This new method aims at studying both the radial-velocity jitter caused by activity and Zeeman signatures reflecting the large-scale magnetic field at the origin of activity. To model the radial-velocity jitter due to rotational modulations, we take advantage of the distortions of the Stokes I profiles that are caused by brightness inhomogeneities at the stellar surface (Hébrard et al., 2015, in prep).

As an example, we outline the results obtained for GJ 358, a moderately active M2-dwarf. From the Stokes V signatures we infer a rotational period of $\sim$25.4 days; using Zeeman Doppler Imaging, we then recover the parent large scale magnetic field. This star exhibits a poloidal component with a polar intensity of -110 G inclined at 45°to the line of sight. We observe that the radial velocities and the longitudinal field vary in quadrature, which suggest that spots cluster at phase $\sim$0.7 (see right panel Fig. 1). By modeling the tiny distortions in Stokes I profile using a modified version of Zeeman Doppler Imaging (Hébrard et al. 2015 in prep.), we obtain a map representing the statistical distribution of spots at the stellar surface. As expected, we find a cluster of spots lying close to the same longitude. The radial velocity jitter of full amplitude of $\sim$ 15 $\mathrm{m\,s^{-1}}$ can be filtered out at a rms precision of 2.8 $\mathrm{m\,s^{-1}}$ close to the intrinsic precision of the data set (see right panel of Fig. 1). In the Lomb-Scargle periodogram of the radial velocities, the periods P_{rot}, $P_{\mathrm{rot}}/2$ and $P_{\mathrm{rot}}/3$ have been filtered, and there is no more prevailing peaks in the periodogram of the residuals.
A similar method has been used the analysis of V830 Tau (Donati et al. 2015) and it will be generalized to the planet search programs in the SPIRou data. In the near-infrared, profile distortions induced by cool spots are smaller than in the visible (Huélamo et al. 2008, e.g.), but the Zeeman broadening is larger, so filtering needs to be adjusted accordingly (Hébrard et al. 2014).

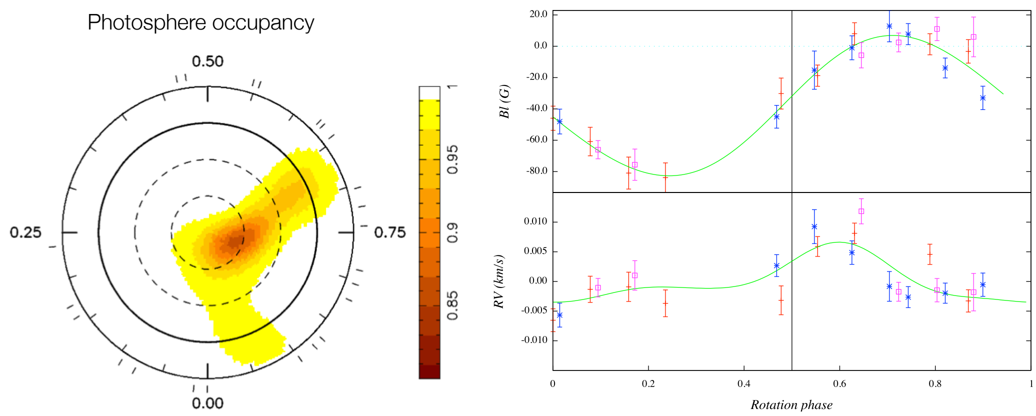

Fig. 1. *Left:* Map of the photosphere occupancy (white for quiet photosphere, brown for spot). The star is viewed in flattened polar projection. The pole is in the center, the bold circle depicts the stellar equator and the outer line represents the -30° latitude. *Right:* Longitudinal field (in G) and radial velocities (in $\mathrm{km\,s^{-1}}$) as a function of the rotation phase, collected with HARPSPol Each color symbol represents a stellar rotation phase. The green curves represent the predicted values.

2.4 Magnetic fields of protostars and cool stars

Our second main scientific goal is to characterise the impact of magnetic fields on the formation of stars and planets. Magnetic fields in the inner disc regions or at protostar surfaces can only be investigated through nIR spectroscopy (Johns-Krull 2007, e.g.) or optical spectropolarimetry (Donati et al. 2005, e.g.). In both cases, magnetic fields are detected through the Zeeman effect on spectral lines, and more specifically through the additional broadening (with respect to non magnetically-sensitive lines of otherwise similar properties) and the polarization structures they generate within line profiles. With SPIRou, we will measure and characterise the structure of the magnetic field of young protostars thanks to the polarimetric capability of SPIRou. The near infrared is needed since these targets are faint in the visible. Moreover the Zeeman effect increases with wavelength.

The questions that SPIRou will be able to handle include: (i) what is the origin of their magnetic fields (e.g. fossil or dynamo), (ii) how do these magnetic fields connect the protostars to their accretion discs, (iii) how do these fields control accretion from the discs and how can they slow down the rotation of the protostars, (iv) how do they participate (along with accretion disc fields) in launching collimated jets, (v) how importantly do they contribute to the photo-evaporation of the disk through the coronal X-rays they indirectly produce, (vi) to what extent do magnetism and magnetospheric accretion modify the internal structure of protostars, and (vii) with which magnetic topologies do protostars start their unleashed spin-up towards the main sequence once they dissipated their accretion discs?

At ages of 0.1-0.5 Myr, low-mass pre-main-sequence stars (class-I protostars) are surrounded by massive accretion discs from which they actively feed, and are embedded in dust cocoons hiding them from view at optical wavelengths. As a result, the large-scale magnetic topology at the surface of a class-I protostars has never been observed and will be assessed for the first time with SPIRou.

With SPIRou data, quantitative studies of how protostars accrete material from their accretion discs and how this process impacts their structure and rotation evolution can be carried out and the corresponding models can be directly confronted to observations. One can for instance retrieve the location and geometry of accretion funnels (Romanova et al. 2011, e.g.), investigate how the resulting accretion shock affects the atmosphere of the star and evaluate the impact of accretion on structure and angular momentum content (Zanni & Ferreira 2013) of the newly born star. In particular, class-I protostars should be well suited for investigating magnetospheric accretion at higher accretion-rate regimes.

With SPIRou, we will be estimating the gaseous content in the inner regions of different types of protostellar accretion discs, investigating their magnetic field strengths and topologies and looking for potential correlations between the disc and field properties to find out whether and how fields can impact discs. Magnetic fields in discs are potentially important since fields are expected to impact significantly the formation, disc-induced migration and orbital inclination of protoplanets. More specifically, discs fields and associated MHD turbulence can potentially inhibit fragmentation through gravitational instabilities and modify the subsequent formation of giant planets. Thanks to our first study on filtering out activity jitter on rotating stars (Petit et al. 2015; Donati et al. 2015), we could also search for hot Jupiters around these targets. Detecting hot Jupiters at the early stage would constrain the theory on the formation and migration of planetary systems.

3 The instrument development status

SPIRou is being developed by seven countries: Canada, France, Switzerland, Taiwan, Brazil, Portugal, Hawaii and 12 institutes in these countries. The consortium is led by IRAP (Toulouse, France).

The science requirements and technical specifications of SPIRou can be summarized as follows:

- Acquire a single-shot spectral domain covering the YJHK domain (0.98-2.35 μm), to benefit the very high spectral radial velocity content in the H and K-band for M-dwarfs and to allow observing the magnetic field of embedded young stars in their early phase.

- Get a spectral resolution of 70K to 75K, in order to optimize the radial-velocity accuracy for lines of slowly rotating M dwarfs.

- Achieve the radial velocity stability of 1m/s, to allow the detection of Earth and Super-Earth exoplanets in the habitable zone of M-dwarfs.

- Provide the linear and circular polarimetric capacity, with maximum 1-2 % crosstalk and down to a sensitivity of 10 ppm (similar to CFHT/ESPaDOnS). This will allow the observations of stellar magnetic fields and the disentangling of the stellar activity and the keplerian signal.

- Obtain a signal-to-noise ratio of 100 per 2km/s pixel for a star of magnitude J=12.0 or K=11; this implies a requirement on the throughput of 15 % and on the thermal background at 2.35 μm of maximum 50 ph/s/Å. This efficiency is required for a large radial-velocity and polarimetric survey.

SPIRou is made of several sub-systems, each of them being simultaneously developed in different institutes of the consortium. The first sub-system is the Cassegrain unit, mounted in the dome at the Cassegrain focus of the 3.6m CFH telescope. It is composed of an atmospheric dispersion corrector, the guide camera with an image stabilisation system and an achromatic polarimeter. The Cassegrain unit is being developed and tested at IRAP, Toulouse. The second sub-system contains the fibers and the pupil slicer. The spectral range requires the use of fluoride fibers; high transmission fibers are chosen to maximize thoughput. The near-field scrambling is obtained with a section of octogonal fibers. The pupil is split into four slices for each science fiber, with 4 pixels separating each fiber. The main piece of SPIRou is the cryogenic spectrograph, located in the coudé room at the third floor of the telescope building. Its thermal control has a specification of 2 mK over a day. The spectrograph design contains a large parabolic mirror, a double-pass prism-train cross-disperser with an R2 diffraction grating, and a fully dioptric camera with a Hawaii 4RG 4kx4k detector array. The spectrograph cryostat, currently being mounted in Victoria (Canada), is shown on Fig. 2. Essential to the radial-velocity accuracy is the calibration & super-stable radial-velocity reference module, also located in the coudé room and fiber linked to the spectrograph; this calibration module is being assembled between Geneva and Observatoire de Haute Provence.

The data reduction pipeline is being developed by the consortium (effort led by LAM, Marseille) and will be delivered to CFHT with the instrument, aiming at a complete extraction of spectra as well as radial-velocity and polarisation signatures available a few minutes after the observations.

The last project review was held in June 2015 at IRAP, Toulouse. The funding process is now finalised, and should be secured at the end of 2015. The integration / validation of the full instrument will be at IRAP, Toulouse and should last 7 months. The integration at system level is expected to start on March 2016, followed by the validation phase on November 2016. The system Acceptance at IRAP will be in April 2017. We expect the final integration on CFHT site to be in summer 2017 for a first light in the last semester of 2017.

Stay tuned by consulting the SPIRou web page `http://spirou.irap.omp.eu/`.

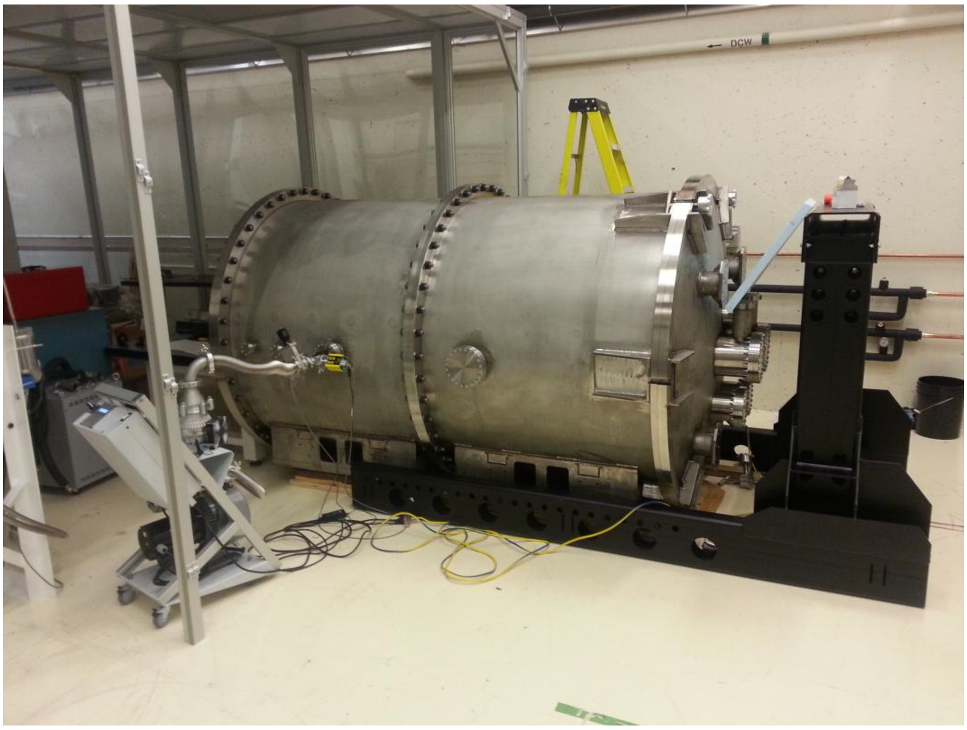

Fig. 2. The SPIRou cryostat, being integrated at NRC Herzberg, Victoria, Canada.

4 The SPIRou Legacy Survey (SLS)

Shortly after its installation on the CFHT, SPIRou will start a series of Legacy Surveys, for a minimum of 300 nights over the first 3 years of operations of the instrument -as approved by the CFHT Board in 2015. The objectives of the surveys are threefold:

- identify several tens of habitable-zone Earth-like planets orbiting M dwarfs in the immediate neighborhood of the Solar System, as well as more than 100 exoplanets with orbital periods ranging from 1 day to 1 year, to derive accurate planet statistics,
- characterize the internal structure of several dozens of telluric planets with moderate equilibrium temperature, by providing mass measurements to the transit candidates discovered by K2, TESS and PLATO,
- explore the impact of magnetic fields on star / planet formation, by detecting and characterizing magnetic fields of various types of young stellar objects.

These three observing programs require large input catalogs of targets for statistical relevance, and a large number of visits per target. With its queue operation mode, the CFHT is well adapted and flexible to handle large surveys, get homogeneous data sets and optimize temporal sampling and critical scheduling. Specific tools are being developed at the observatory to support SPIRou surveys operations.

The radial-velocity **planet-search survey (SLS-PS)** will focus on an input catalog of 330 nearby M dwarfs. They are selected from the catalog by Lépine & Gaidos (2011) and cover a range in mass from 0.08 to 0.5 M_{sun}. Monte Carlo simulations suggest that the SLS-PS should detect $\sim$ 250 new exoplanets, including $\sim$180 with masses less than 5 Earth masses and $\sim$30 of them lying in the habitable zone. Breaking down the full stellar sample in 0.5-dex bins in orbital period and mass, the SLS-PS will provide occurrence rates of Earth-like planets in each mass / period bin with a $\sim$20% accuracy. In particular, the SLS-PS will determine the frequency η_E of habitable-zone Earth-like planets around M dwarfs to an accuracy of $\sim$5%. Extensions of this program are possible and can be carried out after the completion of SLS-PS. The required number of visits per star averages to $\sim$ 50 per star during the survey duration, but this parameter may have to be increased at the expanse of decreasing the sample size, especially if multi-planet systems are frequently found or/and if the stellar jitter remains an issue.

The total time required for the SLS-PS is of the order of 275 nights, counting on $\sim$ 10 min per visits to achieve the required 1 m/s precision on individual radial velocity measurements. As SPIRou observations are done in the spectropolarimetric mode, the magnetic field of the host stars will be monitored at the same frequency than the planetary orbits, offering a unique view on the evolution of magnetic topologies of evolved and quiet fully convective stars. Other activity proxies will also be monitored.

With the future collection of planetary systems to be found by SPIRou, we will be able to bring unprecedented constraints on the formation of planets around low-mass stars, their dynamical evolution and interactions between planets and with the host star. Consequences for further studies are expected to be huge, as tidal locking, orbital properties and stellar wind may be limits to planet habitability and presently require additional observational constraints.

The radial-velocity follow-up observations of transiting planetary candidates is the best way to get rid of false positives (Santerne et al. 2013b) and to measure the mass of the confirmed planets. With mass and radius, the bulk density and global properties of the planetary internal structure can be inferred. In the continuation of successful missions like CoRoT and *Kepler*, NASA is currently operating the K2 mission and is going to launch TESS in 2017. By targeting bright stars, TESS will provide Earth-like planet candidates which radial-velocity follow-up will be possible on ground-based telescopes -unlike most of the *Kepler* candidates. SPIRou at CFHT will be unique to secure radial-velocity measurements on the coolest part of the stellar hosts. Using statistics based on Kepler results, TESS predicts the discovery of several hundreds of Earth-like and super-Earth planets, in addition to thousands of icy and gas giants, for stars brighter than I=12. The list of planet candidates discovered by TESS and their light curves will be made available to the community for complementary observations. Most super-Earth candidates detected by TESS will orbit M dwarfs - with less than 30% of them accessible to optical radial-velocity follow-ups; nIR velocimeters like SPIRou will thus be essential to validate planet candidates.

In the meantime, ground-based transit surveys of M stars are ongoing (e.g., MEarth) or about to start (e.g., ExTrA), with many candidate planets known by 2017. With a first light scheduled in 2016, ExTrA targets stars of late spectral types (M4 to L0) and aims at the smallest planets around the smallest stars. ExTrA should detect a few tens of very-low-mass transiting planet candidates, again to be validated with nIR velocimetry. Expected to even outperform ESPRESSO on the VLT for most types of M dwarfs, SPIRou will be the best and most efficient radial-velocity instrument to monitor in the nIR the candidates visible from CFHT, to confirm or reject their planetary nature and to determine their masses.

The second component of the SLS - **the SLS-TF for Transit Follow-up**, will carry out radial-velocity follow-up observations of the 50 most interesting transiting planet candidates uncovered by future photometry surveys including TESS and ExTrA - for a total of 100 CFHT nights. We will focus on candidates with orbits closest to their habitable zones and/or around the brightest stars for a given spectral type - to select the best ones to be scrutinized in the future by the JWST or the E-ELT for spectral signatures of biomarkers in their atmospheres. The observing strategy includes an estimated number of 70 visits per candidate.

The third component of the SPIRou Legacy Survey is the study of class-I,-II and -III protostars (**SLS-MP: Magnetic Protostar / Planet**). We aim at detecting and mapping the magnetic topologies of young stars and their accretion discs and to explore the origins and evolution of the magnetic field of stars. In this survey, it will also be possible to unveil giant planets in short orbits and put constraints on the formation versus migration timescales for hot-Jupiter like planets - as they survive the system formation processes.

Magnetic fields play a major role in the early evolution of stellar systems. By affecting and often controlling accretion processes, triggering and channeling outflows, and producing intense X-rays, magnetic fields critically impact the physics and largely dictate the angular momentum evolution of pre-main-sequence stars and their accretion discs. Magnetic fields link accreting pre-main-sequence stars to their discs and evacuate the central disc regions; they funnel the disc material onto the stars, generate powerful winds and force classical T Tauri stars to rotate much more slowly than expected from contraction and accretion. Fields of accretion discs trigger instabilities, enhance accretion rates and extract angular momentum through magnetic braking and outflows; they also produce X-rays through flares and shocks, ionizing the disc gas and impacting disc dynamics and planet formation.

The targets are brighter in the nIR than in the optical, whereas the Zeeman effect is stronger at longer wavelengths. Spectropolarimetric observations with SPIRou will thus allow us to survey much larger samples of pre-main-sequence stars than accessible presently, as well as to access younger embedded class-I protostars and their discs on which very little information is yet available.

The SLS-MP survey will consist in collecting spectropolarimetric observations of about 140 young protostars in various stages of evolution, selected in the close star-forming regions of Taurus/Auriga, TW Hya and ρ Ophiuchius. It will, in particular, explore for the first time the magnetic topologies of class-I protostars. The survey will extend over 125 nights as each target requires multiple visits (about 20) to sample the rotation cycle over a couple of cycles. As previously, the MP survey can be extended towards other young systems.

With these three axes, the SPIRou Legacy Survey will gather a large community of scientists interested in the formation, evolution and characteristics of exoplanets and stars. The SPIRou science group is open to any proposal of legacy-type science that would not yet be covered but accessible with the survey observations. Out of these surveys, SPIRou will be able and available to explore many more science topics via open time proposals.

5 Conclusions

The SPIRou near-infrared velocimeter and spectropolarimeter, soon to be installed at the Maunakea CFHT observatory, mainly aims at the specific tasks of investigating planet formation and properties around cool stars and young stars, while describing the magnetic properties of these stars. The polarimetric capability is unique and will widen the future diagnostics of stellar variability for planet search. SPIRou has the potential of finding the telluric exoplanets that space telescopes like JWST will focus on, for atmospheric studies and further habitability explorations. Other near-infrared velocimeters are being built in the world, e.g. CARMENES (Quirrenbach et al. 2010), IRD (Kotani et al. 2014), HPF (Hearty et al. 2014). None of these instruments, however, includes the spectropolarimetric capability (required for stellar activity corrections) nor the essential K band (with a large radial-velocity content for low mass stars and a large flux for embedded sources).

The SPIRou science group is open to any interested member of the CFHT community, especially in the context of the large surveys which will use SPIRou for $\sim$ 70% of the time and at least 300 nights over the 3 first years.

The community is now structured around five main work packages; three focussing on the three components of the SPIRou Legacy Survey. The other two explore topics that are common to all science goals, like radial-velocity optimization, stellar jitter correction or stellar spectroscopic and magnetic characterisation.

The first sub-systems of SPIRou are being delivered to Toulouse, and the integration and tests will take place at IRAP until mid 2017, when the instrument will be shipped to Hawaii. SPIRou should be on the sky at the end of 2017, and probably open to the community in 2018A.

References

Artigau, É., Kouach, D., Donati, J.-F., et al. 2014, in Society of Photo-Optical Instrumentation Engineers (SPIE) Conference Series, Vol. 9147, Society of Photo-Optical Instrumentation Engineers (SPIE) Conference Series, 15

Bonfils, X., Delfosse, X., Udry, S., et al. 2013, A&A, 549, A109

Delfosse, X., Donati, J.-F., Kouach, D., et al. 2013, in SF2A-2013: Proceedings of the Annual meeting of the French Society of Astronomy and Astrophysics, ed. L. Cambresy, F. Martins, E. Nuss, & A. Palacios, 497–508

Donati, J.-F., Hébrard, E., Hussain, G. A. J., et al. 2015, MNRAS, 453, 3706

Donati, J.-F., Paletou, F., Bouvier, J., & Ferreira, J. 2005, Nature, 438, 466

Hearty, F., Levi, E., Nelson, M., et al. 2014, in Society of Photo-Optical Instrumentation Engineers (SPIE) Conference Series, Vol. 9147, Society of Photo-Optical Instrumentation Engineers (SPIE) Conference Series, 52

Hébrard, É. M., Donati, J.-F., Delfosse, X., et al. 2014, MNRAS, 443, 2599

Huélamo, N., Figueira, P., Bonfils, X., et al. 2008, A&A, 489, L9

Johns-Krull, C. M. 2007, ApJ, 664, 975

Kotani, T., Tamura, M., Suto, H., et al. 2014, in Society of Photo-Optical Instrumentation Engineers (SPIE) Conference Series, Vol. 9147, Society of Photo-Optical Instrumentation Engineers (SPIE) Conference Series, 14

Lépine, S. & Gaidos, E. 2011, AJ, 142, 138

Lopez, E. D. & Fortney, J. J. 2014, ApJ, 792, 1

Petit, P., Donati, J.-F., Hébrard, E., et al. 2015, ArXiv e-prints [arXiv] 1503.00180

Quirrenbach, A., Amado, P. J., Mandel, H., et al. 2010, in Society of Photo-Optical Instrumentation Engineers (SPIE) Conference Series, Vol. 7735, Society of Photo-Optical Instrumentation Engineers (SPIE) Conference Series, 13

Romanova, M. M., Long, M., Lamb, F. K., Kulkarni, A. K., & Donati, J.-F. 2011, MNRAS, 411, 915

Santerne, A., Donati, J.-F., Doyon, R., et al. 2013a, in SF2A-2013: Proceedings of the Annual meeting of the French Society of Astronomy and Astrophysics, ed. L. Cambresy, F. Martins, E. Nuss, & A. Palacios, 509–514

Santerne, A., Donati, J.-F., Doyon, R., et al. 2013b, in SF2A-2013: Proceedings of the Annual meeting of the French Society of Astronomy and Astrophysics, ed. L. Cambresy, F. Martins, E. Nuss, & A. Palacios, 509–514

Valencia, D., Guillot, T., Parmentier, V., & Freedman, R. S. 2013, ApJ, 775, 10

Valencia, D., Ikoma, M., Guillot, T., & Nettelmann, N. 2010, A&A, 516, A20

Zanni, C. & Ferreira, J. 2013, A&A, 550, A99

SF2A 2015
F. Martins, S. Boissier, V. Buat, L. Cambrésy and P. Petit (eds)

THE "BINARITY AND MAGNETIC INTERACTIONS IN VARIOUS CLASSES OF STARS" (BINAMICS) PROJECT

C. Neiner[1], J. Morin[2], E. Alecian[1,3] and the BinaMIcS collaboration

Abstract. The "Binarity and Magnetic Interactions in various classes of stars" (BinaMIcS) project is based on two large programs of spectropolarimetric observations with ESPaDOnS at CFHT and Narval at TBL. Three samples of spectroscopic binaries with two spectra (SB2) are observed: known cool magnetic binaries, the few known hot magnetic binaries, and a survey sample of hot binaries to search for additional hot magnetic binaries. The goal of BinaMIcS is to understand the complex interplay between stellar magnetism and binarity. To this aim, we will characterise and model the magnetic fields, magnetospheric structure and coupling of both components of hot and cool close binary systems over a significant range of evolutionary stages, to confront current theories and trigger new ones. First results already provided interesting clues, e.g. about the origin of magnetism in hot stars.

Keywords: stars: magnetic field, binaries: spectroscopic, binaries: close, techniques: polarimetric

1 Introduction

The goals of the "Binarity and Magnetic Interactions in various classes of stars" (BinaMIcS) project are to understand the impact of magnetic fields on stellar formation and evolution, of tidal effects on fossil and dynamo magnetic fields, of magnetism on angular momemtum and mass transfers between binary components, as well as magnetospheric interactions. To address these questions, we are missing observational information on the magnetic field strengths and topologies of a statistically large sample of magnetic close binary systems, in which we expect significant interaction via tidal or magnetospheric interactions. Therefore, BinaMIcS is based on two large programs of spectropolarimetric observations with ESPaDOnS at CFHT (Hawaii) and Narval at TBL (Pic du Midi, France), in addition to theoretical developments and modelling efforts.

Three samples of short-period spectroscopic binaries with two spectra (SB2) are observed:

- known selected cool (< F5) magnetic binaries, to characterise their magnetic properties in details and compare them to single magnetic cool stars
- the few known hot (> F5) magnetic binaries, to characterise their magnetic properties in details and compare them to single magnetic hot stars
- a survey sample of hot binaries, to discover new hot magnetic binaries and compare the occurence of magnetic fields in hot binaries versus single hot stars.

[1] LESIA, Observatoire de Paris, PSL Research University, CNRS, Sorbonne Universités, UPMC Univ. Paris 06, Univ. Paris Diderot, Sorbonne Paris Cité, 5 place Jules Janssen, 92195 Meudon, France
[2] LUPM-UMR 5299, CNRS & Université Montpellier, Place Eugène Bataillon, 34095, Montpellier Cedex 05, France
[3] Univ. Grenoble Alpes, CNRS, IPAG, F-38000 Grenoble, France

© Société Francaise d'Astronomie et d'Astrophysique (SF2A) 2015

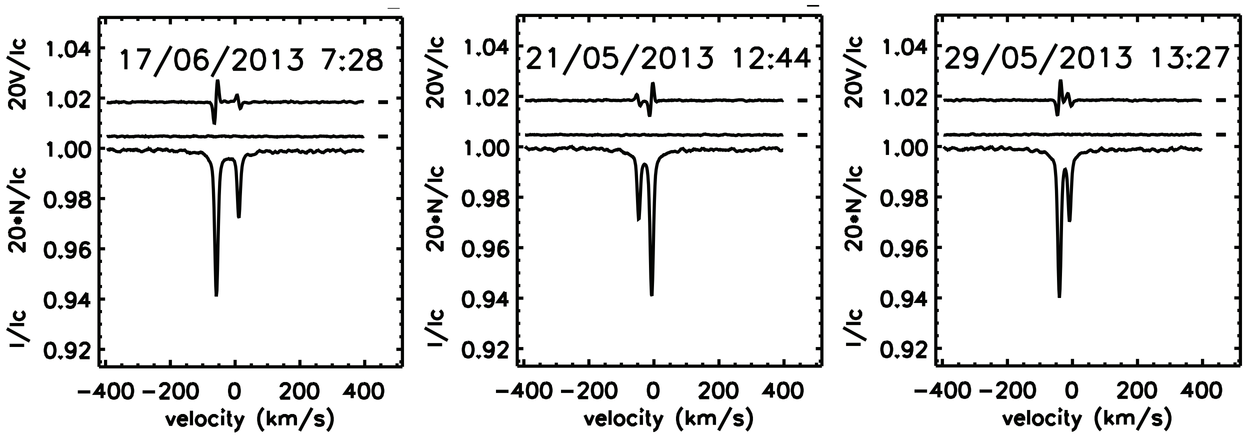

Fig. 1. Three examples of LSD Stokes V (top), null (middle), and intensity profiles (bottom) of the cool binary system BY Dra, taken at various orbital phases. The V and N profiles have been shifted upwards for display purposes. The Stokes V profiles clearly show that both binary components are magnetic.

2 Magnetic hot SB2 systems

Six magnetic SB2 systems with at least one O, B, or A component were known to exist and are currently being characterized in the frame of BinaMIcS. These are HD 37017 (V1046 Ori, Bohlender et al. 1987), HD 37061 (NU Ori, Petit et al. 2011), HD 136504 (ϵ Lup, Hubrig et al. 2011; Shultz et al. 2012), HD 47129 (Plaskett's star, Grunhut et al. 2013), HD 98088 (Folsom et al. 2013), and HD 5550 (Neiner et al., these proceedings, Alecian et al., submitted). Among them, only one is known to host two magnetic stars: ϵ Lup (Shultz et al. 2015). In addition, two newly discovered magnetic SB2 systems with early F stars are being characterized within BinaMIcS: HD 160922 (Neiner & Alecian 2013) and HD 210027 (ι Peg, Neiner & Lèbre 2014).

No other magnetic OBA SB2 system was discovered among the $\sim$200 systems ($\sim$400 stars) observed within the survey sample. Among single hot stars, $\sim$7% are found to host a magnetic field, with a typical strength of a few hundreds to a few thousands gauss (Grunhut & Neiner 2015). These fields are of simple configuration and stable over decades. Moreover, they are of fossil origin, i.e. remnants from the field present in the molecular cloud at the time of stellar formation, possibly enhanced by a dynamo action during the early phases of the life of the star (Borra et al. 1982; Neiner et al. 2015). If similar magnetic fields were present with the same occurence in hot binaries as in single hot stars, we should have detected 20 to 30 magnetic stars in the survey sample. There is thus a clear and strong deficit of magnetic stars in hot short-period spectroscopic binaries.

A possible explanation for this dearth of magnetic fields in hot SB2 systems is provided by stellar formation processes. Stellar formation simulations (e.g. Commerçon et al. 2011) showed that fragmentation of dense stellar cores is inhibited when the medium is magnetic. Therefore, it seems that it is more difficult to form a binary system in the presence of a fossil field and, thus, magnetic hot binaries are rarer.

3 Magnetic cool SB2 systems

The BinaMIcS sample of magnetic cool SB2 systems includes cool main sequence stars, evolved RS CVn objects, and young T Tauri stars. Several of these systems show signatures of magnetic fields in both components. This is the case, for example, of the K4Ve+K7.5Ve system BY Dra (see Fig. 1) or σ^2 CrB (see Neiner & Alecian 2013).

Single magnetic cool stars show various types of magnetic fields, with various levels of complexity, axisymmetry, and strength. Fig. 2 shows known single magnetic cool stars (filled symbols) in a mass versus rotation period diagram. Stars with the strongest fields are the lower mass stars, the slowest rotators, and often have simple poloidal fields. Weak complex fields are found in two regions of the diagram: slowly rotating very low-mass stars, and rapidly rotating higher mass stars. Open symbols in Fig. 2 indicate the position of the cool magnetic binary targets of BinaMIcS. Magnetic maps of these binaries will be compared to the maps of single stars to assess the effect of binarity on stellar dynamo processes.

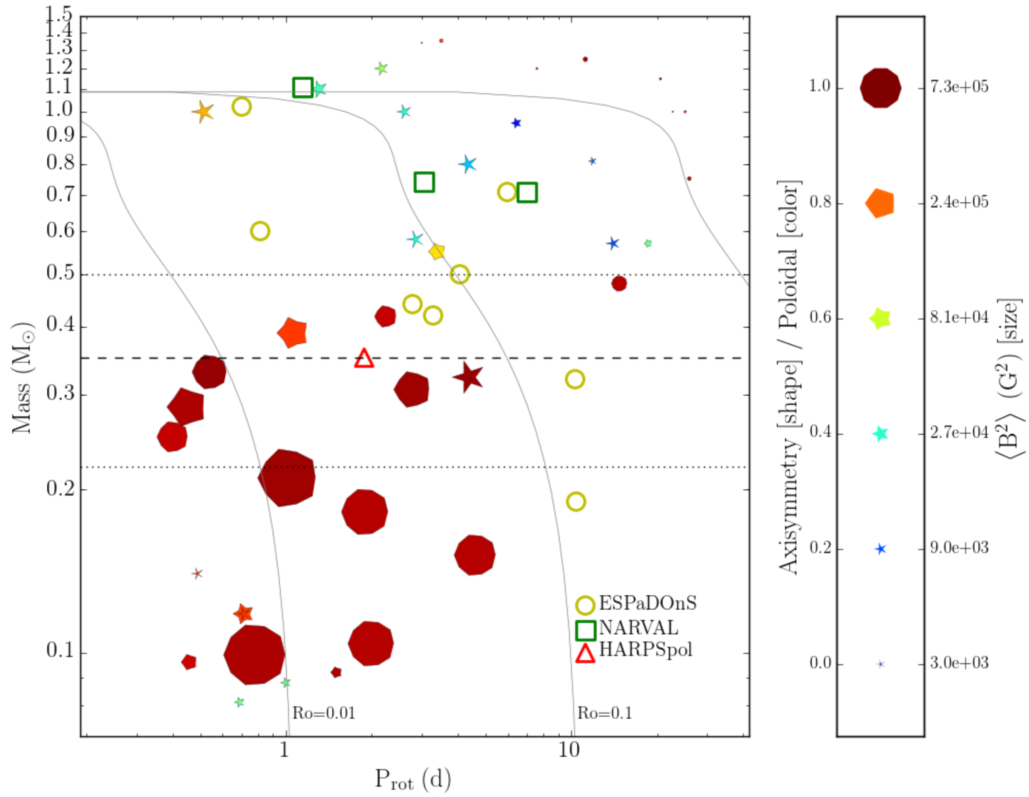

Fig. 2. Mass versus rotation period diagram for single magnetic stars (filled symbols) and cool binaries of the BinaMIcS sample (open symbols). For single stars, the shape of the symbol indicates the axisymmetry of the magnetic field configuration, its color indicates how poloidal the field is, and its size indicates the strength of the field.

4 Conclusions

BinaMIcS aims at studying the effect of magnetism on binary formation and evolution. Individual hot and cool short-period spectroscopic binary (SB2) systems are being studied in great details to infer their magnetic properties. These results will be compared to those obtained for single stars. In addition, the magnetic survey of hot binaries already provided an important result: hot stars in short-period binaries are less often magnetic than when they are single.

We thank the "Programme National de Physique Stellaire" (PNPS) of CNRS/INSU (France) for their financial support to the BinaMIcS project.

References

Bohlender, D. A., Landstreet, J. D., Brown, D. N., & Thompson, I. B. 1987, ApJ, 323, 325

Borra, E. F., Landstreet, J. D., & Mestel, L. 1982, ARA&A, 20, 191

Commerçon, B., Hennebelle, P., & Henning, T. 2011, ApJ, 742, L9

Folsom, C. P., Likuski, K., Wade, G. A., et al. 2013, MNRAS, 431, 1513

Grunhut, J. H. & Neiner, C. 2015, in IAU Symposium, Vol. 305, IAU Symposium, 53

Grunhut, J. H., Wade, G. A., Leutenegger, M., et al. 2013, MNRAS, 428, 1686

Hubrig, S., Ilyin, I., Schöller, M., et al. 2011, ApJ, 726, L5

Neiner, C. & Alecian, E. 2013, in EAS Publications Series, Vol. 64, EAS Publications Series, ed. K. Pavlovski, A. Tkachenko, & G. Torres, 75

Neiner, C. & Lèbre, A. 2014, in SF2A-2014: Proceedings of the Annual meeting of the French Society of Astronomy and Astrophysics, ed. J. Ballet, F. Martins, F. Bournaud, R. Monier, & C. Reylé, 505

Neiner, C., Mathis, S., Alecian, E., et al. 2015, in IAU Symposium, Vol. 305, IAU Symposium, 61

Petit, V., Wade, G., Drissen, L., Montmerle, T., & Alecian, E. 2011, in Astronomical Society of the Pacific Conference Series, Vol. 449, Astronomical Polarimetry 2008: Science from Small to Large Telescopes, ed. P. Bastien, N. Manset, D. P. Clemens, & N. St-Louis, 290

Shultz, M., Wade, G. A., Alecian, E., & BinaMIcS Collaboration. 2015, MNRAS, 454, L1

Shultz, M., Wade, G. A., Grunhut, J., et al. 2012, ApJ, 750, 2

SF2A 2015
F. Martins, S. Boissier, V. Buat, L. Cambrésy and P. Petit (eds)

THE CANADA-FRANCE IMAGING SURVEY: EVOLUTION OF GALAXIES AND CLUSTERS OF GALAXIES

R. Pelló[1]

Abstract. In this paper we discuss the interest of the wide-field CFIS (Canada-France Imaging Survey) regarding extragalactic/cosmology science, focusing on the evolution of galaxies and clusters of galaxies. A deep photometric survey such as CFIS in the Northern hemisphere is presently missing for the needs of different ongoing projects based on photometric redshifts, such as EUCLID or eROSITA.

Keywords: Galaxies, clusters of galaxies, extragalactic surveys

1 Introduction

The CFIS (Canada-France Imaging Survey) is a large program presently under definition in the framework of a call for proposals to be conducted at the CFHT, starting in 2017. This wide-field survey in the Northern hemisphere is expected to be conducted with MegaCam. Its main scientific goals are the study of our Galaxy, the low-surface brightness universe (see also R. Ibata, this conference), as well as extragalactic/cosmology science. As compared to other ongoing or planned surveys, the CFIS is expected to provide a unique combination of image quality, wavelength coverage and depth ($\sim$2 magnitudes deeper than the SDSS; see J.C. Cuillandre, this conference). In this paper we briefly discuss the particular interest of the CFIS regarding the evolution of galaxies and clusters of galaxies used as cosmological probes.

2 Motivation

The motivation behind CFIS is to provide a deep optical survey in the Northern hemisphere, which is presently missing, for the needs of key projects based on photometric redshifts, such as EUCLID (see Laureijs et al. 2011) or eROSITA (see e.g. Merloni et al. 2012). EUCLID (launch expected $\sim$ 2020) has been optimized for the measurement of cosmological weak-lensing and galaxy clustering, including also the use of clusters of galaxies as cosmological probes. eROSITA (launch 2017) is also intended to detect a large sample of clusters of galaxies up to z$\geq$ 1, in order to study the large scale structure in the universe, and to constrain the cosmological models.

We discuss below the impact of CFIS photometry on the expected accuracy for photometric redshifts, as well as the implication for SED-fitting analyses of galaxy populations, and the identification of clusters of galaxies for cosmological studies.

2.1 Photometric redshift accuracy

In order to estimate the accuracy expected on photometric redshifts, and more precisely the impact of CFIS-like observations on their final quality, we have carried-out a series of simulations. Synthetic catalogs were produced, covering a wide parameter space in terms of galaxy types, age of the stellar population and extinction, with a flat N(z) distribution of sources between z= 0 and 5 (to preserve a uniform statistics as a function of refshift). Photometry includes the 4 EUCLID bands (VIS, Y, J and H), and 4 MegaCam filters (g,r,i and z), with and without the u-band. Errors in magnitudes were introduced in a consistent way, assuming a Gaussian error distribution, with S/N scaled to magnitudes in order to reproduce as close as possible the conditions expected for a EUCLID+CFIS survey (see J.C. Cuillandre, this conference). Photometric redshifts were computed with

[1] Université de Toulouse; UPS-OMP; IRAP; 14, avenue Edouard Belin, F-31400 Toulouse, France

© Société Francaise d'Astronomie et d'Astrophysique (SF2A) 2015

the new version (v12.3) of the public code *Hyperz*(*New−Hyperz* *), originally developed by Bolzonella et al. (2000). Only a flat prior in luminosity was used, with a simple cut in the permitted range of luminosities. *New−Hyperz* performs a χ^2 minimization in the parameter space, yielding the best-fit photometric redshift for each input source, as well as a number of fitting subproducts (e.g. absolute magnitudes in the different bands, normalized redshift probability distribution, error bars, secondary solutions, stellar masses, etc...).

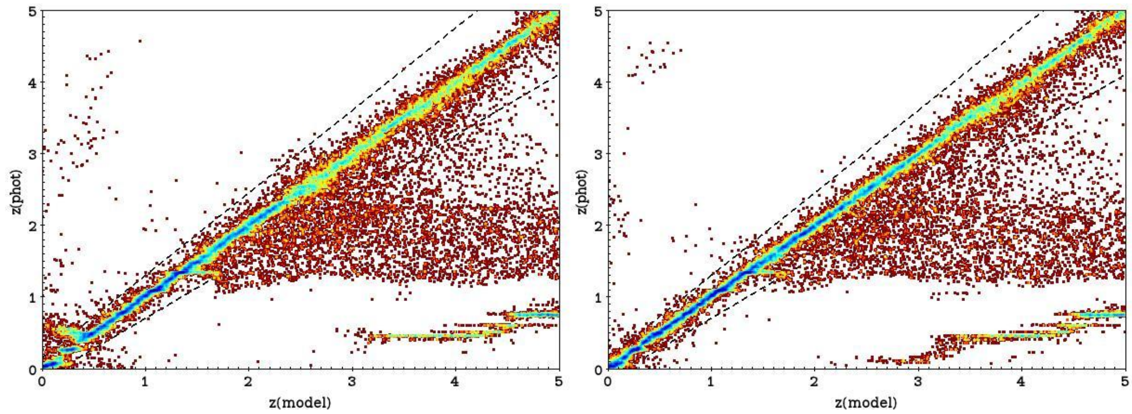

Fig. 1. Left: Comparison between photometric and true redshifts for a simulation of a survey based on EUCLID filters $+griz$ bands. **Right:** Same as in the left panel, for EUCLID filters $+ugriz$ bands. Colors encode the density of test galaxies in this plane using a logarithmic scale.

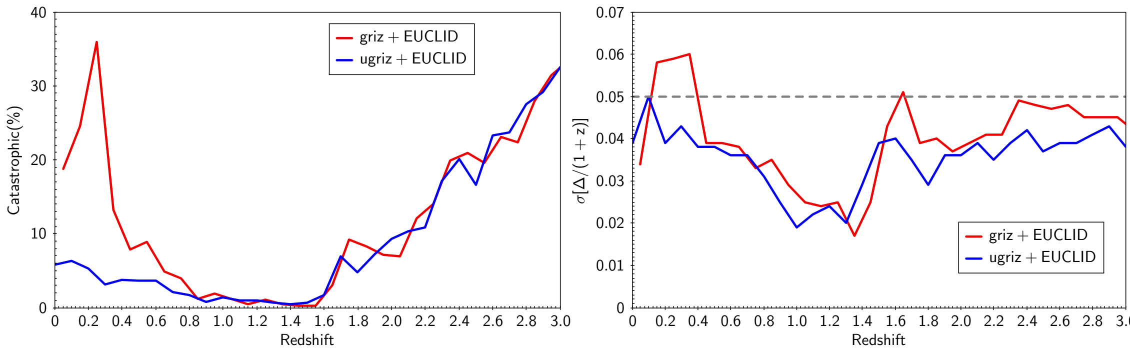

Fig. 2. Left: Fraction of catastrophic identifications expected in the z =0-3 interval based on EUCLID filters + different combinations of filters in the optical wavelengths. **Right:** Same as for the left panel, for the dispersion expected in the photometric redshift determination. Note that, in the two cases, including the u-band has a dramatic effect on the quality of photometric redshifts at $z \leq 0.5$

Fig. 1 displays the comparison between photometric and true redshifts for $\sim 2\times 10^4$ objects in these simulations, with redshifts in the z =0-5 interval and for two different choices of filters (with and without u-band photometry). Fig. 2 presents the fraction of catastrophic identifications (sources with $|z(true) - z(phot)| > 0.15(1 + z(true)))$ and the dispersion expected in the photometric redshift determination within the z =0-3 interval, based on EUCLID filters + different combinations of filters in the optical wavelengths. A CFIS-like survey is clearly needed to reach the requirements of the key projects mentioned above. Including the u-band has a dramatic effect on the quality of photometric redshifts at $z \leq 0.5$.

2.2 Photometric redshits and SED-fitting

Photometric redshits and SED-fitting procedures play an increasingly important role in understanding the physical processes of galaxy assembly through cosmic ages. They allow us to sample the galaxy population

*`http://userpages.irap.omp.eu/~rpello/newhyperz/`

beyond the spectroscopic limits, increasing the size of available samples, therefore improving statistics through the relevant parameter space. Needless to say that this approach has a key role in the identification and study of the sources responsible for the reionization. This situation is not expected to change dramatically in the next coming decade.

Photometric redshits and SED-fitting procedures provide the following important elements when deriving the properties of galaxies:

- A classification of sources into spectro-morphological types, allowing the selection of samples (e.g. for spectroscopic follow up studies).
- A view of the stellar-population properties in galaxies, including dust content, stellar masses, star-formation rates, and possibly other parameters such as the average age of stellar populations when combining photometry with spectroscopic and/or multi-wavelength information. An illustration of the performances expected in this field when combining CFIS-like photometry with EUCLID data is presented in Fig. 3, showing the distribution of stellar masses as a function of redshift for galaxies in the WIRCam WUDS survey, based on a $H + K$ selection on the CFHTLS-D3 field (Groth Strip) (see Pello et al. 2015, in preparation).
- Properties of (extremely) high-redshift galaxies.
- The evolution in the global properties of the galaxy population as a function of redshift and environment: star-formation rate density, luminosity and stellar-mass functions, clustering, ... Different approaches have been used in the literature since the pioneer papers based on pure photometric redshifts and associated PDZ (see e.g. Subbarao et al. 1996; Arnouts et al. 1999; Bolzonella et al. 2002), to modern (massive) surveys making use of spectroscopic data to calibrate photometric redshifts for high-quality results (e.g. Scoville et al. 2007; Ilbert et al. 2013).

Recovering the above properties from broad-band SED-fitting is clearly a degenerate problem, as shown by different authors (see e.g. Maraston et al. 2013; Pforr et al. 2013, and references therein), in particular when relying on photometric redshifts. In this respect, a well suited wavelength coverage is crucial, and the u-band is essential for an optimal exploitation of the key projects mentioned above.

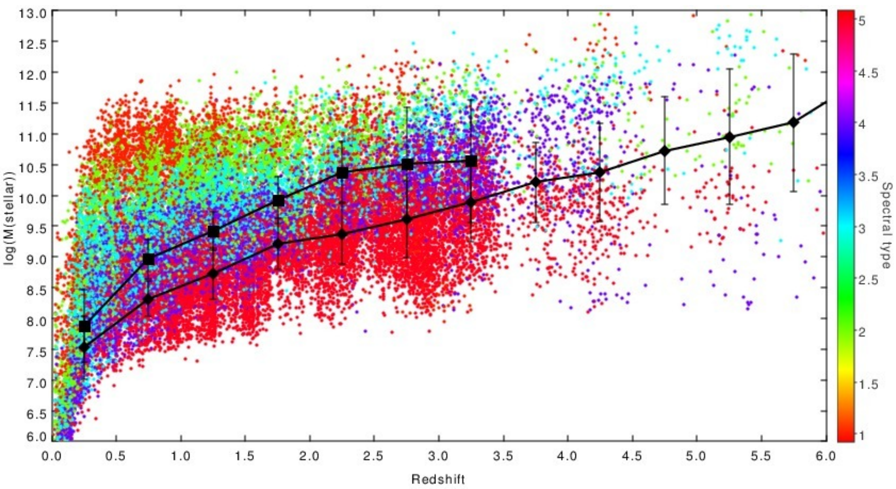

Fig. 3. Distribution of stellar masses as a function of redshift for galaxies in the WIRCam WUDS survey, based on a $H + K$ selection. Colors encode the different spectral types of galaxies, from early types (code 1) to late types (code 5). Black squares and diamonds represent the completeness limits in mass up to $K_s = 24.75$, for early and late-type galaxies respectively. Error bars represent the dispersion within the sample.

2.3 *Clusters of galaxies*

As described in a recent paper by Sartoris et al. (2015), clusters of galaxies selected from EUCLID data are expected to provide important constrains on the cosmological parameters. A large fraction of this sample will be detected using a pure photometric selection (i.e. $\sim 10^6$ clusters are expected with masses above $\sim 10^{14}$ M$\odot$ at a 3σ level, 20% of them at z≥1). Internal calibration in mass will be available for these clusters based on weak-lensing analysis and the dynamics traced by spectroscopy of cluster galaxies, with obvious limitations. Regarding eROSITA, it is expected to perform an all-sky X-ray Survey during its 4-year mission, with a Deep Field Survey on ∼100 deg^2. More than 10^5 clusters are expected to be detected up to z≤1.5, and close to 10^6 AGN (see e.g. Merloni et al. 2012), therefore increasing by a large factor the present sample of ∼20 clusters at z≥1 seen in X-rays. As illustrated in Fig. 2 and 3, the lack of u-band photometry could compromise this exercise at $z \leq 0.5$ in both cases. Clearly the CFIS is ideally suited for the identification of clusters in these surveys based on photometric redshifts.

Photometric redshifts in this context are particularly useful for

- Cluster/structure finding algorithms.
- Determination of cluster redshifts (in complementarity with spectroscopic data).
- Cluster-membership criteria.
- Selection of spectroscopic samples for follow up observations.

Based on current surveys, the accuracy in these determinations is more sensitive to the filter set used rather than the redshift of the cluster, provided that the sensitive rest-frame wavelengths, containing the main spectral features, are covered (e.g. the 4000 Å break). The accuracy on the determination of cluster redshifts is better than for individual galaxies (see e.g. Pelló et al. 2009).

3 Conclusion

In conclusion, a deep photometric survey such as CFIS in the Northern hemisphere is clearly required for the needs of different ongoing extragalactic/cosmology projects based on photometric redshifts, such as EUCLID or eROSITA. It is also needed for target-selection for projects based on (massive) spectroscopy, such as DESI or the Mauna Kea Spectroscopic Explorer (MSE), which is intended to select targets based on CFIS and EUCLID data (see poster by C. Schimd, this conference). It is worth mentioning that follow up observations of CFIS sources will be possible with the TMT.

This work was supported by the French CNRS and the Agence Nationale de la recherche bearing the reference ANR-09-BLAN-0234. WUDS results are based on observations obtained with WIRCam, a joint project of CFHT, Taiwan, Korea, Canada, France, and the Canada-France-Hawaii Telescope (CFHT) which is operated by the National Research Council (NRC) of Canada, the Institute National des Sciences de l'Univers of the Centre National de la Recherche Scientifique of France, and the U. of Hawaii.

References

Arnouts, S., Cristiani, S., Moscardini, L., et al. 1999, MNRAS, 310, 540

Bolzonella, M., Miralles, J.-M., & Pelló, R. 2000, A&A, 363, 476

Bolzonella, M., Pelló, R., & Maccagni, D. 2002, A&A, 395, 443

Ilbert, O., McCracken, H. J., Le Fèvre, O., et al. 2013, A&A, 556, A55

Laureijs, R., Amiaux, J., Arduini, S., et al. 2011, ArXiv e-prints [arXiv] 1110.3193

Maraston, C., Pforr, J., Henriques, B. M., et al. 2013, MNRAS, 435, 2764

Merloni, A., Predehl, P., Becker, W., et al. 2012, ArXiv e-prints [arXiv] 1209.3114

Pelló, R., Rudnick, G., De Lucia, G., et al. 2009, A&A, 508, 1173

Pforr, J., Maraston, C., & Tonini, C. 2013, MNRAS, 435, 1389

Sartoris, B., Biviano, A., Fedeli, C., et al. 2015, ArXiv e-prints [arXiv] 1505.02165

Scoville, N., Aussel, H., Benson, A., et al. 2007, ApJS, 172, 150

Subbarao, M. U., Connolly, A. J., Szalay, A. S., & Koo, D. C. 1996, AJ, 112, 929

SF2A 2015
F. Martins, S. Boissier, V. Buat, L. Cambrésy and P. Petit (eds)

MSE VELOCITY SURVEY

C. Schimd[1], H. Courtois[2] and J. Koda[3]

Abstract. A huge velocity survey based on the Maunakea Spectroscopic Explorer facility (MSE) is proposed, aiming at investigating the structure and dynamics of the cosmic web over 3π steradians up to ~ 1 Gpc and at unprecedented spatial resolution, its relationship with the galaxy formation process, and the bias between galaxies and dark matter during the last three billions years. The cross-correlation of velocity and density fields will further allow the probe any deviation from General Relativity by measuring the the linear-growth rate of cosmic structures at precision competitive with high-redshift spectroscopic redshift surveys.

Keywords: Survey, cosmology, large-scale structure of Universe, dark energy

1 MSE and MSEv

The Maunakea Spectroscopic Explorer (MSE)* is a proposed upgrade of the CFHT 3.6m optical telescope by a 10m-class dedicated multi-object spectroscopic wide-field facility, with completion expected in 2025. With three optical-NIR channels covering the wavelength range $370 - 1400$ nm, a multiplexing of 3200 fibers at spectral resolutions $R = 3000$ and 6500, and 1000 fibers at $R = 40000$, and further IFU capabilities expected for the second light, this instrument will be unique to tackle basic science questions ranging from stellar astrophysics, the physics of the Galaxy and Local Group, the galaxy evolution and clustering across cosmic time, to cosmology.

We propose to realize a velocity survey (MSEv) to measure the redshift of about 2 million of early- an late-type galaxies over $3/4$ of the full sky apart from Milky Way and out to redshift $z \simeq 0.25$, and radial velocities of about half of them over $10,000 - 24,000$ square degrees. Both the Fundamental Plane (FP) and optical Tully-Fisher (TF) techniques will be employed, with galaxy number density and sampling similar to Cosmicflows-2 (CF-2; Tully et al. 2013). The redshift and sky coverage and the total number of MSE velocities is designed to supersede in terms of volume or number density the most recent velocity surveys, such as SFI++ (Springob et al. 2007), 6dFGSv (Springob et al. 2014), and CF-2, and the forthcoming I-band velocity survey TAIPAN (starting around mid-2016; Kuehn et al. 2013). MSEv will further provide the optical-NIR counterpart of the HI surveys ASKAP-WALLABY and WNSHS (Koribalski 2012; Johnston et al. 2008).

2 Science case

Low-redshift growth-rate of structures: dark energy and modified theories of gravity — Peculiar velocities provide a powerful tool to study the distribution of mass directly, without the complicated details of galaxy and star formation, e.g. by applying the *velocity-velocity comparison* (e.g. Kaiser et al. 1991). Focusing on the joint analysis of angle-averaged auto- and cross-power spectra of the density and velocity fields, a preliminary Fisher matrix analysis following Koda et al. (2014) indicates that a minimal MSEv covering $10,000\,\mathrm{deg}^2$ and with a number density of $n_{\rm gal} = 0.003\,h^3\mathrm{Mpc}^{-3}$ (i.e. $\sim 10^6$ galaxies with $z < 0.25$, for which both redshift and distances are measured) will constraint the ratio $\beta = f/b$, between the linear growth-rate and the bias of the tracers, and the amplitude of matter fluctuations, σ_8, at the level of $\delta\beta/\beta = 0.065$ (0.036) and $\delta\sigma_8/\sigma_8 = 0.060$ (0.032) out to redshift $z < 0.1$ (0.2); see Fig. 1. Because of the small volume, these errors increase by a factor $\sim 1.5 - 2.3$ if measuring only the density power spectrum (i.e. redshift space distortions, RSD). Instead, similar precisions to the MSEv joint velocity-density analysis are expected by future spectroscopic redshift surveys at high-redshift such as PFS-SuMIRe, DESI and Euclid, though probing the growth-rate in a more challenging regime.

[1] Aix Marseille Université, CNRS, LAM (Laboratoire d'Astrophysique de Marseille) UMR 7326, 13388, Marseille, France
[2] University of Lyon, UCB Lyon 1/CNRS/IN2P3; IPN Lyon, France
[3] INAF Osservatorio Astronomico di Brera, via E. Bianchi 46, 23807 Merate, Italy

*`http://mse.cfht.hawaii.edu/`

© Société Francaise d'Astronomie et d'Astrophysique (SF2A) 2015

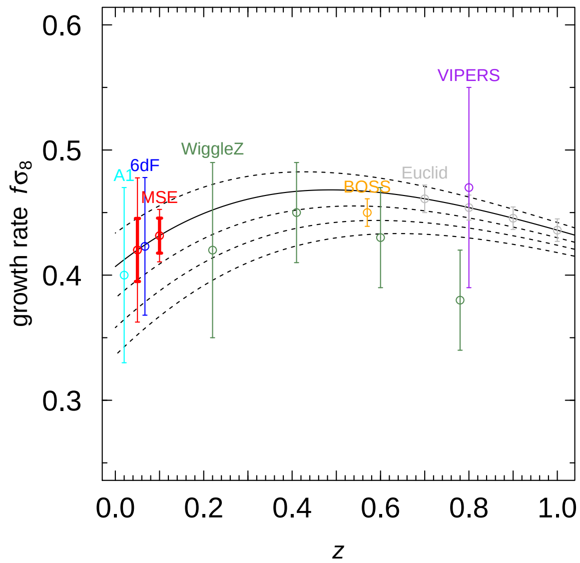

Fig. 1. Fisher matrix 1σ constraints on the linear growth rate $f \approx \Omega_\mathrm{m}^\gamma$ around the fiducial ΛCDM cosmology (solid line, $\gamma = 0.55$; dotted lines are separated by $\delta\gamma = 0.05$, increasing downward), for the minimal MSEv ($10,000\,\mathrm{deg}^2$, $n_\mathrm{gal} = 0.003\ h^3\mathrm{Mpc}^{-3}$). Thick (thin) error bars for the MSEv constraints account for density-velocity cross-correlation (density-only, i.e. RSD, with same number density) up to redshift $z = 0.05$ and $z = 0.1$.

MSEv will allow also a powerful application of the *luminosity fluctuation method* (Feix Nusser & Branchini 2015), which promises to be a powerful test of the current cosmological paradigm. Successfully applied to the velocities reconstructed from $\sim 10^5$ galaxies from the SDSS-DR7, this technique will tremendously benefit of the $\sim 10^6$ MSE peculiar velocities.

From local dynamics to galaxy formation — The low-redshift spacetime symmetries are not evident. The kinematics probed over the huge MSEv volume, which largely encompasses the homogeneity scale (Hogg et al. 2005), will assess the cosmological bulk flow probing its consistency with CMB dipole out to 800 Mpc and allow the test of subtle issues like the backreaction conjecture (Buchert 2008).

MSEv will enable the kinematical classification of the cosmic-web components resolving cosmic structures down to $\lesssim 0.1h^{-1}$Mpc (Hoffman et al. 2012), providing much more details than similar classification algorithms based on density field (see Forero-Romero et al. 2009, and references therein). Moreover, exploiting the high-resolution spectroscopic capabilities of MSE, the knowledge of the velocity-web will provide a unique basis to investigate the tidal torque theory, the alignment of the galaxy spin to the cosmic-web filaments, and the segregation of galaxies and halos with respect to their environment and dynamics.

3 Feasibility study (phase-1)

Spectroscopic and photometric requirements — Both early- and late-type galaxies will be surveyed up to magnitude $i_\mathrm{AB} < 24.5$, to obtain the redshift and equivalent-width of the principal absorption and emission lines (NaD, Mg b, [CaII]; H_α, [OIII], [OII], etc.). The spectra of early-type galaxies should be measured at the same resolution as TAIPAN, i.e. $\sim 70\,\mathrm{km\ s}^{-1}$ rest-frame, while those of late-type galaxies at resolution $< 30\,\mathrm{km\ s}^{-1}$. By comparison with spectra by Keck-II/DEIMOS (Newman et al. 2013) and MMT/Red Channel Spectrograph (Franx 1993), such accuracy can be achieved by exposures of 3,600 s with the mid-resolution MSE channel; see Fig. 2. Besides, accurate photometry (~ 0.1 mag) is needed for pre-imaging (target selection) and measurement of distances, e.g. provided by Pan-STARRS, CFIS, and Euclid, and by LSST and DES for Dec < 30 deg.

Instrumental setup: mini-IFUs — We propose to assess the kinematic of galaxies by fibre-fed mini-IFUs, a technology especially suited to probe the velocity curve of fast rotators but expected to improve the measurement of velocity dispersion of slow rotators and early-type galaxies as well (Krajnović et al. 2011). Each mini-IFU could consist in linear 5- or 7-fibre bundles to simulate long-slits, which nevertheless require alignment to the

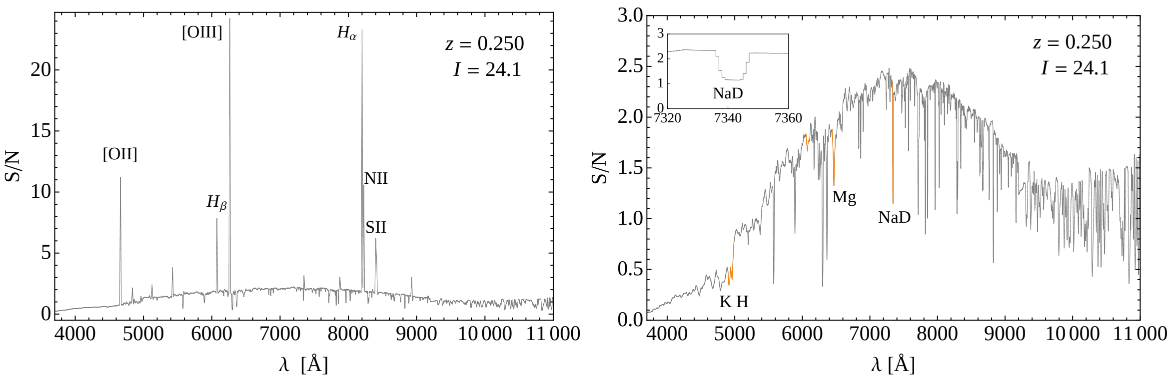

Fig. 2. Synthetic spectra computed with the MSE exposure time calculator (3,600 s exposure-time, mid-resolution). **Left:** elliptical galaxy, centered on the NaD absorption line. **Right:** spiral galaxy, centered on H_α and [OIII] lines.

kinematical axis. A better option would be provided by MaNGA-like close-packed hexagonal mini-IFUs (Drory et al. 2015), each one consisting of 19- or 37-fibre bundles, which do not require any alignment while assuring an optimal measurement of the velocity dispersion. Single fibres of diameter 1.1”-1.5” would guerantee sufficient angular resolution of typical L^*-galaxies out to redshift $z = 0.25$. Using hexagonal mini-IFUs and 4,000 fibres per field-of-view as in the current MSE setup, one obtains $70 - 140$ galaxies per square-degree and $1.7 - 3.7$ millions of L^*-galaxies over $24,000\,\mathrm{deg}^2$ out to $z = 0.25$ at the required number density. A ten-times larger number density of sources with the same field-of-view would likely require a different integral-field technology.

Open issues — i) The typical error on the distance of single galaxies from TF and FP methods is of order 15-20%, improvements on currently devised grouping techniques are needed to assess peculiar velocities down to few-hundreds km s^{-1} at $z \simeq 0.25$. *ii)* The MSE IFU capability, including mini-IFUs, and the observational strategy (bimodal for MSEv) are under discussion in accordance with other MSE projects.

4 Conclusions

MSEv has been recognized as high-value proposal by the MSE Science Executive. The MSE project is entering the phase-2 study.

The authors thank M. Colless, J.-C. Cuillandre, M. Fernandez-Lorenzo, M. Hudson, A. Johnson, N. Kaiser, A. McConnachie, and A. Nusser for fruitful help and discussions.

References

Buchert, T. 2008, GRG, 40, 467
Drory, N. et al. 2015, AJ, 149, 77
Feix, M., Nusser, A., & Branchini, E. 2015, Phys. Rev. Lett., 115, 1301
Forero-Romero, J. E. et al. 2009, MNRAS, 396, 1815
Franx, M. 1993, ApJ 407, L5
Hogg, D. W. et al., 2005, ApJ, 624, 54
Hoffman, Y. et al. 2012, MNRAS, 425, 2049
Johnston, S. et al. 2008, Experimental Astronomy, 22, 151
Kaiser N., et al., 1991, MNRAS 252, 1
Kuehn, K. et al. 2013, Proceedings of the SPIE, 9147, 10
Koribalski, B. 2012, PASA, 29, 359
Krajnović, D. et al. 2011, MNRAS, 414, 2923. See also Emsellem, E. et al. 2011, MNRAS, 414, 888
Koda, J. et al. 2014, MNRAS, 445, 4267
Newman, J. A. et al. 2013, ApJS, 208, 5
Springob, C. M. et al. 2007, ApJS, 172, 599
Springob, C. M. et al. 2014, MNRAS, 445, 2677
Tully, B. et al. 2013, AJ, 146, 86

Session 06

Atelier Jeunes Chercheurs

SF2A 2015
F. Martins, S. Boissier, V. Buat, L. Cambrésy and P. Petit (eds)

PREPARING THE FUTURE OF ASTRONOMY PHDS IN FRANCE

S. Boissier[1], V. Buat[1] and L. Cambresy[2]

Abstract. The numbers of doctors in astronomy formed in France has been increasing for 15 years, a time during which the number of openings for permanent positions has remained constant. As it is well known by the young generations, the pressure on the research position is high, putting many post-doctoral researchers in difficult situations for up to 10 years after their defence. We have to prepare students and post-doctoral researchers to maximize their chances for both academia and the private sector. In this spirit, the 2015 SF2A conference included a lunch meeting with former members of hiring committee and a workshop on the valorization of the astronomy thesis. We believe awareness of both young and senior researchers is important to provide PhDs with a robust background and modern methods, valuable in their future, whichever it is.

Keywords: formation, education

1 Introduction

During the conference, an e-poster was presented in session S06 (`http://sf2a.eu/semaine-sf2a/2015/posterpdfs/2_9_25.pdf`) from which the figures are not reproduced here. In section 2, we remind the evolution of some numbers. In section 3, we stress two actions that were undertaken during the conference in favour of young researchers.

2 Evolution of the number of astronomy PhDs and positions in academia

A compilation of PhDs awarded (or started) in various institutions shows that the number of thesis has been increasing in the last 15 years, at an average rate of 0.63 thesis/years in Paris, 0.2 in Marseille, and 0.25 in Toulouse. There is annual variations and the statistics at any institution is relatively small but the trend is real (likely linked to the possibility to create PhDs fellowship from ANR, ERC, LABEX, etc and to the constant pressure of the community towards its permanent researchers to form students). About 100 thesis in astronomy are started each year in France (D. Mourard* at this conference has indeed given the approximate number of 300 PhD students in INSU laboratories).

In the same period, the number of opened positions has been of around 20 per year for the total of CNRS, CNAP and universities. Perspectives given during the week let us think that this number may not be maintained in the future. We note that due to the autonomy accorded to universities, it is sometimes difficult to have reliable numbers for the university positions.

3 Actions

While many researchers (senior or young) do perform actions in their own laboratories, the SF2A week is the opportunity for them to meet and discuss about them. It is also the unique opportunity to propose new actions at a national level, opened to all.

[1] Aix Marseille Université, CNRS, LAM (Laboratoire d'Astrophysique de Marseille) UMR 7326, 13388, Marseille, France
[2] Observatoire astronomique de Strasbourg, Université de Strasbourg, CNRS, UMR 7550, 11 rue de lUniversité, 67000 Strasbourg, France
*INSU, directeur adjoint scientifique pour l'astronomie-astrophysique

© Société Francaise d'Astronomie et d'Astrophysique (SF2A) 2015

3.1 Lunch meeting on the French permanent positions

A lunch meeting was organised in the presence of several former members of the hiring committees. The application and presentation in front of such committees require young researchers to know a certain number of untold "codes" in order to maximise their chances. It is thus fair that they are discussed with all future candidates (and not just a few chose ones behind closed doors). The lunch meeting was well attended and very successful from this point of view.

3.2 Workshop on the valorization of the astronomy PhD outside academia

Several presentations were given in this worskshop, by Bruno Roussel (Toulouse University), Stéphanie Godier (Recherche et Avenir) and Olivier Iffrig (AUDDASS), showing structures exist to help young researchers to find interesting positions outside academia. An open discussion followed. The workshop was less attended that the lunch meeting presented before because of the occurrence of scientific workshops at the same time, and probably showing that the real goal of young researchers is academia (at odds with the numbers of PhDs we form). We especially encourage AUDDASS in its effort to create a national listing of astronomy PhDs that should help us to keep contact with former students and understand what we (senior scientists) need to include in the formation we provide to them. A real effort on the part of PhD supervisors is may be needed.

4 Conclusion

With the current situation, it is clear that young researchers will have a hard time defending themselves on the academia job market. We have to help all of them to prepare so that the selection process is further improved (all candidates should have access to the same level of information in all fairness). Many of them will have to move to another field of work. It is thus important that the formation delivered during the PhDs provide them with arguments for the private market (modern methods, or tools), and boost their level of confidence. SF2A should play a continuing role in these aspects.

Session 07

Atelier de l'AS SKA-LOFAR

SF2A 2015
F. Martins, S. Boissier, V. Buat, L. Cambrésy and P. Petit (eds)

INTERFEROMETRIC RADIO TRANSIENT RECONSTRUCTION IN COMPRESSED SENSING FRAMEWORK

M. Jiang[1], J. N. Girard[1], J.-L. Starck[1], S. Corbel[1] and C. Tasse[2]

Abstract.
Imaging by aperture synthesis from interferometric data is a well-known, but strong ill-posed inverse problem. Strong and faint radio sources can be imaged unambiguously using time and frequency integration to gather more Fourier samples of the sky. , However, these imagers assumes a steady sky and the complexity of the problem increases when transients radio sources are also present in the data. Hopefully, in the context of transient imaging, the spatial and temporal information are separable which enable extension of an imager fit for a steady sky. We introduce independent spatial and temporal wavelet dictionaries to sparsely represent the transient in both spatial domain and temporal domain. These dictionaries intervenes in a new reconstruction method developed in the Compressed Sensing (CS) framework and using a primal-dual splitting algorithm. According to the preliminary tests in different noise regimes, this new "Time-agile" (or 2D-1D) method seems to be efficient in detecting and reconstructing the transients temporal dependence.

Keywords: interferometry, imaging, transients, sparsity, compressed sensing

1 Introduction

The study of the radio sky at radio wavelengths has increased since the arrival of new sensitive instrumentation. The timescale to produce images in radio was reduced by the development of new imaging techniques taking the full advantage of the instrument. At the same time, the study of known class of transient sources (e.g. pulsars for general relativity tests, Active Galactic Nuclei, etc) and the recent discovery of new class of transients (e.g. Rotating Radio Transients, Fast Radio Bursts, Lorimer type bursts, Lorimer et al. (2007)) has motivated further development for transient detection and characterization.

Imaging via aperture synthesis with interferometric data has been an active field of research for ∼40 years. A radio interferometer gives a limited set of noisy Fourier samples of the sky (the visibilities (Wilson et al. 2009)) inside the field of view of the instrument. An approximate of the sky can be obtained (assuming the small field approximation) by simply taking the inverse Fourier Transform (FT) of those visibilities. Due to the limited number of baselines, the Fourier plane is incomplete and one requires to process this incomplete Fourier map either by solving a deconvolution problem, using tools such as CLEAN and its derivates (e.g. (Högbom 1974; Schwab 1984; Rau & Cornwell 2011)) or by solving the "inpainting" problem by recovering missing information in the Fourier plane. Several teams have addressed this issue within the framework of the recent Compressed Sensing (CS) theory (e.g. (Garsden et al. 2015; Girard et al. 2015) and references therein). In addition, next generation of giant interferometers such as LOFAR (van Haarlem et al. 2013), suffers from "direction-dependent" effects (Tasse et al. 2012) which distort the Fourier relationship between the measurements and the sky (such as array non-coplanarity and dipole projection). In (Garsden et al. 2015), a new imager compatible with LOFAR combined both a sparse approach given by the CS theory and corrections for A and W effects (Tasse et al. 2013). It also demonstrated better angular resolution and lower residuals as compared to classical methods, on simulated and real datasets.

A lot of effort has been put into the development of detection pipelines (e.g. the LOFAR TRAnsient Pipeline – TRAP (Swinbank et al. 2015), based on fast iterative closed-loop performing calibration / imaging / source

[1] Service d'Astrophysique, CEA Saclay, Orme des Merisiers, 91410 GIF-Sur-YVETTE, France
[2] GEPI, Observatoire de Paris-Meudon, 5 rue place Jules Janssen, 92190 Meudon, France

© Société Francaise d'Astronomie et d'Astrophysique (SF2A) 2015

detection / catalogue cross-matching). However, being variable and mostly point-like, the transients imaging suffers from the imaging rate. On the one hand, short time integration enables temporal monitoring of a transient, but each snapshot provides poor visibility coverage. Therefore, the image has low signal-to-noise ratio (SNR) due to large fraction of missing data. On the other hand, long time integration ensures a good sampling, but it will average out the temporal variability of the transient by mixing and diluting "ON" state periods with "OFF" state periods. As a result, a variety of transient radio sources might be missed due to uncertainty or timescale filtering. Consequently, it is difficult to use classical imagers to detect and image transient source when the temporal variability of the transient source is unknown. There is an interest in developing fast imagers, enable to cope with the time variability of the sources. Such imagers can rely on the CS framework to give a quick approximate of the true sky, giving access to faster transients. This motivated the development of a 2D-1D sparse reconstruction imager on the experience obtained in the 2D imaging case.

2 Radio transient reconstruction in compressed sensing framework

2.1 Compressed sensing theory

Shannon theory is commonly known in the domain of signal processing to perfectly reconstruct a regularly sampled signal. However, the innovative sampling and compression theory of recent years, Compressed Sensing (CS) (Candes & Wakin 2008), or Compressive Sensing could go beyond the Shannon limit, at a rate significantly below the Nyquist rate, to capture and represent compressible signals based on the sparsity of observed signals.

The CS theory is a paradigm for finding a nearly exact reconstruction in the case of an undetermined problem. In the radio interferometry imaging problem, as we have fewer observations than unknowns (i.e. the sparsely sampled FT of the sky), the CS theory applies and could enable to produce accurate maps possibly with improved angular resolution. To achieve the perfect reconstruction from few samples, the CS theory relies on two principles: sparsity and incoherence. First, in general, the CS theory exploits the fact that the signal can be sparse or compressive in some dictionary $\mathbf{\Phi}$. For instance, a signal $\mathbf{x}(t)$ may be not sparse in the direct space, but can be sparse in the wavelet space. In such case, $\mathbf{x}(t)$ can be decomposed as its sum of few, but significant, coefficients, as $\mathbf{x} = \mathbf{\Phi}\boldsymbol{\alpha} = \sum_{i=1}^{T} \alpha[i]\varphi_i$, with T relatively small. Second, the incoherence principle states that a sparse signal in the dictionary $\mathbf{\Phi}$ must be as dense as possible in the domain where it is acquired. It means that the sensing vectors must be as different as possible from the atoms of $\mathbf{\Phi}$.

2.2 2D-1D inverse problem formulation

As indicated in the subsection 2.1, the interferometry imaging problem constitutes an ill-posed inpainting problem which can be described mathematically in Eq. (2.1):

$$\mathbf{V} = \mathbf{MFx} + \mathbf{N} \tag{2.1}$$

with $\mathbf{V}$, the measured visibility vector, $\mathbf{M}$ the sampling mask which accounts for incomplete sampling in the Fourier space, $\mathbf{F}$ the FT operator, $\mathbf{x}$ the sky, and $\mathbf{N}$ the noise. The sky $\mathbf{x}$, expressed in the direct space, is a real quantity while the noise $\mathbf{N}$ is complex as it alters both amplitude and phase of the visibility measurements.

By extension, the application to transient imaging leads to recast the entities of Eq. (2.1) as time-dependent entities. In that scope, the data model of the sky $\mathbf{x}$, containing a transient source, will be a cube. At a given frequency, two dimensions are associated with the spatial information and the third dimension describe its time dependence. In the classical 2D case, the masking operator $\mathbf{M}$ is a given, depending on the frequency and time integration. In our case, we have to account for its time-dependence as we considered a ground-based radio interferometer that rotates with Earth (leading to the apparent motion of the sky). $\mathbf{M}$ will sample different region of the sky FT with time which is a cumulative effect to the variation of the sampled FT of the varying sky. The imaging of a transient radio sky, can be regarded as a 2D-1D spatial-temporal image reconstruction problem.

To comply with the CS framework, the choice of the corresponding 2D-1D sparse representation Φ is critical for our problem. Fortunately, as the temporal information is not correlated to the spatial information, we can separate the 2D-spatial dictionary and 1D-temporal dictionary rather than looking for a 3D dictionary. Therefore, as described in (Starck et al. 2009), an ideal wavelet function would be $\psi(x, y, t) = \psi^{(xy)}(x, y)\psi^{(t)}(t)$ where the space (xy) and time (t) are independent. As in Garsden et al. (2015), we selected the 2D starlets (Starck et al. 2010) which have proven to be adapted to astronomical sources. For the 1D temporal transform

$\psi^{(t)}$, we used decimated wavelet functions such as Haar or biorthogonal CDF 9/7 wavelets, depending on the temporal profile of the transient. The whole 2D-1D decomposition scheme is illustrated in Fig. 1. Firstly, assuming a cube of size $N_x \times N_y \times N_z$ where N_z denotes the number of time frames, the starlet transform is operated on each time frame, yielding N_{2D} spatial scales for each frame. Secondly, For each spatial scale, the temporal 1D transform is performed on each pixel column in the temporal direction of each scale. The 1D transform is decimated and will not increase the size of coefficients in time. Thus, we obtain a 2D-1D coefficient set of size $N_{2D} \times N_x \times N_y \times N_z$.

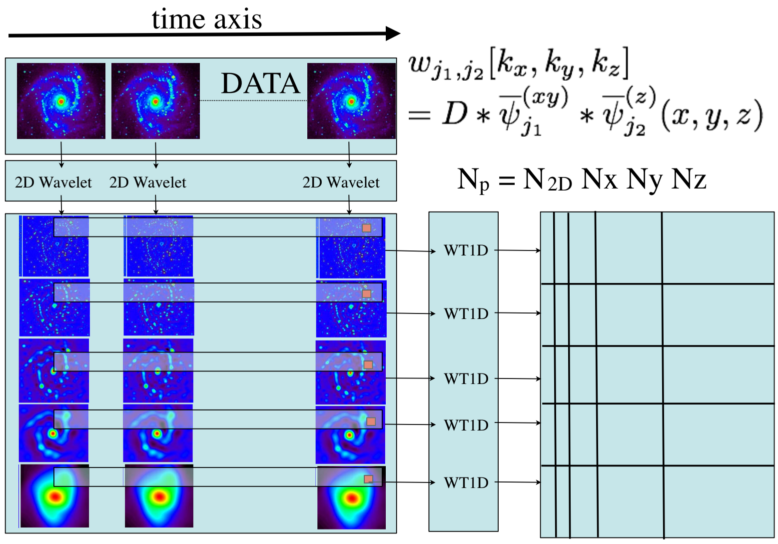

Fig. 1. Illustration of 2D-1D decomposition: For a cube of size $N_x \times N_y \times N_z$, the total number of coefficients will be $N_{2D} \times N_x \times N_y \times N_z$ where N_{2D} is the 2D decomposition scale.

Given this 2D-1D dictionary Φ, the minimization problem can be formulated from Eq. (2.1) in the analysis framework:

$$\mathbf{min}\ ||\mathbf{\Phi}^t\mathbf{x}||_1 \quad s.t. \quad ||\mathbf{V} - \mathbf{MFx}||_2^2 < \epsilon, \tag{2.2}$$

where ϵ denotes the error radius. The objective minimization function takes the form of $||\mathbf{\Phi}^t \cdot ||_1$ where the ℓ_1-norm (summation of absolute values of coefficients) is used to reinforce the sparsity of the solution and ensure the convexity of the problem. However, the ℓ_1-norm involves a soft-thresholding operator which induce bias is solutions (Starck et al. 2010). This is particularly unsuitable for scientific data analysis involving photometry. According to Candes et al. (2007), the reweighted ℓ_1 scheme is one way to handle this issue. To address this issue, we adopted a reweighted ℓ_1 scheme (Candes et al. 2007), by defining a weighting vector $\mathbf{W}$. In addition, as the source photometry is always assumed positive, we impose a positivity constraint as well. Thus, our convex minimization problem can be formulated as:

$$\min_{\mathbf{x}} ||\mathbf{V} - \mathbf{MFx}||_2^2 + ||\mathbf{W} \odot \boldsymbol{\lambda} \odot \mathbf{\Phi}^t\mathbf{x}||_1 + i_{\mathrm{C}^+}(\mathbf{x}), \tag{2.3}$$

where $\boldsymbol{\lambda}$, a scale-dependent vector, is a Lagrangian parameter which depends implicitly on ϵ of the data fidelity in (2.2), the operator $\odot$ denotes the element-by-element multiplication and $i_{\mathrm{C}^+}(x)$ is the indicator function (which is 0 if x belongs to C^+, $+\infty$ otherwise)

As $\boldsymbol{\lambda}$ is not explicitly related to the error radius ϵ, the mathematical relation between $\boldsymbol{\lambda}$ and ϵ is not easy to find out. However, since the real dataset $\mathbf{V}$ is noisy and makes the sparsity constraint decline in the 2D-1D decomposition space, $\boldsymbol{\lambda}$ is closely related to the statistical distribution of decomposition coefficients. Thus, the study of the statistical distribution is important. In practice, several noise driven strategies are available to estimate the statistical distribution. One of the strategies is noise-driven strategy from the residual, which is used hereof. As we will see in section 2.3, the residual is obtained by $\mathbf{R}^{(n)} = \mathbf{V} - \mathbf{MFx}^{(n)}$ in the n-th iteration. Consequently, the statistical distribution $\boldsymbol{\alpha}^{\mathbf{R}^{(n)}} = \mathbf{\Phi}^t\mathbf{F}^t\mathbf{M}^t\mathbf{R}^{(n)}$, and $\boldsymbol{\sigma}$ is accessible by the reliable noise estimator MAD(Median of the Absolute Deviation). Then, $\boldsymbol{\lambda} = k\boldsymbol{\sigma}$ where k defines the level of the significant coefficients which lie within the band $k\sigma$ of the Gaussian distribution.

2.3 Algorithms

According to Candes et al. (2007), the reweighted ℓ_1 scheme is applied as follows:

1. Set the iteration count $n = 0$ and initialize $\mathbf{W}^{(0)} = \mathbf{1}$.
2. Solve the minimization problem (2.3) yielding a solution $\mathbf{x}^{(n)}$, and $\boldsymbol{\alpha}^{(n)}$ is obtained by $\boldsymbol{\alpha}^{(n)} = \boldsymbol{\Phi}^t \mathbf{x}^{(n)}$.
3. Update the weights (see later on).
4. Terminate on convergence or when reaching the maximum number of iterations $N_{\max}$. Otherwise, increment n and go to step 2.

First, a biased solution $\mathbf{x}$ is obtained by the non-reweighted convex optimization, then a weighting step is performed using the following weighting strategy: if $|\alpha_{i,j}| \geq k'\sigma_j$ then $w_{i,j}$=$k'\sigma_j/|\alpha_{i,j}|$, else, $w_{i,j}$=1 (operation later described as function $f(|\alpha_{i,j}|)$. We update the weights for each entity i at scale j, σ_j is the noise standard deviation at scale j. k' acts as a reweight level in scale j. Then, we subsequently apply the proximal theory to solve the minimization problem (2.3) with the Condat-Vũ splitting method (CVSM - Condat (2013); Vũ (2013)). The CVSM introduces a primal-dual pair (x, u) to solve the convex optimization problem (2.3) using forward-backward algorithm. Thus, in summary, the adapted CVSM with reweighted scheme is presented in Algo 1, where the parameters τ and η respect the convergence condition such as $1 - \tau\eta||\Phi||^2 > \tau||\mathbf{MF}||^2/2$, and μ is a relaxation parameter used to accelerate the algorithm. If $\mu = 1$, the algorithm is in the unrelaxed case or no acceleration case. In the Algo 1, the line 3 can be considered as the forward step to converge the non-negative solution from the residual $\mathbf{R} = \mathbf{V} - \mathbf{MFx}$, while the line 4 can be regarded as the backward step to enforce the sparsity constraint by using the soft-thresholding proximity (ST).

Algorithm 1: Analysis reconstruction using CVSM

Data: Visibility $\mathbf{V}$; Mask $\mathbf{M}$
Result: Reconstructed image $\mathbf{x}$

1 Initialize $(\mathbf{x}^{(0)}, \mathbf{u}^{(0)}), \mathbf{W}^{(0)} = \mathbf{1}, \tau > 0, \eta > 0, \mu \in]0, 1]$;
2 **for** $n = 0$ **to** $N_{max} - 1$ **do**
3 $\quad \mathbf{p}^{(n+1)} = \mathrm{Proj}_{\mathrm{C}^+}(\mathbf{x}^{(n)} - \tau\Phi\mathbf{u}^{(n)} + \tau(\mathbf{MF})^*(\mathbf{V} - \mathbf{MFx}^{(n)}))$;
4 $\quad \mathbf{q}^{(n+1)} = (\mathbf{Id} - \mathrm{ST}_{\boldsymbol{\lambda}\odot\mathbf{W}})(\mathbf{u}^{(n)} + \eta\Phi^T(2\mathbf{p}^{(n+1)} - \mathbf{x}^{(n)}))$;
5 $\quad (\mathbf{x}^{(n+1)}, \mathbf{u}^{(n+1)}) = \mu(\mathbf{p}^{(n+1)}, \mathbf{q}^{(n+1)}) + (1 - \mu)(\mathbf{x}^{(n)}, \mathbf{u}^{(n)})$;
6 $\quad \boldsymbol{\alpha}^{(n)} = \boldsymbol{\Phi}^t \mathbf{x}^{(n)}$;
7 $\quad$ Update $\mathbf{W}$ by $w_{i,j}^{(n+1)} = f(|\alpha_{i,j}^{(n)}|)$;
8 **end**
9 **return** $\mathbf{x}^{(N_{\max})}$

3 Experiments

We simulated a sky model of size 32×32×64, i.e. 32×32 pixels on image plane and 64 2-min frames on time. The time-dependent sky model is constituted of a control steady source at the center of the field and a transient source with a gaussian light curve (FWHM = 20 min located at time slice T=24). Both sources have the same peak flux density of 10 arbitrary unit in the sky model. Then, to do the realistic simulation, we generated a 2-hour Fourier sampling mask cube by using an uniform random distribution of 20 antennas observing at the zenith at the latitude of the Nanay Radio Observatory.

To generate the observed visibilities in terms of noise levels, we take the FT of the sky model and apply the mask cube, and then add white gaussian noise with various magnitude ($\sigma = 0.0, 0.5, 1.0, 1.5$ flux unit) on the complex visibilities. Then, by FT inversion, we can obtain the characteristic dirty cube for each case: Fig. 2 (left) shows the transient "OFF" state (first row) and its "ON" state (second row) of the dirty cube. We notice that when the noise level is high, the transient source can be confused with background artifacts.

Figure 2 (right) illustrates the light curve of the transient source central pixel from the sky model cube (dashed curve), the dirty cube (red curve) and the reconstructed cube obtained by the Condat-Vũ algorithm (green curve) described in Sect. 2.3. We can conclude that with no additional noise (but with the sampling noise

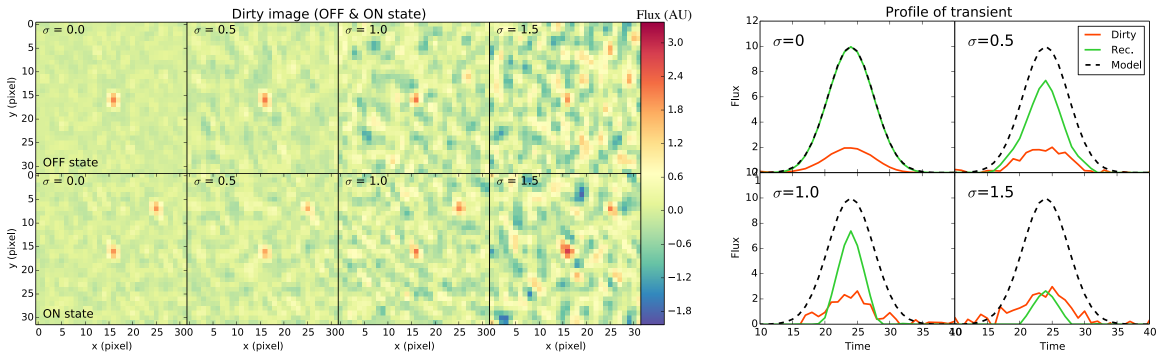

Fig. 2. (left) Dirty images from the benchmark data cube containing two point sources: a central steady source (x=15,y=15) and a transient source (x=24,y=6). First row corresponds to the OFF state (T=10) and second row to the ON state (T=25) at the maximum of the transient. Each column corresponds to various level of additive gaussian noise with $\sigma = 0, 0.5, 1.0, 1.5$ arbitrary flux units. (right) Time profiles at the spatial location of the transient source from the sky model (dash line), the dirty cube (red) and the reconstructed cube (green), for various levels of additive gaussian noise.

due to missing data), our 2D-1D CS method gives a perfect profile reconstruction, with flux unit relative error $\sim 10^{-5}$. As the noise level increases, the flux density of the transient is more spread around the central pixel, resulting in a bias of the peak. However, by summing the flux of the transient on nearby pixels (over a surface equal to the source size), the profile of the transient is again well recovered. Meanwhile, the steady source (not shown) is also well recovered except in the high noise regime where fluctuations are present. From these preliminary results, it seems that our 2D-1D CS reconstruction method is efficient reconstruct the transient in a noisy dataset. The reconstruction time was not monitored but is subject to further study.

4 Conclusions

CS theory offers new tools for solving ill-posed problems such as the imaging problem in radio interferometry. In previous studies, such as Garsden et al. (2015), we have shown that the 2D CS method can outperform classical tools used for deconvolution. In this work, we present an extension of this 2D imager, by recovering the 3D data with the third dimension being the temporal information to detect and reconstruct radio transients. We used respectively a 2D and a 1D wavelet dictionaries to perform 2D-1D reconstruction. In addition, we minimize the convex problem using Condat-Vũ splitting method in the proximal theory framework. The preliminary results based on simulated data cubes containing both steady and transient sources show a good potential for transient imaging. For next steps, we will compare our method with classical deconvolution methods and develop a ”time-agile” imager addressed to the next generation of interferometers, such as LOFAR and SKA, to enable the detection of radio transients. A featured paper is in preparation, and contains extended tests on various dataset (simulated and real datasets containing transient source). As the search for known and unknown transient is a emerging field in radio astronomy, the development of such tools may have a strong impact on transient studies.

We acknowledge the financial support from the UnivEarthS Labex program of Sorbonne Paris Cité (ANR-10-LABX-0023 and ANR-11-IDEX-0005-02) and the Physis project (H2020-LEIT-Space-COMPET).

References

Candes, E. & Wakin, M. 2008, Signal Processing Magazine, IEEE, 25, 21

Candes, E. J., Wakin, M. B., & Boyd, S. P. 2007, ArXiv:0711.1612 [arXiv] 0711.1612

Condat, L. 2013, Journal of Optimization Theory and Applications, 158, 460

Garsden, H., Girard, J. N., Starck, J. L., et al. 2015, A&A, 575, A90

Girard, J. N., Garsden, H., Starck, J. L., et al. 2015, Journal of Instrumentation, 10, C8013

Högbom, J. A. 1974, Astron. Astrophys., 15, 417

Lorimer, D. R., Bailes, M., McLaughlin, M. A., Narkevic, D. J., & Crawford, F. 2007, Science, 318, 777

Rau, U. & Cornwell, T. J. 2011, Astronomy and Astrophysics, 532, A71

Schwab, F. R. 1984, Astronomical Journal, 89, 1076

Starck, J.-L., Fadili, J. M., Digel, S., Zhang, B., & Chiang, J. 2009, Astronomy and Astrophysics, 504, 641

Starck, J.-L., Murtagh, F., & Fadili, M. 2010, Sparse Image and Signal Processing (Cambridge University Press), 53–58

Swinbank, J. D., Staley, T. D., Molenaar, G. J., et al. 2015, Astronomy and Computing, 11, 25

Tasse, C., van der Tol, S., van Zwieten, J., van Diepen, G., & Bhatnagar, S. 2013, Astronomy and Astrophysics, 553, A105

Tasse, C., van Diepen, G., & van der Tol, e. a. 2012, Comptes Rendus Physique, 13, 28

van Haarlem, M. P., Wise, M. W., Gunst, A. W., & et al. 2013, Astronomy and Astrophysics, 556, A2

Vũ, B. C. 2013, Advances in Computational Mathematics, 38, 667

Wilson, T. L., Rohlfs, K., & Hüttemeister, S. 2009, Tools of Radio Astronomy (Springer-Verlag)

SF2A 2015
F. Martins, S. Boissier, V. Buat, L. Cambrésy and P. Petit (eds)

THE ELECTROMAGNETIC INTERACTION OF A PLANET WITH A ROTATION-POWERED PULSAR WIND: AN EXPLANATION TO FAST RADIO BURSTS

F. Mottez[1] and P. Zarka[2]

Abstract. The pulsars PSR B1257+12 and PSR B1620-26 are known to host planets, and other pulsars are suspected to host asteroids or comets. We investigate the electromagnetic interaction of a relativistic and magnetized pulsar wind with a planet or a smaller body in orbit. Many models predict that, albeit highly relativistic, pulsar winds are slower than Alfven waves. In that case, a pair of stationary Alfven waves, called Alfven wings (AW), is expected to form on the sides of the body. They form a magnetic wake into the plasma flow, and they carry a strong electric current. The theory of Alfven wings was initially developed in the context of the electrodynamic interaction between spacecraft and the Earth's magnetosphere, and then of the Io-Jupiter interaction. We have extended it to relativistic winds, and we have studied the possible consequences on radio emissions from pulsar companions. We predict the existence of very collimated radio beams that are seen by an observer as very rare and brief signals. But they are intense enough to be observed from sources at cosmological distances. Thus they could be an explanation to fast radio bursts (FRB). We discuss the properties (polarisation, recurrence) that could make the difference between this model of FRB and others.

Keywords: pulsar, exoplanet, white dwarf, asteroid, magnetosphere, radio emission, Lorimer burst, fast radio bursts, radio transients, Alfvén wings

1 Introduction

Fast radio bursts (FRB) are highly transient events composed of a single radio burst lasting, at a given frequency, a few milliseconds (Lorimer et al. 2007; Keane et al. 2011; Thornton et al. 2013). As pulsar signals, FRB are dispersed in the time-frequency plane due to propagation, but their dispersion measures (DM) are so large that, if interpreted in terms of interstellar and intergalactic electron densities, they correspond to sources at cosmological distances of up to several Gpc ! This is very unlike usual pulsar signals that comme from our galaxy or its close neighbours. At odds with perytons (at first glance similar signals but identified as of terrestrial origin since their first observations), the question of FRB's origin is still open. They could result from flare stars in our galaxy or cataclysmic events, GRBs, Neutron Star mergers, very young pulsars in SuperNova Remnants, all in remote galaxies. If FRB are caused by cataclysmic events, they should happen only once for a given source. For flare stars and young SNR models, FRB would be irregularly repeatable. We propose a model that implies that FRB are periodic. This model considers FRB as a result of the interaction of pulsars and companions orbiting them.

2 Radio emissions by pulsar companions

Pulsars have companions: planets, asteroids, white dwarfs. White dwarfs orbit most millisecond pulsars (Savonije 1987). Their orbital period is typically a few days or weeks (see ATNF database). Among the five known pulsar planets, the orbital periods range from 2.2 hr to a few weeks, and ~ 100 yr for the most distant (Wolszczan & Frail 1992; Thorsett et al. 1993; Bailes et al. 2011). Asteroid belts are also suspected in the vicinity of PSR B1937+21 (Shannon et al. 2013) and PSR 1931+24 (Mottez et al. 2013).

[1] LUTH, Observatoire de Paris, CNRS, Université Paris Diderot, PSL, 5 place Jules Janssen, 92190 Meudon, France.
[2] LESIA, Observatoire de Paris, CNRS, UPMC, Université Paris Diderot, PSL, 5 place Jules Janssen, 92190 Meudon, France.

© Société Francaise d'Astronomie et d'Astrophysique (SF2A) 2015

All these companions are in the pulsar wind. A pulsar wind is an ultra-relativistic plasma flow of unknown density, flowing along the radial direction ($v_W \sim v_r$), with a Lorentz factor that might possibly reach $\gamma_{wind} \sim 10^6$. At least at close distances, a pulsar wind has a magnetic energy density larger than the kinetic energy density of the plasma: $B^2 >> \mu_0 \rho \gamma c^2$ (Michel 1969; Bucciantini et al. 2006). In that case, the Alfvén speed is larger than the plasma speed ($V_A > v_W$), although both velocities are close to c (Mottez & Heyvaerts 2011b). This could be true at the companion's distance, in which case the companion is not shielded behind a shock wave, but is instead in direct contact with the pulsar wind. Then two stationary Alfvén waves called Alfvén wings (AW) are attached to the companion, in the same way as a wake is attached to the rear of a boat on the sea (Neubauer 1980) (see Fig. 1). The AW is fed by a continuous circulation of electric current $I_{AW} \sim 4(E_0 - E_i)R_P/\mu_0 c$. For a pulsar of period $P = 1$s and an Earth-like planet at 0.2 AU, $I_{AW} \sim 10^{11}$ A. For comparision, the Goldreich-Julian current, that is the engine of pulsar magnetic activity, is $I_{GJ} = 2 \times 10^{11}$ A. Because of the high intensity of the AW currents, we can expect powerful radiative processes. For a millisecond pulsar ($P = 10$ ms), $I_{AW} \sim 10^9$ A, which is still considerable (Mottez & Heyvaerts 2011b). Such a current, crossed with the pulsar wind magnetic field, should cause orbital drifts of low mass (asteroid-like) companions (Mottez & Heyvaerts 2011a). Whatever the size of the companion, these currents are also expected to be sources of instabilities and radio waves.

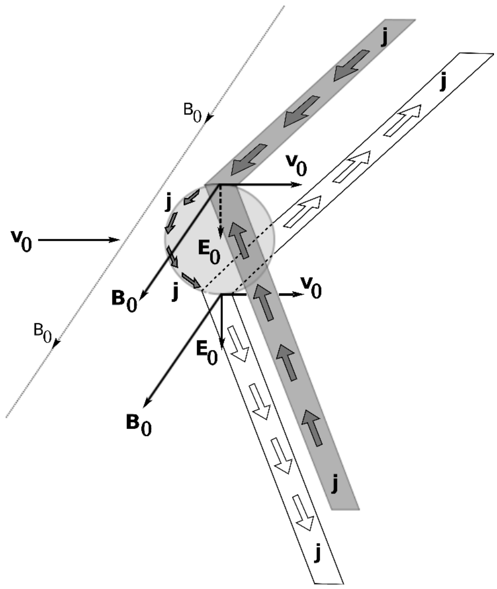

Fig. 1. Schematic view of an unipolar inductor. The unperturbed wind's magnetic field $\vec{B}_0$ and velocity $\vec{v}_0$ are almost, but not exactly, perpendicular. The electric field $\vec{E}_0$ created by the unipolar inductor is perpendicular to these two vectors; it induces an electric current (of density $\vec{j}$) along the body. This current then escapes into the surrounding plasma, forming two structures, each of them consisting of an outwards and an inwards current flow. These currents are unstable to CMI and are the source of radio waves. The angles between radio wave vectors and the current densities $\vec{j}$ mostly depend on the wind Lorentz factor γ_{wind}. When $\gamma_{wind} >> 10^3$, they become extremely narrow $\sim 1/\gamma_{wind}$.

Alvén wings do exist. The satellites Io and Ganymede have AW caused by their interaction with the rotating magnetosphere of Jupiter in which they orbit (Neubauer 1980; Saur et al. 2004). These AW have been studied with the Pioneer and Galileo spacecraft. They intersect the surface of Jupiter, contrary to what we expect with the AW of pulsar companions. It has been shown that the AW of Io and Ganymede generate auroras on Jupiter, that are signatures of plasma acceleration. Alfvén wings are also powerful sources of decametric radio waves triggered by the Cyclotron Maser Instability (CMI) (Mottez et al. 2010). The CMI is an instability that is favoured by the presence of an electric current and accelerated plasma (Freund et al. 1983; Wu 1985), which is therefore typical of Alvén wings. Therefore, we extrapoled the properties of the CMI to the environement of pulsar companions.

We have considered that the source of CMI is a volume of plasma convected by the pulsar wind that passes across the AW. Because this flux of plasma is uninterrupted, this would result in the continuous emission of radio waves, along the AW, by a source that propagates approximately with the wind velocity. Because the wind is highly relativistic, the source of radio waves would propagate, in the observer's frame, almost at the speed of light. Therefore, the emitted waves would sustain a strong relativistic aberration, so that in the observer's reference frame, almost all of the radio energy flux would be confined in a cone of angle $\theta \sim 1/\gamma_{wind}$. The main idea of this model is thus that, because of relativistic aberration with $\gamma_{wind} >> 10^2$, the signal would be produced in an extremely narrow beam, with two practical consequences : we would have very little chance of intercepting it but, when we do, the received photon energy flux would be very high. This is compatible with the rarity of FRB and the possibility of observing them from incredibly remote distances (Mottez & Zarka 2014).

More detailed computations have shown that the range of frequencies in the observer's frame would be compatible with radio frequencies, as displayed in Fig. 2. Because of the motion of the companion along its orbit, the duration of the observed signal would be very brief, compatible with typical FRB duration (5 ms) for a planet at 0.01 to 0.1 AU and $\gamma_{wind} = 10^6$. The amplitude of the radio emission in the reference frame of the source was estimated from Zarka (2007) $P_{radio} = \epsilon \frac{\pi}{\mu_0 c} {R_p}^2 r^{-2} R_*^4 B_*^2 \Omega_*^2$, where R_p is the companion radius, R_* and B_* the neutron star radius and magnetic field, and r the companion's orbital distance. The factor ϵ is estimated to $\sim 10^{-3}$ in Zarka (2007), but we have used a more conservative value $\epsilon = 10^{-4}$. Taking into account the relativistic effects, the predicted flux of the observed signal is $< F >= 4\gamma_{wind}^2 P_{radio} D^{-2} \Delta f^{-1}$, with D the distance of the pulsar and Δf the emission bandwidth. Figure 2 shows that a signal of 1 Jy could indeed be observed from a source at cosmological distances, as suggested by FRB dispersion measures.

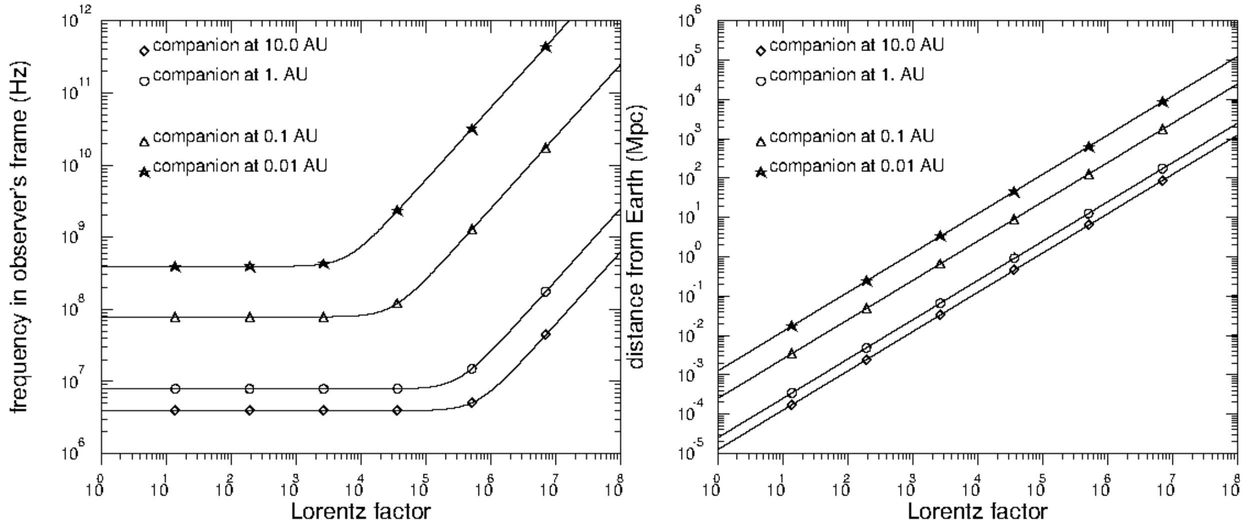

Fig. 2. Left: Frequencies vs Lorentz factor for companions of a typical $P = 10$ ms pulsar. **Right:** Distance at which the flux density of the companion-induced signal reaches 1 Jansky, expressed in Mpc, for various distances from the neutron star to its companion. The neutron star parameters correspond to a typical $P = 10$ ms pulsar.

The model of CMI in the AW of a pulsar companion shows that the shape of the signal is highly dependent on the wind's Lorentz factor. For $\gamma_{wind} \sim 10^6$ and $r \sim 0.01$ AU, the signal is composed of two pulses separated by a time interval of $\sim 1 - 5$ ms. At the time resolution of the radio surveys in which FRB have been detected, these two pulses may be merged and seen as a single pulse.

When $\gamma_{wind} \sim 10^5$ or less, four pulses can be seen, with the second and the third one very close to each other, and much brighter than the first and the fourth ones. This is actually what is seen with a transient event observed only once at the Arecibo radio telescope, and called J1928+15 (Deneva et al. 2009). This signal is composed of three pulses, the second being the most intense. The three pulses are separated by two intervals of about 1 second. We can reproduce this feature with our model and various combinations of parameters (planet distance r, pulsar period P_* and γ_{wind}). We notice that the interpulse duration would not necessarily correspond to the pulsar period P_*.

3 Observations that can help to discriminate our model from others

The following remarks about our pulsar companion model support its compatibility with FRB.

According to the present model, FRB would present the same kind of rarity as main sequence star occultations by planets (as seen with Corot or Kepler), but the aligment needs to be more "perfect" due to the strong focusing of the radio beam.

The line of sight must be in the orbital plane of the neutron star companion. It does not necessarily cross the beam of the pulsar. Even if that was the case, the pulsar signal, being much less focussed by relativistic effects, would not be detectable at cosmological distances. These are the two reasons why FRB are not associated with a regular pulsar signal.

The CMI model presented in this paper predicts only the emission of radio waves, and it is thus consistent with the lack of FRB signal in the optical, X, and γ energy ranges (Petroff et al. 2015a).

Because the CMI signal is circularly polarized in the reference frame of the source, the signal in the reference frame of the observer migh contain a part of polarized signal. This is indeed what was observed with the recent FRB 140514 (Petroff et al. 2015c). More observations of FRB polarization and detailed calculation of the expected polarization (as a function of γ_{wind}) will help to discriminate between the various models proposed to explain FRB.

The most important observation that could help to discriminate our pulsar companion model from others would be the re-occurence of a FRB at the same location and with the same dispersion measure. Up to now, follow-up observation have obtained negative results (Petroff et al. 2015b). But they do not yet constrain the lack of repeatability. A FRB typically lasts 5 ms (at a given frequency) and it might repeat only every few weeks or months. If a FRB is observed a second time, then it will be important to know if the signal is periodic. Up to now, the pulsar companion model is the only one that predicts a periodicity. If a period is found, it will correspond to the orbital period of the pulsar companion, and with that known, other parameters such as the companion's distance and the wind's Lorentz factor can be estimated. This is not only important for the physics of FRB, but for the knowledge of pulsars in general, because the Lorentz factor has never been measured, up to now, in any pulsar wind.

This work is supported by the PNHE programm of the CNRS/INSU.

References

Bailes, M., Bates, S. D., Bhalerao, V., et al. 2011, Science, 333, 1717

Bucciantini, N., Thompson, T. A., Arons, J., Quataert, E., & Del Zanna, L. 2006, MNRAS, 368, 1717

Deneva, J. S., Cordes, J. M., McLaughlin, M. A., et al. 2009, ApJ, 703, 2259

Freund, H. P., Wong, H. K., Wu, C. S., & Xu, M. J. 1983, Physics of Fluids, 26, 2263

Keane, E. F., Kramer, M., Lyne, A. G., Stappers, B. W., & McLaughlin, M. A. 2011, MNRAS, 415, 3065

Lorimer, D. R., Bailes, M., McLaughlin, M. A., Narkevic, D. J., & Crawford, F. 2007, Science, 318, 777

Michel, F. C. 1969, ApJ, 158, 727

Mottez, F., Bonazzola, S., & Heyvaerts, J. 2013, Astronomy and Astrophysics, 555, A126+

Mottez, F., Hess, S., & Zarka, P. 2010, Planet. Space Sci., 58, 1414

Mottez, F. & Heyvaerts, J. 2011a, Astronomy and Astrophysics, 532, A22+

Mottez, F. & Heyvaerts, J. 2011b, Astronomy and Astrophysics, 532, A21+

Mottez, F. & Zarka, P. 2014, A&A, 569, A86

Neubauer, F. M. 1980, Journal of Geophysical Research (Space Physics), 85, 1171

Petroff, E., Bailes, M., Barr, E. D., et al. 2015a, MNRAS, 447, 246

Petroff, E., Johnston, S., Keane, E. F., et al. 2015b, ArXiv e-prints [arXiv] 1508.04884

Petroff, E., Keane, E. F., Barr, E. D., et al. 2015c, MNRAS, 451, 3933

Saur, J., Neubauer, F. M., Connerney, J. E. P., Zarka, P., & Kivelson, M. G. 2004, Plasma interaction of Io with its plasma torus (Cambridge University Press), 537–560

Savonije, G. J. 1987, Nature, 325, 416

Shannon, R. M., Cordes, J. M., Metcalfe, T. S., et al. 2013, ArXiv e-prints [arXiv] 1301.6429

Thornton, D., Stappers, B., Bailes, M., et al. 2013, Science, 341, 53

Thorsett, S. E., Arzoumanian, Z., & Taylor, J. H. 1993, ApJ, 412, L33

Wolszczan, A. & Frail, D. A. 1992, Nature, 355, 145

Wu, C. S. 1985, Space Sci. Rev., 41, 215

Zarka, P. 2007, Planetary and Space Science, 55, 598

SF2A 2015
F. Martins, S. Boissier, V. Buat, L. Cambrésy and P. Petit (eds)

METRIC OBSERVATIONS OF SATURN WITH THE GIANT METREWAVE RADIO TELESCOPE

R. Courtin[1], M. Pandey-Pommier[2], D. Gautier[1], P. Zarka[1], M. Hofstadter[3], F. Hersant[4] and J. Girard[5]

Abstract.
We used the Giant Metrewave Radio Telescope (GMRT, India) to observe Saturn in the metric domain at 0.49 m (610 MHz), 1.28 m (235 MHz), and 2.0 m (150 MHz) -with the aim of constraining the deep atmospheric ammonia and water vapor concentrations around 10−20 kbar. We have obtained a clean detection at 610 MHz, with a disk brightness temperature Tb= 216 ± 32 K, and no significant emission outside of the disk, thus confirming model predictions about the weakness of synchrotron radiation by magnetospheric electrons (Lorenzato et al. 2012, Lorenzato et al. 2012). A marginal detection was obtained at 235 MHz, with Tb= 404 ± 249 K, while an upper limit of 1210 K was set at 150 MHz. Unfortunately, some of the GMRT measurements were affected by strong ionospheric scintillation or radio frequency interferences (RFI). Although the reduction of the LOFAR measurements is much more complex, results are expected in the near future and they will complement nicely with those obtained with the GMRT. We will discuss the constraints resulting from these observations on Saturn's deep atmospheric composition.

Keywords: Saturn; acceleration of electrons; atmosphere; numerical simulations; radio observations

1 Introduction

The bulk abundance of water in Saturn is very poorly known. Various estimates of the upper atmospheric H_2O mole fraction have been obtained in the infrared (Larson et al. 1980; Wilkenstein 1983; Chen et al. 1991; de Graauw 1997; Feuchtgruber et al. 1997) but they all refer to pressure levels above the water condensation cloud expected around 13 bar. Short of sending an atmospheric probe into Saturn to measure the gas composition below that level, we need to rely on remote sensing observations in the microwave domain, at wavelengths on the order of a few tens of centimeters. In the case of Jupiter, this particular method will be implemented during the JUNO mission with the MWR (Micro−Wave Radiometer) instrument (Janssen et al. 2005), which is expected to constrain the deep tropospheric abundances of both of NH_3 and H_2O down to at least 30 bar. For Saturn, however, no such mission is envisaged in the foreseeable future. Therefore, these remote observations must presently be carried out with ground−based radio−telescopes, such as the GMRT in India, the Very Large Array (VLA) in the USA, or the Low Frequency ARray (LOFAR) in the Netherlands, all three of which operate at metric wavelengths.

On the other hand, modeling of the thermochemistry occurring in Saturn's deep troposphere, based on the constraints provided by the observed mole fractions of CO, PH_3 and SiH_4, arrived at the conclusion that oxygen must be enhanced about 3−to−6 times compared to the solar abundance (Visscher and Fegley, 2005). However, the validity of the assumptions used in this model concerning the chemical reactions involved is rather uncertain.

At metric wavelengths, Saturn's radiation originates at deep tropospheric levels, as shown by the contribution functions plotted in Fig. 1. For instance, at 100 cm the contribution function peaks around 100 bar, while

[1] LESIA, Observatoire de Paris,France
[2] CRAL, l'Observatoire de Lyon, France
[3] Jet Propulsion Laboratory, 4800 Oak Grove Drive, Pasadena, CA 91109, USA
[4] LAB, Observatoire Aquitain des Sciences de l'Univers, Bordeaux, France
[5] CEA/Sap-Saclay, Universit Paris Diderot, France

© Société Francaise d'Astronomie et d'Astrophysique (SF2A) 2015

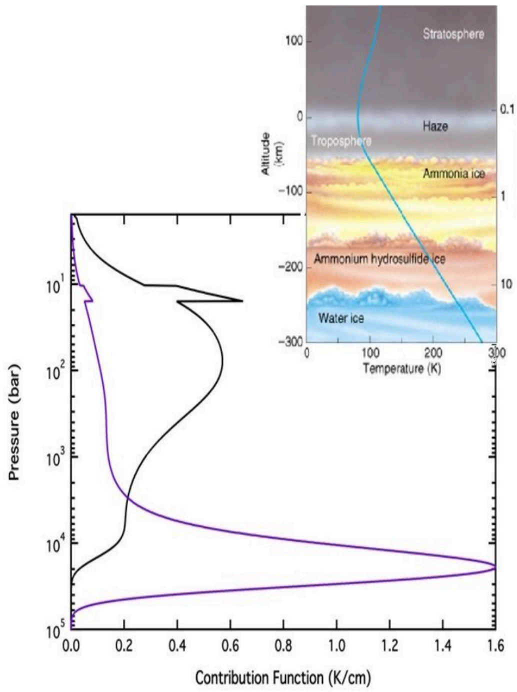

Fig. 1. Contribution functions computed at 1 m (black) and 3 m (purple). The humps at 10−20 bar correspond to the assumed location of the water cloud. Emission near 3 m originates mostly from the 20 kbar level, therefore much deeper than the water cloud.

at 300 cm, the maximum is located around 20 kbar. These contribution functions are calculated under the assumption that the temperature profile follows an adiabat and that the dominant opacity is that of a NH_3-H_2O mixture with mole fractions consistent with those predicted by the Visscher and Fegley model (Gulkis and Hofstadter 2013). Given these assumptions, Saturn's flux density spectrum corresponding to thermal emission can be calculated as a function of the deep−tropospheric water abundance, as shown in Fig. 2.

The absolute level of flux density varies between ∼4 and 20 mJy in the 150−610 MHz frequency range that is accessible with the three ground−based instruments mentioned above. Given the sensitivity of the present detection systems, the expected signal−to−noise ratios are expected to decrease from several hundred at 610 MHz to a few at 150 MHz. But most importantly, we need to measure the flux density with enough accuracy, i.e. less than 10%, to differentiate between the two extreme models, one corresponding to a roughly solar O/H ratio and one with a 30−times enhanced ratio. An impediment to Earth−based remote sensing of Jupiter's deep tropospheric layers at decametric or metric wavelengths stems from the fact that the thermal radiation component is overwhelmed by the synchrotron radiation due to energetic electrons in the Jovian magnetosphere. Such is not the case for Saturn. In modeling the distribution of energetic electrons inside Saturn's magnetosphere, Lorenzato et al. (2012) have shown that losses due to absorption by the dense ring system and icy satellites are the dominant processes. Thus, their model predicts a very weak level of synchrotron emission, on the order of a few tenths of mJy in the 100−300 cm range, whereas the thermal emission is expected to be on the order of a few mJy (see above).

2 Observations

The GMRT observations at 610 and 235 MHz were carried out in order to constrain Saturn's thermal flux density spectrum, and hence the deep tropospheric NH_3 and H_2O concentrations. The measurement of NH_3 and H_2O concentrations allow us to determine the bulk N/H and O/H ratios. The O/H is especially important in terms of cosmological implications and for constraining interior models of Saturn. Other objectives includes the confirmation of a weak−to−negligible magnetospheric synchrotron emission, and that of a possible opacity contribution from weakly ionized water.

Table in Fig. 2 summarize the Saturn observations carried out in 2014 with the GMRT. Unfortunately,

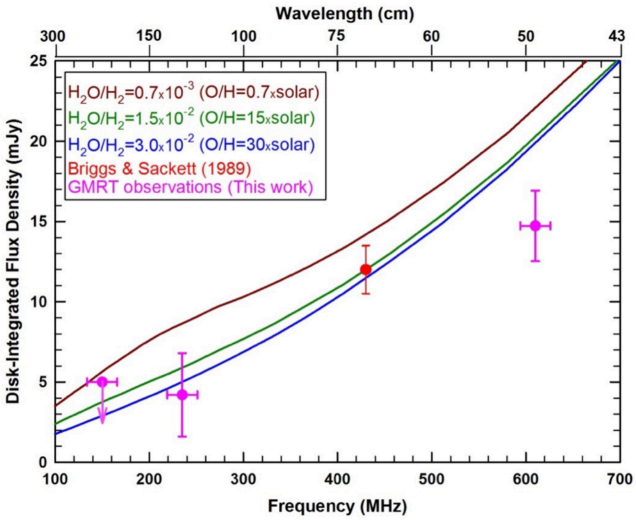

Log of GMRT observations of Saturn			
Date	Central frequency	Duration	Quality / rms noise
March 1, 2014	150 MHz	3 h	Poor (RFI noise)
March 21, 2014	235 MHz 610 MHz	4 h 4 h	Poor (scintillation) / 2 mJy Good / 0.15 mJy
June 20, 2014	150 MHz	4 h	Poor (RFI noise) / 5 mJy
August 16, 2014	235 MHz	4 h	Mediocre (RFI noise) / 2 mJy

Log of LOFAR observations of Saturn			
Date	Central frequency	Duration	Quality
May 21, 2013	116 MHz / 166 MHz	5 h	Poor (scintillation)
May 22, 2013	216 MHz / 244 MHz	5 h	Good
August 25, 2013	216 MHz / 244 MHz	5 h	Good
August 26, 2013	116 MHz / 166 MHz	5 h	Good

Fig. 2. (Panel 1): The GMRT flux densities at 150, 235, and 610 MHz are compared with models of Saturn's thermal radiation assuming various H_2O concentrations. The flux density measured by Briggs and Sackett (1989) at 430 MHz is also shown. In all models, the NH_3 concentration is constrained by another result from Briggs & Sackett (1989) at 1450 MHz. (Panel 2): Log of radio observations on Saturn.

the March 1 (150 MHz), March 21 (235 MHz), and June 20 (150 MHz) GMRT observations, suffered from substantial noise due to ionospheric scintillation and/or radio-frequency interferences (RFI). The on-source time during the observations varied between 3.0 to 4.0 hrs. A total bandwidth of 33.3 MHz (RR correlations only), split into 512 channels, was recorded at 610 MHz. In the case of 235 and 150 MHz the bandwidth was 6 MHz. NRAOs Astronomical Image Processing System (AIPS) was used to carry out the initial calibration of the visibility dataset. The primary calibrator was used to set the flux density scale and derive the bandpass solutions for all the antennas. About 40% of the data, mostly from short baselines, were affected by RFI and subsequently flagged. Gain solutions were obtained for the calibrator sources and together with the bandpass solutions applied to the target field. Channels showing flat bandpass calibration response were used and the rest were discarded as they were too noisy due to the bandpass roll-off. The clean channels were averaged in 10 in order to reduce the size of the data. Cleaned set of averaged channel UV data were used to produce images using 3D technique. Self calibration was applied to the data in order to produce final phase corrected images.

The March 21st GMRT observation at 610 MHz resulted in a high S/N detection of Saturn, along with several extragalactic sources that were used for flux calibration (Figs. 3 and 4). The source was detected at a level of 14.73±1.64 mJy (Tb= 216±32 K) at 610 MHz and 4.2±2.24 mJy at 235 MHz. The error in the flux density measurement is a combination of rms noise in the field, system error and the calibration error in flux density estimate. Note that the noise in 235 MHz is very high as the data was severely affected by RFI and observation was performed when the source was at low elevation. Further deep observations are needed to confirm the detection at 235 MHz.

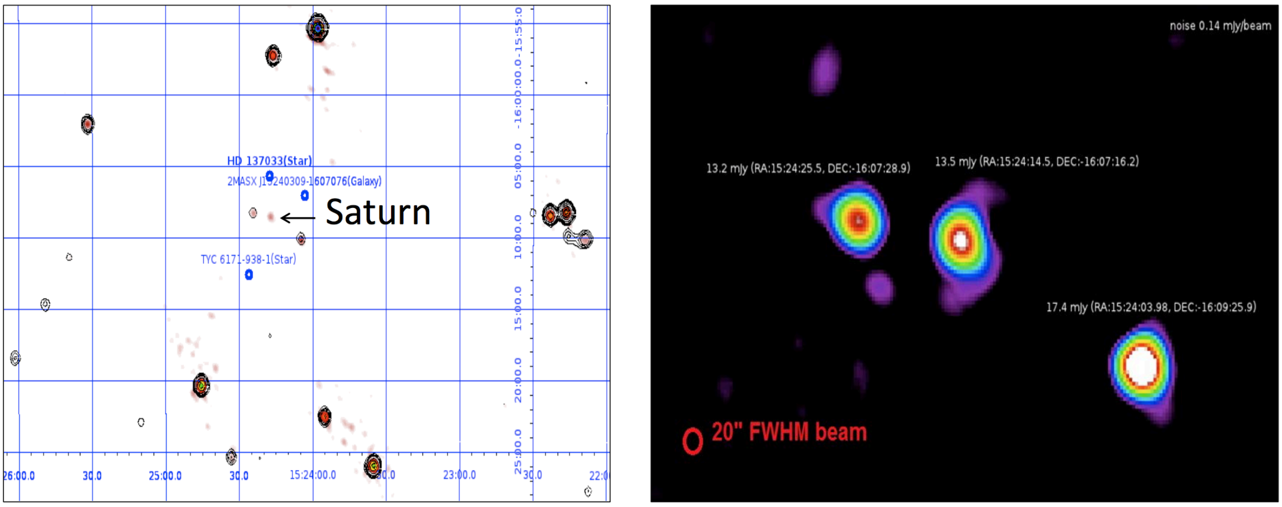

Fig. 3. (Panel 1): GMRT field−of−view for the March 21 observation at 610 MHz. The black contours correspond to known sources in the NVSS catalog. (Panel 2): Zoom on the central part of Panel 1. The size of Saturn's image is consistent with a 18 arsec disk convolved with a beam of 20 arcsec FWHM.

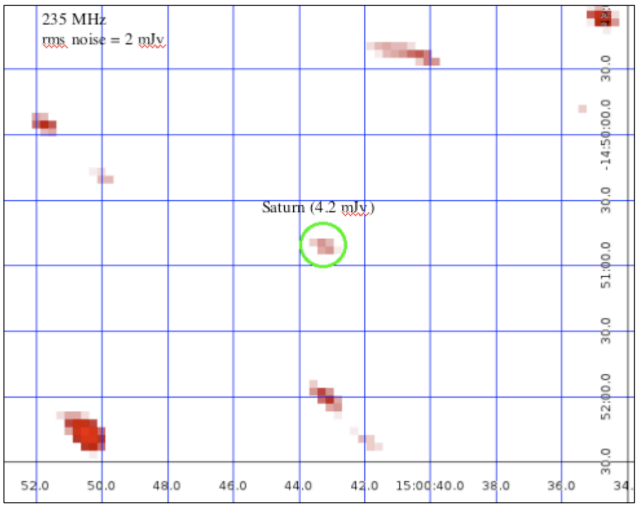

Fig. 4. GMRT field−of−view for the August 16, 2014 observation at 235 MHz (128 cm).

3 Discussion and Conclusion

A comparison of the GMRT results at 150, 235, and 610 MHz with models of Saturn's thermal radiation assuming different values for the water vapor concentration seems to favor water−rich models with an O/H ratio of at least 15 (Fig. 2). This very tentative conclusion needs to be confirmed with additional observations in the metric range. More measurements spread out within the 150-600 MHz interval are needed to confirm the shape of the spectrum and arrive at firmer conclusions. Deeper LOFAR observations will also provide important constraints for the models at frequencies that are complementary to the GMRT ones.

We thank the staff of GMRT, who made these observations possible. The GMRT is run by the National Centre for Radio Astrophysics of the Tata Institute of Fundamental Research.

References

Briggs, F. H. and Sackett, P. D.; 1989; Icarus 80; 77-103

Chen, F. et al.; 1991; J. Geophys. Res.; 96; 17519

deGraauw,T. et al.; 1997; Astron. Astrop.; 321; L13
de Vos, M.; Gunst, A.W.; Nijboer, R; 2009; IEEE Proceedings 97; 1431
Feuchtgruber,H. et al.; 1997; Nature; 389; 159
Gulkis, S. and Hofstadter, M; 2013; Private communication
Janssen, M. A. et al.; 2005; Icarus 173; 447
Larson, H. P. et al.; 1980; Astrophys. J.; 240; 327
Lorenzato, L.; Sicard, A.; Bourdarie, S.; 2012; J. Geophys. Res.; 117; A08214
Lorenzato, et al.; 2012; Thesis 'Modlisation des ceintures de radiation de Saturne'; Univ. Toulouse
Visscher, C. and Fegley B.; 2005; Astrophys. J.; 623; 1221
Wilkenstein, P.; et al.; 1983; Icarus 54; 309

SF2A 2015
F. Martins, S. Boissier, V. Buat, L. Cambrésy and P. Petit (eds)

A STEEP SPECTRUM RADIO HALO IN MERGING GALAXY CLUSTER-MACSJ0416.1-2403

M. Pandey-Pommier[1], R. J. van Weeren[2], G. A. Ogrean[2], F. Combes[3], M. Johnston-Hollitt[4], J. Richard[1], J. Bagchi[5], B. Guiderdoni[1], J. Jacob[6], K. S. Dwarakanath[7], D. Narasimha[8], A. Edge[9], H. Ebeling[10], T. E. Clarke[11] and T. Mroczkowski[11]

Abstract. Steep Spectrum Radio Halos (RH) are very rare diffuse structures existing in the central region of merging galaxy clusters. Due to their steep spectral nature, they are often not detected at higher frequencies and tend to shine only at very low frequencies. They represent a new class of objects that could be either old halos or clusters at a special time of the merger event, when particle acceleration processes have a lower efficiency. The comparison of theoretical predictions with the low frequency observations clearly suggests that there is yet a large population of very faint RHs in galaxy clusters that still remains to be discovered with steep spectrum RHs expected to dominate this undiscovered population. As the number counts of these steep spectrum RHs is scarce, discovery of even a couple of them is important. We present result on cluster $MACSJ0416.1-2403$ (z = 0.396), that host one such steep spectrum RH and emphasize the important contribution of low frequency observations with interferometers like GMRT, MWA, LOFAR, SKA on cluster science and discovery of new population of rare steep spectrum RHs.

Keywords: galaxies: clusters: general, galaxies: clusters: individual: $MACSJ0416.1-2403$: intracluster medium radio halo

1 Introduction

Cluster of galaxies are the largest bound structures in the Universe. They form by mergers with smaller clusters and galaxy groups. These merger events generate shocks, cold fronts, and turbulence within the intracluster medium (ICM), as can be probed by X-ray observations of the intracluster medium (e.g., Markevitch and Vikhlinin 2007; Randall et al. 2008; Zhuravleva et al. 2015). In addition, these merger give rise to diffuse non-thermal radio emission (Giovannini et al. 2009, Feretti et al. 2012, Bonafede et al. 2012, van Weeren et al. 2012, 2014, Giacintucci et al. 2014, Kale et al. 2013, 2015, Ogrean et al. 2015, de Gasperin et al. 2015, Pandey-Pommier et al. 2015). Thanks to X-ray observations, important progress has been made on the study of thermal properties of the ICM and its interactions in galaxy clusters during merger events (Markevitch & Vikhlinin 2007). However, scarce information is available about the non-thermal emitting components in the ICM and their physical properties, that can for example be used to probe the dynamical properties of the cluster (Dursi & Pfrommer 2008; Parrish et al. 2009).

[1] CRAL, l'Observatoire de Lyon,France
[2] Harvard-Smithsonian Center for Astrophysics, 60 Garden Street, Cambridge, MA 02138, USA
[3] LERMA, l'Observatoire de Paris, France
[4] School of Chemical and Physical Sciences, Victoria University of Wellington, PO Box 600, Wellington 6014, New Zealand
[5] Inter University Centre for Astronomy and Astrophysics,(IUCAA), Pune University Campus, Post Bag 4, Pune 411007, India
[6] Newmann Collage, Kerala, India
[7] Raman Research Institute, Bangalore, India
[8] Tata Institute of Fundamental Research, Bombay, India
[9] Department of Physics, Durham University, Durham DH1 3LE, UK
[10] Institute for Astronomy, University of Hawaii, 2680 Woodlawn Drive, Honolulu, HI 96822, USA
[11] U.S. Naval Research Laboratory, 4555 Overlook Ave SW, Washington, DC 20375, USA

© Société Francaise d'Astronomie et d'Astrophysique (SF2A) 2015

The combined study of radio along with multi wavelength properties suggests that, radio halos (RHs) form by electrons that are re-accelerated through scattering with magneto hydro dynamic (MHD) turbulence. Radio relics are thought to trace particles accelerated at shocks. RHs and relics should preferentially be found in massive objects undergoing major mergers, since more energy is released into the ICM during these events. At a later stage in the merger, or during less energetic merger events, clusters might give rise to a fainter class of RHs with steep or ultra steep ($\alpha < -1.5$) spectral nature (Cassano et al. 2015). These ultra steep spectrum radio halos (USSRHs) are under luminous at GHz frequencies and tend to shine only in the MHz range. Thus, low frequency radio observation are crucial for the detection of this rare population of steep or ultra steep spectrum RHs.

In this paper, we present results from Giant Metrewave Radio Telescope (GMRT), Chandra and Jansky Very Large Array (JVLA) observations of a merging galaxy cluster: the Hubble Space Telescope (HST) Frontier Fields cluster $MACSJ0416.1-2403$ (z=0.396, Ebeling et al.2001; Mann & Ebeling 2012).

2 Merging galaxy cluster: $MACSJ$0416.1-2403

HST Frontier Field cluster, $MACSJ$0416.1-2403 was discovered by the Massive Cluster Survey (MACS) as an actively merging system with a luminosity, $L_{X,0.1-2.4keV} = 7.43\pm0.08 \times 10^{44}$ erg s^{-1}, temperature, $T = 10.06^{+0.50}_{-0.49}\ keV$ and elongated central region (Ebeling et al. 2001; Mann & Ebeling 2012, Ogrean et al. 2015).

At optical wavelengths the cluster is known to show strong lensing properties based on the HST data (Postman et al. 2012) and hosts numerous strongly lensed galaxies (refer Fig. 1; Zitrin et al. 2013; Richard et al. 2014, Schirmer et al. 2014; Jauzac et al. 2014; Zitrin et al. 2015; Grillo et al. 2015). Further the HST data also reveal a highly elongated mass distribution, typically seen in merging systems with two mass concentrations associated to two main subclusters involved in the merger, plus two smaller X-ray-dark mass structures north east (NE) and south west (SW) of the cluster center (Jauzac et al. 2015). The combined analysis based on shallow, archival Chandra X-ray data (with poor count statistics) and Dark Matter (DM) distribution map using lensing data by Jauzac et al. (2015), suggested that there exists an offset between the DM and the thermal gas components for the SW subcluster and a good DM-gas alignment for the NE subcluster. Jauzac et al. (2015) concluded that- there are two possible scenarios for the merger event in $MACSJ$0416.1-2403− one pre-merging (lack of offsets) and one post-merging (significant offsets). However, with the recent deep Chandra observation, better constraints (within the uncertainties) on the peak of the X-ray position co-located with the DM centers, was derived, favouring the possibility of $MACSJ$0416.1-2403 being a pre-merging cluster, but the possibility of $MACSJ$0416.1-2403 being a post-merging cluster was not ruled out.

3 Non-thermal emitting components and their spectral properties in $MACSJ$0416.1-2403

Low frequency radio observations are good tracers (in the form of RHs and relics) of the dynamical state of massive galaxy clusters. In the case of most massive merger events, RHs show a typical spectral index of , $\alpha < -1.1$ (where, $S_\nu = \nu^\alpha$, Feretti et al. 2012) and may scale up to Mpc size as seen in the case of $MACSJ0717.5+3745$ (Pandey-Pommier et al. 2013).

At the later stage of major mergers, USSRHs are expected to be formed, that are under luminous at higher frequencies (i.e., above a GHz), due to the energy losses involved. They should still shine brightly at lower frequencies giving rise to a steep spectrum ($\alpha < -1.5$). In the turbulent re-acceleration model (Brunetti et al. 2008, Cassano et al. 2006, Donnert et al. 2013), less energetic merger events, often occurring in less massive systems, are also expected to produce USSRHs. This is caused by an energy cutoff in the particle spectrum because the re-acceleration is inefficient. Less energetic mergers in less massive systems are more frequent than major mergers in the Universe, however, high sensitivity observations are required to detected USSRHs in these less energetic events, due to their faint nature.

In the case of $MACSJ$0416.1-2403, a RH of size 0.65 Mpc and was detected down to 610 MHz (refer Fig. 2 and 3). The halo has an elongated shape and seems to be associated to both the NE and SW subclusters (Ogrean et al. 2015). Using JVLA and GMRT data, a spectral index- $\alpha^{1500MHz}_{610MHz} = -1.6 \pm 0.5$ was estimated with a radio power of $P_{1.4GHz} = (1.3\pm0.3)\times\ 10^{24}$ W Hz^{-1}. The VLA Low Band Ionospheric and Transient Experiment (VLITE) data at 340 MHz also detects the halo at a flux density level of 14.6±7.0 mJy giving a spectral index of $\alpha^{1500MHz}_{340MHz} = -1.5 \pm 0.8$. Given the location of $MACSJ$0416.1-2403 on the $L_x - P_{1.4GHz}$ relation for RHs, it is possible that $MACSJ$0416.1-2403 is either hosting a normal RH or possibly an USSRH formed due to the turbulent re-acceleration in less energetic mergers (refer Fig. 3; Brunetti et al. 2008; Cassano

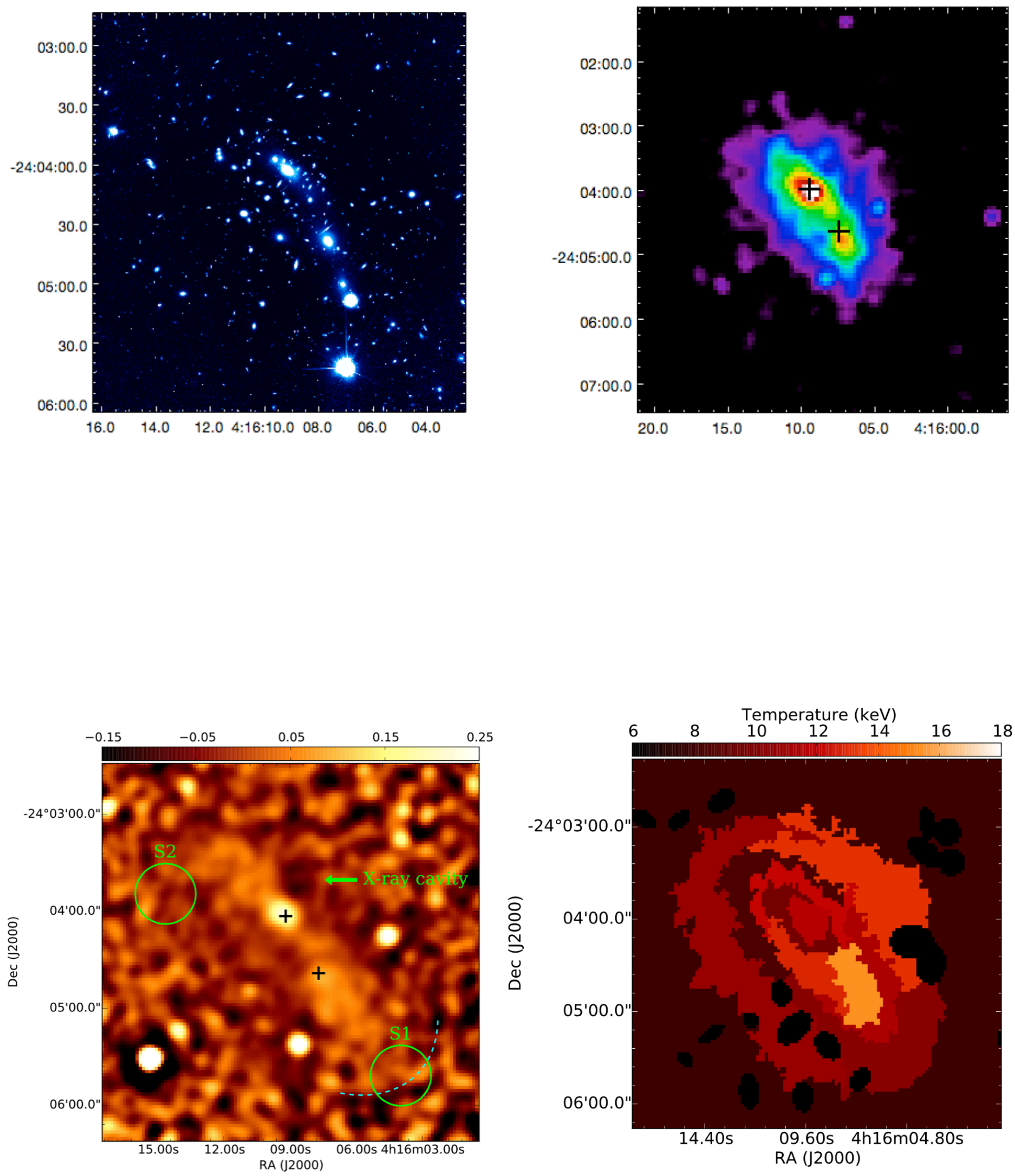

Fig. 1. $MACSJ0416.1$-2403 : *(Top left:)* HST image showing lensed galaxies and elongated mass distribution, *(right:)* Chandra image showing disturbed central region with centers of the DM halos (black crosses) of the NE and SW merging clusters. *(Bottom left:)* Chandra image showing X-ray cavity, positions of the two less massive structures identified by Jauzac et al. (2015) marked as S1, S2. *(right:)* Temperature map showing no strong gradient in the NE and SW merging clusters, (from Ogrean et al. 2015).

et al. 2013; Umetsu et al. 2014). Additional low frequency radio observations (below 610 MHz) are needed to confirm the steepness in the radio spectrum and to establish whether this is an USSRH.

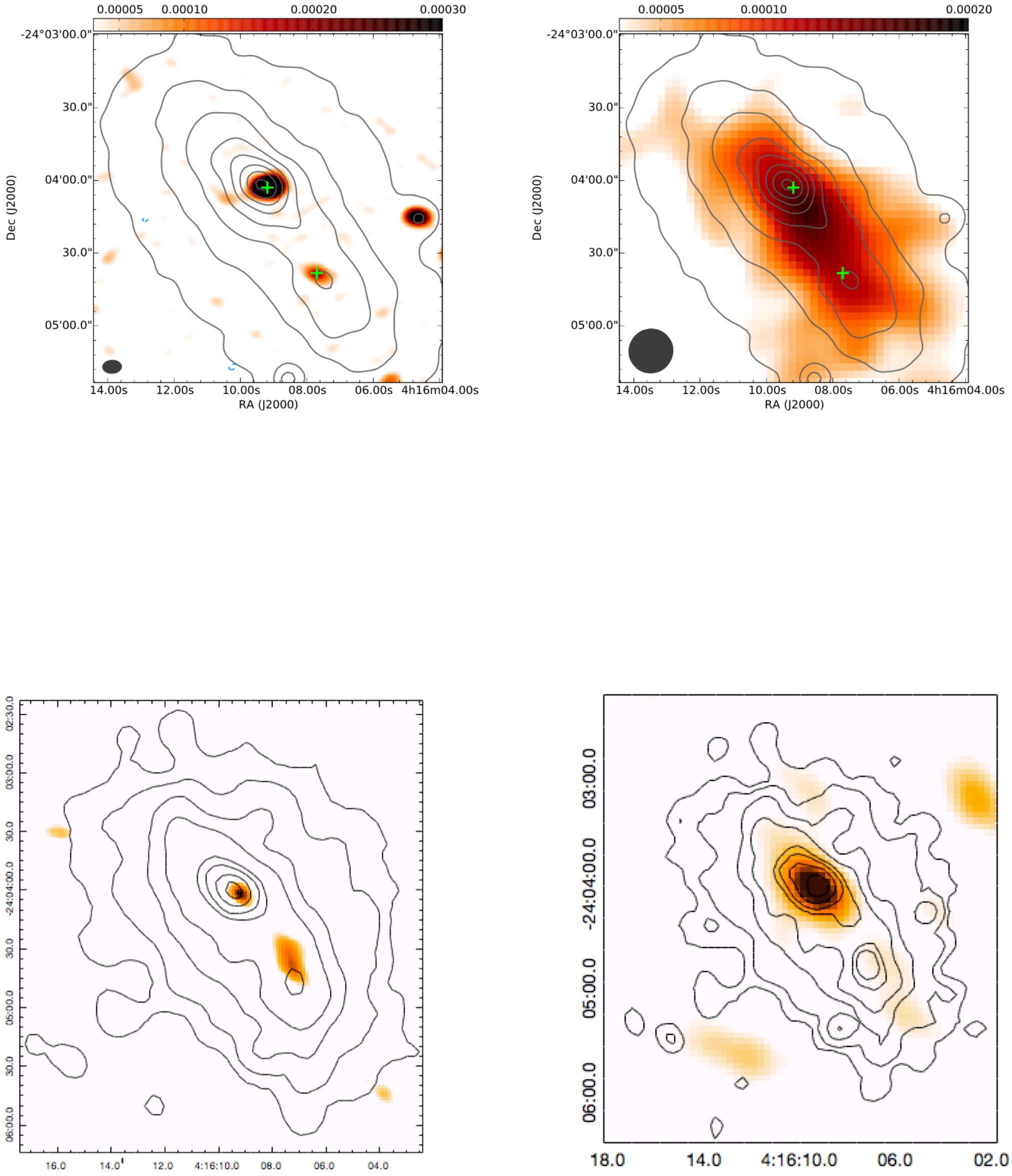

Fig. 2. *(Top left):* JVLA 1-2 GHz high-resolution (7.8 × 5.5 arsec) image showing the compact sources in the cluster region, with the centers of the DM halos marked (green crosses). (*Right:*) 1-2 GHz low resolution image (18 × 18 arsec) of the RH with compact sources subtracted, Ogrean et al. 2015. (*Bottom left:*) GMRT 0.61 GHz high-resolution (7.6 × 4.0 arsec) image showing the compact sources in the cluster region. (*Right:*) low-resolution (20 × 20 arsec) image showing the steep spectrum RH. Chandra contours are overlaid in black.

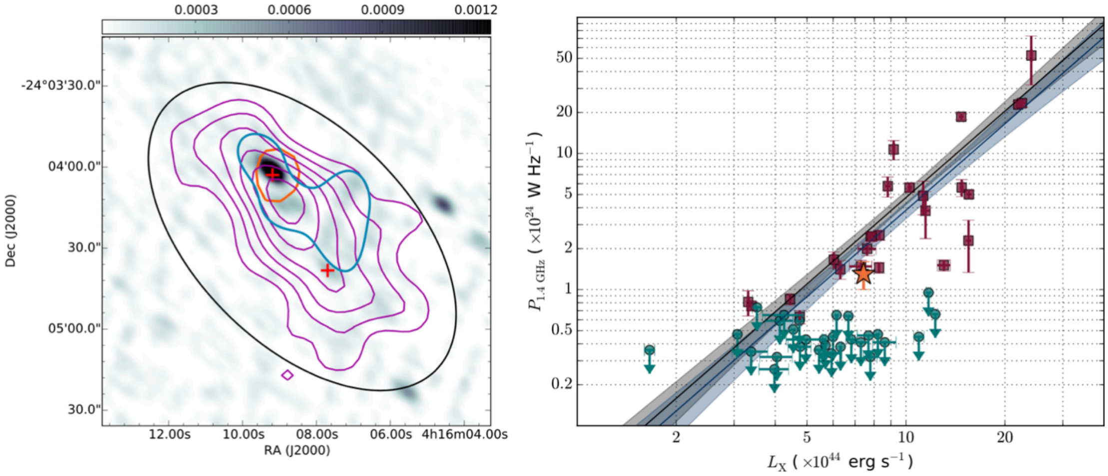

Fig. 3. *(Left):* RH (magenta contours) detected in JVLA data at 1.5 GHz, (blue contours) in GMRT data at 0.61 GHz and in VLITE data (red contours) at 340 MHz for massive cluster $MACSJ$0416.1-2403 overlaid on high resolution JVLA image in grey scale. *(Right)*: $\mathrm{L}_X - P_{1.4GHz}$ diagram in clusters with $MACSJ$0416.1-2403 represented in orange star and upper limits on radio halo power in teal (from Ogrean et al. 2015)

4 Properties of USSRHs in clusters

USSRHs are very rare and faint in nature at GHz frequency range. As of now only 7 clusters viz., A697, A521, A1300, A2256, $RXCJ$1514.91523, Z1953 and A1682 are known to host such USSRHs (Venturi et al. 2008; Macario et al. 2010; Venturi et al. 2013, Giacintucci et al. 2011, Kale et al. 2015). They are less luminous in radio and generated in connection with less energetic phenomena, e.g., major mergers between less massive systems or minor mergers in massive systems towards the end of their activity (Cassano et. al. 2015). Thus, considering the energy input required to initiate merger-events, USSRHs are expected to be more common in the Universe, as compared to major massive mergers which require high energy input (Cassano et al. 2015). Evidently, deep low frequency observations at MHz range with high sensitivity are required for their detection. LOFAR (van Haarlem et al. 2013), MWA (Tingay et al. 2013) and SKA are ideal instruments to detect such new population of USSRHs, with number of these sources being larger in SKA1-LOW surveys thanks to its better sensitivity (Cassano et al. 2015). Simulations suggests that SKA1-LOW may be able to detect ∼2600 halos (including Giant RHs), while LOFAR may detect ∼400 RHs (Cassano et al. 2015), thereby providing better test for theoretical models (Brunetti et al. 2008).

5 Summary and Conclusion

We present a combined radio (GMRT, JVLA, VLITE) and X-ray (Chandra) analysis of the massive galaxy cluster $MACSJ$0416.1-2403 (z = 0.396). Low frequency radio observations with the GMRT down to 610 MHz not only confirmed the presence of a faint RH in $MACSJ$0416.1-2403, in the JVLA data but also provided a better constraint on the radio power. Further, the spectral index estimate between JVLA and GMRT data suggests that the RH in $MACSJ$0416.1-2403 has a steep spectral ($\alpha = -1.6$) nature. Thus, these observations not only highlight the importance of low frequency observation to detect rare steep spectrum RHs but also, the expected major contribution of the SKA, MWA and LOFAR in discovering such rare population RHs, thereby probing the dynamical properties of cluster of galaxies.

We thank the staff of GMRT, who made these observations possible. The GMRT is run by the National Centre for Radio Astrophysics of the Tata Institute of Fundamental Research. This research had made extensive use the data available from public archives from the HST and Chandra.

References

Bonafede, A., Bruggen, M., van Weeren, R., et al. 2012, MNRAS, 426, 40
Brunetti, G., Giacintucci, S., Cassano, R., et al. 2008, Nature, 455, 944
Cassano, R., Brunetti, G., & Setti, G. 2006, MNRAS, 369, 1577
Cassano, R., Ettori, S., Giacintucci, S., et al. 2010, ApJ, 721
Cassano, R., Ettori, S., Brunetti, G., et al. 2013, ApJ, 777, 141
Cassano, R.; Bernardi, G.; Brunetti, G.; et al.; 2015; aska.confE; 73C
de Gasperin, F.; Intema, H. T.; van Weeren, R. J.; et al.; 2015; MNRAS; 453
Donnert, J., Dolag, K., Brunetti, G., & Cassano, R. 2013, MNRAS, 429, 3564
Dursi & Pfrommer, 2008; ApJ; 677; 993D
Ebeling, H., Edge, A. C., & Henry, J. P. 2001, ApJ, 553, 668
Feretti, L., Giovannini, G., Govoni, F., & Murgia, M. 2012,A&A Rev., 20, 54
Giacintucci, S.; Dallacasa, D.; Venturi, T.; et al. 2011, A&A, 534
Giacintucci, S., Markevitch, M., Venturi, T., et al. 2014, ApJ, 781, 9
Giovannini, G., Bonafede, A., Feretti, L., et al. 2009, A&A, 507
Grillo, C., Suyu, S. H., Rosati, P., et al. 2015, ApJ, 800, 38
Jauzac, M., Clement, B., Limousin, M., et al. 2014, MNRAS, 443, 1549
Jauzac, M., Jullo, E., Eckert, D., et al. 2015, MNRAS, 446, 4132
Kale, R., Venturi, T., Giacintucci, S. et al.; 2013, A&A, 557
Kale, R., Venturi, T., Giacintucci, S. et al.; 2015, A&A astropharXiv:1503.02415v1
Macario, G., Venturi, T., Brunetti, G., et al. 2010, A&A, 517
Mann, A. W., & Ebeling, H. 2012, MNRAS, 420, 2120
Markevitch, M., & Vikhlinin, A. 2007, Phys. Rep., 443, 1
Ogrean, G., van Weeren, R.,...PandeyPommier, M., et al. 2015, A&A astropharXiv:1505.05560
Pandey-Pommier, M.; Richard, J.; Combes, F.; et al.; 2013, A&A, 557A
Pandey-Pommier, M.; Richard, J.; Combes, F.; et al.; 2015, A&A, submitted
Parrish, I. J.; Quataert, E.; Sharma, P.; 2009; AIPC; 1201; 358P
Postman M. et al., 2012, ApJS, 199, 25
Randall, S., Nulsen, P., Forman, W. R., et al. 2008, ApJ, 688,208
Richard J. et al., 2014, MNRAS, 444, 268
Schirmer, M., Carrasco, R., Pessev, P., et al. 2014, ArXiv e-prints
Tinagy, S.; Goeke, R.; Bowman, J.; et al.; 2013; PASA; 30; 7T
Umetsu, K., Medezinski, E., Nonino, M., et al. 2014, ApJ, 795, 163
van Haarlem; Wise, M.; Gunst, A.; et al; 2013; A&A; 556A; 2V
van Weeren, R. J., Bonafede, A., Ebeling, H., et al. 2012, MNRAS, 425, L36
van Weeren, R. J., Intema, H. T., Lal, D. V., et al. 2014, ApJ, 781, L32
Venturi, T., Giacintucci, S., Dallacasa, D., et al. 2008, A&A, 484
Venturi, T., Giacintucci, S., Dallacasa, D., et al. 2013, A&A, 551
Zhuravleva, I., Churazov, E., Arevalo, P., et al. 2015, ArXiv e-prints
Zitrin, A., Meneghetti, M., Umetsu, K., et al. 2013, ApJ, 762, L30
Zitrin, A., Fabris, A., Merten, J., et al. 2015, ApJ, 801, 44

GRAVITATIONAL WAVES AND GRBS

S.D. Vergani[1] and E. Chassande-Mottin[2]

Abstract. Owing to new or upcoming facilities (Advanced LIGO/Virgo, SKA with its pathfinders or precursors, CTA, ...) multi-messenger observations will have a strong impact on the field of gamma-ray bursts (GRBs). We are interested in joint radio and gravitational wave (GW) observation of short GRBs. We estimate the prospects for such combined observations with Advanced LIGO/Virgo and the low-frequency radio phased-array NenuFAR. No radio GRB afterglows have been observed so far in the low-frequency band, and our predictions are currently limited by the uncertainty in the radio afterglow models. Our preliminary analysis indicates that there is a limited but non-zero chance to observe with NenuFAR a radio afterglow associated with a GW event.

Keywords: Gravitational waves, Gamma ray bursts, Radio continuum

1 Introduction

GRBs are the most extreme cosmic explosions. Some of them are so bright that even if they are located far away in the Universe their optical counterparts can be observed with naked eye. They are detected from space by satellites thanks to the ash of gamma-ray photons released within a transient relativistic jet, which signals the explosion. The ultra-relativistic jet is produced by a new-born accreting black hole formed after the collapse of a massive star or the merger of two compact objects (see Fig.1). The short lasting (few seconds) gamma-ray *prompt* emission is followed by an *afterglow*, detectable from the X-ray to the radio wavelengths for hours to months, depending on the frequency domain and on its intrinsic brightness.

We can distinguished two classes of GRBs, depending on the duration of their prompt emission (but not only): the *long* and *short GRBs* (Kouveliotou et al. 1993). We now know that long GRBs are associated with the explosions of very massive stars (see e.g. Hjorth & Bloom 2011), whereas we suppose that short GRBs are formed by the merger of two compact objects (stellar black holes and/or neutron stars) but we don't have any direct proof of this. The study of GRBs impacts several branches of physics and astrophysics. Moreover GRBs constitute excellent candidate sources for multi-messenger astrophysics as high-energy neutrinos and gravitational waves are expected in addition to the observed release of electromagnetic energy.

In this proceeding we discuss about the possibility of using radio observations to find the electromagnetic counterparts of gravitational waves (GW) detected by the Advanced LIGO[*]/Virgo[†] interferometers. We will focus in particular on the possible use of the NenuFAR array[‡].

2 GRBs at radio frequencies

GRB afterglows emit through the synchrotron process. The intensity and peak time of GRB radio afterglows depend on the radio frequency observed and on the characteristic of the GRB and its environment. Afterglows become fainter and peak later, as the frequency observed is smaller. GRBs less energetic show fainter radio

[1] GEPI, Observatoire de Paris, CNRS-UMR8111, PSL Research University, Univ. Paris Diderot, 5 place Jules Janssen, 92195, Meudon, France
[2] APC, AstroParticule et Cosmologie, Universit Paris Diderot, CNRS/IN2P3, CEA/Irfu, Observatoire de Paris, Sorbonne Paris Cité, F-75205 Paris Cedex 13, France
[*] `https://www.advancedligo.mit.edu/`
[†] `http://wwwcascina.virgo.infn.it/advirgo/`
[‡] `http://nenufar.obs-nancay.fr/?lang=en`

© Société Francaise d'Astronomie et d'Astrophysique (SF2A) 2015

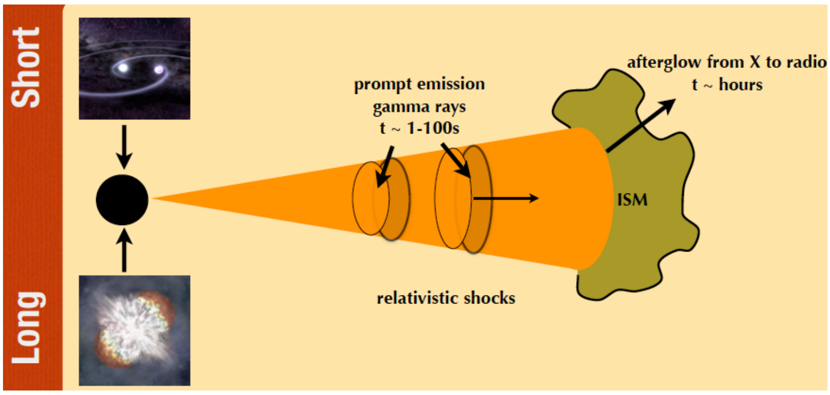

Fig. 1. Cartoon of GRBs following the so-called *fireball* model. The merging of two compact objects (for short GRBs) or the collapse of a very massive rotating star (for long GRBs) give rise to an ultra-relativistic jet within which *internal* shocks produce the *prompt* gamma-ray emission. When the jet encounters the interstellar medium surrounding the progenitor system, the *aftertglow* emission is produces by *external* shocks and can be detected for hours to years, depending on the frequency domain of the observations.

afterglow light-curves that peaks earlier, than those with higher energies. The redshift affects the radio afterglow brightness: GRBs with the same energetic and environment will have fainter afterglows as their redshift increases. The density of the environment will also impact the radio afterglow intensity. Lower densities produce fainter afterglows but the same result is also true at too much high densities due to radio self absorption.

Most of the radio data available to date refer to long GRBs. For GW we are particularly interested to the short GRB class. This class of bursts show fainter and shorter afterglow at any frequencies. In the radio domain, this fact prevented to date to collect a large amount of afterglow radio for short GRBs. Detections are available only for few of them (see Chandra & Frail 2012 for a review).

3 GW and GRBs

Advanced LIGO/Virgo interferometers are about 10 times more sensitive than their predecessors, therefore increasing the explorable volume of the universe by a factor of ∼1000. GW are expected from the merging of compact objects, therefore also in association with short GRBs.

Because of their random orientation, GW events are more likely to come from off-axis coalescing binaries with their orbital momentum not oriented towards the observer. In such case, the associated relativistic jet also does not point towards the observer, thus preventing the observation of the prompt high-energy emission. Those events however be observed as *orphan* afterglows, i.e. transients at optical or radio wavelengths. The radio light-curves of orphan afterglows are similar to those of regular ones, except for the fact that, to detect them, we have to wait for the beaming angle to widen enough to reach our direction. Therefore we see a later rise and peak (see e.g. in Fig. 2) compared to an afterglow seen on-axis. Orphan afterglows represent the bulk of the GRB population despite they have not been detected so far. Ongoing and forthcoming wide and deep surveys are expected (Rossi et al. 2008) to detect orphan afterglows in the optical (Ghirlanda et al. 2015) and in the radio band (Ghirlanda et al. 2014).

The big issue with GW detections will be the huge errors on their position ($> 100\,\mathrm{deg}^2$, reduced to a few $10\,\mathrm{deg}^2$ when the KAGRA[§] and LIGO[¶] india detectors will join the collaboration). Such errors make the identification of the GW electromagnetic counterpart difficult. The large field of view of radio arrays (from a few deg^2 to $> 100\,\mathrm{deg}^2$, depending on the array and its set-up) can be very helpful for the detection of GW counterparts. Radio interferometer will be able to detect and GRB orphan afterglows (and disentangle them form other transient populations; see Fig. 4 of Ghirlanda et al. 2015) and, as the peak of GRB radio afterglow light-curve is shifted towards later times (days, weeks) compared to X-ray or optical, there is no need of extremely rapid follow-up observations.

[§] `http://gwcenter.icrr.u-tokyo.ac.jp/`
[¶] `ttp://gw-indigo.org`

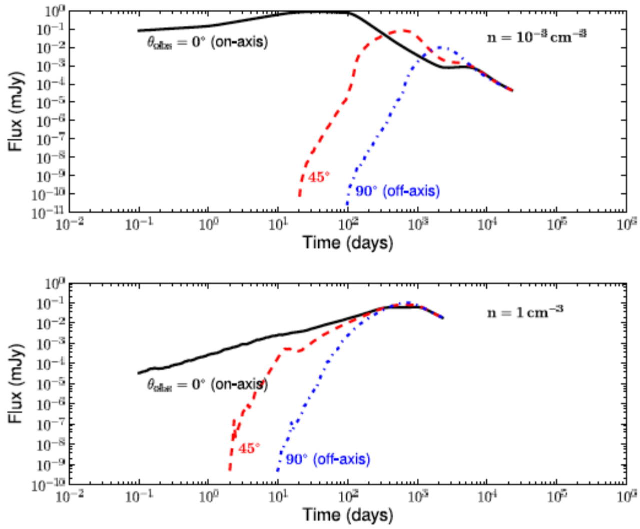

Fig. 2. Examples of GRB radio afterglow light-curves for different observer viewing angles and GRB environment densities. From Feng et al. (2014).

4 GW, short GRBs and NenuFAR

Our aim is to investigate the possibility to detect short GRB counterparts of GW using the phased-array of radio antenna NenuFAR being assembled at the Nanay station (Zarka et al. 2015). Although the radio afterglow is expected to be dimmer at low frequency because of synchrotron self-absorption, it may still be observable with NenuFAR as detectable GW sources are relatively nearby.

To this purpose, we run a simulation using the afterglow modelling of van Eerten & MacFadyen (2012), varying the GRB parameters and combine it with a population synthesis code determining the distribution of GRB rates and redshift. We then define an instrument model and the observing strategy to determine which would be the detectable flux from these events for a given exposure.

We considered initial and final configurations of NenuFAR respectively with 400 and 1800 antennas and chose 80 MHz as the reference frequency of observations. The peak of the GRB afterglow at the radio frequencies appear after at least few days from the GRB explosion. Then, the afterglow starts decaying but it can remain bright enough to be detected for months and even years. For this reason, an efficient strategy to detect the afterglow in the radio is to perform a first observation as soon as the GRB (or the GW) is detected, and then a set of observations starting a few days after the explosion. The first observation will be used to remove confusion and be used as a comparison image, especially at frequencies where quite deep observations of the whole sky are not available.

Several of the parameter and distributions used in the simulations are very uncertain. Not much is known about the real rates and redshift distributions of short GRBs, as well as about the density of the short GRB environment and about the jet opening angles.

We run the simulations considering different environment densities. In Fig. 3 we show the best case for detections ($n \sim 1\,\mathrm{cm}^{-3}$) of our preliminary results.

5 Conclusions

We presented the preliminary results of our investigation on the possibilities to detect short GRB afterglows using NenuFAR, especially looking for the electromagnetic counterparts of GW event detected by the Advanced LIGO/Virgo. Our results show that the probability of detection of such counterparts with NenuFAR is s low but non-zero. Long duration exposures (order of months) are required.

We stress that our predictions are currently limited by the uncertainty in the radio afterglow models. Moreover, there are no detections to date of GRB afterglows at these low frequencies. Detections (or even deep upper limits) with LOFAR may lead to significant change in our conclusions.

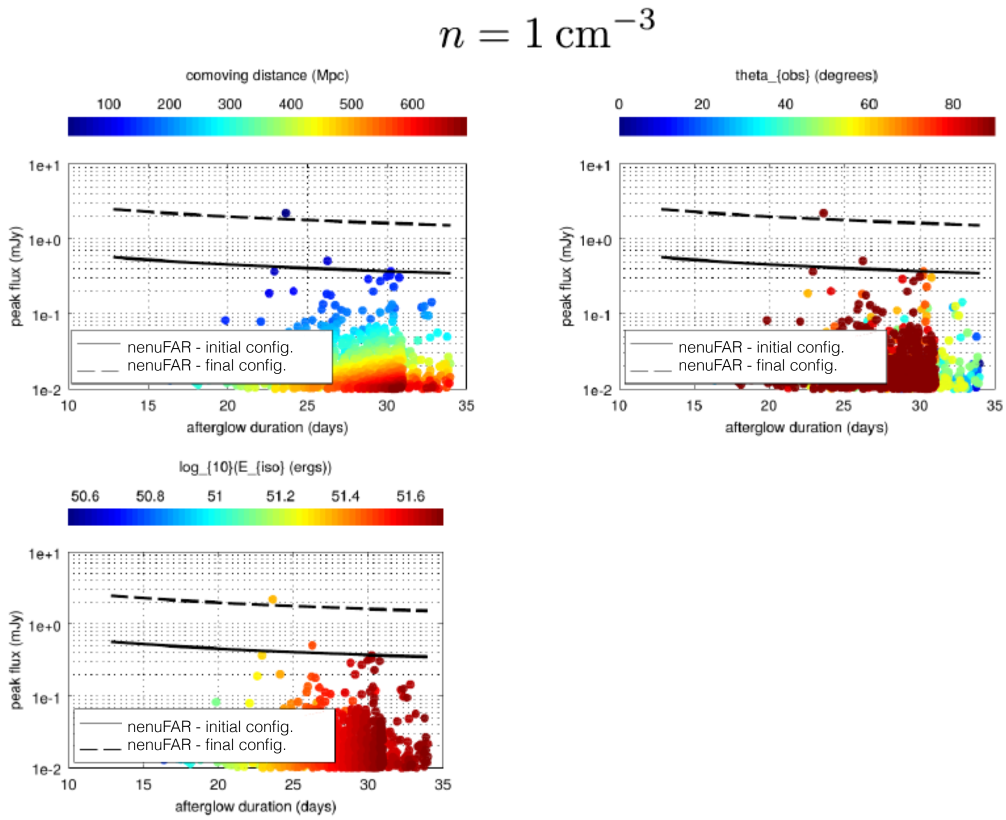

Fig. 3. Peak flux as a function of the afterglow durations from the preliminary results of our simulations, for the case of an environment electron density of $n \sim 1\,\mathrm{cm}^{-3}$. The black (dashed) line represents the flux limit reached by NenuFAR final configuration,1400 antennas (initial configuration, 800 antennas). Each point represent a simulated short GRB whose GW have been hypothetically detected by Advanced LIGO/Virgo. The color code corresponds to different distances (upper left panel), observing angles (upper right panel), and GRB isotropic energy (bottom panel).

References

Chandra, P. & Frail, D. A. 2012, ApJ, 746, 156

Feng, L., Vaulin, R., & Hewitt, J. N. 2014, submitted to MNRAS, ArXiv e-prints: 1405.6219 [arXiv] 1405.6219

Ghirlanda, G., Burlon, D., Ghisellini, G., et al. 2014, PASA, 31, 22

Ghirlanda, G., Salvaterra, R., Campana, S., et al. 2015, A&A, 578, A71

Hjorth, J. & Bloom, J. S. 2011, Chapter 9 in "Gamma-Ray Bursts", eds. C. Kouveliotou, R. A. M. J. Wijers, S. E. Woosley, Cambridge University Press, ArXiv:1104.2274 [arXiv] 1104.2274

Kouveliotou, C., Meegan, C. A., Fishman, G. J., et al. 1993, ApJ, 413, L101

Rossi, E. M., Perna, R., & Daigne, F. 2008, MNRAS, 390, 675

van Eerten, H. J. & MacFadyen, A. I. 2012, ApJ, 751, 155

Zarka, P., Tagger, M., Denis, L., et al. 2015, Proceedings of the 2015 International Conference on Antenna Theory and Techniques (ICATT)

Session 08

Electrodynamique Atmosphérique et Spatiale

PHOTOMETRIC ANALYSIS OF THE CORONA DURING THE 20 MARCH 2015 TOTAL SOLAR ECLIPSE: DENSITY STRUCTURES, HYDROSTATIC TEMPERATURES AND MAGNETIC FIELD INFERENCE.

C. Bazin[1], J. Vilinga [1,2], R. Wittich, S. Koutchmy [1], J. Mouette [1] and C. Nitchelm[3]

Abstract. We present some new accurate CCD photometry analysis of the white light solar corona at the time of the last 20 March 2015 total eclipse (airborne observations on a Falcon 7X and at ground-based-Svalbard). We measured coronal brightness profiles taken along radial directions from 1.001 to 3 solar radii in the northern, southern and equatorial regions, after removing the F-corona and the sky background. These studies allow to evaluate the density gradients, structures and temperature heterogeneity, by considering the Thomson scattering in white light of the K- corona and also emissions of the EUV Fe XII 193A (1 to 2 MK) and Fe XI 171/174 (lower temperature) simultaneously observed by SDO/AIA and SWAP/Proba2 space missions. Some dispersion between the regions is noticed. The limitation of the hydrostatic equilibrium assumption in the solar atmosphere is discussed as well as the contribution of the magnetic field pressure gradients as illustrated by a comparison with the model stationary magnetic corona from Predictive Sc. Inc. These results are compared with the results of the quieter 2010 total solar eclipse corona analyzed with the same method. This photometric analysis of the inner and intermediate white light corona will contribute to the preparation of the Aspiics/Proba 3 flying formation future coronagraphic mission of ESA for new investigation at time of artificial eclipses produced in Space. Note that Aspiics will also observe in the He I D3 line at 5876 A, and will record intensities of the Fe XIV line 5303A simultaneously with the analysis of the orange white- light continuum, including precise polarimetry analysis. .

Keywords: white light corona, CCD photometry, Baumbach fitting, scale height

1 Introduction

We intend to compare some heterogeneity typical values of the temperature and of the density in the corona, using white light observations from recent solar total eclipses, on 22 July 2010 (before maximum of activity), and at the recent 20 March 2015 total eclipse taken well after the maximum of activity. The choice of a five years interval corresponds to an extended period of the activity cycle of the corona. We performed intensity profiles to deduce the brightness in units of the mean solar disc intensity, along the North and the South poles and along equatorial regions, from the limb to 3 solar radii. The simultaneously observed bright star XZ Pisces was identified in images of 2015 and was used as a photometric reference. Its magnitude is 5.6 and sampled on 80 adu in green. The background and sky was subtracted. The exponential decays were applied on the brightnesss profiles to deduce the scale heights assuming an hydrostatic equilibrium. Also we performed Baumbach fitting to compare some values of the power law at distances beyond 2 solar radii. We found that the following polynomial law $P1 * \rho^{-17} + P2 * \rho^{-7} + P3 * \rho^{-3}$ was the best suitable fit on the brightnesss profiles.

2 Brightness profiles and flash spectra analysis

The adjustment with the Baumbach polynomial equation gives a better fitting than with the exponential decay, see also November and Koutchmy, 1996. However, after a further processing (F- corona subtraction), we will used the exponential decay to compare the scale height in 2010 and 2015 in polar and equatorial regions in

[1] Institut d'Astrophysique de paris, 75014 Paris
[2] University of Luanda, Angola
[3] Unity of Astronomy, Antofagasta, Chile

© Société Francaise d'Astronomie et d'Astrophysique (SF2A) 2015

order to straightforwardly deduce the hydrostatic temperatures, see Figure 1. These results show a different behavior of the coronal structure for 2015 compared to 2010. The averaging of the North South Polar Regions and the East and West equators allows to better estimate the gradients. The sky background as well as the F corona was removed. The arrays in figure 2 summarize the results after using an exponential decay for the scale heights and hydrostatic temperatures. The coefficient values with the Baumbach polynomial fitting are indicated for evaluating the density. Comparing the helium shells extensions obtained from the flash spectra made at the same time is interesting. Flash spectra give an evaluation of the activity in the most inner parts of the corona, see Fig. 3. Finally, the following figure 4 aims at showing that the low First Ionization Potential-FIP line of Ti II and He I & He II shells seen in emission and the enhanced brightening indicates that these elements could be ionized in lower altitudes above the photosphere, and close to the Temperature minimum regions. This is done by using high cadence CCD 12 bit imaging, and in 2015 two chanels were used: one at 15 and the other at 214 flash spectra per second, with two computers for the simultaneous acquisitions and GPS chronodation.

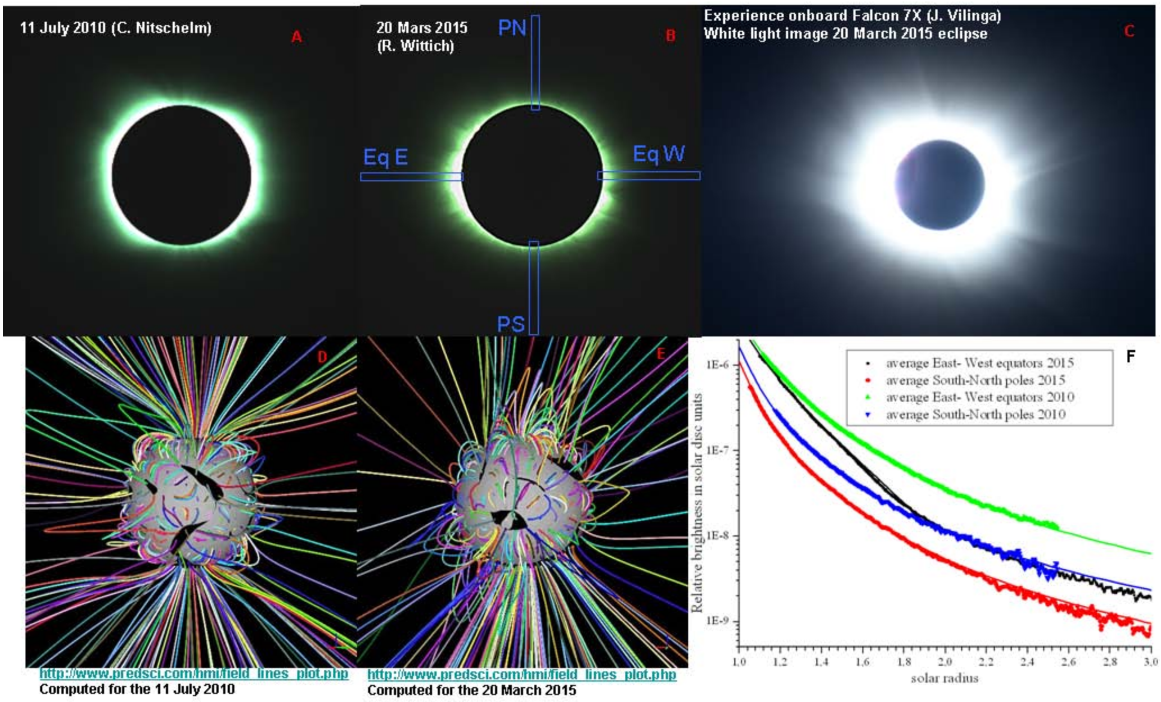

Fig. 1. From left to right and top to bottom are shown: A is the white light images of the total solar eclipses in 2010 (24 ms of exposure time) and B is the corona in 2015 (30 ms of exposure time) to perform the radial brightness profiles. D and E are the set computed magnetic field lines from the date base of `http://www.predsci.com/hmi/field_lines_plot.php` and F are the brightness profiles, near equators and poles for both 2010 and 2015

3 Discussion and Conclusions

The adjustments with the Baumbach polynomial equation see figures 1 and 2 fit better than with the exponential decay. But we used the exponential decay to compare the scale height in 2010 and 2015 in polar and equatorial regions. These results show a different behaviour of the coronal structuration from 2010 and 2015. The averaging of the North South polar regions and the East and West equators allows to better estimate the gradients. The changing of the slope near 1,2 solar radii in 2010 and 1,4 solar radii in 2015 indates some temperature difference and this could indicate that hot plasma penetrate at lower altitudes with a more active Sun but this will be studied in more details The figures 3 and 4 aims to show that the low FIP like Ti II lines and the high FIP He I & He II shells seen in emission and the enhanced brightening indicates that these elements could be ionised in lower altitudes above the photosphre, and close to the Tmin regions. We compare also with coronal holes seen in 2010, 2013 and 2015, for evaluating the scales, extensions of magnetic structures, spicules and jets seen in dark on the limb, see Tavabi 2015. We found some small differences and tendency between the 2010 and the 2015

Regions: 1.005<Rsol<1,4	11/07/2010 Eclipse Scale height Mm and temperature K	20/03/2015 Eclipse Scale height Mm and temperature
East	86 Mm (T = 1,693 MK)	57 Mm (T = 1,122 MK)
West	69 Mm (T = 1,358 MK)	103 Mm (T = 2,027 MK)
North	78 Mm (T = 1,535 MK)	61 Mm (T = 1,200 MK)
South	65 Mm (T = 1,279 MK)	71 Mm (T = 1,397 MK)

Scale heights and temperatures deduced using first order exponential decay fitting with hydrostatic assumptions

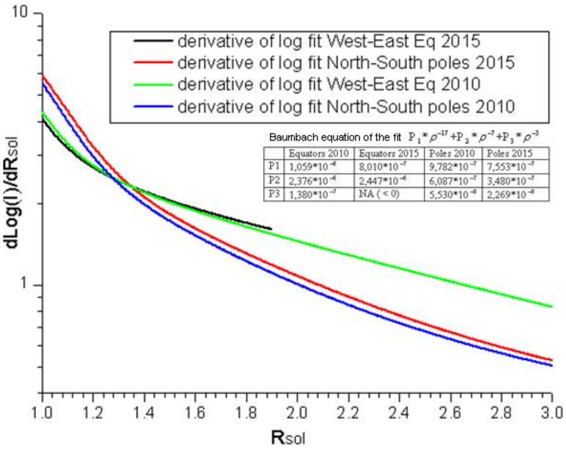

	Equators 2010	Equators 2015	Poles 2010	Poles 2015
P1	$1,059*10^{-6}$	$8,010*10^{-7}$	$9,782*10^{-7}$	$7,553*10^{-7}$
P2	$2,376*10^{-6}$	$2,447*10^{-6}$	$6,087*10^{-7}$	$3,480*10^{-7}$
P3	$1,380*10^{-7}$	NA (< 0)	$5,530*10^{-8}$	$2,269*10^{-8}$

Fig. 2. Scale heights and associated temperatures deduced from the derivative of the logarithm of the Baumbach fit of the brightness radial profiles in white light. The values in the array indicates the Baumbach coefficients of the polynome after fitting.

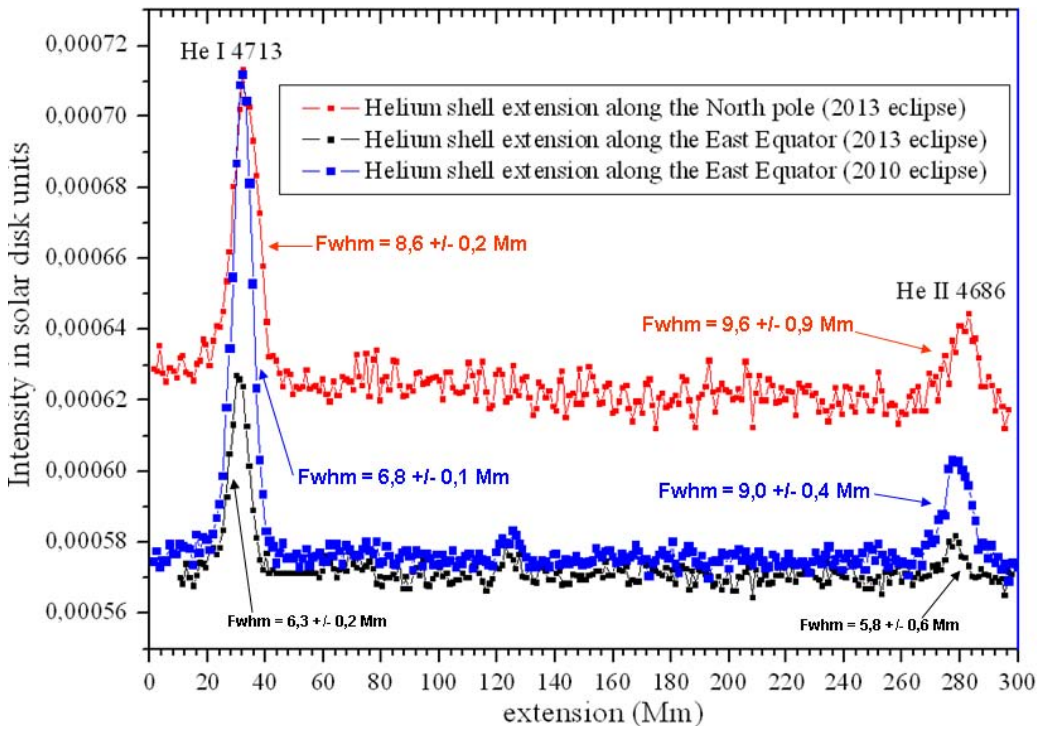

Fig. 3. Helium shell extensions from the 2010 slitless flash spectra in optically thin layers (cool lines) but sensitive to the hot ambiant corona and especially He II which is a high FIP 54 eV, compared with the 2015 slitless flash spectra. In 2015 the clouds masked the end of C2 and the beginning of the totality.

corona. The open lines of force around the Sun show more deviation in equatorial regions in 2015 than it was in 2010. The tendency of the temperature gradients seems highier in 2015 in equatorial regions than in 2010, but the deviations are low. the extension of the helium shells also show a small increase in 2013, than it was mesured in 2013. In conclusion we found that these variations seem to be correlated, and the study of the low altitudes plays an importance using photometry, high cadence CCD flash spectra (with slit spectrograph and slitless), for studying the ionisations processes and associated with the magnetic activity. Some more analysis will be performed.

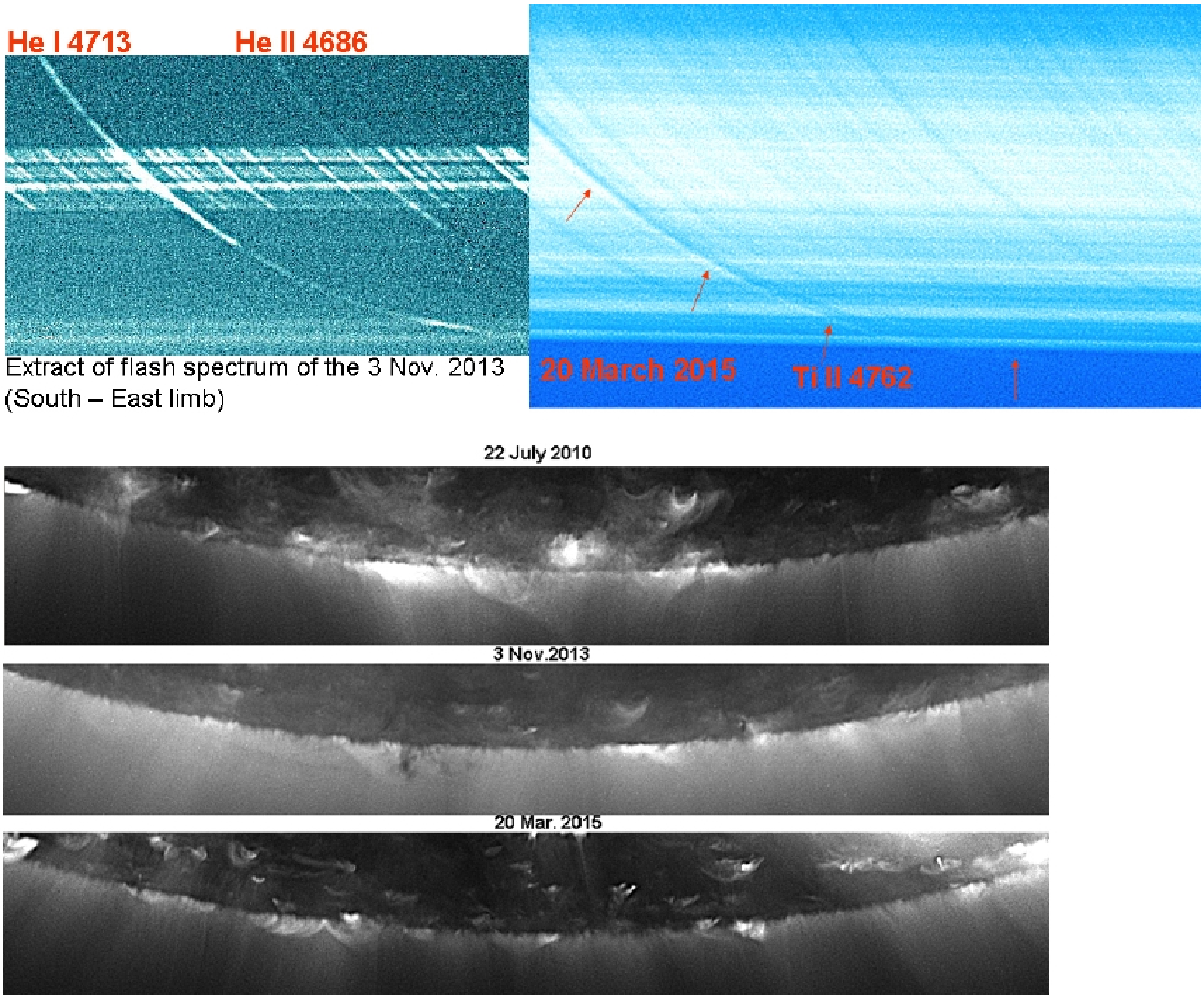

Fig. 4. flash spectra of 2013 and 2015 for comparing the lines apparition close to the continuum and bottom, the coronal holes seen in 2010, 2013 and 2015, for comparing the magnetic structures, spicules and jet seen in dark on the limb

References

Baumbach 1937, S. Astron. Nachrichten, 263, 121

Bazin, C., Koutchmy, S. and Tavabi, E. Journal of Advanced Research, Issue 3, 2013, 307

Lebecq, C., Koutchmy, S., Stellmacher, G. 1985, A&A 152, 175

Lorrain, P. and Koutchmy, S. 1996, Sol. Phys., 165, 115

November, L. & Koutchmy, S. 1996, ApJ, 466, 512

Tavabi, E., Koutchmy, S. and Ajabshirizadeh, A "Limb events brightenings and fast ejection using IRIS Mission Observation" Accepted 1er September 2015 in Sol. Phys. DOI: 10.1007/s11207-015-0771-3

Vernazza J. E., Avrett E. H., Loeser, R. 1981, ApJ Suppl. Series, 45, 635-725

SF2A 2015
F. Martins, S. Boissier, V. Buat, L. Cambrésy and P. Petit (eds)

STUDY OF SECONDARY ELECTRONS AND POSITRONS PRODUCED BY TERRESTRIAL GAMMA-RAY FLASHES

D. Sarria[1], P.-L. Blelly[1,] and F. Forme[1,]

Abstract. Terrestrial Gamma ray Flahes are emissions of X and gamma rays, correlated to thunderstorms. By interacting with the atmosphere, the photons produce a large number of electrons and positrons. Some of these reach altitudes above $\sim$ 100 km that their interactions with the atmosphere become negligible, and they are then guided by Earth's magnetic field lines, forming the so called Terrestrial Electron Beams. The GBM instrument of the Fermi Space Telescope made a particularly interesting measurement of such an event that happened the 12/09/2009.

We perform Monte-Carlo simulations to study this event in detail and we focus on the resulting time histograms. In agreement with previous works, we show that the histogram measured by Fermi GBM can be reproduced from simulations. We then show that the time histogram can be decomposed into three populations of leptons, coming from the hemisphere opposite from the TGF, and mirroring back to the satellite with interactions with the atmosphere or not, and that these we can be clearly distinguished both with their pitch angles.

Keywords: TARANIS, XGRE, IDEE, TGF, Terrestrial gamma ray flash, relativistic, electrons, TEB, pitch angles, gamma rays, x rays, photons

1 Introduction

Terrestrial Gamma Ray flashes (TGF) are bursts of X and gamma photons associated with lightning, and detected mostly from space. TGFs were first presented by Fishman et al. (1994), using data from the BATSE experiment on-board the CGRO spacecraft. Later, TGF were detected from space by RHESSI (Smith et al. 2005), AGILE (Marisaldi et al. 2014) and Fermi (Briggs et al. 2010). TARANIS (XGRE and IDEE instruments) (Lefeuvre et al. 2009) from CNES and ASIM (MXGS instrument) from ESA are planned for the next years and will be dedicated to the study of TGF and secodnary electron emissions.

A comprehensive review of the high energy emissions associated with lightning is presented in Dwyer et al. (2012). The production mechanism of TGFs may be explained by the cold runaway model (Moss et al. 2006; Celestin et al. 2012; Chanrion et al. 2014) or the relativistic feedback model (Dwyer 2012). Observations of TGFs from space, together with their associations with radio emissions from ground, allowed to constrain some important properties (Dwyer & Smith 2005; Cummer et al. 2014). They present :

- A bremsstrahlung type energy spectrum with a maximum energy of about 30 MeV
- A duration between 10 μs and 0.5 ms.
- An emission altitude located between 10 and 20 km (inside or immediately above thunderclouds)
- A fluence of ~ 1 photon/cm^2 at about 500 km altitude, which requires to have at least 10^{16} high energy photons at the source.

Once produced, these primary photons from the TGF interact with the atmosphere. As a result of these interactions, secondary electrons and positrons are produced, and a part of these particles can reach an altitude where they stop interacting significantly with the atmosphere. Their motion is then guided by the geomagnetic

[1] CNRS, IRAP, 9 Av. colonel Roche, BP 44346, F-31028 Toulouse cedex 4, France.

© Société Francaise d'Astronomie et d'Astrophysique (SF2A) 2015

field, forming the so-called Terrestrial Electron Beams (TEBs) (Dwyer et al. 2008). Following field lines, TEBs can travel from an hemisphere to another, and can lead to "false TGF" detections (since they are due to electrons and not to X/gamma-rays), like the anomalous RHESSI TGF event (Smith et al. 2006) detected above a desert. Such events are significantly longer that TGFs, with a typical duration > 1 ms. In some cases, due to the conservation of the first adiabatic invariant, a part of the electrons can mirror and go back to the satellite, leaving a specific signature of a dual pulse in the satellite measurement. Such events could be found in BATSE's data (Dwyer et al. 2008) and later with Fermi GBM, particularly with the 091214 event (Briggs et al. 2011). This event has 1735 counts, about four times more than the other TEB events recorded, making it a perfect candidate for simulations.

For this study, we performed Monte-Carlo simulations, using the MC-PEPTITA Monte-Carlo model, presented into detail in (Sarria et al. 2015). First, we discuss the initial conditions of the simulations to define a "standard" TGF. Then we compare with simulations the TEB lightcurve detected by Fermi GBM, and show how it can be decomposed by looking at the pitch angles of the electrons and positrons.

2 Initial conditions

A simulation is started with a given number of photons N_p. As written before, in a real TGF, in order to have about 1 photon/cm^2 at satellite altitude, it is estimated that 10^{16} high energy photons have to produced at the source. This quantity is not reachable in a reasonable amount of time. We present here simulations with $N_p = 10^8$, high enough to build the distributions with we need low noise. The altitude where the TGF's Bremsstrahlung photons are produced is supposed to be $h = 15$ km, and the latitude (λ) and longitude (ϕ) are set to -13.0^o and $\phi = 32.0^o$. Following Carlson et al. (2011), the angle distribution of the photon beam is assumed to follow a normal distribution that has a σ_θ parameter set to 35^o. Let E be the energy of a TGF photon. We set a standard TGF spectrum with an energy distribution function $P(E) \propto 1/E \exp(-E/\epsilon)$, where ϵ is the cut-off energy, set to 7.3 MeV. This spectrum is reasonably close to the exact spectrum (Dwyer et al. 2012). The minimum energy is set to 10 keV and the upper limit is set to 30 MeV.

The Relativistic Feedback Discharge Model (RFD) (Dwyer 2012) gives time distributions of the primary photons that are symmetrical (the rise time is close to the fall time) for all pulse duration. We make the assumption that it is a normal distribution, with a standard deviation parameter σ_{TGF}. A value of 0.15 ms fits the typical TGF lightcurve shown in Dwyer (2012).

In the simulations, the status (energy, position, velocity, ...) of each lepton is saved when it crosses 565 km altitude, downward or upward. In the example of the Fermi 091214 event, the simulation shows that the center of the electron beam crosses the satellite altitude at two positions: ($\lambda = -8.46^o$,$\phi = 31.7^o$) and ($\lambda = 25.5^o$,$\phi = 31.4^o$). The second value is close to the actual position of Fermi ($\lambda = 25.34^o$,$\phi = 31.42^o$). All the leptons distributions that are discussed hereafter are built considering only the particles in the northern hemisphere, with a radial distance lower than 50 km from the center of the beam.

3 Results

3.1 Basic comparison

Figure 1 shows the time distribution of the electrons and positrons reaching the satellite altitude. We compare the simulated data (blue curve for electrons, green curve for positrons) with the measurement made by Fermi GBM (shown as a the black curve).

A simple model using only three parameters (a time shift $t_s = -19.2$ ms, a scale factor $A = 1/62.9$, and a constant background rate $b = 9$ counts per 0.5 ms) is applied for the simulated time histograms to match the Fermi lightcurve. The two histograms fit very accurately, with a coefficient of determination $r^2 = 0.92$. This is similar to the result of the simulation done by Dwyer et al., presented in (Briggs et al. 2011), and reproduced in figure 1 (magenta curve). This confirms independently that this time histogram is due to electrons that are coming to the satellite from the southern hemisphere (first pulse between 0 ms and 12 ms) with a part that is then bouncing on a magnetic mirror point and reaching the satellite a second time (second pulse between 21 and 27 ms). The positron histogram is similar to the electron histogram, with a scale factor of $A_p = 8$.

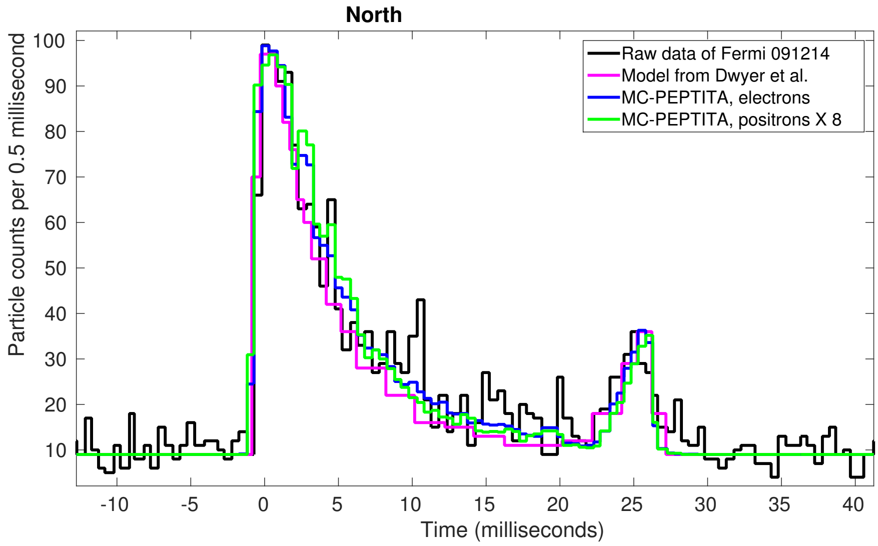

Fig. 1. Time histogram of the Fermi event 091214. Comparison between the Fermi GBM data, the simulations of Dwyer et al. for electrons (both extracted from Briggs et al. (2011)) and MC-PEPTITA simulations (for electrons and positron). The positron histogram is scaled by 8.

3.2 Pitch angle decomposition

Let v be the magnitude of the velocity vector of a lepton, which is constant when the lepton is not interacting with the atmosphere, because of conservation of energy (only the Earth's magnetic field is applied on the particle). Let $v_{\|}$ be the part parallel to its local geomagnetic field. The pitch angle α of a lepton is defined as the angle between its velocity vector and the local magnetic field direction. Figure 2.a. and 2.b. show the lightcruve of leptons crossing satellite altitude ($\sim$ 550 km) in the northern hemisphere. We are using the same definitions of the normal and log-normal distributions that are presented in (Briggs et al. 2010), as well as a Poisson log-likelihood minimization as a method to find the best fits.

Figure 2.a. shows the lightcurve of the leptons that are coming from the southern hemisphere, meaning they have α values between 0^o and 90^o. The lightcurve of the leptons of figure 2.a. is well fit by a log-normal distribution (red) : it has a coefficient of determination $r^2 = 0.99$. This log-normal time distribution is due to differences in time delays due to differences of pitch angles α of the leptons once they escape the atmosphere. Actually, all the leptons will follow very similar magnetic field lines, but the ones with the lowest pitch angles when escaping will have the highest $v_{\|}$ (still in the case where $\alpha < 90^o$). The two quantities are linked with $v_{\|} = v\, cos\,(\alpha)$. α increases along the trajectory of the lepton due to conservation of the first adiabatic invariant. At satellite altitude, the value of v is $\approx 0.98\,c$ on average and the value of $v_{\|}$ is $\approx 0.5\,c$ on average.

The time distribution of figure 2.b. can be split into two parts. From about 5 to 21 ms, we see that the distribution can be very well fit using a gaussian (normal) function. The population located from about 21 to 27 ms can be well fit by a mirrored log-normal function. This model fits well the data since its overall coefficient of determination is $r^2 = 0.98$. The two sub-populations of electrons/positrons can be easily separated with their pitch angles, as shown by figure 2.c. There is a clear difference between the leptons above and below $\alpha \approx 120^o$. Actually, a pitch angle of about 120^o at this position ($h = 565\,\text{km}$, $\lambda = 25.5^o$, $\phi = 31.4^o$) corresponds to electrons that had a mirroring altitude of $\sim$ 100 km, the altitude above which the interactions with the atmosphere occur so infrequently that they are negligible. Therefore, we define 100 km as the limit of the atmosphere in this context. Below $\approx 120^o$, the distribution is weakly spread, and corresponds to the leptons that had a pitch angle between $\approx 60^o$ and 90^o and came back to satellite's altitude after mirroring, without interacting with the atmosphere. Indeed, figure 2.c. shows that the number of leptons between 60^o and 90^o is similar to the number between 90 and $\approx 120^o$, each representing $\approx 11\%$ of the total count. We also know it because the particles are tagged. All the leptons that are coming to the satellite with pitch angles below $\approx 60^o$ were inside the loss cone (the range of angles where the particles have mirroring altitudes inside the atmosphere), but not all of them are absorbed. $\approx 8\%$ of the total count can mirror back to satellite altitude. These leptons interacted weakly enough with the atmosphere, but strongly enough to be scattered back outside

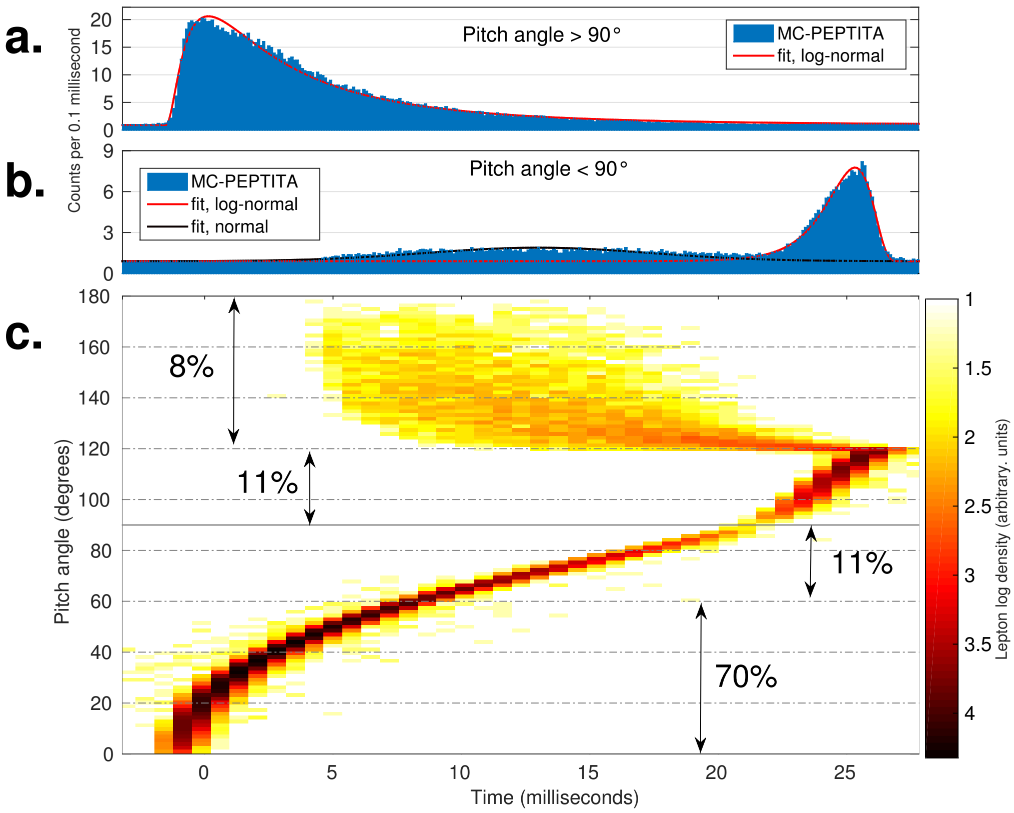

Fig. 2. Time and pitch angles distributions for leptons crossing the altitude of the satellite. The time scale (x-axis) is shared by the three plots. Electrons and positrons coming to the satellite from the southern hemisphere will have a pitch angle α between 0^o and 90^o, whereas leptons coming back to the satellite after mirroring will have pitch angles between 90^o and 180^o. **a.**Simulated time histogram, only for leptons with pitch angles $> 90^o$. The red curve is a log-normal fit. **b.**Simulated time histogram, only for electrons and positrons with pitch angles $< 90^o$. The red curve is a log-normal fit, the black curve is a normal fit. **c.**Density distribution of pitch angle and time. The fractions of the total number of leptons included inside pitch angle ranges are also given.

the atmosphere. Random interactions with the atmosphere result in random time delays, resulting to a time distribution, seen at satellite altitude, with approximately a normal shape.

4 Conclusions

We performed MC-PEPTITA simulations of the Fermi 091214 TGF/TEB event, supposing an initial TGF formed by a photons source, defined with reasonable parameters for its position, energy spectrum, beaming, and time distribution. The lightcurve detected by Fermi is shown to be accurately reproducible from simulations, in agreement with previous work.

Furthermore, we showed that this lightcurve can be decomposed into three components. The first, coming directly from the hemisphere where the TGF was originally emitted, has pitch angles ranging between 0^o and 90^o with a log-normal time distribution. Leptons coming back to the satellite altitude after mirroring have pitch angles between 90^o and 180^o, and can be decomposed into two components : the leptons that have interacted significantly with the atmosphere and the leptons that did not. If they did, their pitch angles range between $\approx 120^o$ and 180^o, and their lightcurve can be well fit by a normal distribution. If they did not, their pitch angles range between 90^o and $\approx 120^o$ and their time distribution can be well fit by a mirrored log-normal function.

The TARANIS satellite, with the XGRE and IDEE instrument, will have the ability to measure the lightcurves and pitch angle distribution of the electrons, and should provide reliable information about these properties.

We would like to thank the "Centre National d'Etudes Spatiales" (CNES), and the "Direction Generale de l'Armement" (DGA) for their support.

This work was granted access to the HPC resources of CALMIP supercomputing center under the allocation 2015-p1505.

References

Briggs, M. S., Connaughton, V., Wilson-Hodge, C., et al. 2011, Geophys. Res. Lett., 38, 2808

Briggs, M. S., Fishman, G. J., Connaughton, V., et al. 2010, Journal of Geophysical Research (Space Physics), 115, 7323

Carlson, B. E., Gjesteland, T., & Østgaard, N. 2011, Journal of Geophysical Research (Space Physics), 116, 11217

Celestin, S., Xu, W., & Pasko, V. P. 2012, Journal of Geophysical Research (Space Physics), 117, 5315

Chanrion, O., Bonaventura, Z., Çinar, D., Bourdon, A., & Neubert, T. 2014, Environmental Research Letters, 9, 055003

Cummer, S. A., Briggs, M. S., Dwyer, J. R., et al. 2014, Geophysical Research Letters, n/a

Dwyer, J. R. 2012, Journal of Geophysical Research (Space Physics), 117, 2308

Dwyer, J. R., Grefenstette, B. W., & Smith, D. M. 2008, Geophysical Research Letters, 35, n/a

Dwyer, J. R. & Smith, D. M. 2005, Geophys. Res. Lett., 32, 22804

Dwyer, J. R., Smith, D. M., & Cummer, S. A. 2012, ssr, 173, 133

Fishman, G. J., Bhat, P. N., Mallozzi, R., et al. 1994, Science, 264, 1313

Lefeuvre, F., Blanc, E., & Pinçon, J. L. 2009, in American Institute of Physics Conference Series, Vol. 1118, American Institute of Physics Conference Series, 3–7

Marisaldi, M., Fuschino, F., Pittori, C., et al. 2014, in EGU General Assembly Conference Abstracts, Vol. 16, EGU General Assembly Conference Abstracts, 11326

Moss, G. D., Pasko, V. P., Liu, N., & Veronis, G. 2006, Journal of Geophysical Research (Space Physics), 111, 2307

Sarria, D., Blelly, P.-L., & Forme, F. 2015, Journal of Geophysical Research: Space Physics, n/a, 2014JA020695

Smith, D. M., Grefenstette, B. W., Splitt, M., et al. 2006, AGU Fall Meeting Abstracts, A1040

Smith, D. M., Lopez, L. I., Lin, R. P., & Barrington-Leigh, C. P. 2005, Science, 307, 1085

Session 09

Evolution des disques protoplanétaires: du milieu interstellaire aux systèmes planétaires

SF2A 2015
F. Martins, S. Boissier, V. Buat, L. Cambrésy and P. Petit (eds)

TRAPPING PROTOPLANETS AT THE SNOWLINES.

K. Baillié[1, 2], S. Charnoz[1,2] and E. Pantin[2]

Abstract. We follow the viscous evolution of protoplanetary disks by modeling self-consistently their dynamics, thermodynamics, photosphere geometry and composition (Baillié & Charnoz., 2014, ApJ and Baillié et al., 2015, A&A). Our hydrodynamical numerical code allows us to estimate the local gradients in temperature and density that drive the type I migration of planetary embryos. In particular, we identify irregular structures in the disk: shadowed regions that are not directly irradiated by the star, temperature plateaux at the sublimation temperature of the main dust components of the disk. These icelines appear to be related with planetary traps. Though planetary embryos can be trapped temporarily in some early transient traps, the other traps (more permanent) will allow protoplanets to survive and favor their growth by collisions between embryos at some specific orbits.

Keywords: Protoplanetary disks, Planets and satellites: formation, Planet-disk interactions, Accretion disks, Planets and satellites: dynamical evolution and stability, Hydrodynamics

1 Introduction

Numerical simulations from Baillié & Charnoz (2014) and Baillié et al. (2015) were able to retrieve observational constraints on surface mass density and geometrical profiles of protoplanetary disks. Their viscous spreading hydrodynamical code involves coupling the photosphere geometry, the disk thermodynamics, its dynamics and the disk composition (through a thorough opacity model based on Helling et al. (2000); Semenov et al. (2003)). In the present work, we estimate the impact of realistic disk profiles on protoplanet migration: we identify favorable locations for planet traps and deserts. We then vary the planet radius and mass to build migration maps showing how planet traps are migrating and surviving along the disk evolution.

2 Model

2.1 Dynamical and thermodynamical evolution

The present numerical model is based on the hydrodynamical code described in Baillié & Charnoz (2014); Baillié et al. (2015), following the viscous evolution of a viscous α disk (Shakura & Sunyaev 1973). Most of the usual asumptions are removed: we follow the disk evolution from an already formed Minimum Mass Solar Nebula and not just its final steady state. We jointly calculate the photosphere geometry: the angle at which the photosphere sees the star is governing the amount of energy that the photosphere is receiving from the star. Therefore, the disk is not only heated by viscous heating but also by stellar irradiation. The iterative process calculating the temperature also calculates a consistent photosphere height, therefore coupling the disk geometry with the disk thermodynamics, which is also linked to the dynamical evolution through the viscosity, as detailed in Equation 2.1 (Lynden-Bell & Pringle 1974) obtained from the mass and angular momentum conservation.

$$\frac{\partial \Sigma(r,t)}{\partial t} = \frac{3}{r}\frac{\partial}{\partial r}\left(\sqrt{r}\,\frac{\partial}{\partial r}\left(\nu(r,t)\,\Sigma(r,t)\,\sqrt{r}\right)\right) \tag{2.1}$$

[1] IPGP / Université Paris Diderot, Paris, France
[2] AIM / CEA, Paris, France

© Société Francaise d'Astronomie et d'Astrophysique (SF2A) 2015

Elements	Sublimation Temperature	Relative Abundances
Water ice	160 K	59.46 %
Volatile Organics	275 K	5.93 %
Refractory Organics	425 K	23.20 %
Troilite (FeS)	680 K	1.57 %
Olivine	1500 K	7.46 %
Pyroxene	1500 K	2.23 %
Iron	1500 K	0.16 %

Table 1. Sublimation temperatures and relative abundances that affect the disk gas opacity.

2.2 Opacity model

The main elements of the disk dust are listed in Table 1 with their sublimation temperatures. As the midplane temperature varies accross the protoplanetary disk, the physical phases of the various elements change as well. This affects the disk opacity which in turn affects the temperature. Therefore, we tabulate the dust opacity as a function of the temperature and we use this updated local opacity in our iterative process for the determination of the temperature and geometry. We use the tabulated values from Helling et al. (2000); Semenov et al. (2003) summarized in Figure 1.

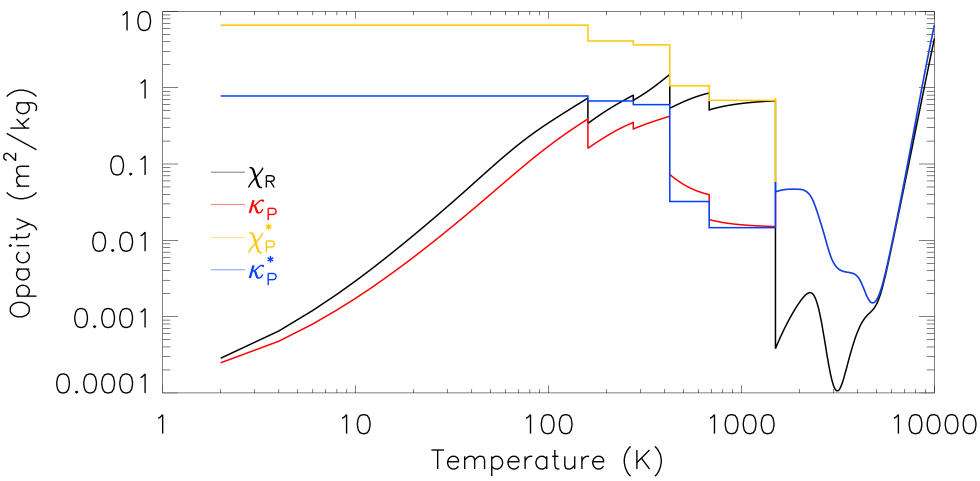

Fig. 1. Opacity variations with local temperature. Black: Rosseland mean opacity in extinction. Red: Planck mean opacity in absorption. Yellow: Planck mean opacity in extinction at stellar irradiation temperature. Blue: Planck mean opacity in absorption at stellar irradiation temperature.

The various opacities show very abrupt drops around the sulbimation temperatures of the dust elements.

3 Impact of the disk evolution on planet migration

An already formed planetary embryo exchanges angular momentum with the disk (Goldreich & Tremaine 1979, 1980) due to the resonances excited by the planet in the disk. The planet exerts a torque on the disk and therefore the disk exerts an opposite torque on the planet. We assume that the disk structure is not modified by the presence of the planet.

3.1 Lindblad torques

Using a two-dimensional approximation, considering laminar disks, a planet on a circular orbit, ignoring the disk self-gravity and assuming thermal equilibrium, Paardekooper & Papaloizou (2008) were able to derive the following formula for the total Lindblad torque exerted by the disk over the planet:

$$\Gamma_{\mathrm{Lindblad}} = -\frac{\Gamma_0(r_P)}{\gamma}\left(2.5 - 1.7\frac{\partial \ln T}{\partial \ln r}(r_P) + 0.1\frac{\partial \ln \Sigma}{\partial \ln r}(r_P)\right), \tag{3.1}$$

with $\gamma = 1.4$, the adiabatic index,
$\Gamma_0(r_P) = \left(\frac{q}{h}\right)^2 \Sigma(r_P)\, r_P^4\, (\Omega(r_P))^2$,
$h = \frac{h_{\mathrm{press}}(r_P)}{r_P}$,
and $\Omega(r_P)$ the Keplerian angular velocity at the planet position in the disk.

3.2 Corotation torques

Corotation resonances are known to exert complicated torques that include linear and nonlinear parts. Paardekooper & Papaloizou (2009b) showed that the corotation torques are generally nonlinear in the usual range of viscosity ($\alpha_{\mathrm{visc}} < 0.1$). The nonlinear contribution, due to the horseshoe drag (Ward 1991) caused by the interaction between the planet and the fluid element moving in its vicinity, is also known for having two possible origins: barotropic, intially formalized by Tanaka et al. (2002), and entropic, detailed by Baruteau & Masset (2008).

Concerning the horseshoe drag, Paardekooper et al. (2011) described the density perturbation generated by the corotation resonances and provided expressions for both the entropy and vortensity (or barotropic) contributions. Assuming a gravitational softening $b = 0.4h_{\mathrm{press}}$, Bitsch & Kley (2011) and Bitsch et al. (2014) summarized these expressions to obtain the following contributing torques:

$$\Gamma_{\mathrm{hs,entro}} = -\frac{\Gamma_0(r_P)}{\gamma^2}\,7.9\left(-\frac{\partial \ln T}{\partial \ln r}(r_P) + (\gamma-1)\frac{\partial \ln \Sigma}{\partial \ln r}(r_P)\right) \tag{3.2}$$

$$\Gamma_{\mathrm{hs,baro}} = -\frac{\Gamma_0(r_P)}{\gamma}1.1\left(\frac{\partial \ln \Sigma}{\partial \ln r}(r_P) + \frac{3}{2}\right) \tag{3.3}$$

It appears that this unsaturated corotation torque strongly depends on the temperature and surface mass density gradients. It also scales with M_{P}^2, as does the Lindblad torque. However, Paardekooper & Papaloizou (2009a) showed that given the viscous, diffusive, and libration timescales, the linear effects of the corotation torques can be saturated for some viscosities and some planet masses. For our disk that evolved for 1 Myr, the viscosity range compared to Fig. 14 from Paardekooper & Papaloizou (2009a) suggests that saturation cannot be neglected for planetary masses higher than $6M_\oplus$. Paardekooper et al. (2011) defined weight functions for the partial saturation of the corotation torque. These functions vary with the half-width of the horseshoe, which depends on the mass of the planet. Appendix A of Bitsch & Kley (2011) summarized this method and added correcting factors. We used a similar torque calculation, which is necessary to take into account the variations with the planet mass.

3.3 Planet migration

The total torque exerted by the disk on the planet is then given by $\Gamma_{\mathrm{tot}} = \Gamma_{\mathrm{Lindblad}} + \Gamma_{\mathrm{hs,entro}} + \Gamma_{\mathrm{hs,baro}}$. This total torque strongly depends on the temperature and surface mass density gradients.

Figure 2 shows a snapshot of the disk profile after 1 million years of evolution: evolved surface mass density and temperature profiles are displayed along with the total torque exerted by the disk on a planet located at a given radial distance r from the star after 1 million years of evolution of the protoplanetary disk.

The regions of negative torques are the regions in which planets will migrate inward while they would migrate outward in the regions of positive total torque. Therefore, we can identify lines of divergence that are going to be depleted in planetary embryos (planet deserts) and lines of convergence where planets will accumulate (planet traps). Traps are very important for two reasons: first they prevent protoplanets from falling onto their host star by inward migration; secondly, they favor accumulation of embryos and therefore their collisions and growth by accretion.

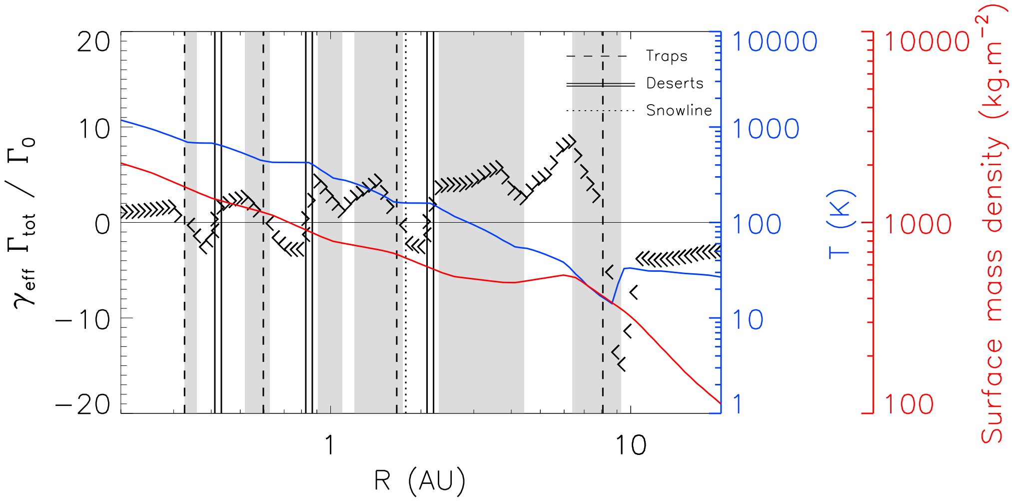

Fig. 2. Total torque exerted by a 1 million-year evolved disk on a 10-$M_{\rm Earth}$ planet versus planet radius. The surface mass density profile appears in red and the temperature profile in blue. Shadowed regions are displayed in gray.

3.4 Evolution of planetary traps and deserts

Figure 3 shows the time evolution of traps and deserts locations. These positions appears to relate quite well with the sublimation lines of the main dust components. In addition, the irradiation-viscous heating barrier seems to generate a population of planet traps that appears to be quite sustainable. Other, more transient trap populations disappear quite early in the disk evolution.

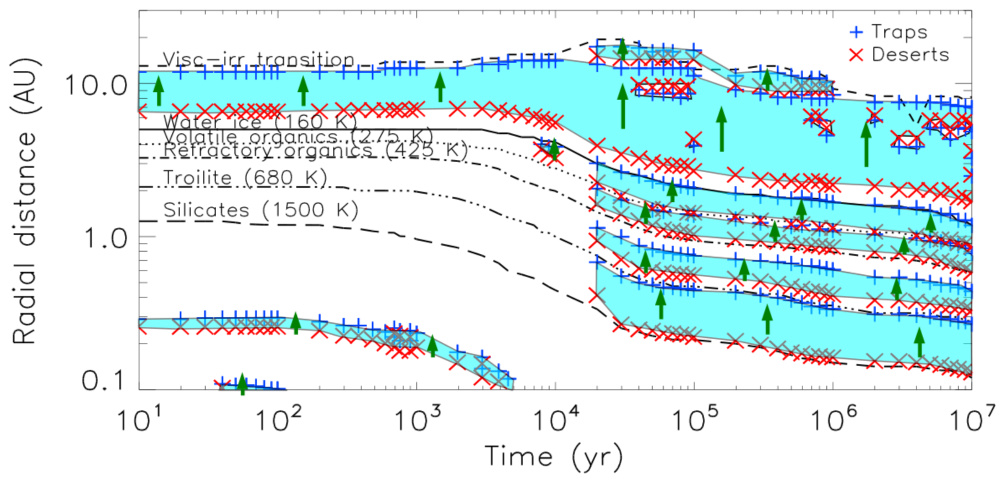

Fig. 3. Time evolution of the locations of planetary traps and deserts for a 10 Earth-masses planet.

Figure 4 displays how the total torque exerted by the disk on the planet depends on the planet mass. It shows islands of outward migration which have planet traps at their outer edge and deserts at their inner edge. As they grow in mass, planet will follow these island borders vertically and will maybe jump from one trap to the inner one as they grow. This work is being investigated currently.

4 Conclusions and perspectives

The proper consideration of the disk composition and the sublimation of the dust main components generates temperature gradient irregularities that could significantly affect the migration torques exerted by the disk on

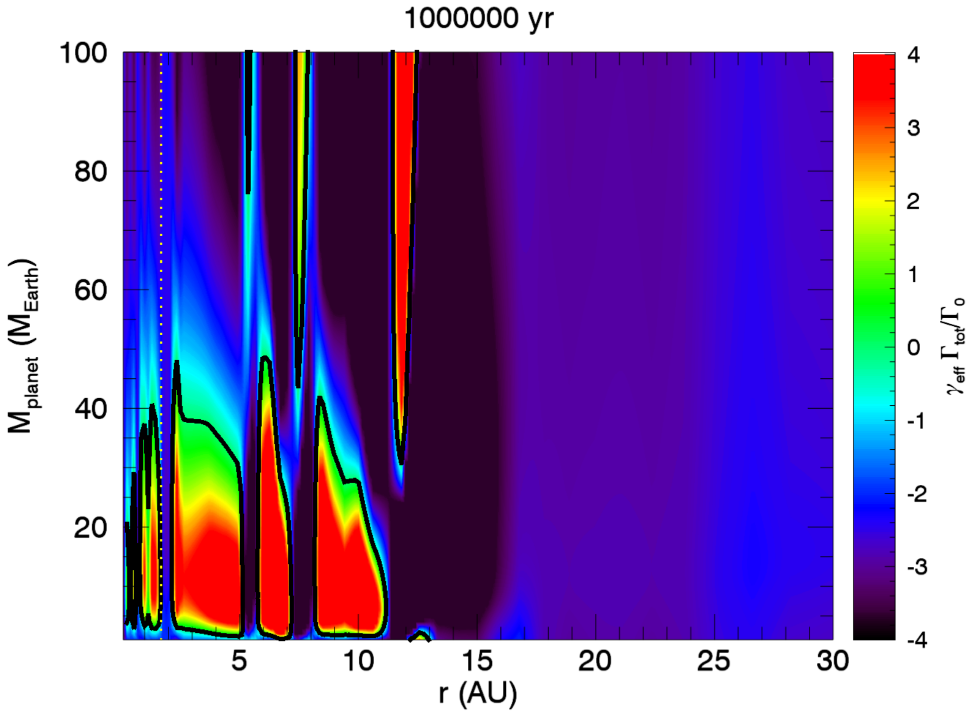

Fig. 4. Total torque exerted by the disk after 1 million year of evolution on a planet versus its radius and mass.

a putative planet. With these refinements, it appears possible to actually trap planets at a specific radius, or to clear a specific position of all planetary embryos. After 1 Myr, we identify several planetary traps and deserts below 10 AU. Most planet traps appear to be related to viscous-irradiation frontier and sublimation lines. They appear early enough in the disk evolution to help protoplanet survive planetary migration and fovor their growth by collisions/accretion.

This work was supported by IDEX Sorbonne Paris Cité. We acknowledge the financial support from the UnivEarthS Labex program of Sorbonne Paris Cité (ANR-10-LABX-0023 and ANR-11-IDEX-0005-02).

References

Baillié, K. & Charnoz, S. 2014, ApJ, 786, 35

Baillié, K., Charnoz, S., & Pantin, E. 2015, A&A, 577, A65

Baruteau, C. & Masset, F. 2008, ApJ, 672, 1054

Bitsch, B. & Kley, W. 2011, A&A, 536, A77

Bitsch, B., Morbidelli, A., Lega, E., & Crida, A. 2014, A&A, 564, A135

Goldreich, P. & Tremaine, S. 1979, ApJ, 233, 857

Goldreich, P. & Tremaine, S. 1980, ApJ, 241, 425

Helling, C., Winters, J. M., & Sedlmayr, E. 2000, A&A, 358, 651

Lynden-Bell, D. & Pringle, J. E. 1974, MNRAS, 168, 603

Paardekooper, S.-J., Baruteau, C., & Kley, W. 2011, MNRAS, 410, 293

Paardekooper, S.-J. & Papaloizou, J. C. B. 2008, A&A, 485, 877

Paardekooper, S.-J. & Papaloizou, J. C. B. 2009a, MNRAS, 394, 2283

Paardekooper, S.-J. & Papaloizou, J. C. B. 2009b, MNRAS, 394, 2297

Semenov, D., Henning, T., Helling, C., Ilgner, M., & Sedlmayr, E. 2003, A&A, 410, 611

Shakura, N. I. & Sunyaev, R. A. 1973, A&A, 24, 337

Tanaka, H., Takeuchi, T., & Ward, W. R. 2002, ApJ, 565, 1257

Ward, W. R. 1991, in Lunar and Planetary Science Conference, Vol. 22, Lunar and Planetary Science Conference, 1463

SF2A 2015
F. Martins, S. Boissier, V. Buat, L. Cambrésy and P. Petit (eds)

EXPOSURE-BASED ALGORITHM FOR REMOVING SYSTEMATICS OUT OF THE COROT LIGHT CURVES

P. Guterman[1,2], T. Mazeh[3] and S. Faigler[3]

Abstract. The CoRoT space mission was operating for almost 6 years, producing thousands of continuous photometric light curves. The temporal series of exposures are processed by the production pipeline, correcting the data for known instrumental effects. But even after these model-based corrections, some collective trends are still visible in the light curves. We propose here a simple exposure-based algorithm to remove instrumental effects. The effect of each exposure is a function of only two instrumental stellar parameters, position on the CCD and photometric aperture. The effect is not a function of the stellar flux, and therefore much more robust. As an example, we show that the $\sim 2\%$ long-term variation of the early run *LRc01* is nicely detrended on average. This systematics removal process is part of the CoRoT *legacy* data pipeline.

Keywords: techniques: photometric, methods: data analysis

1 Introduction

The CoRoT space mission (Baglin et al. 2006) was operating for almost 6 years, producing thousands of continuous photometric light curves. The readout of each CCD exposure transfers simultaneously the flux of 6,000 stars. The temporal series of exposures are processed by the production pipeline, correcting the data for known instrumental effects, such as gain, background, jitter, EMI, SAA discarding, time corrections (Samadi et al. 2006; Auvergne et al. 2009). But even after these model-based corrections, some collective trends are still visible in the light curves (Fig. 1). The flux gradually decreases with unknown shape and a different slope for each star. Previous work to correct these effects has been suggested, including MagZeP (Mazeh et al. 2009), that uses a zero-point magnitude correction, associated with the SysRem systematics algorithm (Tamuz et al. 2005).

Algorithms for removing systematics consist of two parts: 1) identify the *effects* among a set of stars by combining all light curves like SysRem (Tamuz et al. 2005), see also (Ofir et al. 2010), finding combination of a few representative stars (Kovács et al. 2005) or fitting a model for each exposure based on observational (Kruszewski & Semeniuk 2003) or instrumental quantities (Mazeh et al. 2009), then 2) remove them by properly adapting them to each light curve. An effect is a pattern that appears among a large set of independent stars. Effects can be additive, multiplicative or follow any law that needs to be determined. In the common techniques, the effects are derived from a training set of stars using correlation methods like the iterative SysRem (Tamuz et al. 2005). The training set can be a properly selected subset of stars or even the whole set itself.

After their global determination, the effects need to be scaled and subtracted from each of the light curves. Classical fitting techniques like least square are not satisfactory because the resulting coefficient is partly pulled by the light curve's natural shape and disturbs the scientific signal. For example, the gradual loss of sensitivity visible in Fig. 1 correlates with any long-period stellar variability, resulting in removing some real signal. To avoid this critical drawback we propose here a technique similar to MagZeP (Mazeh et al. 2009) that fits the instrumental effects to each exposure independently. The effect of each exposure is a function of only two instrumental stellar parameters, position on the CCD and photometric aperture. The advantage is that the

[1] Division Technique INSU, BP 330, 83507 La Seyne cedex, France
[2] LAM (Laboratoire d'Astrophysique de Marseille), UMR 7326, F-13388 Marseille, France
[3] School of Physics and Astronomy, Tel Aviv University, Tel Aviv 69978, Israel

© Société Francaise d'Astronomie et d'Astrophysique (SF2A) 2015

effect is not a function of the stellar flux, and therefore much more robust.

This paper is structured as follows: Section 2 describes the systematics removal method and its application to CoRoT, Section 3 reviews the derived effects and the performances of the method and Section 4 summarizes and concludes this work.

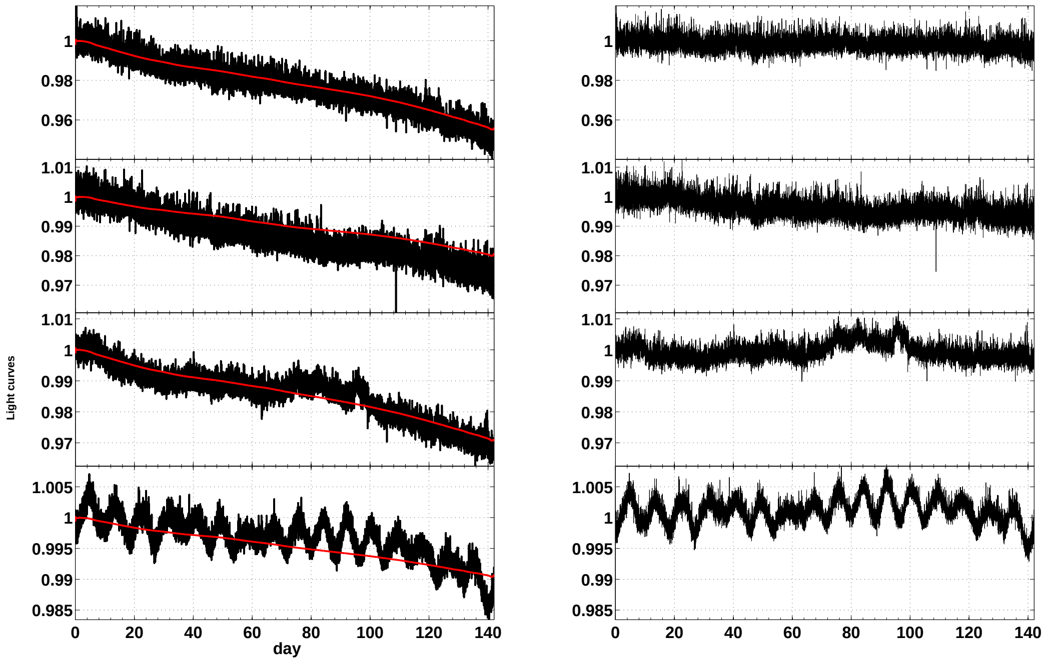

Fig. 1. Corrected stellar trends. Left: Light curves without correction. The considered light curves are from run *LRc01*, CCD 2. The black line is the normalized flux, the red line is the predicted systematic (see below). Right: same curves after correction.

2 Method

We compute the *residual* per pixel of each star by removing its zero point

$$r(t) = \frac{f(t) - \bar{f}}{m}, \tag{2.1}$$

where f is the star's flux and m is the mask surface in pixels. The fluxes are divided by the photometric aperture size m because systematics are at the pixel scale. The average flux $\bar{f}$ is integrated over the first 4 days of the run, before any drift could occur. Thus, all residuals are distributed around zero at the beginning of the run. Fig. 2 (left), which depicts the histogram of the stellar flux during the 4 last days of the run, shows that by the end of the run, the residuals are significantly below zero. The fluxes loose about 30e$^-$/pix on average after 140 days. This offset does not seem proportional to the flux itself, but rather linked to the position of the star on the CCD (right). Moreover, the dependence is close to linear, hence suggesting a model

$$S_{ij} = C_i + A_i x_j + B_i y_j, \tag{2.2}$$

with S_{ij} being the systematic offset of the i^{th} exposure of the j^{th} star located at position x_j, y_j on the CCD. The coefficients A_i and B_i form the position dependence and C_i is the common offset at exposure i. For each exposure we fit the three parameters A_i, B_i and C_i using a robust estimator. Next, we smooth the derived A, B and C temporal curves (Fig. 3), and then subtract the resulting S_{ij} model from each exposure of each star.

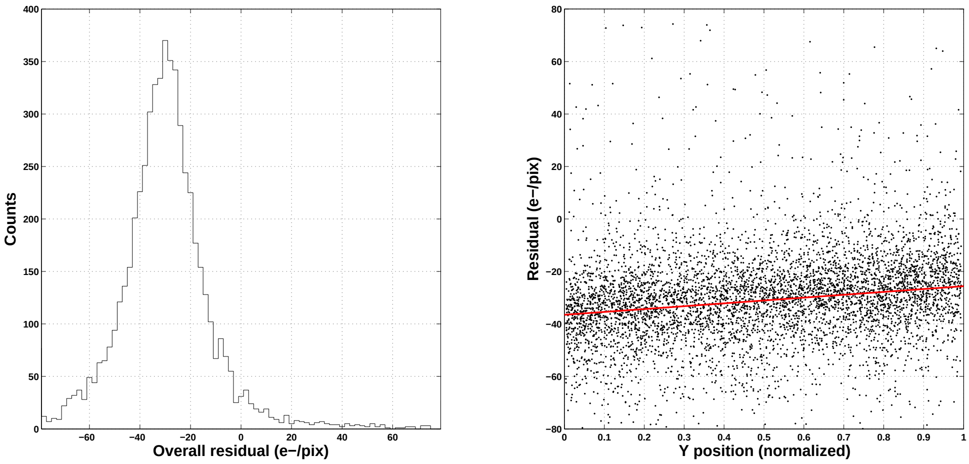

Fig. 2. Systematic offset. Left: an histogram of all light curves residuals for an single exposure at the end of *LRc01*. Right: same residuals as a function of x positions. The red line is the linear approximation of the dependence.

2.1 Processing

Several steps are necessary to process the CoRoT data.

1. Resynchronising the run data

   The CoRoT data is a collection of files, each containing the run light curve of a single star. We pack all the files of a run into a single matrix of star $\times$ exposure that contains the whole data of that run. The difficulty is that although simultaneously acquired, the time label of an exposure differs across files, depending on star position and roundoff errors among others. Consequently we had to gather all measurements within a common 4 sec interval across the whole file set as belonging to the same exposure.

2. Binning to 512 sec

   Some of the stars are sampled at a 32 sec cadence while the rest are at 512 sec cadence. A 512 sec measurement is the onboard concatenation of 16 successive 32 sec exposures. The timestamp is the center of the exposure interval in both cases. The present step consists on binning the data matrix to a common 512 sec time frame in the same way that CoRoT would have done onboard.

3. Deriving the effects coefficients

   We compute the residual of each star (Eq. 2.1) and produce the residual matrix of the run. Then, for each exposure i of that matrix, we estimate the coefficients A_i, B_i and C_i (Eq. 2.2) using robust multi-linear regression (Holland & Welsch 1977). This way, the procedure is insensitive to outliers due to spurious cosmic rays or stellar variability. Another benefit of such an estimator is that there is no need to select a training set.

   The resulting A, B and C temporal coefficients are then strongly smoothed using a 30 days sliding average to remove high-frequency noise caused by the fitting process and modeling imperfections. Fig. 3 shows the temporal evolution of the A, B, C coefficients for *LRc01*.

4. Removing the systematic effects model

   We derive the S_{ij} matrix (Eq. 2.2) and subtract it from the residual matrix. The resulting residuals are then reverted back to light curves through the inverse of Eq. 2.1. This part is performed by the production pipeline that stores the result into a specific extend of the legacy *fits* files. This process takes place after the gap filling and the jumps corrections stages.

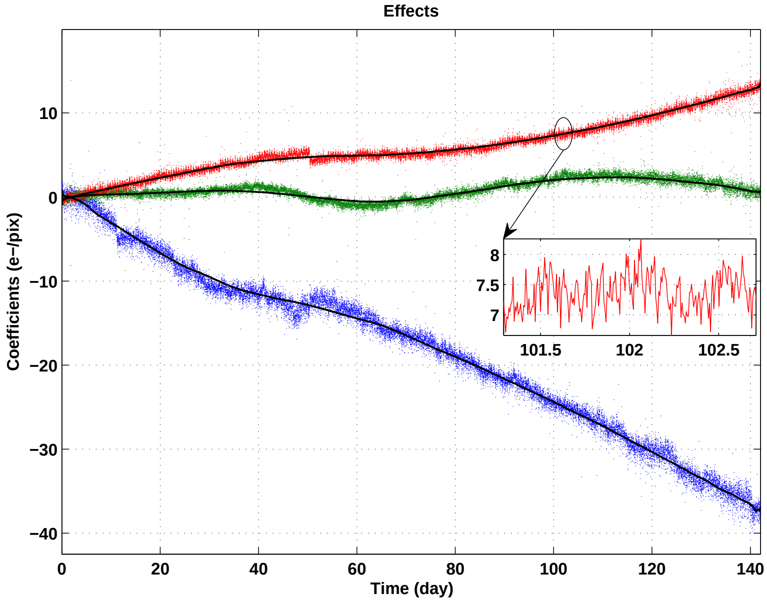

Fig. 3. Effects as a function of time for the long run *LRc01*. Blue-offset C; green-A (x dependence); red-B (y dependence). The magnified section illustrates finer details on a shorter time scale which we ignore. The time is the number of days since the beginning of the run.

3 Results

3.1 Effects

Fig. 3 shows the evolution of the model coefficients during the 142 days of run *LRc01*. In blue, the common offset coefficient C shows that all light curves gradually looses up to 37e$^-$/pix during the 142 days of the run. This long-term trend may reflect the loss of efficiency of the CCD, attributed to aging effects. In red (green), the x (y) coefficients A (B) show patterns of lower amplitude, probably caused by the star shift inside its mask, probably due to small rotational depointing or aberration. The larger value of the B coefficient (red) relative to the A coefficient (green) could come from stretching of the CoRoT PSF along the x direction (Llebaria et al. 2004). Thus, a small displacement in the y direction influences the signal proportionally more than the same displacement along the x axis.

A change of the CCD temperature is visible as a discontinuity at $t \sim 50$ days, particularly in the red curve. Smaller details are visible down to the order of 1e$^-$/pix in the 1.5-day magnified section. The faster oscillations are the residual of the CoRoT satellite orbital period, namely 13.97 day^{-1}. A daily pattern variation is also clearly visible. Although interesting for analysis purposes, such details are removed from the operational coefficients by the smoothing process, because the model is not accurate enough for these patterns.

3.2 Performance

Fig. 4 shows the flux loss histograms in *LRc01* before and after the correction, and illustrates that our method efficiently corrects the flux decrease. Before correction (solid line), the overall difference $\Delta = f_{\text{end}} - f_{\text{begin}}$ spreads around 2% loss in 142 days. This 2% loss is equivalent to $\sim$ 1000e$^-$/pix, assuming an average mask area. After correction (dashed line), in addition to removal of the bias, the histogram is sharper. This reduction of differences between stars illustrates the effectiveness of the position based approach.

While this method is efficient on average, visual inspection of many stars reveals its limitations. For many stars, the systematics model nicely fits the light curve. However, for other stars over/under corrections can be seen. We tested several possibilities for explaining this. We checked the influence of the photometric masks geometry with collective depointing. For this, we used the full pixel images recorded before the run. We also checked the smearing due to readout pattern across columns. We even performed a blind search for correlations

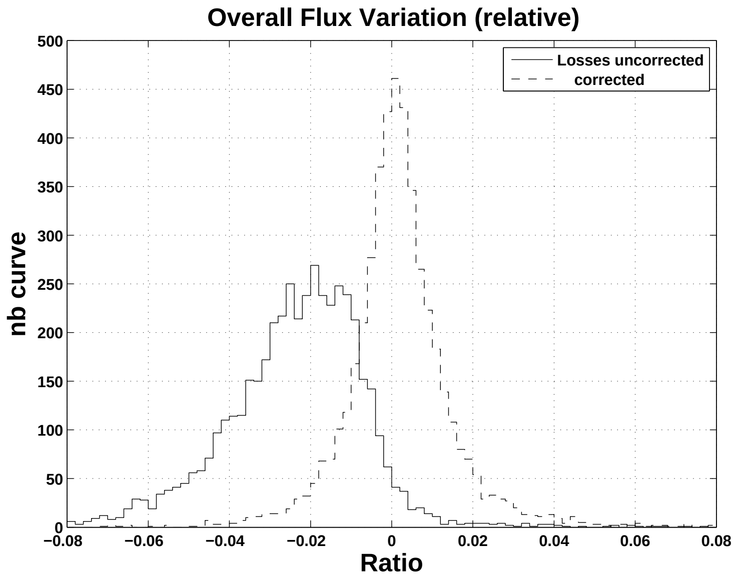

Fig. 4. Results. Black line: histogram of flux losses at the end of run *LRc01*. The loss is intended relatively to the initial flux. Dashed: same after correction.

with combinations of available parameters like spectral type, magnitude, mask surface and others. Eventually we were not able to identify any additional factor that could explain the suspected over/under correction.

4 Summary and conclusions

We present a simple method to remove systematics from the light curves of the CoRoT satellite without altering the scientific information. We apply a 3 parameter linear model per exposure to identify and correct most long-term systematics. The robust estimation algorithm allows to use the full information of the CoRoT sample of a run without selecting a training subset. The derived systematics only depend on the stellar position and mask area and not on the corresponding light curve. Consequently, no fitting based on the light curve itself can modify the real stellar variation, even when it resembles the systematics profile.

As an example, we show that the $\sim 2\%$ long-term variation of the early *LRc01* is nicely detrended on average, and the spread of stars variations is reduced. This systematics removal process is part of the CoRoT *legacy* data pipeline.

Acknowledgements

This research has received funding from the European Community's Seventh Framework Programme (FP7/2007-2013) under grant-agreement numbers 291352 (ERC)

References

Auvergne, M., Bodin, P., Boisnard, L., et al. 2009, A&A, 506, 411
Baglin, A., Auvergne, M., Barge, P., et al. 2006, ESA Special Publication, 1306, 33
Holland, P. W., & Welsch R. E. 1977, Communications in Statistics: Theory and Methods, A6, 813
Kovács, G., Bakos, G., & Noyes, R. W. 2005, MNRAS, 356, 557
Kruszewski, A., & Semeniuk, I. 2003, Acta Astron., 53, 241
Llebaria, A., Auvergne, M., & Perruchot, S. 2004, Proc. SPIE, 5249, 175
Mazeh, T., Guterman, P., Aigrain, S., et al. 2009, A&A, 506, 431
Ofir, A., Alonso, R., Bonomo, A. S., et al. 2010, MNRAS, 404, L99
Samadi, R., Fialho, F., Costa, J. E. S., et al. 2006, ESA Special Publication, 1306, 317
Tamuz, O., Mazeh, T., & Zucker, S. 2005, MNRAS, 356, 1466

SF2A 2015
F. Martins, S. Boissier, V. Buat, L. Cambrésy and P. Petit (eds)

MELTING THE CORE OF GIANT PLANETS: IMPACT ON TIDAL DISSIPATION

S. Mathis [1]

Abstract. Giant planets are believed to host central dense rocky/icy cores that are key actors in the core-accretion scenario for their formation. In the same time, some of their components are unstable in the temperature and pressure regimes of central regions of giant planets and only ab-initio EOS computations can address the question of the state of matter. In this framework, several works demonstrated that erosion and redistribution of core materials in the envelope must be taken into account. These complex mechanisms thus may deeply modify giant planet interiors for which signatures of strong tidal dissipation have been obtained for Jupiter and Saturn. The best candidates to explain this dissipation are the viscoelastic dissipation in the central dense core and turbulent friction acting on tidal inertial waves in their fluid convective envelope. In this work, we study the consequences of the possible melting of central regions for the efficiency of each of these mechanisms.

Keywords: hydrodynamics – waves – celestial mechanics – planets and satellites: interiors – planet-star interactions – planets and satellites: dynamical evolution and stability

1 Introduction and context

While more and more giant gaseous and icy planets are discovered in exoplanetary systems (e.g. Perryman 2011), internal structure of Jupiter, Saturn, Uranus and Neptune are still uncertain (e.g. Guillot 1999; Fortney et al. 2010; Baraffe et al. 2014). More particularly, the mass and the radius of potential central dense cores of rocks and ices are still unknown (e.g. Militzer & Hubbard 2009; Nettelmann 2011; Helled & Guillot 2013) with no firm constrains (Hubbard et al. 2009; Gaulme et al. 2011) while they are key elements for core-accretion formation scenario of these planets (e.g. Pollack et al. 1996; Morbidelli et al. 2015). In this framework, several works have demonstrated that elements constituting these regions (as for example silicates like $MgSiO_3$) are thermodynamically unstable in the pressure and temperature regimes of giant planet interiors (e.g. Wilson & Militzer 2012a,b; Wahl et al. 2013; González-Cataldo et al. 2014; Mazevet et al. 2015). These results demonstrate that central dense regions constituted of heavy elements may dissolve in the envelope. It may lead to an erosion of the core, a redistribution of core materials in the envelope and a modification of the nature of the core-envelope boundary that impact the structure and evolution of giant planets.

At the same time, tidal interactions are one of the key mechanisms that drive the evolution of planetary systems. On one hand, in the solar system, Lainey et al. (2009) and Lainey et al. (2012) have provided new constrains on tidal dissipation in Jupiter and Saturn using high precision astrometry. The obtained values are stronger than those that have been previously proposed in the literature by one order of magnitude, i.e. $Q'_{\rm J} \equiv 10^{5.15}$ and $Q'_{\rm S} \equiv 10^{3.87}$, where Q' is the normalized tidal quality factor defined in Ogilvie & Lin (2007), which is inversely proportional to tidal dissipation. On the other hand, constrains obtained in exoplanetary systems hosting Hot Jupiters lead to a weaker dissipation with $Q'_{\rm HJ} \equiv 10^{6.5}$ (see Ogilvie 2014, and references therein). In giant planets, physical mechanisms driving tidal dissipation are the viscoelastic dissipation in the potential dense central region constituted of rocks and ices (Remus et al. 2012, 2015) and the turbulent friction acting on tidal inertial waves (their restoring force is the Coriolis acceleration) in the deep convective fluid envelope (Ogilvie & Lin 2004). The efficiency of both mechanisms depends on the mass and radius aspect ratios between the core and the envelope and on the nature of the core-envelope boundary (Goodman & Lackner 2009; Ogilvie 2013; Guenel et al. 2014). It is thus necessary to examine the possible consequences of the melting of the core. First, in Sec. 2, we discuss the direct impact of the modification of the mass and the size of the core for each dissipation processes. Next, in Sec. 3, we study the impact of the core-envelope boundary for tidal inertial waves propagating in the fluid envelope. Finally, we conclude and discuss astrophysical consequences and perspectives of this work.

---

[1] Laboratoire AIM Paris-Saclay, CEA/DSM - CNRS - Université Paris Diderot, IRFU/SAp Centre de Saclay, F-91191 Gif-sur-Yvette Cedex, France

© Société Francaise d'Astronomie et d'Astrophysique (SF2A) 2015

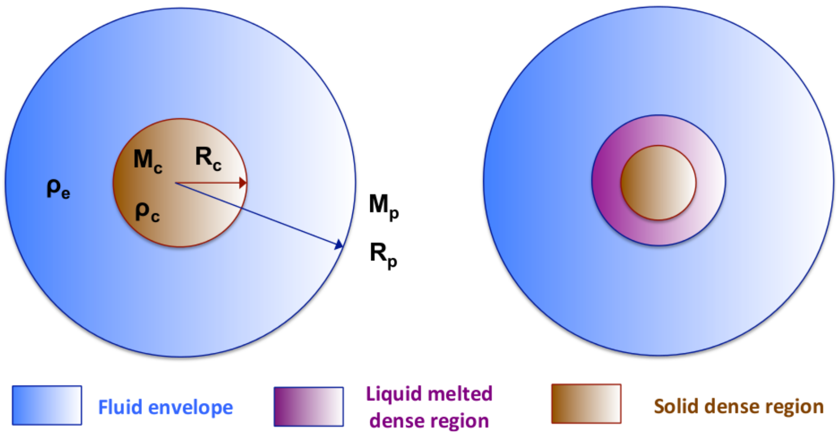

Fig. 1. Left: simplest bi-layer planetary model with a central solid (rocky/icy) core; R_c (R_p) and M_c (M_p) are the radius and the mass of the core (the planet) while ρ_e and ρ_c are the density of the envelope and of the core respectively. **Right:** Three layer planetary model inspired by the results obtained by Mazevet et al. (2015) in the case where central regions melting is occurring.

2 Tidal dissipation mechanisms and their dependences on the mass and the size of the core

Let us first consider simplest bi-layer models of giant planets constituted by an external fluid envelope and a solid core constituted of rocks and ices (see Fig. 1, left-panel). In such a simplified model, two dissipation mechanisms for tidal friction have been identified and studied:

- **The inelastic dissipation:** Rocks and ices can be modeled as viscoelastic materials. Because of the uncertainties on their rheological behavior, the simplest assumption is to assume the linear Maxwell model for which the shear modulus is complex with

$$\mathrm{Re}\left[\bar{\mu}(\omega)\right] = \frac{\eta^2\, G\, \omega^2}{G^2 + \eta^2\, \omega^2} \quad \text{and} \quad \mathrm{Im}\left[\bar{\mu}(\omega)\right] = \frac{\eta\, G^2\, \omega}{G^2 + \eta^2\, \omega^2}, \tag{2.1}$$

where ω is the tidal frequency, G the rigidity and η the viscosity that drives the friction (Remus et al. 2012, 2015). As demonstrated in Ogilvie (2013) and Guenel et al. (2014), it is possible to evaluate a frequency-averaged tidal dissipation, which allows to unravel the impact of internal structure on tidal dissipation. In the case of a viscoelastic core, we obtain:

$$\langle \mathcal{D}_{\rm ve} \rangle_\omega = \int_{-\infty}^{+\infty} \mathrm{Im}\left[k_2^2(\omega)\right] \frac{\mathrm{d}\omega}{\omega} = \frac{\pi\, G\, (3 + 2\mathcal{A})^2\, \mathcal{B}\, C}{\mathcal{D}\, (6\, \mathcal{D} + 4\, \mathcal{ABCG})}, \tag{2.2}$$

with

$$\mathcal{A} = 1 + \frac{5}{2}\gamma^{-1}\alpha^3\,(1-\gamma)\,, \quad \mathcal{B} = \alpha^{-5}\,(1-\gamma)^{-2}\,, \quad C = \frac{19}{2\,\rho_c\, g_c\, R_c}, \quad \mathcal{D} = \left[\frac{2}{3}\mathcal{AB}\,(1-\gamma)\left(1+\frac{3}{2}\gamma\right) - \frac{3}{2}\right]. \tag{2.3}$$

We introduce

$$\alpha = \frac{R_c}{R_p}, \quad \beta = \frac{M_c}{M_p} \quad \text{and} \quad \gamma = \frac{\rho_e}{\rho_c} = \frac{\alpha^3\,(1-\beta)}{\beta\,(1-\alpha^3)} < 1, \tag{2.4}$$

where R_c (R_p) and M_c (M_p) are the radius and the mass of the core (the planet) while ρ_e and ρ_c are the density of the envelope and of the core respectively. We introduce the quadrupolar complex Love number k_2^2, associated with the $(2,2)$ component of the time-dependent tidal potential U that corresponds to the spherical harmonic Y_2^2. It quantifies at the surface of the planet ($r = R_p$) the ratio of the tidal perturbation of its self-gravity potential over the tidal potential in the simplest case of coplanar systems. In the case of dissipative systems, it is a complex quantity which depends on the tidal frequency (ω) with a real part that accounts for the energy stored in the tidal perturbation, while the imaginary part accounts for the energy losses (e.g. Remus et al. 2012).

- **The (viscous) turbulent friction applied on tidal inertial waves:** if we assume that the external fluid envelope is convective, the presence of a close natural satellite or star excites tidal inertial waves if $\omega \in [-2\Omega, 2\Omega]$, where Ω is the angular velocity of the planet. Their restoring force is the Coriolis acceleration. Because of the friction applied by convective turbulence, their kinetic energy is converted into heat that leads to tidal evolution of planet-star/natural satellite systems. Ogilvie (2013) derived the corresponding frequency-averaged dissipation

$$\left\langle \mathcal{D}_{\rm in}^{\rm s}\right\rangle_{\omega} = \int_{-\infty}^{+\infty} \mathrm{Im}\left[k_2^2(\omega)\right] \frac{\mathrm{d}\omega}{\omega} = \frac{100\pi}{63}\epsilon^2 \frac{\alpha^5}{1-\alpha^5}\left[1+\frac{1-\gamma}{\gamma}\alpha^3\right]\left[1+\frac{5}{2}\frac{1-\gamma}{\gamma}\alpha^3\right]^{-2} \tag{2.5}$$

assuming a solid dense core on which tidal waves reflect. It may lead to inertial wave attractors where viscous friction is efficient (Ogilvie 2005). We introduce $\epsilon^2 \equiv \left(\Omega/\sqrt{\mathcal{G}M_{\rm p}/R_{\rm p}^3}\right)^2 = (\Omega/\Omega_{\rm c})^2 \ll 1$, where $\Omega_{\rm c}$ is the critical angular velocity and $\mathcal{G}$ is the gravitational constant. We also define the normalized frequency-averaged tidal dissipation at fixed angular velocity

$$\left\langle \mathcal{D}_{\rm in}^{\rm s}\right\rangle_{\omega}^{\Omega} = \epsilon^{-2}\left\langle \mathcal{D}_{\rm in}^{\rm s}\right\rangle_{\omega}. \tag{2.6}$$

Looking for tidal evolutionary track: In Fig. 2, we represent the variation of $\langle \mathcal{D}_{\rm ve}\rangle_{\omega}$ (assuming the parameters used in Guenel et al. (2014) for Saturn-like planets) and $\left\langle \mathcal{D}_{\rm in}^{\rm s}\right\rangle_{\omega}^{\Omega}$ as a function of the radius and mass ratios $\alpha = R_{\rm c}/R_{\rm p}$ and $\beta = M_{\rm c}/M_{\rm p}$ (respectively in top-left and top-right panels). First, the mass of the material in solid state and thus β is decreased when melting occurs. Next, because of macroscopic transport of heavy elements towards the envelope, its mean density ($\rho_{\rm e}$) is increased while the one of the core ($\rho_{\rm c}$) is decreased (at a fixed core mass, it corresponds to an increase of $R_{\rm c}$). To be able to predict the effect of melting processes, it would thus be necessary to be able to draw planetary evolutionary track in the (α,β) plane and in the corresponding (β,γ) one. Such a methodology has been applied in Mathis (2015) in the case of rotating low-mass stars leading to robust results for the frequency-averaged tidal dissipation in their convective envelope. To compute such a *tidal evolutionary track*, it would be necessary to compute planetary structure and evolution models taking into account melting and related mixing mechanisms (e.g. Leconte & Chabrier 2012) and the most realistic available EOS (e.g. Mazevet et al. 2015). Note also that the value of G depends on the state of materials.

3 The impact of the core-envelope boundary condition

In addition of modifying the radius and mass aspect ratios between the central dense core and the envelope, melting the core of gaseous and icy giant planets may also modify the nature of the boundary condition between these two regions. Indeed, let us focus here on tidal dissipation in the deep hydrogen and helium envelope in two configurations: i) in the first, we consider it surrounds a dense *solid* rocky/icy core (see Fig. 1, left panel); ii) in the second one, we consider the configuration suggested by (Mazevet et al. 2015) where the envelope is above a *liquid* shell of SiO_2 that surrounds a central core of MgO (see Fig. 1, right panel).

Then, tidal dissipation through the viscous dissipation of inertial waves is not the same in the case of a *fluid-solid interface* and of a *fluid-fluid interface*. As in the previous paragraph, we consider the behavior of the frequency-averaged tidal dissipation as introduced by Ogilvie (2013) and computed in the case of gaseous giant planets by Guenel et al. (2014).

In the case of a fluid-solid interface, the frequency-averaged tidal dissipation is given by Eq. (2.5) while in the case of a fluid-fluid interface it becomes

$$\begin{aligned}\left\langle \mathcal{D}_{\rm in}^{\rm f}\right\rangle_{\omega} &= \int_{-\infty}^{+\infty} \mathrm{Im}\left[k_2^2(\omega)\right] \frac{\mathrm{d}\omega}{\omega} = \frac{100\pi}{63}\epsilon^2\left(\frac{\alpha^5}{1-\alpha^5}\right)(1-\gamma)^2 \\ &\times(1-\alpha)^4\left(1+2\alpha+3\alpha^2+\frac{3}{2}\alpha^3\right)^2\left[1+\left(\frac{1-\gamma}{\gamma}\right)\alpha^3\right]\left[1+\frac{3}{2}\gamma+\frac{5}{2\gamma}\left(1+\frac{1}{2}\gamma-\frac{3}{2}\gamma^2\right)\alpha^3-\frac{9}{4}(1-\delta)\alpha^5\right]^{-2}.\end{aligned} \tag{3.1}$$

We also introduce the normalized frequency-averaged tidal dissipation at fixed angular velocity

$$\left\langle \mathcal{D}_{\rm in}^{\rm f}\right\rangle_{\omega}^{\Omega} = \epsilon^{-2}\left\langle \mathcal{D}_{\rm in}^{\rm f}\right\rangle_{\omega}. \tag{3.2}$$

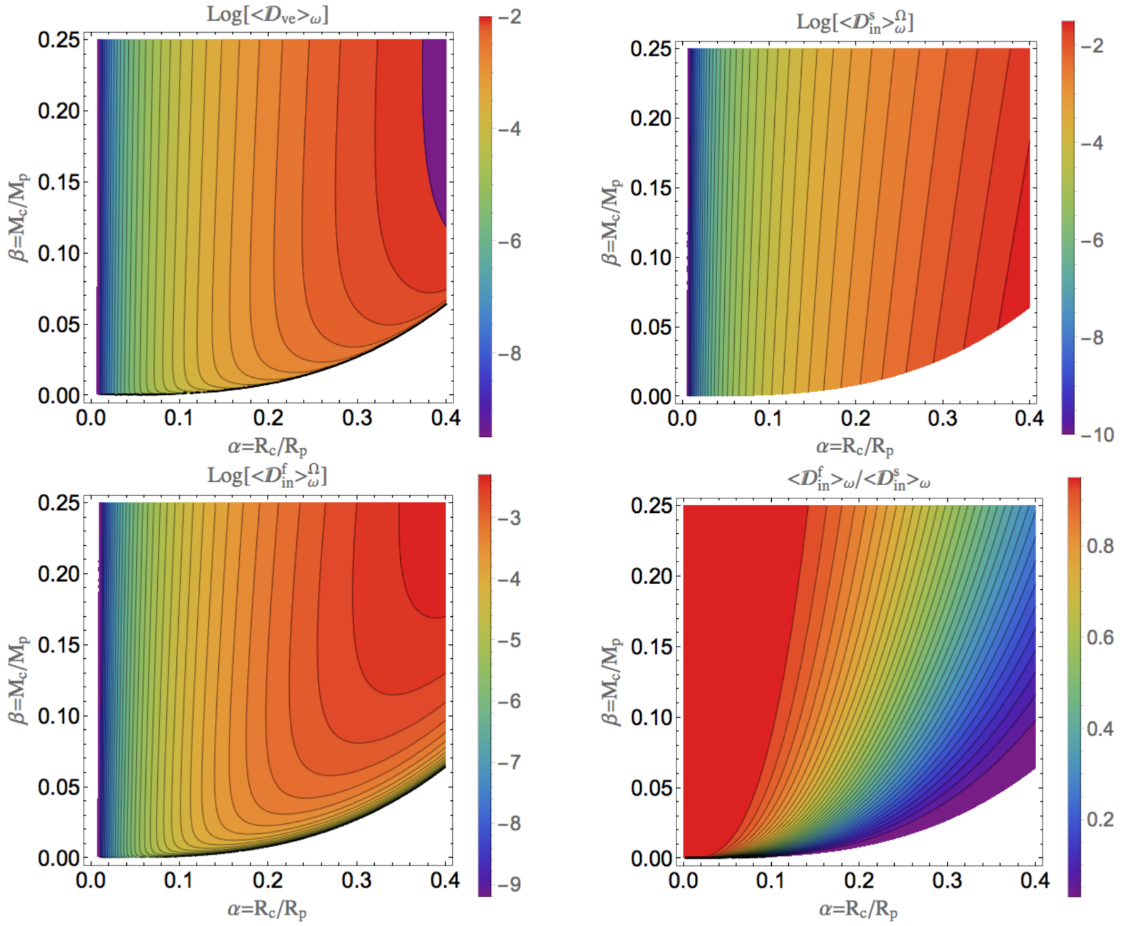

Fig. 2. Variations of $\langle \mathcal{D}_{\rm ve}\rangle_\omega$ (left-top panel), $\left\langle \mathcal{D}_{\rm in}^{\rm s}\right\rangle_\omega^\Omega$ (right-top panel), $\left\langle \mathcal{D}_{\rm in}^{\rm f}\right\rangle_\omega^\Omega$ (left-bottom panel) and $\left\langle \mathcal{D}_{\rm in}^{\rm f}\right\rangle_\omega / \left\langle \mathcal{D}_{\rm in}^{\rm s}\right\rangle_\omega$ (right-bottom panel) as a function of the radius and mass aspect ratios ($\alpha = R_{\rm c}/R_{\rm p}$ and $\beta = M_{\rm c}/M_{\rm p}$ respectively).

In Fig. 2 (left-bottom panel), we represent its variation as a function of $\alpha = R_{\rm c}/R_{\rm p}$ and $\beta = M_{\rm c}/M_{\rm p}$. We immediately see that its behavior is different that the one of $\left\langle \mathcal{D}_{\rm in}^{\rm s}\right\rangle_\omega^\Omega$. First, as observed in Mathis (2015), it is maximum around $\alpha \approx 0.571$ and $\beta \approx 0.501$. Moreover, the maximum of its amplitude is weaker than those of $\left\langle \mathcal{D}_{\rm in}^{\rm s}\right\rangle_\omega^\Omega$. For these reason, we plot in Fig. 2 (right-bottom panel) the ratio $\left\langle \mathcal{D}_{\rm in}^{\rm f}\right\rangle_\omega^\Omega / \left\langle \mathcal{D}_{\rm in}^{\rm s}\right\rangle_\omega^\Omega = \left\langle \mathcal{D}_{\rm in}^{\rm f}\right\rangle_\omega / \left\langle \mathcal{D}_{\rm in}^{\rm s}\right\rangle_\omega$ as a function of α and β. Having a fluid-fluid interface then decreases the strength of tidal dissipation in the external envelope. It is then interesting to evaluate $\left\langle \mathcal{D}_{\rm in}^{\rm f}\right\rangle_\omega / \left\langle \mathcal{D}_{\rm in}^{\rm s}\right\rangle_\omega$ for possible values of $M_{\rm c}$ and $R_{\rm c}$ for Jupiter-, Saturn-, Uranus-, and Neptune-like planets; the obtained results and the used parameters are given in the following table (Guillot 1999; Hubbard et al. 2009; Helled et al. 2011; Podolak & Helled 2012; Nettelmann et al. 2013).

Two conclusions are then obtained. First, for every planets the frequency-averaged tidal dissipation associated with inertial waves reflecting on a fluid-fluid interface is weaker than the one in the case of a fluid-solid interface. Next, as this is shown by Fig. 2 (right-bottom panel), this decrease is much stronger in the case of planets with large radius aspect ratios, that corresponds to the case of icy giant planets for which the strength of the frequency-averaged tidal dissipation corresponds to only 20% of its value in the case of a fluid-solid interface.

4 Conclusions

In this first exploratory work, we have discussed the possible effects of melting mechanisms that may occur in the central dense regions of giant planets. First, we have shown that realistic planetary structure and evolution models are key ingredients to be developed to provide a precise evaluation of mass, radius, and density ratios necessary to get a robust

Parameter	Jupiter	Saturn	Uranus	Neptune
M_p (M_E)	317.830	95.159	14.536	17.147
R_p (R_E)	10.973	9.140	3.981	3.865
M_c (M_E)	6.41	18.65	1.35	2.25
$\alpha = R_c/R_p$	0.126	0.219	0.30	0.35
$\beta = M_c/M_p$	0.020	0.196	0.093	0.131
$\left\langle \mathcal{D}_{\rm in}^{\rm f} \right\rangle_\omega / \left\langle \mathcal{D}_{\rm in}^{\rm s} \right\rangle_\omega$	0.612	0.766	0.237	0.194

Table 1. Values of the parameters used to compute the ratio $\left\langle \mathcal{D}_{\rm in}^{\rm f} \right\rangle_\omega / \left\langle \mathcal{D}_{\rm in}^{\rm s} \right\rangle_\omega$ (Remus et al. 2012; Helled et al. 2011; Podolak & Helled 2012; Nettelmann et al. 2013)

prediction of tidal dissipation. Indeed, these quantities directly impact the amplitude of the frequency-averaged tidal dissipation. Moreover, if melting of rocks and ices is taking place, tidal inertial waves, which propagate in the external envelope, may reflect on a *fluid-fluid* interface instead of a *fluid-solid* interface. In the case of planets having a large core such as icy giant planets, this may lead to a net decrease of tidal dissipation. In a near future, the impact of mixing mechanisms such as double-diffusive instabilities (see e.g Leconte & Chabrier 2012) on tidal dissipation must also be evaluated.

The author acknowledges funding by the European Research Council through ERC grant SPIRE 647383. This work was also supported by the Programme National de Planétologie (CNRS/INSU) and the International Space Institute (ISSI team ENCELADE 2.0).

References

Baraffe, I., Chabrier, G., Fortney, J., & Sotin, C. 2014, Protostars and Planets VI, 763

Fortney, J. J., Baraffe, I., & Militzer, B. 2010, Giant Planet Interior Structure and Thermal Evolution, ed. S. Seager, 397–418

Gaulme, P., Schmider, F.-X., Gay, J., Guillot, T., & Jacob, C. 2011, A&A, 531, A104

González-Cataldo, F., Wilson, H. F., & Militzer, B. 2014, ApJ, 787, 79

Goodman, J. & Lackner, C. 2009, ApJ, 696, 2054

Guenel, M., Mathis, S., & Remus, F. 2014, A&A, 566, L9

Guillot, T. 1999, Planet. Space Sci., 47, 1183

Helled, R., Anderson, J. D., Podolak, M., & Schubert, G. 2011, ApJ, 726, 15

Helled, R. & Guillot, T. 2013, ApJ, 767, 113

Hubbard, W. B., Dougherty, M. K., Gautier, D., & Jacobson, R. 2009, The Interior of Saturn, ed. M. K. Dougherty, L. W. Esposito, & S. M. Krimigis, 75

Lainey, V., Arlot, J.-E., Karatekin, Ö., & van Hoolst, T. 2009, Nature, 459, 957

Lainey, V., Karatekin, Ö., Desmars, J., et al. 2012, ApJ, 752, 14

Leconte, J. & Chabrier, G. 2012, A&A, 540, A20

Mathis, S. 2015, A&A, 580, L3

Mazevet, S., Tsuchiya, T., Taniuchi, T., Benuzzi-Mounaix, A., & Guyot, F. 2015, Phys. Rev. B, 92, 014105

Militzer, B. & Hubbard, W. B. 2009, Ap&SS, 322, 129

Morbidelli, A., Lambrechts, M., Jacobson, S., & Bitsch, B. 2015, Icarus, 258, 418

Nettelmann, N. 2011, Ap&SS, 336, 47

Nettelmann, N., Helled, R., Fortney, J. J., & Redmer, R. 2013, Planet. Space Sci., 77, 143

Ogilvie, G. I. 2005, Journal of Fluid Mechanics, 543, 19

Ogilvie, G. I. 2013, MNRAS, 429, 613
Ogilvie, G. I. 2014, ARA&A, 52, 171
Ogilvie, G. I. & Lin, D. N. C. 2004, ApJ, 610, 477
Ogilvie, G. I. & Lin, D. N. C. 2007, ApJ, 661, 1180
Perryman, M. 2011, The Exoplanet Handbook
Podolak, M. & Helled, R. 2012, ApJ, 759, L32
Pollack, J. B., Hubickyj, O., Bodenheimer, P., et al. 1996, Icarus, 124, 62
Remus, F., Mathis, S., Zahn, J.-P., & Lainey, V. 2012, A&A, 541, A165
Remus, F., Mathis, S., Zahn, J.-P., & Lainey, V. 2015, A&A, 573, A23
Wahl, S. M., Wilson, H. F., & Militzer, B. 2013, ApJ, 773, 95
Wilson, H. F. & Militzer, B. 2012a, Physical Review Letters, 108, 111101
Wilson, H. F. & Militzer, B. 2012b, ApJ, 745, 54

SF2A 2015
F. Martins, S. Boissier, V. Buat, L. Cambrésy and P. Petit (eds)

DIFFRACTIVE TELESCOPE FOR PROTOPLANETARY DISKS STUDY IN UV

W. Roux[1] and L. Koechlin[1]

Abstract.
The direct observation of exoplanetary systems and their environment remains a technological challenge: on the one hand, because of the weak luminosity of objects surrounding the central star, and on the other hand, because of their small size compared to the distance from Earth. The fresnel imager is a concept of space telescope based on focusing by diffraction, developed by our team in Institut de Recherche en Astrophysique et Planétologie (IRAP). Its high photometric dynamics and its low angular resolution make it a competitive candidate. Currently we propose a space mission on board the International Space Station (ISS), observing in the ultraviolet band, in order to validate its capabilities in space and so increase the Technological Readiness Level (TRL), anticipating a larger mission in the future. To reach this goal, we have to provide some evolutions, like improving the design of Fresnel arrays or conceive a new chromatism corrector. This paper presents the evolutions for the ISS prototype and its possible applications like protoplanetary disks imaging.

Keywords: Fresnel Imager, Diffractive telescope, UV astronomy, Protoplanetary disks imaging

1 Introduction

Nowadays, space telescopes are necessary to overcome the Earth atmosphere and observe the Universe, especially in the ultraviolet band. But the weight and size of large focusing systems limit the launch opportunities, thus limiting the field and resolution of available missions. The Fresnel Imager is an innovating alternative to classical optics to avoid these drawbacks, and could be a serious candidate for future missions. This project uses "Fresnel arrays" as primary optics to make images.

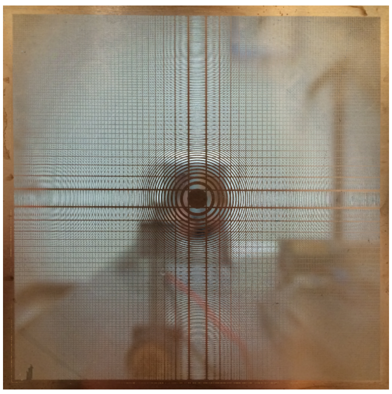

Fig. 1. Last Fresnel array engraved, used for tests in the UV-band. Its focal length is $12.695m$ for $\lambda = 260nm$ ($c = 0.65m$ and $N = 160$).

The Fresnel arrays use the principle of Fresnel zone plates, with the particularity that the pattern is not printed on a transmissive surface but directly engraved in a solid surface (Fig. 1). There is a cophasing relation between each rings, as first experienced by Soret (1875). Thanks to this design, a plane wavefront is made

[1] IRAP, CNRS, Université Paul Sabatier, 14 avenue Edouard Belin 31400 Toulouse, France

© Société Francaise d'Astronomie et d'Astrophysique (SF2A) 2015

spherical and thus focused by diffraction through the numerous void holes in a Fresnel array, so the light is not affected by an optical material that would be present in classical optics.

Actually, with a Fresnel diffractive array made of thin metalized foil, a large aperture around a few meters, the primary system weights about a kilogram. Further than weight, this system is tolerant in terms of manufacturing and positioning (L. Koechlin et al. 2005). Its angular resolution is limited by the aperture, same as classical optics, the width of the point spread function (PSF) is inversely proportional to the diameter of the Fresnel arrays. This system provides a high contrast on compact objects, that is necessary to observe the environment of protoplanetary disks.

Like any optical systems, there are some drawbacks, but they can be corrected by an adapted design. First the chromatism inducing by the fresnel arrays. Actually the focal length is wavelength dependent, so there is a series of focal planes along the optical axis. The system requires a Fresnel blazed lens placed in a pupil plane to correct this dispersion, so currently we are working on a Fresnel blazed mirror (like described below). Our previous design was not adapted to UV and would have caused transmission loss through the optical material. The focal length is also quite long for large apertures because it follows: $f = D^2/(8 * N * \lambda)$, where D is the diameter of aperture, N the number of Fresnel zones, and λ the wavelength. For instance, if we observe at the Lyman-α line ($\lambda = 121nm$), with an aperture $D = 6m$ and $N = 2000$ Fresnel zones, the focal length is $f = 16.6km$. That is why a nominal mission, like studied with Centre National d'Études Spatiales (CNES) from 2008 to 2010 (Hinglais 2011) requires a formation flying (Fig. 2). A first module holds the Fresnel array, and a second one contains the field optics, the chromatism corrector and the instrumentation required for image acquisition, like spectro-imagers and high contrast cameras. Both these modules can be launched by a single Soyuz and placed in orbit around the second Lagrangian point for a 5 year mission (Raksasataya et al. 2010).

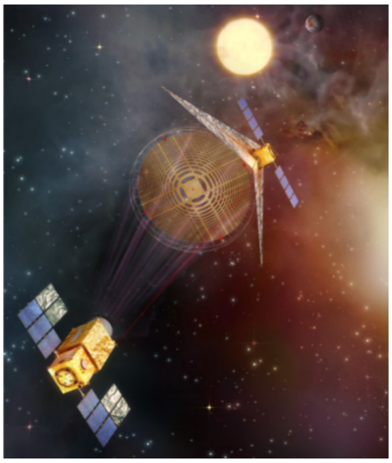

Fig. 2. Artistic view of a possible nominal mission, with the two modules in formation flight: the Fresnel array and the receptor module. (Credit: CNES/GEKO 2008)

2 Future evolutions and probatory mission

Since the presentation of the new developments on the Fresnel Diffractive Imager project at COSPAR Moscow in 2014, we have new leads for a probatory mission on the ISS.

2.1 A new chromatism corrector

We want to replace of the Fresnel blazed lens in the previous prototypes by a Fresnel blazed mirror, to prevent diffusion or transmission loss through fused silica, and so improve the quality of our instrument. This mirror could get an additive concavity to replace the last lens, used for final image focusing. We have calculated this new profile for chromatism correction by reflection. Currently we are investigating what would be the best way to produce this optical element. The previous Fresnel lens was engraved by photolithography, but this method presents some constraints for manufacturing. That's why we are prospecting several companies to engrave this piece with ultraprecision machine systems supporting single point diamond lathing. This new blazed concave grating will be the subject of a future article.

2.2 A new holding bars layout

Until now all Fresnel arrays produced feature a pseudoperiodic bars system to hold the rings in place. As we can see on Fig. 1, there are orthogonal bars every 3 rings. Preliminary studies have shown that regular and equidistant bars could reduce stray light and so raise the dynamic range, but we will make further simulations to enhance these studies. Currently we are developing a new simulation program of light propagation through our instrument to improve the PSF quality, using the new configuration of our prototype.

2.3 New optical tests in the ultraviolet

Due to the new equipment we will produce for the Fresnel Imager, we need a new measurements campaign. Moreover, the last tests in the ultraviolet were not optimal because the CCD camera with a UV sensitive cathode available at the time was not performant in terms of contrast. In February 2015, we met a research team at the Institute for Astronomy and Astrophysics from University of Tübingen in Germany, they work with and develop microchannel plate amplifiers and resistive anode detectors dedicated to UV, and we agreed to work together on a new tests campaign for the Fresnel imager.

2.4 The probatory mission on ISS

The probatory mission on the ISS that we propose consists of two parts on the extremities of the Integrated Truss Structure. The first one consists of the Fresnel array and an orientable mirror that will be used to aim astrophysical targets in the sky, and to compensate the drift of the ISS as well as stabilize images in case of vibrations. The resolution would be $0.15 arcseconds$ for an aperture between 15 and $20cm$. Recently, an agreement of collaboration has been signed with the Institute of Astronomy of the Russian Accademy of Sciences (INASAN), the Universidad Complutense de Madrid (UCM) and the Université Paul Sabatier (UPS) to prepare the future scientific program that would be required for a such mission, and the mission proposal to the Russian space agency ROCOSMOS taking into account the technical constraints.

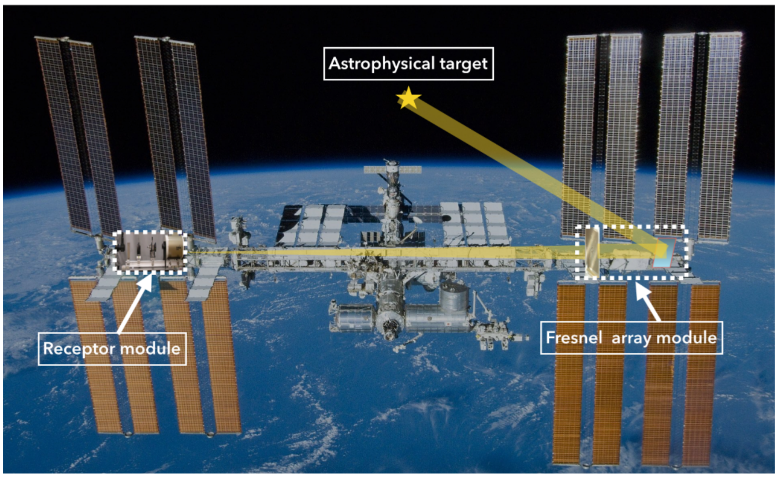

Fig. 3. Scheme of the possible configuration of our prototype on the ISS (Credit: NASA/Crew of STS-132).

3 Science cases in the UV

Due to the capacity of the Fresnel Imager to focus the light by diffraction, with no optical material in the light path, this instrument is more competitive for UV. Actually optical materials scatter and limit the transmission for these wavelengths. The shorter is the wavelength, the more difficult is the challenge. Moreover, the optics can be contaminated by deposited materials on their surface and become opaque to UV.

The UV astronomy is a recent domain of observation because the Earth atmosphere becomes opaque below $320nm$. The interstellar medium becomes opaque anyway below 91.2nm due to the Lyman cutoff, so the observable wavelength domain is limited even from space. The most interesting wavelength to observe with the proposed mission is Lyman-α ($\lambda = 121.6nm$). It corresponds to the most energetic electronic transition in the hydrogen atom. This choice will allow to map the repartition of high energy hydrogen, to examine hot stars environments and stellar formation areas for instance, and the Universe in general but limited to our neighborhood because of the redshift. We could observe numerous other spectral lines in the UV (including life signatures on exoplanets) but for budgetary reasons we will limit to one or two spectral bands for the probatory mission, and up to three ones for a nominal mission.

3.1 *Protoplanetary disks*

The protoplanetary disks are composed of dust and gas orbiting a central star. There are two main sources of UV in a protoplanetary disk (Gómez de Castro 2011). The first is molecular hydrogen in the inner hot gas disk that radiates in Lyman-α, excited by the UV from the central star. The second ones are the accretion shocks, emitting intense UV and X-rays when the matter from the gas disk meets the magnetosphere of the star and hits its surface (Fig. 4).

The imaging of protoplanetary disks is interesting for the study of matter distribution around them and its gravitational drive, to predict their evolutions. That could inform on the role of UV on the disk evolution because we know that UV and X-rays evaporate and blast away the upper and the lower disk surfaces. These studies requires imaging and spectro-imaging at very high angular resolution and contrasts, reachable by a Fresnel Imager with a large aperture.

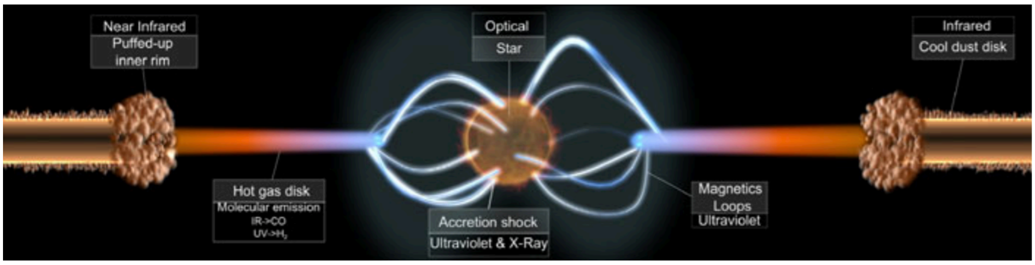

Fig. 4. Representation of the different UV sources in a protoplanetary disk (Credit: A.I. Goméz de Castro).

3.2 *Other science cases*

The study of other astrophysical disks helps to understand the physics behind their formations and evolutions. For instance Active Nucleus Galaxies (AGNs) and quasars (QSOs) present accretion disks orbiting around supermassive black holes, radiating in the UV by thermal emission. Some white dwarfs can also have an accretion disk emitting in the UV.

4 Conclusions

These new leads to improve the Fresnel Diffractive Imager have driven us to build up new collaborations with diverse institutes from Europe and Russia. We except to have results within two or three years with the acceptance of the probatory mission, which will then increase the TRL, provide a modest but valuable scientific return, and allow to prepare a nominal mission. In parallel the reachable science cases will be thoroughly prepared and well defined.

References

Gómez de Castro, A. 2011, Experimental Astronomy, 30, 205

Hinglais, E. 2011, Experimental Astronomy, 30, 85

L. Koechlin, D. Serre, & P. Duchon. 2005, A&A, 443, 709

Raksasataya, T., Deba, P., Rivet, J. P., et al. 2010, Proc. SPIE, 7732, 77322D

Soret, J.-L. 1875, Archive des sciences physiques et naturelles, 52, 320

SF2A 2015
F. Martins, S. Boissier, V. Buat, L. Cambrésy and P. Petit (eds)

TRANSIT-DEPTH METALLICITY CORRELATION: A BAYESIAN APPROACH

P. Sarkis[1] and C. Nehmé[1,2]

Abstract. A negative correlation was previously reported between the transit depth of *Kepler*'s Q1-Q12 gas giant candidates and the stellar metallicity. In this present work, we revisit this correlation to better understand the role of the stellar metallicity in the formation of giant planets, in particular, to investigate the effect of the metallicity on the transit depth. We selected the 82 confirmed giant planets from the cumulative catalogue. This is the first large and homogenous sample of confirmed giant planets used to study this correlation. Such samples are suitable to perform robust statistical analysis. We present the first hierarchical Bayesian linear regression model to revise this correlation. The advantages of using a Bayesian framework are to incorporate measurement errors in the model and to quantify both the intrinsic scatter and the uncertainties on the parameters of the model. Our statistical analysis reveals no correlation between the transit depth of confirmed giant planets and the stellar metallicity.

Keywords: planets and satellites: gaseous planets, stars: solar-type, methods: statistical

1 Introduction

NASA's *Kepler* mission has revolutionized the field of extrasolar planets and now, more than ever, it is possible to put statistical constraints on the observed planet properties and on the theories of planet formation. Thousands of exoplanets have been discovered by *Kepler* which allows one to look at the planets as a population and not as single planets. Clues on the nature of giant planet formation might be revealed from observational trends. With such large and homogenous samples, it is now possible to compare observed correlations to theories. Dodson-Robinson (2012, hereafter DR12) reported a negative correlation between the transit depth of *Kepler*'s gas giant planets and the metallicity of the host star. DR12's sample consisted of 213 giant candidates with estimated radii of $5 - 20R_\oplus$. The author argued that her sample may be contaminated by false positives and interpreted the result as evidence that metal-rich planets of a given mass are denser than their metal-poor counterparts, leading to smaller radii (Fortney & Nettelmann 2010). DR12 did not include in her statistical analysis the uncertainties on the transit depth and on the stellar metallicity although they are very important and could bias the result. In this present work and in order not to contaminate our sample with false positives, we revise the transit depth - metallicity correlation for all the confirmed giant planets detected by *Kepler*. Moreover, we use Bayesian statistics to incorporate the measurement uncertainties in our analysis.

2 Sample Selection

For this study we used the cumulative catalog of planets detected by the NASA *Kepler* mission which, as of April 2015, consisted of the latest Q1-Q16 catalog (Mullally et al. 2015). Following Dodson-Robinson (2012), we define gas giant planets as planets that have a radius between $5R_\oplus < R_p < 20R_\oplus$. We selected only the planets with a SNR > 7.1 to avoid KOIs (or *Kepler* Objects of Interest) with noisy lightcurves. The stellar parameters were taken from the *Kepler* stellar Q1-Q16 database (Huber et al. 2014). We ended up with a sample of 373 giant planets of which 82 are confirmed gas giant exoplanets. Note that the stellar and the planetary parameters provided by *Kepler*'s catalog have asymmetric upper and lower uncertainties. To get the 1σ error bar we calculated their average.

---

[1] Department of Physics & Astronomy, Notre Dame University, Lebanon
pjsarkis01@ndu.edu.lb
[2] CEA Saclay, IRFU, France

© Société Francaise d'Astronomie et d'Astrophysique (SF2A) 2015

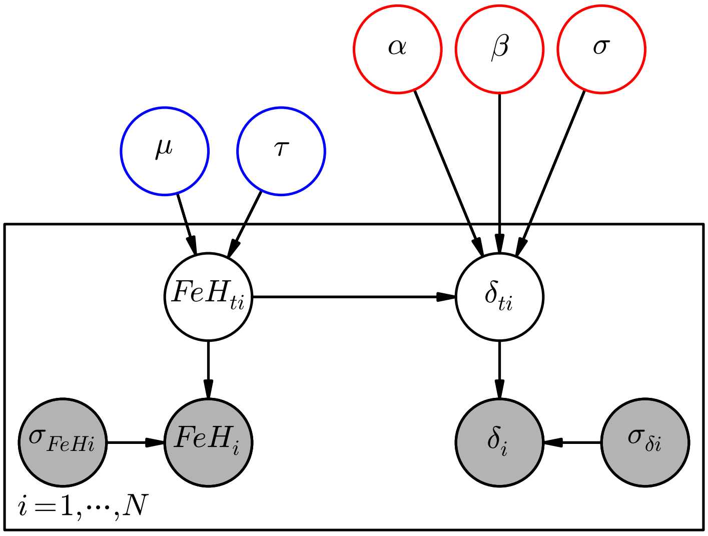

Fig. 1. A graphical model representing our HBM. The gray nodes are the observed parameters. The true missing parameters are in the white nodes. The blue nodes are the nuisance parameters and the parameters of interest are in the red nodes. The arrows indicate the conditional dependence. The definition of each parameter is:

$$\begin{aligned} FeH_i &= \text{ stellar metallicity of the i}^{\text{th}}\text{ planet} \\ \sigma_{FeHi} &= \text{uncertainty on the stellar metallicity of the i}^{\text{th}}\text{ planet} \\ \delta_i &= \text{ transit depth of the i}^{\text{th}}\text{ planet} \\ \sigma_{\delta i} &= \text{ uncertainty on the transit depth of the i}^{\text{th}}\text{ planet} \\ FeH_{ti} &= \text{ true stellar metallicity of the i}^{\text{th}}\text{ planet} \\ \delta_{ti} &= \text{ true transit depth of the i}^{\text{th}}\text{ planet} \\ \mu \text{ and } \tau &= \text{nuissance parameters} \\ \alpha,\ \beta, \text{ and } \sigma &= \text{ parameters of the linear model} \end{aligned}$$

3 The Method: Hierarchical Bayesian Modeling

Hierarchical Bayesian Modeling (hereafter HBM) allows us to derive the uncertainties on the model parameters and to relate the observed data to the true unobserved data. Following Kelly (2007), we constructed the likelihood function in a simple way to relate the parameters of interest to the observed data taking into account the measurement uncertainties. We used this method to study the correlation between the transit depth (δ) and the metallicity (FeH) of the host star. A graphical model of our hierarchical model is given in Fig. 1. Markov Chain Monte Carlo (hereafter MCMC) was performed using the python package PySTAN*, a package for Bayesian inference. We ran the model with 4 Markov Chains, each of 5,000 iterations. The first 50% of each chain were discarded as "burn-in" and the remaining samples were combined ending up with 10,000 samples.

4 Results

The posterior distributions for each of the parameters of interest (α, β, and σ) produced by running MCMC are shown in the left panel of Fig. 2. The equation of the "best-fit" linear model is

$$\delta = (0.07 \pm 0.014) + (0.02 \pm 0.14) FeH \tag{4.1}$$

*`http://mc-stan.org/`

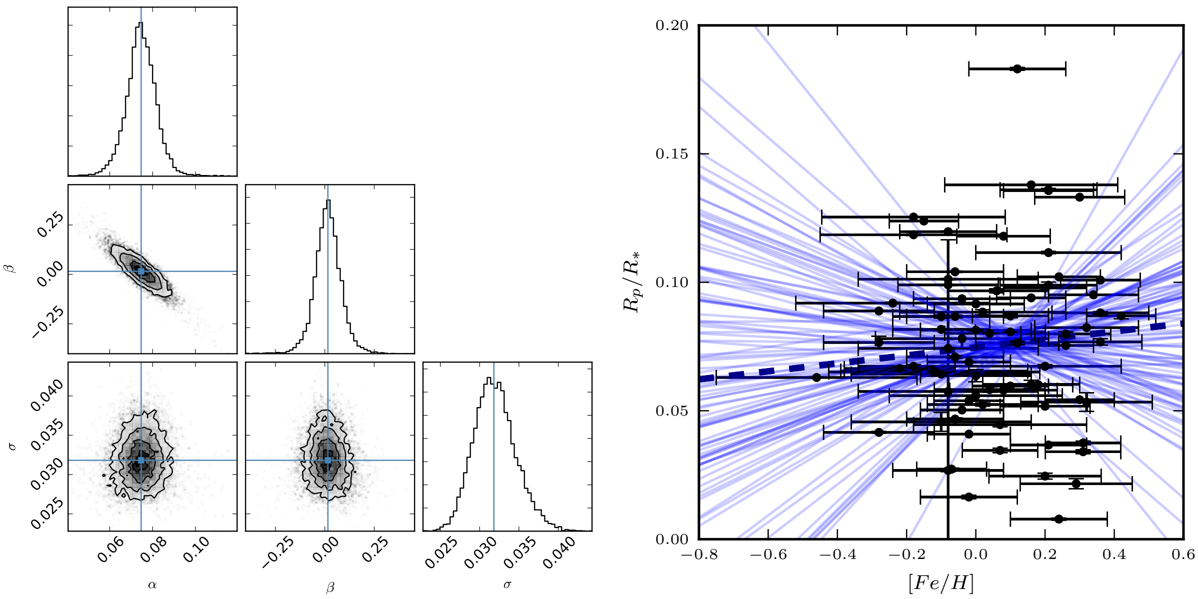

Fig. 2. Left: Posterior probability distributions for the parameters of the model α, β, and σ as computed by MCMC, marginalized over the other parameters. **Right:** Confirmed gas giant explanets and the best fit line. The light blue lines are samples from the MCMC chain.

with an intrinsic scatter of $\sigma = 0.03 \pm 0.005$. The transit depth of each confirmed exoplanet is plotted against the metallicity of the host star along with their uncertainties in the right panel of Fig. 2. The "best-fit" linear model (blue dotted line) is shown along with 100 random samples from the MCMC chain (light blue). It is clear that there is a large intrinsic scatter which leads to the conclusion that there is no correlation between the transit depth and the stellar metallicity.

5 Discussion

In this work, we showed that there is no correlation between the transit depth of *Kepler*'s giant exoplanets and the metallicity of the host star. In particular, we demonstrated that there is a relatively large intrinsic scatter in the relation. This result shows how crucial understanding those discrepancies. Thus, they are directly related to the models of planetary structure and formation.

For future work, this analysis should account for the selection effects and biases present in the *Kepler* survey. Gaidos & Mann (2013) reported the importance of including these effects in any statistical study. The authors also showed that these selection effects lead to biases in the properties of transiting planets and their host stars, hence biasing the correlation.

This research has made use of the data collected by the *Kepler* mission and the NASA Exoplanet Archive, which is operated by the California Institute of Technology, under contract with the National Aeronautics and Space Administration under the Exoplanet Exploration Program.

References

Dodson-Robinson, S. E. 2012, ApJ, 752, 72

Fortney, J. J. & Nettelmann, N. 2010, Space Sci. Rev., 152, 423

Gaidos, E. & Mann, A. 2013, ApJ, 762, 41

Huber, D., Silva Aguirre, V., Mathews, J. M., et al. 2014, ApJS, 211, 2

Kelly, B. C. 2007, ApJ, 665, 1489

Mullally, F., Coughlin, J. L., Thompson, S. E., et al. 2015, ApJS, 217, 31

Session 11

Services de diffusion des données atomiques et moléculaires

SF2A 2015
F. Martins, S. Boissier, V. Buat, L. Cambrésy and P. Petit (eds)

VAMDC CONSORTIUM: A SERVICE TO ASTROPHYSICS

M.L Dubernet[1,2,3], N. Moreau[3,1,2], C.M. Zwölf[3,1,2], Y.A. Ba[3,1,2] and VAMDC Consortium[4]

Abstract. The VAMDC Consortium is a worldwide consortium which federates Atomic and Molecular databases through an e-science infrastructure and a political organisation. About 90% of the inter-connected databases handle data that are used for the interpretation of spectra and for the modelisation of media of many fields of astrophysics. This paper presents how the VAMDC Consortium is organised in order to provide a "service" to the astrophysics community.

Keywords: databases, software, atoms, molecules

1 Introduction

The VAMDC Consortium is issued from two european funded projects: the VAMDC (http://www.vamdc-project.vamdc.eu/) Dubernet et al. (2010) and the SUP@VAMDC (`http://www.sup-vamdc.vamdc.org/`) Zwölf et al. (2014) projects. The main scientific outcome of those two projects are: 1) an e-science infrastructure that interconnects about thirty databases (`http://www.vamdc.eu/activities/research`); 2) a political and technical organisation: "the VAMDC Consortium" that was launched on the 1rst November 2014 through the signature of a Memorandum of Understanding between 15 partners. This structure ensures the organisation and the sustainability of the VAMDC activities. The VAMDC Consortium activities cover 4 domains: research which is the most developed domain, education and industry that are currently in their early development stage, and outreach activities that will be carried out at their own pace depending on the public in contact with the VAMDC partners, and depending on the VAMDC partners' interest.

2 The Political and Technical organisation

The "VAMDC Consortium" Memorandum of Understanding (MoU) handles the following aspects: List of Members, Category of Memberships (Full, Associated Members); Governance with different bodies: Board of Directors, Executive Director Board, Scientific and Technical Board; Voting Rules; Entry into Force, Duration and Termination; Responsibility of members; Definition, Representation, Use of "VAMDC" Brand; Financial Provisions; Description of Activities; Use of foreground; Access Rights, Intellectual Property, List of "VAMDC" products (background).

This MoU is complemented by an "Internal Regulations" Document (IRD) describing in details the implementation of the MoU and a Roadmap that provides the general strategy of the VAMDC Consortium (`http://www.vamdc.eu` - see section "About us"/How to join us).

The Full Members take all decisions in the Board of Directors and both Full and Associated members are part of the Scientific and Technical Board that handles the maintenance, the development and the scientific activities of the VAMDC Consortium. A full description of the functionning can be found in the MoU, in the IRD and in the Roadmap.

[1] LERMA, Observatoire de Paris, PSL Research University, CNRS, UMR8112, 5 Place Janssen, 92195 Meudon, France
[2] Sorbonne University, UPMC Univ Paris 06, CNRS, UMR8112, LERMA, 5 Place Janssen, 92195 Meudon, France
[3] Paris Astronomical Data Center, Observatoire de Paris, PSL Research University, 5 Place Janssen, 92195 Meudon, France
[4] http://www.vamdc.eu

© Société Francaise d'Astronomie et d'Astrophysique (SF2A) 2015

3 The Research Services

The Research Services are organised towards offering a common entry point to all databases thanks to the VAMDC portal (`http://portal.vamdc.eu`), towards offering the possibility to include new data and new databases within the VAMDC e-infrastructure, towards providing software librairies and modules that can be included into customers software, towards providing standalone users oriented software that retrieve and handle atomic and molecular data. The VAMDC e-infrastructure has evolved over the years through successive releases Rixon et al. (2011); Doronin et al. (2012); Dubernet et al. (2015) in order to arrive to the current version of standards and software (release version v12.07).

3.1 Portal

The portal (`http://portal.vamdc.eu`) is the major single entry point to all VAMDC connected databases. It allows a visibility on all available data in the VAMDC connected databases, and in many cases can be the first steps towards discovering data since those databases will respond if they contain the requested data. The portal has been recently upgraded with a new query interface for beginers, called “Guided Query”, and the info section provides tutorials about how to use the different query modes. The tools to visualise the data are homogeneous among the databases and the description of the retrieved data, in particular of quantum numbers, is the same across all databases. Such uniformity implies that the portal cannot offer the same services as the traditionnal graphical user interface of the individual databases. This is the price to pay for accessing a wide range of data. Nevertheless an effort has been made to associate specific visualisation software to each databases (section 3 in in Fig. 1), and this section 3 will continue to improve in order to meet the users needs.

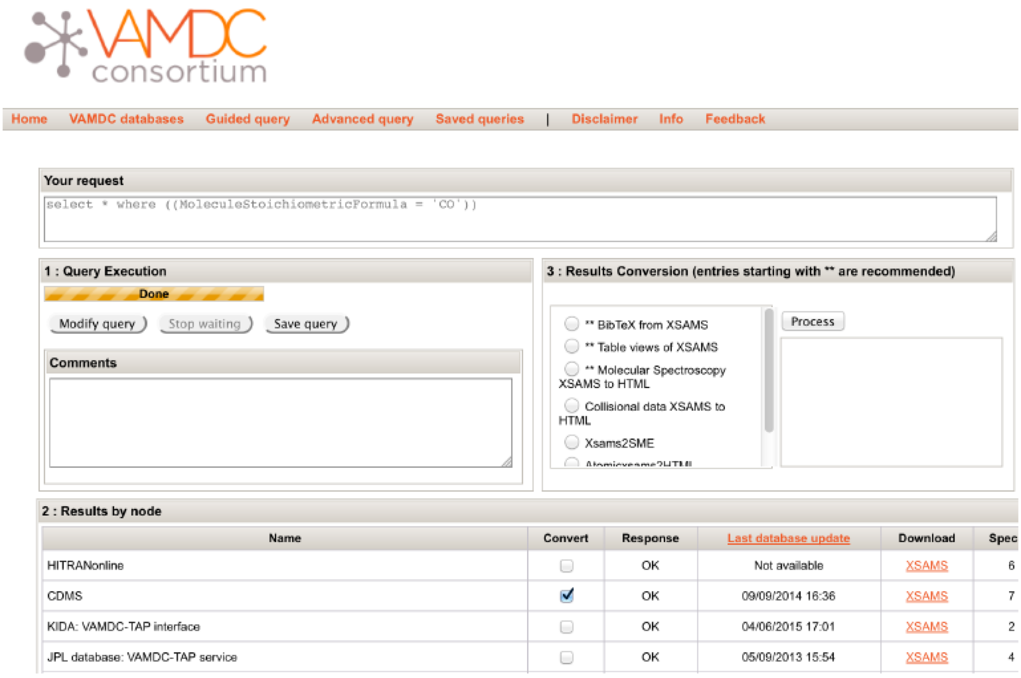

Fig. 1. Visualisation Page of VAMDC Portal

3.2 Services to include new databases

The current VAMDC e-infrastructure includes databases related to atomic and molecular spectroscopy and to heavy particle collisional processes, and is appropriate to the type of currently accessible data. Any producer of data can join the VAMDC infrastructure through different means: 1) they may include their data in existing atomic and molecular databases that are partners of VAMDC; 2) they may create a new database hosted by a partner of VAMDC; 3) they may create a new node in the VAMDC e-infrastructure. In case 1 and 2, the data producers can contact the databases managers directly, when the general support system (support@vamdc.eu) should be contacted in the third case. Furthermore VAMDC aims to provide atomic and molecular data providers and compilers with a large dissemination platform for their work. Currently all products related to VAMDC, portal and tools, explicitly warn that the VAMDC users should cite both the original papers where the data have been published and the relevant databases.

3.3 Libraries and Software

The librairies, software modules and software can be found on the VAMDC website (`http://www.vamdc.eu/software`). The integration of those librairies are documented, supported via tutorials and illustrated in scientific use cases Dubernet et al. (2014). Among the scientific use cases, one might cite the SPECTCOL tool Dubernet et al. (2012) that allows to match spectroscopic data from CMDS Müller et al. (2005, 2012) andJPL (`http://spec.jpl.nasa.gov/`) with collisional data from BASECOL Dubernet et al. (2013)for interstellar applications, the access of VAMDC connected databases through the CASSIS software (`http://cassis.irap.omp.eu`), through the BASS2000 web portal (`http://bass2000.obspm.fr`), the MyXClass software Möller et al. (2015), through the SPECVIEW software (`http://www.stsci.edu/institute/software_hardware/specview/`). Users might want to create new librairies and software, and we provide support for those activities (support@vamdc.eu). The VAMDC Consortium can provide the following services to the users communities: 1) we can improve our current services and tools in order to meet the users requirements; 2) we can port the VAMDC capabilities and facilities into tools developed by institutes outside the consortium; 3) we can provide the scientific community with innovative tools for easily handling and processing results; 4) we can provide "derived products", i.e. products that combination of atomic and molecular data.

4 The Communication Services

The VAMDC Consortium has a large communication platform that is made available to producers and users of data.

The "VAMDC Consortium" communication activities occur through its main website that is the entry point for all customers from research, education, business, outreach, through a virtual tour of the "VAMDC Consortium" (`http://www.vamdc.org/virtual-tour/`) that describes partners and databases, through the News, the Events, the Blogs sections, through the social networks (Facebook, Twitter, ResearchGate, LinkedIn), through the natural channel of dissemination in conferences and workshops, through organising tutorials for different categories of users either through self-organisation or through joining other tutorials linked to atomic and molecular data or to e-infrastructure or to the application fields. We offer a Forum platform that can be used by any groups of data users and data producers. The above communication channels and tools can be used by external customers and by internal VAMDC Consortium members.

5 The Education Services

Education activities cover different target population and different methodologies. The target population is secondary school education, higher education and continuous education. The methodologies include the use of VAMDC in face-to-face education sessions or via on-line teaching. The Education activities are linked to the national Curriculae and must be displayed in the national language at least for all level below university degrees. Nevertheless the coupling of education activities in science and the use of english is often seen as attractive.

Our objectives for Education are the following (`http://www.vamdc.org/activities/education/`): to give easy access to atomic and molecular data and information related to these data; to provide innovative pedagogical resources in agreement with the national curriculae in order to illustrate lectures at all level of education; to re-inforce the link between research and education; to create national networks, and to interconnect them at the international level; to be partners of public institutions; to support teachers and lecturers, and bring them our knowledge on our scientific expertise linked to e-science; to offer training on the developed education tools.

6 Conclusion

The VAMDC Consortium continuously welcomes new members and is opened to welcome new type of data. Two main motivations would be considered in order to extend the scope of VAMDC Consortium: 1) a new community of data provider is interested to beneficiate from our experience and from part of our software,

2) one of our user community needs different types of data to be combined with the set of data already available in the VAMDC e-infrastructure. The inclusion of new types of data would certainly impact some of the "VAMDC Consortium" members, therefore the way of integration within the "VAMDC e-infrastructure" would be discussed within the Board of Directors, and the "VAMDC Consortium" members supporting such changes should make a case showing that this community is strategic for reasons such as increase of visibility, new customers, new stakeholders leading to consolidation of sustainability.

The VAMDC Support has been provided through the VAMDC and the SUP@VAMDC projects funded under the "Combination of Collaborative Projects and Coordination and Support Actions" Funding Scheme of The Seventh Framework Program. Call topic: INFRA-2008-1.2.2 and INFRA-2012 Scientific Data Infrastructure. Grant Agreement numbers: 239108 and 313284.

References

Doronin, M., Dubernet, M. L., Walton, N., et al. 2012, in Astronomical Society of the Pacific Conference Series, Vol. 461, Astronomical Data Analysis Software and Systems XXI, ed. P. Ballester, D. Egret, & N. P. F. Lorente, 331

Dubernet, M., Nenadovic, L., & Doronin, N. 2012, in Astronomical Society of the Pacific Conference Series, Vol. 461, Astronomical Data Analysis Software and Systems XXI, ed. P. Ballester, D. Egret, & N. P. F. Lorente, 335

Dubernet, M. L., Aboudarham, J., Ba, Y. A., et al. 2014, in SF2A-2014: Proceedings of the Annual meeting of the French Society of Astronomy and Astrophysics, ed. J. Ballet, F. Martins, F. Bournaud, R. Monier, & C. Reylé, 17–23

Dubernet, M.-L., Alexander, M. H., Ba, Y. A., et al. 2013, A&A, 553, A50

Dubernet, M. L., Boudon, V., Culhane, J. L., et al. 2010, J. Quant. Spec. Radiat. Transf., 111, 2151

Dubernet, M. L., Rixon, G., Doronin, M., & VAMDC Collaboration. 2015, Highlights of Astronomy, 16, 685

Möller, T., Endres, C., & Schilke, P. 2015, ArXiv e-prints [arXiv] 1508.04114

Müller, H. S. P., Endres, C. P., Stutzki, J., & Schlemmer, S. 2012, in 67th International Symposium on Molecular Spectroscopy, 2

Müller, H. S. P., Schlöder, F., Stutzki, J., & Winnewisser, G. 2005, Journal of Molecular Structure, 742, 215

Rixon, G., Dubernet, M. L., Piskunov, N., et al. 2011, in American Institute of Physics Conference Series, Vol. 1344, American Institute of Physics Conference Series, ed. A. Bernotas, R. Karazija, & Z. Rudzikas, 107–115

Zwölf, C., Dubernet, M.-L., Ba, Y., Moreau, N., & Consortium, V. 2014, in IEEE, IST-Africa Conference Proceedings

SF2A 2015
F. Martins, S. Boissier, V. Buat, L. Cambrésy and P. Petit (eds)

MOLECULES IN STELLAR ATMOSPHERES

T. Masseron[1]

Abstract. In order to analyse "warm" stars (G-type, K or M) spectra -mostly optical-, astronomers need specific and accurate molecular lists, which include, at least, their wavelengths and loggf. A non-negligible number of laboratory data and tools already exist in literature, but it is necessary to convert into format useful for stellar spectroscopists. After addressing the recent progress in the field and illustrating them with astronomical applications, I also mention the remaining needs.

Keywords: molecules, stars, spectroscopy

1 Introduction

Molecules appear in the stellar atmospheres of cool stars, namely all stars wiht effective temperature cooler than ∼6000K. In order to infer stellar parameters and surface abundances, stellar spectroscopists use radiative transfer programs to model the star's spectra. One of the fundamental input to those programs are linelists that allow to reproduce simlutaneously all the bound-bound transitions appearing in the spectra. In parallel, with the advance of modern astronomical facilities, the data quality allow now to resolve the stars spectra down to few $m\AA$, i.e. enough to observe any single transition of any atom or molecule. Therefore, it is important now to ensure that all the linelists used to model stellar spectra achieve at least similar precision.

2 Molecular linelists

Molecular linelists as used by stellar spectroscopists consists mainly in a listing of transition wavelengths, their excitation potential and their oscillator strength. Existing program for simulating molecular structures such as PGopher * allow to derive lines position from laboratory constants, while program such as LEVEL † can compute molecular levels wave function and couple them with a provided transition moments to obtain transition strength. Therefore, the combination of the two codes can provide molecular linelists. This what has been done recently to make an accurate new molecular linelist for CN (Sneden et al. 2014) and C_2 (Brooke et al. 2013). However, thermodynamical conditions in stellar atmosphere often allow to observe more transition than observed in laboratories. By combining the molecular structure codes with a stellar radiative transfer code, we were able to improve the molecular constants and thus the linelists for the CH molecule Masseron et al. (2014).

3 Applications

3.1 The first stars

One of the most exciting results coming from large spectroscopic survey such as SDSS, is the discovery of the most ancient stars in the Galaxy. To hunt such object, stellar spectroscopists are looking for the stars with the most pristine composition possible, in other words with the lowest metallic signature in their spectra. The current record older is SMSSJ03100.36 with only an upper limit on its metallicity such as [Fe/H] < -7.5 (Bessell

[1] Institute of Astronomy, Cambridge, UK

*PGOPHER, a Program for Simulating Rotational, Vibrational and Electronic Structure, C. M. Western, University of Bristol, `http://pgopher.chm.bris.ac.uk`

†R. J. Le Roy, Level 8.2: A Computer Program for Solving the Radial Schrodinger Equation for Bound and Quasibound Levels, University of Waterloo Chemical Physics Research Report CP-663 (2014); see `http://leroy.uwaterloo.ca/programs/.Leroy`

© Société Francaise d'Astronomie et d'Astrophysique (SF2A) 2015

et al. 2015). Indeed, its chemical content is so low that its spectra show almost no lines features except many CH and OH molecular lines. Thus, the proper modelling of those molecular features represent nearly the only constrain we have to understand this stellar relic and constrain its formation as well as the first stages of the Galaxy formation.

3.2 Stellar evolution and Galactic population studies

Carbon and nitrogen elements have two important specificities: they can be altered by almost any kind of stars - in particular during their giant phase, and they also show proeminant molecular spectral features such as the well-known G-band due to the CH molecule. By measuring the C and N content via those molecular features, we were able to show that a large sample of field giant stars show relatively low C/N ratios compared to their main sequence companion. This is explained by the fact that those stars have undergone the first dredge-up, where the CN cycled material formed during the main sequence in the core of the star is brought to the surface (Masseron & Gilmore 2015). We also show that the C/N ratio is generally even more decreased once the stars evolve along the upper part of the red giant branch. But the mechanism responsible for such an extra-mixing is still debated.
Moreover, we also use the fact that the C+N/Fe ratio is expected to be conserved throughout the live of the star, thus reflect its initial content independently of the stellar evolutionary stage. We show in Fig. 1 the C+N/Fe ratio in two Galactic population: the thin and the thick disk. In this figure, those two population show a distinct C+N/Fe pattern testifying for their different chemical evolution.

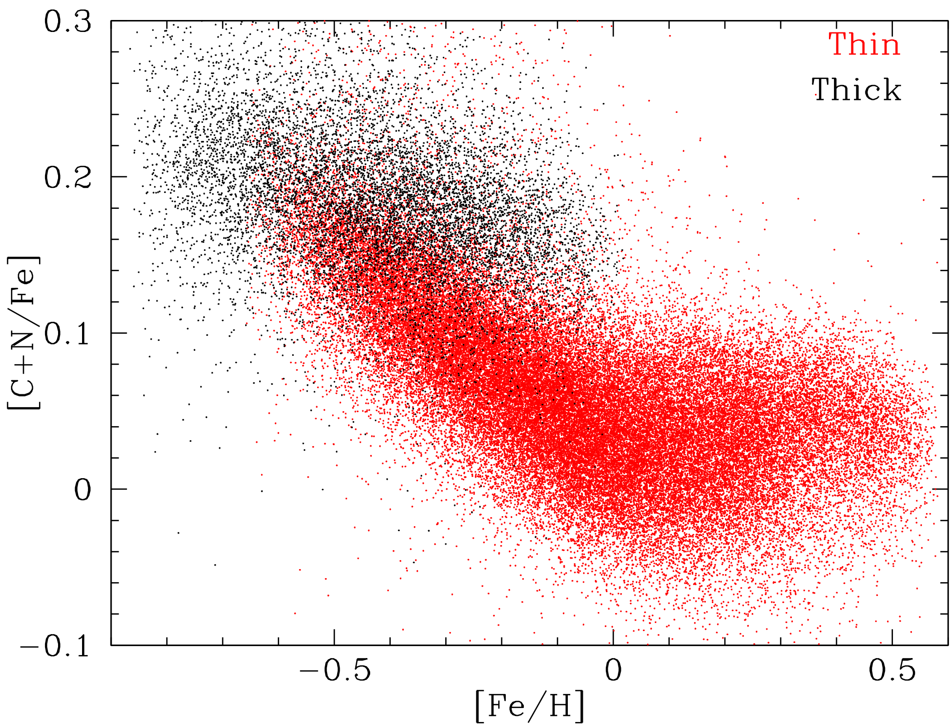

Fig. 1. C+N/Fe ratio in Galactic stars. Red points are thin disk stars while red points are thick disk stars.

4 Conclusions

Despite molecules such as CH and CN are intrinsically very small, their measurement in stars can infer properties of much larger astronomical objects such as stars and our Galaxy. Obviously, the conclusions that can be derive from those molecule are almost entirely dependent on our ability to model them accurately. The examples I show here are based on recently revised molecular linelists that indeed allow to draw some relatively robust conclusions. Nevertheless, it is still not the case for all the molecules present in stellar atmospheres. As an example, I show in Fig. 2 the current status of the TiO molecular linelist as it could be modelled in Gaia spectra. Despite I show here that there is indeed hope for improvement, this still represent only a small portion of the spectrum.

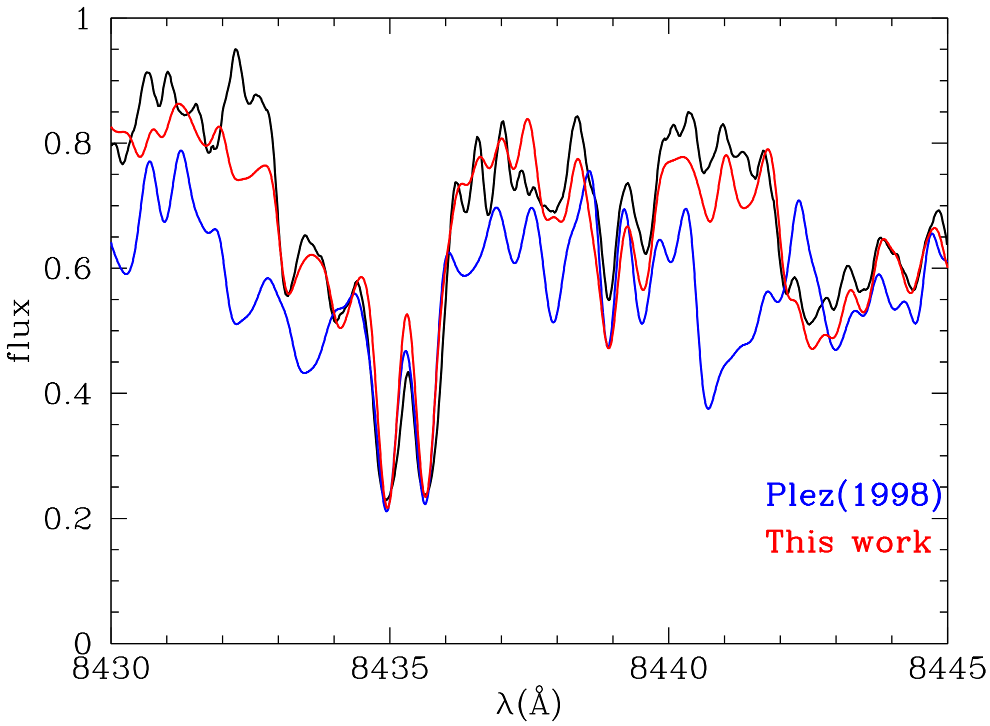

Fig. 2. Example of TiO absorption bands near the Gaia-RVS range. Black: observation. Red: synthesis using my last molecular linelist. Blue: synthesis using the Plez (1998) linelist.

Therefore, in parallel to the efforts made on hydrodynamical stellar simulations, it is crucial to improve fundamental atomic and molecular data. Moreover, molecular measurements in stellar spectra also have the ability to measure more than abundances: they can probe isotopic ratios as well as magnetic field. But for that latter, Lande factors would also need to be calculated via molecular structure programs.

References

Bessell, M. S., Collet, R., Keller, S. C., et al. 2015, ApJ, 806, L16

Brooke, J. S. A., Bernath, P. F., Schmidt, T. W., & Bacskay, G. B. 2013, J. Quant. Spec. Radiat. Transf., 124, 11

Masseron, T. & Gilmore, G. 2015, MNRAS, 453, 1855

Masseron, T., Plez, B., Van Eck, S., et al. 2014, A&A, 571, A47

Plez, B. 1998, A&A, 337, 495

Sneden, C., Lucatello, S., Ram, R. S., Brooke, J. S. A., & Bernath, P. 2014, ApJS, 214, 26

SF2A 2015
F. Martins, S. Boissier, V. Buat, L. Cambrésy and P. Petit (eds)

ATOMIC DATA NEEDS FOR THE MODELLING OF STELLAR SPECTRA

R.Monier[1, 2]

Abstract. The current need for atomic data to model stellar spectra obtained in various wavelength ranges is described. The level of completeness and accuracy of these data is discussed.

Keywords: atomic data

1 Introduction

High quality atomic data are necessary for modelling properly the spectra of stars of various spectral types. The nature of these various data is reviewed here. I also address two crucial issues: i) the completeness of this data and ii) their accuracy.

2 Nature of atomic data

Let us recall that for an atmosphere composed of one layer only, the line profile of an absorption line, I_λ, depends on wavelength as

$$I_\lambda = I_0 \exp(-\tau_\lambda)$$

where I_0 stands for the adjacent continuum and τ_λ is the optical depth which can be expressed as:

$$d\tau_\lambda = -(\kappa_\lambda + l_\lambda)\rho dz$$

where κ_λ and l_λ are the coefficients for continuous and line absorption respectively. The line absorption coefficient can be expressed as:

$$l_\lambda = \lambda_{ij}^2 f_{if} (\frac{N_i}{N}) V$$

where λ_{ij} is the wavelength between the lower level (i) and the higher level (j), f_{ij} the oscillator strength, $\frac{N_i}{N}$ the ratio of absorbers over the total number contributing to the line and V is the normalised Voigt profile.

Under the simple assumption of Local Thermodynamical Equilibrium (LTE), the ratio $\frac{N_i}{N}$ is given by the Saha and Boltzmann equations and the parameters of the transition: the energy E_{ij}, the ionization potential IP, the statistical weight g and the partition function. In the laboratory, the spectroscopist measures the intensity of the line and its position and shape from an emission spectrum. The laser and beam-foil techniques allow to measure the lifetimes of the atomic energy levels and the relative intensities of lines. From these measurements, one can infer:

- the difference in energy between the two levels E_{ij}
- the ionization potential IP
- the degeneracy of the level g
- the transition probability A_{ij}
- the angular momentum quantum number J
- the branching fraction $BF_{ij} = \frac{I_{ij}}{\sum I_j}$

[1] LESIA, UMR 8109, Observatoire de Paris Meudon, Place J.Janssen, Meudon, France
[2] Lagrange, UMR 7293, Universite de Nice Sophia, Nice, France

© Société Francaise d'Astronomie et d'Astrophysique (SF2A) 2015

3 Spectroscopic diagnosis

The local thermodynamical equilibrium (LTE) is verified in a stellar atmosphere when collision processes dominate over radiative processes to populate the levels. If this assumption cannot hold, one should resort to Non Local Thermodynamic Equilibrium (NLTE) and solve the equation of statistical equilibrium:

$$\frac{dn_i}{dt} = \sum_{i \neq j}^{N} n_j P_{ji} - n_i \sum_{i \neq j}^{N} P_{ij} = 0$$

where P_{ij} is the transition probability:

$$P_{ij} = R_{ij}(J_{\nu_0}) + C_{ij}(T)$$

where R_{ij} and C_{ij} refer to the radiative and collicional transitions, J_{ν_0} the local intensity field and T the local temperature. Resolving this equation requires the knowledge of the collision coefficients C_{ij} for the excitation and ionisation of various species of all abundant absorbers. It also requires the knowledge of the photoionization cross sections. As a rule, the occurence of several ionization stages (neutral or ionized) in a stellar spectrum depends on the effective temperature T_{eff}. Typically one does not observe more than three ionization stages in a photosphere if the star does not have a chromosphere, nor a corona.

4 Historical perspective of the production of atomic data

The National Bureau of Standards (NBS) first produced massively atomic data. I refer the reader to NBS monograph 53 published in 1962 (Corliss & Bozman (1962)). It is the first compilation of measured wavelengths and oscillator strengths for 25000 spectral lines observed for 70 chemical elements in the spectral range from 2000 Å up to 9000 Å. This data are affected by systematic errors but some of them are still used today. In 1960, the Massachusets Institute for Technology (MIT) published the MIT wavelength tables which contain about 100000 lines between 2000 Å and 10000 Å. On the other hand, quantum computations have produced massively new atomic data following the MCHF and MCDF formalisms (Multi Configuration Hartree Fock ou Dirac-Fock,Froese Fischer and Taschiev, see http: physics.nist.gov/MCHF, updated Sep 2010)). Similarly Robert Kurucz has produced theoretical calculations (Kurucz (2011)) and so has the team of the Opacity Project (see http:cdsweb.u-strasbg.fr/topbase/op.html)

More recently, the Vienna Atomic Line Database (VALD) has incorporated the new results produced by Kurucz (Kupka et al. (2000)). The National Institute of Standards has produced the NIST database of critically evaluated data on atomic energy levels, wavelengths and transition probabilities and of recent bibliographic data (Kramida (2013), see http:www.nist.gov). The Troisk database also collects new experimental data (Kamid et al (2010)). The trienial reports of Commission 14 (Atomic and Molecular data) of the International Astronomical Union are also important data sources. The DREAM (Database on Rare Earths at Mons University, see w3.umh.ac.be/ astro/dream.shtml, Biemont et al (2005)) provides experimental measurements for the neutral and ionized Lanthanides.

For each of these databases, the question of the completeness and accuracy arise. It all depends on the goal one pursues. The completeness is crucial for opacity computations important for modelling the internal structure and the atmospheric structure of stars. It is necessary to include all strong and weak lines of all elements even if the wavelengths and oscillator strengths are affected by errors. On the other hand, for abundance or velocity fields determinations, one needs high quality atomic data whose errors should be critically evaluated.

5 Stellar spectra at various resolutions

At low resolution (R $\simeq$ 1000), the observed spectra only allow to locate the strongest absorption and emission lines. They can be used to assign a spectral type to a star (Morgan Keenan (MK) spectral tagging). If, in addition, this low resolution data could be calibrated into absolute fluxes, they can be used to test model atmosphere predictions provided the angular diameter of the star is known at various wavelengths.

At intermediate resolution (R $\simeq$ a few 10^3), it is in principle possible to resolve a large number of lines if the lines are not smeared out by rapid rotation. Abundances can be determined by modelling these lines provided they have accurate atomic parameters and they are unblended. The blending depends on the rotation rate and on the individual abundances as well which are a priori unknown.

At high resolution (typically an instrument like the échelle cross-disperser SOPHIE at Observatoire de Haute Provence, R= 75000, or HARPS at ESO, R=115000), one can hope to measure subtle effects of atomic processes on the line profiles such as, for example, isotopic shifts (IS) or hyperfine structure (HFS) or magnetic broadening due to a magnetic field or asymetries in the line wings which are due to depth-dependent convective motions.

6 Problems specific to the ultraviolet region (UV)

The accuracy and completeness of atomic data are rather poor in the UV for elements heavier than the iron-peak elements (Z $\geq$ 28). However, for a few chemical elements, the UV is the only domain where their lines can be found. We can quote Wahlgren (2011) synthesis of the Se II line (Z=34) for the Copernicus spectrum of 3 Cen A (B5 IIIp) which exemplifies well the problem of accuracy. There are no usable Se II lines in the optical range for abundance determinations so this constitutes the first detection of selenium in a star. The oscillator strength for this line stems from a computation but its error is unknown ($\log gf = -0.32$). Adopting this value , the selenium abundance , [Se/H] is found to be 4 times the solar value. However, if one increases $\log gf$ by +0.30, [Se/H] becomes solar. As a consequence, it is not possible to determine accurately the selenium abundance.

6.1 Lack of completeness in the UV

The completeness of atomic data is also an issue in the UV. We can take the example of the spectral synthesis of the hot Am star HD 72660 (Varenne (1999)) at wavelengths shorter than 2000 Å (the far UV). Over the entire far UV many observed lines in the STIS spectrum of HD 72660 do not have counterparts in the synthetic spectrum because their wavelengths and or oscillator strengths are still unknown. So many observed lines cannot be identified. Figure 1 displays the synthesis of the 1655 to 1660 Å wavelength range of the STIS spectrum of HD 72660 which harbours the UV Multiplet 1 resonance lines of C I (indicated by vertical lines, the observed spectrum is in solid lines, the synthetic spectrum in dashed lines). The adopted carbon abundance is that derived from optical spectra by Varenne (1999). The C I lines are properly reproduced, however a number of observed lines are not properly synthezised indicating probably that these lines are still missing in our current linelists. Some of these lines could be Fe II lines measured by Fourier Transform Spectroscopy (FTS) whose oscillator strengths are still unknown. This is due to limited staff resources: several ions should measured by FTS in the laboratory but there is not sufficient funding nor sufficient staff to carry out the experiments. In order to observe at wavelengths shorter than 1400 Å, specific optical materials are necessary (MgF2 beamsplitter). Computed data have complemented laboratory data but their uncertainty is difficult to evaluate if an experimental measurement is not available.

7 Atomic data in the optical

Most of the high excitation lines of iron-peak elements ($E_{low} \geq 60000 cm^{-1}$) do not have oscillator strengths. These lines are formed deep in the atmosphere where LTE prevails and can be used to derive reliable abundances if they have reliable atomic data.

The hot Am star HD 72660 (A1m) whose lines are very sharp ($v \sin i = 6 km.s^{-1}$) can be used to illustrate this problem. The chemical composition of this star is fairly well known from the analysis of lines having accurate NIST data (Varenne (1999)). Using this composition as input to the computation of a synthetic spectrum, one realises three types of problems: i) the oscillator strengths of many lines of the iron-peak elements must be erroneous, ii) weak lines due to the Lanthanides (Ba, Nd, Ce, Eu,...) are poorly synthesized and iii) a number of observed lines remain unidentified. Figure 2 displays the synthesis of the HARPS spectrum of HD 72660 from 4124 Å to 4136 Å. The resonance line of Eu II at 4129.70 Å(with its hyperfine structure of the various isotopes of Europium included) and the Ce II line at 4133.80 Å are clearly detected and are properly reproduced by mild overabundances of about 5 times solar for Europium and 20 times solar for Cerium.

7.1 The case of the low metallicity stars

Several rapid (r) and slow (s) neutron capture elements have been discovered in old stars of very low metallicities. This discovery sets important constraints on the ancient chemical history of the Galaxy. The first works emphasized the detection of light neutron capture elements (Sr, Y, Zr) and of Rare Earths (Ba, La and Eu). For instance, Gilroy et al (1988) compared two metal poor giants of similar fundamental parameters: HD 122563 was found not to be enriched in neutron capture elements whereas HD 115444 turned out to be enriched

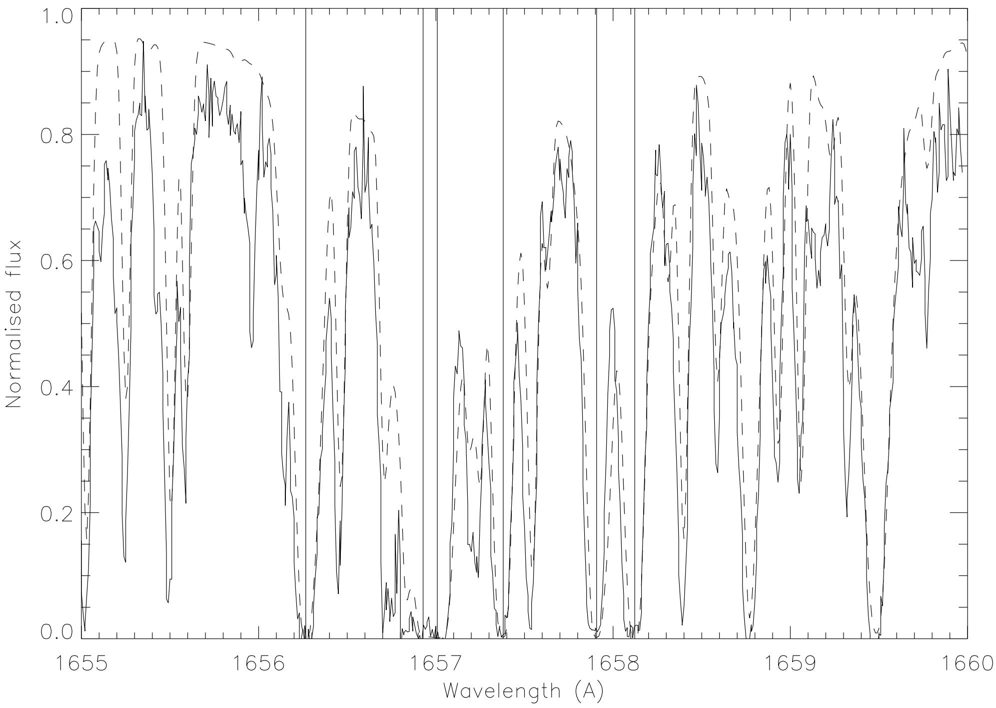

Fig. 1. Synthesis of the C I UV Multiplet 1 for HD 72660 (observed: solid line, model: dashed line)

in neutron capture elements. However, at the time of their analysis, Gilroy et al (1988) could only use a few transitions because few transition probabilities were known and their uncertainties were unknown. Actually, Gilroy et al (1988) used Corliss & Bozman (1962) data for the lines of Dy II and Gd II to derive the abundances of Dysprosium and Gadolinium.

The discovery of cool stars enriched in neutron capture elements has trigered laboratory work. As from 1973, Emile Biémont and his collaborators in Belgium have produced data for Y II, Zr II and Eu II. Other groups in London, Lund and the University of Wisconsin have produced numerous transition probabilities for the Rare Earths from Baryum to Hafnium (Z=72). The teams in London and Lund have focused on elements heavier than Thalium (Ta, Z=73) up to Uranium (U, Z=92). These new data have allowed to greatly improve the abundance patterns of neutron capture elements for metal poor stars (Sneden et al (2014)). Currently, the abundances of 37 neutron capture elements have been determined in CS 22892-052 (Sneden et al (2009)).

8 Atomic data in the Infrared (IR)

The infrared is an important wavelength range for cool stars as their spectral energy distribution reaches a maximum at $\lambda \geq 1\mu m$. The infrared is also instrumental for the study of magnetic fields as the magnetic splitting is proportional to λ^2. It is also important for the measurements of accurate radial velocities, to study molecular species as CO or SiO and atoms (C and N, neutron capture elements) which do not have many lines in the optical range. The IR is also useful to characterize exo-planets between 5 and 10 μm and circumstellar disks. Currently, only 118 oscillator strengths are available at wavelengths greater than 1 μm. For practically

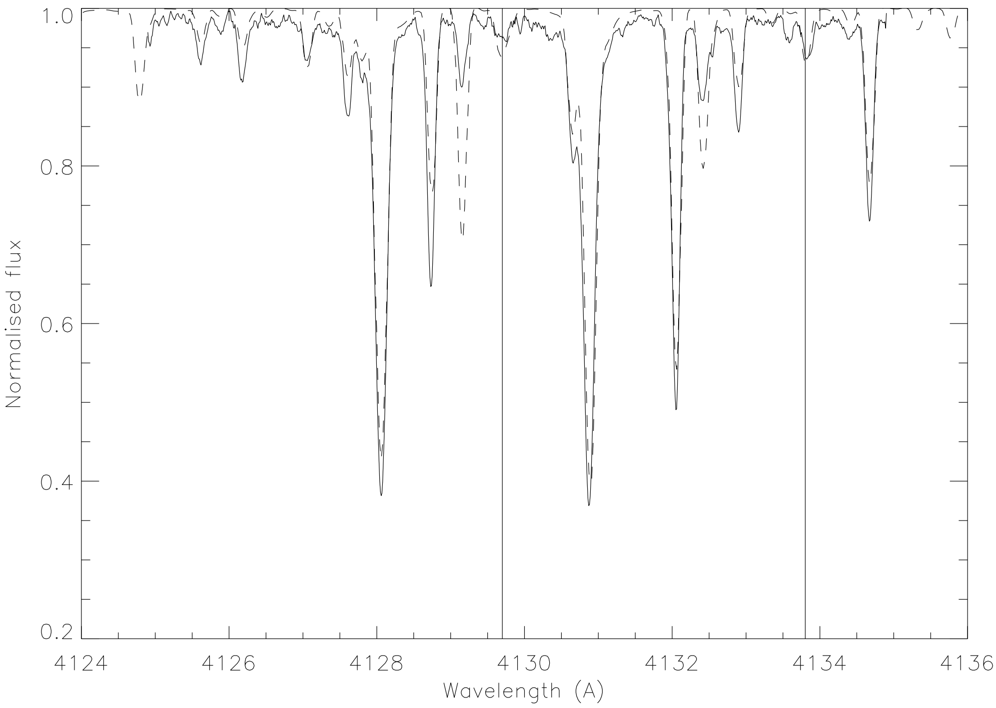

Fig. 2. Detection of Ce II and Eu II lines in HD 72660 (observed: solid line, model: dashed line)

all elements, laboratory spectra are missing for $\lambda \geq 1\mu m$ precluding identifications. Oscillator strengths are missing mostly because branching ratios BF_{ij} are missing.

The branching ratios Bf_{ij} are combined to the lifetimes of the levels τ_j in order to determine the transition probabilities A_{ij}

$$A_{ji} = \frac{BF_{ji}}{\tau_j}$$

and the oscillator strengths f_{ij} are infered by :

$$f_{ji} = 1.499 \times 10^{-8} \frac{g_j}{g_i} \lambda^2 A_{ji}$$

The accuracy on f_{ij} thus depends on the accuracies on λ, τ et BF_{ij}. The main difficulty is to estimate the uncertainty on the BF_{ij}. For solar type stars, spectra like those obtained in the ACE (Advanced Chemistry Experiment) experiment give access to lines which are not acessible in the optical range. The infrared will eventually allow studies of slow and rapid neutron capture elements in evolved stars and in Chemically Peculiar stars.

9 Hyperfine structure and isotopic shifts

The interaction of the magnetic moment of the nucleus , $\vec{\mu_I} = g\frac{e}{2m_p}\vec{I}$ with the magnetic field, $\vec{B_J}$, generated by the orbital motion of the electrons modifies the fine structure. The energy levels are displaced by the quantity:

$$\Delta E_{nhfs} = -\vec{\mu_I}.\vec{B_J} = \frac{A}{\hbar^2}(\vec{I}.\vec{J})$$

The quantum number F verifies:

$$\vec{F} = \vec{I} + \vec{J}$$

and varies from I+J to $|I - J|$).

Each fine structure level is divided into 2I+1 sublevels if $I \leq J$ and into 2J+1 sublevels if $I \geq J$. The magnetic hyperfine splitting ΔE_{mhfs} verifies:

$$\Delta E_{mhfs} = (\frac{A}{2})[F(F+1) - I(I+1) - J(J+1)]$$

In order for instance to properly model the Ni I line at 7414.5 Å in the solar spectrum it is essential to include the hyperfine structure of the 5 isotopes of Nickel: from Ni^{58} up to Ni^{64} (Sneden et al (2014)). The isotopic shifts for Nickel are close to 0.1 Å and are more easily detectable in the infrared.

10 Conclusion

Accurate atomic data are urgently needed in the ultraviolet. The ultraviolet spectra of many elements are still not properly understood. The iron-peak elements have high priorities, in particular Fe II which is ubiquitous and contributes to blends at all wavelengths. In the infrared very few transitions have oscillator strengths. Improving this situation will be essential to the future spatial missions in the IR (SOFIA and JWST) or the VISIR spectrograph at VLT which will be working in the N and Q bands at R=150-30000. For elements having several isotopes, it is highly desirable to include the hyperfine structure and the isotopic shifts for each isotope in order to properly model the observed line profiles at high resolution.

The author thanks Prof. Lydia Tchang-Brillet (Université Pierre et Marie Curie) for her advice at an early stage of this project.

References

Biemont, E., Palmeri, P. and Quinet, P., DREAM - Database on Rare earths at Mons University, 2005

Corliss, C.H., Bozmann, W.R. 1962, National Bureau of Standards, 53

Gilroy, K.K., Sneden, C., Pilachowski, C.A. and Cowan, J.J., 1988, ApJ, 327, 298

Kurucz, R.L. 2011, Can. J. Phys., 417

Kramida, A.E., Atomic energy levels and spectra bibliographic database, version 2.0, NIST, 2013

Kramid, A.E., Ryabtsev, A.V., Vedeneeva, G.Y. and Yakonov E., Bibliography database on atomic spectra, Institue for spectroscopy, Russian Academy of Sciences, Updated May 2010

Kupka F., Ryabchikova T.A., Piskunov N.E., Stempels H.C., Weiss W.W., 2000, Baltic Astronomy, vol. 9, 590-594

Sneden, C., Lawler, J.E., Cowan, J.J., Ivans, I.I. and Den Hartog, E.A., 2009, ApJSup, 182, 80

Sneden, C., Lawler, J.E., Wood, M. D., Den Hartog, E.A. and Cowan, J.J., 2014, Phys. Scr., 89, 114006

Varenne, O., 1999, A&A, 341, 233V

Wahlgren, G., 2011, Can. J. Phys, 89

SF2A 2015
F. Martins, S. Boissier, V. Buat, L. Cambrésy and P. Petit (eds)

CASSIS: A TOOL TO VISUALIZE AND ANALYSE INSTRUMENTAL AND SYNTHETIC SPECTRA.

C. Vastel[1], S. Bottinelli[1], E. Caux[1], J.-M. Glorian[1] and M. Boiziot[1]

Abstract. The advent of high spectral resolution and wide band instruments has left us with an almost overwhelming amount of rich spectra. The analysis of such datasets would be tedious and time consuming, without adequate tools. At IRAP, we have been developing a software, CASSIS, designed to help the astronomer with these tasks. We presented the tool during the SF2A meeting, and the link between databases and interoperability.

Keywords: ISM: molecules, Line: identification, Molecular data, Radiative transfer

1 Introduction

With the wealth of high-resolution, wide-band astronomical spectra that can be and have now been obtained with new generation receivers on ground-based telescopes and with space-based observatories, the need for an efficient and user-friendly software for line analysis has become crucial. Moreover, in order to better understand the physics, dynamics, and chemistry of the observed astronomical objects, it is necessary to develop theoretical models that can be compared with the observations. The goal of the CASSIS software is to provide a set of tools to make such a comparison easier in order to find the best set of parameters that reproduce the observations.
Since 2005, we have developed, at the Institut de Recherche en Astrophysique et Planétologie, the CASSIS line analysis package (Centre d'Analyse Scientifique de Spectres Instrumentaux et Synthétiques[*]) to speed-up the analysis of high spectral resolution spectra (and particularly broad spectral surveys) from ground or space-based telescopes. CASSIS is one "Service d'Observation" of the OVGSO (Observatoire Virtuel du Grand Sud-Ouest) of the OMP (Observatoire Midi-Pyrénées). This package brings together the astronomical data from the telescopes, the telescopes parameters (main bean efficiencies, beam size in order to deal with the beam dilution), the atomic and molecular spectroscopic databases (JPL[†], CDMS[‡], NIST[§]) as well as collisional databases (BASECOL[¶] and LAMDA[‖]) in order to constrain the chemistry and physics of the source, such as the column density (and consequently its abundance), the kinetic or excitation temperature, the molecular hydrogen density, the line width, the line multiplicity.

2 CASSIS design and implementation

2.1 Spectra queries

CASSIS uses the SSA protocol (Single Spectral Access) to access the IVOA (International Virtual Observatory Alliance) services in order to retrieve any spectra (Hubble, Corot, Splatalogue, ISO, etc; the complete list can be found at the http://registry.euro-vo.org webpage) via our SSA module. Also CASSIS uses SAMP (Simple Application Messaging Protocol) that enables astronomy software tools to interoperate and communicate.

[1] Université de Toulouse, UPS-OMP, IRAP, Toulouse, France; CNRS, IRAP, 9 Av. Colonel Roche, BP 44346, F-31028 Toulouse Cedex 4, France
[*] http://cassis.irap.omp.eu
[†] http://spec.jpl.nasa.gov
[‡] http://www.astro.uni-koeln.de/cdms
[§] http://physics.nist.gov/PhysRefData/ASD
[¶] http://basecol.obspm.fr
[‖] http://home.strw.leidenuniv.nl/~moldata

© Société Francaise d'Astronomie et d'Astrophysique (SF2A) 2015

CASSIS can visualise any fits spectra, as well as spectra obtained with the CLASS/GILDAS software, widely used in the millimetre community.

2.2 Molecular databases queries

Line identification and radiative transfer modelling require repeated queries to molecular and atomic databases such as CDMS, JPL, and NIST. CASSIS also provide a database where the ortho/para separation has been performed on some species (H_2D^+, H_2O, H_2CO, NH_3, c-C_3H_2, H_2S and isotopologues) as well as the A/E separation on CH_3OH, CH_3CCH, $HCOOCH_3$. Both CDMS and JPL databases have been used to perform the separation, and the related partition functions are also computed and provided. Regular updates are performed to provide the most recent modifications of the official databases. The whole database is provided during the software installation. CASSIS can also deal with your own private catalog. It is also able to retrieve some useful information for the modelling or identification from databases (CDMS, JPL, BASECOL) through the VAMDC (Virtual Atomic and Molecular Data Centre) TAP protocol (Table Access Protocol) based on IVOA format. TAP provides virtual data and allows to plug in the query language VSS2 and the data model VAMDC-XSAMS (the latter being an output format).

2.3 Radiative transfer modelling

In order to constrain the chemical and physical properties of an astronomical source, you can use the radiative transfer modelling provided by the CASSIS software. All the details on the theory can be found on the CASSIS website (Formalism for the CASSIS software**, author: C. Vastel). Any prediction of spectra can be done from many telescopes provided by the software, using the spectroscopic databases (frequencies, energy levels, statistical weights, Einstein coefficients). Presently a LTE model as well as the RADEX (van der Tak et al. 2007) code are available. These models need some information about the source (size of the source, column density, excitation or kinetic temperature, H_2 molecular density, velocity in the local standard of rest, values of the continuum) which is provided as templates that can be exported or imported into the CASSIS database. The telescopes informations are provided as ASCII files (will soon be xml files) so that any telescope can be very easily added or modified. The software can obviously deal with emission and/or absorption features, depending on the excitation temperature and the value of the continuum. This allows, among a number of tools, to compute synthetic models to be compared with the observations via χ^2 minimization with regular grids of models or using the Markov Chain Monte Carlo algorithm. An example of the main CASSIS user interface is shown in Figure 1. The best fit LTE modelling of the CH species is presented in red, and compared with the Herschel/HIFI observations. The spectroscopic parameters are given when the user clicks on each transition, and the resulting opacity from the LTE modelling are also given.

Currently CASSIS harbours a rotational diagram tool. The observed integrated lines can be fitted (Levenberg-Marquardt or Amoeba fitter) and stored into a file which is called by the rotational diagram tool; the latter then yields the estimated column density and excitation temperature of the studied species (both with error bars) as well as the probability of occurrence (P-value) for a χ^2 value depending on the number of degrees of freedom. A set of results can be obtained varying the source size, but no automated best-fitting tool is available yet. One can also apply the opacity correction module if some of the points might not be optically thin. A change in the temperature for lines of different excitation might indicate that the source has different temperature components or that the lines considered are not optically thin and cannot be easily used to obtain a meaningful excitation temperature. As Goldsmith and Langer (1999) nicely said, this method requires quite a large number of transitions spread over a range of upper state energies. If you plan on performing a population diagram analysis on 2 points only, CASSIS will evidently not be able to provide the errors on the column density and excitation temperature nor the χ^2 and probability values. Note that CASSIS can perform the rotational diagram analysis assuming optically thin lines for multiplet transitions ($\sim$ same frequency, $\sim$ same upper energy), but not on blended transitions ($\sim$ same frequency, different upper energy). Also, the opacity correction cannot be performed on any of these transitions for the moment. After using the Rotational Diagram module, you might want to use the column density and excitation temperature values in the Line Analysis module in order to compare the synthetic spectrum with your observations. An example of the rotational

**http://cassis.irap.omp.eu/docs/RadiativeTransfer.pdf diagram module is shown in Figure 2 on 11 transitions in the Herschel/HIFI frequency range. The blue fit corresponds to a linear fit, giving the excitation temperature and total column density for CO. The red fit corresponds to a linear fit taking into account the opacity effect, more important for low energy levels. It results in a lower excitation temperature and a higher column density.

3 Perspectives

In addition to these features, we propose to provide a tool to interface the results of a number of publicly available codes and the visualization/analysis part of CASSIS. For a given code, the tool would allow the user to define the parameter space to be investigated (range and step for each parameter needed by the code) and where to store the results ; it would then run the code on a dedicated server for all sets of parameter values. Finally, CASSIS would perform the χ^2 minimization as it currently does for LTE and RADEX, and plot the result corresponding to the best set of parameters. The originality of the project presented here resides in the added value for the astronomers. Indeed, presently an astronomer has to define and code in his preferred environment all the steps needed to compare the results of a given model with an astronomical spectrum. He/she has to : (i) identify the lines of a desired species in a generally crowded spectrum (due to the current sensitivity of the instruments) ; (ii) install the available codes and define the grids on which the computation will be done, and (iii) define the minimization algorithm to find the physical parameters that best reproduce his/her data. What we propose to provide with this project is a common environment that will allow the user to easily define the grids on which the computation will be performed, but also a common minimization module for all models. This will allow to perform a comparison of the results of different models, using the same input assumptions. The link to VAMDC (Virtual Atomic and Molecular Database Center) and observational spectral databases via the Virtual Observatory (VO) protocols VAMDC-TAP and SSAP is already implemented in CASSIS, and we will make this VO access functionality also available for databases of physical parameters of astrophysical sources when they will become available. It is useful to check the most up to date spectroscopic data provided through VAMDC, as well as how to deal with the quantum numbers, that can be quite complex to identify from a non-expert in spectroscopy astronomer. Some models (RATRAN, LIME for example) can need large computer resources for large grids of models, therefore the Synthetic Spectra Builder will be developed to run in batch mode on any existing dedicated computing cluster. This will be made available through the STOP (Spectral TOols Platform, 2015, PI: S. Bottinelli) project funded for $\sim$15 months.

4 Conclusions

CASSIS is used in the community to deal with large spectral surveys (Herschel/HIFI, IRAM/30m), but also to prepare proposals for single-dish or interferometric astronomical facilities (IRAM NOEMA, IRAM 30m, ALMA, JCMT, SMA, CSO, HIFI etc...). It has been offered as a HIPE plug-in from version 5.0 of HIPE[††]. HIPE (Herschel Interactive Processing Environment) is a software package to interactively process Herschel data, including finding the data products, interactive analysis, plotting of data, and data manipulation. Using any CASSIS model inside HIPE creates a new HIPE variable. It is possible to overlay any CASSIS model with others CASSIS models or to display it in a new HIPE view. The software is constantly evolving, with the telescopes developments as well as new functionalities from astronomers feedback requests.

References

Goldsmith, Paul F.; Langer, William D., 1999, ApJ 517, 209

van der Tak, F. F. S.; Black, J. H.; Schoier, F. L.; Jansen, D. J.; van Dishoeck, E. F., 2007, A&A 468, 627

[††] http://herschel.esac.esa.int/HIPE_download.shtml

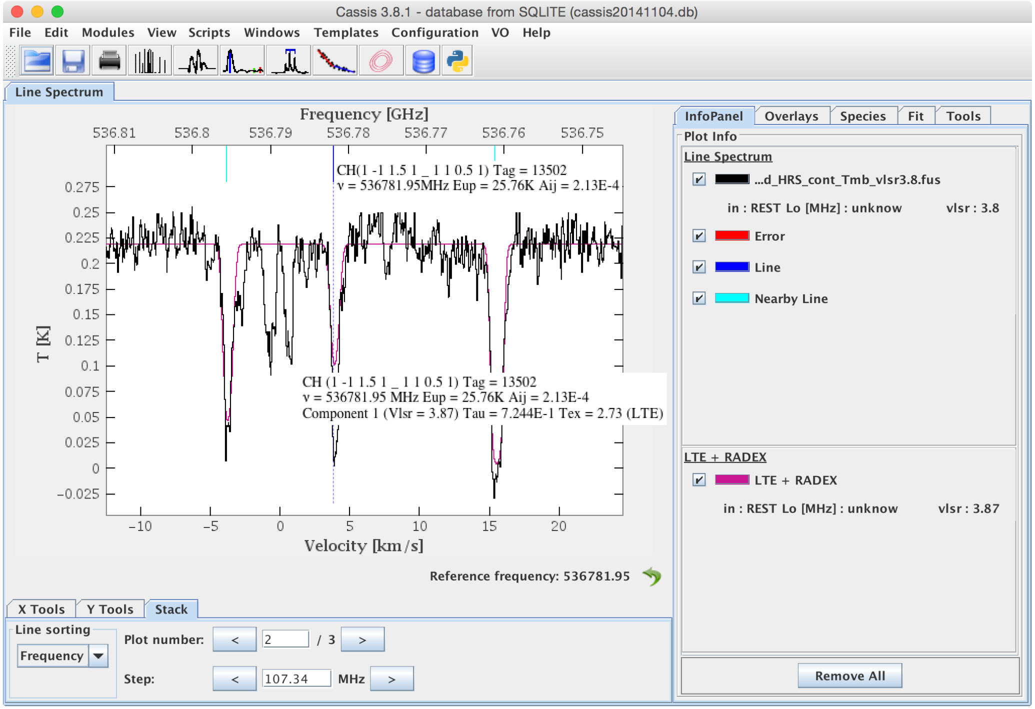

Fig. 1. A screenshot of the main CASSIS window, showing an observed spectrum in black overlaid with a synthetic spectrum in pink. The blue lines indicate the position of the transitions of the species of interest, here CH. A click on these lines display spectroscopic information. Clicking on any modelled line also gives the excitation temperature, Tex, used to produce the model, as well as the opacity, which depends on the assumed column density.

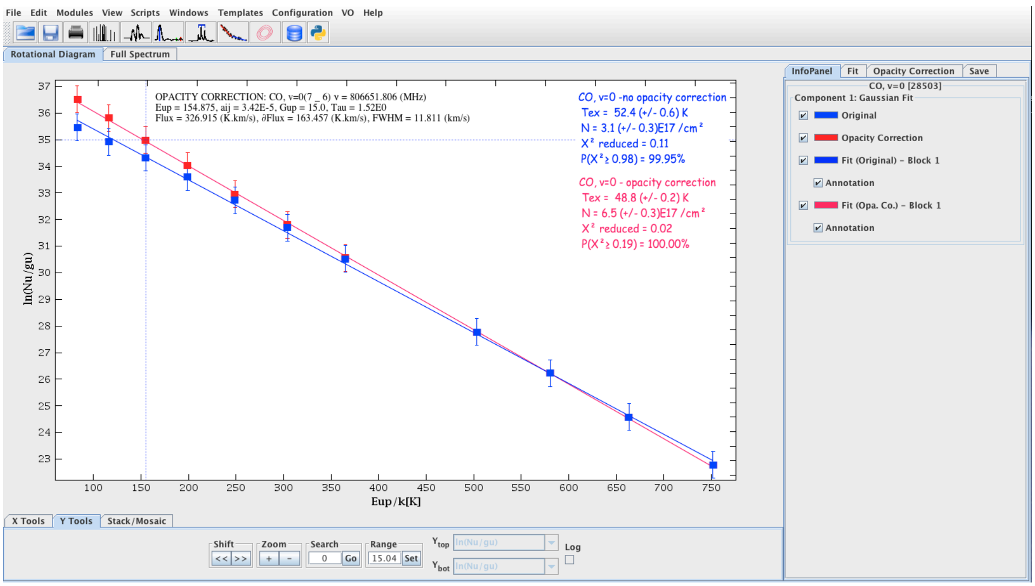

Fig. 2. A screenshot of the CASSIS window, showing the rotational diagram analysis without opacity correction (blue) and with opacity correction (red). Clicking on any line also gives the spectroscopic parameters as well as the line flux.

Session 12

Stades ultimes

SF2A 2015
F. Martins, S. Boissier, V. Buat, L. Cambrésy and P. Petit (eds)

CONSTRAINTS ON THE EXPLOSION MECHANISM AND PROGENITORS OF TYPE IA SUPERNOVAE

S. Blondin[1], Luc Dessart[2], D. John Hillier[3] and Alexei M. Khokhlov[4]

Abstract. We present 1D non-LTE time-dependent radiative-transfer simulations of Type Ia supernova (SN Ia) ejecta resulting from different explosion mechanisms and white dwarf (WD) progenitor masses, and confront our results to SN Ia observations over the first ~ 100 d of their evolution. While the "standard" Chandrasekhar-mass delayed-detonation model reproduces the observed properties of SNe Ia near maximum light over a wide range of peak luminosities, the high luminosity and blue optical colours seen at early times in several SNe Ia appears to require some hydrodynamical interaction affecting the outermost ejecta layers, here in the form of a strong pulsation. Moreover, the fast light-curve evolution of the least luminous SNe Ia seem to require WD progenitors below the Chandrasekhar mass. The observed diversity of the SN Ia population can thus be reproduced with multiple progenitor channels and explosion mechanisms. In this context, departures from spherical symmetry only play a minor role.

Keywords: radiative transfer, supernovae

1 Introduction

Type Ia supernovae (SNe Ia) likely result from the thermonuclear explosion of a C/O white dwarf (WD) star (Hoyle & Fowler 1960). The energy released from fusion of C/O to iron-peak elements unbinds the star, accelerates the ejecta to velocities $\sim$10000 km s^{-1}, and synthesizes copious amounts ($\lesssim 1\,\mathrm{M}_\odot$) of ^{56}Ni to power the light curve ($L_{\rm bol} \approx 10^{43}\,\mathrm{erg\,s^{-1}}$ at peak; Colgate & McKee 1969). The "standard" model for SNe Ia consists of a WD approaching the Chandrasekhar-mass limit ($M_{\rm Ch} \approx 1.4\,\mathrm{M}_\odot$) through accretion of H/He-rich material from a non-degenerate binary companion (Whelan & Iben 1973). Alternatively, such explosions could result from the merger (or collision) of two WDs, in which case the total mass would differ significantly from $M_{\rm Ch}$ (Iben & Tutukov 1984; Webbink 1984; see also van Kerkwijk et al. 2010; Pakmor et al. 2012).

In what follows, we present the results from radiative-transfer simulations for three classes of SN Ia models. The explosion hydrodynamics is described by the reactive flow Euler equations of fluid dynamics which are solved with a one-dimensional Lagrangian hydrodynamics code (see Khokhlov 1991). The calculation is carried out until the ejecta mass shells reach a ballistic regime (homologous expansion), less than ~ 1 min past explosion. Detailed nucleosynthesis is calculated by post processing temperature, density, and neutronization histories of fluid elements with a detailed reaction network.

The long-term evolution is computed with the 1D, time-dependent, non-LTE radiative-transfer code CMFGEN (Hillier & Dessart 2012; Dessart et al. 2014c), which includes the treatment of non-local energy deposition and non-thermal effects (e.g., Dessart et al. 2014b). The output of such calculations are light curves and spectra that can be directly confronted to SN Ia observations.

[1] Aix Marseille Université, CNRS, LAM (Laboratoire d'Astrophysique de Marseille), UMR 7326, 13388 Marseille, France.
[2] Laboratoire Lagrange, UMR 7293, Université Nice Sophia-Antipolis, CNRS, Observatoire de la Côte d'Azur, 06300 Nice, France.
[3] Department of Physics and Astronomy & Pittsburgh Particle Physics, Astrophysics, and Cosmology Center (PITT PACC), University of Pittsburgh, Pittsburgh, PA 15260, USA.
[4] Department of Astronomy & Astrophysics, the Enrico Fermi Institute, and the Computation Institute, The University of Chicago, Chicago, IL 60637, USA.

© Société Francaise d'Astronomie et d'Astrophysique (SF2A) 2015

2 Standard Chandrasekhar-mass models

In this first class of Chandrasekhar-mass models, the burning starts as a subsonic deflagration, followed by a supersonic detonation once the density ahead of the flame front reaches some transition density, ρ_{tr}. By varying ρ_{tr}, one changes the density at which the detonation wave burns the remainder of the WD, hence the production of ^{56}Ni at the expense of intermediate-mass elements, and in turn the peak SN Ia luminosity. In Blondin et al. (2013) we explored a grid of such "delayed-detonation" models with ^{56}Ni masses ranging between $0.12\,M_{\odot}$ and $0.85\,M_{\odot}$, and found an excellent agreement with SN Ia observations near maximum light, from the luminous SN 2009ig to the low-luminosity SN 1999by (Fig. 1, left).

Moreover, an in-depth study of model DDC15 ($M_{^{56}\mathrm{Ni}} = 0.51\,M_{\odot}$) showed that such standard delayed detonations were particularly well suited to SNe Ia with broad Si II 6355 Å lines, such as SN 2002bo (Fig. 1, right; Blondin et al. 2015). The agreement over the first ~ 100 d since explosion suggests the chemical stratification of this model is adequate. Moreover, our assumption of spherical symmetry is not detrimental to reproducing the radiative properties of standard SNe Ia. Interestingly, similar conclusions (chemical stratification and spherical symmetry) are reached from X-ray observations of SN Ia remnants (e.g., Badenes et al. 2006).

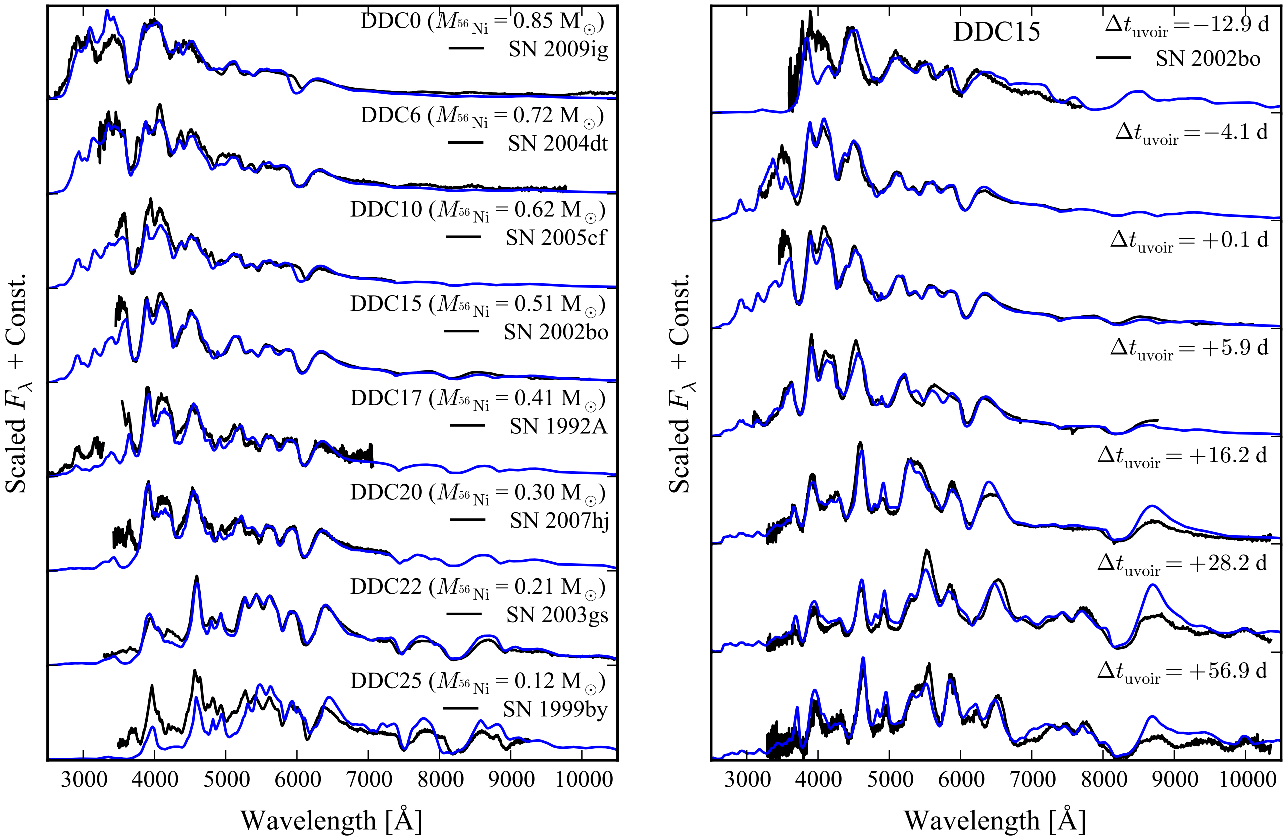

Fig. 1. Left: Comparison of synthetic spectra of standard Chandrasekhar-mass delayed-detonation models (blue) to observed SNe Ia near maximum light (black). The models have been ordered by decreasing ^{56}Ni mass (i.e., decreasing peak luminosity). This figure is similar to Fig. 5 of Blondin et al. (2013) but with updated versions of the models. **Right:** Optical spectroscopic evolution of model DDC15 (blue) compared to SN 2002bo (black), between -12.9 d and $+56.9$ d from ultraviolet-optical-infrared ("uvoir") bolometric maximum. See Blondin et al. (2015) for details.

3 Pulsating Chandrasekhar-mass models

Despite the successes of the standard delayed-detonation model, the predicted luminosity during the first few days past explosion is too low compared to observations (e.g., the nearby SN 2011fe in M101), and the optical colours too red. Moreover, these models are unable to reproduce the narrow Si II 6355 Å line and the slow evolution of its velocity at maximum absorption seen in so-called "low-velocity-gradient" (or LVG) SNe Ia, nor the absorption features associated with C II 6580 Å that probe the initial WD composition.

All these problems are overcome with the class of models known as pulsating delayed-detonations (PDD). In our setup, the deflagration is artificially quenched, allowing the inner WD layers to recollapse before the detonation is initiated — the outermost layers escape burning altogether. The hydrodynamical interaction between the (outgoing) detonation wave and the infalling WD material produces a dense shell with a steep density fall-off on its outer edge (the "cliff" at $\sim 15000\,\mathrm{km\,s^{-1}}$ in model PDDEL4; see Fig. 2, upper left panel) and a larger temperature in the outer low-density shocked material compared to a standard delayed-detonation model with a similar ^{56}Ni mass (DDC15; Fig. 2, lower left panel). The result is a higher luminosity at early times, more compatible with that observed for SN 2011fe (Fig. 2, upper right panel), as well as bluer optical colours reflected in the SED at two weeks before maximum light (Fig. 2, lower right panel).

Moreover, the presence of unburnt carbon at lower velocities combined with the higher temperature favours the emergence of C II 6580 Å absorption features seen in some early-time SN Ia spectra. Last, the presence of a density "cliff" results in a slower evolution of the spectrum-forming region in velocity space, and hence offers a natural explanation for SNe Ia of the LVG subclass. Interestingly, the association of C II detections with LVG events has been confirmed observationally by several authors (e.g., Parrent et al. 2011).

Such a "pulsation" configuration affects the outer ejecta layers and hence can bring diversity at early times in a spherically-symmetric ejecta and independent of the ^{56}Ni mass, which affects the evolution around maximum light and beyond. Despite the artificial setup, these models illustrate the impact of a hydrodynamical interaction on the predicted observables, as could arise for instance in a binary WD merger event.

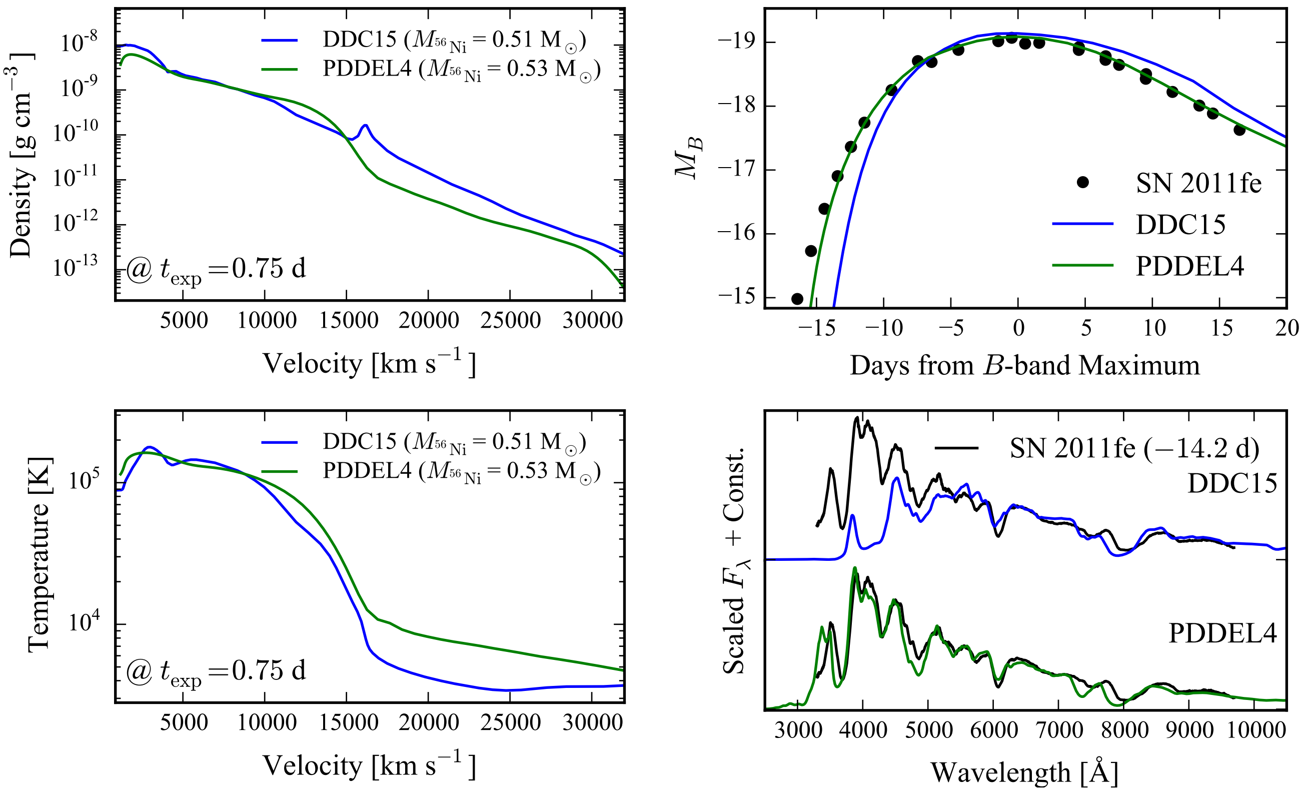

Fig. 2. Left: Density (upper panel) and temperature (lower panel) profiles at 0.75 d past explosion for the standard Chandrasekhar-mass delayed-detonation model DDC15 (blue) and the pulsating Chandrasekhar-mass delayed-detonation model PDDEL4 (green). Note the density "cliff" at $\sim$15000 km s^{-1} and the hotter outer ejecta layers in the pulsating model. **Right:** Comparison of the absolute B-band light curves (upper panel) and spectra at −14 d from maximum light (lower panel) of models DDC15 and PDDEL4 to corresponding observations of SN 2011fe. The model spectra have been scaled to match the V-band flux of SN 2011fe. The hotter outer ejecta in the pulsating model result in a more luminous and bluer event at early times. See Dessart et al. (2014a) for details.

4 Sub-Chandrasekhar-mass models

With the two classes of Chandrasekhar-mass delayed-detonation models discussed above it appears one can reproduce the full range of observed SN Ia luminosities while accounting for some diversity at a given peak luminosity. However, these models fail to reproduce the fast light-curve evolution for the least luminous events, similar to the prototypical SN 1991bg (cf. the V-band light curve for model DDC25 compared to the "91bg-like" SN 1999by in the right panel of Fig. 3). The main reason lies in the amount of mass above the (centrally concentrated) ^{56}Ni-rich layers: for our Chandrasekhar-mass model DDC25, 99% of the total ^{56}Ni mass ($\sim 0.12\,M_\odot$) is located at a mass coordinate $\lesssim 0.8\,M_\odot$, i.e. $\sim 0.6\,M_\odot$ below the WD surface layers (Fig. 3, left).

The explosion of WDs below the Chandrasekhar mass offers an attractive alternative to the delayed-detonation models. For these low-mass WDs, the ignition of the C/O fuel can result either indirectly through the surface detonation of a thin He-rich accreted layer leading to compression of the core ("double-detonation"), or through a WD-WD merger whose combined mass is less than $\sim 1.4\,M_\odot$.

In our sub-Chandrasekhar-mass model SCH2p0, corresponding here to the pure detonation of a $0.88\,M_\odot$ C/O WD star, the same amount of ^{56}Ni extends over a larger fraction of the total ejecta mass, leading to a shorter diffusion time for radiation, and hence a faster rise to peak (~ 16 d cf. ~ 21 d to bolometric maximum). The post-maximum luminosity decline is also faster, since the lower ejecta densities favour the direct escape of γ-rays and leakage of optical photons. Sub-Chandrasekhar-mass models thus lead to narrower light curves for a given ^{56}Ni mass (and hence peak luminosity), in better agreement with the observed width-luminosity relation of Phillips (1993) for the least luminous events.

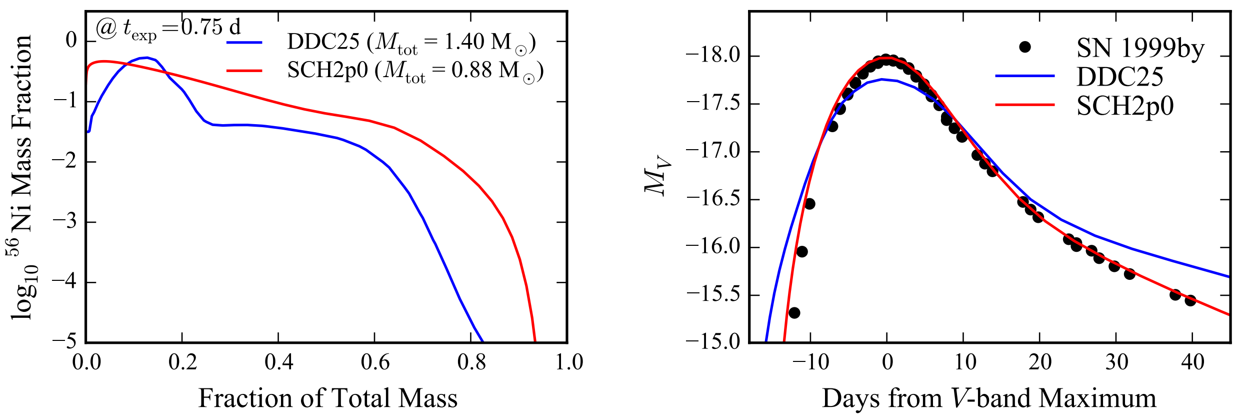

Fig. 3. Left: Abundance profile for ^{56}Ni vs. the fractional mass coordinate ($\equiv M_{\rm Lagrangian}/M_{\rm tot}$) for the standard Chandrasekhar-mass delayed-detonation model DDC25 (blue) and the sub-Chandrasekhar-mass model SCH2p0. **Right:** Absolute V-band light curves of both models compared to the low-luminosity ("91bg-like") SN 1999by, for which we assume a distance modulus of 30.97 mag and a host-galaxy visual extinction $A_V = 0.11$ mag. The lower ejecta mass for model SCH2p0 results in a faster light-curve evolution around maximum light.

5 Conclusions

We have presented three classes of SN Ia models resulting from different explosion mechanisms and white dwarf (WD) progenitor masses. Neither model on its own is able to reproduce the full range of SN Ia properties, suggesting the observed diversity results from multiple progenitor scenarios and explosion mechanisms. Differentiating between these different scenarios requires detailed radiative-transfer calculations, currently only feasible in 1D. While the explosion is expected to be an intrinsically multi-dimensional process, the resulting SN Ia ejecta appear well reproduced by spherically-symmetric models. We will nonetheless compare our 1D models to angle-averaged versions of multi-D calculations in the future.

All our model results are available online at: `https://www-n.oca.eu/supernova/home.html`**.**

LD and SB acknowledge financial support from the European Community through an International Re-integration Grant, under grant number PIRG04-GA-2008-239184, from "Agence Nationale de la Recherche" grant ANR-2011-Blanc-SIMI-5-6-007-01, and from the "Programme National de Physique Stellaire" (PNPS). DJH acknowledges support from STScI theory grant HST-AR-12640.01, and NASA theory grant NNX14AB41G. This work was granted access to the HPC resources of CINES under the allocation c2013046608 and c2014046608 made by GENCI (Grand Equipement National de Calcul Intensif).

References

Badenes, C., Borkowski, K. J., Hughes, J. P., Hwang, U., & Bravo, E. 2006, ApJ, 645, 1373

Blondin, S., Dessart, L., & Hillier, D. J. 2015, MNRAS, 448, 2766

Blondin, S., Dessart, L., Hillier, D. J., & Khokhlov, A. M. 2013, MNRAS, 429, 2127

Colgate, S. A. & McKee, C. 1969, ApJ, 157, 623

Dessart, L., Blondin, S., Hillier, D. J., & Khokhlov, A. 2014a, MNRAS, 441, 532

Dessart, L., Hillier, D. J., Blondin, S., & Khokhlov, A. 2014b, MNRAS, 439, 3114

Dessart, L., Hillier, D. J., Blondin, S., & Khokhlov, A. 2014c, MNRAS, 441, 3249

Hillier, D. J. & Dessart, L. 2012, MNRAS, 424, 252

Hoyle, F. & Fowler, W. A. 1960, ApJ, 132, 565

Iben, Jr., I. & Tutukov, A. V. 1984, ApJS, 54, 335

Khokhlov, A. M. 1991, A&A, 245, 114

Pakmor, R., Kromer, M., Taubenberger, S., et al. 2012, ApJ, 747, L10

Parrent, J. T., Thomas, R. C., Fesen, R. A., et al. 2011, ApJ, 732, 30

Phillips, M. M. 1993, ApJ, 413, L105

van Kerkwijk, M. H., Chang, P., & Justham, S. 2010, ApJ, 722, L157

Webbink, R. F. 1984, ApJ, 277, 355

Whelan, J. & Iben, I. J. 1973, ApJ, 186, 1007

SF2A 2015
F. Martins, S. Boissier, V. Buat, L. Cambrésy and P. Petit (eds)

NUMERICAL SIMULATIONS OF AXISYMMETRIC BONDI-HOYLE ACCRETION ONTO A COMPACT OBJECT

I. El Mellah[1] and F. Casse[1]

Abstract. Compact bodies which are not at rest compare to an homogeneous ambient environment are believed to undergo Bondi-Hoyle axisymmetric accretion as soon as their relative velocity reaches supersonic levels. Contrary to its spherical counterpart, B-H accretion presents flow structures difficult to analytically derive, hence the need for numerical investigations. The broad dynamics at stake when a tiny compact object engulfs surrounding material at a much larger scale has made numerical consistency a polemical issue as it has prevented both scales to be grasped for reasonable wind velocities. We designed a numerical setup which reconciliates the requirement for finite size accretor with steady states properties of the Bondi-Hoyle flow independent of the size of the inner boundary. The robustness of this setup is evaluated accordingly to predictions concerning the mass accretion rate evolution with the Mach number at infinity and the topology of the sonic surface as determined by Foglizzo & Ruffert (1996). It provides an estimation of the mass accretion rates and thus, of the expected X-ray luminosity for an idealized B-H configuration which might not be too far off for isolated compact objects like runaway neutron stars or hyper-luminous X-ray sources.

Keywords: subject, verb, noun, apostrophe

1 Introduction

Accretion of matter by a gravitationally centred field has been an active topic of study over the last decades, as the X-ray satellites unveiled more and more systems where such an interplay was believed to occur in some way. Starting with the Bondi's spherical model of a non-zero temperature stationary flow at infinity (Bondi 1952) enabled quantitative predictions to be derived but soon turned out to be irrelevant in most astrophysical configurations, where the relative motion of the accreting body compare to the ambient medium did matter : super-giant X-ray binaries (Walter et al. 2015), runaway neutron stars (Cordes et al. 1993), symbiotic binaries (Theuns et al. 1996; de Val-Borro et al. 2009), hyper-luminous X-ray sources Pfahl et al. (2002),... Many interpretations had everything to gain at seeing axisymmetric models of accretion to be developed. Well before X-ray pathfinders, Hoyle, Lyttleton and afterwards, Bondi had laid the foundations of an axisymmetric model of a zero temperature supersonic flow at infinity, henceforward referred to as B-H or wind accretion (Hoyle & Lyttleton 1939; Bondi & Hoyle 1944). It is usually the starting point to investigate the influence of more sophisticated considerations as inhomogeneities (Ruffert 1996, 1999), hydrodynamical terms (Horedt 2000), finite size accretors (Ruffert 1994a), small or large scale magnetic fields (Igumenshchev & Narayan 2002; Igumenshchev 2006; Pang et al. 2011), orbital effects (Theuns & Jorissen 1993), radiative feedback (Park & Ricotti 2013), turbulence (Krumholz et al. 2006), net vorticity (Krumholz et al. 2005), etc ; the wind accreting systems grew as they ramified.

In parallel, the new computational capacities offer us the opportunity to unveil the physical phenomena at stake behind the scenes with the search for numerical setups able to reproduce the observational classification. Numerical simulations of B-H accretion started to blossom in the late 80's with a series of works investigating the influence of the hydrodynamical (HD) terms. The stability of the B-H flow was put into question with numerical results glimpsing various instabilities without being able to agree whether their origin was physical or not (see Foglizzo et al. 2005, and references therein). Progress were made in simulating accretion onto not compact objects but the wide dynamics introduced by the small size of a compact object compare to its gravitational

[1] Laboratoire AstroParticules et Cosmologie - Université Paris 7 Diderot - Paris, France

© Société Francaise d'Astronomie et d'Astrophysique (SF2A) 2015

sphere of influence on non-relativistic winds has prevented numerical simulations to converge to a B-H accretion solution around a compact object up to now. A major theoretical step was undertaken with the study of spherical accretion of a flow with a non vanishing velocity at infinity, mixing ballistic and pressure effects all together (Theuns & David 1992). The same blending remained to be done for axisymmetric geometries until Foglizzo & Ruffert (1996), henceforth FR96, linked the sonic surface* of a B-H flow to the simpler one of the spherical configuration.

In this proceeding, our primary goal is to describe a robust axisymmetric numerical setup we designed to take the most of the high performance computing methods implemented in the MPI-parallelized Adaptive Mesh Refinement Versatile Advection Code (MPI-AMRVAC). We constantly monitored our results to compare them to firmly established analytical constraints, derive accurate numerical mass accretion rates and study the steady state structure of the flow (transverse profiles, sonic surface...). Using a continuously nested logarithmic mesh with a shock-capturing algorithm and specific boundary conditions, we can resolve the flow from the vicinity of the central compact object up to the significant deflection scale, at an affordable computational price and with realistic wind velocities. According to the properties of B-H accretion on finite size objects recalled in Ruffert (1994a), we can finally reach numerical regimes where the size of the inner boundary no longer alters the flow properties. We solve the full set of HD Eulerian equations, including the energy one, with the less restrictive adiabatic assumption instead of considering a polytropic flow and identifying the adiabatic and the polytropic indexes. We investigate the evolution of the properties of the B-H accretion flows we obtain with the Mach number of the flow at infinity, from slightly subsonic to highly supersonic setups.

2 Theoretical overview

2.1 *The ballistic Hoyle-Lyttleton flow and its Bondi-Hoyle refinement*

In their seminal paper, Hoyle & Lyttleton (1939) portrayed a homogeneous supersonic planar flow with a relative velocity and a density at infinity of $\mathbf{v}_\infty$ and ρ_∞, deflected by the gravitational field of a point mass M. As a first approximation, they neglected the influence of the HD terms and solved the equations of motion for a test-mass ; compare to Bondi's spherical model (Bondi 1952), thermodynamics was sacrificed in favour of a more realistic symmetry. In this ballistic framework, the explicit expressions of the trajectories can easily be derived (Bisnovatyi-Kogan et al. 1979). Yet, once the flow reaches the line lying downstream of the gravitational body, dissipative effects are likely to lead to a substantial damping of the orthoradial component of the velocity field, letting the test-mass worn out with a total mechanical energy which turns out to be negative for particles with an impact parameter ζ verifying the Hoyle-Lyttleton accretion condition :

$$\zeta < \zeta_{\text{HL}} = \frac{2GM}{v_\infty^2} \tag{2.1}$$

ζ_{HL} is commonly referred to as the accretion radius or the stagnation point even if, in this picture, particles are left with a non-zero velocity provided by the remaining radial component. G stands for the usual gravitational constant. Given the symmetry of the problem, one can expect that all independent particles in a cylinder of cross section $\pi\zeta_{\text{HL}}^2$ will eventually be trapped in the gravitational potential. Those considerations led Hoyle & Lyttleton to suggest an accretion rate of :

$$\dot{M}_{\text{HL}} = \pi\zeta_{\text{HL}}^2\rho_\infty v_\infty = \frac{4\pi G^2M^2\rho_\infty}{v_\infty^3} \tag{2.2}$$

As a first attempt to include HD effects, accretion column models were developed considering a thin but non zero accretion wake (see Edgar 2004, for a pedagogical review). Those two-flow models (supersonic B-H deflected flow supplying matter and momentum / one-dimensional channelled flow along the column) led to a non linear system of ordinary differential equations describing the dynamics of the accretion column ; investigations of the latter suggested that the position of the stagnation point and thereby, the value of the mass accretion rate, could vary by an order-of-unit factor around the Hoyle Lyttleton mass accretion rate given by (2.2). Yet, for the sake of solvability, those studies either neglected the pressure force in the wake (Edgar 2005) or assumed a polytropic relation between pressure and density to bypass the energy equation (Horedt 2000). In a more pragmatic approach, Bondi was led by the similarities between the spherical and the axisymmetric mass accretion rates

*To be understood as the surface where the flow speed oversteps the local sound speed.

formulae to suggest a first interpolation formula between those asymptotic cases, as a first empirical attempt to account for thermal and kinetic effects all together :

$$\dot{M}_{\rm BH} = \dot{M}_{\rm HL} \left(\frac{{\mathcal{M}_\infty}^2}{{\mathcal{M}_\infty}^2 + 1} \right)^{\frac{3}{2}} \tag{2.3}$$

where $\mathcal{M}_\infty$ is the Mach number of the incoming flow, v_∞ / c_∞.This formula matches the HL mass accretion rate at high Mach numbers but not the Bondi one for low Mach numbers. The non physical origin of this formula led several authors to pinpoint the likely discrepancies which one would observe as soon as a comparison with actual solutions of Eulerian equations are undertaken. The numerical simulations were to confirm this presentiment.

2.2 *Sonic surface of Bondi-Hoyle flows*

In the spherical Bondi accretion formalism, the sonic radius locates the uniquely determined position where a stationary subsonic inflowing gas becomes supersonic :

$$r_0 = \frac{5-3\gamma}{4} \frac{GM}{c_\infty^2 + \frac{\gamma-1}{2} v_\infty^2} \tag{2.4}$$

The intrinsic multi-dimensionality of the Hoyle-Lyttleton flow has prohibited until now any comparable level of detail, concerning the analytical properties of the sonic surface, to be reached. FR96 started to bridge the analytical gap between the spherical Bondi accretion of a flow at rest at infinity and the ballistic pressureless Hoyle-Lyttleton accretion, as they proved a topological property of the sonic surface of B-H flows in relation with the radius of their isotropic counterpart, r_0, with the same Bernoulli's invariant value. They showed that the B-H sonic surface must intersect at least once the sphere of radius r_0. The main analytical constrain entailed by this property is the necessity for the sonic surface of flows with $\gamma = 5/3$ to be anchored into the inner boundary of a simulation, whatever its size since the sonic radius vanishes. FR96 also derived an interpolation formula based on asymptotic expansions near the accretor and considerations about the sonic surface. They suggest, providing an unknown constant of unity-order, that the interpolation formula they determined could fit the stationary mass accretion rates measured.

2.3 *Designing a Bondi-Hoyle axisymmetric setup*

We derive the structure of the B-H flow relying on the MPI-AMRVAC code, further described in Porth et al. (2014). Briefly, the MPI-AMRVAC package consists in a multi-dimensional finite-volume code able to solve, in multiple geometries, the set of equations of hydrodynamics or magnetohydrodynamics for an ideal gas, either in a classical or relativistic framework. In the present proceeding, we called upon a shock-capturing second order in time and space Total Vanishing Diminishing Lax-Friedrichs (TVDLF) scheme and a Koren slope limiter (Koren 1993) to solve the conservative HD equations. So as to properly physically handle the shock, we relax the polytropic assumption and consider the adiabatic energy equation, which might already unveil results beyond the theoretical expectations. Indeed, the main drawback of the polytropic assumption is to add an additional degree of freedom with the polytropic index Γ. Γ has no reason to be equal to the adiabatic index γ (determined by the chemical nature of the flow), as long as the flow is not isentropic (Horedt 2000), which is not our case here because of the expected shock formation. If this founding hypothesis alleviates the introduction of an additional degree of freedom, the price to pay is to refrain the comparison of our results to prediction relying on $\gamma = 5/3$ for it is the adiabatic index of any flow hot enough to be composed of monoatomic (if not, ionized) particles. It also encloses our reflection to compact objects undergoing *adiabatic* wind accretion.

Since the current proceeding reports on axisymmetric properties of the B-H flow, we can work on a spherical 2.5D mesh, where the third component is the longitudinal one, φ, always null. Thus, the cells do respect the full 3D geometry information but the flow is assumed to be invariant by rotation around the polar axis, which spares the mesh to span a third dimension. The incoming wind velocity at infinity is then collinear to the polar axis. Given the reported reasonable stability of the 3D B-H flow against transverse instabilities as the "flip-flop" one at stake in some 2D cylindrical B-H configuration (Blondin & Pope 2009), both theoretically (Soker 1990) and numerically (Blondin & Raymer 2012), we expect such a configuration to give birth to a relatively robust equilibrium from which full 3D simulation should not depart much.

A regular 2.5D spherical grid would suffer two major drawbacks. First, to get a decent radial resolution next to the inner boundary, we would have to work with a huge number of radial cells, which would be painfully time-consuming and would not tell us much more about the relevant dynamics. In addition, the cell aspect ratio $\Delta r/r\Delta\theta$ cannot remain constant all along a radius ; r varying from the inner to the outer boundary by a factor 10^2 to 10^4 (depending on the simulation), a regular grid would give highly deformed cells. As indicated by its name, MPI-AMRVAC presents the capacity to adaptively refine the mesh where needed. A safer swindle (initially introduced for B-H flows by Fryxell & Taam 1988) is to work with a constant aspect ratio, in other words, with a radial step proportional to the radius (hence the " logarithmic grid" designation). It enables us to keep a homogeneous "relative resolution", from the vicinity of the compact object up to the accretion radius. We typically work with $N_\theta = 64$ latitudinal cells and $N_r = 128$,176 or 224 radial cells, depending on the size of the inner radius of the grid ; once the latter is set, we tune the aspect ratio around the unity value to make the outer radius approximately constant from a simulation to another. Given the angular resolution, this approach leads to a radial cell size of the order of a twentieth of the inner boundary one next to it.

The Eulerian equations are associated with usual polar symmetry and antisymmetry conditions along the polar axis. For the outer radial boundary conditions, far ahead the shock, where the flow is supersonic, we prescribe the ballistic solution for v_r and v_θ and the permanent regime solution deduced for ρ from the mass conservation equation by Bisnovatyi-Kogan et al. (1979). We extended the latter to the total specific energy density e. It assures that the gravitational ballistic deflection of the initially planar flow, from infinity to the outer boundary, is taken into account. The downstream outer boundary condition is a continuous one and to avoid any spurious reflection of pressure waves, we set its size r_{out} such as the velocities at the boundary are supersonic. Typically, it requires $r_{\text{out}} \sim 8\zeta_{\text{HL}}$.

Concerning the inner boundary conditions, much caution must be taken. Straightforward absorbing conditions (floor density and continuous velocities e.g., provided they leave the simulation space) do alter the stability of the flow without guarantee of fitting the continuity of the radial flows. One has to not prevent the stationary solution the mass and energy continuity equations to be achieved, e.g. by ensuring the continuity of $\rho v_r r^2$ at the inner boundary : so as to do so, we computed the density in the inner ghost cells with a first order Taylor-Young expansion and deduced the corresponding radial velocities from the continuity of the radial mass flux $\rho v_r r^2$. For the total specific energy e, the conserved quantity is given by the Bernoulli's condition considered for a permanent flow : $(e + P + \rho\varphi)v_r r^2$. The value of v_θ is much less critical and is also set via a simple first order expansion. Such inner boundary condition entitle the flow to reach a permanent regime as the ones described further.

3 Results and comments

3.1 Structure of the shock and sonic surface

First comments can be made about the large scale geometry of the shocks we obtained. Whatever the Mach number as long as we deal with a supersonic unperturbed flow at infinity, the shock is clearly detached, with a shock front at a distance of the compact object large compare to the size of the inner boundary but of the order of a fraction of the critical impact parameter ζ_{HL}. The opening angle of the shock evolves along the axis, with a concave shape for the shock and smaller opening angles for larger Mach numbers. Concerning the transverse profiles in the tail, we first notice that the shock forms a hollow cavity, in agreement with one of the solutions proposed by Bisnovatyi-Kogan et al. (1979).

Although immune against non axisymmetric instabilities as the flip-flop one, our simulations could lead to longitudinal or axisymmetric transverse instabilities (Cowie 1977; Foglizzo et al. 2005). However, the relative distance to the previous state - defined as the standard deviation point by point between the state values (mass density, impulsion, total specific energy density) at a given time step and the previous one - tends to be smaller than 0.0001% once the steady state is reached : no acoustic cycle takes place to maintain or amplify an oscillation in the tail, in spite of the actual production of entropy at the detached shock interface. This stability of the bow shock should not be attributed to an accretor too large given the ratios $\zeta_{\text{HL}}/r_{\text{in}}$ we used but might be linked to a solver excessively diffusive or a spatial resolution too low.

We observe a slight beaming effect along the pole in the B-H simulated flow, probably due to a mesh-alignment effect. We believe it essentially alters neither the conclusions we came to nor the trends we derive for the mass accretion rate or the geometry of the shock for instance. Yet, it must be acknowledged that the quantitative information concerning the latter one might give slightly underestimated positions of the forward shock because of a numerical driving in of artificially focused flow along the axis.

The main result concerning the small scale structure of the flow concerns the aforementioned sonic surface. Our simulations confirm Foglizzo and Ruffert's analytical prediction about the topology of the sonic surface for an adiabatic flow with $\gamma = 5/3$: whatever the size of the inner boundary (left panel of Figure 2 and right panel of Figure 1) or the Mach number of the flow, the sonic surface is always anchored into the inner boundary. It extends along the wake of the accretor, the axisymmetry of the cause being preserved in the consequence. For supersonic flows, the density distribution is mostly isotropic and the streamlines, radial, in the vicinity of the inner boundary. Thus, the accretion is regular in the sense that there is no infinite mass accretion rate direction, although the local mass accretion rate is enhanced by a factor of a few in the back hemisphere compare to the front hemisphere. As a consequence, the non isotropy of the mass accretion rates around the inner boundary is mostly due to the non isotropy of the velocity field ; along the mock accretion line, in the wake of the accretor, the flow has been more reaccelerated than upstream after the shock.

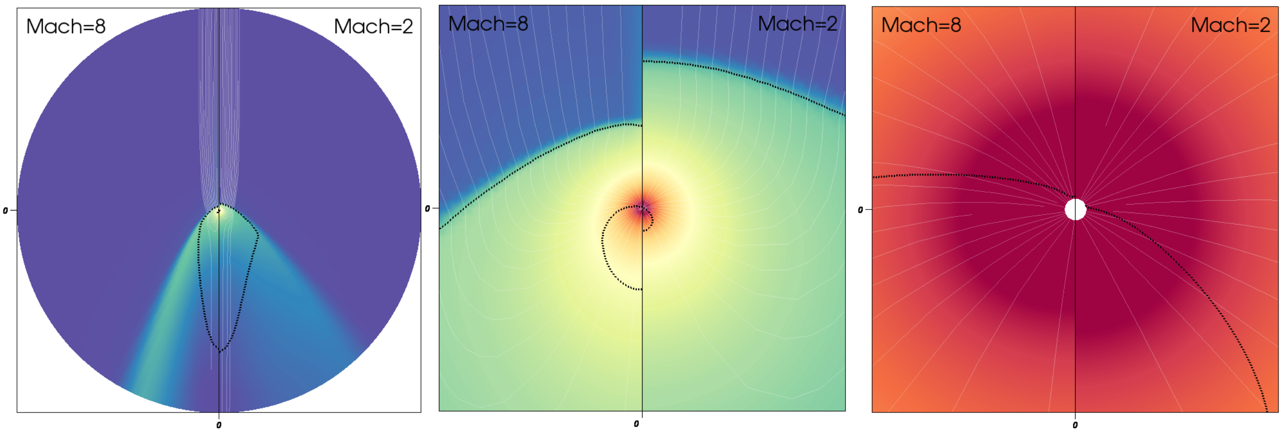

Fig. 1. Logarithmic colour maps of the density for $\mathcal{M}_\infty = 8$ (left panels) and $\mathcal{M}_\infty = 2$ (right panels). Streamlines have been represented in solid white within the accretion cylinder and the dotted black contours stand for Mach-1. Zoom in on the central area by a factor of 20 (centre) and 400 (right).

3.2 Global mass accretion rates

To compare the steady state mass accretion rates at any Mach number, we introduced a homogeneous normalisation variable $\dot{M}_0$ to prevent any privileged point of view between the low and the high $\mathcal{M}_\infty$. The steady-state mass accretion rates $\langle \dot{M} \rangle$ are computed by averaging the instantaneous ones (i.e. the spatially averaged mass accretion rates in the vicinity of the inner boundary, well below the shock front radius) for $t > 10$ crossing-times, once the steady state is reached. The obtained $\langle \dot{M} \rangle$ are presented in the right panel of Figure 2. Data dispersion is dominated by systematics whom influence is given by the two sets of points from the different inner boundary sizes. As expected, the traditional Bondi formula, in blue dotted, matches the Hoyle-Lyttleton mass accretion rate at high Mach numbers, which itself turns out to be an overestimation of the actual mass accretion rate by approximately 30% : it is consistent with the previous reports of $\dot{M}_{\text{HL}}$ being a slight overestimation of the numerically observed mass accretion rates in the asymptotically supersonic regime - see, e.g., Figure 7 of Edgar (2004). Yet, since (2.3) does not properly include thermodynamics (e.g. it does not depend on the adiabatic index), it is a poor estimation in the subsonic regimes, overestimating $\dot{M}$ by a factor up to 4 for $\gamma = 5/3$.

Foglizzo and Ruffert's interpolation formula, represented in red dashes in the right panel of Figure 2, is given by the following interpolation formula :

$$\dot{M}_{\text{FR}} = \dot{M}_{\text{B}} \left[\frac{(\gamma+1)\,{\mathcal{M}_{\text{eff}}}^2}{2+(\gamma-1)\,{\mathcal{M}_{\text{eff}}}^2} \right]^{\frac{\gamma}{\gamma-1}} \left[\frac{\gamma+1}{2\gamma{\mathcal{M}_{\text{eff}}}^2-\gamma+1} \right]^{\frac{1}{\gamma-1}} \tag{3.1}$$

with $\mathcal{M}_{\text{eff}}$ the effective Mach number which depends on a free parameter λ assessing the aforementioned discrepancy between $\dot{M}_{\text{HL}}$ and the observed mass accretion rate at high $\mathcal{M}_\infty$:

$$\dot{M}_{\text{FR}} \xrightarrow[\mathcal{M}_\infty \to \infty]{} \lambda \dot{M}_{\text{HL}} \tag{3.2}$$

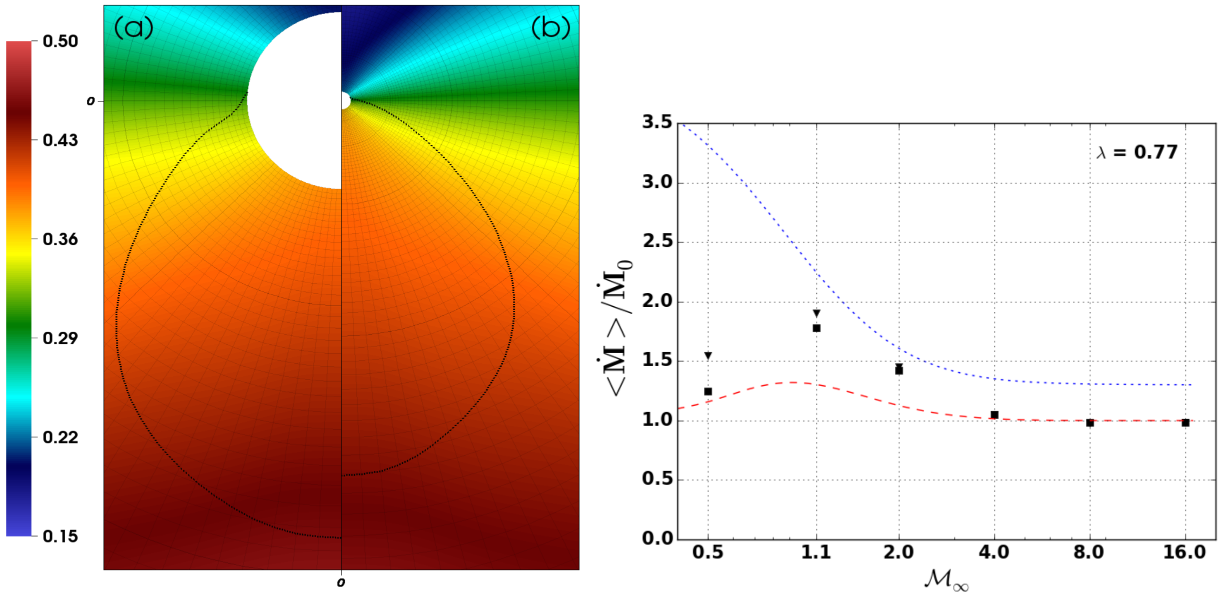

Fig. 2. Left : Colour map of the mass accretion rate for $\mathcal{M}_\infty = 2$ and, for (a), $r_{\rm in} = 10^{-2}\zeta_{\rm HL}$ and for (b), $r_{\rm in} = 10^{-3}\zeta_{\rm HL}$. The scale is linear (arbitrary units) and the inflowing mass is counted positively. The thick dotted black line is the sonic surface, anchored into the inner boundary in both cases. The radial logarithmic mesh is over plotted. Zoom in by a factor 500 on the central area of the simulation. **Right :** Mass accretion rates $\dot{M}$ as a function of the Mach number $\mathcal{M}_\infty$, normalized with the empirical mass accretion rate $\dot{M}_0$. In black are the numerically computed ones for $\zeta_{\rm HL}/r_{\rm in} = 10^2$ (triangles) and $\zeta_{\rm HL}/r_{\rm in} = 10^3$ (squares). The blue dotted line is the Bondi interpolation formula and the red dashed is the FR96's one.

$$\frac{\mathcal{M}_{\rm eff}}{\mathcal{M}_\infty} \sim \frac{1}{2^\gamma \lambda^{\frac{\gamma-1}{2}}} \sqrt{\frac{2}{\gamma}} \frac{(\gamma+1)^{\frac{\gamma+1}{2}}}{(\gamma-1)^{\frac{5(\gamma-1)}{4}}(5-3\gamma)^{\frac{5-3\gamma}{4}}} \tag{3.3}$$

Physically, λ accounts for an essential non-ballistic feature of the flow, whatever high the Mach number can be. Foglizzo and Ruffert's formula must be understood as a lower limit since it neglects the matter being accreted from a subsonic region whom angular extension becomes larger as $\mathcal{M}_\infty$ decreases.

Although pretty similar to Ruffert's numerical conclusions (Ruffert 1994b; Ruffert & Arnett 1994), our results do not show any decreasing trend at high Mach number and match the interpolation formula $\dot{M}_{\rm FR}$ in the asymptotically supersonic regime for $\lambda \sim 0.77$, down to $\mathcal{M}_\infty = 4$, at a few percents precision level. We also grasp the main feature of the axisymmetric B-H accretion flow that is to say an amplification by a few 10% of $\dot{M}$ around $\mathcal{M}_\infty = 1$ compare to the interpolation formulae (3.1) and the expression of $\dot{M}_0$ verifying $\dot{M} \xrightarrow{\mathcal{M}_\infty \to 0} \dot{M}_{\rm B}$ and $\dot{M} \xrightarrow{\mathcal{M}_\infty \to \infty} \sim \dot{M}_{\rm HL}$. It must be noticed that for $\mathcal{M}_\infty = 0.5$, 1.1 & 2, the mass accretion rates measured are not yet independent of the inner boundary size, which is in agreement with the zero value of the sonic radius : since the sonic surface is anchored into the accretor, there is always directions of accretion where the flow is not supersonic. The smaller the inner boundary size, the closer the simulation from the model drawn in FR96, which is confirmed by the data being closer from their interpolation formula for $r_{\rm in} = 10^{-3}\zeta_{\rm HL}$ than for $r_{\rm in} = 10^{-2}\zeta_{\rm HL}$. It can also be seen from direct visualization of the sonic surface which tends to occupy an angular region around the inner boundary larger for smaller inner boundary radii. Given those elements, those numerical $\dot{M}$ must be seen as upper limits of the ones one would get for a smaller absorbing inner boundary.

4 Conclusions

Numerical simulations with an inner boundary size smaller than 10^{-3} critical impact parameter $\zeta_{\rm HL}$ converge towards common steady states. Given the mass accretion rates we could compute from the latter, we can affirm that the mass interpolation formula derived in FR96 turns out to grasp the qualitative behaviour of flows with a

Mach number at infinity around 1, even if the neglecting of the mass accreted from the subsonic directions makes it an underestimation by a few 10%. The numerical robustness of our results is confirmed by the accordance between the large and small scale properties of the flow, in particular the geometry of the sonic surface : in agreement with FR96's topological comment on the latter, we find sonic surfaces systematically anchored into the inner boundary as soon as the flow is supersonic at infinity.

The present study has discarded the orbital effects like the ones present in binaries (see Theuns & Jorissen 1993; Theuns et al. 1996, for SPH simulations). Yet, if the orbitally induced torque remains small enough, those axisymmetric simulations are not expected to depart much from the actual configuration of Super-giant X-ray binaries where the mass transfer is believed to occur mainly through fast stellar winds. Thanks to our numerical setup, which reconciles the requirement for physical size of the accretor together with the necessity to include the accretion radius within the simulation space, we can start to consider the wind accretion of angular momentum in full 3D simulations in order to unveil the properties of the possibly subsequently formed accretion disc.

We gratefully thank Thierry Foglizzo for fruitful exchanges and the MPI-AMRVAC development team, in particular Oliver Porth, Rony Keppens and Zakaria Meliani, for useful assistance. IEM thanks the organizing committee of the *Journées de la SF2A 2015* for giving him the occasion to present his results at the Paul Sabatier University of Toulouse. We acknowledge the financial support from the UnivEarthS Labex program of Sorbonne Paris Cite (ANR-10-LABX-0023 and ANR-11-IDEX-0005-02).

References

Bisnovatyi-Kogan, G. S., Kazhdan, Y. M., Klypin, A. A., Lutskii, A. E., & Shakura, N. I. 1979, Sov. Astron., 23
Blondin, J. M. & Pope, T. C. 2009, Astrophys. J., 700, 95
Blondin, J. M. & Raymer, E. 2012, Astrophys. J., 752, 30
Bondi, H. & Hoyle, F. 1944, Mon. Not. R. Astron. Soc., 104, 273
Bondi, . 1952, Mon. Not. R. Astron. Soc., 112
Cordes, J. M., Romani, R. W., & Lundgren, S. C. 1993, Nature, 362, 133
Cowie, . 1977, Mon. Not. R. Astron. Soc., 180, 491
de Val-Borro, M., Karovska, M., & Sasselov, D. 2009, arXiv.org, 1148
Edgar, R. G. 2004, New Astron. Rev., 48, 843
Edgar, R. G. 2005, Astron. Astrophys., 434, 41
Foglizzo, T., Galletti, P., & Ruffert, M. 2005, Astron. Astrophys., 2201, 15
Foglizzo, T. & Ruffert, M. 1996, Astron. Astrophys., 361, 22
Fryxell, B. a. & Taam, R. E. 1988, Astrophys. J., 335, 862
Horedt, G. P. 2000, Astrophys. J., 541, 821
Hoyle, F. & Lyttleton, R. A. 1939, Math. Proc. Cambridge Philos. Soc., 35, 405
Igumenshchev, I. V. 2006, Astrophys. J., 649, 31
Igumenshchev, I. V. & Narayan, R. 2002, Astrophys. J., 566, 137
Koren, B. 1993, Notes Numer. Fluid Mech., 45, 117
Krumholz, M. R., McKee, C. F., & Klein, R. I. 2005, Astrophys. J., 618, 757
Krumholz, M. R., McKee, C. F., & Klein, R. I. 2006, Astrophys. J., 638, 369
Pang, B., Pen, U.-L., Matzner, C. D., Green, S. R., & Liebendörfer, M. 2011, Mon. Not. R. Astron. Soc., 415, 1228
Park, K. & Ricotti, M. 2013, Astrophys. J., 767, 163
Pfahl, E., Rappaport, S., & Podsiadlowski, P. 2002, Astrophys. J., 571, L37
Porth, O., Xia, C., Hendrix, T., Moschou, S. P., & Keppens, R. 2014, Astrophys. J. Suppl. Ser., 214, 4
Ruffert, M. 1994a, Astrophys. J., 427, 342
Ruffert, M. 1994b, Astron. Astrophys. Suppl. 106
Ruffert, M. 1996, 814, 793
Ruffert, M. 1999, 06, 17
Ruffert, M. & Arnett, D. 1994, Astrophys. J., 427, 351
Soker, N. 1990, Astrophys. J., 358, 545
Theuns, T., Boffin, H., & Jorissen, A. 1996, 000, 13
Theuns, T. & David, M. 1992, Astrophys. J., 384, 587
Theuns, T. & Jorissen, A. 1993, Mon. Not. R. Astron. Soc., 265, 946
Walter, R., Lutovinov, A. A., Bozzo, E., et al. 2015, eprint arXiv:1505.03651 [arXiv] arXiv:1505.03651v1

SF2A 2015
F. Martins, S. Boissier, V. Buat, L. Cambrésy and P. Petit (eds)

THE SUPERNOVA-DRIVEN INTERSTELLAR MEDIUM

O. Iffrig[1] and P. Hennebelle[1, 2]

Abstract. Stellar feedback is thought to be responsible for the regulation of star formation in the interstellar medium. In particular, supernovae inject a significant amount of energy and momentum into the ISM. However, the dynamical range of length scales swept by supernovae are too large to be handled at once with current computational resources. We present a two-step study: first we performed numerical simulations of a single supernova event inside a turbulent cloud, which then enabled us to extract a sub-grid model for larger-scale simulations of stratified disk-like structures. In the latter case, we focus on the influence of supernovae on the properties of the gas, namely turbulence and star formation. We also emphasize the strong dependence with respect to the employed sub-grid feedback scheme.

Keywords: ISM: supernova remnants, ISM: structure, turbulence, stars: formation

1 Introduction

1.1 Context

Star formation rates estimated by assuming a gravitational collapse within a few free-fall times are several orders of magnitude higher than the observed star formation rates (Zuckerman & Evans 1974; Dobbs et al. 2014). Therefore, other physical processes are involved in regulating star formation. Three main processes have been considered efficient: magnetic field (Shu et al. 1987), turbulence (Mac Low & Klessen 2004) and stellar feedback (e.g. Agertz et al. 2013). While a substantial magnetic field intensity has been measured in molecular clouds (Crutcher 2012), its influence remains too weak to explain the difference. Thus, turbulence and stellar feedback are believed to contribute significantly. However, turbulence decays quickly (Mac Low & Klessen 2004), therefore it has to be driven, either by large-scale structure such as spiral arms, or by stellar feedback. Thus, stellar feedback has a double role in the dynamics of the ISM: on the one hand it regulates star formation by injecting energy into the gas, and on the other hand it drives turbulence, which in turns regulates star formation.

Motivated by these results, we studied the impact of one of the most energetic stellar feedback processes, namely supernovae. We first quantified the momentum injected into the interstellar medium by a supernova, before running self-consistent simulations at larger scale, checking the influence of the feedback scheme. Then, motivated by a seemingly consistent feedback model, we perform high-resolution runs to study the properties of the supernova-driven interstellar medium. The next subsection presents the numerical code we use and some technical features. The following section shows the results of cloud-scale (a few parsecs) simulations of one single supernova event (Iffrig & Hennebelle 2015), the following one the results of kiloparsec-scale simulations of a supernova-regulated galactic disk, and the last section concludes this discussion.

1.2 Numerical method

To perform the numerical simulations, we used the RAMSES code (Teyssier 2002). It is a second-order Godunov code solving the magnetohydrodynamics (MHD) equations with self-gravity, using a constrained transport scheme for the magnetic field (Fromang et al. 2006). We also used a cooling function accounting for both the various cooling processes relevant to the ISM (Sutherland & Dopita 1993; Wolfire et al. 2003; Audit &

[1] Laboratoire AIM, Paris-Saclay, CEA/IRFU/SAp – CNRS – Université Paris Diderot, 91191 Gif-sur-Yvette Cedex, France
[2] LERMA (UMR CNRS 8112), Ecole Normale Supérieure, 75231 Paris Cedex, France

© Société Francaise d'Astronomie et d'Astrophysique (SF2A) 2015

Hennebelle 2005), and a UV background heating model, leading to a cooling function similar to the one used in Joung & Mac Low (2006).

The equations we solve are:

$$\partial_t \rho + \vec{\nabla} \cdot (\rho \vec{v}) = 0, \tag{1.1}$$

$$\partial_t (\rho \vec{v}) + \vec{\nabla} \cdot \left(\rho \vec{v} \otimes \vec{v} + \left(P + \frac{B^2}{8\pi} \right) \vec{I} - \frac{\vec{B} \otimes \vec{B}}{4\pi} \right) = -\rho \vec{\nabla} \phi, \tag{1.2}$$

$$\partial_t E + \vec{\nabla} \cdot \left(\left(E + P - \frac{B^2}{8\pi} \right) \vec{v} + \frac{1}{4\pi} \vec{B} \times \left(\vec{v} \times \vec{B} \right) \right) = -\rho \vec{v} \cdot \vec{\nabla} \phi - \rho \mathcal{L}, \tag{1.3}$$

$$\partial_t \vec{B} - \vec{\nabla} \times \left(\vec{v} \times \vec{B} \right) = 0, \tag{1.4}$$

$$\Delta \phi - 4\pi G \rho = 0, \tag{1.5}$$

where ρ, $\vec{v}$, P, $\vec{B}$, ϕ, E and $\mathcal{L}$ respectively being the density, velocity, pressure, magnetic field, gravitational potential, total (kinetic plus thermal plus magnetic) energy and cooling function.

Supernova feedback is injected at chosen time and location, either from pre-defined values, or depending on the evolution of the supernova. The details will be given in the next sections. Ejecta, momentum and (kinetic and thermal) energy are injected directly around the chosen location in one single time step. The injection radius is chosen to be a sphere of at least two computing cells.

Sink particles (Krumholz et al. 2004) are used in the self-consistent disk simulations in order to track star formation sites. One massive star is assumed to be formed when a sink has accreted more than 120 $M_\odot$. This threshold is used to trigger supernova feedback in the fiducial scheme.

The turbulent initial conditions are generated using an analytic density profile and a random velocity field sampled with a power-law Kolmogorov spectrum with random phase distribution. A constant magnetic field is imposed within the whole box. The simulation starts by letting the gas evolve to a self-consistent state where turbulence is fully developed.

2 Single supernova simulations

First, we ran simulations to quantify the momentum injected by a supernova into the interstellar medium. The detailed results are shown in Iffrig & Hennebelle (2015). This study served as a basis for the larger-scale simulations.

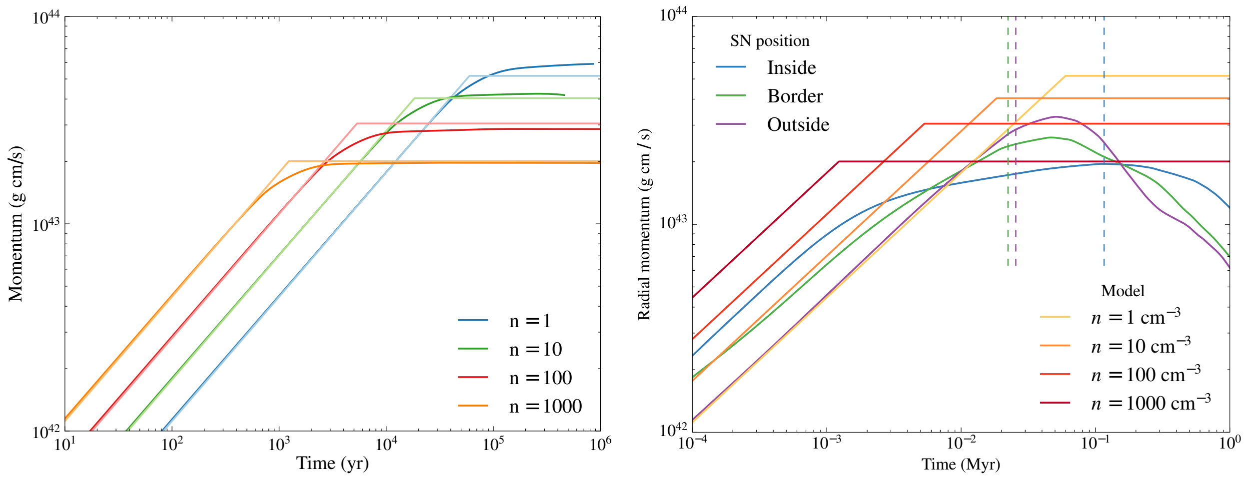

Fig. 1. Integrated radial momentum injected by a single supernova. **Left:** Supernova in a uniform medium for different ambient densities. **Right:** Supernova in a turbulent cloud-like medium.

Box size (pc)	Density (cm^{-3})	Temperature (K)
160	1	4907.8
80	10	118.16
80	100	36.821
40	1000	19.911

n_0 (cm^{-3})	t_{tr} (10^4 yr)	p_f (10^{43} g cm s^{-1})
1	2.99	5.18
10	0.919	4.04
100	0.267	3.04
1000	0.0616	2.01

Table 1. Left: Initial conditions for the uniform runs. The gas is initially at rest. **Right:** Transition time t_{tr} and final momentum p_f as a function of the ambient density n_0, estimated with the model.

2.1 Uniform density runs

We first assessed our scheme by running three-dimensional simulations of a supernova in a uniform medium. We were able to reproduce the well-known supernova remnant evolution models (e.g. Oort 1951; Sedov 1959; Chevalier 1974; Cioffi et al. 1988; Blondin et al. 1998), and derived a simple model from these. The simulation results are consistent with the model.

We simulated the explosion of a supernova in densities of 1, 10, 100 and 1000 cm^{-3}. The temperature is chosen so that the gas is at thermal equilibrium with respect to the heating and cooling processes. The simulation box size is chosen so that the remnant does not escape the box. The values of these parameters are summarized in Table 1 left. We inject 10^{51} erg of thermal energy at the center of the simulation box.

According to the Sedov-Taylor (Sedov 1959) model, the radial momentum of the supernova remnant can be expressed as

$$p_{43} = 1.77\ n_0^{1/5} E_{51}^{4/5} t_4^{3/5}, \tag{2.1}$$

where p_{43} is the total momentum in units of 10^{43} g cm s^{-1}, n_0 is the particle density in cm^{-3}, E_{51} is the supernova energy in units of 10^{51} erg, and t_4 is the age of the remnant in units of 10^4 yr.

We define the transition time t_{tr} as the moment when the age of the remnant becomes equal to the cooling time τ_{cool} of the shell which is given by

$$\tau_{cool} = \frac{3}{2} k_B \frac{n_s T_s}{n_s^2 \Lambda_s}, \tag{2.2}$$

where n_s and T_s are the gas density and temperature of the shell, and Λ_s the net cooling (in erg cm^3 s^{-1}). This transition time corresponds to the transition from the Sedov-Taylor adiabatic phase to a momentum-conserving snowplow (Oort 1951). We do not take into account the pressure-driven snowplow stage (Cioffi et al. 1988) because it does not change the final momentum significantly, and is not distinguishable from the transition between the two other stages we consider.

To model analytically the second stage, we solve numerically the equation $t_{tr} = \tau_{cool}$. For the highest ambient densities ($n_0 \gtrsim 10$), the momentum injection is reasonably well fitted by the momentum-conserving snowplow model with the final momentum p_f taken to be the momentum of a Sedov-Taylor blast wave at $2t_{tr}$ (the numerical values are given in Table 1 right). Some small deviations are found with the lowest density case because the pressure within the shell is still higher than the surrounding pressure and the shell keeps accelerating. When the surrounding gas density varies by 3 orders of magnitude, the total momentum varies by a factor of about 3. The injected radial momentum in the simulations is shown on Figure 1 left. The results are consistent with the model and confirm this weak dependency.

2.2 Turbulent runs

The interstellar medium being highly turbulent (e.g. Hennebelle & Falgarone 2012), it presents large density contrasts which may strongly affect the dynamics of a supernova remnant sweeping through it. Thus, we needed to simulate a more realistic cloud-like medium which is expected to exist in the vicinity of an exploding star. To achieve this, we generate a cloud-like medium from a spherically symmetric density distribution

$$\rho(r) = \frac{\rho_0}{1 + \left(\frac{r}{r_0}\right)^2} \tag{2.3}$$

where $\rho_0 = 9370$ cm^{-3} and $r_0 = 1.12$ pc. The total mass enclosed in this cloud is 10^4 $M_\odot$. The cloud is surrounded by a halo of density $\rho_0/100$, mimicking the H_I halo around molecular clouds. A turbulent velocity field is added on top of this density distribution to generate a turbulent medium where gravity and turbulence contain the same energy. This cloud is surrounded by uniform 1 cm^{-3} medium at thermal equilibrium. We let the cloud evolve for 1.25 Myr (roughly 1 crossing time) in order for the turbulent fluctuations to build up. Then, a supernova is injected at a chosen location, as shown in Figure 2. The three runs referred to as "Inside", "Border" and "Outside" correspond to supernovae exploding in ambient densities of 700, 20 and 1.2 cm^{-3}.

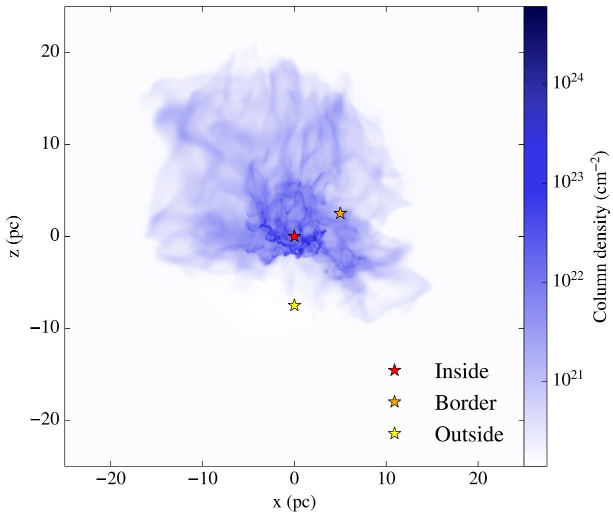

Fig. 2. Positions of the supernovae in the simulated cloud.

We calculated the radial momentum (with respect to the location of the supernova) injected by the explosion. The results are shown in Figure 1 right. Despite a slightly different evolution, the injected momentum is coherent with the trends given by the model. Especially, the final momentum has the predicted order of magnitude of 10^{43} g cm/s. The decrease of the momentum at late times corresponds to matter flowing out of the simulation box.

It is worth noting that most of the gas expelled from the cloud has a low to intermediate (less than 100 cm^{-3}) density, although a supernova inside the cloud is able to push denser gas too. The evolutions of mass and momentum for different density thresholds are shown in Figure 3 and Figure 4. A supernova may therefore not prevent star formation efficiently, but has some significant effects on the intermediate density gas, which would otherwise have collapsed later on by the effect of gravity.

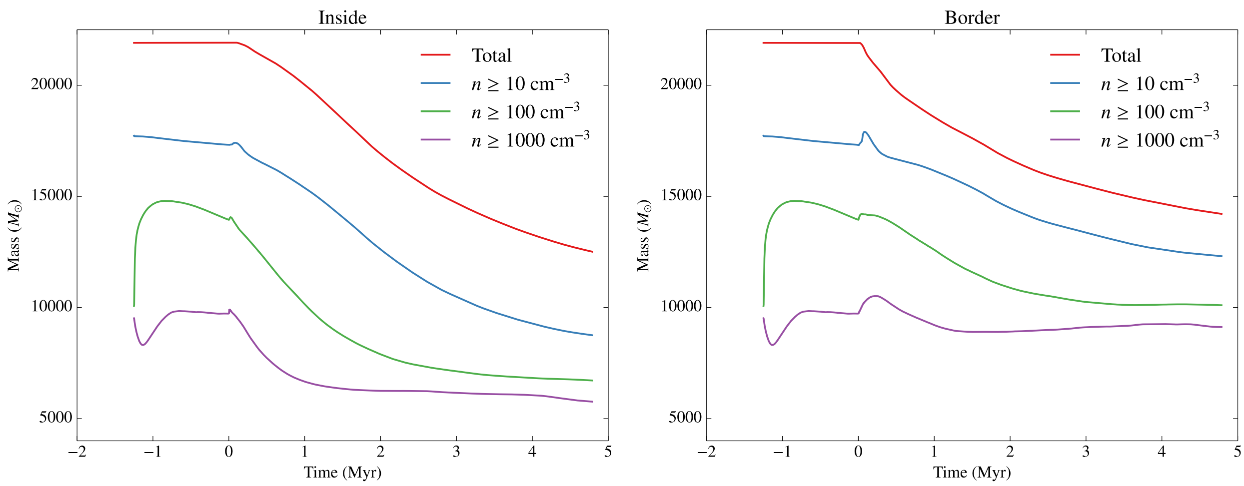

Fig. 3. Evolution of mass for different density thresholds as a function of time. **Left:** Supernova inside the cloud. **Right:** Supernova at the border of the cloud. The dashed lines correspond to the first outflow from the simulation box.

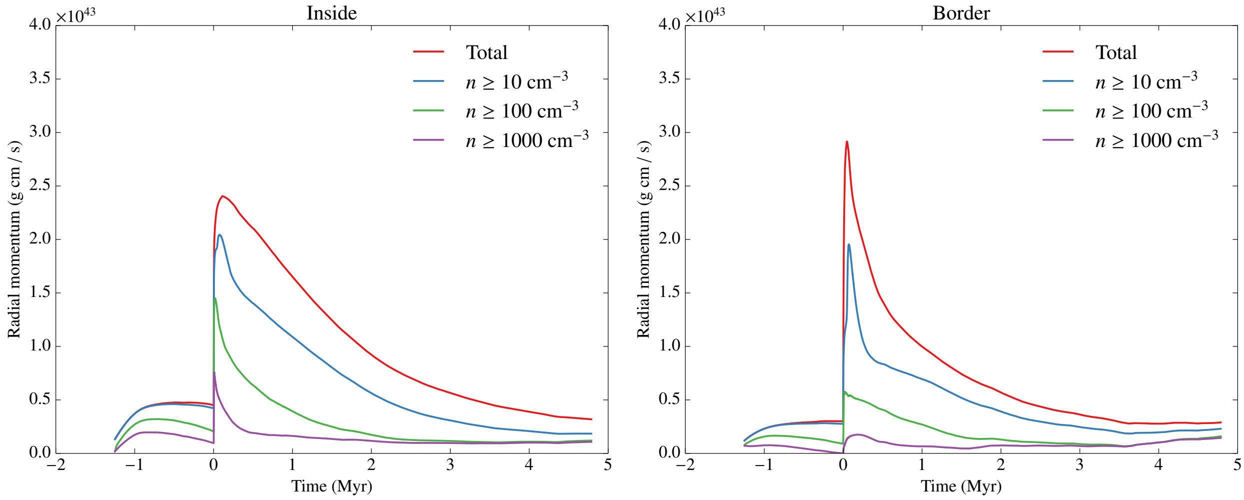

Fig. 4. Evolution of radial momentum for different density thresholds as a function of time. **Left:** Supernova inside the cloud. **Right:** Supernova at the border of the cloud.

2.3 Summary

Based on the standard supernova remnant evolution models, we were able to derive a simple model for the injection of momentum into the interstellar medium. We successfully compared it to the results of simulations of a uniform medium swept up by a supernova remnant, as well as those of a more realistic environment. The model gives us a simple prescription of a few 10^{43} g cm/s momentum injected for an initial energy of 10^{51} erg, almost regardless of the surrounding density. The precise distribution of this momentum to the gas strongly depends on the location of the explosion: if the supernova happens inside a cloud, the bubble will be pushing the dense gas around it until it can escape through more diffuse chimneys. A supernova exploding outside a cloud will mainly push lower-density gas, and thus cannot prevent immediate star formation, but still injects sufficient energy and momentum to prevent ~ 100 cm^{-3} gas to collapse.

This model is, however, useful as sub-grid physics for a larger-scale simulation where supernovae are injected self-consistently with respect to star formation sites. The next section presents our tests of this model in simulations of a part of a galactic disk.

3 Large-scale study of a stratified galactic disk with supernova feedback

The previous study of the momentum injected by a supernova into cloud-like medium, and also its emphasis on the sensitivity to the correlation between supernovae and star formation sites triggered our interest for self-consistent simulations. We considered a 1 kpc simulation cube containing a stratified galactic disk with an initially gaussian density profile

$$n(z) = n_0 \exp\left(-\left(\frac{z}{z_0}\right)^2\right) \tag{3.1}$$

with $n_0 = 1.5$ cm^{-3} and $z_0 = 150$ pc. The temperature is initially set to 8000 K, which corresponds to warm neutral gas. A turbulent velocity field is imposed on this initial condition, as described in Section 1.2. We also added a mean-field gravitational potential accounting for the distribution of stars and dark matter

$$g(z) = -\frac{a_1 z}{\sqrt{z^2 + z_0^2}} - a_2 z \tag{3.2}$$

with $a_1 = 1.42 \times 10^{-3}$ kpc Myr^{-2}, $a_2 = 5.49 \times 10^{-4}$ Myr^{-2} and $z_0 = 180$ pc, as used by Joung & Mac Low (2006). We performed simulations on a 256^3 grid to test different feedback schemes (for more detailed results, see Hennebelle & Iffrig 2014), before scaling up to 1024^3 for our fiducial scheme (see below).

The supernova energy is injected as kinetic (momentum) and thermal energy, using the prescriptions of 10^{51} erg energy and 2×10^{43} g cm/s momentum. These quantities are distributed in a sphere of at least 2 computational cells.

3.1 Scheme

In order to assess the importance of the correlation between supernovae and star forming regions, we ran several simulations with different feedback prescriptions. For the simplest one (referred to as "random"), we use a uniform distribution in the galactic plane, a gaussian distribution in altitude, and a fixed rate of $1/50\ \mathrm{yr}^{-1}$ in time. The second one has the same rate in time, but with a correlation to the densest point in the simulation.

The more realistic runs use sink particles to track star-forming regions, and we assume there is one supernova per 120 $M_{\odot}$ of accreted gas. In order to assess the correlation between the supernova and the location of the sink, we used two schemes. The fiducial one (referred to as "sphere") puts the supernova randomly in a sphere of 10 pc around the sink. The second one (referred to as "shell") puts the supernova farther away, that is in a shell between spheres of 10 pc and 20 pc respectively.

As expected, there are strong differences between the results of these runs. Figure 5 shows column density maps for the various schemes. Without feedback, the gas quickly collapses due to gravity, forming dense filaments. A randomly distributed feedback causes a big gas dispersion, but does not prevent run-away gravitational collapse. The fiducial scheme is able to ensure an equilibrium between star formation and gravitational collapse. Finally, a correlation with more distance between the sink particles and the supernovae entails very efficient feedback which effectively prevents star formation, but completely destroys the disk structure.

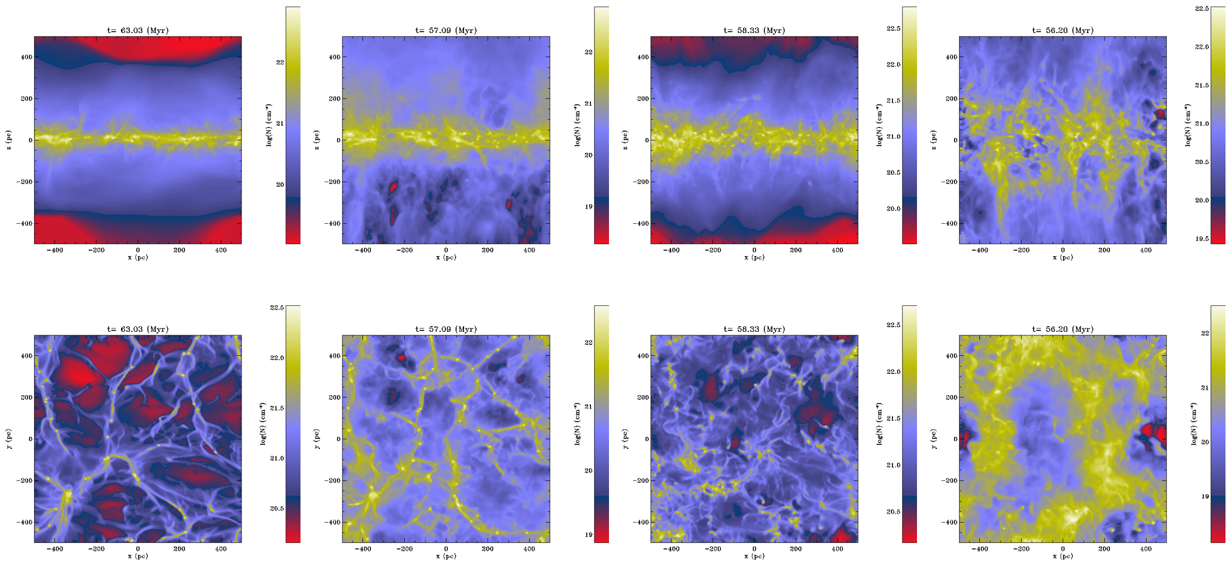

Fig. 5. Column density maps of the galactic disk simulations for different feedback schemes. **From left to right:** no feedback, random, sphere, shell. **Top:** Edge-on view. **Bottom:** Face-on view.

3.2 Star formation

The star formation efficiency can be estimated by tracking the mass accreted by sinks throughout the simulation. The absolute results have to be handled very carefully, but they provide at least a means of comparing the impact of each feedback scheme on star formation. The results are summarized in Figure 6. We observe that correlated feedback is indeed able to reduce star formation rate by a factor around 10, but since the evolution seems to be still out of equilibrium, this factor may still decrease. These results put forward the "sphere" scheme as our fiducial scheme, for it is able to sustain a vertical equilibrium as well as to regulate star formation. Note however that supernova feedback alone does not explain all of the discrepancy between observed star formation rates and estimations based on gravitational collapse.

3.3 Turbulence

The fiducial scheme being successfully assessed, we performed a higher resolution run in order to study in more details the properties of the supernova-driven interstellar medium. We scaled the resolution down to 1 pc, using

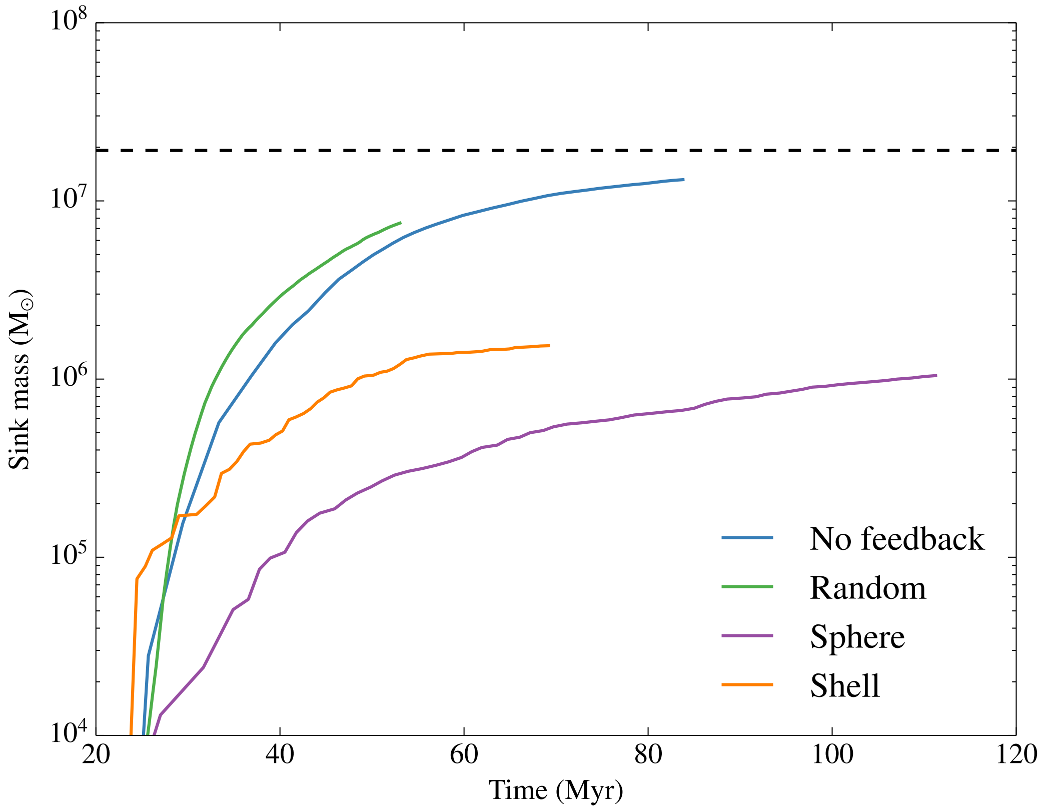

Fig. 6. Star formation efficiency, as measured with the total mass accreted by sink particles. The dashed line corresponds to the initial gas mass.

a 1024^3 uniform grid. This grid enables us to compute power spectra to quantify the properties of turbulence. A column density map of our fiducial run with enhanced resolution is shown on Figure 7.

Given this 1 pc resolution, we calculated Fourier power spectra of several physical quantities, plotted on Figure 8, and compared them to well-known models of turbulence (e.g. Kolmogorov 1941; Fleck 1996; Kritsuk et al. 2007). Given the artificial viscosity introduced by the numerical scheme, the smallest scales are not reliable to derive physical conclusions (see Kritsuk et al. 2007, and references therein for more details). However, there is a small inertial range showing power-law behaviour coherent with the predictions of Kolmogorov (1941) and Fleck (1996) with a compression degree $\alpha = 1/6$. The injection scale is not clearly appearing because the simulations do not include any large scale forcing: the turbulence is sustained by the supernovae.

4 Conclusions

We performed simulations of supernovae exploding in both uniform and turbulent medium. With help of the uniform medium simulations, we derived a simple prescription for the momentum a supernova should inject into the surrounding gas. The simulations of a single supernova interacting with a molecular cloud confirm the validity of this prescription, although the precise dynamics strongly depend on the relative location of the supernova and the cloud, making clear the need of self-consistent simulations.

Using these results, we studied the influence of the feedback scheme in self-consistent simulations of a 1 kpc cube of a galactic disk. The study shows important variability with respect to the scheme. A correlation between supernovae and star formation sites seems to be enough to maintain a vertical equilibrium, also decreasing the star formation rate significantly, but not enough to explain the big discrepancy between observed star formation rates and the rates corresponding to gravitational collapse acting alone. This result is however bound to change because supernovae are not the only significant feedback process. Stellar winds and radiation happen before supernovae and inject a similar energy into the surrounding medium. Therefore, taking them into account may further reduce the star formation rate, explaining the remaining difference.

The high resolution runs performed allow us to quantify the properties of a supernova-driven interstellar medium. This medium exhibits power spectra compatible with well-known turbulence models. A further study (in preparation) will provide more detailed results on the structure of the simulated medium.

References

Agertz, O., Kravtsov, A. V., Leitner, S. N., & Gnedin, N. Y. 2013, ApJ, 770, 25

Audit, E. & Hennebelle, P. 2005, A&A, 433, 1

Blondin, J. M., Wright, E. B., Borkowski, K. J., & Reynolds, S. P. 1998, ApJ, 500, 342

Chevalier, R. A. 1974, ApJ, 188, 501

Cioffi, D. F., McKee, C. F., & Bertschinger, E. 1988, ApJ, 334, 252

Crutcher, R. M. 2012, ARA&A, 50, 29

Dobbs, C. L., Krumholz, M. R., Ballesteros-Paredes, J., et al. 2014, Protostars and Planets VI, 3

Fleck, Jr., R. C. 1996, ApJ, 458, 739

Fromang, S., Hennebelle, P., & Teyssier, R. 2006, A&A, 457, 371

Hennebelle, P. & Falgarone, E. 2012, A&A Rev., 20, 55

Hennebelle, P. & Iffrig, O. 2014, A&A, 570, A81

Iffrig, O. & Hennebelle, P. 2015, A&A, 576, A95

Joung, M. K. R. & Mac Low, M.-M. 2006, ApJ, 653, 1266

Kolmogorov, A. 1941, Akademiia Nauk SSSR Doklady, 30, 301

Kritsuk, A. G., Norman, M. L., Padoan, P., & Wagner, R. 2007, ApJ, 665, 416

Krumholz, M. R., McKee, C. F., & Klein, R. I. 2004, ApJ, 611, 399

Mac Low, M.-M. & Klessen, R. S. 2004, Reviews of Modern Physics, 76, 125

Oort, J. H. 1951, in Problems of Cosmical Aerodynamics, 118

Sedov, L. I. 1959, Similarity and Dimensional Methods in Mechanics

Shu, F. H., Adams, F. C., & Lizano, S. 1987, ARA&A, 25, 23

Sutherland, R. S. & Dopita, M. A. 1993, ApJS, 88, 253

Teyssier, R. 2002, A&A, 385, 337

Wolfire, M. G., McKee, C. F., Hollenbach, D., & Tielens, A. G. G. M. 2003, ApJ, 587, 278

Zuckerman, B. & Evans, II, N. J. 1974, ApJ, 192, L149

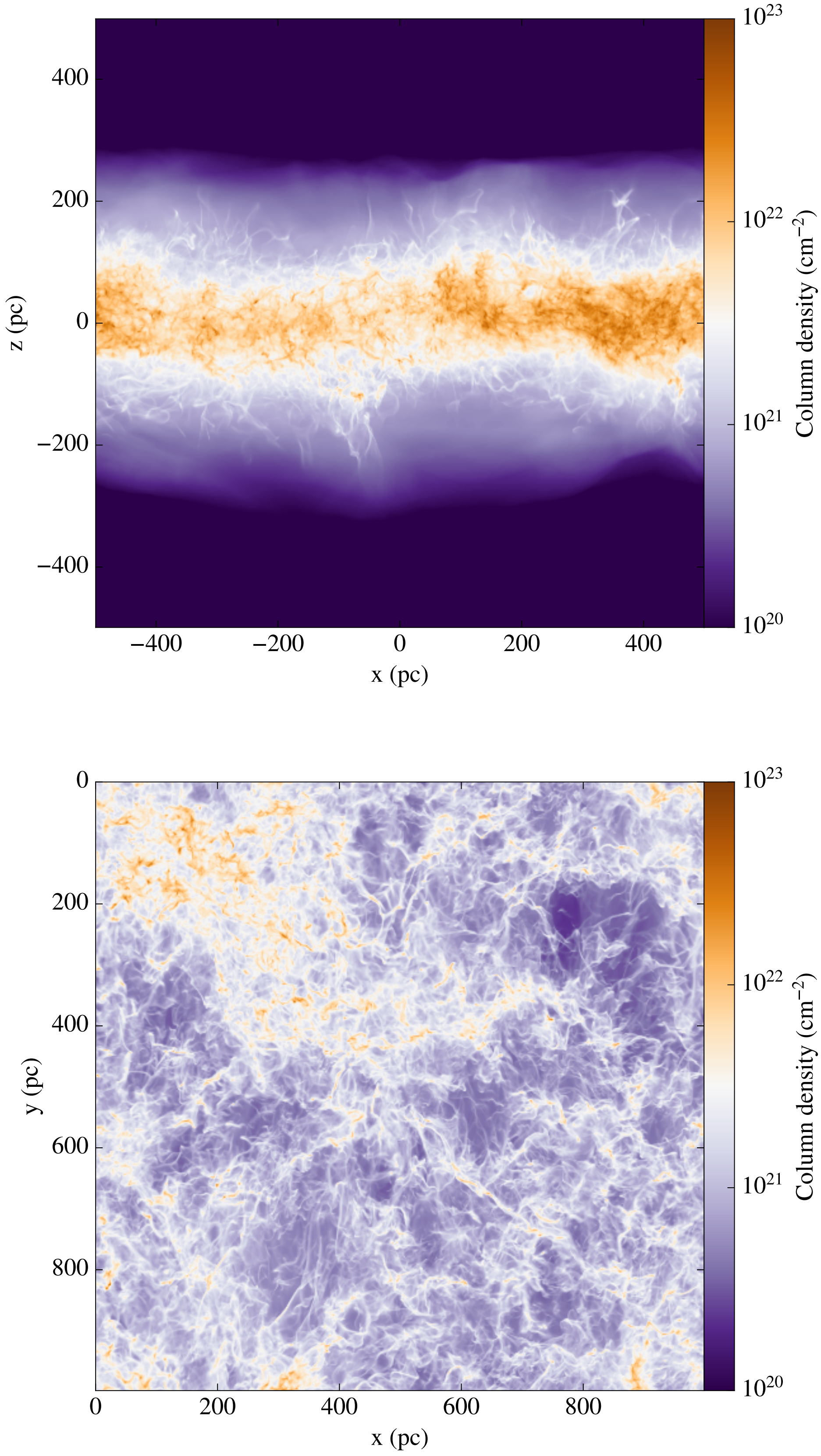

Fig. 7. Column density maps of the high-resolution fiducial run. **Top:** edge-on view. **Bottom:** face-on view.

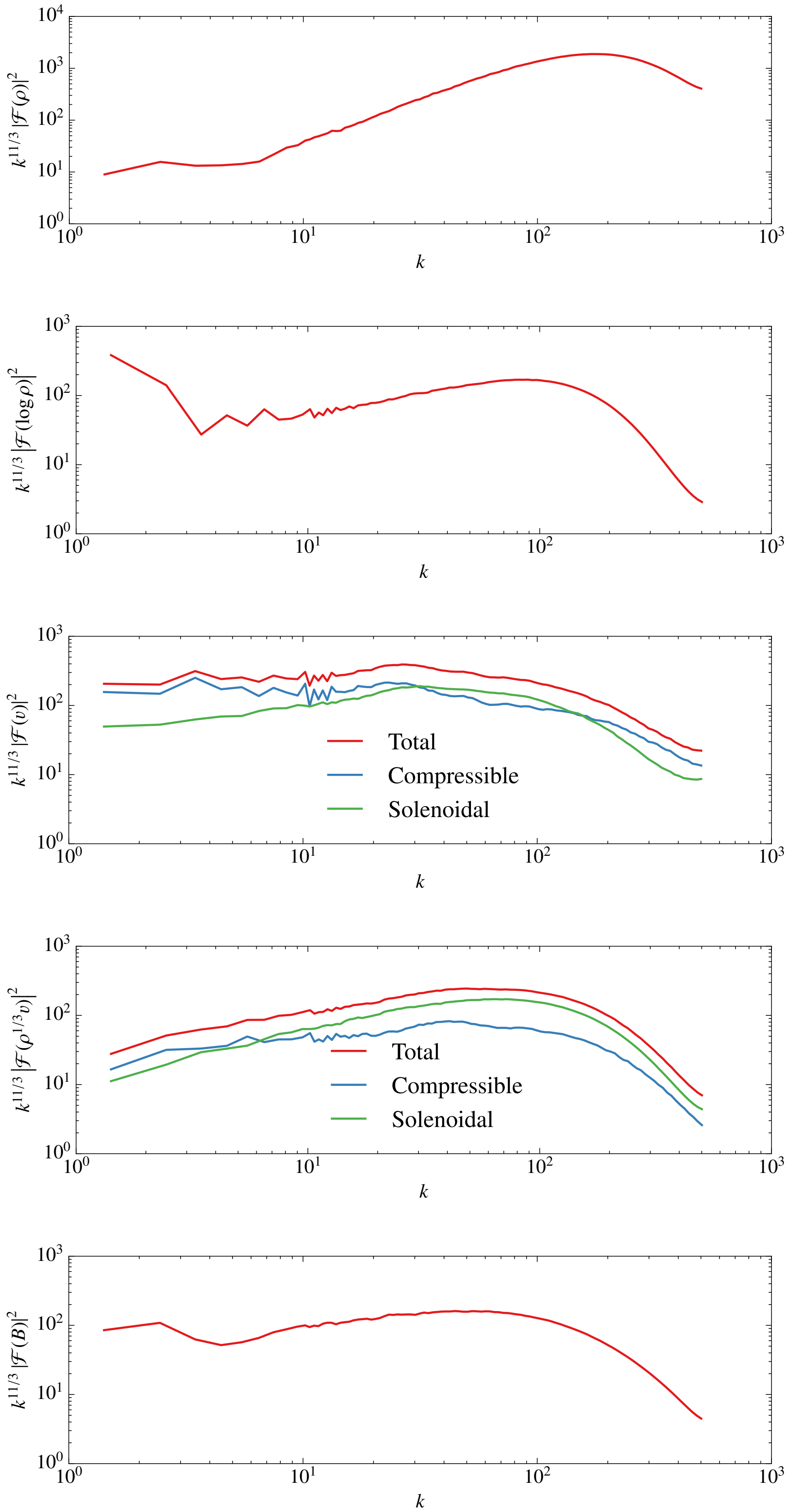

Fig. 8. Power spectra for the disk simulations. **From top to bottom:** density, log. density, velocity, density-weighted velocity (see Kritsuk et al. 2007), magnetic field. The power spectra are compensated by $k^{11/3}$, so a purely Kolmogorov spectrum would appear flat.

SF2A 2015
F. Martins, S. Boissier, V. Buat, L. Cambrésy and P. Petit (eds)

MASS LOSS OF MASSIVE STARS

F. Martins[1]

Abstract. In this contribution we review the properties of the winds of massive stars. We focus on OB stars, red supergiants, Luminous Blue Variables (LBVs) and Wolf-Rayet stars. For each type of star, we summarize the main wind properties and we give a brief description of the physical mechanism(s) responsible for mass loss.

Keywords: stars: massive; stars: winds, outflows; stars: mass loss

1 Introduction

Massive stars experience episodes of mass loss throughout their evolution. Either through continuous winds or bursts, large amounts of mass are ejected in the immediate surrounding. This deeply affects not only the star's evolution, but also the structure of the interstellar medium, and thus the appearance of supernovae which occur in such environments.

Mass loss is one of the main drivers of massive stars evolution (Chiosi & Maeder 1986). During their lifetime, massive stars may lose up to 90% of their initial mass through stellar winds (Maeder & Meynet 1991). This strongly impacts on their internal structure and thus their evolution. Meynet et al. (2015) showed that changing the mass loss rate by a factor of ten only in the (short) red supergiant phase can affect the end point of stellar evolution: a star may become a supernova either as a red or as a blue supergiant depending on the mass loss history in the red supergiant phase.

The material ejected just before the explosion of a supernova also impacts on the appearance of the supernova itself. Depending on the density of the medium into which the supernova expands, its spectrum may be very different. For instance, type IIn supernovae are thought to have a spectrum dominated by nebular emission (Schlegel 1990; Chugai et al. 2004). In addition, different types of core-collapse supernovae are formed depending on the physical properties of the progenitor. As illustrated above, the progenitor's appearance will strongly depend on the mass loss history of its parent star.

In this review, we describe the wind properties of massive stars in different evolutionary state (OB, red supergiant, LBV, Wolf-Rayet). We summarize the main properties and give a brief overview of the mechanism(s) driving the outflows.

2 OB stars

Massive stars are born as O or B stars. This phase is defined by effective temperatures higher than about 15000 K. It corresponds to the main sequence and slightly beyond when including "blue supergiants", i.e. stars not on the main sequence any more but hot enough to have a spectral type O or B. Massive stars spend 85-90% of their lifetime on the main sequence. A 15 $M_{\odot}$ star will stay 13 Myr on the main sequence for a lifetime of 15 Myr. For a 60 $M_{\odot}$ star, the numbers are 3.5 Myr and 4 Myr respectively.

During this phase, massive stars eject material in the interstellar medium at a rate between 10^{-9} and 10^{-5} $M_{\odot}$ yr^{-1} depending on the initial mass and exact evolutionary state. The wind terminal velocities from 500 to 4000 km s^{-1} in the most extreme cases, with values usually between 1000 and 3000 km s^{-1}.

Winds of OB stars are explained by the radiatively driven wind theory. First developed by Lucy & Solomon (1970) and Castor et al. (1975) (see later developments by Pauldrach et al. 1986; Vink et al. 2001), it describes

[1] LUPM, CNRS & Université de Montpellier, Place Eugène Bataillon, F-34095, Montpellier Cedex 05, France

© Société Francaise d'Astronomie et d'Astrophysique (SF2A) 2015

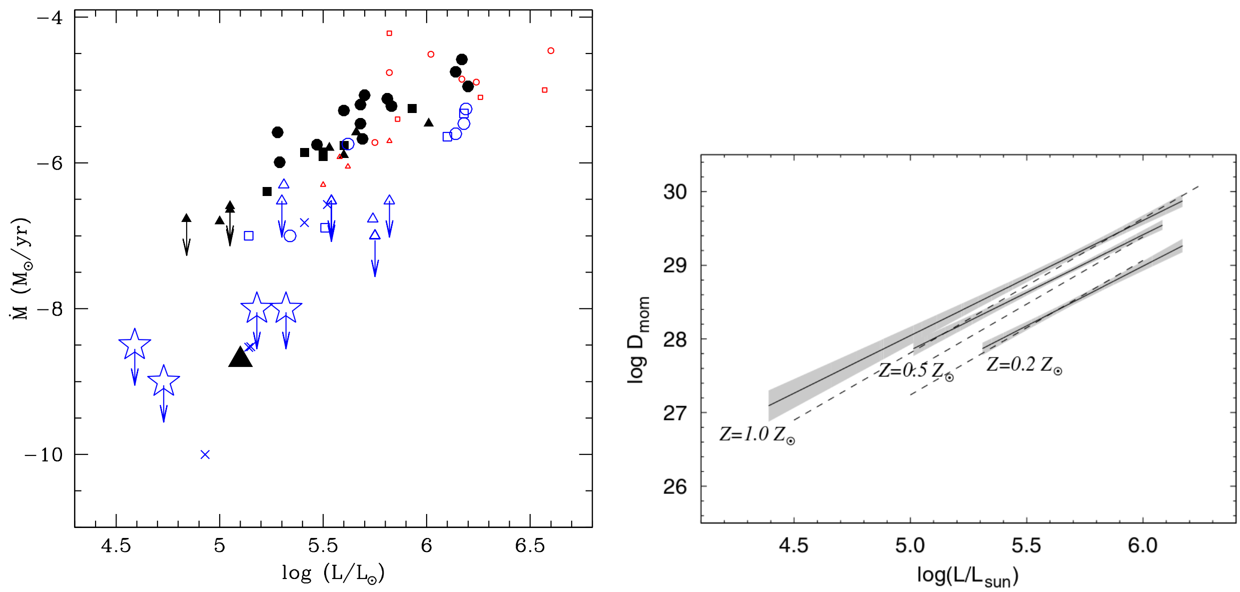

Fig. 1. Mass loss rates of OB stars and their relation to luminosity. **Left:** Mass loss rate as a function of luminosity for stars in the Galaxy (black symbols), the LMC (red) and the SMC (blue). Reproduced from Martins et al., 2004, A&A, 420, 1087. **Right:** Wind momentum - luminosity relation at different metallicities. The wind momentum is directly proportional to the mass loss rate. Reproduced from Mokiem et al., 2007, A&A, 473, 603

how a transfer of momentum from photons to matter occurs through radiation absorption by metallic lines in stellar atmospheres. Momentum is subsequently redistributed to the bulk atmospheric material through collisional coupling. This translates into the development of a steady-state stellar wind. Computations by Vink et al. (2001) show quantitatively that absorption through iron atoms is responsible for about 50% of the wind acceleration at solar metallicity, CNO ions being the next main contributors. At lower metallicity, CNO ions become the dominant wind drivers.

The radiation driven wind theory predicts that the resulting mass loss should scale with a power of the luminosity. Fig. 1 reveals that this is confirmed observationally: more luminous stars have on average higher mass loss rates. Since acceleration is due to metallic lines, stars in low-metallicity environments should have lower mass loss rates. This is confirmed empirically by the work of Mokiem et al. (2007) (see right panel of Fig. 1). A scaling relation $\dot{M} \propto Z^{0.83}$ is obtained when studying the winds of OB stars in the Galaxy and the Magellanic Clouds.

In the context of the radiation driven wind theory, terminal velocities are expected to scale with the escape velocity. Garcia et al. (2014) show that this is true, although the scatter is large. Leitherer et al. (1992) found a weak metallicity dependence of the wind terminal velocity: $v_\infty \propto Z^{0.13}$.

Even though radiatively driven winds are continuous, they are not homogeneous. This is due to the intrinsic instability of the driving mechanism. The radiative acceleration being proportional to the velocity gradient, any change in the later will lead to a runaway change in the former. Consequently, regions of higher-than-average velocities follow regions of lower-than-average velocities. Due to mass conservation, this translates into inhomogeneities in the density distribution. A clumping factor is defined as the ratio of the density of the densest regions to the average density. Most studies indicate a value of ∼3, although larger values can be found (Bouret et al. 2005).

3 Red supergiants

After the main sequence, at solar metallicity, stars with masses between ∼8 and ∼25 M$_\odot$ quickly (i.e. within 0.2-0.5 Myr) cross the HR diagram to become red supergiants (RSG). The RSG phase lasts 5 to 10% of the stellar lifetime (2.5 Myr for a 9 M$_\odot$ star with a lifetime of 30 Myr; 0.3 Myr for a 25 M$_\odot$ star with a lifetime of 7 Myr).

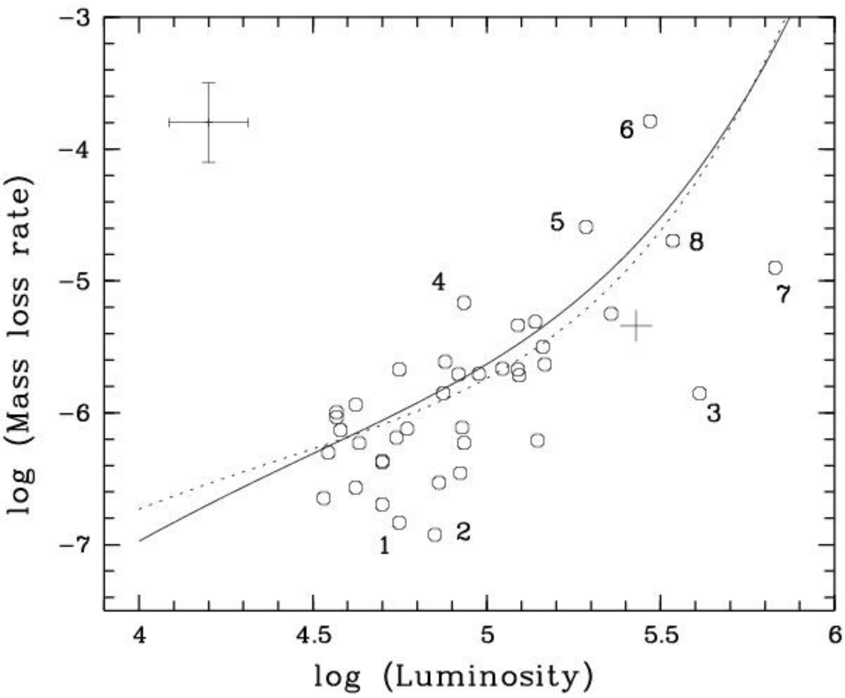

Fig. 2. Mass loss rate as a function of luminosity for red supergiants. The solid and dotted lines are the De Jager rates for different temperatures. Reproduced from Mauron & Josselin, 2011, A&A, 526, A56.

Although short, the RSG phase strongly impacts on the neighbouring environment. In that phase, mass loss rates range from 10^{-7} to 10^{-4} $M_{\odot}$ and the wind velocities are typically of 10 to 40 km s^{-1}. Hence, the wind density is about a thousand times larger than in the OB phase. Fig. 2 shows mass loss rate as a function of luminosity for a sample of red supergiant studied by Mauron & Josselin (2011). Two key features are seen. First, there seems to be a trend of higher mass loss rates for higher luminosities. Second, at a given luminosity, the dispersion in mass loss rates is about a factor of ten. Mauron & Josselin (2011) also show that measurements for the same star but with different diagnostics lead to variation in mass loss rates of the same order (factor of ten). Consequently, the mass loss rates of red supergiants remain poorly constrained empirically.

The mechanism responsible for the ejection of matter in RSGs is not understood. By analogy with lower mass AGB stars, acceleration of photospheric material by stellar pulsations followed by radiation pressure on dust grains formed above the photosphere may trigger stellar winds. However, for red supergiants, there are no pulsations on the stellar surface. An alternative mechanism may be convection since recent high-resolution images indicate the presence of very large spots on the photosphere (Haubois et al. 2009). Such spots may be convection patterns. Magnetic loops at the surface (Aurière et al. 2010) may be an alternative possibility to trigger large scale motions. Another problem for red supergiant is the formation of dust. The seeds of such grains are not identified, and the conditions above the photosphere imply that dust formation can occur only a few stellar radii above the photosphere. The action of radiation pressure thus takes over at large distances from the surface, which may not be sufficient to trigger the stellar wind.

Whatever the mechanism at the origin of RSGs' stellar winds, a typical feature is inhomogeneity in the ejecta. Infrared observations of the closest objects reveal the presence of filaments and regions of overdensity (see e.g. Fig. 6 of Kervella et al. 2011).

4 Luminous Blue Variables

Stars more massive than about 25 $M_{\odot}$ do not go through a RSG phase. For more massive stars, the redward evolution at high luminosity implies that the star reaches the Eddington limit above which it is not bound anymore. Observationally, this limit is seen as the 'Humphreys-Davidson' limit (Humphreys & Davidson 1979): no stars are observed rightward of this limit in the HR diagram. Stars reaching this part of the HR diagram are

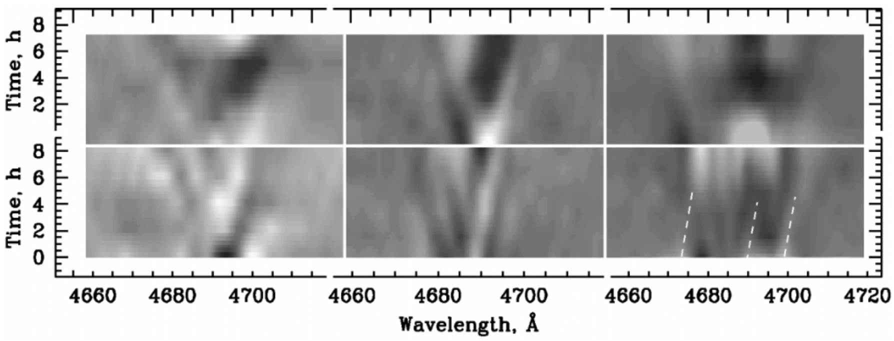

Fig. 3. Interpolated time series of the difference between individual and average line profiles around HeII 4686 for three WR stars in the SMC. Reproduced from Marchenko et al., 2007, ApJ, 656, L77.

usually classified as Luminous Blue Variables (LBV). As stems from their name, such objects show a variety of variable patterns, both photometrically and spectroscopically.

There are two main groups of LBVs. The first one is made of stars showing photometric modulation of the order 1 to 2 magnitudes at most. In the HR diagram, these stars are seen to evolve horizontally on short timescales. The rapid changes in effective temperature associated to a constant luminosity imply expansion/contraction of the stars (Clark et al. 2005). In that phase, where stars are also known as S-Dor variables, mass loss rates range from a few 10^{-6} to 10^{-4} $M_{\odot}$. The wind velocities are between 100 and 500 km s^{-1}. Mass loss rates vary with changes in T_{eff} and radius (they are higher when the star is cooler/bigger) - see Stahl et al. (2001); Vink & de Koter (2002).

The second group is made of only two objects: η Car and P-Cygni. These are the true LBVs. They experience huge photometric variability and massive ejections. η Car became a LBV in the 1840's, when it brightened from a V magnitude of 2 to -1. It then fainted down to a magnitude of 8 at the beginning of the XX^{th} century, and kept becoming brighter from then, reaching mV = 4.5 nowadays. At the same time, it experienced a short but intense eruptive phase during which it expelled about 10 $M_{\odot}$ in 10 years, creating the so-called Homunculus nebula. LBVs are thus characterized by very strong mass loss rates of the order of a few tens of $M_{\odot}$ yr^{-1}. The ejections are not homogeneous, as the structure of the Homunculus reveals: filaments, spikes, debris, knots are observed (Morse et al. 2001).

The origin of stellar winds in LBVs is poorly understood. Radiative driving remains the best theoretical ground. In the S-Dor phase, changes in the effective temperature imply modification of the ionization structure, which in turn change the number of ions absorbing photons and thus accelerating the upper layers. This may explain the increase of mass loss rates at cooler temperatures since more atomic transitions from less ionized iron atoms are available (Vink & de Koter 2002). For the giant eruptions of LBVs, continuum driving (and not line-driving) may be the key factor (Owocki et al. 2004). This requires the presence of a clumped medium to be efficient.

5 Wolf-Rayet stars

Stars more massive than 25 $M_{\odot}$ (et solar metallicity) end their lives as Wolf-Rayet stars (WR). The WR phase takes up to 5% of the star's lifetime. Typically, a 40 $M_{\odot}$ star will spend 0.2 Myr as a WR for a total lifetime of 5 Myr. During that phase, Wolf-Rayet stars have strong stellar winds characterized by mass loss rates of 10^{-6} to 10^{-4} $M_{\odot}$ yr^{-1} and velocities of 800 to 2500 km s^{-1}. The wind density is thus $\sim$10 times higher than in an OB star.

The current understanding of WR winds is based on the radiation driven wind theory (Castor et al. 1975). To reach mass loss rates about one order of magnitude higher than in OB stars, it is necessary to invoke multiple scattering of photons, contrary to OB stars where photons are usually absorbed and re-emitted only once (on average). A correlation between mass loss rate and luminosity seems to exist (e.g. Fig. 7 of Crowther 2007). In addition, mass loss rates scale with metallicity (Crowther et al. 2002). These facts are consistent with the expectation of radiative driving through metallic lines.

Another characteristics shared by WR and OB stars' winds is the presence of inhomogeneities. Due to the higher density of WR stars' winds, such clumps can be directly observed. Fig. 3 shows time series of spectra

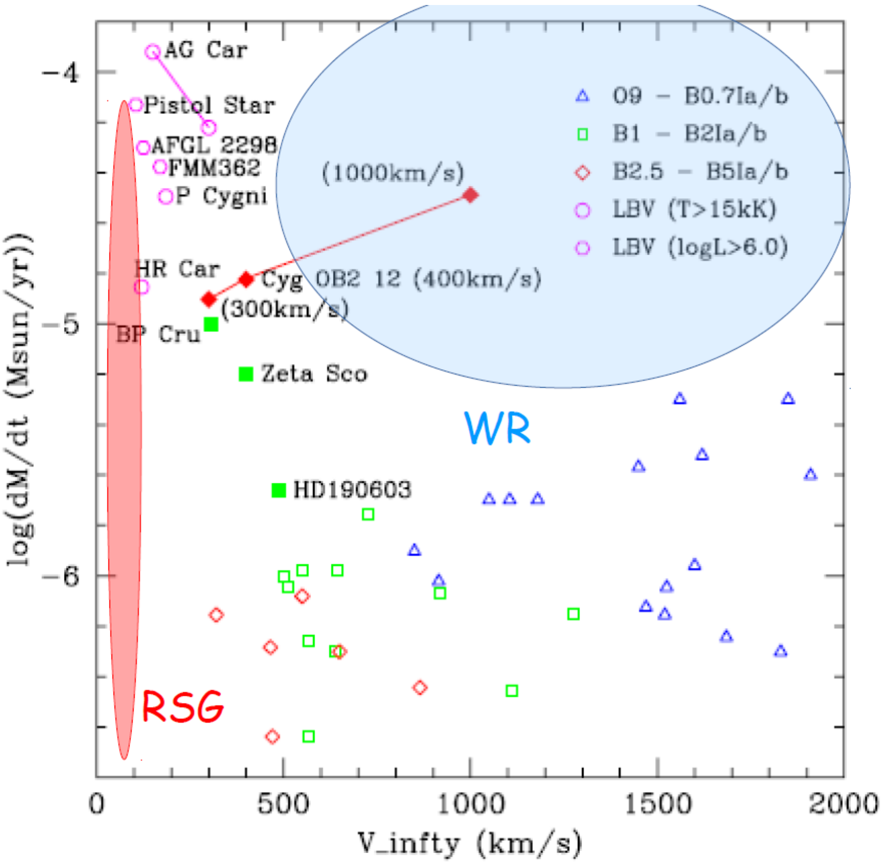

Fig. 4. Mass loss rate as a function of wind velocity for various types of stars. Circles (triangles/squares/diamonds) stand for LBVs (OB stars). The position of red supergiants (WR stars) is shown by the left (right) ellipse. Adapted from Clark et al., 2012, A&A, 541, A145.

centered on HeII 4686 for three WR stars. The presence of overdensities moving from the line center to the wings is clearly seen. This is interpreted as the presence of clumps originating close to the surface and following the wind motion up to high velocities, and thus up to the outer atmosphere.

6 Conclusions

In this short review we have summarized the main characteristics of the winds of massive stars in four different evolutionary phases: OB, red supergiant, LBV and WR. Fig. 4 gathers the mass loss rates and wind velocities of stars in these different phases. Wind densities can be extracted from this figure, considering that they are proportional to the mass loss rate divided by the wind velocity.

We also highlighted the timescales of the different phases. Most of the time is spent in the OB phase. The latest phases (RSG, LBV, WR) are much shorter, but immediately precede the supernova explosion, and thus affect the appearance of the SN. The nature of the progenitor depends on the entire history of mass loss over the star's lifetime.

FM thanks the organizers for the invitation to give this review and for a fruitful meeting.

References

Aurière, M., Donati, J.-F., Konstantinova-Antova, R., et al. 2010, A&A, 516, L2
Bouret, J.-C., Lanz, T., & Hillier, D. J. 2005, A&A, 438, 301
Castor, J. I., Abbott, D. C., & Klein, R. I. 1975, ApJ, 195, 157
Chiosi, C. & Maeder, A. 1986, ARA&A, 24, 329

Chugai, N. N., Blinnikov, S. I., Cumming, R. J., et al. 2004, MNRAS, 352, 1213
Clark, J. S., Larionov, V. M., & Arkharov, A. 2005, A&A, 435, 239
Crowther, P. A. 2007, ARA&A, 45, 177
Crowther, P. A., Dessart, L., Hillier, D. J., Abbott, J. B., & Fullerton, A. W. 2002, A&A, 392, 653
Garcia, M., Herrero, A., Najarro, F., Lennon, D. J., & Alejandro Urbaneja, M. 2014, ApJ, 788, 64
Haubois, X., Perrin, G., Lacour, S., et al. 2009, A&A, 508, 923
Humphreys, R. M. & Davidson, K. 1979, ApJ, 232, 409
Kervella, P., Perrin, G., Chiavassa, A., et al. 2011, A&A, 531, A117
Leitherer, C., Robert, C., & Drissen, L. 1992, ApJ, 401, 596
Lucy, L. B. & Solomon, P. M. 1970, ApJ, 159, 879
Maeder, A. & Meynet, G. 1991, A&AS, 89, 451
Mauron, N. & Josselin, E. 2011, A&A, 526, A156
Meynet, G., Chomienne, V., Ekström, S., et al. 2015, A&A, 575, A60
Mokiem, M. R., de Koter, A., Vink, J. S., et al. 2007, A&A, 473, 603
Morse, J. A., Kellogg, J. R., Bally, J., et al. 2001, ApJ, 548, L207
Owocki, S. P., Gayley, K. G., & Shaviv, N. J. 2004, ApJ, 616, 525
Pauldrach, A., Puls, J., & Kudritzki, R. P. 1986, A&A, 164, 86
Schlegel, E. M. 1990, MNRAS, 244, 269
Stahl, O., Jankovics, I., Kovács, J., et al. 2001, A&A, 375, 54
Vink, J. S. & de Koter, A. 2002, A&A, 393, 543
Vink, J. S., de Koter, A., & Lamers, H. J. G. L. M. 2001, A&A, 369, 574

Session 13

Atelier du PNPS

SF2A 2015
F. Martins, S. Boissier, V. Buat, L. Cambrésy and P. Petit (eds)

*

A NEW WAY TO STUDY THE STELLAR PULSATION FIRST POLAR MISSION PAIX

M. Chadid[1]

Abstract. In the context of long and continuous timeseries photometry and after the MOST, CoRoT, KEPLER space missions and large geographic longitude ground–based networks, a new way is offered by the polar location helping to cope with the problem associated with the Earth day–night cycle. In this paper, we present the first long timeseries photometry from the heart of Antarctica -Dome Charlie- and we discuss briefly our new results and perspectives on the pulsating stars from Antarctica, especially the connection between temporal hydrodynamic phenomena and cyclic modulations. Finally, we highlight the impact of PAIX -the robotic Antarctica photometer- on the stellar pulsation study.

Keywords: Polar mission, robotic Antarctica photometer -PAIX-, stellar pulsation, Asteroseismology, observation, oscillations, hydrodynamics, space missions.

1 Introduction

Stellar oscillations and Asteroseismogy are currently one of the fundamental techniques to improve our understanding of the internal structure of stars. On the observational side, progress is limited by the data accuracy needed to detect numerous modes of oscillations with small amplitudes and by the discontinuous nature of typical ground-based data strings which often introduces ambiguities in the determination of oscillation frequencies. Space missions such as MOST (Matthews 1998), CoRoT (Chadid et al. 2010a) and KEPLER (Borucki et al. 2007) enable to overcome both difficulties, and indeed have considerably enhanced the scope of asteroseismological methods. However, the outcome of the space missions (MOST, COROT and KEPLER) on the stellar oscillation fields shows large gaps in terms of the flexibility during the observing runs, the choice of targets, the repair of failures and the inexorable high costs. Now the time has came to implement a new way to study the stellar oscillations with long uninterrupted and continuous observations over 150 days from the ground, south polar site –Dome Charlie– the great image quality and the high time coverage with PAIX. This photometer is made of the low–cost commercial components, and achieves astrophysical measurement time-series of stellar pulsation fields, challenging photometry from space. In this talk, we briefly describe the polar mission PAIX and the first outcome of the stellar pulsation from the heart Antarctica during 1 polar night.

2 Getting the PAIX Science for the Least Money

2.1 PAIX Mission, Polarcraft, Concept and Description

PAIX –Photometer AntarctIca eXtinction– gives new insight to cope with unresolved stellar enigma and stellar oscillation challenges and is a great opportunity to benefit from an access to one of the best astronomical site on Earth –Dome Charlie– at a height of 3300 m on $75^{deg}06^{min}04^{s}S, 123^{deg}20^{min}52^{s}$ E of Antarctica plateau, where the seeing reaches a median value of 1 arcsec during the polar night (Vernin et al. (2009) and Giordano et al. (2012)). PAIX is attached to the Cassegrain focus of a 40-cm Ritchey-Chretien optical telescope, with a F/D ratio of 10, located at Dome C in the open field, without any shelter, installed at ice level. The set–up of PAIX was improved by the use of a new camera SBIG ST10–XME, yielding images of 728 x 490 pixels with 3 x 3 binning across a 12.4 x 8.3 arcmn field of view. The camera is cooled with a Peltier assembly, with temperature

*Based on observations collected from Antarctica at Dome C, by use of PAIX telescope, during the polar night 2009

[1] Université Nice Sophia-Antipolis, Observatoire de la Côte d'Azur, UMR 7293, Parc Valrose, 06108 Nice Cedex 02, France

© Société Francaise d'Astronomie et d'Astrophysique (SF2A) 2015

regulation. The quantum efficiency is 60%, 85%, 80% and 55% at respectively 400, 550, 700 and 800 nm. PAIX challenges space telescopes and even has more advantages than CoRoT and KEPLER in observing in UBVRI bands and then collecting multicolor light curves simultaneously of several targets in the same field of view 12.4 arcmin x 8.3 arcmin.
PAIX has been antarctized to run under extreme conditions at temperatures as low as -80 deg.C, and has been designed and built by PaixTeam where the operating headquarters and the Principal Invistigator M. Chadid are located at Université de Nice Sophia–Antipolis and Observatoire de la Côte d'Azur.

2.2 PAIX Robotisation and Observations

The observations are collected under the extreme conditions of the climate, humain survival and isolation that prevail in the heart of Antarctica, by the use of PAIX.
A continuous, uninterrupted series of multi-color photometric observations is collected all along one polar night – 150 nights — from April to October, with Earth's day–night duty cycle of 80 % with 40–60 s of integration times and a high optical photometric accuracy of 0.025 mag for a 12 mag V–magnitude (Chadid et al. 2010b).
PAIX shows a tremendous increase of the productivity with the development of a new remote control software PACS –PAIX Acquisition and Control Software– and then is automatically operated without any human on-site intervention (except under extreme weather conditions or major power failure). For the first time, remote polar observations is finally possible from anywhere in the world towards the heart of Antarctica, Dome Charlie. Remote observing sequences are scripted and data series are automatically transferred through VPN tunnel to a server located in Nice (Figure. 1).

3 Stellar pulsation study

3.1 Antarctica RR Lyrae survey

We present the first optical photometric data collected by the use of PAIX from Dome Charlie. A continuous and uninterrupted series of photometric observations, of the Blazhko* RR Lyrae star S Arae, was collected during one polar night – 150 nights — from 18 April to 20 Septembre 2009. Figure. 2 shows the PAIX light curve of S Arae. The V-magnitude varies between 10 and 11.5 mag, with an accuracy of 0.025 mag, in a period of 0.452 d and a Blazhko period of 48.544±0.045 d. A total of 89736 CCD frames, during 323 pulsation cycles and 3 Blazhko cycles, were acquired with 40 to 60 s integration times, allowing an average time resolution T/P around 0.15 % of the pulsation period, where T is the exposure time and P is the period of the pulsation. The PAIX data were analyzed using the software PDM13 (Zalian et al. 2014). Besides the main pulsation period of 0.452 d and the Blazhko period of 47.264 d, the frequency analysis shows three new significant frequencies that we interpreted as a first radial overtone (0.319 d) and two non–radial modes (0.338 d and 0.263 d) never detected so far in an RR ab type (Chadid et al. 2014).

3.2 Possible explanation of the Blazhko effect

Figure. 3 presents the light curve of S Arae, showing the *lump*, *bump* and *hump* (Chadid & Preston 2013). The most striking feature is that the descending branch of the light curve demonstrates the existence of new bumps at phases $\varphi = 0.10$ and $\varphi = 0.70$. We call them *jump* and *rump*. The *jump* occurs just after maximum light and the *rump* appears very close to the *bump*. They might be a consequence of a multi–shock structure, the atmosphere of the Blazhko star S Arae is crossed by several shock waves with different amplitudes and physical origins. In this condition, the shocks develop a stationary coronal structure and drive an outflowing wind. The latter minimize gradually the overall compression of the atmosphere and then the strength of κ–γ mechanisms. Perhaps, the outflowing wind plays a major role of a trigger mechanism acting on the κ and γ mechanisms. We suggest that the Blazhko effect is a consequence of a dynamical interaction between a multi–shock structure and the outflowing wind of a coronal structure (Chadid et al. 2014).

*Chadid (2011)

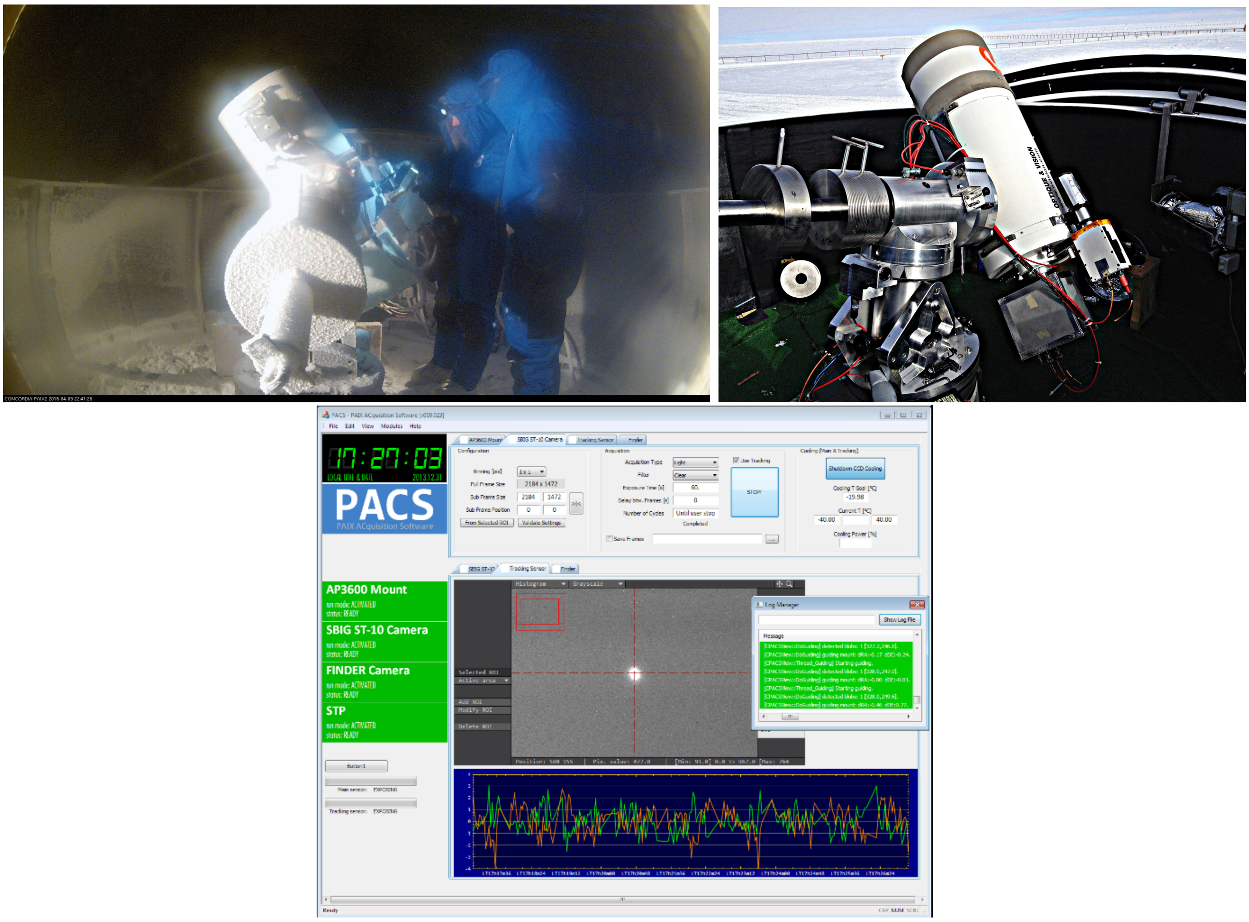

Fig. 1. Top*:* The robotic Antarctica photometer –PAIX– during the polar night (on the left) and during the polar day (on the right) in the heart of Antarctica at Dome Charlie. Remote observing sequences are scripted and data series are automatically transferred through a VPN tunnel to a server located in Nice. PAIX is antarctized to run under extreme conditions at temperatures as low as -80 deg.C. **Bottom:** Screen capture of the remote PAIX Acquisition and Control Software PACS.

4 Conclusions

PAIX – robotic Antarctica photometer – polar mission is a great opportunity for monitoring stars with excellent time-sampling and unprecedented photometric precision over up to 150 days, and could even challenge the photometry from space for less Money. As an important benefit, high-quality RR Lyrae polar light curves are obtained with a quasi-uninterrupted coverage over several pulsation and Blazhko cycles. The PAIX polar data, are the most accurate and continuous data set of oscillating and pulsating stars ever obtained from the ground-based observation networks. Due to the proper data sampling and high precision we got new results towards understanding of the atmospheric dynamics and the pulsation behaviour in the pulsating stars type RR Lyrae. We describe the still puzzling Blazhko phenomenon on a higher level and we suggest a new explanation of the Blazhko effect.

I thank Yveline Lebreton and Boris Dintrans for inviting me to give this talk.
Special thanks go to US Air Force Research Laboratory, Agence Nationale de la Recherche (ANR-05-BLAN-0033-01), Conseil des Programmes Scientifiques et Technologiques (CPST) for their great support and the Polar Institut Paul Emile Victor (IPEV) for the precious infrastructure helps.
I am indebted to all people who partcipates to the Antarctica expeditions within the PAIX program.

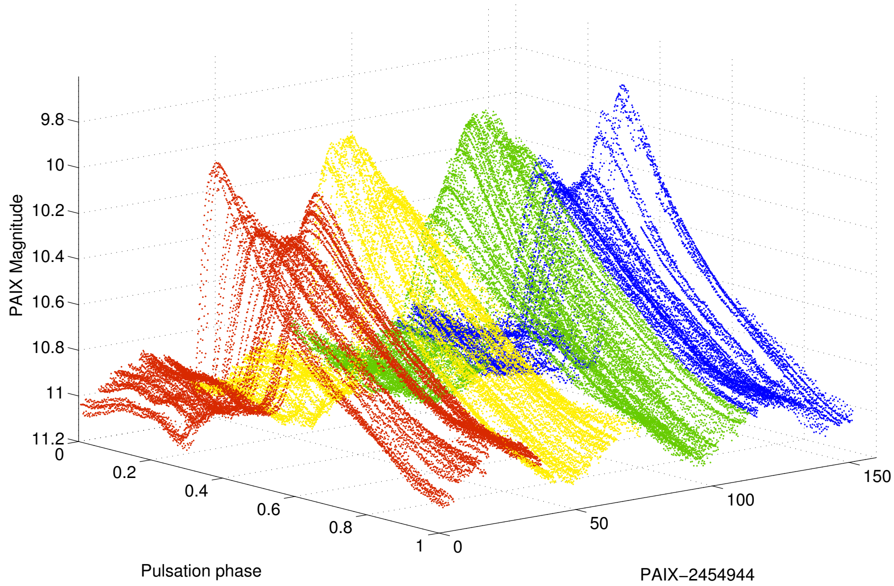

Fig. 2. Three–dimensional PAIX light curve of S Arae over 150 days –one polar night– folded with the pulsation period (0.452) over 3 Blazhko cycles and showing a strong Blazhko strength.

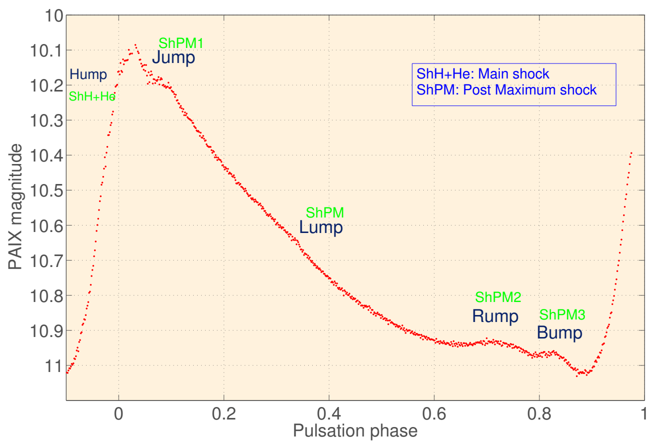

Fig. 3. PAIX light curve of S Arae showing the hump, jump, lump, rump and bump

References

Borucki, W. J., Koch, D. G., Lissauer, J., et al. 2007, in Astronomical Society of the Pacific Conference Series, Vol. 366, Transiting Extrapolar Planets Workshop, ed. C. Afonso, D. Weldrake, & T. Henning, 309

Chadid, M. 2011, in RR Lyrae Stars, Metal-Poor Stars, and the Galaxy, ed. A. McWilliam, 29

Chadid, M., Benkő, J. M., Szabó, R., et al. 2010a, A&A, 510, A39

Chadid, M. & Preston, G. W. 2013, MNRAS, 434, 552

Chadid, M., Vernin, J., Mekarnia, D., et al. 2010b, A&A, 516, L15

Chadid, M., Vernin, J., Preston, G., et al. 2014, AJ, 148, 88

Giordano, C., Vernin, J., Chadid, M., et al. 2012, PASP, 124, 494

Matthews, J. 1998, JRASC, 92, 314

Vernin, J., Chadid, M., Aristidi, E., et al. 2009, A&A, 500, 1271

Zalian, C., Chadid, M., & Stellingwerf, R. F. 2014, MNRAS, 440, 68

SF2A 2015
F. Martins, S. Boissier, V. Buat, L. Cambrésy and P. Petit (eds)

CLUES ABOUT THE FIRST STARS FROM CEMP-NO STARS

A. Choplin[1], G. Meynet[1] and A. Maeder[1]

Abstract. The material used to form the CEMP-no stars presents signatures of material processed by the CNO cycle and by He-burning from a previous stellar generation called the source stars. In order to reproduce the relative abundance ratios like for instance C/N or ^{12}C/^{13}C, some mixing between the two burning regions must have occured in the source stars and only the outer layers of the stars, with modest amount coming from the CO core, must have been expelled either through stellar winds or at the time of the (faint) supernova event. With new models at low metallicity including rotational mixing, we shall discuss how the variety of abundances observed for CEMP-no stars can be reproduced.

Keywords: stars: evolution, rotation, massive, abundances, nucleosynthesis, chemically peculiar

1 Introduction

Iron deficient zones in the universe are of particular interest since they were preserved from chemical enrichment, hence delivering clues on the early universe. Carbon enhanced metal poor stars (CEMP) are iron deficient stars with an excess of carbon relatively to the sun. The two common criteria defining a CEMP star are* [Fe/H] < -1 and [C/Fe] > 0.7 (Aoki et al. 2007). s- and r-elements were detected in some of those stars, leading to 4 subclasses : CEMP-s, CEMP-r/s, CEMP-r and CEMP-no stars (Beers & Christlieb 2005). CEMP-no denote CEMP stars without significant amounts of s- or r- elements. This latter category is of particular interest since it dominates at [Fe/H] < -3 (Aoki 2010; Norris et al. 2013), allowing us to approach the primordial universe even closer. Among the scenarios explored to explain CEMP-no stars, there is the "spinstar" scenario (Meynet et al. 2006, 2010; Hirschi 2007; Maeder et al. 2015), which suggests that CEMP-no formed in a region previously enriched by a material coming from fast rotating, low metallicity, massive stars, experiencing strong mixing, mass loss and eventually a supernova at the end of their lives. For main sequence CEMP-no stars at least, no in situ changes of the surface abundances are expected and observed surface abundances are believed to be the same as at the time of the star formation. Recently, Maeder et al. (2015) suggested that the variety of CEMP-no abundances can be explained by a material having been processed back and forth by H- and He-burning regions before being ejected by the spinstar. Also shown in Maeder et al. (2015) is that changing the initial CNO distribution in the spinstar will increase the fit between model and observations in 2D abundance diagrams like log(^{12}C/^{13}C) vs. [C/N].

We discuss two 32 $M_\odot$ models of spinstars computed with the geneva code. Ejecta of the models (wind and supernova) are compared to observed CEMP-no abundances through the 2D abundance diagram [C/N] vs. log(^{12}C/^{13}C). We discuss the impact of taking non-solar initial CNO abundances and emphasize the need for a strong interaction between H- and He-burning shells, in order to synthesize the material needed to build CEMP-no stars.

2 Physical ingredients

The two 32 $M_\odot$ models discussed were computed at $Z = 10^{-5}$, with an initial rotation rate† of $v/v_{crit} = 0.7$, which corresponds to an initial equatorial velocity of 680 km/s. The evolution is stopped at the end of the

[1] Department of Astronomy, University of Geneva, Versoix, Switzerland

*[X/Y] = $\log_{10}(N_X/N_Y)$ - $\log_{10}(N_{X\odot}/N_{Y\odot})$ with $N_{X,Y}$ the number density of elements X and Y, $\odot$ denoting the abundances in the sun.

†v_{crit} is the velocity at which the gravitational acceleration is exactly compensated by the centrifugal force at the equator.

© Société Francaise d'Astronomie et d'Astrophysique (SF2A) 2015

neon photodisintegration phase, after the carbon burning. Mass loss prescription is taken according to Vink et al. (2001) when $T_{eff} > 3.95$ and to de Jager et al. (1988) otherwise. We used the recipes of Zahn (1992) and Maeder (1997) for horizontal turbulence and shear mixing, respectively. The only difference between the two models is their initial composition : while the first model has a solar-scaled mixture (Asplund et al. 2005), the second one presents a modified α-enhanced mixture (α-mod). In the latter mixture [C/N], [O/N] and $^{12}C/^{13}C$ are put to 2, 1.6 and 30, according to suggestions of Maeder et al. (2015) for [C/N] and [O/N] and to prediction of galactic chemical evolution models at low metallicity of Chiappini et al. (2008) for $^{12}C/^{13}C$.

3 Results

Thick tracks in fig.1 show the integrated abundances in the wind as evolution proceeds for the two models. Comparing the two thick paths, one sees that both are going toward the CNO-equilibrium point : the CNO cycle is at work in such massive stars and transforms ^{12}C into ^{14}N and ^{13}C, leading to lower and lower [C/N] and $\log(^{12}C/^{13}C)$ in the wind. Since the initial [C/N] is higher in the α-mod mixture, it better fits the observations and cover the whole range of observed [C/N] and almost all the range of $^{12}C/^{13}C$. However, it seems that wind cannot provide a material with $-1 <$[C/N]< 1 together with $\log(^{12}C/^{13}C) \sim 0.5$, where most CEMP-no are lying. Moreover, both models lose only $\sim 0.5\ M_{\odot}$ through winds, which is probably too low to form a new (even low mass) star. More massive models of spinstars should be modeled since they are likely to eject more mass through winds. A way to get more available mass in the ISM with the present models is to add a supernova to the wind.

Thin curves in fig.1 show the integrated abundances in the ejecta as inner and inner layers of the final stellar structure are added to the wind. Although simple, such a supernova simulation allow us to explore all possible mass cuts[‡]. Even though the red track is going toward higher [C/N], both of those thin curves are similar and can be divided in three parts:

1. Outer layers ($20 < M_{cut} < 31\ M_{\odot}$) of the stars are added to the wind. The CNO cycle was at work here, so that the ejecta is more and more enriched in ^{13}C and ^{14}N, reducing [C/N] and $\log(^{12}C/^{13}C)$ ratios from ~ -2 and ~ 0.75 to ~ -2.6 and ~ 0.6 (see fig.1).

2. Middle layers are added ($13 < M_{cut} < 20\ M_{\odot}$). $^{12}C/^{13}C$ is at CNO equilibrium in this region but not [C/N] : there is an excess of ^{12}C compared to ^{14}N. This ^{12}C comes from the He-burning shell which has strongly interacted with the H-shell during the carbon burning phase, leading to [C/N] of ~ -1 and 0 for solar and α-mod models respectively. Rotational mixing is likely playing an important role to build this special regions in the star, where some He-burning products have moved from the He-shell to the H-shell. The physical process leading to a zone in the star with CNO equilibrium values for $^{12}C/^{13}C$ but not for [C/N] is likely due to the fact that $(^{12}C/^{13}C)_{eq}$ is reached quicker that $[C/N]_{eq}$ when the CNO-cycle operates.

3. Inner layers are added ($M_{cut} < 13\ M_{\odot}$). The He-shell burning shell is reached, leading to a big rise of both [C/N] and $^{12}C/^{13}C$ since a He-burning region is ^{12}C-rich but ^{13}C- and ^{14}N-poor.

As we see, $^{12}C/^{13}C$ ratio is able to constrain M_{cut} : if too deep layers are expelled, $^{12}C/^{13}C$ in the ejecta become too high compared to the range of observed value. Only modest amount of He-burning region should be expelled : ejecting 1 $M_{\odot}$ of the He-shell of the model with α-mod mixture leads to $\log(^{12}C/^{13}C) = 1.7$, which correspond to maximum observed values.

Considering also the wind ejecta, we see that starting with an α-mod mixture in the spinstar improves the fit regarding to a solar mixture : all the range in [C/N] is covered and adding a (faint) supernova to the wind provides a material which corresponds to many observed [C/N] and $^{12}C/^{13}C$ ratios at the surface of CEMP-no stars. A word of caution, however, regarding the ejecta : while wind, and especially mechanical wind Decressin et al. (2007), is expected to stay in the neighbourhood of the star, the supernova ejecta is likely to go further so that the different ejecta should be considered separately. Moreover, some dilution with the ISM can occur, leading to a mixed material made of processed and pristine material. Those points should be taken into account in the future.

[‡]mass coordinate inside the star delimiting the part which is expelled from the part which is kept into the remant.

One of the other next step is to consider more chemical species (O, Ne, Na, Mg, Al...) in order to increase the level of constraint. Different initial masses must also be investigated, especially to have an idea on which kind of progenitor is preferred to form CEMP-no stars.

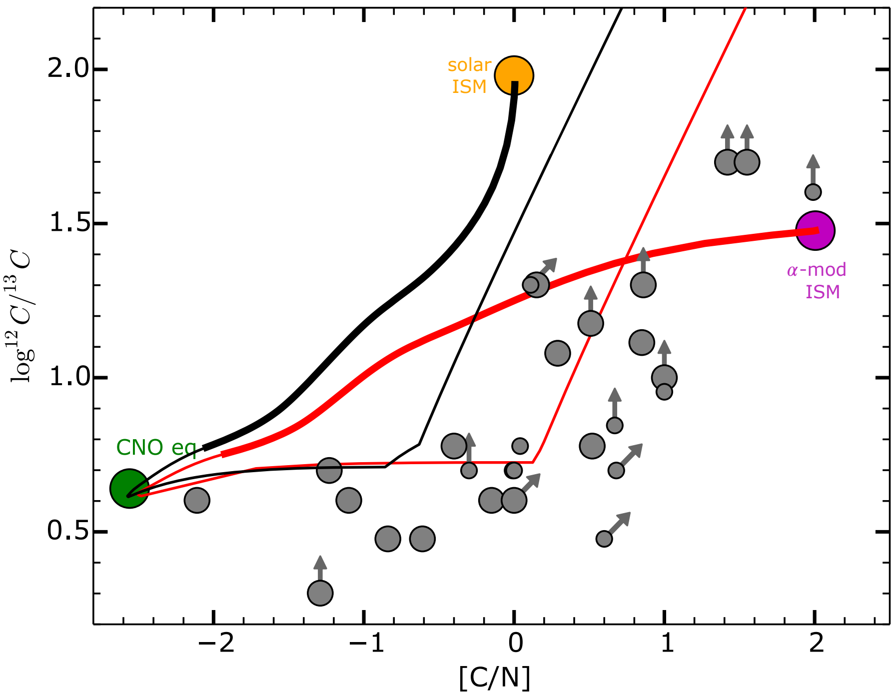

Fig. 1. [C/N] vs. $\log(^{12}C/^{13}C)$ diagram. Grey dots are observed CEMP-no stars from Norris et al. (2013), Masseron et al. (2010), Allen et al. (2012) and Hansen et al. (2015) (except for 6 stars, the rest of the sample is the same as Maeder et al. (2015), see their table 1 for more details). Small points are MS stars or subgiants while bigger points apply for bright giants. A vertical arrows is drawn when $^{12}C/^{13}C$ is a lower limit. Oblique arrows indicate a lower limit for $^{12}C/^{13}C$ and an upper limit for Nitrogen at the same time. Yellow and green circles denote values in the sun and when the CNO-cycle is at equilibrium, respectively. Purple circle represent the initial α-mod mixture. Thick tracks show integrated abundances ratios in the wind as evolution proceeds and thin lines show the integrated abundances in the ejecta as inner and inner layers of the final stellar structure are added to the wind.

4 Conclusions

We discussed the possibility of building observed CEMP-no stars with ejecta of spinstars. The two models presented differed only by their initial CNO distribution. The model with a non-solar initial CNO distribution improves the fit in two ways : first the initial [C/N] is taken higher than solar, so that the whole range of observed [C/N] is covered with wind ejecta. Second, CEMP-no with $-1 <$ [C/N] < 1 together with $\log(^{12}\mathrm{C}/^{13}\mathrm{C}) \sim 0.7$ are well covered by the α-mod model if adding a supernova to the wind. Various mass cuts in the spinstar can explain different observed CEMP-no. The special material, with CNO equilibrium values for $^{12}C/^{13}$C but not for [C/N], is made available during carbon burning phase, owing to a strong interaction between H- and He-burning shells. Regardless of the initial CNO distribution, $^{12}\mathrm{C}/^{13}\mathrm{C}$ appears to be a great ratio to constrain the mass cut at the time of the supernova : if too deep layers are added to the wind, He-burning region is reached and $^{12}\mathrm{C}/^{13}\mathrm{C}$ becomes too high compared to observed ratios.

References

Allen, D. M., Ryan, S. G., Rossi, S., Beers, T. C., & Tsangarides, S. A. 2012, A&A, 548, A34

Aoki, W. 2010, in IAU Symposium, Vol. 265, IAU Symposium, ed. K. Cunha, M. Spite, & B. Barbuy, 111–116

Aoki, W., Beers, T. C., Christlieb, N., et al. 2007, ApJ, 655, 492

Asplund, M., Grevesse, N., & Sauval, A. J. 2005, in Astronomical Society of the Pacific Conference Series, Vol. 336, Cosmic Abundances as Records of Stellar Evolution and Nucleosynthesis, ed. T. G. Barnes, III & F. N. Bash, 25

Beers, T. C. & Christlieb, N. 2005, ARA&A, 43, 531

Chiappini, C., Ekström, S., Meynet, G., et al. 2008, A&A, 479, L9

de Jager, C., Nieuwenhuijzen, H., & van der Hucht, K. A. 1988, A&AS, 72, 259

Decressin, T., Meynet, G., Charbonnel, C., Prantzos, N., & Ekström, S. 2007, A&A, 464, 1029

Hansen, T., Hansen, C. J., Christlieb, N., et al. 2015, ArXiv e-prints [arXiv] 1506.00579

Hirschi, R. 2007, A&A, 461, 571

Maeder, A. 1997, A&A, 321, 134

Maeder, A., Meynet, G., & Chiappini, C. 2015, A&A, 576, A56

Masseron, T., Johnson, J. A., Plez, B., et al. 2010, A&A, 509, A93

Meynet, G., Ekström, S., & Maeder, A. 2006, A&A, 447, 623

Meynet, G., Hirschi, R., Ekstrom, S., et al. 2010, A&A, 521, A30

Norris, J. E., Yong, D., Bessell, M. S., et al. 2013, ApJ, 762, 28

Vink, J. S., de Koter, A., & Lamers, H. J. G. L. M. 2001, A&A, 369, 574

Zahn, J.-P. 1992, A&A, 265, 115

SF2A 2015
F. Martins, S. Boissier, V. Buat, L. Cambrésy and P. Petit (eds)

GAIA RADIAL VELOCITIES: FIRST COMPARISONS WITH GROUND VALUES

F. Crifo[1], G. Jasniewicz[2], D. Katz[1,], O. Marchal[1,], P. Panuzzo[1,], P. Sartoretti[1,], C. Soubiran[3] and C. Zurbach[2,]

Abstract. After several months of Gaia-RVS observations, many radial velocities are now available and can be compared to existing ground values. An extended catalogue of 10227 reliable ground-based RV has been compiled from different sources including our own observations of standard star candidates, and objects with good archive spectra.

First conclusions are:

Some 4000 comparison stars already observed several times during the 3 first months of operation show a gaussian dispersion around the ground-based value on the order of 1.1km/s; some stars show a slight evolution of their RVS measurements and are probably binaries; some RVS observations show "irregularities" now explored in details.

It is particularly important to note that our 2798 primary standard star candidates (extended list), are very stable over the Gaia mission. For the others, the last ground-based campaign anticipated 10 years ago to assess their stability, should be now started.

Keywords: stars, radial velocities, sb2, Gaia

1 Introduction

The Gaia satellite with its Radial Velocity Spectrometer (RVS) has been working regularly since July 2014. Many radial velocities have already been acquired. In order to enlarge the number of standard stars, an extended catalogue of reliable ground-based RV has been already compiled from different sources including both our own observations of standard stars candidates, and other objects with good archive or literature measurements. This catalogue is used for calibration and evaluation of accuracy of the instrument. It contains 10227 objects and its description is for the moment restricted inside the DPAC Consortium; 2798 of these stars are called "primary standards" (highest quality).

It should be noted that the "RVS values" presented in this paper are not yet provided by the general reduction pipeline, but by the simplified pipeline developed at Meudon for the commissioning. They are therefore not "final".

2 General results

Within the RVS observations, those concerning the stars in our extended catalogue (primary and secondary stars) have been extracted, and compared to the ground values. The result is shown on the histogram of Fig. 1 left; it contains 11787 observations made between july and october 2014, and concerning 3783 objects with more than 3 observations each. In x, the quantity ($RV_{RVS} - RV_{ground}$). The standard deviation is 1.14 km/s. (Expected values at end of mission: 1 km/s for such bright objects).

[1] GEPI (UMR 811 du CNRS; Université Paris 7, FRANCE), Observatoire de Paris, 92190 MEUDON, FRANCE
[2] LUPM UMR 5299 CNRS/UM2, Université Montpellier II, CC 72, 34095 Montpellier Cedex 05, FRANCE
[3] LAB, UMR 5804 - Université de Bordeaux - CNRS, 2 rue de l'Observatoire, F-33270 FLOIRAC, FRANCE

© Société Francaise d'Astronomie et d'Astrophysique (SF2A) 2015

3 Some examples

3.1 A nice double star

The star HIP 70674 shown on Fig. 1 right is listed as double star in the SB9 catalogue (Pourbaix et al. (2004), Halbwachs et al. (2014)). Each calcium line shows a double peak. The distance between the two peaks varies with time.

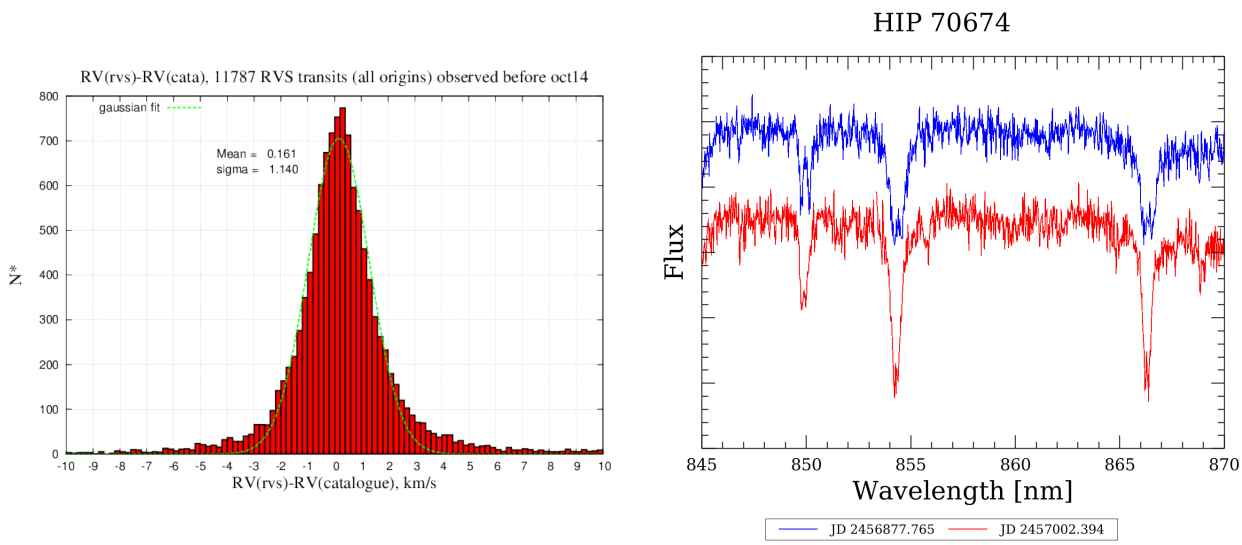

Fig. 1. Left: 11787 transits for 3783 primary and secondary standard stars already observed. **Right:** A double star at 2 different epochs.

3.2 Ground and space measurements

Data from both ground and space are available for the observed standard stars. On Fig. 2 they all are plotted on a common graph for HIP 32769. The zero-shift between the histogram centre (see fig. 1) and the ground values has not yet been removed. A slight drift in time is possible: therefore this object will be remeasured in our ground-based observing programme, phase 2 (during mission). It might be an unknown long-period double star.

4 Ground observations, phase 2

For the RVS calibration, 1420 candidate standard stars had been selected several years ago (see Crifo et al. (2010), Soubiran et al. (2013) and intensively observed from the ground between 2006 and 2013; 1300 more have been recently selected within the archive data from Elodie, Sophie and Harps: a total of 24865 individual measurements. Most objects proved to be quite stable in RV; but some are less: figure 3 shows the variability found within the basic list of 1420; the maximum acceptable value for variability being set at 0.3 km/s.

For slightly more than 1000 of these stars, the long-term stability (until end of mission: 2019?) has to be assessed. Therefore it is now time to start the Phase 2 of our observing programme, on the SOPHIE (north) and CORALIE (south) spectrographs. Figure 4 shows the fraction of stars to be reobserved in the North: those with only few measurements; or a short time basis; or quite old data; or a possible small drift.

5 Conclusion

From these very first data it appears that the RVS gives good, accurate spectra; and that the agreement with ground-based data is good too. The second phase of ground observations for the candidate standards can now be started.

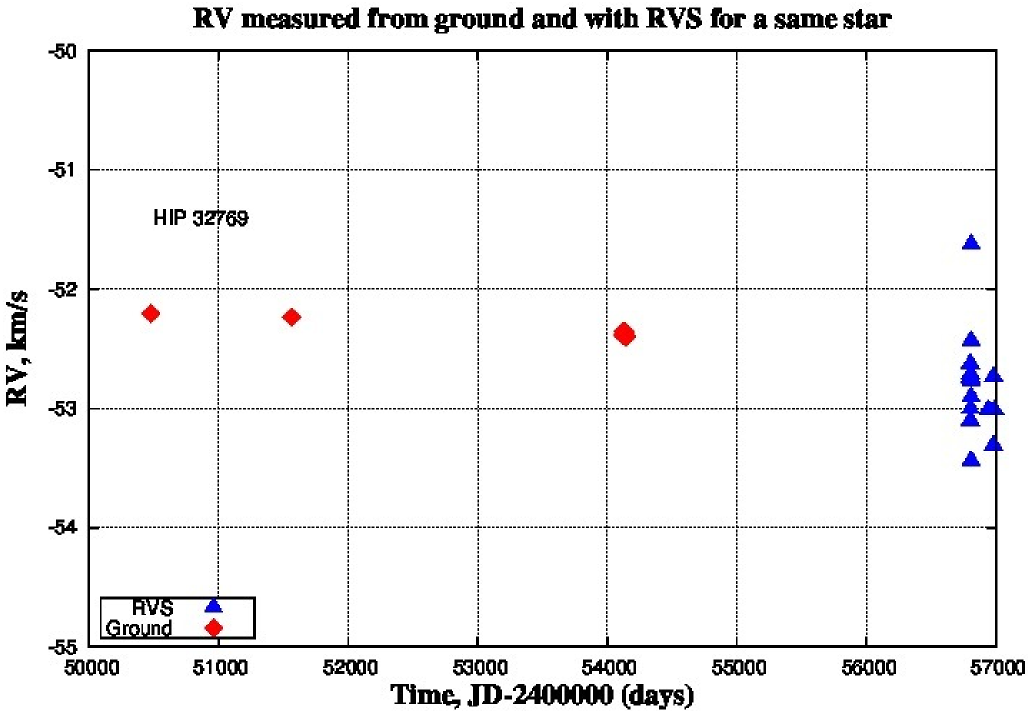

Fig. 2. Ground and space observations for a same star: possible drift?

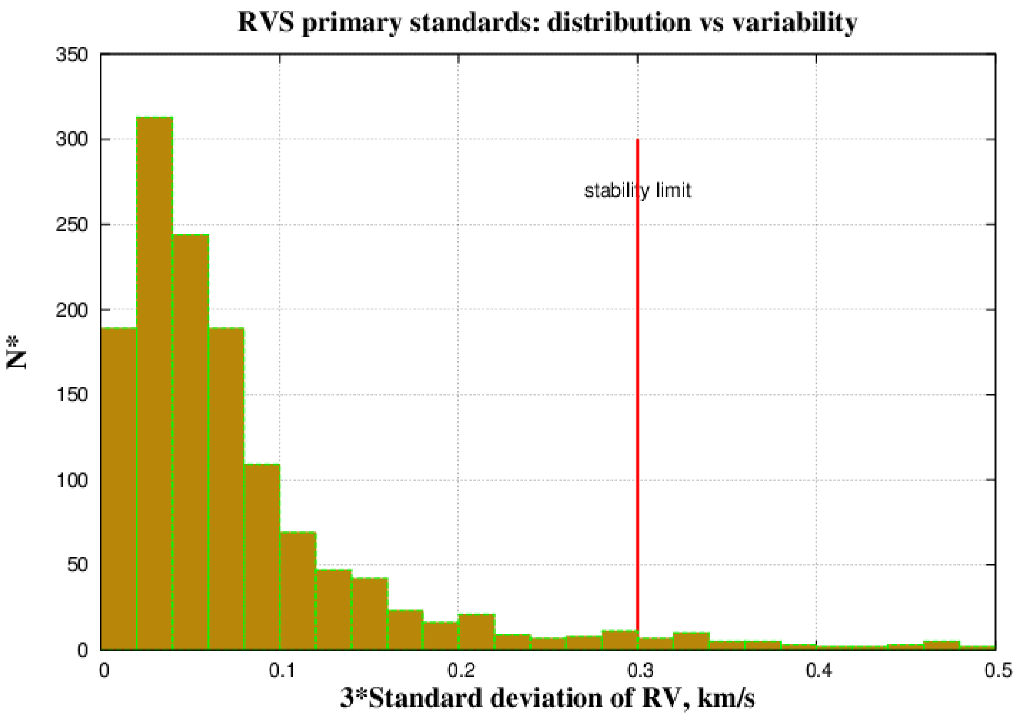

Fig. 3. Variability among the basic list of 1420 candidate standard stars

The authors are members of the Gaia Data Processing and Analysis Consortium (DPAC) and this work has been supported by the following funding agencies: Observatoire de Paris, Université de Bordeaux, Université de Montpellier, INSU, CNRS, CNES.

Material used in this work has been provided by the Coordination Unit 6 (CU6) of DPAC. They are gratefully acknowledged for their contribution.

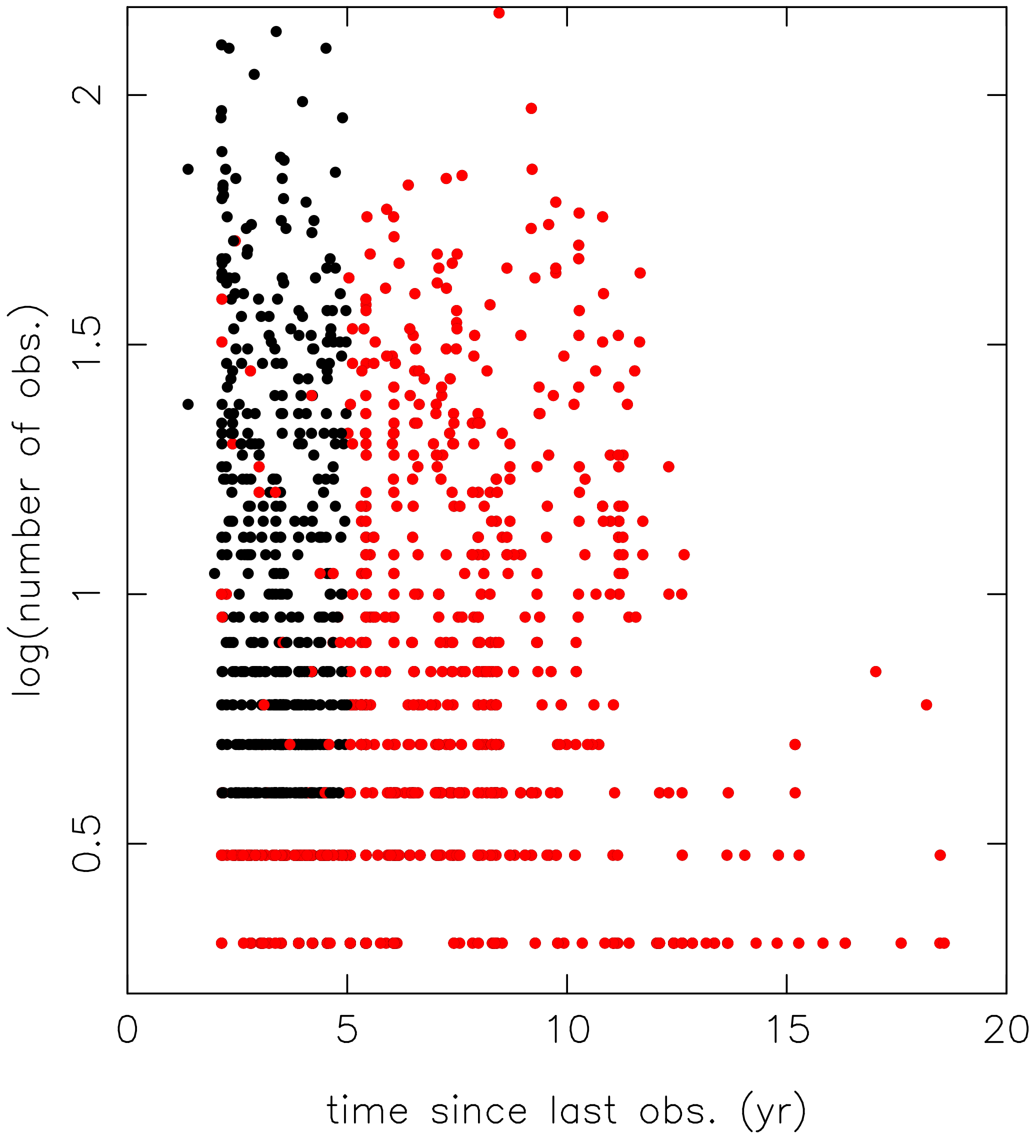

Fig. 4. Northern candidate standards: those in red should be remeasured.

The ground-based observers at Observatoire de Haute-Provence, Observatoire du Pic du Midi and Observatoire de Genève who acquired a good part of the telescope data on the standard stars, and the CDS Strasbourg, are also kindly thanked.

References

Crifo, F., Jasniewicz, G., Soubiran, C., et al. 2010, A&A, 524, A10

Halbwachs, J.-L., Arenou, F., Pourbaix, D., et al. 2014, MNRAS, 445, 2371

Pourbaix, D., Tokovinin, A. A., Batten, A. H., et al. 2004, A&A, 424, 727

Soubiran, C., Jasniewicz, G., Chemin, L., et al. 2013, A&A, 552, A64

SF2A 2015
F. Martins, S. Boissier, V. Buat, L. Cambrésy and P. Petit (eds)

FINGERING INSTABILITIES INDUCED BY THE ACCRETION OF PLANETARY MATTER ONTO STARS : THE LITHIUM CASE. APPLICATION TO THE 16 CYGNI STELLAR SYSTEM.

M. Deal[1,2], O. Richard[1] and S. Vauclair[2,3]

Abstract. The 16 Cygni system is composed of two solar analogs with similar masses and ages. They have been observed by *Kepler* for asteroseismology, and their radii have been precisely determined from interferometry. A red dwarf is in orbit around 16 Cygni A whereas 16 Cygni B hosts a giant planet. The abundances of heavy elements are similar in the two stars but lithium is much more depleted in 16 Cygni B that in 16 Cygni A, by a factor of at least 4.7. We show that fingering convection induced by the accretion of planetary matter onto 16 Cygni B can account for this difference in lithium abundances. This is a general result which may be applied to all planetary-host stars.

Keywords: 16 Cyg system, stellar evolution, accretion, fingering convection, lithium abundance

1 Introduction

The bright solar analogs 16 Cyg A and 16 Cyg B represent a very interesting stellar system for many reasons. The two stars are separated enough to be studied in the same way as two isolated stars, with no common dynamical effects. This situation allows for precise differential studies between a planet-host star and a non-planet-host star with similar birth conditions. The presence of the brown dwarf around 16 Cyg A may be the reason why no accretion disk could have developed around it, whereas a planetary disk remained around 16 Cyg B, including the observed giant planet, and probably smaller still unobserved bodies. The metallic abundances of these two stars are very close but the surface lithium abundance of 16 Cyg B is smaller than that of 16 Cyg A by at least a factor 4.7 (King et al. 1997). The interest of this study is that these stars have the same birth site and the same age, with masses of the same order, so that their past evolution is similar for most aspects. The observed differences between them must basically be due to the presence of a planetary disk around 16 Cyg B. We studied the properties of these two stars by computing models with the Toulouse Geneva Evolution Code (TGEC). We identified the stellar oscillation frequencies (computed with the PULSE code of Brassard & Charpinet 2008) with the Kepler observations to derive the best models. We then tested the effect of accreting planetary matter on the lithium abundance of 16 Cyg B.

2 Fingering (thermohaline) convection

In stars, fingering (thermohaline) convection occurs every time heavy matter comes upon lighter one, in the presence of a stable temperature gradient. This may happen in several cases, and particularly in the case of accretion of planetary matter (Vauclair 2004; Garaud 2011; Théado & Vauclair 2012; Deal et al. 2013).

Fingering convection is characterised by the so-called density ratio R_0 which is the ratio between thermal and compositional gradients:

$$R_0 = \frac{\nabla - \nabla_{ad}}{\nabla_\mu}.$$

[1] Laboratoire Univers et Particules de Montpellier (LUPM), UMR 5299, Université de Montpellier, CNRS, Place Eugne Bataillon 34095 Montpellier Cedex 5 France
[2] CNRS, IRAP, 14 avenue Edouard Belin, 31400 Toulouse, France
[3] Université de Toulouse, UPS-OMP, IRAP, France

© Société Francaise d'Astronomie et d'Astrophysique (SF2A) 2015

Table 1. Properties of 16 Cygni A and B from this work

	16 Cygni A	16 Cygni B
$T_{\rm eff}$ (K)	5821 ± 25	5747 ± 25
log g	4.29 ± 0.01	4.36 ± 0.01
Mass ($M_\odot$)	1.10 ± 0.01	1.06 ± 0.01
Radius ($R_\odot$)	1.24 ± 0.01	1.13 ± 0.01
Luminosity ($L_\odot$)	1.58 ± 0.03	1.25 ± 0.03
Age (Gyrs)	6.4 ± 0.4	6.4 ± 0.4
Z_i	0.024	0.024
Y_i	0.26	0.26
Z_{surf}	0.0221	0.0223
Y_{surf}	0.2226	0.2265

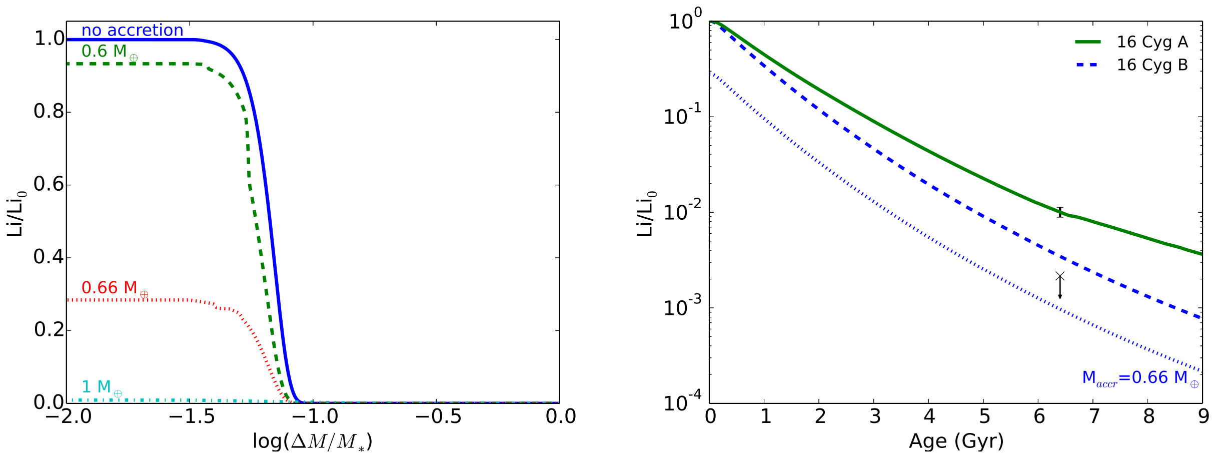

Fig. 1. Left: Lithium abundance profiles just after the accretion of different masses at the beginning of the MS for 16 Cygni B models. **Right:** Time variations of the lithium surface abundances. The black crosses are the observed lithium abundances (King et al. 1997). The solid and dashed lines represent respectively the models computed for 16 Cyg A and B without any accretion whereas the dotted line corresponds to the models of 16 Cyg B computed with an accreted mass of 0.66 $M_\oplus$.

This instability can only develop if the thermal diffusivity is larger than the molecular one. This means that a heavy blob of fluid falls in the star and keeps falling because heat diffuses more rapidly than the chemical elements. Fingering convection cannot occur if the ratio of the diffusivities becomes smaller than ratio of the gradients, which leads to the following condition:

$$1 < R_0 < \frac{1}{\tau}$$

where τ is the inverse Lewis number, ratio of molecular and thermal diffusivity. For values of $R_0 < 1$ the region is dynamically convective (Ledoux criteria) and for values of $R_0 > 1/\tau$ the region is stable.

3 Accretion

We computed models of 16 Cyg A and B with initial parameters as given in Table 1, which fit precisely the observed oscillation frequencies (Deal et al. 2015). Here we show how the accretion of planetary matter (earth composition) on 16 Cyg B at the beginning of the MS induces fingering convection, which decreases the surface lithium abundance (left panel of Fig. 1).

Accreted masses lighter than 0.6 $M_\oplus$ only have a small impact on the Li surface abundance because the μ-gradient is not large enough. For larger accreted masses, fingering convection mixes elements down to the lithium destruction zone and may reduce significantly the Li surface abundance.

4 Results

The Li abundance ratio between 16 Cyg A and B is too large to be accounted for by traditional mixing processes like rotation and/or internal waves. Beginning with the same initial lithium, the ratio at the age of the stars is less than 3, whereas the observed ratio is larger than 4.7 (right panel of Fig. 1). Another process is needed to explain the Li destruction in 16 Cygni B. We claim that this process is the fingering convection induced by planetary matter accretion.

We computed models of 16 Cyg B in which we assumed accretion-induced fingering convection at the beginning of the evolution. Later on, lithium was supposed to decrease with time in the same way for the two stars. We show that in this case, an accretion mass of 2/3 $M_\oplus$ is enough to account for the larger depletion observed in 16 Cyg B.

Furthermore the observed Li surface abundance of 16 Cyg B is an upper limit so that a larger accretion mass may be needed to explain the observations.

5 Conclusion

The accretion of planetary matter onto stars leads to fingering convection which has to be taken into account when computing the abundance variations of the elements. Due to this extra mixing, the accreted heavy elements are diluted inside the star, so that no overabundance remains at the surface. Meanwhile, lithium may be destroyed if the mixing zone reaches the lithium destruction region. A fraction of earth mass is enough to account for the observations in the 16 Cygni system.

This extra mixing may happen in many cases, every time stars accrete heavy matter. The 16 Cygni system is very instructive in that respect. We are going to study this effect in more details, for other stars, including very metal poor stars, CEMPs and other cases. We will also computed models with the Montreal-Montpellier code, which treats the diffusion processes with a numerical scheme different from the TGEC one, to test the robustness of our results.

References

Brassard, P. & Charpinet, S. 2008, Ap&SS, 316, 107

Deal, M., Deheuvels, S., Vauclair, G., Vauclair, S., & Wachlin, F. C. 2013, A&A, 557, L12

Deal, M., Richard, O., & Vauclair, S. 2015, ArXiv e-prints 1509.06958 [arXiv] 1509.06958

Garaud, P. 2011, ApJ, 728, L30

King, J. R., Deliyannis, C. P., Hiltgen, D. D., et al. 1997, AJ, 113, 1871

Théado, S. & Vauclair, S. 2012, ApJ, 744, 123

Vauclair, S. 2004, ApJ, 605, 874

SF2A 2015
F. Martins, S. Boissier, V. Buat, L. Cambrésy and P. Petit (eds)

HOST'S STARS AND HABITABILITY

F. Gallet[1], C. Charbonnel[1, 2] and L. Amard[1, 3]

Abstract. With about 2000 exoplanets discovered within a large range of different configurations of distance from the star, size, mass, and atmospheric conditions, the concept of habitability cannot rely only on the stellar effective temperature anymore. In addition to the natural evolution of habitability with the intrinsic stellar parameters, tidal, magnetic, and atmospheric interactions are believed to have strong impact on the relative position of the planets inside the so-called habitable zone. Moreover, the notion of habitability itself strongly depends on the definition we give to the term "habitable". The aim of this talk is to provide a global and up-to-date overview of the work done during the last few years about the description and the modelling of the habitability, and to present the physical processes currently includes in this description.

1 Introduction

Thanks to the increase of the accuracy and precision of modern techniques of observation, the size and mass of detected exoplanet have continuously decreased since the first detection of 51 Peg b ($\approx 150 M_\oplus$, Mayor & Queloz 1995). While the first exoplanets detected were gaseous so called hot Jupiter, the detection of telluric planet starts to be quite common. Among these newly detected planets, there is one interesting example, Kepler 186 f (Quintana et al. 2014) orbiting around an M-type star, that possesses a radius very close to the Earth's one (1.11 $R_\oplus$) but unfortunately without precise mass estimation (0.32-3.77 $M_\oplus$). Tidal interactions between the two bodies are very active (because the planet is quite close from its star, i.e., 0.35-0.4 AU) and act at strongly modifying the orbital motion of the planet. Constraining habitability of such planet is thus quite challenging and motivating since all the physical mechanisms at act in stellar vicinity have to be taken into account. To fully understand the habitability of an exoplanet we first need to understand its evolution as a function of the stellar parameters. The aim of this work is to highlight the impact of stellar parameter such as metallicity, mass, and rotation on the habitable zone limits.

2 Habitability

2.1 Definition

The habitability of an exoplanet is defined by two characteristics: the fact that the planet is inside the habitable zone and that the physical ingredients, that are required to host and sustain life, are present. The habitable zone (hereafter HZ) is classically defined as the region where a rocky planet can maintain, given its atmosphere, liquid water on its surface (see Kopparapu et al. 2013, 2014; Linsenmeier et al. 2015; Torres et al. 2015). Kasting et al. (1993) provide a simple analytic expression to get the HZ limits (hereafter HZL)

$$d = \left(\frac{L/L_\odot}{S_{eff}}\right)^{0.5} \mathrm{AU}, \tag{2.1}$$

where d is the inner or outer edge of the HZ, and S_{eff} is the effective stellar flux (Kasting et al. 1993; Kopparapu et al. 2013, 2014) define as the ratio between the outgoing IR flux from the planet and the net incident flux from the star

$$S_{eff} = \frac{F_{IR}}{F_{inc}}. \tag{2.2}$$

[1] Department of Astronomy, University of Geneva, Chemin des Maillettes 51, 1290 Versoix, Switzerland
[2] IRAP, UMR 5277, CNRS and Université de Toulouse, 14, av. E.Belin, F-31400 Toulouse, France
[3] LUPM, UMR 5299, CNRS and Université Montpellier II, place E. Bataillon, 34 090 Montpellier, France

© Société Francaise d'Astronomie et d'Astrophysique (SF2A) 2015

Using the 1-D radiative-convective climate cloud-free model developed by the Kasting's group, Kopparapu et al. (2013, 2014) provide a parametric equation to calculate the HZL

$$S_{eff} = S_{eff\odot} + aT_* + bT_*^2 + cT_*^3 + dT_*^4 \tag{2.3}$$

where $T_* = T_{eff} - 5780$ and $S_{eff\odot}$ is estimated by assuming that the total incident flux at the top of the atmosphere is the present solar constant at Earth's orbit. The inner limit of the HZ is usually described as the runaway greenhouse limit where the green house effect starts to have a positive feedback, i.e. the limit where the surface temperature $T_{surf} > 647$ K at which oceans are entirely evaporated. The outer edge of the HZ is defined by the maximum greenhouse limit where the greenhouse effect starts to be reduced by the Rayleigh scattering by the CO_2. This limit corresponds to a surface temperature of about 273 K.

2.2 The 1 $M_\odot$ star

This study is based on a grid of standard stellar models computed with the code STAREVOL for a range of initial masses between 0.5 and 2 $M_\odot$ and for four values of metallicity [Fe/H]=0.26, 0, -0.56, and -2.16. The grid of models will be published in a forthcoming paper of Amard et al. (in prep.). For the 1 $M_\odot$ star, we use the standard and rotating stellar models from Lagarde et al. (2012) and refer to this paper for a detailed description of the model and of the evolution code STAREVOL.

2.2.1 Evolution of the limits of the habitable zone

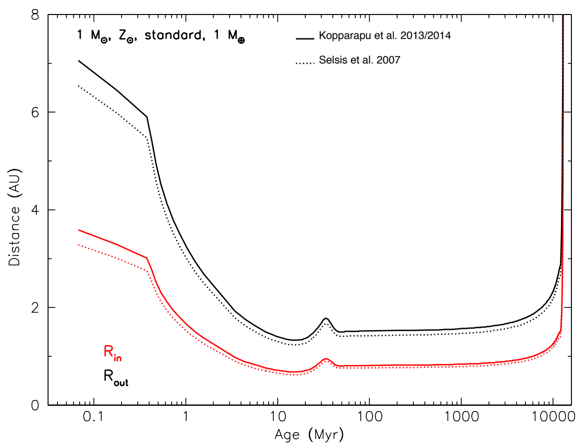

Fig. 1. Evolution of the HZL as a function of age for a 1 $M_\odot$ with solar metallicity. Red and black lines represent the inner and outer edge of the HZ, respectively. The solid, and dotted lines are associated to HZ's prescription from Kopparapu et al. (2014) and Selsis et al. (2007), respectively.

Here we focus on solar-type star with solar metallicity and use the non-rotating model from Lagarde et al. (2012). Figure 1 shows the temporal evolution of inner (red) and outer (black) edge of the HZ from the early pre-main-sequence (PMS) to the end of the main-sequence (MS) phase. The PMS phase along the Hayashi track (Hayashi 1961) is associated to a rapid and sharp decrease of the HZL. After the Hayashi track (between 2 10^2 and 1.5 10^7 years) the HZL of the star reach a minimum value of about 0.68 AU for the inner edge of the HZ (HZ_{in}) and 0.70 AU for the outer edge of the HZ (HZ_{out}). The HZL then increases following the increase of stellar luminosity towards the zero age main-sequence (ZAMS, that is located in Figure 5 at the "bump"). At the end of the PMS (about 30 Myr), the star reaches the ZAMS where the stellar structure temporally stops to evolve followed by the stop of the evolution of the HZL. Finally, during the MS phase (from 30 Myr up to about 5 Gyr) the HZL remains more or less constant at about 1.5 AU for the outer edge and 0.8 AU for the inner edge. At the end of the MS (from 5-6 Gyr) and towards the red giant branch (RGB) the HZL sharply increases following the increase of stellar luminosity.

2.2.2 Metallicity effect

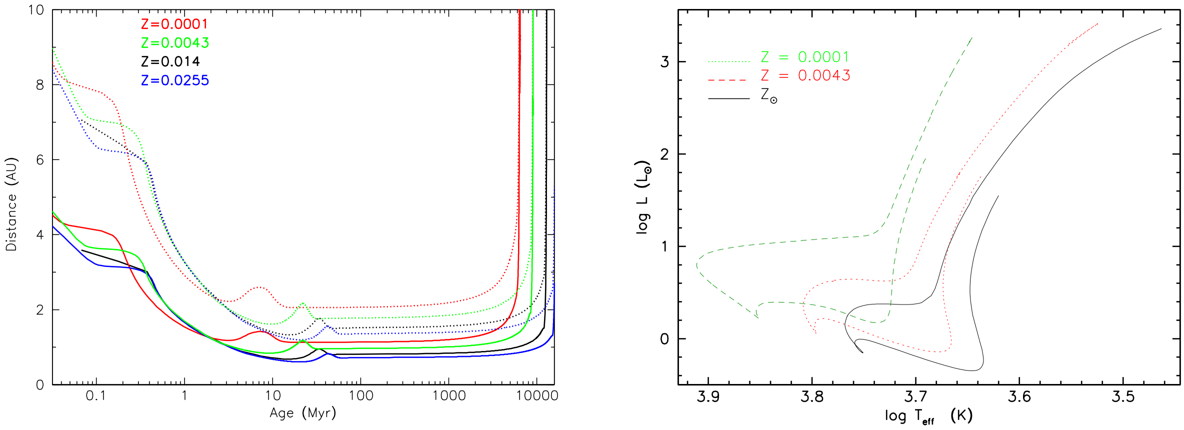

Fig. 2. Left: HZL as a function of the effective temperature for a 1 M$_\odot$ star and for four values of the metalliciy metallicity. The solid and dashed lines represent the inner and outer edge of the HZ, respectively. **Right:** Tracks in the HRD.

Metallicity is one of the main parameters that modify significantly the stellar structure and evolution. Here we study the impact of metallicity from [Fe/H] = 0.26 to [Fe/H] = -2.16 corresponding to Z=0.0255 to Z=0.0001 ([Fe/H] = 0 is the solar metallicity). The main effect of metallicity is to induce, due to opacity effect, a shift in both effective temperature and luminosity that increase, at a given evolution phase, for decreasing metallicity. Figure 2 (left) shows the impact of metallicity on the evolution of the inner and outer edge of the HZ for the case of the 1 M$_\odot$ star. For low metallicities the HZL reaches higher values when the star arrives on the ZAMS, and during the whole MS phase. At 100 Myr, HZ_{in} increases from 0.72 AU (Z= 0.0255) to 1.14 AU (Z= 0.0001) corresponding to an increase of 58%. For HZ_{out}, the increase rate is about the same (52%) with an increase from 1.36 (Z= 0.0255) to 2.08 (Z= 0.0001) AU.

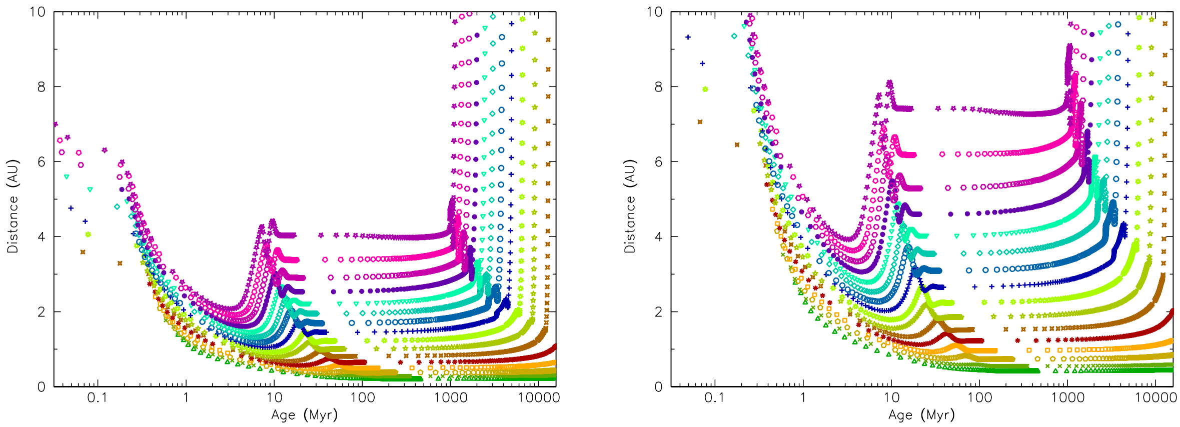

Fig. 3. Evolution of the inner (**Left**) and outer (**Right**) edge of the HZ as a function of time for stars between 0.5 (green triangle) and 2 (purple inclined star) M$_\odot$.

2.3 Mass dependence

The stellar mass is also one of the major quantities that significantly modify the internal structure and intrinsic parameters (such as effective temperature, luminosity, lifetime) as well as their evolution for a given star. The shape of the HZL evolution strongly depends on the stellar mass considered. At a given time, luminosity and effective temperature increase for increasing mass. The direct effects on the HZ are to increase both inner and outer edge of the HZ as well as to increase the size of the HZL. At ZAMS, the HZL increase from ≈ 0.5 AU for the 0.5 $M_{\odot}$ star to more than 8 AU for the 2 $M_{\odot}$. The width of the HZ also increases for increasing stellar mass. On average, for a non-rotating star with solar metallicity, the width of the HZ is about 0.27 AU for a 0.5 $M_{\odot}$ and 3.25 AU for a 2 $M_{\odot}$. The fact that the width of the HZ of low mass star is, on average, wider than higher mass star could suggests that these stars are more willing to host habitable planet (i.e., the probability for a planet to be found inside the HZ is higher).

3 Conclusions and perspectives

To assess the habitability of an exoplanet we need to precisely define the location of the HZL. In most of the studies from the literature, these limits are only discussed for a given age and regardless of the temporal progress of stellar evolution. However, and as briefly shown here, the HZ strongly varies along the life of planet host stars, and depends on their mass and metallicity. In this work we looked at the effect of stellar parameters on the HZL along the stellar evolution from the early PMS to the tip of the RGB, as well as the effects of mass and metallicity. We show that the HZL is very sensitive to the metallicity and stellar mass that almost entirely control the HZL. These parameters are then crucial to be determined observationally when one looking for planetary habitability. In a forthcoming paper we will also studied the impact of rotation and stellar activity on the evolution of the HZL.

The authors would like the warmly thanks the organizers of the 2015 SF2A meeting in Toulouse! The authors acknowledge financial support from the Swiss National Science Foundation (FNS) and from the French Programme National National de Physique Stellaire PNPS of CNRS/INSU. This work results within the collaboration of the COST Action TD 1308.

References

Hayashi, C. 1961, PASJ, 13, 450

Kasting, J. F., Whitmire, D. P., & Reynolds, R. T. 1993, Icarus, 101, 108

Kopparapu, R. K., Ramirez, R., Kasting, J. F., et al. 2013, ApJ, 765, 131

Kopparapu, R. K., Ramirez, R. M., SchottelKotte, J., et al. 2014, ApJ, 787, L29

Lagarde, N., Decressin, T., Charbonnel, C., et al. 2012, A&A, 543, A108

Linsenmeier, M., Pascale, S., & Lucarini, V. 2015, Planet. Space Sci., 105, 43

Mayor, M. & Queloz, D. 1995, Nature, 378, 355

Quintana, E. V., Barclay, T., Raymond, S. N., et al. 2014, Science, 344, 277

Selsis, F., Kasting, J. F., Levrard, B., et al. 2007, A&A, 476, 1373

Torres, G., Kipping, D. M., Fressin, F., et al. 2015, ApJ, 800, 99

SF2A 2015
F. Martins, S. Boissier, V. Buat, L. Cambrésy and P. Petit (eds)

FREE INERTIAL MODES IN DIFFERENTIALLY ROTATING CONVECTIVE ENVELOPES OF LOW-MASS STARS : NUMERICAL EXPLORATION

M. Guenel[1], C. Baruteau[2], S. Mathis[1] and M. Rieutord[2]

Abstract. Tidally-excited inertial waves in stellar convective regions are a key mechanism for tidal dissipation in stars and therefore the evolution of close-in binary or planetary systems. As a first step, we explore here the impact of latitudinal differential rotation on the properties of free inertial modes and identify the different families of modes. We show that they differ from the case of solid-body rotation. Using an analytical approach as well as numerical calculations, we conclude that critical layers — where the Doppler-shifted frequency vanishes — could play a very important role for tidal dissipation.

Keywords: hydrodynamics - waves - planet-star interactions

1 Introduction

Star-planet tidal interactions may result in the excitation of inertial waves in the convective region of stars. Their dissipation plays a prominent role in the long-term orbital evolution of short-period planets (Ogilvie & Lin 2007; Lai 2012; Valsecchi et al. 2014; Mathis 2015). Furthermore, turbulent convection sustains differential rotation in the envelope of low-mass stars, with an equatorial acceleration (as in the Sun) or deceleration which can modify the waves' propagation properties (Brun & Toomre 2002; Brown et al. 2008; Gastine et al. 2014). In this work, we explore the general properties of free linear inertial modes in a differentially rotating homogeneous isentropic fluid in a spherical shell. We assume that the angular velocity background flow depends on the latitudinal coordinate only, close to what is expected in the external convective envelope of low-mass stars. We use i) an analytical approach in the inviscid case to get the dispersion relation, study the existence of attractor cycles and identify the different families of inertial modes ; ii) high-resolution numerical calculations based on a spectral method for the viscous problem.

2 Physical model

We consider that the convective envelope of a low-mass star is a spherical shell of external radius R and aspect ratio η ($0 < \eta < 1$), extending from the boundary of the radiative core of radius ηR to the surface. For the sake of simplicity, we assume that the fluid is homogeneous with density ρ_0 and has a constant kinematic viscosity ν.

2.1 Hydrodynamic equations

Since we want to study the propagation of inertial waves — whose restoring force is the Coriolis acceleration — in a differentially rotating fluid, we linearize the Navier-Stokes equations around the steady state where the fluid has a non-uniform dimensionless angular velocity Ω. We normalize all frequencies by Ω_{ref} which we define as the angular velocity at the poles and all distances by R. We thus look for dimensionless velocity perturbations ($\mathbf{u}$) and reduced pressure perturbations (p) of dimensionless angular frequency ω_p (in the inertial frame) and azimuthal wavenumber m. This means they are proportional to $\exp(i\omega_p t + im\varphi)$.

[1] Laboratoire AIM Paris-Saclay, CEA/DSM/IRFU/SAp - Université Paris Diderot - CNRS, 91191 Gif-sur-Yvette, France
[2] IRAP, Observatoire Midi-Pyrénées, Université de Toulouse, 14 avenue Edouard Belin, 31400 Toulouse, France

© Société Francaise d'Astronomie et d'Astrophysique (SF2A) 2015

In an inertial frame, this yields the following system (e.g. Baruteau & Rieutord 2013) :

$$\left\{\begin{array}{l} i\tilde{\omega}_p\mathbf{u} + 2\Omega\mathbf{e_z}\times\mathbf{u} + x\sin\theta\,(\mathbf{u}\cdot\nabla\Omega)\,\mathbf{e}_\varphi = -\nabla p + E\Delta\mathbf{u}, \\ \nabla\cdot\mathbf{u} = 0, \end{array}\right. \tag{2.1}$$

where $\tilde{\omega}_p = \omega_p + m\Omega$ is the dimensionless Doppler-shifted frequency, $\mathbf{e_z}$ is the unit vector along the rotation axis, x is the dimensionless spherical radius and the Ekman number $E = \nu/R^2\Omega_{\rm ref}$ is the dimensionless viscosity.

Note that we will numerically solve the vorticity equation

$$\left\{\begin{array}{l} \nabla\times\left(i\tilde{\omega}_p\mathbf{u} + 2\Omega\mathbf{e_z}\times\mathbf{u} + x\sin\theta\,(\mathbf{u}\cdot\nabla\Omega)\,\mathbf{e}_\varphi\right) = E\nabla\times\Delta\mathbf{u}, \\ \nabla\cdot\mathbf{u} = 0, \end{array}\right. \tag{2.2}$$

in the following section in order to get rid of the ∇p term.

In addition to Eqs. (2.2), we use stress-free boundary conditions ($\mathbf{u}\cdot\mathbf{e_r} = 0$ and $\mathbf{e_r}\times[\sigma]\mathbf{e_r} = \mathbf{0}$, where $[\sigma]$ is the viscous stress tensor) at the inner and outer boundaries of the spherical shell.

2.2 Differential rotation profile

As motivated in the introduction, we use a conical differential rotation profile that only depends on the colatitude θ, which reads :

$$\Omega(\theta) = 1 + \varepsilon\sin^2\theta, \tag{2.3}$$

so that the dimensionless angular velocity of the background flow is 1 at the poles and $1+\varepsilon$ at the equator. The quantity ε is a parameter that describes the behavior of the differential rotation :

- $\varepsilon > 0$ is for solar differential rotation (equatorial acceleration),
- $\varepsilon < 0$ is for anti-solar differential rotation (equatorial deceleration).

2.3 Dispersion relation and inviscid analysis

When viscosity is neglected, Eqs. (2.1) is equivalent to a mixed-type second-order partial differential equation (PDE) for p only. Then we can infer analytically the propagation properties of inertial waves in the inviscid limit through the solution's characteristic trajectories in the domains where this PDE is of hyperbolic type (Rieutord et al. 2001; Baruteau & Rieutord 2013). In solid-body rotation with angular velocity $\Omega_{\rm ref}$, the Doppler-shifted frequency is restricted to $[-2\Omega_{\rm ref}, 2\Omega_{\rm ref}]$ and these trajectories are straight lines with a fixed inclination angle

$$\lambda = \sin^{-1}\left(\frac{\Omega_p + m\Omega_{\rm ref}}{2\Omega_{\rm ref}}\right) = \sin^{-1}(\tilde{\omega}_p/2)$$

with respect to the rotation axis. When differential rotation is included, we can numerically integrate these trajectories for any parameters using a ray tracing code. We found that they sometimes converge towards limit cycles called "wave attractors" that have previously been found in the case of solid-body rotation (Rieutord et al. 2001). Some of the figures shown in the following section feature overplotted white curves that were obtained using this method. We also found that the aforementioned PDE is not always hyperbolic in the whole shell, leading to different dynamics of the characteristic trajectories (latitudinal trapping, focusing towards a wedge, etc).

This analysis shows that two kinds of inertial modes may exist with differential rotation : D modes which can propagate in the entire spherical shell, and DT modes which can only propagate in part of the shell (Baruteau & Rieutord 2013). We also derive analytically the dispersion relation as well as the expressions of the phase and group velocities, and we show that when $m \neq 0$, critical layers (or corotation resonances) defined by $\tilde{\omega}_p = 0$ are singularities of the inviscid problem. For more details, see Guenel et al. (2015, submitted to A&A).

3 Numerical calculations

3.1 Numerical method

In this section, we show several results we obtained by solving numerically Eqs. (2.2) — along with stress-free boundary conditions — using a unique decomposition of the unknown velocity field $\mathbf{u}$ onto vectorial spherical

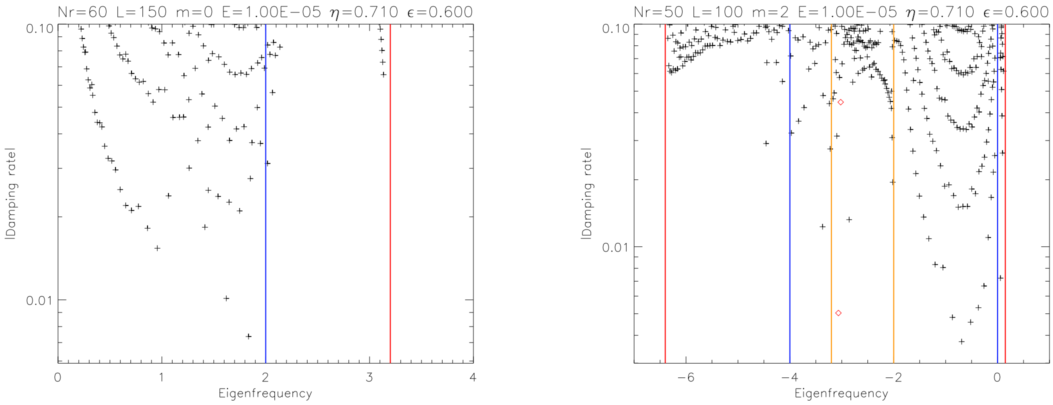

Fig. 1. Distribution of eigenvalues in the complex plane for $m = 0$ (left) and $m = 2$ (right), with $E = 10^{-5}$, $\eta = 0.71$ and $\varepsilon = 0.60$. Unstable eigenvalues with a positive damping rate are depicted by the red squares. The vertical blue (resp. red) line depicts the transition between the D and DT modes (resp. DT and non-existant modes) frequency ranges. Critical layers exist between the two orange lines.

harmonics (Rieutord 1987) :

$$\mathbf{u}(x,\theta,\varphi) = \sum_{l=0}^{\infty}\sum_{m=-l}^{l}\left\{u_m^l(x)\mathbf{R}_l^m(\theta,\varphi) + v_m^l(x)\mathbf{S}_l^m(\theta,\varphi) + w_m^l(x)\mathbf{T}_l^m(\theta,\varphi)\right\} \tag{3.1}$$

with $\mathbf{R}_l^m = Y_l^m(\theta,\varphi)\mathbf{e_r}$, $\mathbf{S}_l^m = \nabla_\mathbf{H} Y_l^m$ and $\mathbf{T}_l^m = \nabla_\mathbf{H} \times \mathbf{R}_l^m$ where $Y_l^m(\theta,\varphi)$ is the usual spherical harmonic of degree l and order m normalized on the unit sphere, and $\nabla_\mathbf{H} = \mathbf{e}_\theta\,\partial_\theta + \mathbf{e}_\varphi(\sin\theta)^{-1}\,\partial_\varphi$ is the horizontal gradient.

This decomposition yields a linear system of coupled ordinary differential equations involving u_m^l, v_m^l, w_m^l, which can be discretized in the radial direction on the Gauss-Lobatto collocation nodes (N_r points). We also truncate the system at a maximum spherical harmonic degree L. The linear solver we use (see Rieutord 1987) can compute directly the set of eigenvalues of the sparse matrix for moderate resolutions. It can also be used to compute individual pairs of eigenvalues and eigenmodes at higher resolutions.

3.2 Exploration of the modes

As a first step, we computed numerically the entire set of eigenvalues using a QZ-factorization method at moderate resolutions and therefore Ekman numbers E above 10^{-6}. The algorithm is designed to obtain the least-damped modes, which means that eigenvalues whose absolute damping rate exceeds $\sim 10^{-1}$ can be safely ignored. In Fig. 1, we show the results of two of these computations for a star with the solar aspect ratio $\eta = 0.71$ and $\varepsilon = 0.60$ (the Sun is actually around $\varepsilon = 0.30$), for $m = 0$ (left) and $m = 2$ (right). The main results we obtained from these computations are the following :

- the least-damped modes are always in the frequency range that corresponds to D modes ;
- eigenvalues in the DT frequency range are rare and have higher absolute damping rates ;
- when $m \neq 0$ and a critical layer exists in the shell, unstable eigenvalues exist for E as high as 10^{-5}.

Then, we computed various eigenmodes for different parameters , as shown by the few examples in Fig. 2. We briefly sum up our findings below :

- D modes have properties that are very similar to inertial modes in the case of solid-body rotation : characteristic trajectories are curved but wave attractors still exist in narrow frequency bands and patterns of shear layers form around them (see the top-left panel of Fig. 2). Their damping rate usually scales as $E^{1/3}$ as in solid-body rotation.
- DT modes with small damping rates are rare as indicated by the diagrams shown in the previous paragraph. Moreover, the shear layers that compose them often focus towards the intersection of a turning surface with the inner or outer boundary of the shell (see the top-right panel of Fig. 2).

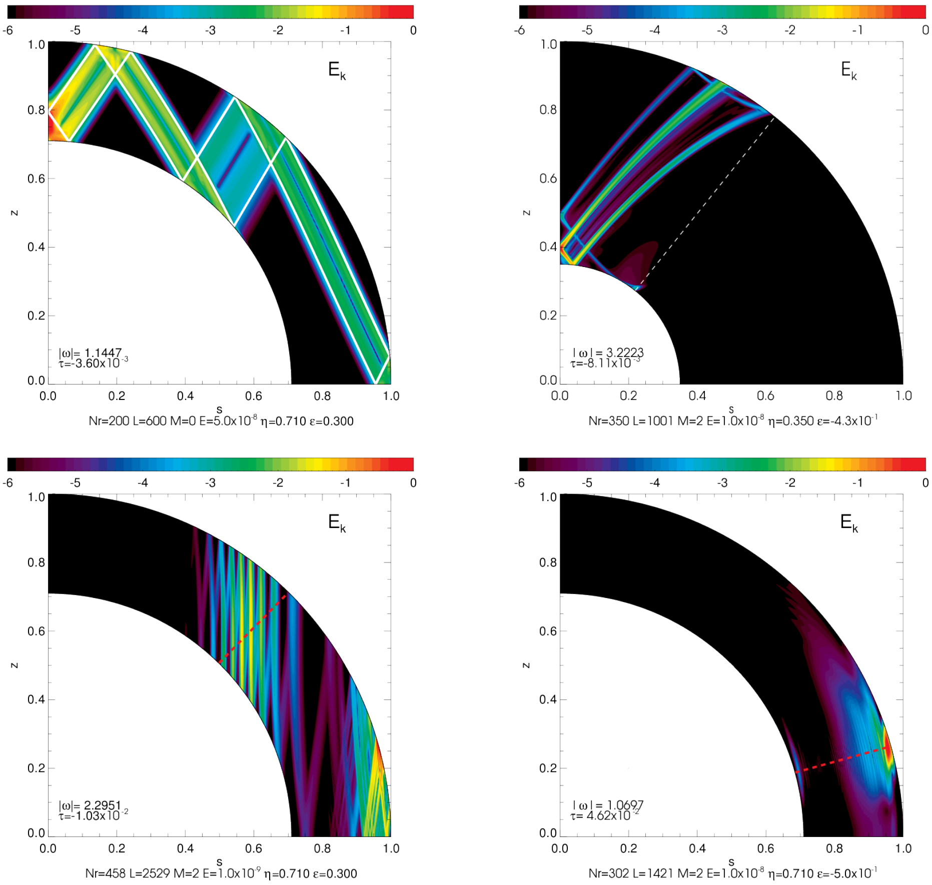

Fig. 2. Meridional cuts of the normalized kinetic energy of different inertial modes. **Top-left :** Axisymmetric D mode. The attractor of characteristics for these parameters is overplotted by the white curve. **Top-right :** DT mode with focusing towards a wedge at the intersection of a turning surface, depicted by the white-dashed line, with the inner boundary of the shell. **Bottom-left :** Stable non-axisymmetric D mode with critical layer (depicted by the red-dashed line). **Bottom-right :** Unstable non-axisymmetric D mode with corotation resonance.

- When a corotation resonance exists inside the shell, both stable and unstable modes exist (see the bottom panels of Fig. 2). The characteristic trajectories and the shear layers that follow them may become vertical at the resonance with a local accumulation of kinetic energy. On the other hand, unstable modes show no recognizable shear layer patterns and they may play a prominent role in the dissipation and/or exchange of angular momentum with the mean flow (see Grimshaw 1979; Watson 1981).

4 Conclusions

We find that modes that can propagate in the whole differentially rotating convective envelope of a low-mass star behave the same way as with solid-body rotation. However, other families of inertial modes exist, which can propagate only in a restricted part of the convective zone. Most importantly, non-axisymmetric oscillation modes may be unstable when a critical layer exists in the convective zone. These new properties of free inertial modes with differential rotation could significantly change our understanding of the tidal dissipation and the dynamics of short-period systems. This is related to the tidally-forced regime which we will study in the near future.

S. Mathis and M. Guenel acknowledge funding by the European Research Council through ERC grant SPIRE 647383. This work was also supported by the Programme National de Plantologie (CNRS/INSU) and the CoRoT-CNES grant at Service d?Astrophysique (CEA Saclay).

References

Baruteau, C. & Rieutord, M. 2013, Journal of Fluid Mechanics, 719, 47
Brown, B. P., Browning, M. K., Brun, A. S., Miesch, M. S., & Toomre, J. 2008, ApJ, 689, 1354
Brun, A. S. & Toomre, J. 2002, ApJ, 570, 865
Gastine, T., Yadav, R. K., Morin, J., Reiners, A., & Wicht, J. 2014, MNRAS, 438, L76
Grimshaw, R. 1979, Geophysical and Astrophysical Fluid Dynamics, 14, 303
Lai, D. 2012, MNRAS, 423, 486
Mathis, S. 2015, A&A, 580, L3
Ogilvie, G. I. & Lin, D. N. C. 2007, ApJ, 661, 1180
Rieutord, M. 1987, Geophysical and Astrophysical Fluid Dynamics, 39, 163
Rieutord, M., Georgeot, B., & Valdettaro, L. 2001, Journal of Fluid Mechanics, 435, 103
Valsecchi, F., Rasio, F. A., & Steffen, J. H. 2014, ApJ, 793, L3
Watson, M. 1981, Geophysical and Astrophysical Fluid Dynamics, 16, 285

ACCURATE STELLAR MASSES FOR SB2 COMPONENTS: INTERFEROMETRIC OBSERVATIONS FOR GAIA VALIDATION*

J.-L. Halbwachs[1], H.M.J. Boffin[2], J.-B. Le Bouquin[3], B. Famaey[1], J.-B. Salomon[1], F. Arenou[4], D. Pourbaix[7,5], F. Anthonioz[3], R. Grellmann[6], S. Guieu[3], P. Guillout[1], A. Jorissen[7], F. Kiefer[8], Y. Lebreton[4,9], T. Mazeh[8], A. Nebot Gómez-Morán[1], H. Sana[10] and L. Tal-Or[8]

Abstract. A sample of about 70 double-lined spectroscopic binaries (SB2) is followed with radial velocity (RV) measurements, in order to derive the masses of their components when the astrometric measurements of Gaia will be available. A subset of 6 SB2 was observed in interferometry with VLTI/PIONIER, and the components were separated for each binary. The RV measurements already obtained were combined with the interferometric observations and the masses of the components were derived. The accuracies of the 12 masses are presently between 0.4 and 7 %, but they will still be improved in the future. These masses will be used to validate the masses which will be obtained from Gaia.

In addition, the parallaxes derived from the combined visual+spectroscopic orbits are compared to that of Hipparcos, and a mass-luminosity relation is derived in the infrared H band.

Keywords: binaries: spectroscopic, binaries: visual, stars: fundamental parameters, stars: individual:HIP 12272, HIP 14124, HIP 14157, HIP 20601, HIP 104987, HIP 117186

1 Introduction

An observation program is on going since 2010 at the OHP observatory with the T193/Sophie, in order to improve the orbital elements of a selection of 200 known spectroscopic binaries (SBs) (Halbwachs & Arenou 2009; Halbwachs et al 2014). Our long-term goal is the derivation of accurate stellar masses from the orbital elements of the double-lined spectroscopic binaries (SB2s), taking into account the astrometric measurement of the Gaia satellite. The diagram in Fig. 1 illustrates the progress of the programme. As explained in Halbwachs et al (2014), a reliable SB2 orbit may be obtained when the number of RV measurements of each component is at least 11, and when the period was enterily covered by the observation. A third condition is not visible on this diagramme, however: the measurements must be adequately distributed in orbital phase.

During the second semester of last year, interferometric measurements were performed at ESO, with the VLTI and the PIONIER instrument. Our purpose was to derive masses in order to check the reliability of those that will be obtained from Gaia. Six binaries were observed, which are HIP 12272, HIP 14124, HIP 14157, HIP 20601, HIP 104987 and HIP 117186. Four of them are taken from our sample, but two (HIP 14124 and HIP 14157) are southern stars which are not observable from Haute-Provence. They are included in a programme which is carried on from the Roque de los Muchachos Observatory, with the Hermes instrument.

* BASED ON OBSERVATIONS PERFORMED AT ESO AND AT THE HAUTE-PROVENCE OBSERVATORY

[1] Observatoire Astronomique de Strasbourg, Université de Strasbourg, CNRS, UMR 7550, 11, rue de l'université, F-67000 Strasbourg, France
[2] ESO, Av. Alonso de Cordova 3107, 19001 Casilla, Santiago 19, Chile
[3] UJF-Grenoble 1/CNRS-INSU, UMR 5274, Institut de Plantologie et dAstrophysique de Grenoble (IPAG), 38041 Grenoble, France
[4] GEPI, Observatoire de Paris, CNRS, Université Paris Diderot, 5 place Jules Janssen, 92195, Meudon, France
[5] F.R.S.-FNRS, Rue d'Egmont 5, 1000 Bruxelles, Belgium
[6] Physikalisches Institut der Universität zu Köln, Zülpicher Strasse 77, D-50937 Köln, Germany
[7] Institut d'Astronomie et d'Astrophysique, Université libre de Bruxelles, boulevard du Triomphe, 1050 Bruxelles, Belgium
[8] School of Physics and Astronomy, Tel Aviv University, Tel Aviv 69978, Israel
[9] Institut de Physique de Rennes, Université de Rennes 1, CNRS UMR 6251, F-35042 Rennes, France
[10] Institute of Astronomy, KU Leuven, Celestijnenlaan 200D, 3001 Leuven, Belgium

© Société Francaise d'Astronomie et d'Astrophysique (SF2A) 2015

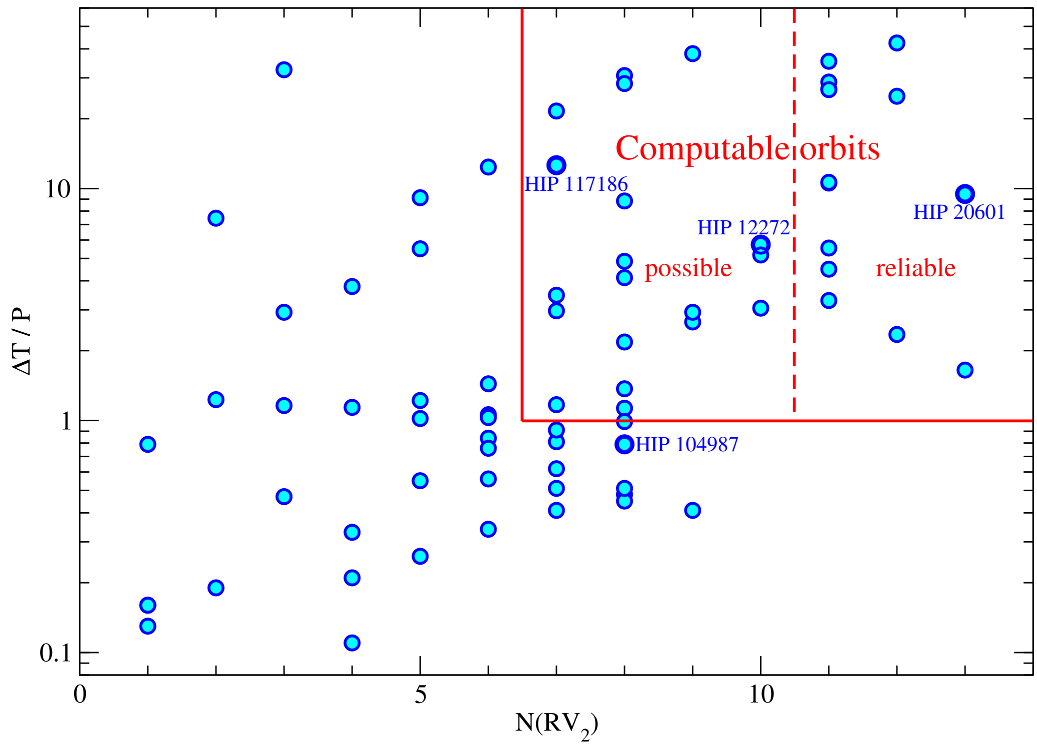

Fig. 1. The number of covered periods vs the number of detections of the secondary dip of the SB2, after semester 2014B. The HIP numbers of the stars observed with the VLTI are indicated.

2 Derivation of the masses, parallaxes and H IR magnitudes

None of the stars observed with PIONIER is fulfilling the conditions to obtain a reliable and definitive orbit. Nevertheless, the stars observed at OHP have all enough measurements to derive a preliminary SB2 orbit. Moreover, the ancient measurements are taken into account, in addition to the RV coming from our own observations.

Between four and nine interferometric measurements were obtained for each star, covering at least 25 % of the period. This sufficient to derive a visual orbit, but we consider that 6 observations covering half of the period are a minimum to compute reliable elements: a visual orbit consists in 7 elements (e, P, T_0, a, i, ω, Ω), and 6 2-dimension measurements lead to a solution with 6 degrees of freedom. This is just enough for the verification and for the correction of the uncertainties. As a consequence, the results hereafter must also be considered as preliminary for unsufficient interferometric measurements, for three of the six stars: HIP 12272, HIP 14124, and HIP 104987.

The RV and the interferometric measurements are used to derive simultaneously the orbital elements of the binaries, and therefore the masses of the components and the parallaxes of the systems. In addition, the flux ratios in the infrared H band are also obtained. Since the total H magnitudes are known thanks to Cutri et al. (2003), the indidual magnitudes of the stars were also computed, and therefore the absolute H magnitudes. The results are presented in Table 1.

3 The mass-luminosity diagram

The positions of our stars in the mass-luminosity diagram are directly taken from Tab. 1 and plotted in the left panel of Fig. 2. The four stars lighter than the Sun have masses which are compatible with the relation of Henry & McCarthy (1993), although they all are a few percent larger.

Table 1. The orbital elements of the 6 binaries, and the masses and absolute magnitudes of the 12 components.

HIP	P	T_0(JD)	e	ω_1	Ω_1	i	a	$\mathcal{M}_{1,2}$	ϖ	$H_{abs\ 1,2}$	n_{VLTI}
	(d)	2400000+		(°)	(°)	(°)	(mas)	($\mathcal{M}_\odot$)	mas	(mag)	$\Delta T/P$
12272	269.344	53352.65	0.1347	62.5	351.11	35.6	17.4	1.64	15.50	1.497	4
	±0.0049	±1.33	±0.0041	±1.8	±0.53	±1.0		±0.12	±0.49	±0.083	0.27
								1.076		3.373	
								±0.077		±0.087	
14124	362.996	43069.06	0.6841	301.77	151.48	84.82	39.3	1.390	29.17	2.725	7
	±0.052	±0.20	±0.0053	±0.88	±0.15	±0.12		±0.066	±0.61	±0.061	0.28
								1.084		3.482	
								±0.037		±0.067	
14157	43.32031	51487.5000	0.7595	174.67	19.141	92.24	5.8	0.981	19.558	3.645	10
	±0.00013	±0.0081	±0.0010	±0.18	±0.082	±0.18		±0.0.10	±0.078	±0.031	> 1
								0.8819		4.073	
								±0.0089		±0.032	
20601	156.38023	56636.6695	0.85142	201.943	340.513	103.163	11.3	0.9763	16.714	3.688	6
	±0.00027	±0.0018	±0.00016	±0.061	±0.056	±0.074		±0.0031	±0.035	±0.047	0.72
								0.7250		4.687	
								±0.0015		±0.049	
104987	98.8026	52719.7	0.0049	55.	216.7	151.56	12.2	2.14	18.46	-1.08	5
	±0.0062	±6.1	±0.0040	±22.	±1.2	±0.51		±0.12	±0.35	±0.20	0.25
								1.796		1.05	
								±0.092		±0.20	
117186	85.8238	56402.540	0.32728	175.90	16.930	88.054	4.7	1.673	8.450	1.282	7
	±0.0013	±0.081	±0.00077	±0.37	±0.047	±0.043		±0.031	±0.083	±0.038	0.68
								1.399		2.173	
								±0.038		±0.040	

4 Comparison of the parallaxes with Hipparcos

Since Fekel (2015) have found a stellar system with a parallax significantly different from that provided by Hipparcos 2, it is relevant to compare our parallaxes to that coming from this catalogue. This is done on the right panel of Fig. 2. Although the individual stars have all parallaxes with errors smaller than 2 σ, this figure suggests that the small parallaxes of Hipparcos 2 could be systematically underestimated. However, this impression must still be confirmed on the basis on more data.

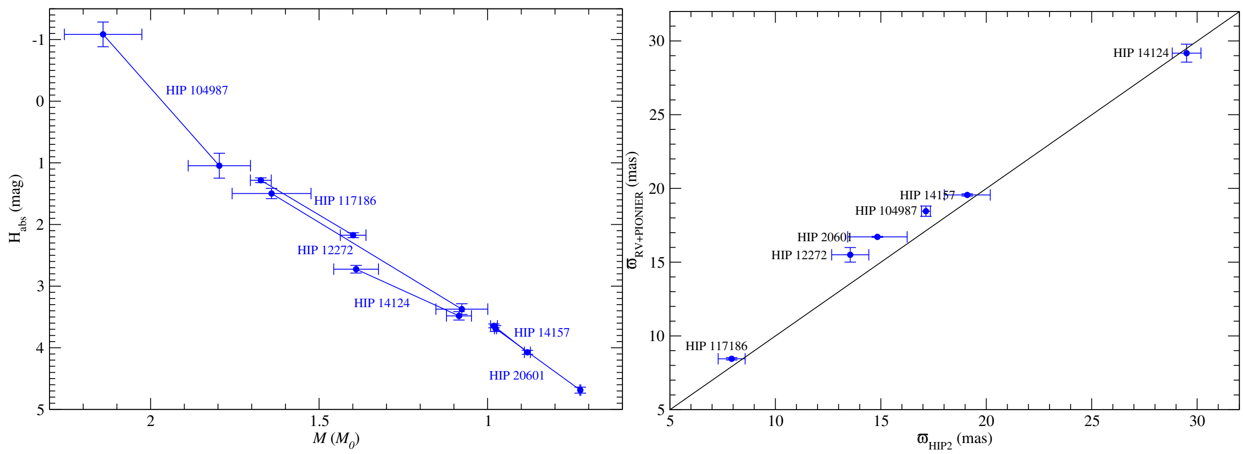

Fig. 2. Left: The twelve binary components in the masse-luminosity diagramme; H_{abs} is the absolute magnitude in the infrared 2-Mass H band. **Right:** Comparison of our parallaxes to that of Hipparcos 2. The Hipparcos 2 parallaxes were corrected for the orbital motion only for the three binaries well-observed with the VLTI (HIP 14157, HIP 20601 and HIP 117186).

5 Conclusions

We have obtained relevant masses and parallaxes for 6 binaries and their components.The results presented here are preliminary, but a study of the three binaries well observed with the VLTI will be detailled in a forthcoming refereed paper (Halbwachs et al 2016)

This project was supported by the french INSU-CNRS "Programme National de Physique Stellaire" and "Action Spécifique *Gaia*". PIONIER is funded by the Université Joseph Fourier (UJF), the Institut de Planétologie et d'Astrophysique de Grenoble (IPAG), and the Agence Nationale pour la Recherche (ANR-06-BLAN-0421, ANR-10-BLAN-0505, ANR-10-LABX56). The integrated optics beam combiner is the result of a collaboration between IPAG and CEA-LETI based on CNES R&T funding. The HERMES spectrograph is supported by the Fund for Scientific Research of Flanders (FWO), the Research Council of K.U.Leuven, the Fonds National de la Recherche Scientifique (F.R.S.-FNRS), Belgium, the Royal Observatory of Belgium, the Observatoire de Genève, Switzerland and the Thüringer Landessternwarte Tautenburg, Germany. We are grateful to the staff of the Haute–Provence Observatory, and especially to Dr F. Bouchy, Dr H. Le Coroller, Dr M. Véron, and the night assistants, for their kind assistance. This research has received funding from the European Community's Seventh Framework Programme (FP7/2007-2013) under grant-agreement numbers 291352 (ERC). This work made use of the Smithsonian/NASA Astrophysics Data System (ADS) and of the Centre de Donnees astronomiques de Strasbourg (CDS).

References

Cutri, R.M., Skrutskie, M.F., van Dyk, S. et al. 2003, 2Mass All Sky Catalog of point sources, Vizier Online Data Catalogue 2246,0

Fekel, F. 2015, AJ 149, 83

Halbwachs, J.-L., & Arenou, F. 2009, Proceedings SF2A 2009, M. Heydary–Malayeri, C. Reylé et R. Samadi édr., p. 53

Halbwachs, J.-L., Arenou, F., Famaey, B., et al. 2014, Proceedings SF2A 2014, J. Ballet, F. Martins, F. Bournaud, R. Monier, C. Reylé édr., p. 427

Halbwachs, J.-L., Arenou, F., Pourbaix, D., et al. 2014, MNRAS 445, 2371

Halbwachs, J.-L., Boffin, H.M.J., Le Bouquin, J.-B., et al. 2016, MNRAS (submitted)

Henry, T.J., McCarthy, D.W. 1993, AJ 106, 773

SF2A 2015
F. Martins, S. Boissier, V. Buat, L. Cambrésy and P. Petit (eds)

THE FIRST HOMOGENEOUS SET OF STELLAR PARAMETERS OF THE REFERENCE O-TYPE STARS: PRELIMINARY RESULTS

A. Hervé[1 2]

Abstract. Massive stars play a key role in various fields of astrophysics. In the 70s, the two dimensional spectral classification of O stars was developed by Walborn. Standard stars have been selected to be the reference object of each stellar type / luminosity class. These standard stars are still used today for the classification of the any newly discovered O stars. However, the stellar properties of these reference objects have never been determined in a homogeneous way. Consequently, there is no reference set of stellar parameters for these classification O stars. We propose to determine the stellar properties of all reference O stars using use state-of-the-art atmosphere models We will provide the community with a homogeneous catalog of high signal to noise, high resolution spectra as well as the stellar parameters for each reference stars. We present preliminary results for the standard O-type dwarfs.

Keywords: Stars: atmospheres Stars: fundamental parameters Stars: abundances

1 Introduction

Massive stars are the cornerstones of modern astrophysics. The heaviest elements of the universe are synthesized in their core and during the supernova explosion. This matter is subsequently released in the interstellar medium through their powerful stellar wind and on galactic scales at their death as supernovae. The mechanical energy associated to these flows triggers molecular cloud collapse and can lead to the birth of new stars. The strong UV radiation of massive stars is responsible for HII regions. And finally, these stars are the likely progenitors of long-soft GRBs. The classification of O-type stars started at the end of the 70's. Using low resolution, limited signal-to-noise spectra, Walborn (Walborn 1971, 1972) identified key lines varying across the population of O stars. Using these morphological modifications, he built a two dimensional classification of O stars, defining spectral types between O4 and O9.7 and luminosity classes from dwarfs (V) to bright supergiants (Ia). This classification is still relevant today. The relative strength of the HeI and HeII lines is used to define the spectral type. The strength and shape of specifics lines (ex: HeII 4686 Å) are used to determine the luminosity class of the early stellar types while the ratio of HeI and Si IV lines are used for late type stars. In order to establish a universal classification, Walborn selected one reference star for each type and luminosity class. These stars are still used today as reference stars. Since the studies of Walborn, numerous surveys have provided spectra of hundreds of O stars - VLT-FLAMES survey (Evans et al. 2005), TARENTULA survey (Evans et al. 2010), GOSS survey (Sota et al. 2011). Consequently, the classification of the newly discovered O stars is based on the comparison of the spectra of these objects to the standard O-type stars. Despite their crucial role, the stellar properties of the entire sample of standard O stars have never been studied homogeneously. Occasionally some of them have been analysed as part of specific studies. So currently, the astrophysics community does not have access to a high resolution, high signal to noise spectra database of reference O-type stars. More important, we do not have access to accurate stellar parameters of the standard stars.

In section 2, we present our data. In the section 3, we present the methodology for the spectroscopic analysis and in the section 4, we show the first results for the dwarfs.

[1] Astronomical Institute ASCR, Fricova 298, 251 65 Ondrejov, Czech Republic
[2] LUPM, Université de Montpellier, CNRS, Place Eugène Bataillon, F-34095 Montpellier, France

© Société Francaise d'Astronomie et d'Astrophysique (SF2A) 2015

2 Observations

For the determination of the properties of the massive stars, we need high-resolution and high-signal-to-noise ratio (SNR) spectra for all the standard O-type stars. We have obtained spectra with the échelle spectrograph $SOPHIE$ on the 193cm telescope at the Observatoire de Haute Provence for the stars observable from the north hemisphere. We thus observed the north hemisphere reference O-type stars during 7 nights in August 2014 and 1 night in December 2014. To complete our sample with the south hemisphere stars, we have extracted from the $FEROS$ archive the spectra publicly available. The quality of some data is not good enough for our project. We have thus obtained new observation time with FEROS at the 2.2m telescope at la Silla. The future observations are planned in October 2015 and March 2016.

When available, we also use IUE archive data.

3 Spectroscopic analysis

We use the code CMFGEN (Hillier & Miller 1998) to determine the fundamental properties of the sample stars. CMFGEN computes non-LTE and spherical models of massive stars atmospheres and the code takes into account line-blanketing and the presence of stellar wind. The hydrodynamical structure (density, velocity) is given as an input. The expansion of the wind is described by the so-called β law. In order to decrease the computation time and the size of the problem, a super level approached is used. In our model and in order to take into account the effect of line-blanketing, we have included the following elements in our calculations: H, He, C, N, O, Ne, Si, S, Ar, Ca, Fe and Ni. Once the atmospheric structure is obtained, a formal solution of the radiative transfer equation, including the proper line profiles, is performed. A depth variable microturbulent velocity starting from 10 $km.s^{-1}$ at the photosphere and reaching 10% of the terminal velocity at the top of the atmosphere is assumed.

To compare the synthetic spectra to the observation we convolve the synthetic spectra by the rotational velocity of the star and by a macroturbulent velocity.

To constrain the stellar and wind parameters, we follow the methodology established for the analysis of the O-type stars of the MIMES survey and presented in Martins et al. (2015)

First, we need to determine the projected rotational velocity of the stars. We use the Fourier transformation method (Gray 1976; Simón-Díaz & Herrero 2007). We apply this method to the non blend O iii λ5592 line. Then we convolve our synthetic spectra by the result of the first zero in the Fourier transformation. The uncertainty on $V sini$ is $\sim$10 $km.s^{-1}$

To mimic the effect of the macroturbulent velocity, we fit the O iii 5592 line with different synthetic spectra convolved by a Gaussian profile (in addition to the convolution by rotational broadening). Using a χ^2 method, we determine the best value of the macroturbulent velocity. Then, we convolve the whole synthetic spectrum by the rotational velocity and the macroturbulent velocity.

To determine the effective temperature, we use the presence of two consecutive ionization level of helium in the optical band. In practice, we use the He i λ4471 He ii λ4542, as main indicator. We can also use He i λ4026, He i λ4388, He i λ4713, He i λ4922, and the He ii λ4200, He ii λ5412 as secondary indicators.

Concerning the surface gravity we use the the wings of Balmer lines (except Hα which is very sensitive to the presence of a stellar wind) as main diagnostic of log g. As $SOPHIE$ and $FEROS$ are échelle spectrographes, the normalisation of the spectra is difficult and can lead to difference in the determination of the surface gravity. To determine the position of continuum in spectra, we use a synthetic spectrum to determine region in échelle spectra where no lines are present.

For the determination of the mass loss rate and the clumping parameters, we fit the intensity of the Balmer lines.

We will also determine the abundances of the the CNO elements from the fit of the different lines present in the optical band. The list of CNO lines and methodology to determine the abundances and their uncertainty is presented in Martins et al. (2015)

Concerning the luminosity of the O-type stars, we use the calibration of Martins et al. (2005).

For the majority of the stars, IUE spectra are available. We thus use the blue-ward extension of the absorption part of the Civ $\lambda\lambda$ 1548, 1551 PCygni profiles to determine the terminal velocity of the wind (Prinja et al. 1990). The typical uncertainty is $\sim$ 100 km.s^{-1}. If UV spectra is not available we use theoretical values of Muijres et al. (2012).

Table 1. Our preliminary results concerning the effective temperature, surface gravity, rotational velocity and macro-turbulent velocity for a sub-sample of the reference O-dwarfs.

ST	star	log $\frac{L}{L_\odot}$ (1)	T_{eff} kK	*logg*	V*sini* $km.s^{-1}$	vmac $km.s^{-1}$
4	HD46223[2]	5.68	41.5	3.83	59	51
5	HD46150[2]	5.51	40.0	3.92	66	52
5.5	HD93204	5.41	$38.3^{+0.2}_{-0.5}$	$3.61^{+0.08}_{-0.05}$	120	35
6	HD42088	5.30	$37.9^{+2.5}_{-2.2}$	$3.86^{+0.25}_{-0.25}$	40	44
6.5	HD12993	5.20	$37.0^{+3.0}_{-3.0}$	$3.84^{+0.40}_{-0.30}$	79	39
7	HDE242926	5.10	$36.2^{+5.0}_{-4.0}$	$3.82^{+0.50}_{-0.40}$	100	41
7.5	HD152590	5.00	$35.4^{+2.5}_{-1.5}$	$3.90^{+0.25}_{-0.15}$	50	20
8.	HD191978	4.90	$34.5^{+1.0}_{-1.5}$	$3.89^{+0.13}_{-0.23}$	60	58
8.5	HD14633	4.82	$33.9^{+1.8}_{-2.0}$	$3.98^{+0.20}_{-0.20}$	117	55
9	10LAC	4.72	$34.7^{+0.8}_{-0.7}$	$4.08^{+0.07}_{-0.08}$	15	15
9.5	AE Aur[1]	4.62	$33.3^{+2.0}_{-2.}$	$4.01^{+0.2}_{-0.2}$	15	30

(1) Luminosities are from Martins et al. (2005).
(2) We are currently calculating models to determine the uncertainties.

4 First results

In a first step we have computed a grid of synthetic spectra with the radiative code CMFGEN. This grid have been computed using the theoretical values of stellar and wind parameters for each spectral type / luminosity class presented in Muijres et al. (2012). In order to determine the effective temperature and surface gravity with accuracy as well as their uncertainties, we have computed and added more models in our grid. Fitting simultaneously the HeI, HeII lines and the wings of the Balmer lines, we determined the surface gravity and effective temperature of a sample of O-dwarfs stars (see Table 1). From our results, we can see, as expected, the temperature is increasing from the late type to the early type. The variation of temperature is included between few hundred of Kelvin to less than two thousands kelvin from one stellar type to another. We note the exception of 10 Lac. We also obtained large error bars for the parameters of HDE242926. This is due to the low SNR (SNR $\sim$ 100) of the spectrum for this star in comparison to the other objects (SNR $\sim$ 400). Concerning the surface gravity, we determined values in agreement with the status of dwarf for all these stars. The only exception is HD93204. The surface gravity of this star is closer to the traditional value of a giant. In Figure 1, we present our best fit model of HD191978 one of the standard O8V. The simultaneous fit of the wing of the balmer lines and the HeI and HeII lines present in the spectrum allow us to determine the surface gravity and the effective temperature. Then we have found a mass loss rate of 5.6×10^{-10} $M_\odot.yr^{-1}$ by the fit of the intensity of the Balmer lines. In Figure 2, we show the analysis of the carbon and nitrogen abundances of HD191978. Using all the carbon (nitrogen) lines available in the visible band, we proceeded to a the χ^2 analysis of the carbon (nitrogen) abundances. The minimisation of the χ^2 allows us to determine the carbon (nitrogen) surface abundance of the star. We found solar abundances for carbon and nitrogen. So our results do not show any chemical enrichment, as expected for a dwarf.

5 Conclusions

With our *SOPHIE* spectra, our *FEROS* observations and *FEROS* public archives, we are building a high-resolution high-signal-to-noise ratio spectra catalog of all the standard O-type stars. Using the state-of-the-art radiative transfer code, we are currently analysing the the spectra of this sample. We will thus determine with accuracy the stellar and wind parameters (Teff, logg, $\dot{M}$, clumping properties and chemical composition) for each stars. Using these reference stars, we will thus constrain the variation of the properties of the O-type stars from one spectral type / luminosity class to another.

Once our analysis finished, we will provide the community with a homogeneous catalog of high-signal-to-noise ratio, high-resolution spectra as well as the stellar parameters for each reference stars.

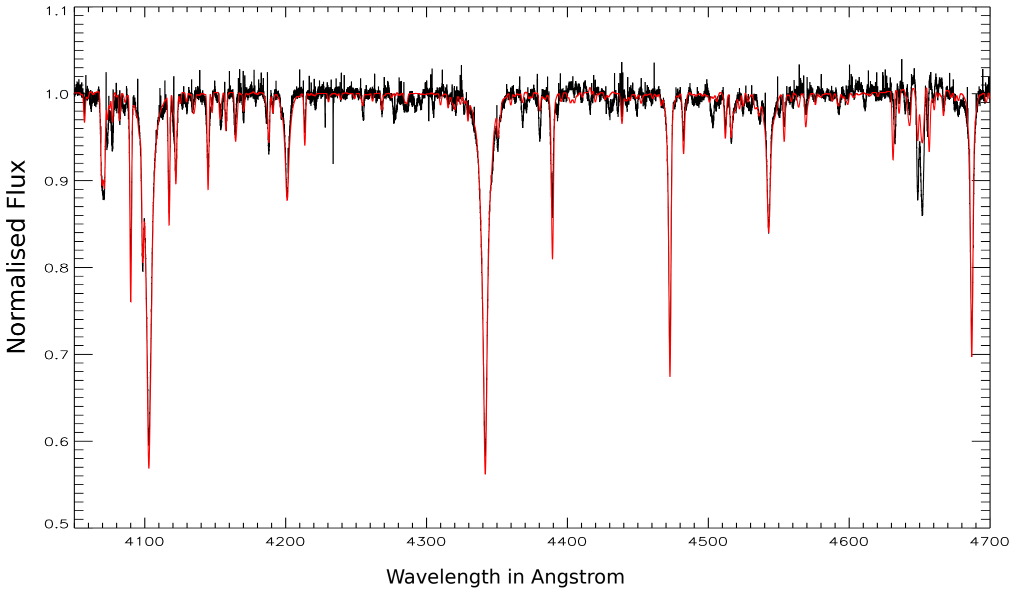

Fig. 1. Our best fit model (in red) compared to the *SOPHIE* spectrum of HD191978 (in black).

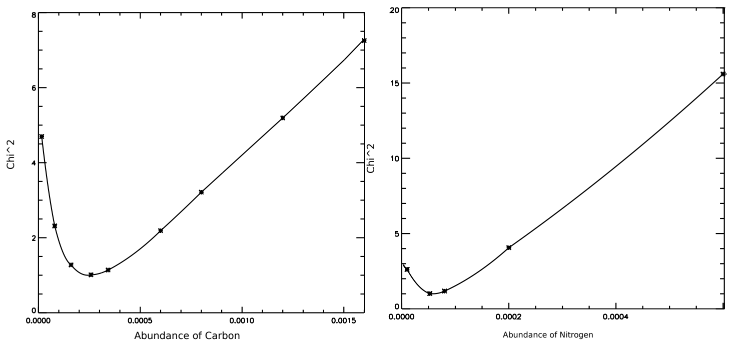

Fig. 2. Left: The bold solid curve shows the χ^2 of the analysis combining the carbon lines present in the optical band of HD191978. The black points correspond to the abundance of the different models used to determine the carbon abundance. Right: The same than on the left but for the nitrogen.

AH is supported by the grant 14-02385S from GA ČR. AH thank the Agence Nationale de la Recherche for financial support (grant ANR-11-JS56-0007).

References

Evans, C. J., Bastian, N., Beletsky, Y., et al. 2010, in IAU Symposium, Vol. 266, IAU Symposium, ed. R. de Grijs & J. R. D. Lépine, 35–40

Evans, C. J., Smartt, S. J., Lee, J.-K., et al. 2005, A&A, 437, 467

Gray, D. F. 1976, The observation and analysis of stellar photospheres

Hillier, D. J. & Miller, D. L. 1998, ApJ, 496, 407

Martins, F., Hervé, A., Bouret, J.-C., et al. 2015, A&A, 575, A34

Martins, F., Schaerer, D., & Hillier, D. J. 2005, A&A, 436, 1049

Muijres, L., Vink, J. S., de Koter, A., et al. 2012, A&A, 546, A42

Prinja, R. K., Barlow, M. J., & Howarth, I. D. 1990, ApJ, 361, 607

Simón-Díaz, S. & Herrero, A. 2007, A&A, 468, 1063

Sota, A., Maíz Apellániz, J., Walborn, N. R., et al. 2011, ApJS, 193, 24

Walborn, N. R. 1971, ApJS, 23, 257

Walborn, N. R. 1972, AJ, 77, 312

SF2A 2015
F. Martins, S. Boissier, V. Buat, L. Cambrésy and P. Petit (eds)

SEARCHING FOR A VARIABILITY OF INTERSTELLAR REDDENING IN THE LINE OF SIGHT OF NGC 4833

J. Itam-Pasquet[1], G. Jasniewicz[1], D. Puy[1,] and D. Pfenniger[2]

Abstract. The globular cluster NGC 4833 lies near the galactic plane. It is known to exhibit a strong differential reddening caused by several galactic interstellar clouds in its line of sight. Based on two optical observation runs made in 2006 within and separated by a 6-month interval, we intend to detect the photometric variations (colors and magnitudes) of stars in NGC 4833 due to the varying interstellar reddening.

Keywords: dust, extinction, globular cluster NGC 4833

1 Introduction

Light passing through clouds of atomic and/or molecular hydrogen is significantly obscured by the dust they contain. One of the main questions in the study of the Interstellar Medium (ISM) is the size of the smallest structure of these neutral clouds. This structure could be hierarchical or fractal, extending down to AU-sized clumps. Pfenniger et al. (1994) proposed that the baryonic dark matter associated with galaxies might consist of tiny cold gas clouds. They based this suggestion on galaxy dynamics and evolution, emphasizing the astrophysical appeal of dark matter in this form. Pfenniger & Combes (1994) further proposed that the fractal structure seen in CO at large scales might extend down to AU scales, and could be associated with the outer Milky Way disk, as seen in CO and HI. The extreme properties of these elementary cloudlets in the coldest cases (3K) would be: $10^9 cm^{-3}$; column density, $10^{24} cm^{-2}$; size, 30 AU; and mass, $10^{-3} M_\odot$. Since then, significant evidence has been accumulated for the existence of AU-sized structures in the cold ISM, or the existence of molecular gas not detected by CO emission. One of the latest examples is the spectroscopic results of Boissé et al. (2013), which further reinforce the proposal that there are few-AU structures in the ISM. We therefore propose to measure variable extinction towards the NGC 4833 globular cluster, using BVI photometry. We report photometric observations of several hundreds of stars in NGC 4833, repeated over a 6-month interval. Our goal is to look for magnitude variations over time, among these stars. Indeed, as NGC 4833 lies at a distance of 6500 pc from the Sun, it moves $\simeq 8.04\, mas.yr^{-1}$, equivalent to $52\, AU.yr^{-1}$ and more than 4 AU per month. Therefore, within a six-month period, NGC 4833 moves about 26 AU, which is comparable to the size of the small-scale structures of the ISM.

2 Observations and Data Reductions

Photometric observations of NGC 4833 were performed at La Silla, Chile, with the ESO Multi-Mode Instrument (EMMI). Two observation runs separated by a 6-month interval were done. The first run was performed on January 20-22, 2006, and the second on July 15-17, 2006. For each run, four stellar fields (F_1, F_2, F_3, F_4) around NGC 4833 were selected. Each stellar field was observed using three exposure times: 60s, 420s and 900s (filter B); 12s, 90s, and 600s (filter V); and 6s, 40s and 200s (filter I). Bias, dome and sky flat-fields were collected in the usual way.

For photometry reduction, we used the DAOPHOT II Stetson (1994) crowded-field photometry package. Using stars common to all filters, we compiled a BVI photometry list, keeping only those stars which errors do not exceed 0.05 mag and spatial restraint of 0.2 pixels.

[1] Laboratoire Univers et Particules de Montpellier, CNRS/Université de Montpellier, Place Eugène Bataillon, F-34095 Montpellier
[2] Observatoire de Genève, Chemin des Maillettes, CH-1290 Sauverny

© Société Francaise d'Astronomie et d'Astrophysique (SF2A) 2015

3 Highlighting Color Variations Within Six Months

3.1 Color magnitude diagrams

We assembled B-V and V-I color magnitude diagrams (CMDs hereafter) as shown in Fig.1. For each observation, the magnitudes of stars measured depended on atmospheric extinction. It is well-known that this extinction is a function of spectral type. Thus, in this study, we restricted our targets to the same luminosity class (dwarfs) and to a short temperature interval ($0.50 \leq (B-V) \leq 1.0$). Accordingly, 5,800 dwarfs, well-identified at epoch 0 and 1, satisfied these criteria. The probability of star membership will be discussed in an upcoming paper by Itam-Pasquet at al (in preparation).

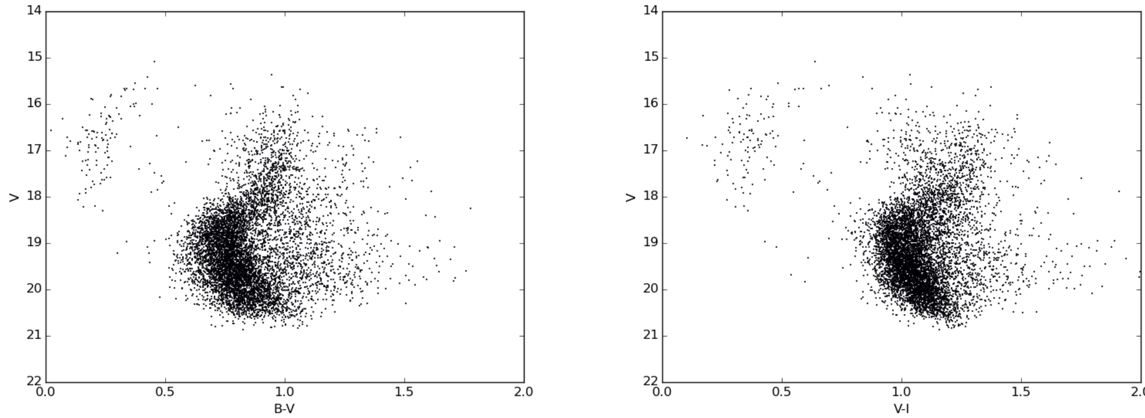

Fig. 1. Left: (B-V) CMD of NGC 4833. **Right:** (V-I) CMD of NGC 4833.

3.2 (B-V) Color maps

(B-V) color variations can be expressed as follows: $\Delta(B-V) = (B-V)_{jan} - (B-V)_{jui}$, and errors related to these variations are written as: $\delta(\Delta(B-V)) = \delta(B-V)_{jan} + \delta(B-V)_{jui}$. We built a (B-V) variation map (see Fig.2, left panel), selecting only stars which satisfied: $\Delta(B-V) > \delta(\Delta(B-V))$. In Fig.2, the right panel represents the same map as in the left panel does, but it includes the position of stars in order to weigh variations. The center of the map displays an area of high weight including with many variation clumps, suggesting that these variations are not homogeneous.

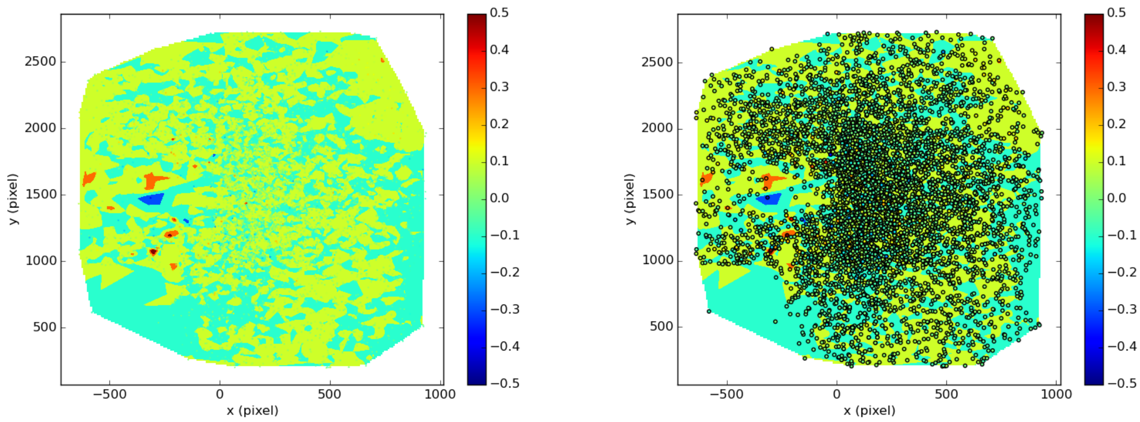

Fig. 2. Left: Map of (B-V) variations. **Right:** Map of (B-V) variations with stars. The X-axis and the Y-axis represent the pixel coordinates of stars.

4 Searching for Variations of Magnitudes Based on Variable Interstellar Reddening (VIR)

4.1 Methodology

We aim to check if photometric variations follow a simplified model of interstellar extinction. Indeed, in this model, we consider that the galactic extinction curve is constant over time. Each star observed at epoch 1 (first observing run) was directly compared to the same star observed at epoch 2 (second observing run). If time variations are due to Variable Interstellar Reddening (VIR hereafter), one expects that the following VIR-test is satisfied:

$$|\Delta(B)| = 1.4 * |\Delta(V)| \pm \eta \tag{4.1}$$

$$|\Delta(I)| = 0.6 * |\Delta(V)| \pm \eta \tag{4.2}$$

with $\Delta(\lambda_F) = m_1(\lambda_F) - m_2(\lambda_F)$ and a parameter η, which determines the robustness of the test and will be defined in the following section.

4.2 Discarding intrinsic variable stars

Kopacki (2014) listed the well known variable stars in NGC 4833 and placed them in a CMD, allowing us to verify that candidates are not known as intrinsic variable stars. In our selected region of the CMD, mostly binary variable stars (especially WUMa-type ones) are found among dwarfs. In fact, Milone et al. (2012) measured the fraction of binary stars in NGC 4833, and found a low value of 0.058 ± 0.006. In other words, out of the 5,800 stars selected among dwarfs in NGC 4833, only 336 might statistically be binaries. In order to further lower this number, we chose η so that binaries could not verify equations 4.1 and 4.2. We randomly selected two different phases from the B, V and I light curves of several WUMa stars, and checked if the magnitude variations between the two phases satisfied equations 4.1 and 4.2. After 50,000 simulations for each WUMa, we chose $\eta = 0.3$ to design a robust VIR test at which binaries fell under a small ratio $< 5\%$.

4.3 VIR test results for NGC 4833' stars and error discussion

The formula of error for our VIR-test can be expressed as follows:

$$E\left(\frac{\Delta(\lambda_F)}{\Delta(\lambda_V)}\right) = \frac{\Delta(\lambda_F) * E(\Delta(\lambda_V)) + \Delta(\lambda_V) * E(\Delta(\lambda_F))}{(\Delta(\lambda_V))^2} \tag{4.3}$$

Of the 5,800 stars selected in the CMD, only 46 had an error ratio $< \eta = 0.3$ mag (see Fig.3). Thus, we could only apply the VIR-test (equations 4.1 and 4.2) to 46 stars, which is too small a statistic to be significant. Furthermore, none of the 46 stars passed the VIR-test. Therefore, with this method, because of the high error values of magnitude ratios, we could not verify if photometric variations were compatible with a VIR.

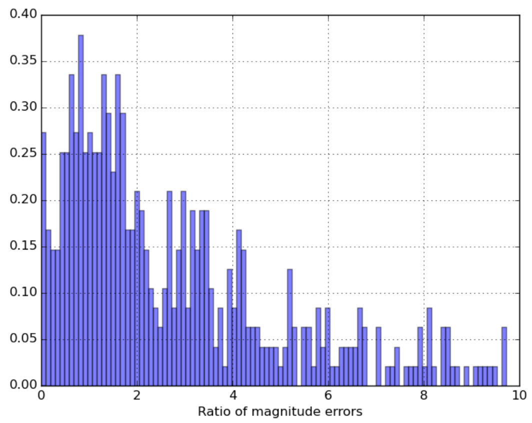

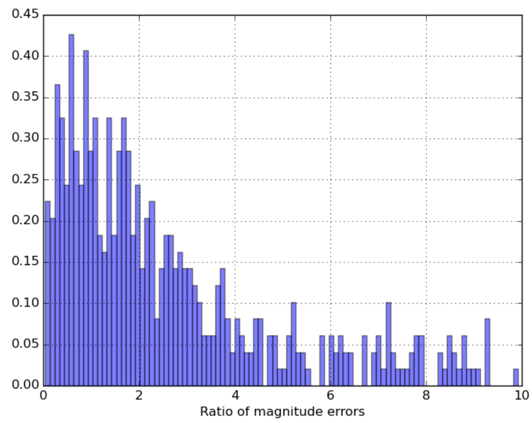

Fig. 3. Histograms of ratio of magnitude errors with $\lambda_F = B$ (see equation 4.3 and left panel) and with $\lambda_F = I$ (right panel).

4.4 Confidence in results

In the following, we assume that all stars are members of NGC 4833. In order to show that the photometric variations of magnitudes do not occur by chance, we want the distribution of magnitude variations over a period of 6 months (called "data" hereafter) to fit within a known distribution. Thusly, we are able to compute the occurrence likelihood of each magnitude variation. Kolmogorov-Smirnov and Wilcoxon statistic tests yield a significant p-value for a logistic distribution with $\mu = -0.001 \pm 0.0005$ and $s = 0.026 \pm 0.0002$ (see Fig.4). For variations $> |0.05|$ mag the probability that they are not due to chance is $> 86\%$, which is significant.

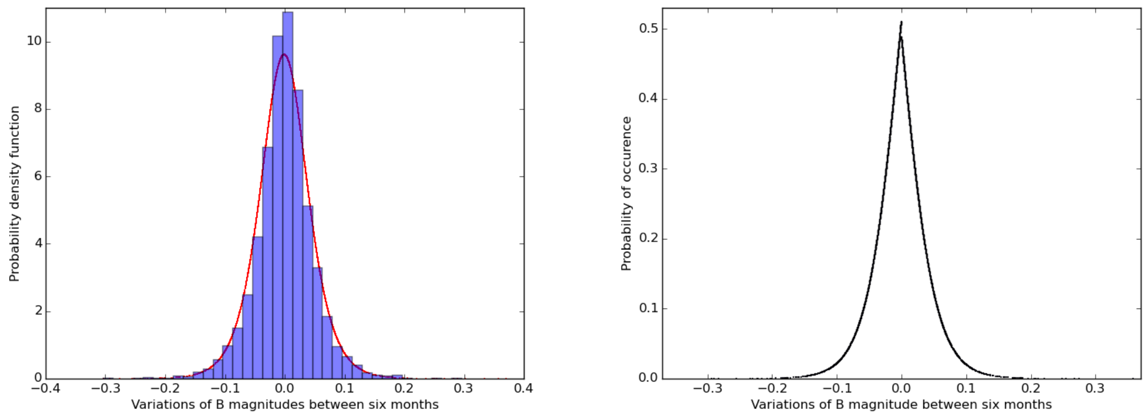

Fig. 4. Left: Fit of a logistic distribution of our data with $\mu = -0.001 \pm 0.0005$ and $s = 0.026 \pm 0.0002$. **Right:** Probability of occurrence (on y-axis) of a variation in magnitude within six months (on x-axis).

5 Conclusions

The study of the NGC 4833 globular cluster, is particularly relevant because it lies behind dusty regions. We believe that the interstellar medium in the foreground, is composed of large and small structures of several AUs. Because of these structures and of NGC 4833's velocity, variations of the reddening over time may occur. The magnitude error ratios are too high to determine if the variations are compatible with a VIR, but statistical analysis shows that the likelihood that variations $> |0.05|$ are not due to chance is $> 86\%$. Moreover, the (B-V) color map of NGC 4833 highlights variations with time. In future work, we will plan to compare our data to that of Melbourne et al. (2000), who carried out optical observations of NGC 4833 in 1995. The comparison will give us an opportunity to extend our study of this cluster to a time span of 11 years. In addition, we will create a model based on a given structure and a dynamic of clouds in the foreground to constrain the existence of these photometric and color variations.

We wish to acknowledge Valentin D. Ivanov for his help, the CNRS & the CNES for their financial support and the Graduate School for Information, Structures and Systems sciences (I2S) for their logistical support.

References

Boissé, P., Federman, S. R., Pineau des Forêts, G., & Ritchey, A. M. 2013, A&A, 559, A131

Kopacki, G. 2014, in IAU Symposium, Vol. 301, IAU Symposium, ed. J. A. Guzik, W. J. Chaplin, G. Handler, & A. Pigulski, 441–442

Melbourne, J., Sarajedini, A., Layden, A., & Martins, D. H. 2000, AJ, 120, 3127

Milone, A. P., Piotto, G., Bedin, L. R., et al. 2012, A&A, 540, A16

Pfenniger, D. & Combes, F. 1994, A&A, 285, 94

Pfenniger, D., Combes, F., & Martinet, L. 1994, A&A, 285, 79

Stetson, P. B. 1994, PASP, 106, 250

SF2A 2015
F. Martins, S. Boissier, V. Buat, L. Cambrésy and P. Petit (eds)

ABUNDANCE DETERMINATIONS FOR THE F DWARFS MEMBERS OF THE HYADES FROM SOPHIE HIGH RESOLUTION SPECTRA

T. Kılıçoğlu[1], R. Monier[2,3] and M. Gebran[4]

Abstract.
The mean chemical composition of open clusters can be derived from the chemical abundance analysis of F-type main-sequence stars, as they have convective layers which homogenize the material in their outer layers and thus keep track of the initial composition of the cluster. We present a preliminary abundance analysis of 5 F-type members of the Hyades open cluster using the high resolution spectra retrieved from SOPHIE archive. Our aim is to derive the elemental abundances of these stars as well as the mean abundance distribution of the cluster. The analysis was carried out by iteratively adjusting LTE synthetic spectra for several chemical elements: C, O, Na, Mg, Al, Si, S, Ca, Sc, Ti, V, Cr, Mn, Fe, Co, Ni, Cu, Zn, Ga, Sr, Y, Zr, Ba, La, Ce, Pr, Nd, Sm, Eu, and Gd. This is the first abundance determination of the Lanthanides in the Hyades F dwarfs. Each element was found to be marginally/slightly overabundant relative to solar, except for Zn, Ga, Y, and Pr which are solar, and for Sr, Ba, La, Ce, Sm, and Gd which are overabundant. The mean iron abundance of the cluster is found to be [Fe/H] = 0.21 dex.

Keywords: Open clusters and associations: individual: Hyades, Stars: abundances, Stars: individual: HD 18404, Stars: individual: HD 26345, Stars: individual: HD 27534, Stars: individual: HD 28736, Stars: individual: HD 28911

1 Introduction

The deep convection zones of the F type main-sequence stars homogenize the gas in their outer layers. The derived photospheric abundances of these stars should thus reflect their original values at the time when cluster formed and provide the mean original chemical composition of the cluster.

The Hyades Open Cluster is one of the most important laboratory for stellar astrophysicists due to its brightness and large number of members. The carbon and iron abundances have been derived by Friel & Boesgaard (1990) and Boesgaard & Friel (1990) for 14 F-type stars. Thorburn et al. (1993) also derived lithium abundance of several F-type members. A detailed abundance analysis of this cluster (including both chemically normal and peculiar stars) was carried out by Varenne & Monier (1999) and, recently by Gebran et al. (2010). For the abundance analysis of F-type stars, Gebran et al. (2010), however, used mono-order AURELIE spectra, which allowed to derive the abundance for a limited number of elements with a fairly large uncertainty.

Our aim is to derive the mean chemical abundances for F-type stars members of the Hyades precisely, using the high resolution and high signal-to-noise echelle SOPHIE spectra which span a much wider wavelength range, from 3900 Å to 6860 Å, than AURELIE spectra did. We selected HD 18404, HD 26345,HD 27534, HD 28736, and HD 28911 to derive their abundances. This study is a part of a long-term ongoing project which includes 25 F-type members of Hyades and we present here our first results.

[1] Ankara University, Faculty of Science, Department of Astronomy and Space Sciences, 06100, Tandoğan, Ankara, Turkey
[2] LESIA, UMR 8109, Observatoire de Paris Meudon, Place J. Janssen, Meudon, France
[3] Laboratoire Lagrange UMR 7293, Université de Nice Sophia, Nice, France
[4] Notre Dame University, Faculty of Natural & Applied Sciences, Louaize, Lebanon

© Société Francaise d'Astronomie et d'Astrophysique (SF2A) 2015

2 Spectral Data

The spectra and radial velocities of HD 18404 (F5IV), HD 26345 (F6V), HD 27534 (F5V), HD 28736 (F5V), and HD 28911 (F5V) were retrieved from the SOPHIE archive. The spectral data spans the wavelengths between 3872 and 6942 Å, with a resolution of about R=75000.

In the event more than one spectrum was available for a given star, we co-added these spectra to increase the signal-to-noise (S/N) ratio. The spectra were then normalised to a local continuum using low-order spline functions.

3 Abundance Analysis

Model atmospheres were computed using ATLAS9 (Kurucz 1993; Sbordone et al. 2004; Sbordone 2005) code assuming LTE (Local Thermodynamic Equilibrium) approximation and RE (Radiative Equilibrium). The synthetic spectra were computed using SYNSPEC48 (Hubeny & Lanz 1992). We have slightly modified this code to compute the chi-squares between observed and synthetic spectra.

In order to derive the atmospheric parameters of the five cluster members, we initially used Strömgren's uvbyβ photometry of these stars (Crawford et al. 1966; Crawford & Perry 1966; Eggen 1982, 1985; Hauck & Mermilliod 1998; Olsen 1994) and Napiwotzki et al.'s (1993) calibration of this photometry in terms of T_e and log g. We then compared the observed and the theoretical hydrogen Balmer line profiles (H_β, H_γ, H_δ) computed for these parameters to improve the effective temperature of the stars more accurately (Fig. 1). As the hydrogen Balmer lines are not very sensitive to surface gravity changes at these effective temperatures, the surface gravities were adopted from photometry. The derived effective temperatures from Strömgren photometry and from hydrogen Balmer lines were found to agree with each other. The microturbulent velocity of the stars varies between 1.6 and 2.0 km s^{-1}. The derived atmospheric parameters and final adopted values are collected in Table 1.

The linelist of R. L. Kurucz (gfhyperall.dat) was used as an initial source of atomic data and then was updated using the NIST (Kramida et al. 2013) and VALD (Piskunov et al. 1995; Ryabchikova et al. 1997; Kupka et al. 1999, 2000) databases.

In order to derive the elemental abundances, we iteratively adjusted the synthetic spectra to the observed spectrum for each star. The final outputs of this adjusting process are illustrated in Fig. 1. We only analyzed

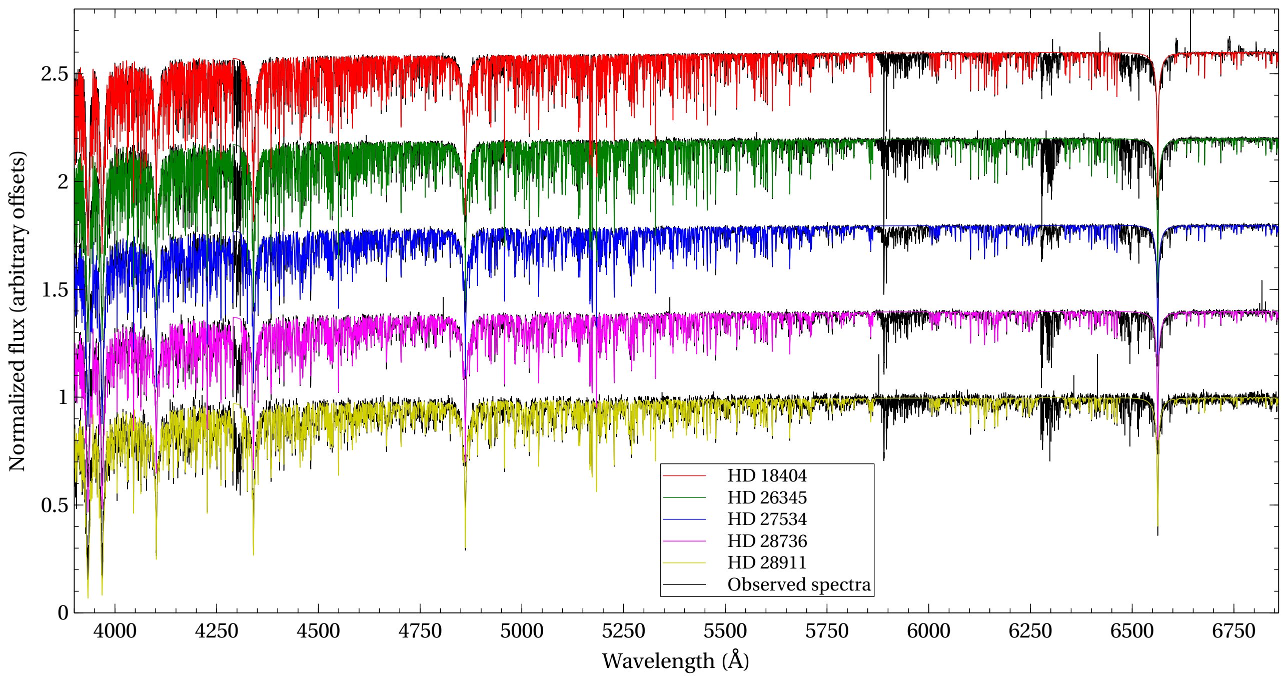

Fig. 1. Comparison of the observed and synthetic spectra for the derived elemental abundances

Table 1. Atmospheric parameters of the program stars

		HD 18404	HD 26345	HD 27534	HD 28736	HD 28911
	H_β	6800	6900	6750	6800	6800
	H_γ	6800	6850	6600	6800	6900
T_e(K)	H_δ	6850	6900	6700	6800	6800
	Strömgren $uvby\beta$	6917	6866	6665	6833	6767
	Adopted	6850 ± 100	6900 ± 100	6700 ± 100	6800 ± 100	6800 ± 100
log g	Strömgren $uvby\beta$	4.25	4.23	4.08	4.17	4.16
	Adopted	4.25 ± 0.05	4.25 ± 0.10	4.10 ± 0.30	4.15 ± 0.10	4.15 ± 0.10

the spectral region from 3900 Å to 6860 Å as the spectra are too noisy outside this range. We discarded the following wavelength intervals: 5870-6000, 6270-6330 and 6470-6600 Å because of the telluric lines. We also rejected the 4290-4310 Å interval because we had difficulties to normalize to a local continuum in that region.

4 Results and Discussion

Fig. 2 displays the derived elemental abundances of 30 chemical elements for each star. To our knowledge, the abundances of many lanthanides (La, Ce, Pr, Nd, Sm, Eu, and Gd) were derived for the first time in this study for the Hyades. We found that the abundances of Zn, Ga, Y and Pr are normal, Mg, S, Sc, Ti, Mn, Cu, and Zr are marginally overabundant ($\sim +0.10$ dex), while C, O, Na, Si, Ca, V, Cr, Fe, Co, Ni and Nd are slightly overabundant ($\sim +0.25$ dex), Sr, Ba, La, Ce, Sm, and Gd are overabundant ($\sim +0.40$ dex) relative to solar abundances (Grevesse & Sauval 1998). We did not find significant variations of the abundances from one star to another. The apparent star-to-star abundance variations for O, Ga, and Eu most likely are caused by the limited number of lines analyzed and differences in the projected rotational velocities between the program stars.

We compared our derived mean abundances for the F stars in the Hyades with those determined by Gebran et al. (2010) taking into account typical uncertainties of about ± 0.20 dex in Fig. 2. The mean abundances in these two study are similar in the limit of uncertainties, except for C and Fe. The differences between the two study most likely arise from the different resolution and wavelength coverage of the two instruments used in the analyses. However, the found C enrichment for these F stars in this study is unexpected. A fine analysis on several high quality C I lines is clearly necessary for a better conclusion. The first results presented in this study reveal that the F stars of Hyades cluster are more enriched in metals (i.e., [Fe/H]=0.21 dex) than previously reported (0.13 by Boesgaard & Friel (1990) and 0.05 by Gebran et al. (2010)). Our ongoing project on a large number of F-type members in Hyades will help us to derive a more precise distribution of elemental abundances for the cluster. A differential abundance analysis may also help to eliminate the systematic instrumental errors on derived abundances.

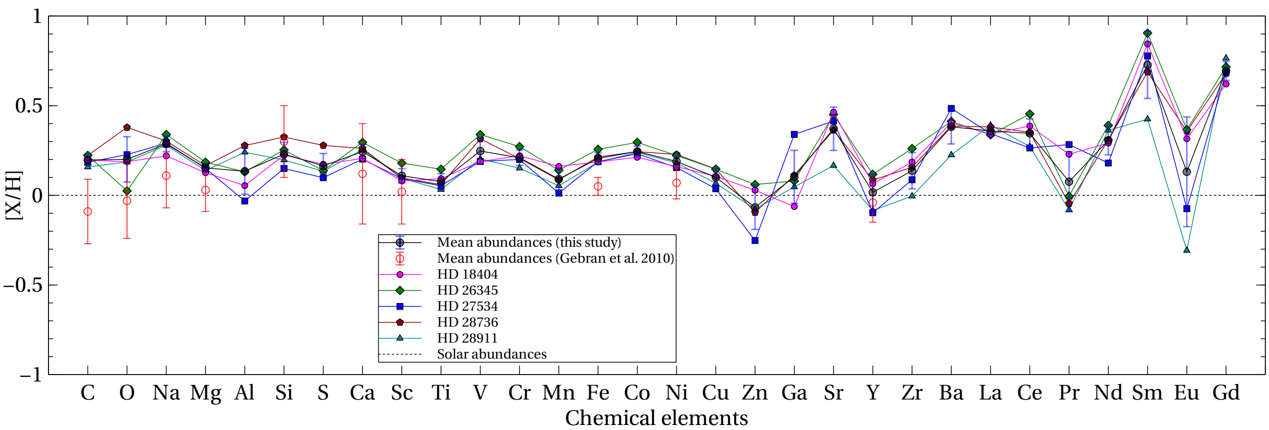

Fig. 2. Derived abundances for the program stars

We thank the OHP night assistants for their efficient support. This research made use of the SIMBAD, WEBDA, ADS, VALD, and NIST databases and R.L. Kurucz's web page. This research was supported by the Scientific and Technological Research Council of Turkey (TÜBİTAK, Project no. 1001-112T119).

References

Boesgaard, A. M. & Friel, E. D. 1990, ApJ, 351, 467

Crawford, D. L., Barnes, J. V., Faure, B. Q., Golson, J. C., & Perry, C. L. 1966, AJ, 71, 709

Crawford, D. L. & Perry, C. L. 1966, AJ, 71, 206

Eggen, O. J. 1982, ApJS, 50, 221

Eggen, O. J. 1985, PASP, 97, 807

Friel, E. D. & Boesgaard, A. M. 1990, ApJ, 351, 480

Gebran, M., Vick, M., Monier, R., & Fossati, L. 2010, A&A, 523, A71

Grevesse, N. & Sauval, A. J. 1998, Space Sci. Rev., 85, 161

Hauck, B. & Mermilliod, M. 1998, A&AS, 129, 431

Hubeny, I. & Lanz, T. 1992, A&A, 262, 501

Kramida, A., Yu. Ralchenko, Reader, J., & and NIST ASD Team. 2013, NIST Atomic Spectra Database (ver. 5.1), [Online]. Available: `http://physics.nist.gov/asd`. National Institute of Standards and Technology, Gaithersburg, MD.

Kupka, F., Piskunov, N., Ryabchikova, T. A., Stempels, H. C., & Weiss, W. W. 1999, A&AS, 138, 119

Kupka, F. G., Ryabchikova, T. A., Piskunov, N. E., Stempels, H. C., & Weiss, W. W. 2000, Baltic Astronomy, 9, 590

Kurucz, R. 1993, ATLAS9 Stellar Atmosphere Programs and 2 km/s grid. Kurucz CD-ROM No. 13. Cambridge, Mass.: Smithsonian Astrophysical Observatory, 1993., 13

Napiwotzki, R., Schoenberner, D., & Wenske, V. 1993, A&A, 268, 653

Olsen, E. H. 1994, A&AS, 106, 257

Piskunov, N. E., Kupka, F., Ryabchikova, T. A., Weiss, W. W., & Jeffery, C. S. 1995, A&AS, 112, 525

Ryabchikova, T. A., Piskunov, N. E., Kupka, F., & Weiss, W. W. 1997, Baltic Astronomy, 6, 244

Sbordone, L. 2005, Memorie della Societa Astronomica Italiana Supplementi, 8, 61

Sbordone, L., Bonifacio, P., Castelli, F., & Kurucz, R. L. 2004, Memorie della Societa Astronomica Italiana Supplementi, 5, 93

Thorburn, J. A., Hobbs, L. M., Deliyannis, C. P., & Pinsonneault, M. H. 1993, ApJ, 415, 150

Varenne, O. & Monier, R. 1999, A&A, 351, 247

SF2A 2015
F. Martins, S. Boissier, V. Buat, L. Cambrésy and P. Petit (eds)

γ^2 VELORUM: COMBINING INTERFEROMETRIC OBSERVATIONS WITH HYDRODYNAMIC SIMULATIONS

A. Lamberts[1] and F. Millour[2]

Abstract. Colliding stellar winds in massive binary systems have been studied through their radio and strong X-ray emission for decades. More recently, spectro-interferometric observations in the near infrared have become available for certain binaries, but identifying the different contributions to the emission remains a challenge. Multidimensional hydrodynamic simulations reveal a complex double shocked structure and can guide the analysis of observational data. In this work, we analyse the wind collision region in the WR+O binary, γ^2 Velorum. We combine multi-epoch AMBER observations with mock data obtained with hydrodynamic simulations with the RAMSES code. We assess the contributions of the wind collision region in order to constrain the wind structure of both stars.

Keywords: stars:binaries:spectroscopic, stars:Wolf-Rayet, stars:winds, outflows, techniques:interferometric, methods:numerical, stars:individual:γ^2 Velorum

1 Introduction

The strong photon field of massive stars enables them to drive supersonic winds ($v \simeq 1000 - 3000$ km s^{-1}) with mass loss rates varying from $10^{-8} M_\odot \mathrm{yr}^{-1}$ for O stars to $10^{-5} M_\odot$ yr^{-1} for Wolf-Rayet (WR) stars. These winds are a crucial aspect to the evolution of massive stars. They also impact their surrounding medium, by the injection of momentum and metals during the final stages. Colliding wind binaries provide a unique opportunity to probe the structure of stellar winds. The interaction of both winds creates a warm and dense shocked region, with strong X-ray emission (Stevens et al. 1992). The geometry of the shock cone can be inferred from phase-locked variability in UV, optical and IR emission lines, as well as non-thermal radio-observations in certain systems. As such colliding wind binaries provide much more observables than isolated systems and provide crucial information on stellar winds.

γ^2 Velorum is the closest known WR+O binary and is an ideal target for in depth study of the colliding wind region (St.-Louis et al. 1993; Willis et al. 1995; Henley et al. 2005). Detailed modelling of the of the optical and infrared spectra (De Marco & Schmutz 1999; De Marco et al. 2000) allows to determine most of the stellar and wind parameters for both stars, but direct observation of the O-star remains a challenge, as it is strongly embedded in the wind collision zone. Infrared interferometry offers a unique opportunity to put constraints on the spatial extension of the wind collision zone and its relative flux. Previous work (Millour et al. 2007) based on AMBER observations refined the spectral types of the stars and highlighted the presence of strong residuals in the data but was unable to attribute them to the wind collision region.

In this work, we present a direct comparison of interferometric data and mock data from hydrodynamic simulations. The 3D simulations present an accurate model of the temperature and density in the wind collision region, from which we can derive the corresponding emitted flux. The resulting extended emission is well matched by the data. This work is the first identification of a wind collision region with interferometric data in the infrared.

[1] Department of Physics, University of Wisconsin-Milwaukee, 3135 N. Maryland Avenue, Milwaukee, WI 53211, USA
[2] Laboratoire Lagrange, UMR 7293 UNS-CNRS OCA, Boulevard de l'Observatoire, B.P. 4229 F, 06304 Nice Cedex 4, France

© Société Francaise d'Astronomie et d'Astrophysique (SF2A) 2015

2 Combining interferometric data and hydrodynamic simulations

2.1 Observations and data analysis

We use interferometric data obtained with AMBER (Astronomical Multi-BEam Recombiner (Petrov et al. 2007)) on the Very Large Telescope Interferometer (VLTI). AMBER provides spectra in the J,H and K bands, with a maximal resolution of $\Delta\lambda/\lambda = 12000$. While multiple observations from 2004 until 2012 provide a good coverage of the $79d$ orbital period, the work we present here focuses on the orbital phase $\phi \simeq 0.8$, where the binary is in the plane of the sky. Using the `fitOmatic` software (developed in house, see Millour et al. (2009)), we isolate two different spectra. The first one is clearly associated with the luminous WR star, while the second one is spatially associated with the region around the O-star. As such, it probably includes features from the O-star wind and the WR star wind but also the wind collision region. This is suggested by the presence of important residuals when substracting the WR spectrum from the O-star spectrum.

While detailed modeling of the spectral lines is beyond the scope of our work we use hydrodynamic simulations to reproduce the continuum emission and derive visibility curves.

2.2 Numerical simulations and mock data

We use the RAMSES code (Teyssier 2002) to solve the equations of hydrodynamics in three dimensions. The code is based on a second order Godunov method on a Cartesian grid. It allows for adaptive mesh refinement (AMR), meaning that the resolution can be locally increased according to the properties of the flow. It is perfectly suited for the study of colliding wind binaries, where refinement according to density gradients will naturally enhance the resolution around the shocks (see e.g. Lamberts et al. (2011)).

The winds are generated in two spherical regions, which are reset at each timestep. The winds are spherical and are launched with their terminal velocity. We include orbital motion of the stars and radiative cooling in the shocked region. We model a region covering six times the binary separation. The amount of flux in the shocked region outside of our simulation domain is negligible. We use the wind and stellar parameters derived in De Marco et al. (2000) and the orbital parameters from Schmutz et al. (1997).

Figure 1 shows the density, velocity and temperature in the orbital plane for the orbital phase $\phi = 0.8$. The temperature map clearly highlights the warm shocked region. At the apex, the wind velocity is very low but then increases up to supersonic values further out. Both shocked winds are separated by a contact discontinuity, as can be seen on the density map. Due to the lower density, the O-star wind is less subject to radiative cooling and has a temperature of more than 10^8 K at the apex of the shock. The WR wind on the other hand cools down to about 10^7 K in the whole shocked region. The shocked region presents a limited development of both the Kelvin-Helmholtz and the non-linear thin shell instability (Vishniac 1994), which should not be sufficient to yield any temporal variability in the system.

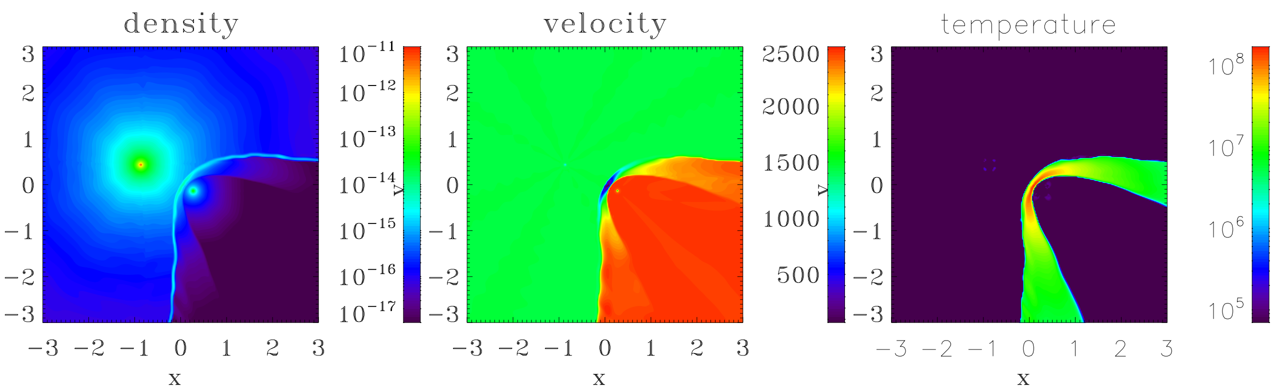

Fig. 1. Density (g cm^{-3}), velocity (km s^{-1}) and temperature (K) in the orbital plane of γ^2 Vel at $\phi = 0.8$. The lengthscale is given in units of the binary separation. The WR star is on the top left, the O star on the bottom right.

To compare with the emission from the unshocked winds, we compute the free-free emission from the wind collision region only. First, we compute the emissivity in all shocked cells (those with $T \geq 10^5$ K) and then we take into account the absorption along the line of sight. As we included a passive scalar in the simulation, we can distinguish both winds and account for the chemical enrichment of the WR wind. The emission of the WR wind is determined by a model derived from Dessart et al. (2000) and the O star is considered as a point source (i.e. the contribution of its free wind is neglected). Figure 2 shows the resulting emission map at $2\mu m$. The map shows extended emission from the shocked region. At this stage, we have not determined the exact impact on the emitted spectra.

However, we have assessed the contribution of this extended source on the visibility of the system. The visibility is an interferometric measurement related to the spatial extension of a source. A low visibility indicates an extended emitting region. The left panel of figure 3 shows the observed visibility curve in γ^2 Vel (in red) as well as a mock curve (in black) based on a model including the emission from both stars and the Wolf-Rayet wind, but no wind collision region. The model does not match the data, indicating an extended source contributes to the emission. The right panel shows mock visibility curves extracted from the simulation. Again, the black curves assumes the wind collision region does not contribute to the emission. The green and red curves assume an arbitrary contribution of 2.5% and 5% of the total flux respectively. While the quantitative analysis is still in progress, these plots show that the wind collision region impact the total emission and can be detected with infrared interferometry.

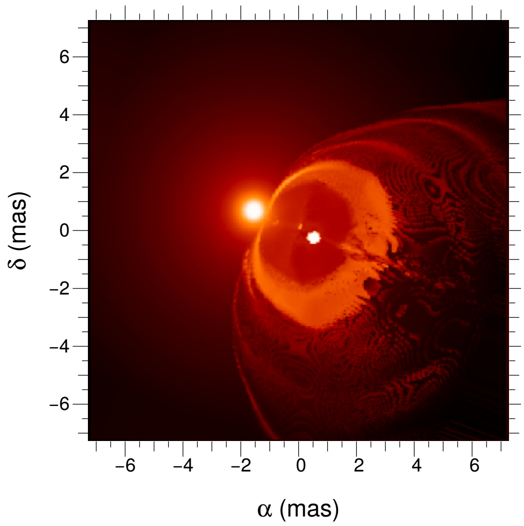

Fig. 2. Flux at 2μ at $\phi = 0.8$. The color scale is arbitrary and logarithmic.

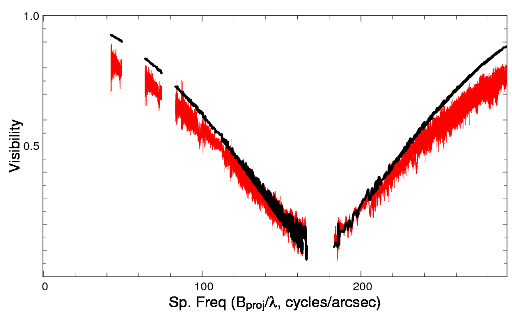

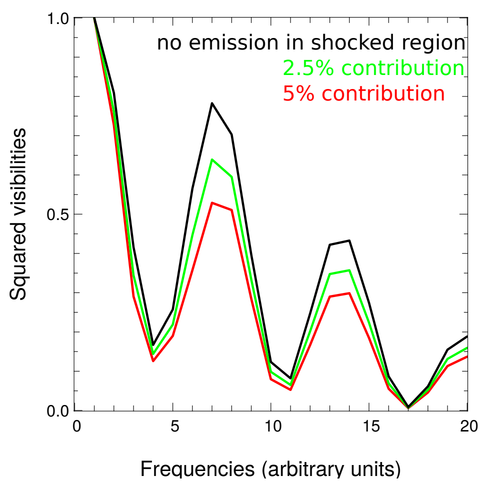

Fig. 3. Left: Observed (red) and mock visibility curve, assuming two stars without wind collision region. Right: Visibility curves with different respective contributions, based on the numerical simulation.

3 Looking further

In this work we confirm the first detection of a wind collision region with infrared interferometry. Although γ^2 Vel is an ideal target for such observations, the identification of the wind collision region is not straightforward, due to the complex geometry of the system. Therefore, we have performed three-dimensional hydrodynamic simulations to model the structure of the system and determine its continuum emission. The resulting emission map shows that the wind collision region displays extended emission and decreases the visibility curve of the system. Our preliminary qualitative analysis matches the data and allows us to confirm the detection of the wind collision region. Further work will include more quantitative results including several orbital phases.

Acknowledgments: This work was initiated by Olivier Chesneau, who passed away before seeing the confirmation of the detection. We thank him for his insight to start this collaboration between observation and theory. Astrid Lamberts is supported by the UWM Research Growth Initiative, the NASA ATP program through NASA grant NNX13AH43G, and NSF grant AST-1255469. Simulations were performed at the NASA Advanced Supercomputing Division.

References

De Marco, O. & Schmutz, W. 1999, A&A, 345, 163

De Marco, O., Schmutz, W., Crowther, P. A., et al. 2000, A&A, 358, 187

Dessart, L., Crowther, P. A., Hillier, D. J., et al. 2000, MNRAS, 315, 407

Henley, D. B., Stevens, I. R., & Pittard, J. M. 2005, MNRAS, 356, 1308

Lamberts, A., Fromang, S., & Dubus, G. 2011, MNRAS, 418, 2618

Millour, F., Chesneau, O., Borges Fernandes, M., et al. 2009, A&A, 507, 317

Millour, F., Petrov, R. G., Chesneau, O., et al. 2007, A&A, 464, 107

Petrov, R. G., Malbet, F., Weigelt, G., et al. 2007, A&A, 464, 1

Schmutz, W., Schweickhardt, J., Stahl, O., et al. 1997, A&A, 328, 219

St.-Louis, N., Willis, A. J., & Stevens, I. R. 1993, ApJ, 415, 298

Stevens, I. R., Blondin, J. M., & Pollock, A. M. T. 1992, ApJ, 386, 265

Teyssier, R. 2002, A&A, 385, 337

Vishniac, E. T. 1994, ApJ, 428, 186

Willis, A. J., Schild, H., & Stevens, I. R. 1995, A&A, 298, 549

SF2A 2015
F. Martins, S. Boissier, V. Buat, L. Cambrésy and P. Petit (eds)

THEORETICAL ANALYSIS OF THE MG(3 ^{3}P)-MG(4^{3}S) LINE SHAPE IN COOL DZ WHITE DWARFS

T. Leininger[1], F. X. Gadéa[1] and N. F. Allard[2, 3]

Abstract. We present a determination of the Mg(3 ^{3}P)-Mg(4 ^{3}S) collisional line profiles using very recent *ab initio* potential energies. Results are reported for the conditions prevailing in cool DZ white dwarf atmospheres.

Keywords: white dwarfs - Stars: atmospheres - Lines: profiles

1 Introduction

Traces of heavy metal in cool DZ white dwarfs are now attributed to the accretion of circumstellar dust. This dust is thought to originate from the tidal disruption of some rocky material. They provide a unique opportunity to study the composition of extra-solar planetary systems. The determinations of precise atmospheric parameters and abundances require accurate description of the line profiles of the identified features. This work is a continuation of our studies of sodium and ionized calcium resonance lines perturbed by helium (Allard 2013; Allard & Alekseev 2014; Allard et al. 2014). The triplet $3p$-$4s$ line profiles of Mg perturbed by helium are calculated for the physical conditions encountered in the atmospheres of cool white dwarfs that exhibit a strong asymmetry in their spectra. We show that a line satellite band located in the near blue wing of the Mg line is responsible of an asymmetry not correctly considered by modelers of cool DZ white dwarfs. The asymmetrical shapes of spectral lines have been extensively investigated for many years because of their importance in experimental and theoretical work (Allard & Kielkopf 1982). Line profile calculations in our work have been done in unified line-shape semiclassical theory (Anderson 1952) using new *ab initio* potential energies that take into account the long range part. The analysis was based on line broadening theory reported in Allard et al. (1999). Several theoretical computed profiles are used to illustrate the evolution of the line satellite with pressure.

2 Potentials

The *ab initio* computation of the adiabatic potential energy curves of MgHe have been carried out using a large core pseudopotential for Mg complemented by operatorial Core Polarisation Potential (CPP) (Fuentealba et al. 1983) with the MOLPRO package. The large basis set we built was inspired from the standard (pseudopotential) basis set (Fuentealba et al. 1982) and the one used in rather high Rydberg calculations (Khemiri et al. 2013) leading to a 10s9p6d3f3g basis set. For He, the huge 30s17p10d6f3g basis set of Deguilhem and coworkers (Deguilhem et al. 2009) has been used. State specific orbitals were obtained from CASSCF calculations (Werner & Knowles 1985) , where the active space consisted of 4 electrons distributed in all orbitals up to the 4s orbital of Mg. These orbitals were then used in subsequent MRCI (Werner & Knowles 1988) calculations to obtain the potential energy curves as well as static and transition dipole moments for all allowed transitions. For this 4 electrons system, this leads to almost full CI quality calculations.

Potential energy curves $V(R)$ for the MgHe molecule in the $3p\,^3$P and $4s\,^3$S states are shown in Fig. 1, where R denotes the internuclear distance between the radiator and the perturber.

[1] Laboratoire de Chimie et Physique Quantiques, UMR5626, CNRS, Université de Toulouse, 118 route de Narbonne, F-31400 Toulouse, France
[2] Observatoire de Paris GEPI, UMR 8111, CNRS, 61, Avenue de l'Observatoire, F-75014 Paris, France
[3] Institut d'Astrophysique de Paris, UMR 7095, CNRS, Université Pierre et Marie Curie, 98bis Boulevard Arago, F-75014 Paris, France

© Société Francaise d'Astronomie et d'Astrophysique (SF2A) 2015

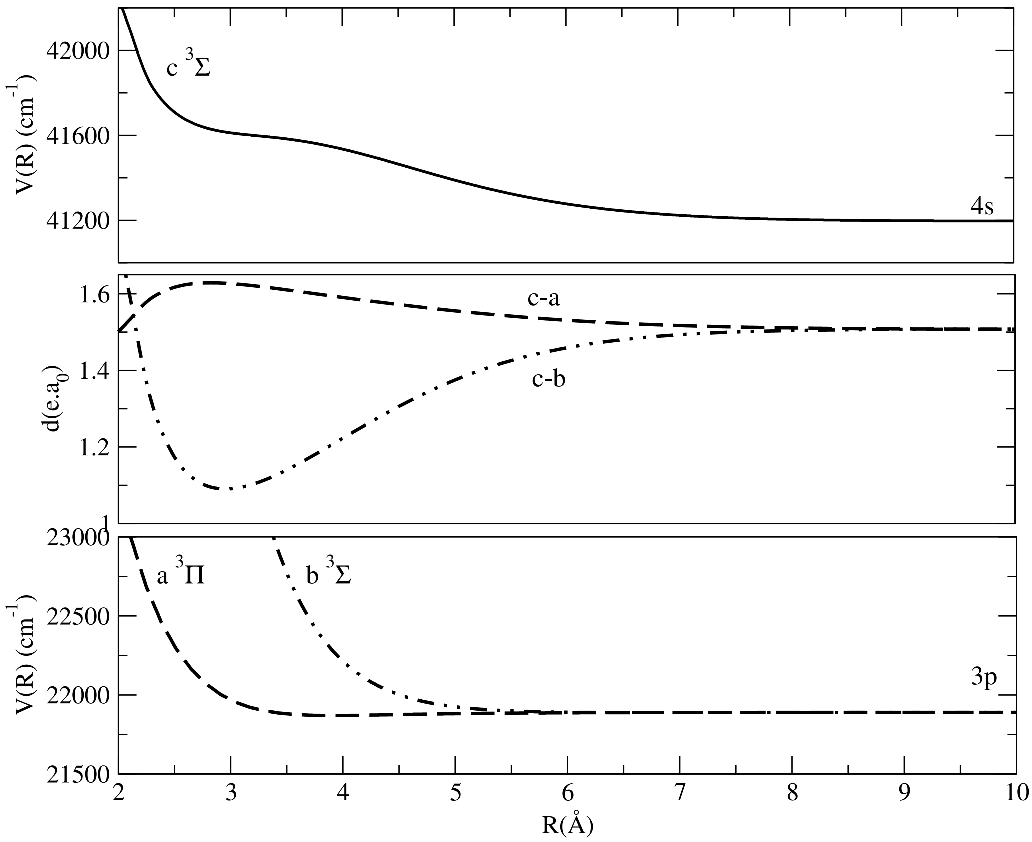

Fig. 1. Potential energies for the triplet $4s$ and $3p$ states of the Mg–He molecule and transition dipole moments.

3 Density dependence of the line profile

In radiative collision transitions it is the difference potential between the final and initial states that determines the frequency and the energy emitted or absorbed by a single photon. The unified theory of Anderson (1952) predicts that there will be satellites centered periodically at frequencies corresponding to the extrema of the difference potential between the upper and lower states. Hence the interpretation of the asymmetrical shape of the $3p \rightarrow 4s$ line requires us to study ΔV, as shown in Fig. 2-left. The difference potential maxima are respectively 400 and 165 cm^{-1} for $3p\,^3\Pi \rightarrow 4S\,^3\Sigma$ and $3p\,^3\Sigma \rightarrow 4s\,^3\Sigma$. Figure 2-right shows the individual components for comparison, weighted as if they were the only contribution to the profile. The distinct wide shoulder at about 240 cm^{-1} due to the $3p\,^3\Pi \rightarrow 4S\,^3\Sigma$ transition, yields unresolved line satellite in the blue wing about 5120 Å (Fig. 3-right). The other maximum at ΔV= 165 cm$^-1$ does not give the slightest hint of a blue shoulder, the corresponding individual profile simply appears to have a blue asymmetry.

In Fig. 3 we show the variation of the line profiles at 6000 K with increasing helium density. When the density is about 1.75× 10^{21} cm^{-3} the development of the blue wing leads to the overwhelming of the line by the satellite. The line satellite becomes higher than the main line for $n_{\rm He}$ = 2.5× 10^{21} cm^{-3} which has totally disappeared for $n_{\rm He}$ = 4× 10^{21} cm^{-3}.

4 Conclusion

The purpose of this study was to establish the link of the strong asymmetry observed in spectral features observed in cool DZ white dwarfs with the existence of an unresoved blue satellite. This effect is of increasing importance with He density, and as a result, the profile shifts towards the position of the satellite band. The asymmetry in the Mg profile is uncorrectly identified as due to quasistatic broadening since Wehrse & Liebert (1980) but the line shape does not depend on the assumption that the interaction is given by a van der Waals approximation.

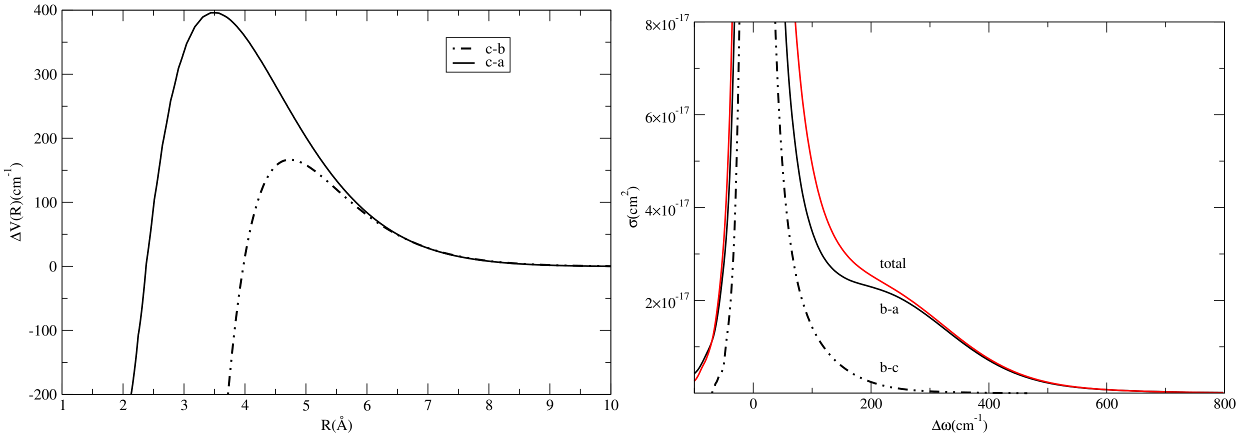

Fig. 2. Left: ΔV for the two transitions contributing to $3p \to 4s$ line. **Right:** Individual components of the line compared to the total profile. (T=6000 K and $n_{\rm He}$= 10^{20} cm^{-3}).

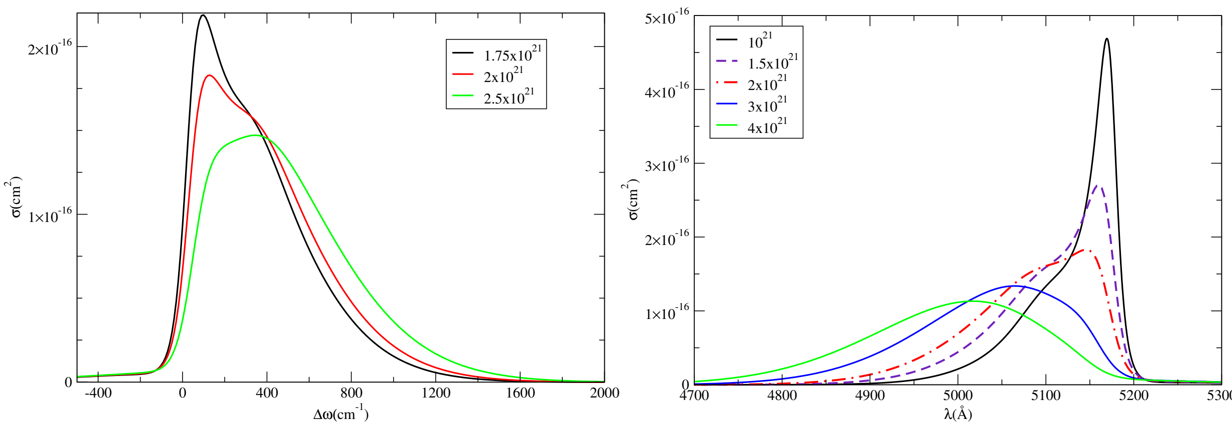

Fig. 3. Evolution of the unified profiles with increasing helium density. **Left:** $n_{\rm He}$= 1.75 to 2.5× 10^{21} cm^{-3}. **Right:** $n_{\rm He}$= 1 to 4× 10^{21} cm^{-3}.

References

Allard, N. F. 2013, in EAS Publications Series, Vol. 63, EAS Publications Series, 403–406
Allard, N. F. & Alekseev, V. A. 2014, Advances in Space Research, 54, 1248
Allard, N. F., Homeier, D., Guillon, G., Viel, A., & Kielkopf, J. 2014, Journal of Physics Conference Series, 548, 012006
Allard, N. F. & Kielkopf, J. F. 1982, Rev. Mod. Phys., 54, 1103
Allard, N. F., Royer, A., Kielkopf, J. F., & Feautrier, N. 1999, Phys. Rev. A, 60, 1021
Anderson, P. W. 1952, Phys. Rev., 86, 809
Deguilhem, B., Leininger, T., Gadéa, F. X. & Dickinson, A. S. 2009, J. Phys. B: At. Mol. Opt. Phys. 42, 015102
Fuentealba, P., Stoll, H., v. Szentpaly, L., Schwerdtfeger, P., & Preuss, H. 1983, J. Phys. B 16, L323
Fuentealba, P., Preuss, H., Stoll, H., & v. Szentpaly, L. 1982, Chem. Phys. Lett. 89, 418
Khemiri, N., Dardouri, R., Oujia, B., & Gadéa, F. X. 2013, J. Phys. Chem. 117, 8915
Wehrse, R. & Liebert, J. 1980, A&A, 86, 139
Werner, H. J., & Knowles, P. J. 1985, J. Chem. Phys. 82, 5053
Werner, H. J., & Knowles, P. J. 1988, J. Chem. Phys. 89, 5803

SF2A 2015
F. Martins, S. Boissier, V. Buat, L. Cambrésy and P. Petit (eds)

THE VARIATION OF THE TIDAL QUALITY FACTOR OF CONVECTIVE ENVELOPES OF ROTATING LOW-MASS STARS ALONG THEIR EVOLUTION

S. Mathis[1]

Abstract. More than 1500 exoplanets have been discovered around a large diversity of host stars (from M- to A-type stars). Tidal dissipation in their convective envelope is a key actor that shapes the orbital architecture of short-period systems and that still remains unknown. Using a simplified two-layer assumption and grids of stellar models, we compute analytically an equivalent modified tidal quality factor, which is proportional to the inverse of the frequency-averaged dissipation due to the viscous friction applied by turbulent convection on tidal waves. It leads the conversion of their kinetic energy into heat and tidal evolution of orbits and spin. During their Pre-Main-Sequence, all low-mass stars have a decrease of the equivalent modified tidal quality factor for a fixed angular velocity of their convective envelope. Next, it evolves on the Main Sequence to an asymptotic value that is minimum for $0.6M_{\odot}$ K-type stars and that increases by several orders of magnitude with increasing stellar mass. Finally, the rotational evolution of low-mass stars strengthens tidal dissipation during the Pre-Main-Sequence.

Keywords: hydrodynamics – waves – celestial mechanics – planet-star interactions – stars: evolution – stars: rotation

1 Introduction and context

Since twenty years, more than 1500 exoplanets have been discovered (e.g. Perryman 2011). The orbital architecture of their systems is strongly different from the one we know for our solar system (e.g. Fabrycky et al. 2014). It stimulates a lot of studies of their dynamical evolution and stability (e.g. Bolmont et al. 2012; Laskar et al. 2012). In such studies, tidal interactions are one of the principal physical mechanisms that must be modeled, particularly for short-period systems. Indeed, the dissipation of the kinetic energy of tidal flows/displacements in stellar and planetary interiors leads to a modification of the semi-major axis and the eccentricity of the orbits, of the rotation of celestial bodies and of the relative inclination of the spins (Hut 1980, 1981). In this framework, a large majority of works proposed to use the so-called *tidal quality factor* Q to parametrize this dissipation and the related friction processes (Kaula 1964). As in the case of the theory of forced damped oscillators, the dissipation is strong and the evolution is rapid when the quality factor is small and vice-versa. Two ways are then proposed to choose a value for Q: i) one can choose to calibrate it on observations or on formation scenario (Goldreich & Soter 1966; Hansen 2012); ii) one choose to compute it using an ab-initio treatment of dissipative mechanisms acting on tidal motions (e.g. Mathis & Remus 2013; Ogilvie 2014; Le Bars et al. 2015). In the second case, it is now demonstrated that tidal dissipation is a complex function of the internal structure of celestial bodies, of their dynamical properties (their rotation, stratification, viscosity, thermal diffusivity, etc.) and of the forcing frequency (e.g. Efroimsky & Lainey 2007; Mathis & Remus 2013; Ogilvie 2014; Auclair Desrotour et al. 2015, and references therein). Such dependences have a strong impact on the dynamical evolution of systems (Auclair-Desrotour et al. 2014).

To obtain a coherent picture of the dynamics of exoplanetary systems it is thus necessary to have a correct evaluation of tidal dissipation in their host stars along their evolution; for instance this dissipation has a strong impact on the orbital configuration of short-period systems. From now on, stellar mass range spreads from M red dwarfs to intermediate-mass A-type stars. In this context, tidal friction in the rotating turbulent convective envelopes of these low-mass stars plays an important role for tidal migration, circularization of orbits, synchronization and alignment of spins (e.g. Winn et al. 2010; Albrecht et al. 2012; Lai 2012; Ogilvie 2014; Valsecchi & Rasio 2014, and references therein for hot-Jupiter systems). In stellar convective layers, tidal flows are constituted of large-scale non-wavelike/equilibrium flows driven by the adjustment of the hydrostatic structure of stars because of the presence of the planetary/stellar companion (Zahn 1966; Remus et al.

[1] Laboratoire AIM Paris-Saclay, CEA/DSM - CNRS - Université Paris Diderot, IRFU/SAp Centre de Saclay, F-91191 Gif-sur-Yvette Cedex, France

© Société Francaise d'Astronomie et d'Astrophysique (SF2A) 2015

2012) and the dynamical tide constituted by inertial waves, which have the Coriolis acceleration as restoring force (e.g. Ogilvie & Lin 2007). In this framework, both the structure and rotation of stars strongly varies along their evolution (e.g. Siess et al. 2000; Gallet & Bouvier 2013, 2015). Moreover, as reported by Ogilvie (2014), observations of star-planet and binary-star systems show that tidal dissipation varies over several orders of magnitude. Therefore, the key questions that must be addressed for dynamical studies is *how does the tidal quality factor of the convective envelope of low-mass stars vary as a function of stellar mass, evolutionary stage, and rotation?*

Using results presented in Mathis (2015), we introduce here an equivalent modified tidal quality factor, which has been defined by Ogilvie & Lin (2007) and is proportional to the inverse of the frequency-averaged dissipation. We compute it as a function of the mass, the age, and the rotation of stars using realistic computed grids of stellar models which can be used for dynamical studies of star-planet systems in a first step. In sec. 2, we introduce the assumptions and the formalism that allows us to analytically evaluate this quantity as a function of the structure and rotation of stars (Ogilvie & Lin 2007; Ogilvie 2013). In sec. 3, we compute it as a function of stellar mass and evolutionary stage at fixed angular velocity using grids of stellar models for low-mass stars from 0.4 to $1.4 M_{\odot}$. In sec. 4, we present our conclusions.

2 Tidal dissipation modelling

In this work, we adopt a simplified two-layer model of a star A of mass $M_{\rm s}$ and mean radius $R_{\rm s}$ hosting a point-mass tidal perturber B of mass m orbiting with a mean motion n (e.g. Ogilvie 2013; Penev et al. 2014, and Fig. 1). In this model, both the central radiative region and the convective envelope are assumed to be homogeneous with respective constant densities $\rho_{\rm c}$ and $\rho_{\rm e}$. The convective layers of A are assumed to be in a moderate solid-body rotation with an angular velocity Ω so that $\epsilon^2 \equiv \left(\Omega/\sqrt{\mathcal{G}M_{\rm s}/R_{\rm s}^3}\right)^2 = (\Omega/\Omega_{\rm c})^2 \ll 1$, where $\Omega_{\rm c}$ is the critical angular velocity and $\mathcal{G}$ is the gravitational constant. Therefore, the centrifugal acceleration, which scales as Ω^2, is not taken into account. It surrounds the radiative core of radius $R_{\rm c}$ and mass $M_{\rm c}$.

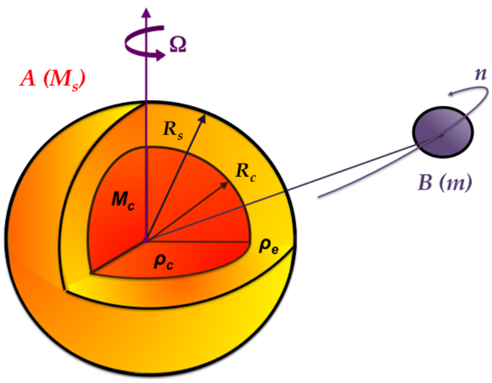

Fig. 1. Two-layer low-mass star A of mass $M_{\rm s}$ and mean radius $R_{\rm s}$ and point-mass tidal perturber B of mass m orbiting with a mean motion n. The radiative core of radius $R_{\rm c}$, mass $M_{\rm c}$, and density $\rho_{\rm c}$ is surrounded by the convective envelope of density $\rho_{\rm e}$.

Tidal dissipation in the convection zone of A originates from the excitation by B of inertial waves, which have the Coriolis acceleration as restoring force and are excited if the tidal forcing frequency $\omega \in [-2\Omega, 2\Omega]$. They are damped by the turbulent friction, which is modelled using a turbulent viscosity (see e.g. Ogilvie & Lesur 2012, and references therein). Its analytical evaluation in our two-layer model was conducted by Ogilvie (2013) who assumed an incompressible convective envelope, which corresponds to inertial waves with shorter wavelength than the characteristic length of variation of the density. In this modeling, the dissipation of tidal internal gravity waves in the stable radiative core is not taken into account (Barker & Ogilvie 2010; Ivanov et al. 2013) and the higher-frequency acoustic waves are filtered out. It allows us to compute the frequency-averaged tidal dissipation given in Ogilvie (2013) (Eq. B3) and to introduce an

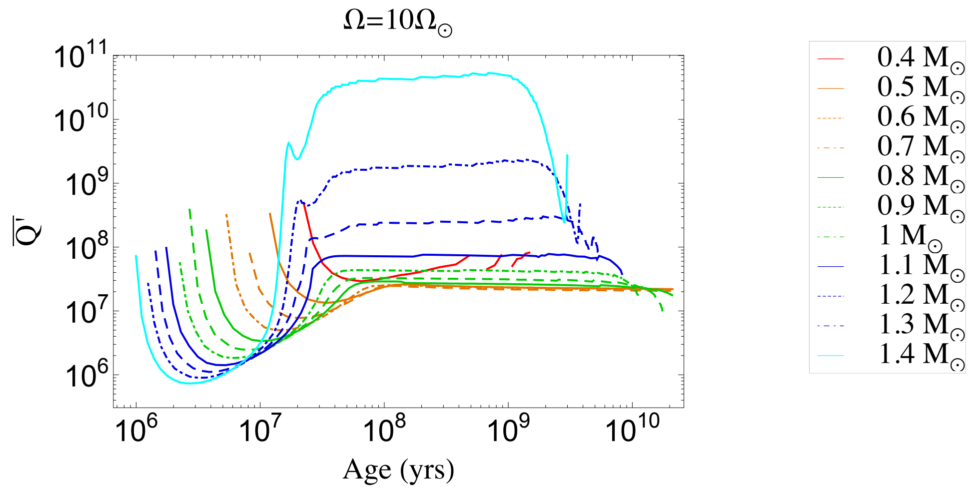

Fig. 2. Evolution of the frequency-averaged modified tidal quality factor, $\overline{Q'}$, for $\Omega = 10\Omega_{\odot}$, where $\Omega_{\odot}$ is the solar angular velocity, as a function of time for stellar masses (M_s) from 0.4 to $1.4M_{\odot}$.

equivalent modified tidal quality factor, $\overline{Q'}$, as defined by Ogilvie & Lin (2007)*:

$$\frac{3}{2\overline{Q'}} = \frac{k_2}{\overline{Q}} = \int_{-\infty}^{+\infty} \mathrm{Im}\left[k_2^2(\omega)\right] \frac{\mathrm{d}\omega}{\omega} = \left\langle \mathrm{Im}\left[k_2^2(\omega)\right]\right\rangle_{\omega} = \frac{100\pi}{63}\epsilon^2\left(\frac{\alpha^5}{1-\alpha^5}\right)(1-\gamma)^2$$
$$\times(1-\alpha)^4\left(1+2\alpha+3\alpha^2+\frac{3}{2}\alpha^3\right)^2\left[1+\left(\frac{1-\gamma}{\gamma}\right)\alpha^3\right]\left[1+\frac{3}{2}\gamma+\frac{5}{2\gamma}\left(1+\frac{1}{2}\gamma-\frac{3}{2}\gamma^2\right)\alpha^3-\frac{9}{4}(1-\delta)\alpha^5\right]^{-2} \quad (2.1)$$

with

$$\alpha = \frac{R_c}{R_s}, \quad \beta = \frac{M_c}{M_s} \quad \text{and} \quad \gamma = \frac{\rho_e}{\rho_c} = \frac{\alpha^3(1-\beta)}{\beta(1-\alpha^3)} < 1. \quad (2.2)$$

We introduce the quadrupolar complex Love number k_2^2, associated with the $(2,2)$ component of the time-dependent tidal potential U that corresponds to the spherical harmonic Y_2^2. It quantifies at the surface of the star ($r = R_s$) the ratio of the tidal perturbation of its self-gravity potential over the tidal potential in the simplest case of coplanar systems. In the case of dissipative convective envelopes, it is a complex quantity which depends on the tidal frequency (ω) with a real part that accounts for the energy stored in the tidal perturbation while the imaginary part accounts for the energy losses (e.g. Remus et al. 2012). We also recall the correspondance with the commonly used real hydrostatic quadrupolar Love number k_2, which is independent of ω in the case of fluid layers, and an equivalent tidal quality factor $\overline{Q}$. The dissipation being averaged in frequency (with the corresponding notation $\langle ...\rangle_{\omega}$), its complicated frequency-dependence in a spherical shell (Ogilvie & Lin 2007) is filtered out. The dissipation at a given frequency could thus be larger or smaller than its averaged value by several orders of magnitude.

3 Tidal dissipation along stellar evolution and the variation of $\overline{Q'}$

Following Mathis (2015), we compute the variation of the equivalent modified tidal quality factor $\overline{Q'}$ (Eq. 2.1) as a function of stellar mass, age and rotation. To reach this objective, we compute the radius and mass aspect ratios (respectively α and β) as function of time using grids of stellar models from 0.4 to $1.4M_{\odot}$ for a metallicity $Z = 0.02$ computed by Siess et al. (2000) using the STAREVOL code. It allows us to plot in Fig. 2 the variation of $\overline{Q'}$ with time with taking into account the simultaneous variations of α, β, and R_s. On the Pre-Main-Sequence (hereafter PMS), it decreases towards the minimum value, which decreases with stellar mass, corresponding to the region around ($\alpha_{\max} \approx 0.571, \beta_{\max} \approx 0.501$)

*We point out here that equivalent quality factors $\overline{Q'}$ and $\overline{Q}$, which are proportional to the inverse of the frequency-averaged dissipation $\left\langle \mathrm{Im}\left[k_2^2(\omega)\right]\right\rangle_{\omega}$, where $\langle ...\rangle_{\omega} = \int_{-\infty}^{\infty} ...\mathrm{d}\omega/\omega$, are not equivalent to potentially defined frequency-averaged quality factors $\langle Q'(\omega)\rangle_{\omega}$ and $\langle Q(\omega)\rangle_{\omega}$. In this framework, the relevant physical quantity being $\left\langle \mathrm{Im}\left[k_2^2(\omega)\right]\right\rangle_{\omega}$, we prefer to define directly equivalent quality factors from it.

where the dissipation is maximum for all stellar masses. This is due to the formation and the growth of the radiative core that leads to spherical shell configurations where dissipative inertial wave attractors may take place (Ogilvie 2005; Goodman & Lackner 2009). The time coordinate of this minimum is smaller if stellar mass is higher because of the corresponding shorter life-time of the star. Then, $\overline{Q'}$ increases to rapidly reach its almost constant value on the Main Sequence (hereafter MS). As already pointed out, and expected from observational constraints (e.g. Albrecht et al. 2012) and previous theoretical works (Ogilvie & Lin 2007; Barker & Ogilvie 2009), it increases with stellar mass from $0.6 M_\odot$ K-type to A-type stars by several orders of magnitude (≈ 3 between 0.6 and $1.4 M_\odot$) because of the variation in the thickness of the convective envelope, which becomes thinner †. For $0.4 M_\odot$ M-type stars, the radiative core has an evolution where it finally disappears. Therefore, the configuration converges on the MS to the case of fully convective stars with the weak dissipation of normal inertial modes (Wu 2005). Finally, for higher mass stars, we can see a final decrease of $\overline{Q'}$ because of the simultaneous extension of their convective envelope and contraction of their radiative core during their Sub Giant phase leading again the star towards the region of maximum dissipation in the (α, β) plane.

It is also crucial to discuss consequences of the rotational evolution of low-mass stars. As we know from observational works and related modelling (e.g. Gallet & Bouvier 2013, 2015, and references therein), their rotation follows three phases of evolution: i) stars are trapped in co-rotation with the surrounding circumstellar disk; ii) because of the contraction of stars on the PMS their rotation (and thus ϵ) increases; and iii) stars are braked on the MS because of the torque applied by pressure-driven stellar winds (e.g. Réville et al. 2015, and references therein) and ϵ decreases. As a detailed computation of stellar rotating models is beyond the scope of the present work, we have here computed $\overline{Q'}$ for an intermediate rotation $\Omega = 10\Omega_\odot$ (the values for $\Omega = \Omega_\odot$ and $\Omega = 100\Omega_\odot$ will be 100 times higher and lower respectively). From results obtained by Gallet & Bouvier (2013, 2015), we can easily infer that $\overline{Q'}$ decreases during the PMS because of the growth of the radiative core and of the angular velocity. On the MS, $\overline{Q'}$ increases because of the evolution of the structure of the star and of its braking by stellar winds.

4 Conclusions

All low-mass stars have a decrease of the equivalent modified tidal quality factor for a fixed angular velocity in their convective envelope for tidal frequencies lying within the range $[-2\Omega, 2\Omega]$ so that inertial waves can be excited until they reach a critical aspect and mass ratios close to $(\alpha_{\max}, \beta_{\max})$ during the PMS. Next, it evolves on the MS to an asymptotic value that reaches a minimum for $0.6 M_\odot$ K-type stars and then increases by several orders of magnitude with increasing stellar mass. Finally, the rotational evolution of low-mass stars strengthens the importance of tidal dissipation during the PMS as pointed out by Zahn & Bouchet (1989).

In the near future, it would be important to relax current assumptions by taking into account density stratification, differential rotation, magnetic field, non-linear effects (and related possible instabilities) and the dissipation of tidal gravito-inertial waves in stellar radiative cores (e.g. Baruteau & Rieutord 2013; Schmitt 2010; Favier et al. 2014; Ivanov et al. 2013) to get a complete picture (Guillot et al. 2014). Finally, it will be interesting to explore advanced phases of stellar evolution.

This work was supported by the Programme National de Planétologie (CNRS/INSU) and the CoRoT-CNES grant at Service d'Astrophysique (CEA-Saclay).

References

Albrecht, S., Winn, J. N., Johnson, J. A., et al. 2012, ApJ, 757, 18

Auclair-Desrotour, P., Le Poncin-Lafitte, C., & Mathis, S. 2014, A&A, 561, L7

Auclair Desrotour, P., Mathis, S., & Le Poncin-Lafitte, C. 2015, A&A, 581, A118

Barker, A. J. & Ogilvie, G. I. 2009, MNRAS, 395, 2268

Barker, A. J. & Ogilvie, G. I. 2010, MNRAS, 404, 1849

Baruteau, C. & Rieutord, M. 2013, Journal of Fluid Mechanics, 719, 47

Bolmont, E., Raymond, S. N., Leconte, J., & Matt, S. P. 2012, A&A, 544, A124

Efroimsky, M. & Lainey, V. 2007, Journal of Geophysical Research (Planets), 112, 12003

† In the cases of F- and A-type stars, a convective core is present in addition to the envelope. We neglect its action assuming that it corresponds to the regime of weak dissipation in a full sphere (Wu 2005).

Fabrycky, D. C., Lissauer, J. J., Ragozzine, D., et al. 2014, ApJ, 790, 146
Favier, B., Barker, A. J., Baruteau, C., & Ogilvie, G. I. 2014, MNRAS, 439, 845
Gallet, F. & Bouvier, J. 2013, A&A, 556, A36
Gallet, F. & Bouvier, J. 2015, ArXiv e-prints [arXiv] 1502.05801
Goldreich, P. & Soter, S. 1966, Icarus, 5, 375
Goodman, J. & Lackner, C. 2009, ApJ, 696, 2054
Guillot, T., Lin, D. N. C., Morel, P., Havel, M., & Parmentier, V. 2014, in EAS Publications Series, Vol. 65, EAS Publications Series, 327–336
Hansen, B. M. S. 2012, ApJ, 757, 6
Hut, P. 1980, A&A, 92, 167
Hut, P. 1981, A&A, 99, 126
Ivanov, P. B., Papaloizou, J. C. B., & Chernov, S. V. 2013, MNRAS, 432, 2339
Kaula, W. M. 1964, Reviews of Geophysics and Space Physics, 2, 661
Lai, D. 2012, MNRAS, 423, 486
Laskar, J., Boué, G., & Correia, A. C. M. 2012, A&A, 538, A105
Le Bars, M., Cébron, D., & Le Gal, P. 2015, Annual Review of Fluid Mechanics, 47, 163
Mathis, S. 2015, A&A, 580, L3
Mathis, S. & Remus, F. 2013, in Lecture Notes in Physics, Berlin Springer Verlag, Vol. 857, Lecture Notes in Physics, Berlin Springer Verlag, ed. J.-P. Rozelot & C. . Neiner, 111–147
Ogilvie, G. I. 2005, Journal of Fluid Mechanics, 543, 19
Ogilvie, G. I. 2013, MNRAS, 429, 613
Ogilvie, G. I. 2014, ARA&A, 52, 171
Ogilvie, G. I. & Lesur, G. 2012, MNRAS, 422, 1975
Ogilvie, G. I. & Lin, D. N. C. 2007, ApJ, 661, 1180
Penev, K., Zhang, M., & Jackson, B. 2014, PASP, 126, 553
Perryman, M. 2011, The Exoplanet Handbook
Remus, F., Mathis, S., & Zahn, J.-P. 2012, A&A, 544, A132
Réville, V., Brun, A. S., Matt, S. P., Strugarek, A., & Pinto, R. F. 2015, ApJ, 798, 116
Schmitt, D. 2010, Geophysical and Astrophysical Fluid Dynamics, 104, 135
Siess, L., Dufour, E., & Forestini, M. 2000, A&A, 358, 593
Valsecchi, F. & Rasio, F. A. 2014, ApJ, 786, 102
Winn, J. N., Fabrycky, D., Albrecht, S., & Johnson, J. A. 2010, ApJ, 718, L145
Wu, Y. 2005, ApJ, 635, 688
Zahn, J. P. 1966, Annales d'Astrophysique, 29, 489
Zahn, J.-P. & Bouchet, L. 1989, A&A, 223, 112

SF2A 2015
F. Martins, S. Boissier, V. Buat, L. Cambrésy and P. Petit (eds)

THE PECULIAR ABUNDANCE PATTERN OF THE NEW HG-MN STAR HD 30085

R.Monier[1,2], M.Gebran[3], F.Royer[4] and R.E.M.Griffin[5]

Abstract. Using high-dispersion, high-quality spectra of HD 30085 obtained with the echelle spectrograph SOPHIE at l'Observatoire de Haute Provence, we show that this star contains strong lines of the *s*-process elements Sr II, Y II and Zr II. Line syntheses of the lines yield large overabundances of Sr, Y, Zr which are characteristic of HgMn stars. The Sr-Y-Zr triad of abundances is inverted in HD 30085 compared to that in our solar system. The violation of the odd-even rule suggests that physical processes such as radiative diffusion, chemical fractionation and others must be at work in the atmosphere of HD 30085, and that the atmosphere is stable enough to sustain them.

Keywords: stars: individual, stars: Chemically Peculiar

1 Introduction

HD 30085, currently assigned a spectral type of A0 IV, is one of the 47 northern slowly-rotating early-A stars stars studied by Royer et al. (2014). It shows strong lines of Mn II and Hg II, and recently Monier et al. (2015) synthesized several lines of Mn II, Fe II and Hg II which are present in spectra observed with SOPHIE, using model atmospheres and spectrum synthesis that include hyperfine structure of various isotopes where relevant. The synthetic spectra were adjusted iteratively to the observed high-resolution, high signal-to-noise spectra in order to derive the abundances of those elements. The analysis yielded over-abundances of 40 times solar for Mn and 32000 times solar for Hg, thus demonstrating unquestionably that the star needs to be re-classified as an HgMn star. In this paper we focus on lines of Sr, Y, Zr which are also strong in the spectrum of HD 30085, and derive the element abundances.

2 Observations and reduction

HD 30085 was observed twice at l'Observatoire de Haute Provence in February 2012 and December 2013, using the high-resolution mode (R =75000) of SOPHIE. Three 15-minute exposures were obtained in February 2012 and coadded to create a mean spectrum with a $\frac{S}{N}$ ratio of about 316. A single 20-minute exposure was acquired in December 2013, with a $\frac{S}{N}$ of $\sim$300.

3 Lines of Sr II, Zr II and Y II in HD 30085

The strongest lines of Sr II, Y II and Zr II in our line catalogue are conspicuous in the SOPHIE spectra of HD 30085. They are listed in Table 1 along with the measured equivalent width and derived abundance for each transition. Only a few of these lines are unblended; most of the blends are with lines of Cr II, Mn II and Fe II, whose abundances were derived in Monier et al. (2015). Fig. 1 displays the resonance-line profile of Sr II at 4305 Å and that of Zr II at 4496 Å to illustrate their strengths and the overabundances of those species.

[1] LESIA, UMR 8109, Observatoire de Paris Meudon, Place J.Janssen, Meudon, France
[2] Lagrange, UMR 7293, Universite de Nice Sophia, Nice, France
[3] Department of Physics and Astronomy, Notre Dame University - Louaize, PO Box 72, Zouk Mikael, Lebanon
[4] GEPI, UMR 8111, Observatoire de Paris Meudon, Place J.Janssen, Meudon, France
[5] Dominion Astrophysical Observatory, 5071 West Saanich Road, Victoria, BC, V9E 2E7, Canada

© Société Francaise d'Astronomie et d'Astrophysique (SF2A) 2015

Lines used for abundance analysis					
Wavelengths (Å)	Identification	Multiplet	EW	Abundance	Comment
4077.71	Sr II	M 2	74.0	40 $\odot$	blend
4161.80	Sr II	M 3	11.0	40 $\odot$	
4215.52	Sr II	M 2	64.7	40 $\odot$	blend
4305.45	Sr II	M 3	14.6	40 $\odot$	
4177.53	Y II		46.0	300 $\odot$	blend
4235.73	Y II		18.3	300 $\odot$	
4309.63	Y II		42.1	250 $\odot$	blend
4358.73	Y II		31.8	300 $\odot$	blend
4398.01	Y II		49.6	250 $\odot$	blend
4422.59	Y II		32.9	500 $\odot$	blend
4682.32	Y II		15.1	300 $\odot$	blend
4823.30	Y II		16.1	275 $\odot$	blend
4883.68	Y II		50.9	500 $\odot$	
4900.12	Y II		49.4	500 $\odot$	blend
5205.72	Y II		48.2	500 $\odot$	
5497.41	Y II		31.4	500 $\odot$	blend
5662.93	Y II		51.2	500 $\odot$	
4443.00	Zr II		27.4	200 $\odot$	
4457.43	Zr II		10.0	100 $\odot$	
4496.98	Zr II		22.2	200 $\odot$	
5112.30	Zr II		12.6	150 $\odot$	

Table 1. The strongest lines of Sr II, Y II and Zr II in HD 30085

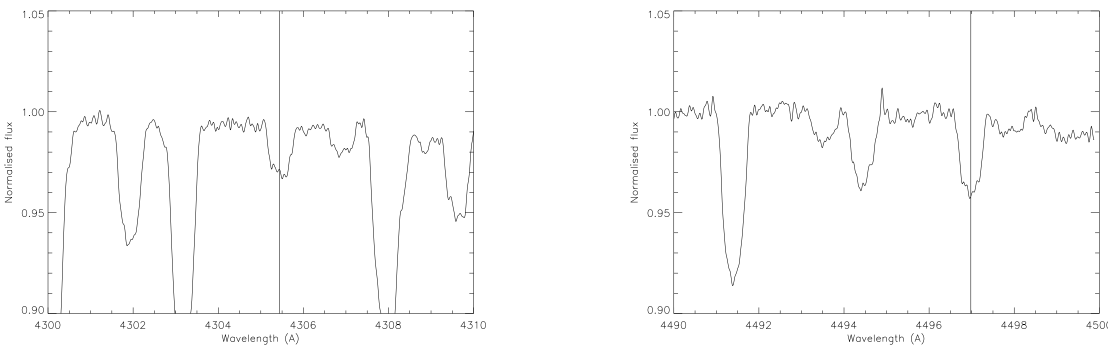

Fig. 1. Left: Sr II line at 4305 Å (left). **R**ight: Zr II line at 4496 Å (right).

4 Model atmospheres and spectrum synthesis

The effective temperature $T_{\rm eff}$ and surface gravity $\log g$ of HD 30085 were first evaluated using Napiwotzky et al's (1993) *uvbybeta* calibration of Stromgren's photometry. The derived values were $T_{\rm eff} = 11300 \pm 200$ K, $\log g = 3.95 \pm 0.25$.

First a plane-parallel model atmosphere assuming radiative equilibrium and hydrostatic equilibrium was computed using the ATLAS9 code (Kurucz 1992), but with the linux version that uses the new ODFs maintained by F. Castelli on her website*. A line-list was built by starting from Kurucz's (1992) "gfhyperall.dat" file †, which includes hyperfine splitting levels, and was upgraded by appealing to the NIST Atomic Spectra Database

*http://www.oact.inaf.it/castelli/

†http://kurucz.harvard.edu/linelists/

‡ and the VALD database operated at Uppsala University (Kupka et al. 2000)§. A grid of synthetic spectra was then computed with SYNSPEC48 (Hubeny & Lanz 1992), specifically to model the Sr II, Y II and Zr II lines. We adopted a projected rotational velocity $v_e \sin i = 26$ km s^{-1} and a radial velocity $v_{rad} = 8.20$ km.s^{-1} from Royer et al. (2014). In Fig. 2, the observed line-profile of Y II at 5662.93 Å is compared with the synthetic one computed for an overabundance of Yttrium of 500 ⊙; that overabundance provided the best fit to the observed profile.

5 Evidence for Sr-Y-Zr excesses

The abundances of Strontium, Yttrium and Zirconium that were derived from each analysed transition are listed in Table 1. The four lines of Sr II yielded a consistent overabundance of 40 ⊙. In contrast, the Y II lines yielded overabundances ranging from 250 ⊙ to 500 ⊙, the scatter in the values probably reflecting inacuracies in the atomic data of those elements. Similarly, the Zr II lines yielded overabundances ranging from 100 to 200 ⊙. We thus find that Y is more abundant than Sr and Zr in HD 30085, which is the opposite of what is observed in the solar system.

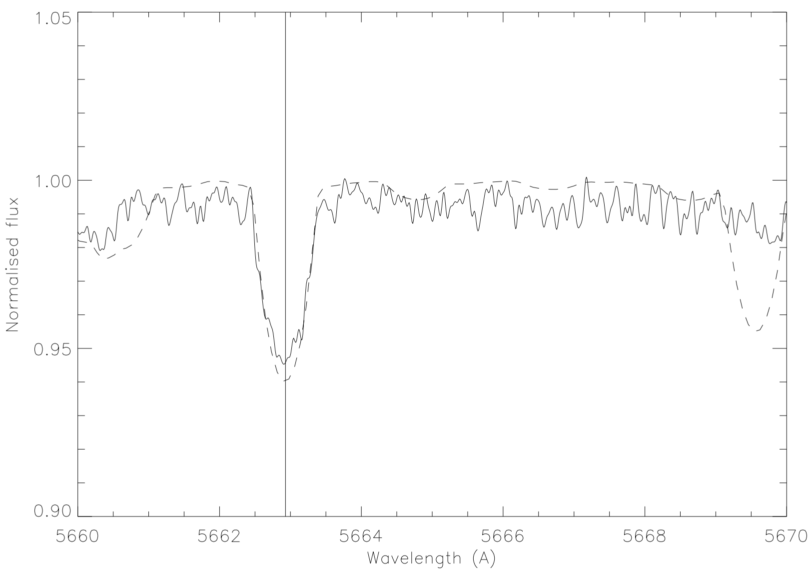

Fig. 2. Synthesis of the Y II line at 5662 Å (observed: thick line, synthetic: dashed lines for a 500 ⊙ overabundance)

6 Conclusions

Lines of Sr II, Y II and Zr II are enhanced in HD 30085. Line synthesis reveals large overabundances in these *s*-process elements, Y being more abundant than Sr and Zr. This violation of the odd-even rule shows that the Sr-Y-Zr triad of abundances is inverted in HD 30085 compared to the solar system pattern. It strongly suggests that physical processes such as radiative diffusion and chemical fractionation are at work in the atmosphere of HD 30085, and that its atmosphere is stable enough for long enough to sustain such processes. Sr, Y and Zr are of interest for nucleosynthetic studies because they comprise the first blocking place in the neutron absorption cross-section for *s*-process syntheses of heavy elements in red giants. We conclude that HD 30085 has overabundances of Sr, Y, Zr which are characteristic of an Hg-Mn star. A detailed abundance analysis of other elements in this star is currently in progress in order to complement the abundances reported here.

‡http://physics.nist.gov/cgi-bin/AtData/qlinesform

§http://vald.astro.uu.se/ vald/php/vald.php

The authors acknowledge very efficient support from the night assistants at Observatoire de Haute Provence. They have used the NIST Atomic Spectra Database and the VALD database operated at Uppsala University (Kupka et al., 2000) to upgrade atomic data.

References

Hubeny, I., Lanz, T. 1992, A&A, 262, 501

Kupka F., Ryabchikova T.A., Piskunov N.E., et al., 2000, Baltic Astronomy, vol. 9, 590-594

Kurucz, R.L. 1992, Rev. Mexicana. Astron. Astrofis., 23, 45

Monier, R., Gebran, M., Royer, F. 2015, A&A, 577A, 96M

Napiwotzki, R., Schoenberner, D., Wenske, V. 1993, A&A, 268, 653

Royer, F., Gebran, M., Monier, R., et al., 2014 , A&A, 562A, 84R

SF2A 2015
F. Martins, S. Boissier, V. Buat, L. Cambrésy and P. Petit (eds)

DISCOVERY OF NEW CHEMICALLY PECULIAR LATE B-TYPE STARS: HD 67044

R.Monier[1,2], M.Gebran[3] and F.Royer[4]

Abstract. Using high dispersion high quality spectra of HD 67044 obtained with the echelle spectrograph SOPHIE at Observatoire de Haute Provence, we show that this star contains strong lines of Silicon, Titanium, Chromium, Yttrium, Zirconium and Europium. Line synthesis of these lines yield overabundances which range from 3 $\odot$ up to 200 $\odot$. We therefore propose that HD 67044 be reclassified as a late Chemically Peculiar B star of the SiCrEu type.

Keywords: stars: individual, stars: Chemically Peculiar

1 Introduction

HD 67044 currently assigned a B8 spectral type is one of the slowly rotating B stars situated in the northern hemisphere which we are currently observing. The selection criteria for this sample of stars are a declination higher than -15^o, spectral class B8 or B9, luminosity class V or IV, and a magnitude V brighter than 7.85. Most of the stars of this B8-9 sample have just recently been observed in December 2014. We are currently performing a careful abundance analysis study of high resolution high $\frac{S}{N}$ ratio spectra of these objects and sort them out into chemically normal stars (ie. whose abundances do not depart more than $\pm$ 0.15 dex from solar), new spectroscopic binaries and new chemically peculiar B stars (CPs) which had remained unoticed so far.We present here new abundance determinations for HD 67044 which allow us to propose that this star is a new CP late B star. Monier et al. (2015) have recently published the discovery of 4 new HgMn stars (3 from this late-B stars sample and one from a sample of 47 early A types stars verifying the same criteria). Royer et al. (2014) have published the analysis of the sample of 47 early A stars having low apparent projected velocities in the northern hemisphere up to V=6.65 mag. A careful abundance analysis of high resolution high $\frac{S}{N}$ ratio spectra of these objects has sorted out the sample into 17 chemically normal stars, 12 spectroscopic binaries and 13 Chemically Peculiar stars (CPs) among which 5 are new CP stars.

2 Observations and reduction

HD 67044 has been observed once at Observatoire de Haute Provence using the High Resolution (R =75000) mode of SOPHIE in December 2014. A 40 minutes exposure was secured in December 2014 with a $\frac{S}{N}$ ratio of about 130.

3 The nature of the new CP star HD 67044

Several spectral regions have been used to readdress the spectral type of HD 67044. The star being a late B-type dwarf, the chemical peculiarity could be either i) of the HgMn type, ii) or of the Si type or iii) of the SrCrEu type, or iv) a hybrid of the last two. We therefore investigated several spectral regions containing strong resonance or low excitation lines of Hg, Mn, Si, Sr, Cr and Eu. First, the red wing of H_ϵ harbors the Hg II λ 3984 Å line and several Zr II and Y II lines likely to be strenghtened in late B star of the Hg-Mn type. The

[1] LESIA, UMR 8109, Observatoire de Paris Meudon, Place J.Janssen, Meudon, France
[2] Lagrange, UMR 7293, Universite de Nice Sophia, Nice, France
[3] Department of Physics and Astronomy, Notre Dame University - Louaize, PO Box 72, Zouk Mikael, Lebanon
[4] GEPI, UMR 8111, Observatoire de Paris Meudon, Place J.Janssen, Meudon, France

© Société Francaise d'Astronomie et d'Astrophysique (SF2A) 2015

Classification lines			
Laboratory Wavelengths (Å)	Identification	Multiplet	Abundance
3982.44	Y II		200 $\odot$
3983.87	Hg II	M 2	not detected
3990.96	Zr II		70 $\odot$
3998.82	Zr II		70 $\odot$
4077.71	Sr II		1 $\odot$
4128.07	Si II	M 2	2-3 $\odot$
4130.88	Si II	M 2	2-3 $\odot$
4136.92	Mn II		about $\odot$
4205.04	Eu II		70 $\odot$
4215.52	Sr II		1 $\odot$
4305.44	Sr II		1 $\odot$
4558.65	Cr II	M 1	10 $\odot$

Table 1. Classification lines and determined abundances for HD 67044

region from 4125 Å to 4145 Å contains the classification Si II doublet (M 2), the Mn II line at 4136 Å and the Sr II resonance line at 4129.72 Å likely to be strengthened respectively in a Bp Si star, in a star enriched in Mn, and a SrCrEu Bp star. The regions 4070-4080 Å, 4210-4220 Å and 4300-4310 Å contain the resonance lines of Sr II at 4077.71 Å and 4215.52 Å and the low-excitation line at 4305.44 Å. The 4200-4210 Å region contains the Eu II resonance line at 4205.04 Å. The 4550-4560 Å region contains the strongest expected Cr II line at 4558.65 Å. We fail to detect the Hg II line at 3984 Å. The Mn II line at 4136.92 Å is not particularly strong, nor are the Sr II lines. In contrast, the lines of Si II (Multiplet 2), Cr II, Y II , Zr Ii and Eu II are strong in HD 67044. This leads us to rule out that HD 67044 be a new HgMn star. It probably rather is a new CP star of the SiCrEu type.

4 Model atmospheres and spectrum synthesis

The effective temperature and surface gravity of HD 67044 were first evaluated using $B - V = -0.04$ and the effective temperature calibration versus $B - V$ in Underhill & Doazan (1982). This yields $T_{eff} = 10200$ K in good agreement with Huang et al. (2010) who derived $T_{eff} = 10519$K and $\log g = 3.72$ which we have adopted for the surface gravity.

A plane parallel model atmosphere assuming radiative equilibrium and hydrostatic equilibrium has been first computed using the ATLAS9 code (Kurucz 1992), specifically the linux version using the new ODFs maintained by F. Castelli on her website. The linelist was built starting from Kurucz's (1992) gfhyperall.dat file* which includes hyperfine splitting levels. This first linelist was then upgraded using the NIST Atomic Spectra Database† and the VALD‡ database operated at Uppsala University (Kupka et al. 2000).

5 Evidence for Si, Ti, Cr, Y, Zr and Eu excesses

A grid of synthetic spectra was computed with SYNSPEC48 (Hubeny & Lanz 1992) to model the Si II, Ti II, Cr II, Mn II, Fe II, Y II, Zr II and Eu II lines. Computations were iterated varying the unknown abundance $[\frac{X}{H}]$ until minimisation of the chi-square between the observed and synthetic spectrum. Figure 1 displays the synthesis of 3 lines: Y II 3982.44 Å, Zr II 3990.96 Å, and Zr II 3998.82 Å. The observed line profiles, rectified to the red wing of H_ϵ are compared to the synthetic spectrum providing the best fit to the oberved one. The model is computed for an overabundance of Yttrium of 200 $\odot$ and a Zirconium overabundance of 70 $\odot$ (solid line: observed normalised spectrum, dashed lines: synthetic spectrum).

*http://kurucz.harvard.edu/linelists/
†http://physics.nist.gov/cgi-bin/AtData/linesform
‡http://vald.astro.uu.se/ vald/php/vald.php

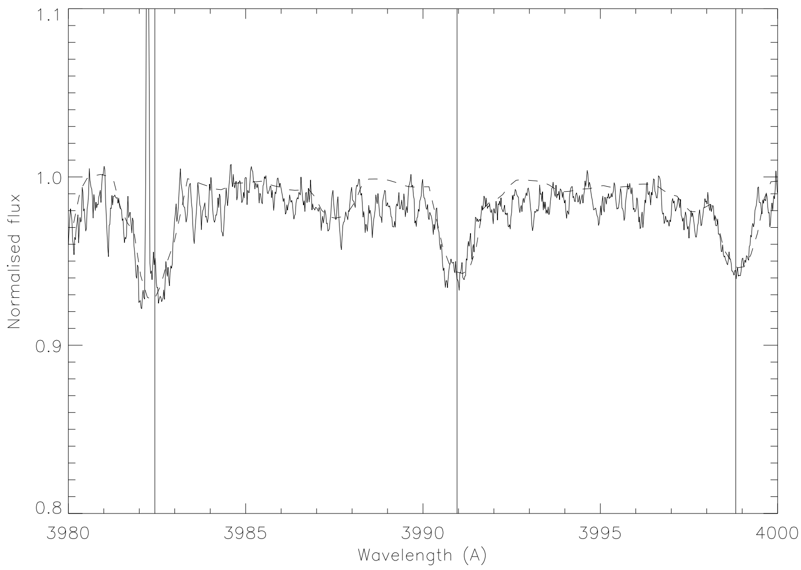

Fig. 1. Synthesis of the Y II and Zr II lines in the red wing of H_ϵ (observed: solid line, model: dashed line)

6 Conclusions

HD 67044 has overabundances which are characteristic of an SiCrEu star. We thus propose that it should be reclassified as a late Chemically Peculiar B star of the SiCrEu type. It displays a mild overabundance of Silicon and large overabundances of Titanium, Chromium, Yttrium, Zirconium and Europium which range from 10 $\odot$ to about 200 $\odot$. We are currently determining more abundances for this peculiar star.

The authors acknowledge very efficient support from the night assistants at Observatoire de Haute Provence. They have used the NIST Atomic Spectra Database and the VALD database operated at Uppsala University (Kupka et al., 2000) to upgrade atomic data.

References

Underhill, A., & Doazan, V. 1982, Journal of the British Astronomical Association, 92, 290

Huang, W., Gies, D. R., & McSwain, M. V. 2010, ApJ, 722, 605

Hubeny, I., Lanz, T. 1992, A&A, 262, 501

Kupka F., Ryabchikova T.A., Piskunov N.E., et al. 2000, Baltic Astronomy, vol. 9, 590-594

Kurucz, R.L. 1992, Rev. Mexicana. Astron. Astrofis., 23, 45

Monier, R., Gebran, M., Royer, F. 2015, A&A, 577A, 96M

Royer, F., Gebran, M., Monier, R., et al. 2014 , A&A, 562A, 84R

SF2A 2015
F. Martins, S. Boissier, V. Buat, L. Cambrésy and P. Petit (eds)

THE MAGNETIC FIELD OF THE HOT SPECTROSCOPIC BINARY HD 5550

C. Neiner[1], E. Alecian[1,2] and the BinaMIcS collaboration

Abstract. HD 5550 is a spectroscopic binary composed of two A stars observed with Narval at TBL in the frame of the BinaMIcS (Binarity and Magnetic Interactions in various classes of Stars) Large Program. One component of the system is found to be an Ap star with a surprisingly weak dipolar field of ∼65 G. The companion is an Am star for which no magnetic field is detected, with a detection threshold on the dipolar field of ∼40 G. The system is tidally locked, the primary component is synchronised with the orbit, but the system is probably not completely circularised yet. This work is only the second detailed study of magnetic fields in a hot short-period spectroscopic binary. More systems are currently being observed with both Narval at TBL and ESPaDOnS at CFHT within the BinaMIcS project, with the goal of understanding how magnetism can impact binary evolution and vice versa.

Keywords: stars: individual: HD 5550, stars: early-type, stars: magnetic field, binaries: spectroscopic, stars: chemically peculiar

1 Observations of HD 5550

HD 5550 is a spectroscopic double-line (SB2) binary system composed of two A-type components (Carrier et al. 2002). HD 5550 was previously reported to be an Ap SrCrEu star (Renson et al. 1991). Carrier et al. (2002) also reported that the secondary has chemical peculiarities, but they could not distinguish more precisely the peculiar type of this component.

We observed HD 5550 in the frame of the BinaMIcS (Binarity and Magnetic Interactions in various classes of Stars) project, with the goal to understand the interplay between magnetism and binarity (see Neiner et al., these proceedings). Twenty-five high-resolution spectropolarimetric observations were obtained with Narval at the Bernard Lyot Telescope (TBL, Pic du Midi, France) and were used to check for the presence of a magnetic field in both components.

We first disentangled the spectra of the two components to be able to analyse them separately. The binary orbit has a period $P_{\rm orb} = 6.82054$ d (Carrier et al. 2002) and is almost circularised with an eccentricity e=0.005. We then used Zeeman and Atlas9 LTE models on the disentangled spectra to derive the stellar parameters of both components: we confirmed that the primary component is an Ap star and found that the secondary is an Am star, with overabundance of the iron-peak elements, extreme overabundance of Ba, and underabundance of Ca. Finally, we applied the Least-Square Deconvolution (LSD) technique to produce averaged Stokes I and V spectra of each component and we measured the magnetic field in both stars.

2 Magnetic results

2.1 Primary Ap star

We found that the primary Ap star is magnetic with clear Zeeman signatures (see Fig. 1). The longitudinal field B_l values are systematically negative and vary from −26 to −12 G, with typical error bars of 4 G.

From the variations of the Stokes V profiles, and the corresponding B_l values, we found that the field is modulated by the rotation period $P_{\rm rot} \sim 6.84$ d. This period is compatible with the orbital period $P_{\rm orb} \sim 6.82$ d, i.e. the rotation of the star is synchronised with the binary orbit.

[1] LESIA, Observatoire de Paris, PSL Research University, CNRS, Sorbonne Universités, UPMC Univ. Paris 06, Univ. Paris Diderot, Sorbonne Paris Cité, 5 place Jules Janssen, 92195 Meudon, France
[2] Univ. Grenoble Alpes, CNRS, IPAG, F-38000 Grenoble, France

© Société Francaise d'Astronomie et d'Astrophysique (SF2A) 2015

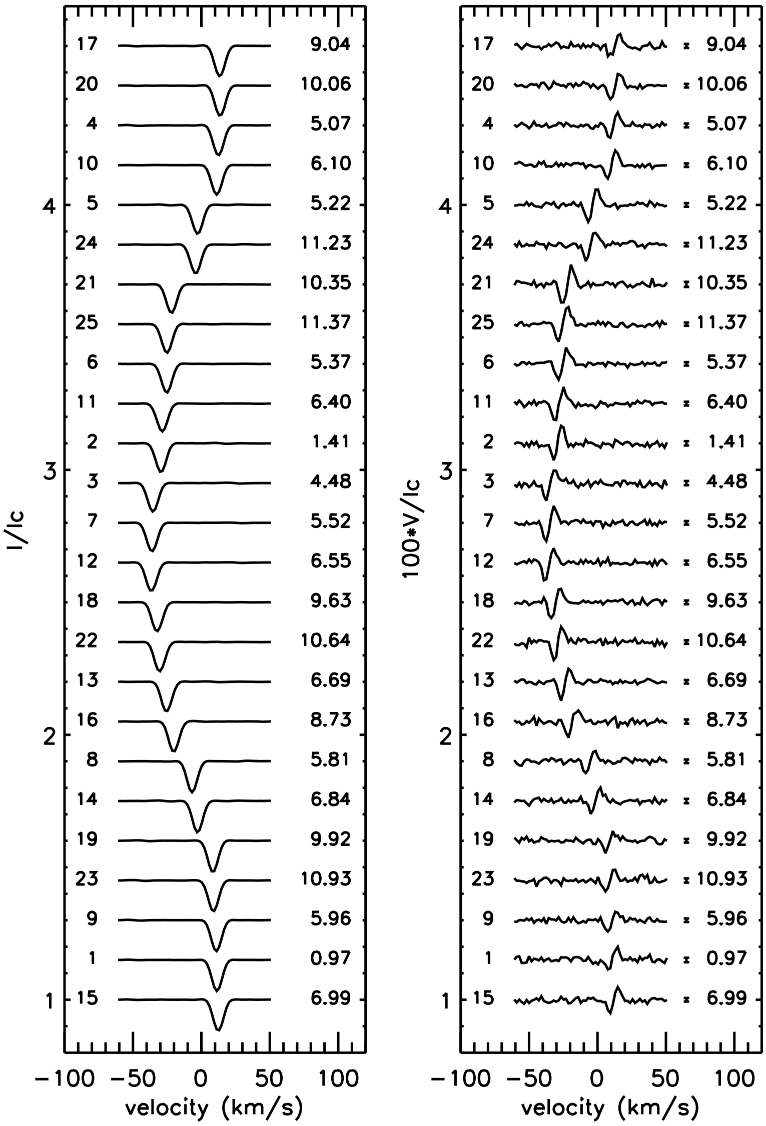

Fig. 1. LSD I/Ic (left) and V/Ic (right) profiles of the primary component of HD 5550, ordered by increasing orbital phase. Taken from Alecian et al., submitted to A&A.

An oblique dipole model of the Zeeman signatures shows that the polar field strength is only $B_{\rm pol} = 65 \pm 20$ G, with an inclination $i \sim 32°$ and an obliquity $\beta \sim 156°$. This is the weakest magnetic field known in an Ap star. Indeed, typical magnetic field strengths in Ap/Bp stars are of the order of 1 kG, with a range between 300 G and 30 kG (e.g. Borra & Landstreet 1980; Landstreet 1992; Bagnulo et al. 2006). The dipolar field value of HD 5550 falls in the dichotomy desert proposed by Aurière et al. (2007) between strong and ultra-weak fields.

2.2 Seconday Am star

We did not detect a magnetic field in the secondary Am star. The longitudinal field values we measured by integrating the LSD I and V profiles are all consistent with 0 G, with uncertainties of 3-4 G.

To determine the upper limit on the possible undetected magnetic field of the secondary star, we first fitted the LSD I profiles with Gaussian profiles. We then computed 1000 synthetic Stokes V profiles for various values of the polar magnetic field $B_{\rm pol}$. Each of these models uses a random inclination angle i, obliquity angle β, and rotational phase. We added a white Gaussian noise to each modeled profile with a null average and a variance corresponding to the signal-to-noise of the observed profile. We then computed the detection probability of a magnetic field as a function of B_{pol} for each observation, and combined them to obtain the detection probability function for the full dataset. Above a 90% detection probability, we consider that we would have detected the field in our dataset. We therefore established that the upper limit of the magnetic field of the secondary Am component, which could have remained hidden in our observations, is $\sim$40 G.

Only a few Am stars are known to host a magnetic field so far and all of them have ultra-weak fields, with longitudinal components of less than 1 G (Petit et al. 2011; Blazère et al. 2015). If such an ultra-weak field were present in the Am component of HD 5550, it would have remained undetected in our observations.

3 Conclusions

Spectropolarimetric Narval observations of HD 5550 showed that it is a binary system composed of a weakly magnetic Ap star and an Am star found to be non-magnetic with the achieved precision. With HD 98088 (Folsom et al. 2013), this is the second hot magnetic spectroscopic binary studied in details. Studying more hot magnetic binaries, which is one of the goals of the BinaMIcS project, will allow us to understand the interplay between magnetism and binarity in hot systems.

We thank the "Programme National de Physique Stellaire" (PNPS) of CNRS/INSU (France) for their financial support to the BinaMIcS project.

References

Aurière, M., Wade, G. A., Silvester, J., et al. 2007, A&A, 475, 1053

Bagnulo, S., Landstreet, J. D., Mason, E., et al. 2006, A&A, 450, 777

Blazère, A., Petit, P., Lignières, F., et al. 2015, in IAU Symposium, Vol. 305, IAU Symposium, 67

Borra, E. F. & Landstreet, J. D. 1980, ApJS, 42, 421

Carrier, F., North, P., Udry, S., & Babel, J. 2002, A&A, 394, 151

Folsom, C. P., Likuski, K., Wade, G. A., et al. 2013, MNRAS, 431, 1513

Landstreet, J. D. 1992, A&A Rev., 4, 35

Petit, P., Lignières, F., Aurière, M., et al. 2011, A&A, 532, L13

Renson, P., Gerbaldi, M., & Catalano, F. A. 1991, A&AS, 89, 429

SF2A 2015
F. Martins, S. Boissier, V. Buat, L. Cambrésy and P. Petit (eds)

NUMERICAL SIMULATIONS OF ZERO-PRANDTL-NUMBER THERMOHALINE CONVECTION

V. Prat[1], F. Lignières[2, 3] and N. Lagarde[4]

Abstract. Thermohaline (or fingering) convection has been used to explain chemical anomalies at the surface of red giant stars. However, recent numerical simulations suggest that the efficiency of thermohaline convection is lower than expected, and thus not sufficient to explain the observations.

One of the uncertainties of these simulations is that they have been performed in a parameter range for the Prandtl number (i.e. the ratio between viscosity and thermal diffusivity) which is far from what can be found in stellar interiors.

Using the small-Péclet-number approximation, we are able for the first time to perform simulations of thermohaline convection in a parameter domain which is relevant for stellar physics. In the present paper, we discuss the validity of this approximation and compare our results with previous simulations and models.

Keywords: Hydrodynamics, instabilities, turbulence, stars: evolution, stars: interiors

1 Introduction

Thermohaline convection (also known as fingering convection) is a mixing process which occurs in flows with stable thermal stratification and unstable chemical stratification. Originally studied in oceanography when a layer of warm salty water lays above a layer of cold fresh water (see for example Stern 1960), it has been introduced in an astrophysical context for the first time by Ulrich (1972).

In stellar interiors, the unstable chemical gradient necessary to raise the instability can have various causes. In particular, it can happen in ^{3}He-shell-burning regions of evolved stars (Charbonnel & Zahn 2007; Denissenkov 2010). It can also be due to heavy infalling material from a planetary system (Vauclair 2004; Garaud 2011; Deal et al. 2013) or a more evolved companion (Stancliffe et al. 2007). Another possibility is the accumulation of heavy elements such as iron thanks to radiative levitation (Théado et al. 2009; Vauclair & Théado 2012; Zemskova et al. 2014).

Thermohaline convection is characterised by three dimensionless numbers: (i) the so-called "density ratio" $R_0 = -{N_\mathrm{T}}^2/{N_\mu}^2$, where N_T and N_μ are the thermal and chemical Brunt-Väisälä frequencies measuring thermal and chemical stratification, (ii) the diffusivity ratio $\tau = \kappa_\mu/\kappa_\mathrm{T}$, where κ_μ and κ_t are the chemical and thermal diffusivities, and (iii) the Prandtl number $Pr = \nu/\kappa_\mathrm{T}$, where ν is the viscosity. According to Baines & Gill (1969), thermohaline convection occurs when

$$1 < R_0 < \frac{1}{\tau}. \tag{1.1}$$

The stellar regime is characterised by very low values of the diffusivity ratio τ and the Prandtl number, along with high values of the density ratio (see Garaud et al. 2015). Because of the very low Prandtl number, the flows are very turbulent and numerical simulations of astrophysical thermohaline convection is computationally expensive.

[1] Max-Planck Institut für Astrophysik, Karl-Schwarzschild-Str. 1, 85748, Garching bei München, Germany
[2] Université de Toulouse; UPS-OMP; IRAP; 14, avenue Édouard Belin, F-31400 Toulouse, France
[3] CNRS; IRAP; 14, avenue Édouard Belin, F-31400 Toulouse, France
[4] School of Physics and Astronomy, University of Birmingham, Edgbaston, Birmingham B15 2TT, UK

© Société Francaise d'Astronomie et d'Astrophysique (SF2A) 2015

Recent simulations in 2D (Denissenkov 2010) and 3D (Traxler et al. 2011; Brown et al. 2013) have been performed with Prandtl numbers down to 10^{-2}. Brown et al. (2013) also proposed an analytical model for thermohaline convection with a free parameter they calibrate thanks to their numerical simulations. Although there is a good agreement between the model and the numerical results, the explored parameter domain is still far from what can be found in stellar interiors.

This is our main motivation to apply the small-Péclet-number approximation (SPNA, see Lignières 1999). Assuming that because of the very high thermal diffusivity, advection is unable to modify the thermal background, the SPNA consists in a Taylor expansion in the Péclet number $Pe = UL/\kappa_{\mathrm{T}}$, where U and L are typical velocity and length scales. This approximation has been successfully used to investigate the very-high-thermal-diffusivity limit of the transport generated by the shear instability in stellar radiative zones (Prat & Lignières 2013, 2014).

The purpose of this paper is to apply the SPNA to the problem of thermohaline convection in order to reach the zero-Prandtl limit likely to describe the stellar regime. We first describe our configuration in Sect. 2, and present our results in Sect. 3. Finally, we discuss the consequences of this work and conclude in Sect. 4.

2 Configuration

In this paper, we study thermohaline convection in the Boussinesq approximation. It means that density fluctuations are neglected, except in the buoyancy term. We choose a configuration with uniform background temperature and mean molecular weight gradients $\mathrm{d}T_0/\mathrm{d}z$ and $\mathrm{d}\mu_0/\mathrm{d}z$. The dimensionless equations for the velocity $\vec{v}$ and temperature and mean molecular weight fluctuations θ and μ' are

$$\vec{\nabla} \cdot \vec{v} = 0, \tag{2.1}$$

$$\phi \left[\frac{\partial \vec{v}}{\partial t} + (\vec{v} \cdot \vec{\nabla})\vec{v} \right] = -\vec{\nabla} P + Ra_\mu (R_0 \theta - \mu') \vec{e}_z + \Delta \vec{v}, \tag{2.2}$$

$$\frac{\partial \theta}{\partial t} + \vec{v} \cdot \vec{\nabla} \theta + v_z = \frac{1}{\tau} \Delta \theta, \tag{2.3}$$

$$\frac{\partial \mu'}{\partial t} + \vec{v} \cdot \vec{\nabla} \mu' + v_z = \Delta \mu', \tag{2.4}$$

where $\phi = \kappa_\mu/\nu = \tau/Pr$ is the inverse of the Schmidt number, $Ra_\mu = \beta(\mathrm{d}\mu_0/\mathrm{d}z)L^4/(\nu\kappa_\mu)$ the chemical Rayleigh number, $\beta = (\partial \ln \rho/\partial \mu)_{P,T}$ the chemical contraction coefficient and L a typical length. These equations have been obtained by using L, L^2/κ_μ, κ_μ/L, $L\mathrm{d}T_0/\mathrm{d}z$, $L\mathrm{d}\mu_0/\mathrm{d}z$ and $\rho_0\nu\kappa_\mu/L^2$ as length, time, velocity, temperature, mean molecular weight and pressure units.

This adimensionalisation is different from the one used for example by Brown et al. (2013), which is not appropriate to investigate the limit of very high thermal diffusivities. In particular, they use a thermal diffusive time as time unit, which tends to zero when Pr tends to zero. In contrast, all our unit scales remain finite in this limit. Thus, we can use the SPNA, which modifies Eqs. (2.2) and (2.3):

$$\phi \left[\frac{\partial \vec{v}}{\partial t} + (\vec{v} \cdot \vec{\nabla})\vec{v} \right] = -\vec{\nabla} P + Ra_\mu (R_0 \tau \psi - \mu') \vec{e}_z + \Delta \vec{v}, \tag{2.5}$$

$$v_z = \Delta \psi, \tag{2.6}$$

with $\psi = \theta/\tau$. This removes the numerical issue posed by the large factor $1/\tau$ in the right-hand side of Eq. (2.3), and the stability is now given by the number $r = R_0\tau$, which according to Eq. (1.1), must verify

$$0 < r < 1. \tag{2.7}$$

We used the code Snoopy (Lesur & Longaretti 2011) to perform direct numerical simulations solving these equations. It uses a Fourier colocation method in all directions with periodic boundary conditions for fluctuations and a Runge-Kutta time scheme. A typical run is 256^3 grid points distributed over 128 cores.

3 Results

We performed first full Boussinesq simulations with decreasing Prandtl numbers down to $6.67 \cdot 10^{-3}$ and one SPNA simulation (corresponding to $Pr = 0$), all with the same values $r = 2/3$ and $\phi = 1$. The turbulent diffusion coefficient is defined as

$$D_\mu = -\frac{\langle \mu' v_z \rangle}{\mathrm{d}\mu_0/\mathrm{d}z}, \tag{3.1}$$

where $\langle\rangle$ denotes the temporal and spatial average. This coefficient is related to the chemical Nusselt number Nu_μ, used notably in Traxler et al. (2011) and Brown et al. (2013), thanks to the relation

$$Nu_\mu = 1 + \frac{D_\mu}{\kappa_\mu}. \tag{3.2}$$

One of our simulations was performed at $Pr = 1/3$, $\tau = 1/3$ and $R_0 = 2$, which is close to one simulation of Traxler et al. (2011). We found a Nusselt number of 9.75, in agreement with their value of 9.5 ± 0.3. The results of our simulations are plotted in Fig. 1. It shows that the SPNA is able to describe well the transport by thermohaline convection in the limit of very small Prandtl numbers. One can also see that the corresponding

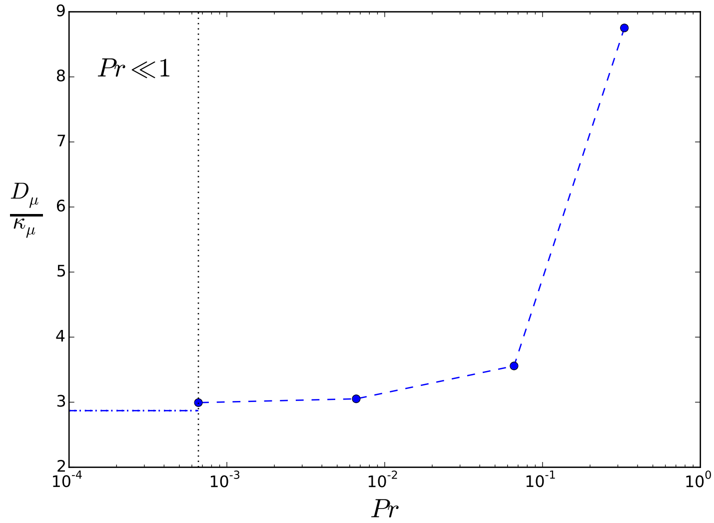

Fig. 1. Turbulent diffusion coefficient as a function of the Prandtl number at $r = 2/3$ and $\phi = 1$. Blue dots are full Boussinesq simulations and the dash-dotted line is a SPNA simulation.

asymptotic regime is almost already reached at $Pr \sim 10^{-2}$, which is the smallest value used by Brown et al. (2013).

Then we performed two series of SPNA simulations, one at constant $\phi = 1$ and various values of r, the other at constant $r = 3.33 \cdot 10^{-3}$ and various values of ϕ. Both results are plotted in Fig. 2, along with the predictions of Brown et al. (2013). The first interesting remark is that our simulations globally follow the trends given by Brown et al. (2013). However, there are sometimes significant discrepancies, especially for very small values of r or when ϕ is greater than one. The latter case is not really an issue, because we expect ϕ to be smaller than one in stellar radiative zones. These discrepancies may be due to the saturation mechanism, which is the most uncertain part of the model of Brown et al. (2013).

4 Conclusions

This study is the first application of the SPNA to thermohaline convection and our results validate its use in this context. Thanks to this approximation, we are able to reach the regime of very low Prandtl numbers, and thus to perform simulations with realistic stellar parameters. Simulations at very small r and ϕ are still challenging, but managable.

As we have seen in the previous section, our results are in relatively good agreement with the predictions of Brown et al. (2013). However, there are significant discrepancies, in particular for very small values of r and ϕ, for which we find a transport coefficient larger than the one given by Brown et al. (2013). For typical models of red giants, r and ϕ can reach values from 1 down to 10^{-5} and 10^{-4}, respectively (Lagarde 2012).

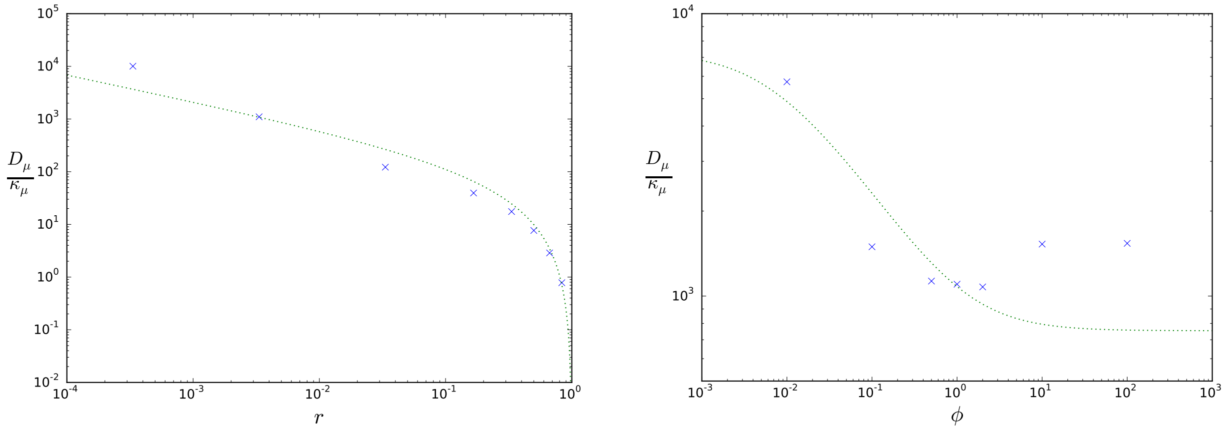

Fig. 2. Left: Turbulent diffusion coefficient as a function of r at $\phi = 1$. **Right:** The same as a function of ϕ at $r = 3.33 \cdot 10^{-3}$. The dotted lines correspond to the model of Brown et al. (2013).

The discrepancies between our simulations and Brown et al. (2013) thus occur in a regime which is relevant for red giants, and could possibly lead to a much higher mixing coefficient in the corresponding regions. This could help to reduce the disagreement between observed chemical abundances of red giants and predictions of stellar evolution using Brown et al. (2013), as highlighted by Wachlin et al. (2014). A more extensive study of the diffusion coefficient in this regime is thus needed.

VP thanks Geoffroy Lesur for his help with the Snoopy code. NL acknowledges financial support from Marie Curie Intra-European fellowship (FP7-PEOPLE-2012-IEF).

References

Baines, P. G. & Gill, A. E. 1969, J. Fluid Mech., 37, 289
Brown, J. M., Garaud, P., & Stellmach, S. 2013, ApJ, 768, 34
Charbonnel, C. & Zahn, J.-P. 2007, A&A, 467, L15
Deal, M., Deheuvels, S., Vauclair, G., Vauclair, S., & Wachlin, F. C. 2013, A&A, 557, L12
Denissenkov, P. A. 2010, ApJ, 723, 563
Garaud, P. 2011, ApJ, 728, L30
Garaud, P., Medrano, M., Brown, J. M., Mankovich, C., & Moore, K. 2015, ApJ, 808, 89
Lagarde, N. 2012, PhD thesis, Faculté des sciences de l'Université de Genève
Lesur, G. & Longaretti, P.-Y. 2011, A&A, 528, A17
Lignières, F. 1999, A&A, 348, 933
Prat, V. & Lignières, F. 2013, A&A, 551, L3
Prat, V. & Lignières, F. 2014, A&A, 566, A110
Stancliffe, R. J., Glebbeek, E., Izzard, R. G., & Pols, O. R. 2007, A&A, 464, L57
Stern, M. E. 1960, Tellus, 12, 172
Théado, S., Vauclair, S., Alecian, G., & LeBlanc, F. 2009, ApJ, 704, 1262
Traxler, A., Garaud, P., & Stellmach, S. 2011, ApJ, 728, L29
Ulrich, R. K. 1972, ApJ, 172, 165
Vauclair, S. 2004, ApJ, 605, 874
Vauclair, S. & Théado, S. 2012, ApJ, 753, 49
Wachlin, F. C., Vauclair, S., & Althaus, L. G. 2014, A&A, 570, A58
Zemskova, V., Garaud, P., Deal, M., & Vauclair, S. 2014, ApJ, 795, 118

SF2A 2015
F. Martins, S. Boissier, V. Buat, L. Cambrésy and P. Petit (eds)

ASTEROSEISMIC HARE & HOUND EXERCISES: THE CASE OF β CEPHEI STARS

S.J.A.J. Salmon[1], J. Montalbán[2], A. Miglio[3], A. Noels[4], M.-A. Dupret[4], P. Eggenberger[5] and S. Turck-Chièze[1]

Abstract. The β Cephei pulsating stars present a unique opportunity to test and probe our knowledge of the interior of massive stars. The information that we can get depends on the quality and number of observational constraints, both seismic and classical ones. The asteroseismology of β Cephei stars proceeds by a forward approach, which can result in multiple solutions, without clear indication on the level of confidence. We seek a method to derive confidence intervals on stellar parameters and investigate how these latter behave depending on the seismic data accessible to the observer. We realise forward modelling with the help of a grid of pre-computed models. We also use Monte-Carlo simulations to build confidence intervals on the inferred stellar parameters. We apply and test this method in a series of hare and hound exercises on a subset of theoretical models simulating observed stars. Results show that a set of 5 frequencies (with knowledge of their associated angular degree) yields precise seismic constraints. Significant errors on the determination of the extent of the central mixed region may result when the theoretical models do not present the same chemical mixture as the observed star.

Keywords: Asteroseismology, Stars: variables: general

1 Introduction

There are now more and more evidence for the presence of extra-mixing at the edge of the convective core in main-sequence B stars, revealed by constraints from eclipsing binaries or required to fit stellar cluster observation with help of isochrones (see e.g. Ribas et al. 2000; Gallart et al. 2005, respectively). However, the efficiency and exact nature of the processes at work remain an open issue for stellar physics(see e.g. the review by Chiosi 2007). Fortunately, among the richness of pulsating stars across the Hertzsprung-Russell diagram, main-sequence B stars can present β Cephei pulsations, which are excited by the κ mechanism (Moskalik & Dziembowski 1992). Such oscillations may present both a pressure and gravity mode character. Because these modes probe in part the layers at the border of the convective core, they offer strong constraints on the deep layers of β Cephei stars.

A goal of asteroseismology is to interpret the properties of these pulsations to deliver information on the internal conditions of stars. As a main success, the observation of rotational splitting in at least four β Cephei stars led to first constraints on the ratio of core to surface rotation rates (see e.g. the review by Goupil 2011). It also succeeded in retrieving estimates of the mass, radius and amount of core overshooting for about ten β Cephei (see review by Aerts 2013). These constraints on the core overshooting are of prime importance to get an insight on the physics underlying the extra-mixing processes. In particular, the convective core of B stars recedes during the main sequence and a chemical composition gradient ($\nabla\mu$) develops in the radiative layers at its border. The limits and shape of this gradient depend on the nature of extra-mixing: for e.g. overshooting (if described as instantaneous mixing) simply extends the limit of the central fully mixed region while mixing induced by rotation is thought to act as a diffusive process, smoothing $\nabla\mu$ (e.g. Meynet et al. 2013).

[1] Laboratoire AIM, CEA/DSM-CNRS-Université Paris 7, Irfu/Service d'Astrophysique, CEA-Saclay, 91191, Gif-sur-Yvette, France
[2] Dipartimento di Fisica e Astronomia, Università di Padova, Vicolo dell'Osservatorio 3, I-35122 Padova, Italy
[3] School of Physics and Astronomy, University of Birmingham, Edgbaston, Birmingham, B15 2TT, UK
[4] Département d'Astrophysique, Géophysique et Océanographie, Université de Liège, Allée du 6 Aot 17, B4000 Liège, Belgium
[5] Geneva Observatory, University of Geneva, Chemin des Maillettes 51, CH-1290 Sauverny, Switzerland

© Société Francaise d'Astronomie et d'Astrophysique (SF2A) 2015

The overshooting ($\alpha_{\rm OV}$) values determined with asteroseismology in most of the previous studies correspond to an instantaneous mixing prescription. As such, they give the limit of the extra-mixing region –i.e. the extra region fully mixed at the top of the formal boundary of the convective core– in terms of local pressure scale height (H_p). A step further, obtaining constraints on the shape and extent of $\nabla\mu$ would be very valuable for a better understanding of the extra-mixing processes. Dziembowski & Pamyatnykh (2008) attempted to determine the chemical composition transition in the overshoot region for the two β Cephei stars ν Eri and 12 Lac, but they could not draw a clear conclusion.

The quality and the nature of the constraints also depend on the seismic observables. Considering four β Cephei stars observed with intensive and coordinated follow-up, the number of frequency modes detected went from 6 to 13 (ν Eri – De Ridder et al. 2004 ; HD 129929 – Aerts et al. 2004 ; θ Oph – Briquet et al. 2007 ; 12 Lac – Desmet et al. 2009). In each case, the number of axisymmetric modes with a clear angular degree identification was limited to 3.

As a consequence, it is important to address the following questions concerning the study of β Cephei stars: i) what are the classical and seismic observables necessary for a good seismic modelling; ii) how do the seismic inferences depend on the stellar models and their input physics; iii) can we constrain further the $\nabla\mu$ region in these stars. To investigate these issues, we have carried out a series of hare and hound exercises (see also the previous work of Thoul et al. 2003). We consider as "observed" stars a set of stellar models (the hares) covering a wide range of parameters representative of β Cephei stars. We also vary the input physics of these models.

Section 2 briefly details our seismic modelling method while Section 3 presents the results of the hare and hound exercises, illustrated for one particular case. The paper ends with perspective and conclusion sections.

2 The modelling process

We use a forward approach scheme by comparing theoretical frequencies to those observed with the following merit function:

$$\chi^2 = \frac{1}{N_{\rm obs}} \sum_{i=1}^{N_{\rm obs}} \frac{(\nu_{\rm obs,i} - \nu_{\rm th,i})^2}{\sigma_i^2}. \tag{2.1}$$

$N_{\rm obs}$ is the number of observed frequencies ($\nu_{\rm obs,i}$), σ_i^2 the error on $\nu_{\rm obs,i}$, and $\nu_{\rm th,i}$ the theoretical frequencies. The theoretical frequencies come from a pre-computed grid of models initially presented in Briquet et al. (2009). The stellar models and their oscillation frequencies were obtained with the stellar evolution code CLES (Scuflaire et al. 2008b) and the oscillation code LOSC (Scuflaire et al. 2008a), respectively. The revised solar mixture from Asplund et al. (2005, ; AGS05, hereafter) and the OP opacities (Badnell et al. 2005) were adopted. Other details on the input physics are summarised in Briquet et al. (2009).

The stellar parameters of the grid cover the following ranges: M from 7.6 to 18.6 M$_\odot$ by step of 0.1 M$_\odot$ for the mass, X from 0.68 to 0.74 (step of 0.02) for the initial H mass fraction, Z from 0.010 to 0.018 (step of 0.002) for the metallicity and $\alpha_{\rm OV}$ from 0 to 0.50 (step of 0.05) for the instantaneous overshooting parameter. We use in this work the adiabatic oscillation frequencies, which were computed from angular degrees $\ell = 0$ to 3 for each of the models on the main-sequence phase.

In our approach, we determine the theoretical model of the grid that corresponds to the global minimum of Eq. 2.1. The stellar parameters of this model give the seismic inferred parameters of the observed star. To estimate the uncertainty on the solution, we introduce Monte Carlo simulations. We generate randomly new set of frequencies (pseudo-observed frequencies). For each of these sets, we determine a corresponding best-fit model (the one minimising Eq. 2.1 on the grid). We then gather the stellar parameters of each of the solutions and build distributions for every parameter. These distributions are next used to derive confidence intervals on the different inferred stellar parameters. The pseudo-observed frequencies are drawn from Gaussian distributions centered on the original observed frequencies. The values of the standard deviations reproduce the typical theoretical errors made on the computation of oscillation frequencies. We estimate it to be of the order of 10^{-2} c/d (see Salmon 2014). More details on this method are given in Salmon (2014) and will be the object of a forthcoming paper.

3 The hare and hound exercises

In Salmon (2014), we have presented the results of several hare and hound exercises dedicated to β Cephei models. We have checked different sets of seismic constraints to establish the minimum requirements allowing to derive accurate seismic inferences. We have as well estimated the impact of the physics on the seismic inferences. In that aim, the input physics of stellar models used as an observed star were set different from that of the models in the grid. For the target stars to be representative of typical β Cephei stars, we have selected models with stellar masses from 9 to 14 $M_\odot$ and at different evolutionary stages with X_C from 0.2 to 0.5 for the central H mass fraction. The role of the input micro-physics is tested by selecting either OPAL (Iglesias & Rogers 1996) or OP opacities and either GN93 (Grevesse & Noels 1993) or AGS05, for the chemical mixture.

Table 1. Stellar parameters of the target star t1 and solutions from the seismic modelling when 3 and 5 identified frequencies are considered, named t1-3freq and t1-5freq, respectively.

Model	M (in $M_\odot$)	R (in $R_\odot$)	X_{initial}	Z_{initial}	α_{ov}	X_C
t1	14	7.48	0.70	0.014	0.20	0.288
t1-3freq	15.6	10.18	0.70	0.018	0.45	0.237
t1-5freq	13.8	7.45	0.68	0.014	0.20	0.274

To illustrate the dependency of the seismic inferences on the available observational data, we present here one exercise where the target star is a stellar model (called t1, hereafter) with exactly the same input physics as in the theoretical grid. The frequencies of this model are computed with the non-adiabatic code MAD (Dupret 2001), which leads to frequencies different by about 10^{-4} (up to 10^{-2}) c/d from the adiabatic ones. In this way, we avoid any bias in the search of the solution. Indeed frequencies of the model t1 and those of the same model in the grid would have perfectly matched, in an unrealistic manner.

We have analysed different cases, considering that 3 to 5 frequencies were observed, with or without identification of the angular degree ℓ. In this paper we compare in particular a case with 3 identified frequencies (1 $\ell = 0$; 1 $\ell = 1$; 1 $\ell = 2$) to one with 5 identified frequencies (1 $\ell = 0$; 2 $\ell = 1$; 2 $\ell = 2$). The results of the modelling are given in Table 1, where t1-3freq and t1-5freq are the best-fit models for the 3 and 5 frequency cases, respectively. The solution with 3 observed frequencies shows that the mass and radius are overestimated, as well as α_{OV} which is erroneously derived. Fig. 1 clearly illustrates in its top panel that the solution is not satisfactory in this case, with the global minimum of χ^2 failing to match the parameters of the target star. The ridges with lower values of χ^2 correspond to models with the same dynamical timescale, which is constrained by the presence of a radial mode ($\ell = 0$) in the set of observed frequencies. With the help of Monte-Carlo simulations, we are able to refine the solution but find large uncertainties at the 1-σ level of confidence of 22% and 31% respectively on M and R.

However, with additional constraints, the solution can reach a higher level of accuracy. In the bottom panel of Fig. 1, the χ^2 global minimum is indeed found very close to that of the target star when 5 identified frequencies are considered. This statement is confirmed by the Monte-Carlo simulations that indicate an uncertainty[*] of 1% on M and R at the 1-σ level. Not depicted, the limits of the central mixed region and the extent of $\nabla\mu$ are also inferred[†] with 1% precision in terms of mass fraction (m/M), quantity of prime importance for stellar physics.

We derived other results with the help of additional exercises (see Salmon 2014), which can be summarised as follows:

- for a given input physics and when the number of identified frequencies is < 5 or part or them are unidentified, the additional knowledge of classical parameters (T_{eff}, $\log g$) can however result in an accurate seismic modelling,
- when the target star and the theoretical grid do not present the same chemical mixture, global parameters such as M and R are still retrieved, although with a lower precision. Yet, the location of the central mixed region can be poorly constrained in terms of m/M, even if the α_{OV} seems correctly inferred. That is the models have the same α_{OV}[‡] but the mass of their central mixed regions is significantly different,
- when the target star presents a different macro-physics (for e.g. turbulent mixing induced by rotational mixing), the modelling process is unable to make the distinction since it as it has not been designed for it (instantaneous mixing in the grid models).

[*]this value is probably underestimated since we are in an ideal situation where target star and models present the same input physics
[†]this is also probably underestimated
[‡]the other inferred parameters do not match exactly those of the target star

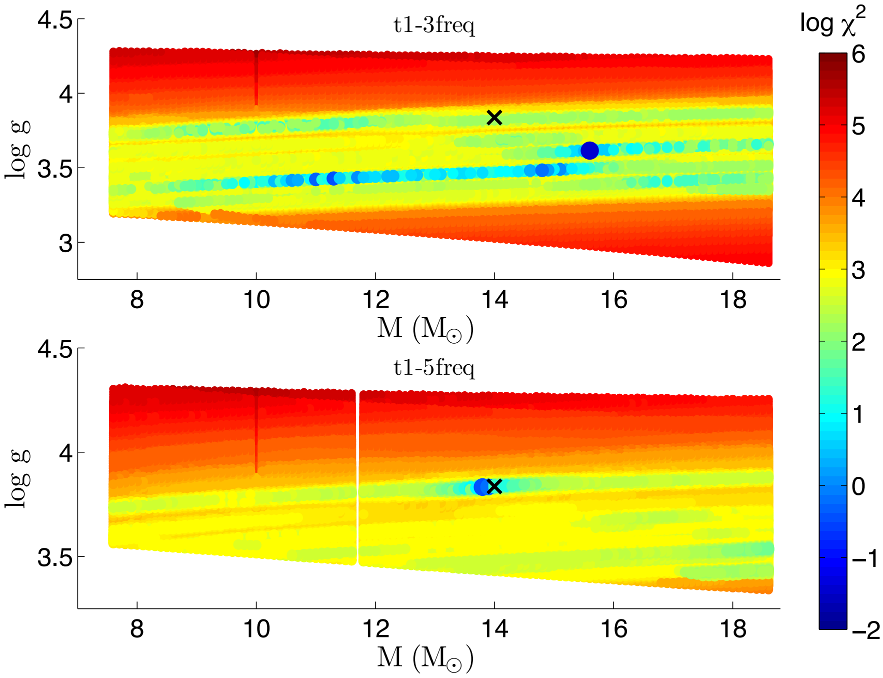

Fig. 1. Values of χ^2 as a function of M and surface gravity ($\log g$) for given $X_{\rm initial}$, $Z_{\rm initial}$, and $\alpha_{\rm ov}$, corresponding to those of the t1-3freq (top panel) and t1-5freq (bottom panel) best-fit models, respectively. The black cross indicate the M and $\log g$ values of the target star t1.

4 Perspectives: opacity and driving of the modes

In our hare and hound exercises, we have carried out a seismic analysis based on theoretical adiabatic frequencies. With the help of non-adiabatic computations, one can determine which modes are expected to be excited. The κ mechanism is known as the driving mechanism of oscillations in β Cephei stars (Moskalik & Dziembowski 1992). This latter works as a heat-engine mechanism, activated by the presence of the iron-group element peak of opacity at a temperature of about 200,000 K in β Cephei stars. The efficiency of the mechanism is very sensitive to the size and shape of the opacity peak (e.g. Pamyatnykh 1999), and so on the opacity data.

Several seismic studies of β Cephei stars were realised with help of a non-adiabatic approach. However requiring the excitation of the fitting theoretical frequencies revealed a discrepancy with observation. Dziembowski & Pamyatnykh (2008) could not find modes theoretically excited in the range of the low frequencies observed in the hybrid pulsators ν Eri and 12 Lac, whether the OPAL or OP opacities were used. Zdravkov & Pamyatnykh (2009) reached the same conclusion for the γ Peg star. More recently, observations of β Cephei candidates in the Magellanic Clouds presented a new challenge, since pulsations were not expected from a theoretical point of view at such low metallicities (see Salmon et al. 2012, and references therein).

All this suggests that current stellar opacities could be underestimated in the iron-group elements peak(Zdravkov & Pamyatnykh 2009; Salmon et al. 2012; Cugier 2014). Analysis of spectral opacity computations obtained with different opacity codes revealed differences with OP (OPAL could not be compared), in particular for Ni (Turck-Chièze et al. 2013). This could led to important changes in the Rosseland mean opacity values (Turck-Chièze & Gilles 2013). More recently, Bailey et al. (2015) found a large disagreement between the experimental measurement of Fe spectral opacity and theoretical computations, for conditions close to that of the solar base of the convective zone. These new issues have called for new opacity computations.

In the frame of the OPAC collaboration, solar models calibrated with the new OPAS opacities (designed for solar conditions of temperature and density, see Mondet et al. 2015) present a base of the convective zone and sound speed profile that reduce the disagreement with the helioseismic inferences (Le Pennec et al., submitted). Concerning B stars, more complete computations of iron-group elements have not led to major changes in the OPAL opacities (Iglesias 2015). However, the future release of ATOMIC opacities computed with new computer facilities by the Los Alamos team might help to solve part of the observational challenge of β Cephei stars(Walczak et al. 2015). With help of these new opacities, we plan to include in the future non-adiabatic approach in our modelling scheme. We suggest then to reanalyse well-known pulsators such as ν Eri and 12 Lac, and see what are the consequences of these new opacity data.

5 Conclusions

Asteroseismology of β Cephei stars is a powerful tool to derive constraints on their global parameters and the size of their central mixed regions, provided a sufficient number of seismic and/or classical observables are known. In particular, our study has shown the crucial need for the identification of angular degree of modes. Hence we suggest that new observing campaigns of β Cephei stars shall focus on this objective.

The Monte Carlo simulations we have introduced have revealed their potential to derive confidence levels. They could also help refining the solutions derived by the forward approach.

Considering the impact of the input physics selected in the theoretical models, it appears as essential to introduce a chemical mixture representative of the observed stars to get an unbiased estimate of the central mixed region extent. As a consequence it calls for additional observations when studying β Cephei stars, in particular the determination of individual element abundances.

Finally, we shall probably need to implement new parameters in the modelling process to access information on the shape and extent of the chemical composition gradient, and hence on the nature of extra-mixing in main-sequence B stars.

References

Aerts, C. 2013, in EAS Publications Series, Vol. 64, EAS Publications Series, 323–330

Aerts, C., Waelkens, C., Daszyńska-Daszkiewicz, J., et al. 2004, A&A, 415, 241

Asplund, M., Grevesse, N., & Sauval, A. J. 2005, in Astronomical Society of the Pacific Conference Series, Vol. 336, Cosmic Abundances as Records of Stellar Evolution and Nucleosynthesis, ed. T. G. Barnes III & F. N. Bash, 25

Badnell, N. R., Bautista, M. A., Butler, K., et al. 2005, MNRAS, 360, 458

Bailey, J., Nagayama, T., Loisel, G., et al. 2015, Nature, 517, 56

Briquet, M., Morel, T., Thoul, A., et al. 2007, MNRAS, 381, 1482

Briquet, M., Uytterhoeven, K., Morel, T., et al. 2009, A&A, 506, 269

Chiosi, C. 2007, in IAU Symposium, Vol. 239, IAU Symposium, ed. F. Kupka, I. Roxburgh, & K. L. Chan, 235–246

Cugier, H. 2014, A&A, 565, A76

De Ridder, J., Telting, J. H., Balona, L. A., et al. 2004, MNRAS, 351, 324

Desmet, M., Briquet, M., Thoul, A., et al. 2009, MNRAS, 396, 1460

Dupret, M. A. 2001, A&A, 366, 166

Dziembowski, W. A. & Pamyatnykh, A. A. 2008, MNRAS, 385, 2061

Gallart, C., Zoccali, M., & Aparicio, A. 2005, ARA&A, 43, 387

Goupil, M. 2011, in Lecture Notes in Physics, Berlin Springer Verlag, Vol. 832, Lecture Notes in Physics, Berlin Springer Verlag, ed. J.-P. Rozelot & C. Neiner, 223

Grevesse, N. & Noels, A. 1993, in Origin and Evolution of the Elements, ed. N. Prantzos, E. Vangioni-Flam, & M. Casse, 15–25

Iglesias, C. A. 2015, MNRAS, 450, 2

Iglesias, C. A. & Rogers, F. J. 1996, ApJ, 464, 943

Meynet, G., Ekstrom, S., Maeder, A., et al. 2013, in Lecture Notes in Physics, Berlin Springer Verlag, Vol. 865, Lecture Notes in Physics, Berlin Springer Verlag, ed. M. Goupil, K. Belkacem, C. Neiner, F. Lignières, & J. J. Green, 3–642

Mondet, G., Blancard, C., Cossé, P., & Faussurier, G. 2015, ApJS, 220, 2

Moskalik, P. & Dziembowski, W. A. 1992, A&A, 256, L5

Pamyatnykh, A. A. 1999, Acta Astronomica, 49, 119

Ribas, I., Jordi, C., & Giménez, Á. 2000, MNRAS, 318, L55

Salmon, S. 2014, PhD thesis, *Impact of micro-physics and macro-physics on the seismic properties of main-sequence B-type stars*, Université de Liège

Salmon, S., Montalbán, J., Morel, T., et al. 2012, MNRAS, 422, 3460

Scuflaire, R., Montalbán, J., Théado, S., et al. 2008a, Ap&SS, 316, 149

Scuflaire, R., Théado, S., Montalbán, J., et al. 2008b, Ap&SS, 316, 83

Thoul, A., Ausseloos, M., Barban, C., et al. 2003, Communications in Asteroseismology, 143, 25

Turck-Chièze, S. & Gilles, D. 2013, in European Physical Journal Web of Conferences, Vol. 43, European Physical Journal Web of Conferences, 1003

Turck-Chièze, S., Gilles, D., Le Pennec, M., et al. 2013, High Energy Density Physics, 9, 473

Walczak, P., Fontes, C. J., Colgan, J., Kilcrease, D. P., & Guzik, J. A. 2015, A&A, 580, L9

Zdravkov, T. & Pamyatnykh, A. A. 2009, in American Institute of Physics Conference Series, Vol. 1170, American Institute of Physics Conference Series, ed. J. A. Guzik & P. A. Bradley, 388–390

SPECTROPOLARIMETRIC STUDY OF THE COOL RV TAURI STAR R SCUTI

B. Tessore[1], A. Lèbre[1] and J. Morin[1]

Abstract.
With the spectropolarimeter Narval at TBL we have initiated in spring 2015 a 2-year campaign dedicated to a sample of cool and evolved stars including pulsating RV Tauri stars. We monitor net circular and linear polarisation in the spectral lines of R Scuti, the brightest of such variable targets. Our aim is to study the surface magnetic field and the linear polarisation associated with specific spectral lines. We confirm a definite detection of the surface magnetic field of R Sct, with an average longitudinal component $B_\ell = 0.9 \pm 0.5$ G. We also unveil our first results on linear polarisation.

Keywords: stars: late-type, stars: R Sct, stars: magnetic field, line: profiles, polarisation

1 Introduction

Magnetic fields of cool evolved stars, have previously been detected with radio observations in circumstellar envelopes (Vlemmings 2012), but still, little is known on the surface magnetic field. Surface magnetic fields in evolved stars are often invoked (Pascoli & Lahoche 2008) to explain the mass loss and the shaping of the circumstellar envelope in the Asymptotic Giant Branch (AGB) phase and beyond. Recently, magnetic field at the surface of the radially pulsating AGB Mira star, χ Cygni has been detected by Lèbre et al. (2014). The latter, point out a relation between this detection and the radiative shock waves known to propagate periodically through the stellar atmosphere.
Like Mira stars, RV Tauri stars are pulsating variable targets but they present a succession of deep and shallow minima in their light curve. R Sct is the brightest RV Tauri star and it is suspected to be in a post-AGB evolutionary stage (van Winckel 2003). Radiative shock waves are also known to propagate through its atmosphere (Lebre & Gillet 1991). It is therefore possible to follow and to detect the presence of a shock wave, through high resolution spectroscopy. Indeed atomic lines present typical signature tracing the presence of shock waves such as strong emission in Balmer lines and doubling of photospheric lines (Lebre & Gillet 1992). In R Sct, the radiative shock waves may also enhance the surface magnetic field and ease its detection. In order to provide new observational constraints on magnetic field - shock waves interaction, R Sct is monitored with spectropolarimetry along its pulsation period. Observations of R Sct in all Stokes parameters (I, U, Q, V) are performed with the new generation spectropolarimeter Narval at TBL (Pic du Midi). Figure 1 shows the light curve of R Sct and the observation dates. The star is preferentially observed around its maxima of luminosity, so as to optimise the signal-to-noise ratio (S/N) and to avoid molecular blending occurring at low temperature.
The surface magnetic field is measured from polarisation in spectral lines induced by the Zeeman effect.
Circular polarisation (Stokes V), as well as linear polarisation (Stokes U and Q), are analysed with the Least-Square Deconvolution (LSD) method (Donati et al. 1997). To detect very weak polarisation signals (down to $10^{-5} \times I_c$), the LSD technique combines polarimetric signatures present in thousands of spectral lines to compute for each Stokes parameter an average line profile with enhanced S/N. A numeric mask, gathering atomic data extracted from the VALD database (Kupka et al. 1999) and optimised for the stellar parameters ($T_{\rm eff}$ and log g) of R Sct is used for the LSD analysis (Sabin et al. 2015).

[1] LUPM, Université de Montpellier, CNRS, Place Eugène Bataillon, 34095, France

© Société Francaise d'Astronomie et d'Astrophysique (SF2A) 2015

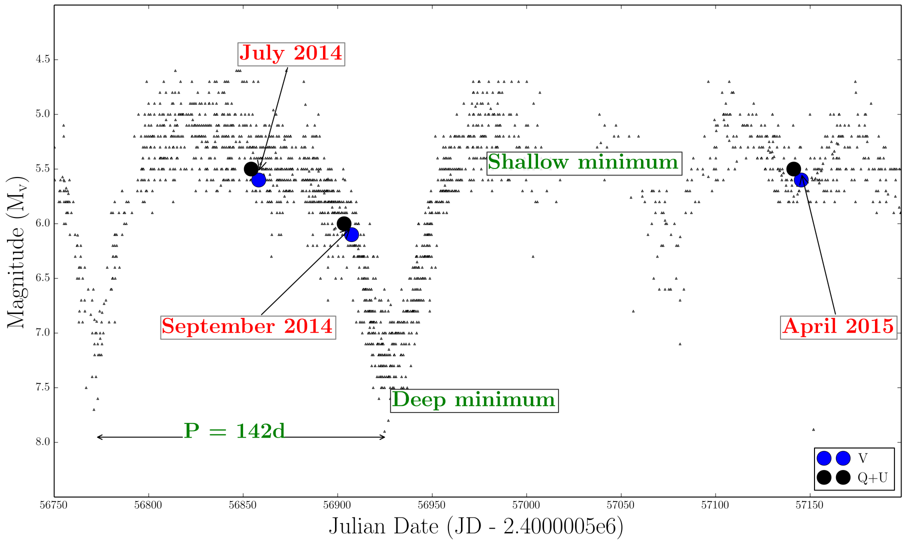

Fig. 1. Observations of R Sct along its pulsation period (P = 142 d). The light curve comes from the American Association of Variable Star Observers database (`https://www.aavso.org/`).

2 Circular polarisation: surface magnetic field

Figure 2 presents the Stokes V profiles at different epochs after analysis with the LSD method. Stokes V profiles are shown in the left panel of Fig.2. The same optimised mask for R Sct was used for all epochs.
From a mean LSD Stokes V profile, the mean longitudinal component of a surface magnetic field can be computed using the first moment method (Rees & Semel 1979):

$$B_\ell = -2.14 \times 10^{11} \frac{\int vV(v)\, dv}{\lambda gc \int [I_c(v) - I(v)]\, dv}$$

where I, I_c, V, g, λ, v and c are respectively, intensity, continuum intensity, circular polarisation, Landé factor, wavelength (nm), velocity (km/s) and celerity of light in vacuum (km/s), and B_ℓ is the projection of magnetic field along the line-of-sight (in Gauss). The magnetic field at the surface of cool evolved stars is expected to be at the Gauss level, according to the measurement of magnetic field in their circumstellar envelopes (Vlemmings 2012). Moreover, from spectropolarimetric facilities, Aurière et al. (2010) confirm that trend in the Red SuperGiant (RSG) star Betelgeuse, where a longitudinal magnetic field of approximately 1 G is measured. Lèbre et al. (2014) also measure a Gauss-level magnetic field in the AGB star χ Cygni. Sabin et al. (2015) report a longitudinal magnetic field $B_\ell = 0.6 \pm 0.6$ Gauss in R Sct from the Narval observations of 21-23 July 2014. This first detection of a surface field in RV Tauri star needs to be confirmed and further investigated. Our own investigations confirm this definite detection – according to a standard statistical criterion based on Donati et al. (1997) – only for the 21-23 July 2014, but not for other epochs. Right panel of Fig. 2 shows that the Zeeman signature (detected in Stokes V profile) is centered with the blue component of the Stokes I line profile. We therefore consider that a more physically meaningful value of $B_\ell = 0.9 \pm 0.5$ G is obtained by considering only the blue component of the intensity in its computation with the first moment method. The double-component structure in the mean intensity line, is indeed typical of a shock wave presence in the photospheric region. The blue component is therefore related to the material moving upward with the passage of the wave. We note that for the April 2015 observations no magnetic field is detected, whereas the pulsation phase ($\phi = 0.56$) is close to that of 21-23 July 2014 ($\phi = 0.62$). However the shape of the cycles of 2014 and 2015 look different, pointing out different physical conditions and the non-rigorous reproducibility of the cycles. This is confirmed by the fact that the mean intensity profile of April 2014 does not exhibit the typical double-component. All these observations strengthen our idea that a shock wave may enhance the magnetic field and hence may ease its detection.

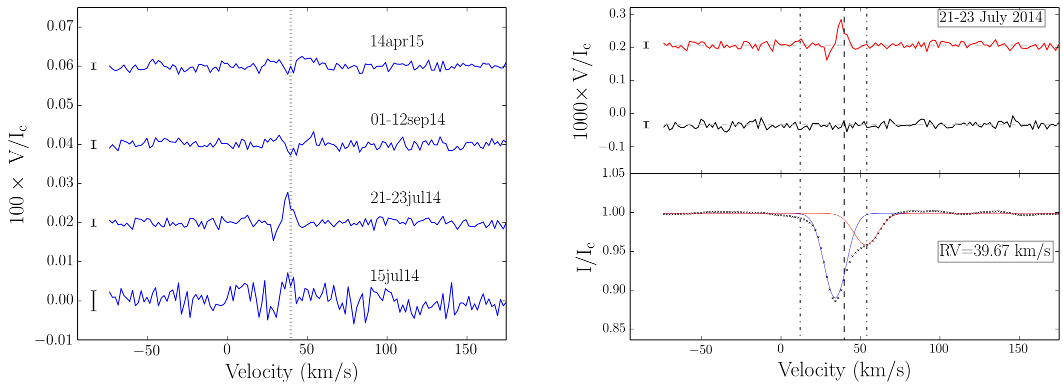

Fig. 2. Left: Circular polarised spectra of R Sct at different phases along its pulsation period. These data are collected with the spectropolarimeter Narval. The S-shape of the 21-23 July detection is typical of a weak dipole field. The gray dashed line shows the central radial velocity of the star. **Right:** The resulting LSD profile for the detection of July. Top panel: Stokes V in red, Null polarisation in black. Bottom panel: intensity profile. The blue and red components of the intensity profile are shown so as to highlight the connection between surface magnetic field and shock waves. The dashed and the dot-dashed are respectively, the central radial velocity of the star (RV = 39.67 km/s) and the bounds used for the first moment method (12 − 57 km/s).

3 Linear polarisation: from LSD profiles to individual lines view

In the weak field approximation – which is perfectly valid as we deal with Gauss and sub-Gauss level for the surface magnetic field strength – the circular polarisation amplitude is about one order greater than the linear polarisation one. In the cool evolved stars which present strong net linear polarisation, on the contrary, the measured amplitude of Stokes Q and U are systematically one order of magnitude larger than Stokes V. We can therefore rule out the Zeeman effect as a major contributor to the observed linear polarisation structures. Other contributions to linear polarisation are related to anisotropies of the radiation field. In this context, linear polarisation is compared with what we know about the solar case. In that case the linear polarisation has two contributions: (i) depolarisation of the continuum by absorption and scattering lines and (ii) intrinsic polarisation of lines. For the Sun, the anisotropy of the radiation field is related to center-to-limb variation (Stenflo & Keller 1997) which is a centro-symmetric effect. Thus the disk-integrated linear polarisation would be zero. Therefore, on spatially unresolved stars, the detection of net linear polarisation traces the presence of surface inhomogeneities. Recently, (Aurière et al. in prep.) have discovered linear polarisation in the spectrum of the RSG star Betelgeuse. For this case, the proposed main contributor to the observed linear polarisation is the depolarisation of continuum by lines through Rayleigh scattering due to photospheric spots. Lèbre et al. (2015) have also measured net linear polarisation in the spectral lines of the variable Mira star χ Cygni; however no linear polarisation signals were found in spectral lines of non-pulsating AGB stars hosting surface magnetic field. Figure 3 displays Stokes Q and U LSD profiles of R Sct. Strong signatures are detected for all epochs except 15 July 2014. In the right panel of Fig. 3, linear polarisation is represented in terms of linear polarisation rate $\mathrm{P}_\ell = \sqrt{\mathrm{Q}^2 + \mathrm{U}^2}/\mathrm{I_c}$. Time variation of P_ℓ is observed with an increasing amplitude toward minimum luminosity. Linear polarisation in the spectral lines of R Sct is so strong – at the level of a percent of the unpolarised continuum – that it can be measured in individual lines. Figure 4 depicts the linearly polarised spectrum of R Sct around the strontium I line at 460.7 nm. This spectral line – known to show strong polarisation in the second solar spectrum – is clearly detected in linear polarisation for R Sct. Comparing the behaviour of polarised lines in the spectrum of R Sct with the second solar spectrum will help us to improve our understanding of the origin of linear polarisation in R Sct.

4 Summary

We have initiated a large campaign of observations over two years with the spectropolarimeter Narval. We aim to detect magnetic field at the surface of cool evolved stars, to highlight the nature of the interaction between magnetic field and shock waves for a sample of variable stars and to determine the origin of linear polarisation.

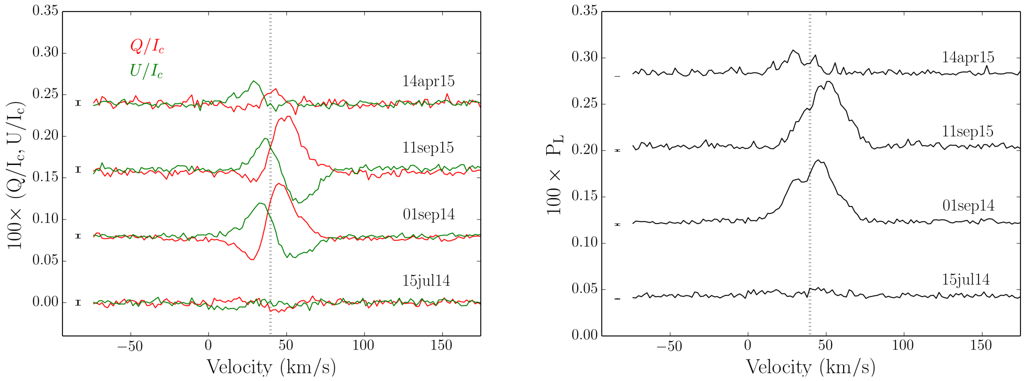

Fig. 3. Left: Linear polarisation profiles, Stokes Q and U. **right:** Linear polarisation rate.

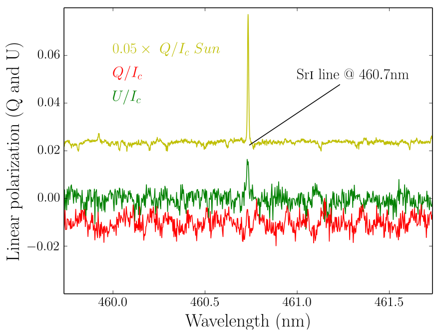

Fig. 4. The linearly polarised spectrum of R Sct around the SrI line at 460.7 *nm*. A clear polarisation is detected. The second solar spectrum (yellow) is shown for comparison (Stenflo 2014).

The main results we have obtained so far are: 1) Zeeman signature in net circular polarisation seems to be related to the atmospheric dynamics, 2) considering 1) we report a better estimation of $B_\ell = 0.9 \pm 0.5$ G and 3) non-Zeeman net linear polarisation is very strong and could be related to surface inhomogeneities.

Ongoing observations with Narval and ESPaDOnS (CFHT, Hawaii) will help us to confirm the systematic connection between surface magnetic field and photospheric dynamics and to study the physical origin of linear polarisation in RV Tauri stars and AGB stars.

We acknowledge financial support from "Programme National de Physique Stellaire" (PNPS) of CNRS/INSU, France, and the "Société Française d'Astronomie et d'Astrophysique" (SF2A).

References

Aurière, M., Donati, J.-F., Konstantinova-Antova, R., et al. 2010, A&A, 516, L2

Donati, J.-F., Semel, M., Carter, B. D., Rees, D. E., & Collier Cameron, A. 1997, MNRAS, 291, 658

Kupka, F., Piskunov, N., Ryabchikova, T. A., Stempels, H. C., & Weiss, W. W. 1999, A&AS, 138, 119

Lèbre, A., Aurière, M., Fabas, N., et al. 2014, in IAU Symposium, Vol. 302, IAU Symposium, ed. P. Petit, M. Jardine, & H. C. Spruit, 385–388

Lèbre, A., Aurière, M., Fabas, N., et al. 2015, in IAU Symposium, Vol. 305, IAU Symposium, 47–52

Lebre, A. & Gillet, D. 1991, A&A, 251, 549

Lebre, A. & Gillet, D. 1992, A&A, 255, 221

Pascoli, G. & Lahoche, L. 2008, PASP, 120, 1267

Rees, D. E. & Semel, M. D. 1979, A&A, 74, 1

Sabin, L., Wade, G. A., & Lèbre, A. 2015, MNRAS, 446, 1988

Stenflo, J. O. & Keller, C. U. 1997, A&A, 321, 927
van Winckel, H. 2003, ARA&A, 41, 391
Vlemmings, W. 2012, in IAU Symposium, Vol. 283, IAU Symposium, 176–179

Session 14

L'univers (sub-)millimétrique haute résolution angulaire: la révolution d'ALMA et de NOEMA

SF2A 2015
F. Martins, S. Boissier, V. Buat, L. Cambrésy and P. Petit (eds)

WATER AND COMPLEX ORGANIC MOLECULES IN THE WARM INNER REGIONS OF SOLAR-TYPE PROTOSTARS

A. Coutens[1], J. K. Jørgensen[1], M. V. Persson[2], J. M. Lykke[1], V. Taquet[2], E. F. van Dishoeck[2, 3], C. Vastel[4, 5] and S. F. Wampfler[1]

Abstract. Water and complex organic molecules play an important role in the emergence of Life. They have been detected in different types of astrophysical environments (protostars, prestellar cores, outflows, protoplanetary disks, comets, etc). In particular, they show high abundances towards the warm inner regions of protostars, where the icy grain mantles thermally desorb. Can a part of the molecular content observed in these regions be preserved during the star formation process and incorporated into asteroids and comets, that can deliver it to planetary embryos through impacts? By comparison with cometary studies, interferometric observations of solar-type protostars can help to address this important question. We present recent results obtained with the Plateau de Bure interferometer about water deuteration, glycolaldehyde and ethylene glycol towards the low-mass protostar NGC 1333 IRAS2A.

Keywords: astrochemistry, astrobiology, ISM: individual objects: NGC 1333 IRAS2A, stars: formation , stars: protostars, ISM: molecules

1 Introduction

Star-forming regions are known to show a very rich chemistry. Numerous molecules are especially detected towards Class 0 protostars, both in the warm inner regions and in the cold outer envelope. The presence of these molecules can be explained both by gas phase and grain surface chemistry. A lot of complex organic molecules (COMs) are found in the inner regions (e.g., Bottinelli et al. 2004, 2007; Bisschop et al. 2008) and are thought to be released in the gas phase with water once the temperature is sufficiently high ($T > 100\,\mathrm{K}$) to desorb the icy grain mantles. These regions are called hot corinos (Ceccarelli 2004).

Asteroids and comets are also chemically rich. Water was detected in different comets (e.g., Mumma et al. 1986) and asteroids (Campins et al. 2010; Küppers et al. 2014). COMs such as ethylene glycol and formamide are also known to be present in comets (Biver et al. 2014). Glycine, an amino-acid, was even found by Elsila et al. (2009) in the cometary samples of the STARDUST mission. A lot of COMs, amino acids and sugars were also found in meteorites (e.g., Schmitt-Kopplin et al. 2010). It was consequently suggested that water and prebiotic molecules (i.e. amino-acids and sugars) could have been delivered to Earth by impacts of asteroids and/or comets, which would have probably played an important role in the emergence of Life.

The question then arises: can the molecular content observed during the Class 0 stage be preserved during the star formation process (at least partially) until the formation of planets, comets and asteroids or is it completely reprocessed? To answer this question, it is therefore important to study the chemistry in the warm inner regions of protostars, where planets are supposed to form at a later stage. The aims are first to compare it with comets and asteroids and determine any similarity or variation between molecules, and secondly to better understand how this Class 0 molecular content formed.

We present recent results obtained with the Plateau de Bure Interferometer (PdBI) towards low-mass protostars. Section 2 is focused on water deuterium fractionation, while Section 3 is dedicated to glycolaldehyde and ethylene glycol. Perspectives are presented in Conclusion.

[1] Centre for Star and Planet Formation, Niels Bohr Institute & Natural History Museum of Denmark, University of Copenhagen, Øster Voldgade 5-7, DK-1350 Copenhagen K., Denmark
[2] Leiden Observatory, Leiden University, P.O. Box 9513, 2300 RA Leiden, The Netherlands
[3] Max-Planck-Institut für Extraterrestrische Physik, Giessenbachstrasse 1, D-85748 Garching, Germany
[4] Université de Toulouse, UPS-OMP, IRAP, F-31062 Toulouse, France
[5] CNRS, IRAP, 9 Av. Colonel Roche, BP 44346, F-31028 Toulouse Cedex 4, France

© Société Francaise d'Astronomie et d'Astrophysique (SF2A) 2015

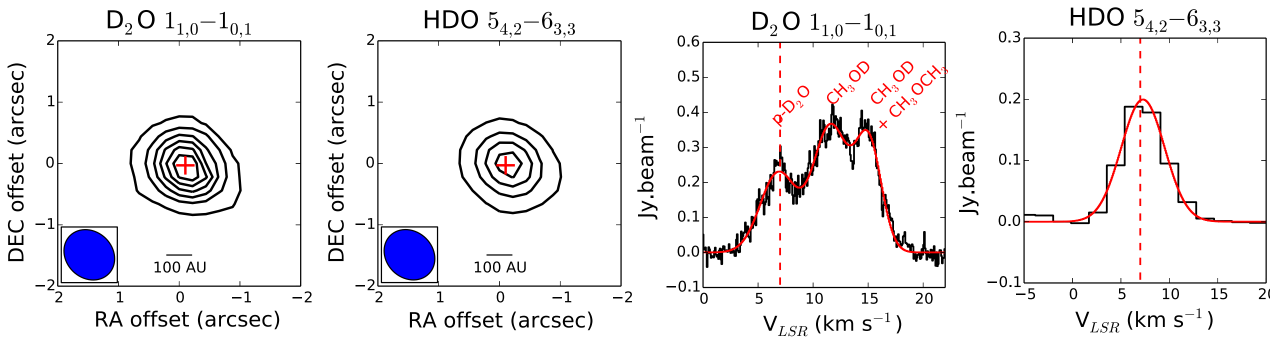

Fig. 1. Observations of the D_2O $1_{1,0}$-$1_{0,1}$ and HDO $5_{4,2}$-$6_{3,3}$ transitions towards the protostar NGC 1333 IRAS2A with the PdBI. Left panels: integrated intensity maps. Right panels: continuum subtracted spectra. Figure from Coutens et al. (2014).

2 Water deuteration

The determination of deuterium fractionation ratios is very helpful to understand how molecules form and to follow their evolution. Indeed, the deuterium fractionation can be enhanced by a few reactions, such as the reaction $H_3{}^+ + HD \rightarrow H_2D^+ + H_2$ that is only efficient at low temperatures and high densities. If molecules formed in a cold and dense environment, their deuterium fractionation ratios should therefore be higher by several orders of magnitude than if they formed in the gas phase at high temperature.

Water can form through different mechanisms: i) ion-molecule gas phase reactions, ii) high-temperature gas phase reactions (typical of shocks or hot cores) and iii) hydrogenation of atomic and molecular oxygen on grain surfaces (in cold and dense regions) (see van Dishoeck et al. (2013) for more details). With the determination of the water deuterium fractionation ratios and chemical modeling, it is then possible to constrain the origin of water.

2.1 *HDO/H_2O ratios towards solar-type protostars and comets*

The HDO/H_2O ratio* was determined in the inner regions of several Class 0 protostars by Persson et al. (2014) using PdBI data. The values range between 6×10^{-4} and 2×10^{-3} (see Figure 6 in Persson et al. 2014). Comets also show various values. The ratios found in Oort cloud comets are on average slightly lower than in the warm inner regions of protostars (Bockelée-Morvan 2011), but could be consistent with some of the protostars. The HDO/H_2O ratio is lower for two Jupiter family comets that were studied with the HIFI spectrometer onboard Herschel and consistent with the terrestrial value ($\sim 3 \times 10^{-4}$, Hartogh et al. 2011; Lis et al. 2013), but the in-situ measurement obtained towards another Jupiter family comet in the framework of the Rosetta mission is higher and in agreement with the protostellar values (Altwegg et al. 2015). The similarity of the HDO/H_2O ratios suggest that at least a part of the cometary water content could originate from the first phases of star formation. It is also supported by a theoretical study that showed that a total reprocessing of the chemistry in the protoplanetary disk would lead to HDO/H_2O ratios that are too low compared to the values found in comets and Earth's oceans (Cleeves et al. 2014).

2.2 *Determination of the D_2O/HDO ratio towards NGC 1333 IRAS2A*

Although D_2O has not been detected towards comets so far, interferometric studies of this isotopologue towards low-mass protostars can help to understand the origin of water in the warm inner regions of these objects. Observations of the D_2O $1_{1,0}$–$1_{0,1}$ transition were carried out towards the source NGC 1333 IRAS2A with the PdBI, leading to the first interferometric detection of D_2O towards a low-mass protostar (Coutens et al. 2014, see Fig. 1). The D_2O/HDO ratio was found to be surprisingly high ($\sim 1.2 \times 10^{-2}$) compared to the HDO/H_2O ratio ($\sim 1.7 \times 10^{-3}$). None of the grain surface chemical models (including the doubly deuterated form of water) published so far show a D_2O/HDO ratio higher than the HDO/H_2O ratio. This consequently suggests that

*The HDO/H_2O ratio is equal to twice the water D/H ratio.

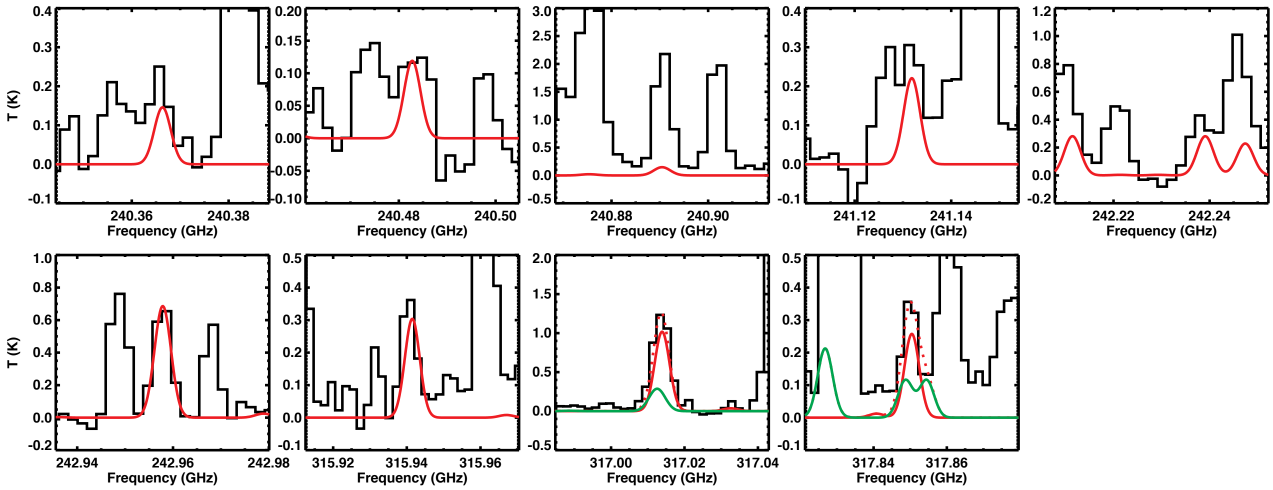

Fig. 2. Observed lines of glycolaldehyde toward the protostar NGC 1333 IRAS2A (in black). The LTE modeling of glycolaldehyde is shown in red. The contribution of methyl formate is shown in green. Figure from Coutens et al. (2015).

either an ingredient is missing in the understanding of deuterium fractionationation processes, or that high temperature gas phase reactions also take place in the warm inner regions of protostars. Indeed, in the second case, the thermal desorption of the icy grain mantles would explain the high D_2O/HDO ratios, while the high temperature gas phase reactions would produce a lot of H_2O (but only a little of deuterated water), which would lead to a decrease of the HDO/H_2O ratio.

3 Glycolaldehyde and ethylene glycol

Glycolaldehyde (CH_2OHCHO) is the simplest form of sugar and is thought to play a role in the formation of biological molecules. It was also shown that this molecule could survive during impact delivery to planetary bodies (McCaffrey et al. 2014). The reduced alcohol of this species is named ethylene glycol $(CH_2OH)_2$. While ethylene glycol was detected towards three comets, glycolaldehyde was not[†], leading to an ethylene glycol-to-glycolaldehyde (hereafter EG/GA) ratio higher than 3–6 (Crovisier et al. 2004; Biver et al. 2014). Glycolaldehyde was detected for the first time towards a low-mass protostar (IRAS 16293-2422) with the Atacama Large Millimeter/submillimeter Array (ALMA) by Jørgensen et al. (2012). Local thermal equilibrium analyses of glycolaldehyde and ethylene glycol give a lower EG/GA ratio of about 1 (Jørgensen et al. in prep.), which would suggest that a reprocessing of the chemistry takes place between the Class 0 stage and the formation of comets.

We analyzed some observations of another low-mass protostar, NGC 1333 IRAS2A, to determine if the EG/GA ratio was similar to IRAS 16293-2422. Eight lines of glycolaldehyde and more than thirty lines of ethylene glycol were successfully detected towards this source (Coutens et al. 2015, see Fig. 2). The EG/GA ratio was estimated at about 5, which means that it is consistent with the lower limits found in comets and higher than the value in IRAS 16293-2422. Several hypotheses can be proposed to explain the different ratios measured in NGC 1333 IRAS2A and IRAS 16293-2422. If the EG/GA ratio was initially the same on grains, it would indicate that some gas phase reactions are able to destroy (or possibly form) one of the two molecules more efficiently (after their desorption in the hot corino). A different sublimation temperature for the two molecules could also be possible. More experimental and theoretical work would be needed to know if these scenarios are possible. Experimental studies show, however, that the EG/GA ratio can vary on the grains (Öberg et al. 2009). It is especially sensitive to the CH_3OH:CO composition of the UV irradiated ices. A composition of pure CH_3OH leads to high EG/GA ratios (> 10), while a CH_3OH:CO 1:10 ice mixture produces low EG/GA ratios (< 0.25). It could consequently mean that ices in NGC 1333 IRAS2A were richer in methanol than in IRAS 16293-2422. This scenario seems plausible, as the gas-phase abundance of CH_3OH is higher towards

[†]A first detection of glycolaldehyde was recently presented in Goesmann et al. (2015).

NGC 1333 IRAS2A, while the CO abundances are similar (Schöier et al. 2002; Jørgensen et al. 2002, 2005). It is possible that CH_3OH formed more efficiently (by hydrogenation of CO) in NGC1333 IRAS2A, because this source shows lower H_2 densities than IRAS 16293-2422 (see Fig. 5 in Coutens et al. 2015). If ethylene glycol forms through hydrogenation of glycolaldehyde, it would explain why the EG/GA ratio is higher when the CH_3OH/CO ratio is higher.

4 Conclusion

Studying the chemistry in Class 0 protostars is important to understand how the molecules form and how they evolve between this stage and the formation of comets, asteroids and planets. Recent studies on deuterated water and COMs show that similarities can be observed between low-mass protostars and comets. The results on glycolaldehyde and ethylene glycol in NGC 1333 IRAS2A and IRAS 16293-2422 illustrate the need for investigating a higher number of sources, first to know if the chemistry in low-mass protostars is relatively similar and secondly to understand possible variations. Precise D_2O/HDO ratios will be soon obtained for the protostar IRAS 16293-2422 in the framework of an ALMA project (Coutens et al. in prep). With ALMA and the NOrthern Extended Millimeter Array (NOEMA), it will also be possible to investigate intermediary stages (Class I and Class II protostars) to better understand the evolution of the chemistry from the Class 0 stage to the formation of planets.

The research of AC, JKJ, and JML was supported by the Lundbeck foundation. Research at Centre for Star and Planet Formation is funded by the Danish National Research Foundation. The research leading to these results has received funding from the European Commission Seventh Framework Programme (FP/2007-2013) under grant agreement No. 283393 (RadioNet3).

References

Altwegg, K., Balsiger, H., Bar-Nun, A., et al. 2015, Science, 347, 1261952
Bisschop, S. E., Jørgensen, J. K., Bourke, T. L., Bottinelli, S., & van Dishoeck, E. F. 2008, A&A, 488, 959
Biver, N., Bockelée-Morvan, D., Debout, V., et al. 2014, A&A, 566, L5
Bockelée-Morvan, D. 2011, in IAU Symposium, Vol. 280, IAU Symposium, ed. J. Cernicharo & R. Bachiller, 261–274
Bottinelli, S., Ceccarelli, C., Neri, R., et al. 2004, ApJ, 617, L69
Bottinelli, S., Ceccarelli, C., Williams, J. P., & Lefloch, B. 2007, A&A, 463, 601
Campins, H., Hargrove, K., Pinilla-Alonso, N., et al. 2010, Nature, 464, 1320
Ceccarelli, C. 2004, in Astronomical Society of the Pacific Conference Series, Vol. 323, Star Formation in the Interstellar Medium: In Honor of David Hollenbach, ed. D. Johnstone, F. C. Adams, D. N. C. Lin, D. A. Neufeeld, & E. C. Ostriker, 195
Cleeves, L. I., Bergin, E. A., Alexander, C. M. O. ., et al. 2014, Science, 345, 1590
Coutens, A., Jørgensen, J. K., Persson, M. V., et al. 2014, ApJ, 792, L5
Coutens, A., Persson, M. V., Jørgensen, J. K., Wampfler, S. F., & Lykke, J. M. 2015, A&A, 576, A5
Crovisier, J., Bockelée-Morvan, D., Biver, N., et al. 2004, A&A, 418, L35
Elsila, J. E., Glavin, D. P., & Dworkin, J. P. 2009, Meteoritics and Planetary Science, 44, 1323
Goesmann, F., Rosenbauer, H., Bredehöft, J. H., et al. 2015, Science, 349, 020689
Hartogh, P., Lis, D. C., Bockelée-Morvan, D., et al. 2011, Nature, 478, 218
Jørgensen, J. K., Favre, C., Bisschop, S. E., et al. 2012, ApJ, 757, L4
Jørgensen, J. K., Schöier, F. L., & van Dishoeck, E. F. 2002, A&A, 389, 908
Jørgensen, J. K., Schöier, F. L., & van Dishoeck, E. F. 2005, A&A, 437, 501
Küppers, M., O'Rourke, L., Bockelée-Morvan, D., et al. 2014, Nature, 505, 525
Lis, D. C., Biver, N., Bockelée-Morvan, D., et al. 2013, ApJ, 774, L3
McCaffrey, V. P., Zellner, N. E. B., Waun, C. M., Bennett, E. R., & Earl, E. K. 2014, Origins of Life and Evolution of the Biosphere, 44, 29
Mumma, M. J., Weaver, H. A., Larson, H. P., Williams, M., & Davis, D. S. 1986, Science, 232, 1523
Öberg, K. I., Garrod, R. T., van Dishoeck, E. F., & Linnartz, H. 2009, A&A, 504, 891
Persson, M. V., Jørgensen, J. K., van Dishoeck, E. F., & Harsono, D. 2014, A&A, 563, A74
Schmitt-Kopplin, P., Gabelica, Z., Gougeon, R. D., et al. 2010, Proceedings of the National Academy of Science, 107, 2763
Schöier, F. L., Jørgensen, J. K., van Dishoeck, E. F., & Blake, G. A. 2002, A&A, 390, 1001
van Dishoeck, E. F., Herbst, E., & Neufeld, D. A. 2013, Chemical Reviews, 113, 9043

AGN FEEDBACK AND JET-INDUCED STAR FORMATION

Q. Salomé[1], P. Salomé[1], F. Combes[1 2] and S. Hamer[1]

Abstract. We studied the impact of the AGN in radio galaxies on star formation along the radio jet. Our main goal was to determine whether star formation is more efficient in the shocked region along the jet.

A first large scale work based on IRAM-30m CO observations of 3C 285 and Minkowski's Object has shown the star-forming spots located a few tens of kpc along the radio jet appears to form stars at least as efficiently as typical spiral galaxies or even boosted. This result supports the AGN positive feedback scenario.

On the opposite, a small scale multi-wavelength analysis of the northern filaments of Centaurus A tends to quench star formation in the filaments, maybe due to the AGN negative feedback.

Keywords: Methods:data analysis, Galaxies:evolution, interactions, star formation, Radio lines:galaxies

1 Introduction

AGN are thought to play a role in galaxy evolution (and formation), but it is yet not clear how the so-called AGN feedback affects star formation. On the one hand, a *negative* feedback could prevent or regulate star formation through the energy released by the AGN (Heckman & Best 2014 and references therein). On the other hand, it is expected that the propagation of jet-driven shocks can accelerate the gas cooling and trigger star formation (Best & Heckman 2012; Ivison et al. 2012), producing an AGN *positive* feedback.

Leroy et al. (2008, 2013) compared the molecular gas content of nearby galaxies with SFR tracers. They found that the star formation efficiency depends mostly if not only on the amount of molecular gas. However, some environmental effects may also influence star formation (Daddi et al. 2010; Genzel et al. 2010).

Evidence of jet-induced star formation has been claimed only for a few objects: (1) Centaurus A (Schiminovich et al. 1994; Charmandaris et al. 2000); (2) Minkowski Object (van Breugel et al. 1985); (3) 3C 285 (van Breugel & Dey 1993); (4) at z = 3.8, the radio source 4C 41.17 (Bicknell et al. 2000; De Breuck et al. 2005; Papadopoulos et al. 2005).

To better understand the impact of the AGN interaction with the intergalactic medium on star formation, we conducted two studies at large (3C 285 and Minkowski's Object) and small scales (the northern filaments of Centaurus A). Our main goal was to determine whether star formation is more efficient in the shocked region along the jet. Throughout this work, we assume the cold dark matter concordance Universe, with $H_0 = 70 km.s^{-1}.Mpc^{-1}$, $\Omega_m = 0.30$ and $\Omega_\Lambda = 0.70$.

2 Hint of jet-induced star formation in 3C 285 and Minkowski's object

3C 285 is a double-lobed powerful FR-II radio galaxy where both lobes have a complex filamentary structure. In the eastern radio lobe, there is a radio jet with unresolved radio knots. A slightly resolved object in Hα emission is located near the eastern radio jet (**3C 285/09.6**; van Breugel & Dey 1993). 3C 285/09.6 is a small, kiloparsec-sized object where star formation seems to be triggered by the jet.

Minkowski's Object (MO) is a star-forming peculiar object near the double-lobed FR-I radio source NGC 541 in the galaxy cluster Abell 194 (Croft et al. 2006), located in a large optical bridge that connects NGC 541 with the interacting galaxies NGC 545/547. VLA observations show two HI clouds "wrapped" around the eastern jet with a total HI mass of 4.9×10^8 $M_\odot$ (Croft et al. 2006).

We have observed the CO(1-0) and CO(2-1) emission along the jet axis of the radio galaxies 3C 285 and NGC 541. The observations were made with the IRAM 30m telescope on March and June 2014, using the EMIR receiver with the

[1] LERMA, Observatoire de Paris, CNRS UMR 8112, 61 avenue de l'Observatoire, 75014 Paris, France
[2] Collège de France, 11 place Marcelin Berthelot, 75005 Paris

© Société Francaise d'Astronomie et d'Astrophysique (SF2A) 2015

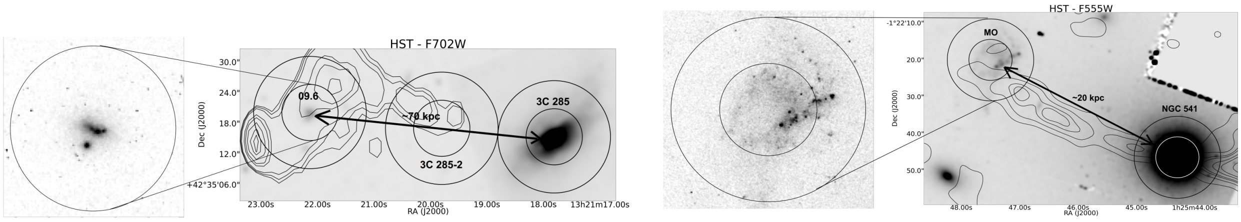

Fig. 1: Contour map of 3C 285 and NGC 541 observed at 21 cm (van Breugel & Dey 1993; van Breugel et al. 1985), overlaid on a slightly smoothed optical image. The observed positions are shown by the CO(1-0) and CO(2-1) IRAM 30m beams (circles). Details of 3C 285/09.6 and Minkowski's Object.

WILMA backend (bandwidth of 3.7 GHz; resolution of 2 MHz). Three regions were observed in March 2014: the central galaxy 3C 285, 3C 285/09.6, and an intermediate position (3C 285-2) along the jet (cf. Fig. 1). In June 2014, observations pointed at NGC 541 and Minkowski's Object (cf. Fig. 1).

CO luminosities The central galaxies were detected in both CO(1-0) and CO(2-1), whereas there is no detection for the other positions. Each line was fitted by a gaussian in order to get its characteristics (see Salomé et al. 2015 for the details). The CO luminosity L'_{CO} was calculated with the formula from Solomon et al. (1997) and the molecular gas mass was estimated using a standard Milky Way conversion factor of 4.6 $M_\odot.(K.km.s^{-1}.pc^2)^{-1}$ (Solomon et al. 1997).
Star formation rate and depletion time The Hα and IR emission is often used as tracers of star formation. We derived a star formation rate from the Hα (Baum & Heckman 1989; van Breugel & Dey 1993) and IR emission (computed with Herschel-SPIRE data from the archive), following the methods of Kennicutt & Evans (2012) and Calzetti et al. (2007). The total SFR is the sum of the SFR derived from the Hα and the IR emission. The molecular gas depletion time is the time to consume all the molecular gas with the present star formation rate: $t^{mol}_{depl} \sim M_{H_2}/SFR$.

Source	3C 285	3C 285/09.6	NGC 541	MO
SFR ($M_\odot.yr^{-1}$)	14.53	0.62	0.095	0.47
t_{dep} (Gyr)	0.71	< 1.0	1.79	0.02

Table 1: SFR and depletion for the different objects observed with the IRAM 30m.

A Kennicutt-Schmidt law? We have calculated the gas and SFR surface densities (Σ_{gas}, Σ_{SFR}; the values can be found in Salomé et al. 2015). The Σ_{SFR} vs Σ_{gas} diagram (see figure 2, Bigiel et al. 2008; Daddi et al. 2010), shows that the two star-forming regions 3C 285/09.6 and MO stand at least on or even above the KS-law, with molecular gas depletion time < 1 Gyr in 3C285/09.6 and down to < 20 Myr for the Minkowski's Object in regions of ~ 36 kpc and ~ 9 kpc. This supports the AGN positive feedback scenario that predicts an enhanced star formation activity along the shocked region inside the radio-jets.

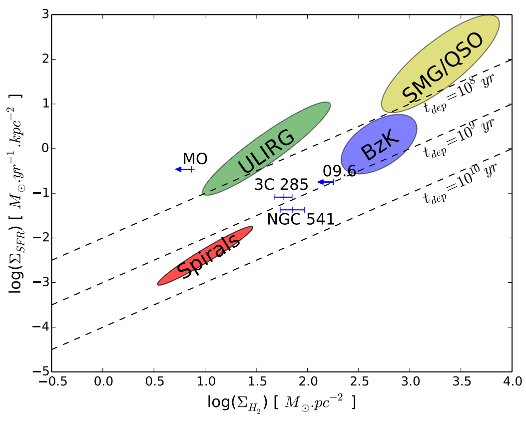

Fig. 2: Σ_{SFR} vs. Σ_{gas} diagram for the sources studied in Salomé et al. (2015). The diagonal dashed lines show lines of constant SF efficiency, indicating the level of Σ_{SFR} needed to consume 1%, 10%, and 100% of the gas reservoir in 10^8 years. Thus, the lines also correspond to constant gas depletion times of, from top to bottom, 10^8, 10^9, and 10^{10} yr The coloured regions come from Daddi et al. (2010).

3 Centaurus A

NGC 5128 (also known as **Centaurus A**) is a giant nearby early type galaxy surrounded by faint arc-like stellar shells (at several kpc around the galaxy). In the shells, HI emission has been detected (Schiminovich et al. 1994) and CO emission was observed at the intersection with the radio jet (Charmandaris et al. 2000). In addition, large amount of dust

($\sim 10^5$ M$_\odot$) lies around the northern shell region (Auld et al. 2012).
Along the radio-jet, optically bright filaments (so-called inner and outer filaments) have been observed (Morganti et al. 1991). These filaments located along the direction of the northern radio jet (at a distance of $\sim$ 7.7 kpc and $\sim$ 13.5 kpc, respectively) are the place of star formation (Auld et al. 2012).

We gathered archival data of the outer filaments in FUV (GALEX), FIR (Herschel) and CO (SEST and ALMA). We also searched for HCN/HCO$^+$ (ATCA) and observed optical emission lines (VLT/MUSE) in the filaments. Here we summarise the main results of this study, more details can be found in an other SF2A proceeding.

Molecular gas masses of a few $10^5 - 10^6$ M$_\odot$ were detected in several of the 44″ ($\sim$ 0.72 kpc) SEST beam of the map. The Σ_{SFR} vs Σ_{gas} diagram (Bigiel et al. 2008; Daddi et al. 2010) shows that the central galaxy is forming stars very efficiently, similar to ULIRG, whereas star formation at all the CO-SEST positions seems to be **quenched**.

4 Conclusion

CO emission has not been detected by the IRAM 30m telescope in 3C 285/09.6 and Minkoski's Object. Upper limits at 3σ provides molecular gas masses smaller than $\sim 10^7 - 10^8$ M$_\odot$. These masses lead to molecular depletion times $\leq$ 1 Gyr and $\leq$ 0.02 Gyr, respectively. In addition, the KS-diagram indicates that the star formation is at least as efficient as inside spiral galaxies and even boosted in the case of MO.

Using a standard conversion factor, the whole region of Centaurus A northern filaments contains $M_{H_2} = 2 \times 10^7$ M$_\odot$ with a very long depletion time $t_{dep} \sim 10$ Gyr.

Both objects have different behaviours, leading to a hint of environmental effects. This study is the first step towards a detailed understanding of the feedback effect.

References

Auld, R., Smith, M. W. L., Bendo, G., et al. 2012, MNRAS, 420, 1882
Baum, S. A. & Heckman, T. 1989, ApJ, 336, 681
Best, P. N. & Heckman, T. M. 2012, MNRAS, 421, 1569
Bicknell, G. V., Sutherland, R. S., van Breugel, W. J. M., et al. 2000, ApJ, 540, 678
Bigiel, F., Leroy, A., Walter, F., et al. 2008, AJ, 136, 2846
Calzetti, D., Kennicutt, R. C., Engelbracht, C. W., et al. 2007, ApJ, 666, 870
Charmandaris, V., Combes, F., & van der Hulst, J. M. 2000, A&A, 356, L1
Croft, S., van Breugel, W., de Vries, W., et al. 2006, ApJ, 647, 1040
Daddi, E., Elbaz, D., Walter, F., et al. 2010, ApJ, 714, L118
De Breuck, C., Downes, D., Neri, R., et al. 2005, A&A, 430, L1
Genzel, R., Tacconi, L. J., Gracia-Carpio, J., et al. 2010, MNRAS, 407, 2091
Heckman, T. M. & Best, P. N. 2014, ARA&A, 52, 589
Ivison, R. J., Smail, I., Amblard, A., et al. 2012, MNRAS, 425, 1320
Kennicutt, R. C. & Evans, N. J. 2012, ARA&A, 50, 531
Leroy, A. K., Walter, F., Brinks, E., et al. 2008, AJ, 136, 2782
Leroy, A. K., Walter, F., Sandstrom, K., et al. 2013, AJ, 146, 19
Morganti, R., Robinson, A., Fosbury, R. A. E., et al. 1991, MNRAS, 249, 91
Papadopoulos, P. P., Greve, T. R., Ivison, R. J., & De Breuck, C. 2005, A&A, 444, 813
Salomé, Q., Salomé, P., & Combes, F. 2015, A&A, 574, A34
Schiminovich, D., van Gorkom, J. H., van der Hulst, J. M., & Kasow, S. 1994, ApJ, 423, L101
Solomon, P. M., Downes, D., Radford, S. J. E., & Barrett, J. W. 1997, ApJ, 478, 144
van Breugel, W., Filippenko, A. V., Heckman, T., & Miley, G. 1985, ApJ, 293, 83
van Breugel, W. J. M. & Dey, A. 1993, ApJ, 414, 563

SF2A 2015
F. Martins, S. Boissier, V. Buat, L. Cambrésy and P. Petit (eds)

STAR FORMATION EFFICIENCY IN THE OUTER FILAMENTS OF CENTAURUS A

Q. Salomé[1], P. Salomé[1], F. Combes[1 2], S. Hamer[1] and I. Heywood[3 4]

Abstract. We present a multi-wavelength study of the northern filaments of Centaurus A (at a distance of ∼ 20 kpc from the galaxy center) based on FUV (GALEX), FIR (Herschel) and CO (SEST and ALMA) emission. We also searched for HCN and HCO^+ (ATCA) and observed optical emission lines (VLT/MUSE) in different places of the filament. An upper limit of the dense gas of $L'_{HCN} < 4.8 \times 10^3$ K.km.s^{-1}.pc^2 at 3σ leads to a dense-to-molecular gas fraction < 23% in this region.

We compared the CO masses with the SFR estimates and found very long depletion times (11 Gyr on 730 pc scales) and a large scatter in the KS-relation with a standard conversion factor. Applying a metallicity correction to the CO/H_2 conversion factor would lead to even more massive clouds with higher depletion times.

Using ALMA archive data, we found 3 unresolved CO(2-1) clumps of size < 37×21pc and masses around $10^4 M_\odot$. The 3 clumps show resolved line profiles ($\Delta v \sim 10$km.s^{-1}) and are all three dynamically clearly separated by $\sim 10-20$km.s^{-1}. We derived a virial parameter $\alpha_{vir} \sim 10 - 16$ which indicates that the clumps are not gravitationally bound and input of energy likely inhibits star formation.

Keywords: Methods:data analysis, Galaxies:evolution, interactions, star formation, Radio lines:galaxies

1 Introduction

AGN are supposed to regulate gas accretion and thus slow down star formation (negative feedback). However, evidence of AGN **positive feedback** has also been observed in a few radio galaxies. In a previous work (Salomé et al. 2015), we studied two of the most famous example of **jet-induced star formation**: 3C 285/09.6 (van Breugel & Dey 1993) and Minkowski's Object (van Breugel et al. 1985). Here we study another famous example: the outer filaments of Centaurus A (Mould et al. 2000; Oosterloo & Morganti 2005).

NGC 5128 (or Centaurus A) is a giant nearby early type galaxy that is surrounded by faint arc-like stellar shells (at several kpc around the galaxy). In the shells, HI emission has been detected (Schiminovich et al. 1994) and CO emission was observed at the intersection with the radio jet (Charmandaris et al. 2000). In addition, large amount of dust ($\sim 10^5 M_\odot$) lies around the northern shell region (Auld et al. 2012).

Along the radio-jet, optically bright filaments (so-called inner and outer filaments) have been observed (Morganti et al. 1991). These filaments located along the direction of the northern radio jet (at a distance of ∼ 7.7 kpc and ∼ 13.5 kpc, respectively) are the place of star formation (Auld et al. 2012).

We gathered archival data of the outer filaments in FUV (GALEX), FIR (Herschel) and CO (SEST and ALMA). We also searched for HCN/HCO^+ (ATCA) and observed optical emission lines (VLT/MUSE) in the filaments.

Our main goal was to determine whether star formation is more efficient in the shocked region along the jet. Throughout this work, we assume the cold dark matter concordance Universe, with $H_0 = 70$km.s^{-1}.Mpc^{-1}, $\Omega_m = 0.30$ and $\Omega_\Lambda = 0.70$.

2 Results

Star formation rate For all the CO positions, we derived a SFR from the FIR and FUV emission (Kennicutt 1998; Kennicutt & Evans 2012). The FIR emission also enabled us to estimate the molecular gas-to-dust ratios.

[1] LERMA, Observatoire de Paris, CNRS UMR 8112, 61 avenue de l'Observatoire, 75014 Paris, France
[2] Collège de France, 11 place Marcelin Berthelot, 75005 Paris
[3] CSIRO Astronomy & Space Science, P.O. Box 76, Epping, NSW 1710, Australia
[4] Department of Physics & Electronics, Rhodes University, P.O. Box 94, Grahamstown 6140, South Africa

© Société Francaise d'Astronomie et d'Astrophysique (SF2A) 2015

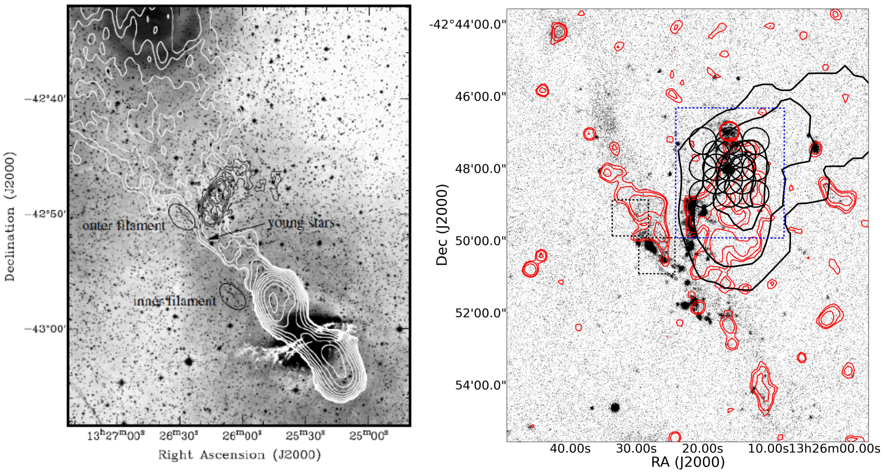

Fig. 1: *Left:* Optical image of Cen A in the range $\lambda = 3850 - 5400$ Å showing the diffuse emission and the location of the so-called inner and the outer filaments. The white contours denote the radio continuum emission of the inner lobes and the large-scale jet. The black contours refer to the north-east outer HI cloud. *Right:* FUV image of the outer filament from GALEX. The black and red contours correspond to the HI and the Herschel-SPIRE 250 μm emission, respectively. The circles show the positions observed (black; Charmandaris et al. 2000) and ATCA (red). The dashed boxes show the field of view of MUSE observations (Santoro et al. 2015).

Filaments oxygen abundance We computed oxygen abundance maps following the method of Pettini & Pagel (2004). The maps show that (i) there is no major metallicity difference between the inner and the outer filaments, (ii) there is no major metallicity gradient along each filament and (iii) both filament have relatively high abundances (roughly solar), but with local variations, even if as far as several kpc away from the center of NGC 5128.

Molecular gas mass CO emission was detected in almost all the positions of the 3×3 half beam central map. It has also been detected in the two positions 44″ upward and downward the central position. We found CO luminosities L'_{CO} of a few $10^5 - 10^6$ K.km.s^{-1}.pc^2 (with a standard conversion factor). Taking into account local low-metallicity corrections (Leroy et al. 2013) to the standard CO/H_2 conversion factor would lead to higher molecular masses and thus larger depletion times. **Dense gas tracers** HCN and HCO$^+$ were not detected with ATCA. We derived upper limits at 3σ assuming a line width of the order of the one detected in CO ($\sim$ 10km.s^{-1}): $L'_{HCN} < 4.8 \times 10^3$ K.km.s^{-1}.pc^2 and $L'_{HCO^+} < 4.8 \times 10^3$ K.km.s^{-1}.pc^2. This leads to a dense-to-molecular gas fraction < 23%. **Clumpy CO emission** CO(2-1) emission is detected by ALMA and reveals the presence of 3 distinct unresolved clumps. They show resolved line profiles (Δv $\sim$ 10 km.s^{-1}) and are dynamically separated by $\sim 10 - 20$ km.s^{-1}. The total integrated flux of the clumps is $S_{CO}\Delta v \sim 3.0$ Jy.km.s^{-1}, leading to $M_{H_2} \sim 8.7 \times 10^4$ $M_\odot$ with a standard CO/H_2 conversion factor. From FUV emission, we derived a SFR of $\sim 1.4 \times 10^{-5}$ $M_\odot$.yr^{-1} on scale of a few pc.

The **virial parameter** $\alpha_{vir} = 5\sigma_c^2 R_c/(GM_c)$ (Bertoldi & McKee 1992) measures the ratio of the kinetic to gravitational energy of the clouds. For the ALMA clumps, we found $\alpha_{vir} \sim 10 - 16$ (8 km.s^{-1}, 20 pc, 4×10^4 $M_\odot$), so an input of kinetic energy may have happened and could explain why these clouds appear inefficient (large depletion time) to form stars despite their surface density $N_{H_2} \geq 10^{20}$ cm^{-2}.

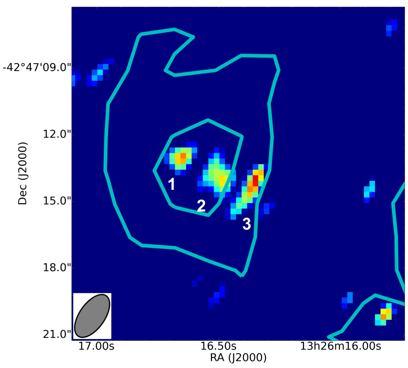

Fig. 2: ALMA CO(2-1) integrated emission line over Δv $\sim$ 30 km.s^{-1}. The contours show the FUV emission from GALEX.

Clump	offset	v_0 (km.s^{-1})	Δv (km.s^{-1})	M_{H_2} (10^4 $M_\odot$)
1	5.8″, −17.25″	∼ −231	12.5	4.0 ± 1.7
2	4.4″, −18.2″	∼ −222	8.0	2.6 ± 1.7
3	2.0″, −19.3″	∼ −214	7.5	2.1 ± 1.5

Table 1: CO(2-1) emission line properties for each clump (central velocity, FWHM and molecular gas mass estimated with a standard and fixed conversion factor with no metallicity correction). Offsets from the ALMA phase center: $\alpha = 13^h26^m16^s.1$, $\delta = -42{:}46{:}55.7$ are given in the first column.

3 Conclusion

The $\Sigma_{\rm SFR}$ vs $\Sigma_{\rm gas}$ diagram (see figure 3; Bigiel et al. 2008; Daddi et al. 2010) shows that, while the central galaxy is forming stars very efficiently (Espada et al. 2009), similar to ULIRG, the positions where CO has been detected in the filaments have large depletion times indicating very inefficient star formation. This trend would be even stronger if we take into account local metallicity correction. High spatial and spectral resolution of the CO line emission by ALMA hints for a large $\alpha_{\rm vir}$, in agreement with a kinetical energy injection in the molecular gas, preventing further collapse and thus star formation in the filaments aligned with the AGN jet direction.

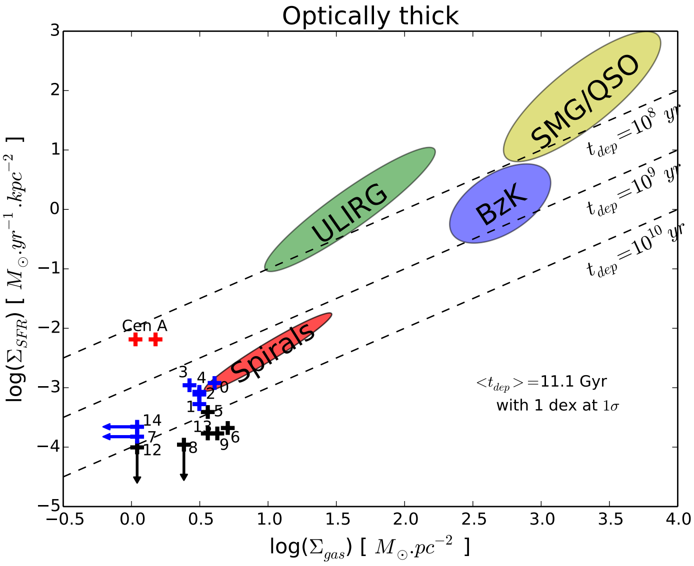

Fig. 3: $\Sigma_{\rm SFR}$ vs. $\Sigma_{\rm gas}$ for the different regions of CO emission. The diagonal dashed lines show lines of constant SFE, indicating the level of $\Sigma_{\rm SFR}$ needed to consume 1%, 10%, and 100% of the gas reservoir in 10^8 years. Thus, the lines also correspond to constant gas depletion times of, from top to bottom, 10^8, 10^9, and 10^{10} yr. The coloured regions come from Daddi et al. (2010). The blue and black colors separate the CO positions in two groups, depending on the depletion time. The red crosses correspond to the central galaxy.

References

Auld, R., Smith, M. W. L., Bendo, G., et al. 2012, MNRAS, 420, 1882
Bertoldi, F. & McKee, C. F. 1992, ApJ, 395, 140
Bigiel, F., Leroy, A., Walter, F., et al. 2008, AJ, 136, 2846
Charmandaris, V., Combes, F., & van der Hulst, J. M. 2000, A&A, 356, L1
Daddi, E., Elbaz, D., Walter, F., et al. 2010, ApJ, 714, L118
Espada, D., Matsushita, S., Peck, A., et al. 2009, ApJ, 695, 116
Kennicutt, R. C. & Evans, N. J. 2012, ARA&A, 50, 531
Kennicutt, Jr., R. C. 1998, ApJ, 498, 541
Leroy, A. K., Walter, F., Sandstrom, K., et al. 2013, AJ, 146, 19
Morganti, R., Robinson, A., Fosbury, R. A. E., et al. 1991, MNRAS, 249, 91
Mould, J. R., Ridgewell, A., Gallagher III, J. S., et al. 2000, ApJ, 536, 266
Oosterloo, T. A. & Morganti, R. 2005, A&A, 429, 469
Pettini, M. & Pagel, B. E. J. 2004, MNRAS, 348, L59
Salomé, Q., Salomé, P., & Combes, F. 2015, A&A, 574, A34
Santoro, F., Oonk, J. B. R., Morganti, R., Oosterloo, T. A., & Tremblay, G. 2015, A&A, 575, L4
Schiminovich, D., van Gorkom, J. H., van der Hulst, J. M., & Kasow, S. 1994, ApJ, 423, L101
van Breugel, W., Filippenko, A. V., Heckman, T., & Miley, G. 1985, ApJ, 293, 83
van Breugel, W. J. M. & Dey, A. 1993, ApJ, 414, 563

Author Index

© Société Francaise d'Astronomie et d'Astrophysique (SF2A) 2015